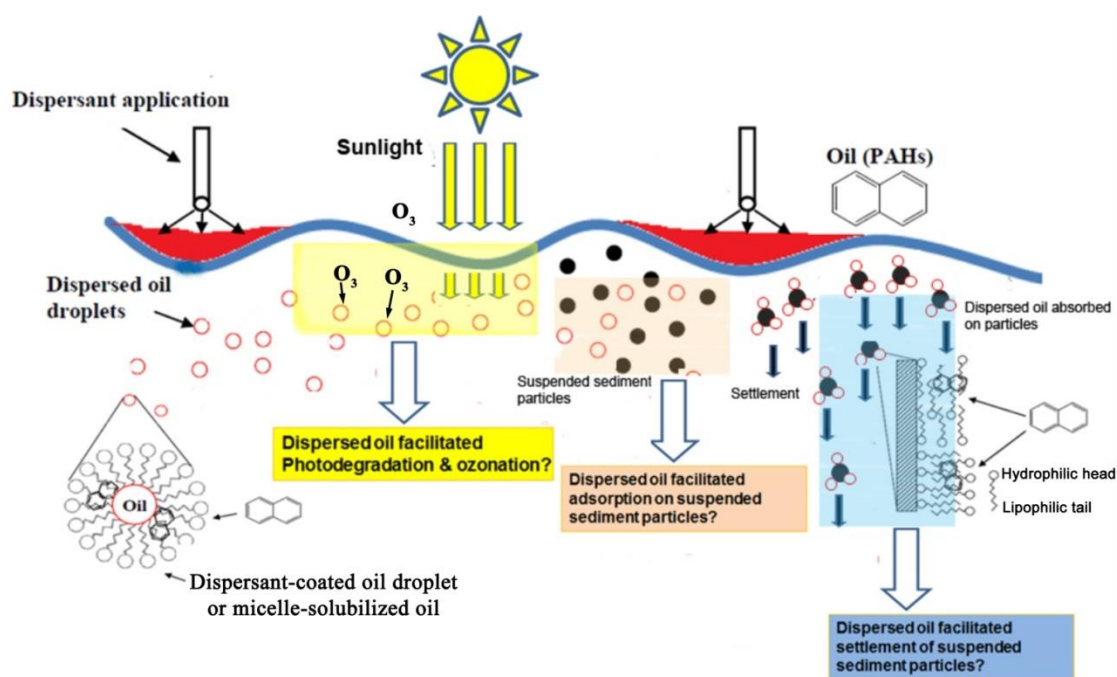


# Oil and Dispersed Oil-Sediment Interactions in the Marine Environment and Impacts of Dispersants on the Environmental Fate of Persistent Oil Components



# **Oil and Dispersed Oil-Sediment Interactions in the Marine Environment and Impacts of Dispersants on the Environmental Fate of Persistent Oil Components**

Author

Dongye (Don) Zhao

Prepared under BOEM Contract  
M12AC00013

by

Auburn University  
Department of Civil Engineering  
238 Harbert Engineering Center  
Auburn, AL 36849

Published by

**U.S. Department of the Interior  
Bureau of Ocean Energy Management  
Gulf of Mexico OCS Region**

**New Orleans, LA  
June 2017**

## **DISCLAIMER**

Study concept, oversight, and funding were provided by the US Department of the Interior, Bureau of Ocean Energy Management, Environmental Studies Program, Washington, DC, under Cooperative Agreement Number M12AC00013. This report has been technically reviewed by BOEM and it has been approved for publication. The views and conclusions contained in this document are those of the authors and should not be interpreted as representing the opinions or policies of the US Government, nor does mention of trade names or commercial products constitute endorsement or recommendation for use.

## **REPORT AVAILABILITY**

To download a PDF file of this Gulf of Mexico OCS Region report, go to the U.S. Department of the Interior, Bureau of Ocean Energy Management, Environmental Studies Program Information System website and search on OCS Study BOEM 2016-0xx.

This report can be viewed at select Federal Depository Libraries. It can also be obtained from the National Technical Information Service; the contact information is below.

U.S. Department of Commerce  
National Technical Information Service  
5301 Shawnee Rd.  
Springfield, Virginia 22312  
Phone: (703) 605-6000, 1(800) 553-6847  
Fax: (703) 605-6900  
Website: <http://www.ntis.gov/>

## **CITATION**

Zhao D., Cai Z., Liu W., Gong Y., Fu J., Ji H., Duan J., Zhao X., Xie W. 2016. Oil and dispersed oil-sediment interactions in the marine environment and impacts of dispersants on the environmental fate of persistent oil components. U.S. Dept. of the Interior, Bureau of Ocean Energy Management, Gulf of Mexico OCS Region, New Orleans, LA. OCS Study BOEM 2017-042. 280 p.

## **ACKNOWLEDGMENTS**

This work was a joint effort between the Auburn University research team and Bureau of Ocean Energy Management (BOEM), Gulf of Mexico OCS region. In particular, we are grateful to the Project Officer, Dr. S. Erin O'Reilly, for her tireless technical guidance, assistance and discussion throughout this research. We also thank our Contracting Officer Ms. Dominique Bruce Morton for her diligent help with all the contracting paper work and for keeping all administrative issues on track. Lastly, we thank our editor Ms. Elaine Leyda for her thorough editing of the final report.



# Contents

List of Figures .....	vii
List of Tables .....	xii
Abbreviations.....	xiv
<b>1. Introduction .....</b>	<b>1</b>
<b>1.1. Background .....</b>	<b>1</b>
1.1.1. Marine oil pollution.....	1
1.1.2. Interactions between oil and sediments .....	1
1.1.3. Application of oil dispersant and its effects on oil-sediment interactions .....	3
<b>1.2. Research Goal and Objectives .....</b>	<b>6</b>
<b>1.3. Summary of Findings .....</b>	<b>7</b>
<b>2. New Methods for Oil Dispersant Measurement.....</b>	<b>9</b>
<b>2.1. A Surface Tension Based Method for Measuring Oil Dispersant Concentration in Seawater .....</b>	<b>9</b>
2.1.1. Methods and materials for dispersant measurement.....	10
2.1.2. Analysis of dispersant samples .....	11
2.1.3. Effects of environmental factors on surface tension analysis .....	14
2.1.4. Accuracy of the method.....	17
2.1.5. Conclusions .....	17
<b>2.2. A New Technique for Determining Critical Micelle Concentrations of Surfactants and Oil Dispersants via UV Absorbance of Pyrene.....</b>	<b>18</b>
2.2.1. Methods for critical micelle concentration measurements .....	19
2.2.2. Methodological mechanism of the new method .....	19
2.2.3. The red shift of maximum absorption wavelength as an indicator of CMC .....	21
2.2.4. Determination of critical micelle concentration by various methods .....	22
2.2.5. Ratio of pyrene and surfactant molecules in micelles .....	26
2.2.6. Conclusions .....	27
<b>3. Effects of Dispersant on Sorption and Desorption and Transport of Oil and Oil Components</b>	<b>28</b>
<b>3.1. Effects of Oil Dispersant and Oil on Sorption and Desorption of Phenanthrene with Gulf Coast Marine Sediments .....</b>	<b>28</b>
3.1.1. Materials and methods for phenanthrene sorption and desorption .....	29
3.1.2. Sorption and desorption of Corexit EC9500A .....	33
3.1.3. Effects of dispersant on sorption and desorption kinetics of phenanthrene .....	35
3.1.4. Effects of dispersant on sorption and desorption isotherms of phenanthrene .....	39

3.1.5. Effects of WAO and DWAO on sediment sorption of phenanthrene .....	42
3.1.6. Conclusions .....	45
<b>3.2. Effects of Oil Dispersant on Solubilization, Sorption, and Desorption of Polycyclic Aromatic Hydrocarbons in Sediment-Seawater Systems .....</b>	<b>46</b>
3.2.1. Materials and methods for solubilization, sorption and desorption of polycyclic aromatic hydrocarbons .....	47
3.2.2. Dispersant-facilitated solubilization of PAHs .....	48
3.2.3. Effects of dispersant on sorption and desorption of PAHs.....	51
3.2.4. Effects of WAO and DWAO on sorption of PAHs .....	58
3.2.5. Conclusions .....	59
<b>3.3. Effects of Oil Dispersants on Desorption of Aged Oil Components from Jimmy Bay Sediment .....</b>	<b>59</b>
3.3.1. Materials and methods .....	60
3.3.2. Results and discussion .....	62
3.3.3. Conclusions .....	66
<b>3.4. Formation of Marine Snow and Its Effect on Oil Transport .....</b>	<b>67</b>
3.4.1. Materials and methods for marine snow formation and analysis.....	68
3.4.2. Formation of MS and MOS .....	69
3.4.3. Formation mechanism of MOS and effects of oil and dispersant .....	74
3.4.4. Distribution of <i>n</i> -alkanes in aqueous and MS and MOS phases .....	77
3.4.5. MS-MOS-facilitated uptake and transport of oil hydrocarbons .....	79
3.4.6. Environmental Significance and Implications .....	80
<b>3.5. Effects of Oil Dispersant on Settling Performance of Suspended Sediment Particles and Vertical Transport of Oil Contaminants.....</b>	<b>81</b>
3.5.1. Materials and methods for sediment settling tests.....	82
3.5.2. Effect of dispersants on sediment settling .....	85
3.5.3. Effects of dispersant under various environmental conditions.....	91
3.5.4. Effect of dispersant on sediment-facilitated distribution and transport of oil components ...	97
3.5.5. Conclusions .....	102
<b>4. Effects of Dispersant on Photodegradation of Oil and Oil Components .....</b>	<b>103</b>
<b>4.1 Effects of Dispersant on UV-Facilitated Photodegradation of Oil PAHs in Seawater ....</b>	<b>103</b>
4.1.1. Materials and methods for pyrene photodegradation under UV light .....	104
4.1.2. UV-spectroscopic studies of pyrene in dispersant solutions .....	106
4.1.3. Effects of dispersant on photodegradation of pyrene under UV and sunlight.....	107
4.1.4. Effects of dispersant on volatilization and photodegradation of pyrene .....	109

4.1.5. Roles of radicals, photodegradation mechanisms, and effects of dispersant .....	109
4.1.6. Effects of environmental factors on photodegradation of pyrene in dispersant solutions ...	114
4.1.7. Conclusions .....	117
<b>4.2. Effects of Oil Dispersant on Simulated Sunlight-Facilitated Photodegradation of Oil PAHs in Seawater .....</b>	<b>117</b>
4.2.1. Materials and methods .....	118
4.2.2. Effects of dispersants on PAHs photolysis .....	120
4.2.3. Effects of individual dispersant components on PAH photolysis.....	124
4.2.4. Chemical mechanisms of dispersant-enhanced PAH photolysis .....	127
4.2.5. Photodegradation pathways of anthracene and 9,10-DMA.....	131
4.2.6. Conclusions .....	132
<b>4.3. A Mechanistic Investigation into Sunlight-Facilitated Photodegradation of Pyrene in Seawater with Oil Dispersants .....</b>	<b>133</b>
4.3.1. Materials and methods for PAHs photodegradation experiments.....	134
4.3.2. Effects of oil dispersants on pyrene photodegradation .....	135
4.3.3. Mechanisms of dispersant effects .....	136
4.3.4. Effects of dispersants on pyrene photodegradation pathway .....	140
4.3.5. Photochemical stability of dispersants .....	143
4.3.6. Conclusions .....	144
<b>5. Photocatalytic Degradation of PAHs by Engineered Catalysts .....</b>	<b>145</b>
<b>5.1. Photodegradation of Oil PAHs by Co-Deposited Titanate Nanotubes .....</b>	<b>145</b>
5.1.1. Synthesis of Co-deposited TNTs and material characterization methods.....	146
5.1.2. Photocatalytic degradation methods .....	147
5.1.3. Photocatalytic activity of Co-deposited TNTs under different synthesis conditions.....	147
5.1.4. Morphology, crystal phases and compositions of Co-deposited TNTs.....	149
5.1.5. Photocatalytic degradation of phenanthrene by Co-deposited TNTs .....	152
5.1.6. Mechanisms for enhanced photocatalytic activity of Co-TNTs-600 .....	154
5.1.7. Conclusions .....	160
<b>5.2. Photodegradation of Oil PAHs by Pt-Deposited Titanate Nanotubes.....</b>	<b>161</b>
5.2.1. Synthesis of Pt-deposited TNTs.....	161
5.2.2. Experimental methods.....	162
5.2.3. Photocatalytic activity of Pt(0)-TNTs prepared under various conditions.....	162
5.2.4. Morphology, crystal phases and compositions of Pt-deposited TNTs.....	163
5.2.5. Photocatalytic degradation of phenanthrene by various Ti-based materials .....	167
5.2.6. Mechanisms for enhanced photocatalytic activity of Pt-deposited TNTs .....	168

5.2.7. Conclusions .....	171
<b>5.3. Photodegradation of Oil PAHs by SiO<sub>2</sub>/TiO<sub>2</sub> Composites.....</b>	<b>172</b>
5.3.1. Synthesis of SiO <sub>2</sub> /TiO <sub>2</sub> .....	172
5.3.2. Experimental methods: adsorption and photocatalysis .....	172
5.3.3. Characterization of TiO <sub>2</sub> /SiO <sub>2</sub> .....	173
5.3.4. Adsorption of phenanthrene by various TiO <sub>2</sub> /SiO <sub>2</sub> composite materials .....	174
5.3.5. Photocatalysis of phenanthrene by various TiO <sub>2</sub> /SiO <sub>2</sub> composite materials.....	178
5.3.6. Reusability of TiO <sub>2</sub> /SiO <sub>2</sub> -800 .....	179
5.3.7. Conclusions .....	180
<b>5.4. Removal of Oil Components by Activated Charcoal Supported Titanate Nanotubes through Adsorption and Photocatalysis .....</b>	<b>180</b>
5.4.1. Synthesis of TNTs@AC .....	181
5.4.2. Methods on adsorption and photocatalysis .....	181
5.4.3. Characterizations of TNTs@AC .....	183
5.4.4. Adsorption of phenanthrene by TNTs@AC.....	186
5.4.5. Photo-regeneration of TNTs@AC and material reuse after phenanthrene adsorption.....	192
5.4.6. Adsorption and photodegradation of oil components in DWAO by TNTs@AC.....	194
5.4.7. Photodegradation of adsorbed oil components by TNTs@AC .....	199
5.4.8. Conclusions .....	200
<b>6. Ozonation of Oil and Oil Components and Effects of Dispersant .....</b>	<b>201</b>
<b>6.1. Effects of Dispersant on Ozonation of Oil PAHs by Surface-Level Ozone .....</b>	<b>201</b>
6.1.1. Materials and methods.....	201
6.1.2. Oxidation of 1-methylnaphthalene by Surface-Level Ozone.....	202
6.1.3. Oxidation of 1-methylfluorene by Surface-Level Ozone.....	208
<b>6.2. Effects of Dispersant on Ozonation of WAOs and DWAOs by Surface-Level Ozone.....</b>	<b>213</b>
6.2.1. Effects of oil dispersant on ozone oxidation of DPHs in seawater .....	213
6.2.2. Influence of ozone concentration and water chemistry on ozonation of DPHs in DWAO .....	218
6.2.3. Ozonation mechanisms of DWAO.....	231
<b>6.3. Removal of DWAOs by combined ozonation and photodegradation.....</b>	<b>234</b>
<b>7. Summary and Observations .....</b>	<b>238</b>
<b>8. References.....</b>	<b>241</b>

## List of Figures

Figure 1. <i>DwH</i> oil spill satellite image. ....	1
Figure 2. Formation and movement of various types of OSAs in marine systems. ....	2
Figure 3. Mechanisms of chemical dispersion of oil. ....	6
Figure 4. Three regions of a typical surface tension to $\ln$ [surfactant] plot. ....	9
Figure 5. Correlation between equilibrium surface tension and $\ln$ [Corexit EC9500A] in seawater. ....	12
Figure 6. Correlation between equilibrium surface tension and $\ln$ [Corexit EC9500A]. ....	14
Figure 7. Correlation between equilibrium surface tension and $\ln$ [Corexit EC9500A]. ....	15
Figure 8. Equilibrium surface tension against $\ln$ [Corexit EC9500A] at various DOM levels (measured as TOC).....	15
Figure 9. Correlation of equilibrium surface tension with $\ln$ [Corexit EC9500A] in seawater and sediment extracts.....	16
Figure 10. Relationship between UV absorption and aqueous concentration of pyrene in Tween 80 solution. ....	20
Figure 11. UV spectrum and red shift. ....	22
Figure 12. Correlations of UV absorbance with surfactant concentration. ....	25
Figure 13. Sorption and desorption isotherms of Corexit EC9500A. ....	34
Figure 14. Sorption kinetics of phenanthrene onto (a) loamy sand and (b) sandy loam sediments. ....	35
Figure 15. Desorption kinetics of phenanthrene from (a) loamy sand and (b) sandy loam sediments. ....	38
Figure 16. Effects of Corexit EC9500A on sorption isotherms of phenanthrene. ....	39
Figure 17. Effects of Corexit EC9500A on desorption hysteresis of phenanthrene on sediments. ....	40
Figure 18. Phenanthrene uptake by (a) loamy sand and (b) sandy loam sediments. ....	41
Figure 19. Effects of aging time on phenanthrene uptake. ....	42
Figure 20. Effects of WAO and DWAO on sorption kinetics of phenanthrene. ....	43
Figure 21. GC-MS analysis of WAO and DWAO. ....	43
Figure 22. Hydrocarbon compositions of WAO and DWAO. ....	45
Figure 23. Apparent solubility of three model PAHs. ....	50
Figure 24. Sorption kinetics of PAHs onto (a) sandy loam and (b, c, d) loamy sand sediments. ....	52
Figure 25. Sorption isotherms of PAHs with (a) sandy loam, and (b, c, d) loamy sand sediments. ....	53
Figure 26. Sorption and desorption isotherms of PAHs. ....	55
Figure 27. Equilibrium distribution coefficients of PAHs. ....	56
Figure 28. Equilibrium distribution coefficients of 1-methylnaphthalene. ....	57
Figure 29. Effects of WAO and DWAO on sorption kinetics of PAHs onto a loamy sand sediment. ....	58
Figure 30. Distributions of <i>n</i> -alkanes in the sediment. ....	62
Figure 31. Distributions of PAHs in sediment. ....	63
Figure 32. Desorption kinetics of TPHs (a), <i>n</i> -alkanes (b) and parent PAHs (c). ....	64
Figure 33. Different fractions of <i>n</i> -alkanes and PAHs desorbed. ....	65
Figure 34. Successive desorption kinetics of various oil components. ....	66
Figure 35. Morphological changes of particle aggregates. ....	72

Figure 36. Changes of particle parameters.....	73
Figure 37. Changes in total bacterial number and extracellular polymeric substances.....	75
Figure 38. Mass distributions of <i>n</i> -alkanes in seawater (a) and in particle aggregates (b).....	77
Figure 39. Schematic diagram on the fate and transport of oil during formation of marine oil snow. ....	79
Figure 40. Effects of oil dispersants on the settling kinetics of marine sediments. ....	86
Figure 41. Effects of oil dispersants on particle size distribution of marine sediments.....	87
Figure 42. Settling kinetics of OS sediment particles and zeta potential of sediment. ....	88
Figure 43. Distributions of particle size (a) and settling velocity (b) of sediment particles. ....	88
Figure 44. Effects of dispersant components on settling and zeta potential of sediment particles. ....	89
Figure 45. Effects of dispersant components on particle size. ....	90
Figure 46. Influences of pH on settling kinetics and zeta potential of OS sediment. ....	92
Figure 47. Settling kinetics of OS sediment particles at various NaCl concentrations in the absence (a) or presence (b) of dispersant Corexit EC9527A. ....	93
Figure 48. Effects of humic acid on settling of OS sediment. ....	94
Figure 49. Effects of temperature on settling kinetics of sediment particles.....	95
Figure 50. Effects of WAO and DWAO on settling of OS sediment particles.....	96
Figure 51. Sorption kinetics of phenanthrene and pyrene.....	97
Figure 52. TPH distributions on seawater surface, in seawater column or sediment.....	98
Figure 53. Total PAHs distributions on seawater surface, in seawater column or sediment.....	99
Figure 54. Total alkanes distributions on seawater surface, in seawater column or sediment. ....	99
Figure 55. Mass distributions of PAHs on seawater surface (a) and in seawater column (b). ....	100
Figure 56. Mass distributions of various PAHs in sediment (a) and PAHs in crude oil (b).....	101
Figure 57. A schematic of the experimental set-up.....	104
Figure 58. UV-vis absorption spectra of pyrene. ....	106
Figure 59. First-order kinetic plots of pyrene dissipation. ....	108
Figure 60. Production of intermediate 1-hydroxypyrene.....	113
Figure 61. Effects of environmental conditions on photodegradation of pyrene with dispersant. ....	115
Figure 62. Absorption spectra of humic acid and pyrene.....	116
Figure 63. Effects of Corexit EC9500A on photodegradation of anthracene (a) and 9,10-DMA (b) in seawater.....	120
Figure 64. UV-Vis absorption spectra of anthracene (a) and 9,10-DMA (b).....	121
Figure 65. Fitting the first-order kinetic model to the experimental rate data.....	122
Figure 66. Effects of model oil dispersants on photodegradation of 9,10-DMA in seawater. ....	123
Figure 67. Effects of dispersant components on photodegradation of 9,10-DMA in seawater.....	124
Figure 68. UV-Vis absorption spectra of 9,10-DMA, Tween 85, and Corexit EC9500A in seawater.....	125
Figure 69. Vertical distribution of 9,10-DMA concentration in the photo-reactor. ....	126
Figure 70. Effects of key components of SPC 1000 on photodegradation of 9,10-DMA in seawater.....	127
Figure 71. Effects of DO on photodegradation of anthracene (a) and 9,10-DMA (b). ....	128
Figure 72. Effects of radical scavengers on photolysis of anthracene and 9,10-DMA. ....	130

Figure 73. Fluorescence spectra of anthracene (a) and 9,10-DMA (b).....	131
Figure 74. Proposed photodegradation pathways. ....	132
Figure 75. Effects of various dispersants on photodegradation of pyrene in seawater.....	135
Figure 76. Mechanistic investigation on dispersants facilitated pyrene photodegradation. ....	138
Figure 77. Mechanistic investigation on dispersants facilitated pyrene photodegradation. ....	139
Figure 78. Proposed pathway of pyrene photodegradation in seawater.....	141
Figure 79. Photodegradation products expressed as peak areas from GC-MS chromatograms. ....	143
Figure 80. Photocatalytic degradation of phenanthrene by Co-deposited TNTs. ....	148
Figure 81. TEM images of (a) TiO <sub>2</sub> (P25), (b) TNTs, (c) Co-TNTs-600, and (d) EDS spectra of Co-TNTs-600. .....	150
Figure 82. XRD patterns of various Ti-based materials.....	150
Figure 83. FTIR spectra of various Ti-based materials. ....	151
Figure 84. Photocatalytic degradation of phenanthrene by various Ti-based materials. ....	152
Figure 85. Apparent rate constants ( $k_1$ ) and removal efficiencies ( $R$ ). ....	153
Figure 86. DRS UV-vis spectra of TNTs and Co-TNTs-600. ....	154
Figure 87. PL spectra of various Ti-based materials under solar irradiation. ....	155
Figure 88. XPS spectra of TNTs and Co-TNTs-600.....	156
Figure 89. Schematic illustration of enhanced photocatalytic activity of Co-TNTs-600.....	157
Figure 90. Total ion chromatograms of phenanthrene and degradation byproducts.....	158
Figure 91. Mass spectra of phenanthrene and degradation byproducts. ....	159
Figure 92. Proposed degradation pathway of phenanthrene by Co-TNTs-600 under solar light.....	160
Figure 93. Photocatalytic degradation of phenanthrene by various Pt(0)-TNTs. ....	163
Figure 94. TEM images of (a) TiO <sub>2</sub> (P25), (b) TNTs, and (c) Pt(0)-TNTs-600; and (d) EDX spectra of Pt(0)- TNTs-600. ....	164
Figure 95. XRD patterns of various Ti-based materials.....	165
Figure 96. FTIR spectra of various Ti-based materials. ....	165
Figure 97. XPS spectra.....	166
Figure 98. Photocatalytic degradation of phenanthrene. ....	167
Figure 99. DRS UV-vis spectra of TNTs, Pt(0)-TNTs-600 and Pt(IV)-TNTs-600. ....	168
Figure 100. Contributions of UV and visible irradiation to photocatalytic degradation of phenanthrene. .....	169
Figure 101. PL spectra of various Ti-based materials under solar irradiation. ....	170
Figure 102. Schematic illustration of enhanced photocatalytic activity.....	171
Figure 103. TEM and HRTEM images. ....	173
Figure 104. XRD patterns of various TiO <sub>2</sub> /SiO <sub>2</sub> composites. ....	174
Figure 105. Adsorption kinetics of phenanthrene by various SiO <sub>2</sub> /TiO <sub>2</sub> composite materials. ....	175
Figure 106. Adsorption isotherms of phenanthrene by various SiO <sub>2</sub> /TiO <sub>2</sub> composite materials. ....	176
Figure 107. Photocatalytic degradation of phenanthrene. ....	178
Figure 108. Removal of phenanthrene by TiO <sub>2</sub> /SiO <sub>2</sub> -800 with and without pre-adsorption. ....	179
Figure 109. Reusability of TiO <sub>2</sub> /SiO <sub>2</sub> -800 for removal of phenanthrene over 5 consecutive cycles.....	180

Figure 110. SEM images of (a) AC and (b, c) TNTs@AC; EDS spectra of (d) AC and (e) TNTs@AC. ....	183
Figure 111. XRD patterns of TNTs, AC and TNTs@AC.....	184
Figure 112. XPS spectra of AC and TNTs@AC. ....	185
Figure 113. Phenanthrene adsorption kinetics and isotherms.....	187
Figure 114. Effects of environmental conditions.....	189
Figure 115. (a, b) TEM of TNTs@AC, (c, d) HRTEM of single TNTs, and (e) EDS line spectra of TNTs walls. .....	190
Figure 116. A conceptualized representation on the bottle-filling mechanism. ....	191
Figure 117. Photo-degradation of adsorbed phenanthrene by TNTs@AC.....	192
Figure 118. Schematic of a two-step adsorption-photodegradation process.....	193
Figure 119. Adsorption kinetics of TPHs, <i>n</i> -alkanes and PAHs in DWAO by TNTs@AC. ....	194
Figure 120. Distribution of <i>n</i> -alkanes in DWAO during adsorption by TNTs@AC. ....	196
Figure 121. Distribution of PAHs in DWAO during adsorption by TNTs@AC. ....	197
Figure 122. Adsorption isotherms of: (a) TPHs, (b) <i>n</i> -alkanes and (c) PAHs in DWAO by TNTs@AC. ....	198
Figure 123. Photodegradation kinetics of oil components.....	200
Figure 124. Volatilization and ozonation of 1-methylnaphthalene.....	203
Figure 125. Dispersant effects on volatilization and ozonation of 1-methylnaphthalene. ....	204
Figure 126. Effects of pH on the ozonation of 1-methylnaphthalene. ....	205
Figure 127. Ozonation kinetics of three alkylated PAHs.....	206
Figure 128. Volatilization, direct ozonation and total oxidation of 1-methylnaphthalene. ....	207
Figure 129. Volatilization and ozonation of 1-methylfluorene.....	208
Figure 130. Dispersant effects on the volatilization and ozonation of 1-methylfluorene.....	209
Figure 131. Effects of pH on the ozonation of 1-methylfluorene.....	210
Figure 132. Volatilization, direct ozonation and total oxidation of 1-methylfluorene.....	211
Figure 133. Volatilization and ozonation of 1-methylfluorene in the absence of dispersant. ....	212
Figure 134. Volatilization and ozonation of 1-methylfluorene in the presence of dispersant.....	213
Figure 135. Volatilization and ozonation of oil components in WAO and DWAO solutions. ....	214
Figure 136. Distributions of <i>n</i> -alkanes in WAO (a) and DWAO (b) before and after ozonation.....	215
Figure 137. Distributions of PAHs in WAO (a) and DWAO (b) before and after ozonation.....	216
Figure 138. Volatilization and ozonation of parent PAHs and alkylated PAHs. ....	217
Figure 139. Ozonation of oil components at various ozone concentrations.....	218
Figure 140. Ozonation of parent PAHs (a) and alkylated PAHs (b) in DWAO. ....	219
Figure 141. Effects of pH on ozonation of TPHs, <i>n</i> -alkanes and total PAHs in DWAO.....	220
Figure 142. Distributions of <i>n</i> -alkanes (a) and PAHs (b) in DWAO after 24h ozonation. ....	221
Figure 143. Effects of pH on ozonation of parent and alkylated PAHs in DWAO. ....	222
Figure 144. Effects of humic acid on ozonation of oil components.....	224
Figure 145. Distributions of <i>n</i> -alkanes (a) and PAHs (b) in DWAO after 24 h ozonation.....	226
Figure 146. Ozonation of (a) TPHs, (b) <i>n</i> -alkanes and (c) PAHs at various salinity levels. ....	227
Figure 147. Distributions of <i>n</i> -alkanes (a) and PAHs (b) in DWAO after 24 h ozonation.....	228



Figure 148. Effects of Corexit EC9500A on ozonation of PAHs in DWAO. ....	230
Figure 149. Fluorescence EEM spectra of DWAO. ....	231
Figure 150. Transient concentrations of oil components, ozone and hydroxyl radicals. ....	232
Figure 151. Distributions of oil components upon total and direct ozonation. ....	234
Figure 152. Removal of oil components by combined ozonation and photodegradation. ....	236

## List of Tables

Table 1. Chemical constituents of dispersants Corexit EC9500A and Corexit EC9527A <sup>a</sup> .....	4
Table 2. Salient physical and chemical properties of marine sediments used in this work .....	10
Table 3. Comparison of Corexit EC9500A concentrations in seawater measured by TOC analysis and by the surface tension based method .....	17
Table 4. CMCs of surfactants or dispersants obtained from different methods in this work and reported data from open publications.....	24
Table 5. Salient physical and chemical properties of marine sediments used in this work .....	30
Table 6. Equilibrium sorption parameters for phenanthrene onto loamy sand and sandy loam sediments in the absence or presence of various concentrations of the dispersant. ....	36
Table 7. The best-fitted values of phenanthrene diffusivities and the corresponding mean weighted square error (MWSE) in the absence or presence of the dispersant. ....	37
Table 8. Equilibrium sorption parameters for phenanthrene onto loamy sand and sandy loam sediments in the absence or presence of various concentrations of the dispersant. ....	39
Table 9. Parameters for the solubilization of three PAHs.....	50
Table 10. Equilibrium sorption parameters for PAHs onto sediments in the absence and presence of dispersant Corexit EC9500A.....	54
Table 11. TPHs concentration in the sediment via sequential extraction .....	62
Table 12. Observations of marine snow formation during roller table experiments .....	71
Table 13. Physicochemical characteristics of sediment samples.....	83
Table 14. First-order photodegradation rate constants for pyrene in the absence or presence of Corexit EC9500A under UV and sunlight irradiations .....	108
Table 15. First-order rate constants for pyrene volatilization and/or UV-mediated photodegradation with or without Corexit EC9500A. ....	109
Table 16. Contributions of radicals ( $\cdot\text{OH}$ , $^1\text{O}_2$ and $\text{O}_2^{\cdot-}$ ) to pyrene photodegradation with or without Corexit EC9500A .....	111
Table 17. First-order rate constants for pyrene photodegradation in 18 mg/L dispersant solutions as a function of IS, humic acid, pH, and temperature.....	114
Table 18. The first-order photodegradation rate constants ( $k$ ) of anthracene and 9,10-DMA under solar irradiation. ....	122
Table 19. Best-fitted first-order photodegradation rate constants ( $k_1$ ) of anthracene in the presence of individual dispersant components under solar irradiation .....	124
Table 20. First-order rate constants ( $k_1$ ) in the initial stage of anthracene and 9,10-DMA photodegradation with or without DO.....	128
Table 21. Contributions of different reactive species to photodegradation of pyrene under simulated solar irradiation.....	142
Table 22. Salient physical parameters of TiO <sub>2</sub> , TNTs, and Co-TNTs-600 .....	151
Table 23. Elemental weight percentages in Pt(0)-TNTs-600 and Pt(IV)-TNTs-600 .....	166
Table 24. Parameters of kinetic models for phenanthrene adsorption onto various SiO <sub>2</sub> /TiO <sub>2</sub> materials .....	175

Table 25. Parameters of isotherm models for phenanthrene adsorption onto various SiO <sub>2</sub> /TiO <sub>2</sub> materials .....	177
Table 26. Atomic percent of different compositions of C 1s and O 1s .....	186
Table 27. Kinetic model parameters for adsorption of phenanthrene by TNTs@AC.....	187
Table 28. Isotherm model parameters for adsorption of phenanthrene by AC, TNTs, and TNTs@AC....	188
Table 29. Kinetic parameters for adsorption of TPHs, <i>n</i> -alkanes and PAHs in DWAO by TNTs@AC.....	194
Table 30. Isotherm parameters for adsorption of TPHs, <i>n</i> -alkanes and PAHs in DWAO by TNTs@AC....	199
Table 31. Parameters of first-order kinetic model for photocatalytic degradation of TPHs, <i>n</i> -alkanes and PAHs by TNTs@AC .....	200
Table 32. First-order rate constants for 1-methylnaphthalene volatilization and ozonation .....	203
Table 33. First-order rate constants for 1-methylnaphthalene volatilization and ozonation in the presence of dispersant at 18 mg/L .....	205
Table 34. First-order rate constants for 1-methylnaphthalene volatilization and ozonation in the presence of 200 ppb ozone.....	207
Table 35. First-order rate constants for 1-methylnaphthalene volatilization and ozonation in the presence of dispersant at 18 mg/L .....	209
Table 36. First-order rate constants for 1-methylfluorene ozonation (200 ppb ozone) .....	211
Table 37. First-order ozone oxidation rate constants for TPHs, <i>n</i> -alkanes and TPAHs in WAO and DWAO. ....	217
Table 38. First-order ozone oxidation rate constants for TPHs, <i>n</i> -alkanes and TPAHs in DWAO when exposed to various concentrations of atmospheric ozone.....	219
Table 39. First-order rate constants for various PAHs at an ozone concentration of 200 ppbv .....	220
Table 40. First-order ozone oxidation rate constants for TPHs in DWAO in the presence of various concentrations of humic acid.....	225
Table 41. First-order ozone oxidation rate constants for TPHs, <i>n</i> -alkanes and TPAHs in DWAO.....	232
Table 42. First-order reaction rate constants for TPHs, <i>n</i> -alkanes and TPAHs in DWAO for different reaction mechanisms .....	237

## Abbreviations

AC	Activated charcoal
AH	Aromatic hydrocarbons
BET	Brunauer-Emmett-Teller
BH	Branched aliphatic hydrocarbons
BJH	Barret-Joyner-Halender
CEC	Cation exchange capacity
CH	Cyclic aliphatic hydrocarbons
CMC	Critical micelle concentration
CNMs	Carbon nanomaterials
CNTs	Carbon nanotubes
CPI	Carbon preference index
DCM	Dichloromethane
DEA	Diethanolamine
DI	Deionized
DLVO	Derjaguin–Landau–Verwey–Overbeek
DMA	Dimethyl anthracene
DO	Dissolved oxygen
DOC	Dissolved organic carbon
DOM	Dissolved organic matter
DOR	Dispersant oil ratio
DOSS	Dioctyl sodium sulfosuccinate
DPHs	Dissolved petroleum hydrocarbons
DTPHs	Dissolved total petroleum hydrocarbons
DWAO	Dispersed water accommodated oil
<i>DwH</i>	<i>Deepwater Horizon</i>
EDS	Energy dispersive spectra
EPA	Environmental Protection Agency
EPS	Extracellular polymeric substances
EIWR	Elmer’s Island Wildlife Refuge
FTIR	Fourier transform infrared
GB	Grand Bay
GC-FID	Gas chromatography-flame ionization detector
GC-MS	Gas chromatography-mass spectrometry

HA	Humic acid
HLB	Hydrophilic-lipophilic Balance
HPLC	High Performance Liquid Chromatography
HMWHs	High molecular weight hydrocarbons
HPLC-MS	High performance liquid chromatography-mass spectrometry
HRTEM	High resolution transmission electron microscopy
ICP-OES	Inductively coupled plasma-optical emission spectroscopy
IR	Infrared
IS	Ionic strength
LC-MS-MS	Liquid chromatography with tandem-mass spectrometry
LH	Linear aliphatic hydrocarbons
LMW	Low molecular weight
LMWHs	Low molecular weight hydrocarbons
LSC	Louisiana sweet crude oil
MMWHs	Medium molecular weight hydrocarbons
MOS	Marine oil snow
MS	Marine snow
MWSE	Mean withed square error
NOMs	Natural organic matters
NTU	Nephelometric turbidity unit
OS	Ocean Springs National Seashore Park
OSAs	Oil-SPM aggregates
OSC	On-scene coordinator
PAHs	Polycyclic aromatic hydrocarbons
PL	Photoluminescence
PTFE	Polytetrafluoroethylene
Py	Pyrene
ROS	Reactive oxygen species
RRT	Regional response team
SBE	Sigmoidal-Boltzmann equation
SDS	Sodium dodecyl sulfate
SDSS	Surfactant sodium dioctyl sulfosuccinate
SOM	Soil organic matter
SPM	Suspended particulate material

SW	Seawater
TAB	Trimethylammonium bromide
TBOT	Tetrabutyl titanate
TBN	Total bacterial number
TEM	Transmission electron microscopy
TOF	Time of flight
TPAHs	Total polycyclic aromatic hydrocarbons
TPHs	Total petroleum hydrocarbons
TNTs	Titanate nanotubes
TOC	Total organic carbon
UV	Ultraviolet
UV-DRS	UV-visible diffuse reflectance spectra
VOCs	Volatile organic compounds
WAO	Water accommodated oil
XPS	X-ray photoelectron spectroscopy
XRD	X-ray diffractometer

# 1. Introduction

## 1.1. Background

### 1.1.1. Marine oil pollution

Oil can be released into the marine environment from routine or accidental releases as a result of human activities, including drilling for oil, manufacturing processes, storing oil, transporting oil, and waste management (NRC 2003). For example, an offshore oil well blowout or pipe line rupture can release large amounts of oil into the marine environment. The 2010 *Deepwater Horizon (DwH)* oil spill released an estimated 4.9 million barrels of South Louisiana Sweet Crude oil (LSC) into the Gulf of Mexico, resulting in the largest marine oil spill in the U.S. history and perhaps the second largest in world history (**Figure 1**) (Pallardy 2016) after the first Gulf War oil spill in Kuwait (Abbriano et al. 2011, Graham et al. 2010, Hemmer et al. 2011). Oil tankers carrying millions of gallons of oil can also pose a significant threat to the marine environment in the event of ship collisions or grounding (Bandara et al. 2011, Lytle and Peckarsky 2001). In addition to anthropogenic releases, natural seepage also releases significant amounts of oil into the marine environment.



Figure 1. *DwH* oil spill satellite image.

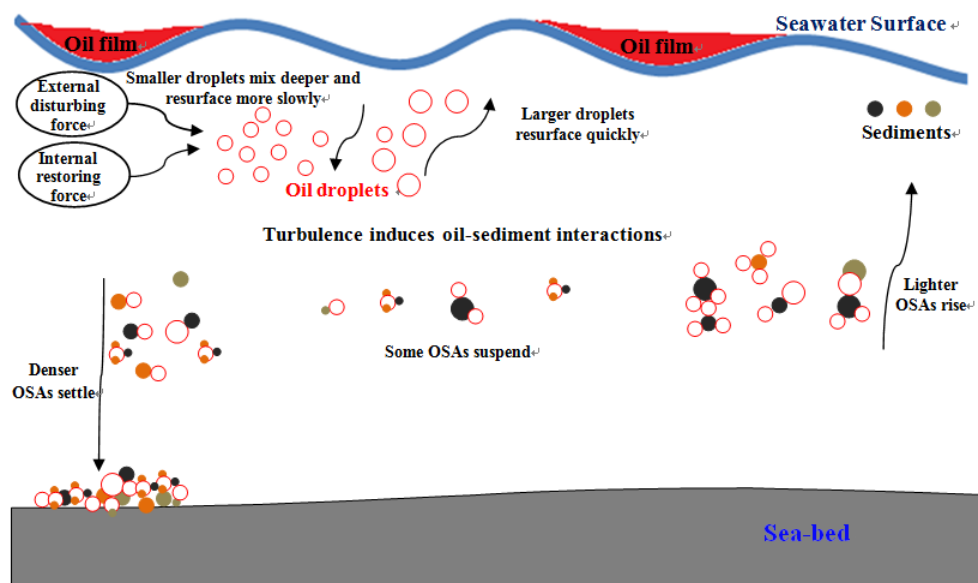
### 1.1.2. Interactions between oil and sediments

Once oil is released into the marine environment, it undergoes complex physical, chemical, and biological transformations, including spreading, drifting, dispersion, stranding, and weathering. The important weathering processes include evaporation, dissolution, biodegradation, emulsification (i.e., “mouse” formation), and photo-oxidation (NRC 2003). Though fine droplets may be dispersed into the water column, monocyclic compounds (e.g., benzene and alkyl-substituted benzenes) with  $\log K_{ow}$  values between 2.1 and 3.7 and some lower molecular weight, 2-3 ring polycyclic aromatic hydrocarbons

(PAHs) with log  $K_{ow}$  values between 3.7 and 4.8 may undergo partial dissolution (NRC 2005b, Payne et al. 2003). These environmental processes can be strongly affected by interactions between dissolved and dispersed oil components and sediment particles.

Sediments have long been recognized as an important vector in the transport of oil from one environmental compartment (i.e., phase) to another following an oil spill event in the aquatic environment. Studies have shown that interactions between oil and sediments have an important role in dispersion and degradation of spilled oil (Muschenheim and Lee 2002). In near shore waters, naturally dispersed oil droplets may aggregate with suspended particulate material (SPM), such as clay minerals or organic matter to form oil-SPM aggregates (OSAs). Terminologies, such as oil-clay flocculation, oil-SPM interactions, oil-mineral aggregation, and oil-fines interactions, have been used to describe this natural process (Khelifa et al. 2002, 2005, Muschenheim and Lee 2002, Omotoso et al. 2002, Owens 1999, Owens and Lee 2003, Payne et al. 2003). Interactions between oil and SPM have been documented in several laboratory and field studies.

Typically, OSAs are formed in two consecutive steps (**Figure 2**). First, oil film is broken into oil droplets, which can be realized via two types of forces, external disturbing forces produced by the flow field, such as inertia or viscous force, and internal restoring forces of oil, such as the interfacial tension to sustain the oil droplet shape (Hinze 1955). The main affecting parameters for this step are the mixing energy, oil viscosity, and interfacial tension between oil and seawater. Second, oil droplets interact with SPM to form OSAs. This step is actually the interaction between SPM and polar compounds within oil droplets (Delvigne and Sweeney 1988).



**Figure 2. Formation and movement of various types of OSAs in marine systems.**

Due to their toxic, mutagenic, carcinogenic and persistent properties, PAHs are one of the principal contaminants of environmental concern associated with oil spills (Nam et al. 2008). The commonly found PAHs in the water phase are those with relatively lower numbers of benzene rings (e.g., naphthalene, phenanthrene, fluorene and pyrene) because of their relatively higher solubility. Elevated concentrations of naphthalene, phenanthrene, pyrene, chrysene, and benzo(a)pyrene were observed in the water column during and after the 2010 *DwH* oil spill (EPA 2010, Reddy et al. 2012a). All these PAHs are included in the list of EPA's 16 priority pollutant PAHs (Bojes and Pope 2007). Introduction of an oil phase into



sediment-water systems has significant influence on the PAHs distribution. Conventional knowledge and models on the fate and distribution of PAHs in the sediment-water systems are often challenged in systems affected by oil spills.

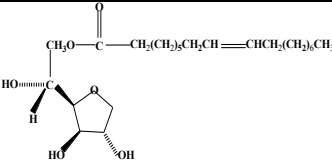
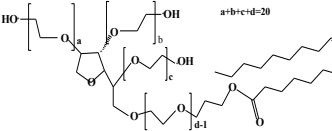
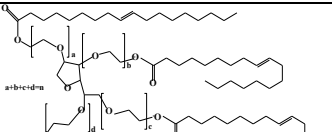
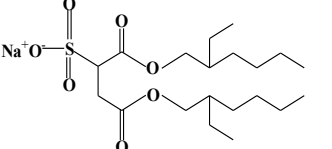

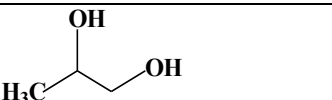
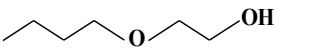
### 1.1.3. Application of oil dispersant and its effects on oil-sediment interactions

The application of oil dispersants has been a critical response measure to mitigate impacts of marine oil spill for decades (Franklin and Warner 2011). On June 3, 1979, the Ixtoc I well in the Bay of Campeche, Mexico, suffered a major blowout, which resulted in the release of half a million metric tons (140 million gallons) of oil into the Gulf of Mexico (OSIR 1980). The U.S. EPA estimated that 1–2.5 million gallons of dispersants (mainly Corexit EC9527A) were sprayed during almost 500 aerial flights over the surface oil slick. In 2000, around 2000 barrels of SLC oil were released into the Gulf of Mexico from a 24-inch pipeline 65 miles south of Houma, Louisiana. In response to the oil spill, 3000 gallons of Corexit EC9527A were employed to disperse the oil (Stoermer 2001). During the *DwH* oil spill, BP applied approximately 2.1 million gallons of oil dispersants (Corexit EC9500A and Corexit EC9527A), of which 1.4 million gallons of the dispersants were applied at the surface and 0.77 million gallons at the wellhead (Kujawinski et al. 2011).

Generally, oil dispersants are complex mixtures of surfactants, solvents, and other additives. Solvents are added primarily to promote the dissolution of surfactants, reduce the dispersant's viscosity and enhance its solubility in spilled oil. Additives may improve the dissolution of the surfactants into an oil slick and increase the long-term stability of the dispersant (NRC 2005c). Commercial chemical dispersants usually consist of two or more surfactants. These surfactants in fixed ratios can emulsify oil, and the hydrocarbon-based solvents can help break up large clumps of high molecular weight, more viscous oil (Kujawinski et al. 2011, Ramachandran et al. 2004). Mechanistically, oil dispersants can break oil slicks into fine droplets by lowering the oil-water interfacial tension, thereby enhancing dispersion and dissolution of hydrophobic oil components into the water column (NRC 2005c). Typically, oil dispersants contain a mixture of nonionic surfactants, such as sorbitan monooleate (Span 80) and ethoxylated sorbitan monooleate (Tween 80), and anionic surfactants, such as sodium dioctyl sulfosuccinate (DOSS) (Thibodeaux et al. 2011). For example, Corexit EC9527A consists of two nonionic surfactants (48%) including ethoxylated sorbitan mono- and trioleates (Tween 80 and Tween 85) and an anionic surfactant (35%) (DOSS) in an aqueous hydrocarbon solvent of ethylene glycol monobutyl ether (17%) (Scelfo and Tjeerdema 1991). Corexit EC9500A contains the same surfactants as Corexit EC9527A, but it does not contain 2-butoxy ethanol, which is an ingredient in Corexit EC9527A (Nalco 2010). **Table 1** presents the key chemical ingredients in these dispersants.

About 0.3 million gallons of Corexit EC9527A were applied in the early stage of the *DwH* oil spill, but that formulation was later replaced with Corexit EC9500A (1.8 million gallons) due to the fear of the higher toxicity of the former (Benner Jr 2010, Kujawinski et al. 2011). However, both dispersants are EPA-approved and by far the most prevalent of all dispersants held in industry stockpiles in the U.S. (OSB 2005).

**Table 1. Chemical constituents of dispersants Corexit EC9500A and Corexit EC9527A<sup>a</sup>**

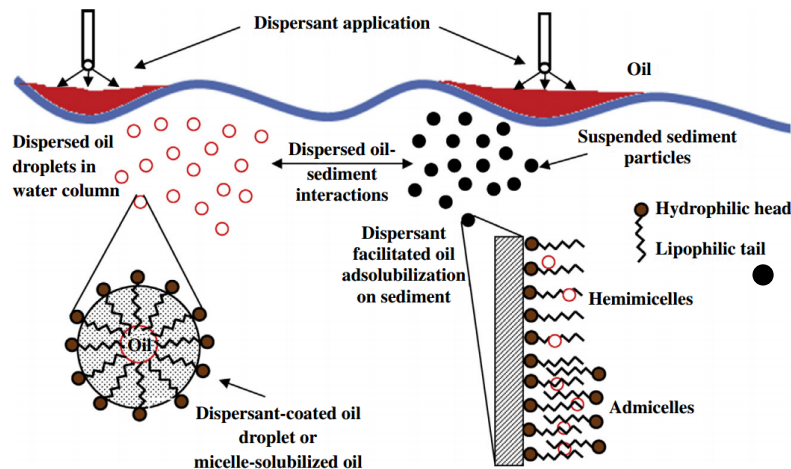
Name	CAS number	Ionic property	Synonym	Molecular formula	MW (g/mol)	HLB	Chemical structure
<b>Span 80</b>	1338-43-8	Neutral surfactant	Sorbitan, mono-(9Z)-9-octadecenoate	C <sub>24</sub> H <sub>44</sub> O <sub>6</sub>	428.61	4.3	
<b>Tween 80</b>	9005-65-6	Neutral surfactant	Sorbitan, mono-(9Z)-9-octadecenoate, poly(oxy-1,2-ethanediyl) derivs.	C <sub>64</sub> H <sub>124</sub> O <sub>26</sub>	1310	15	
<b>Tween 85</b>	9005-70-3	Neutral surfactant	Sorbitan, tri-(9Z)-9-octadecenoate, poly(oxy-1,2-ethanediyl) derivs	C <sub>60</sub> H <sub>108</sub> O <sub>8</sub> <sup>-</sup> (C <sub>2</sub> H <sub>4</sub> O) <sub>n</sub>	1838.57	11	
<b>DOSS</b>	577-11-7	Anionic surfactant	Butanedioic acid, 2-sulfo-, 1,4-bis(2-ethylhexyl) ester, sodium salt (1:1)	C <sub>20</sub> H <sub>37</sub> SO <sub>7</sub> Na	444.57	10.9	
<b>DPnB</b>	29911-28-2	Solvent	Propanol, 1-(2-butoxy-1-methylethoxy)	C <sub>10</sub> H <sub>22</sub> O <sub>3</sub>	190		
<b>PG</b>	57-55-6	Solvent	Propylene Glycol, 1,2,-propanediol, 1,2-dihydroxypropane	CH <sub>3</sub> CHOHCH <sub>2</sub> OH	76.1		
<b>Distillates</b>	64742-47-8	Solvent	Distillates (petroleum), hydrotreated light	N/A	N/A	N/A	
<b>2-butoxy-ethanol,<sup>b</sup></b>	111-76-2	Solvent	2-Butoxyethanol	C <sub>6</sub> H <sub>14</sub> O <sub>2</sub>	118.17		

<sup>a</sup>After Gong et al. (2014a), Kover et al. (2014), and Zhao et al. (2016b); <sup>b</sup>This chemical component is not included in Corexit EC9500A.

Typically, dispersants are sprayed on surface oil slicks to break up oil into small droplets which increases its surface area by lowering the oil-water interfacial tension. When used in the right amount and circumstances, the application of chemical dispersants may promote biodegradation of oil in the water column and eliminate or significantly reduce the impacts of oil on sensitive shorelines and habitats (Lessard and Demarco 2000). The current U.S. environmental regulations require special permissions from the Regional Response Team (RRT) and On-scene Coordinator (OSC) for uses of oil dispersants in shallow waters or on beaches. Limited “pre-approved” zones are usually granted for using dispersant countermeasures in waters beyond ~5 kilometers off the shoreline and at water depths greater than 10 meters (NRC 2005). More stringent rigorous scientific investigations are needed to decide the suitability of the potential uses of dispersants in nearshore and shallow waters (NRC 2005).

**Figure 3** depicts the mechanisms of chemical dispersion of surface oil in aquatic systems containing suspended sediment particles. Dispersant and surfactant-facilitated dissolution or solubilization of oil is achieved through formation of surfactant-coated oil droplets or partitioning of oil into the surfactant micelles. The resulting dispersed oil droplets may agglomerate with SPM (Guyomarch et al., 1999; Guyomarch et al., 2002; Khelifa et al., 2008; Li et al., 2007; Mackay and Hossain, 1982). From the standpoint of dispersant-oil-sediment interactions (**Figure 3**), the concentration of SPM in undisturbed offshore water is usually low compared to that in nearshore water, which partially accounts for the regulators’ caution of nearshore uses. Nonetheless, at least a fraction of the oil dispersants applied offshore and dispersed oil may reach sediment through a number of transport pathways. First, dispersants and dispersed oil can be advectively transported to nearshore sediments by both surface water wave actions, underwater current and dispersed oil plumes. Second, dispersants and dispersed oil can be transported to the bottom sediment by oil-plume settling, and formation and the subsequent settling of marine snow or marine oil snow. Third, re-suspended sediments and drilling mud at the drilling site may harvest considerable amounts of dispersants and dispersed oil. Though more robust field data are yet to be collected, a number of field observations following the *DwH* oil spill support these proposed mechanisms, including the observed large amounts of oil on the beaches and in the nearshore water, accumulation of oil at the bottom sediments, and migration of massive oil plumes. Also, it is noteworthy that as part of the efforts to shut off oil flow into the Gulf during the *DwH* oil spill, heavy drilling mud was pumped into the crippled blowout preventer on top of the well (Klemas, 2010). As a result, a portion of the oil on the bottom near the wellhead is associated with this use of the drilling mud.

The observed oil plumes and oil accumulation on the seafloor following the *DwH* oil spill may be ascribed to, at least in part, sediment facilitated transport, dispersion and sedimentation of the oil. Understanding the dispersant-oil-sediment interactions may facilitate more accurate estimate of transport, budget, mass balance and distribution of dispersed oil in various environmental compartment, which in many cases may account for the “lost oil” that has been largely omitted in the official oil budget estimate.



**Figure 3. Mechanisms of chemical dispersion of oil.**

Left: accumulation of dispersant molecules at oil-water interface facilitates formation of fine oil droplets that become entrained in the water column. Right: accumulation of dispersants at sediment-water interface facilitates sorption (adsolubilization) of oil on the solid phase. Alternatively, dispersed oil droplets may also form agglomerates with SPM, which can be stable colloids or re-suspended (temporarily stable) sediment particles.

## 1.2. Research Goal and Objectives

The overall goal of this proposed research is to fill in some of the critical knowledge gaps in how oil, dispersants, and sediments interact, how such interactions impact weathering of oil components, and how deepwater conditions alter the interactions. This study systematically examined how dispersants affect the fundamental physicochemical processes that govern the interactions between key oil components (e.g., C10–C30 aliphatic compounds and common PAHs) and sediment particles, and chemical reactions affecting the fate of oil components. The study also aims to investigate the roles of natural catalytic photochemical degradation and ozonation of persistent oil components in systems simulating the Gulf Coast ecosystems (estuaries and marshes), and to develop cost-effective technologies for enhancing the natural weathering processes. The specific objectives are to:

- 1) Determine the role and mechanism of the oil dispersants in sorption and desorption of persistent oil components with representative coastal and deep-sea sediments;
- 2) Test how oil-dispersant-sediment interactions change the settling behavior of SPM, oil and oil components associated thereon, and the effects of oil and oil dispersants on the formation of marine oil snow;
- 3) Determine the desorption rate and extent of persistent oil components from representative field contaminated sediments and effect of dispersant on the desorption process;
- 4) Evaluate the effects of dispersants on the natural photodegradation of the persistent oil components in various phases (seawater-dissolved, sediment-sorbed, and dispersed microdroplets);
- 5) Develop a new technology for enhancing the natural photodegradation of spilled oil by developing a new class of low-cost and ‘green’ photocatalysts;
- 6) Determine the role of surface-level ozone oxidation in weathering of oil and PAHs in seawater and sediment, and examine how dispersants and sediment sorption affect the reactions; and

7) Investigate the synergistic effects of photochemical degradation and ground-level ozone oxidation in the presence of catalysts.

The research findings will fill critical knowledge gaps on the environmental distribution and natural attenuation of dispersed oil due to adsorption-desorption, photochemical and surface-level ozone oxidation, and can potentially lead to the development of cost-effective technologies that can rapidly and completely degrade persistent oil components by enhancing the natural weathering processes. Specifically, this study offers the following benefits: **a)** understanding the dispersant-oil-sediment interactions will facilitate more accurate estimate of transport, budget, mass balance and distribution of dispersed oil in various environmental compartments, which in many cases may account for the large fractions of the oil that has not been accounted for in current oil budget estimate; **b)** it will facilitate sounder assessment of weathering and environmental fate of dispersed oil; **c)** understanding effects of dispersants on key transport processes and weathering reactions will aid in more reliable assessment of environmental impacts of the *DWH* oil spill and future spill incidents that involve extensive uses of dispersants; and **d)** a solid understanding of the rate and extent of catalytic photodegradation and ozonation of oil and PAHs will greatly facilitate sounder and more accurate assessment of the long-term risks of oil spills on the Gulf Coast ecosystems, whereas the improved engineered technology will arm the remediation engineers with a powerful tool to mitigate the environmental impacts and greatly shorten the restoration timeframe.

### 1.3. Summary of Findings

The key findings are summarized as follows:

1) A new method was developed for measuring dispersant concentration in seawater based on surface tension measurement;

2) A new method for determining critical micelle concentration (CMC) of surfactants and oil dispersants via UV absorbance of pyrene was established;

3) The dispersant can linearly enhance the solubilities of PAHs, the deepwater conditions diminished the dispersant effect on solubilization of PAHs;

4) Increasing the concentration of dispersants increases sediment uptake of PAHs;

5) Oil dispersants increase the desorption of oil contaminants from aged oil-contaminated sediments;

6) Oil dispersants, dispersed oil droplets and dissolved oil greatly facilitate the formation of marine snow and marine oil snow;

7) Oil dispersants accelerate the settling performance of suspended sediment particles;

8) The presence of oil dispersants reduces the volatilization of PAHs, but enhances photodegradation of oil components;

9) A new class of highly effective cobalt or platinum-deposited photocatalysts was synthesized, which can facilitate rapid photochemical degradation of oil PAHs under solar light;

10) A new class of TiO<sub>2</sub>/SiO<sub>2</sub> composite materials with both high adsorption capacity and photocatalytic activity were synthesized, which can effectively remove and degrade dispersed oil and PAHs in seawater;

**11)** A new class of photo-regenerable activated charcoal supported titanate nanotubes (TNTs@AC) was synthesized, which can initially concentrate oil components through adsorption and destroy the compounds through subsequent photocatalysis;

**12)** Surface-level ozone can degrade total petroleum hydrocarbons (TPHs), *n*-alkanes and PAHs in water accommodated oil (WAO) and dispersed water accommodated oil (DWAO), and oil dispersants increase the ozonation rate;

**13)** Combining ozonation and photocatalytic degradation with TiO<sub>2</sub>/SiO<sub>2</sub> greatly enhances for weathering of persistent oil components in DWAO.

## 2. New Methods for Oil Dispersant Measurement

### 2.1. A Surface Tension Based Method for Measuring Oil Dispersant Concentration in Seawater

Oil dispersants have been widely used to mitigate environmental impacts of spilled oil (Cai et al. 2016, Fu et al. 2014, Gong et al. 2014a, Zhao et al. 2015). Yet it has been challenging to quantitatively analyze oil dispersants conveniently and economically. This is not only due to the complex nature of the mixture of a variety of dispersants and solvents, but also the proprietary and incomplete information on the type and quantity of the dispersant components. For instance, the most common practice for analyzing Corexit EC9500A in water has been to analyze one or some of the key dispersant components that can be quantified following the standard methods, e.g., GC-MS (Gas Chromatography-Mass Spectrometry), LC-MS-MS (Liquid Chromatography with Tandem Mass Spectrometry), HPLC-MS (High Performance Liquid Chromatography-Mass Spectrometry) (Kujawinski et al. 2011). However, these methods bear the following drawbacks: 1) they are quite costly and time- and labor-consuming, especially for the LC-MS-MS method, 2) the results for individual components may not reflect the integrity of the dispersant as a whole, and 3) the undisclosed components in a dispersant are often neglected.

It has been observed that surface tension ( $\gamma$ ) is correlated with the concentration of a surfactant ((Fu et al. 2015, Menger et al. 2009, Myers 1999). Specifically, Menger et al. (2009) observed that when  $\gamma$  is plotted against  $\ln[\text{surfactant}]$ , the curve can be divided into three distinct regions (**Figure 4**): Region A:  $\gamma$  slightly decreases with increasing surfactant concentration; Region B:  $\gamma$  decreases sharply and almost linearly with increasing surfactant concentration; and Region C: the slope abruptly levels off (i.e.,  $\gamma$  remains nearly constant) at the surfactant concentration above the critical micelle concentration, defined as the concentration of a surfactant at which micelles start to form (Myers 1988). Conventionally, it is assumed that the surfactant is saturated at the air-water interface throughout Region A (Perez et al. 1998, Vader 1960), which allows the calculation of the area-per-molecule via the classic Gibbs equation (Menger et al. 2009). In an effort to determine the CMC value of oil dispersants, Gong et al. (2014b) observed that the natural logarithm of Corexit EC9500A concentration is linearly correlated to  $\gamma$  of the solution. The concentration of the dispersant may be measured by indirectly measuring the combined effect of the dispersant components, i.e., by gauging the surface tension of a dispersant solution.

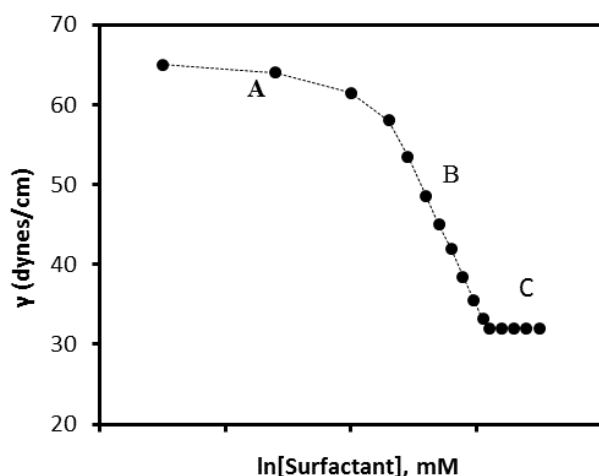


Figure 4. Three regions of a typical surface tension to  $\ln[\text{surfactant}]$  plot.

Based on the linear correlation between  $\gamma$  and dispersant concentration, we developed and validated a

new analytical method for simple and rapid quantification of oil dispersants in seawater. To illustrate the concept, Corexit EC9500A was used as the model dispersant and Gulf coast seawater as the prototype solution matrix. The specific objectives were to: 1) establish the linear correlation between  $\gamma$  and  $\ln$  [dispersant concentration], 2) assess the effects of environmental factors, such as salinity, pH, and dissolved organic matter (DOM) on the correlation, and 3) identify the applicable conditions as well as constraints of the method. The new method is expected to provide a convenient and economical analytical tool for researchers and practitioners in the field of oil spill and marine pollution.

## 2.1.1. Methods and materials for dispersant measurement

### 2.1.1.1. Materials

Seawater samples were collected at Grand Bay, Alabama in the Gulf of Mexico (N30.37873, W88.30679) on November 2012. They were stored in sealed containers at 4 °C and filtered through 0.22  $\mu\text{m}$  membrane of cellulose esters to remove suspended solids before use. Marine sediment was collected from the Ocean Springs National Seashore Park, Mississippi (N30.39772, W88.79175). The sediment corresponds to the loamy sand based on the USDA Soil Taxonomy used for soil classification and the organic matter content was 1.6 wt.% (sediment analysis was performed by the Soil Testing Laboratory at Auburn University, and the physicochemical characteristics of sediment are shown in **Table 2**).

**Table 2. Salient physical and chemical properties of marine sediments used in this work**

pH <sup>a</sup>	SOM <sup>b</sup> %	Cation Exchange Capacity Meq/100g				Taxonomy <sup>c</sup>	Sand <sup>d</sup> %	Silt <sup>d</sup> %	Clay <sup>d</sup> %
6.4	1.6	6.6				Loamy sand	81.6	15.3	3.1
Ca ppm	K ppm	Mg ppm	P ppm	Al ppm	B ppm	Zn ppm	Mn ppm	Na Ppm	Fe ppm
441.9	182.7	314.5	9.1	87.7	3.23	5.2	3.9	4118.4	73.1

<sup>a</sup> Sediment pH was measured on a 1:1 sediment:water mixture via the Reference Soil Test Methods (UGA 1983)

<sup>b</sup> SOM (soil organic matter) was obtained based on the empirical relationship:  $\text{SOM} = 1.72 \times \text{TOC}$  (Davies 1974)

<sup>c</sup> Sediment texture was conducted following the hydrometer method (Bouyoucos 1962)

<sup>d</sup> Categorized based on U.S. Department of Agriculture-definition

Note: Metal contents were measured per EPA method 3050B. Soil calcium, magnesium, potassium and sodium were first extracted per the Mehlich 1 procedure, filtered through a #1 Whatman qualitative filter paper, and then determined by a Varian Vista-MPX Radial Spectrometer.

All chemicals used in this study were of analytical or higher grade, and were used as received, including humic acid (Fluka Chemie AG), sodium hydroxide (NaOH, Fisher Scientific), and hydrochloric acid (HCl, 36.5–38.0%, Mallinckrodt Chemical). Corexit EC9500A was acquired by the courtesy of Nalco Company. A Corexit EC9500A stock solution was prepared at 1 g/L by mixing Corexit EC9500A and the filtered seawater in a glass flask under magnetic stirring for one hour, and then the desired working solutions (up to 200 mg/L) were obtained by diluting the stock solution with seawater. Serial dilution was avoided to reduce cumulative error (Scelfo and Tjeerdema 1991).

### 2.1.1.2. Effects of environmental factors

Effects of environmental factors on the viability of the surface-tension based method were assessed at various solution salinities, pH levels, and DOM concentrations. The pH of the seawater was adjusted using HCl (0.5 M) or NaOH (0.5 M) solution from the initial 7.9 to the final value of 6.0, 7.0 or 9.0. Different DOM concentrations were achieved by diluting a DOM stock solution (550 mg/L as TOC), which was obtained by dissolving the standard humic acid into seawater. This Fluka reference humic acid has been commonly used as a model DOM in aquatic systems. The humic acid consist of the three main



fractions with molecular weights of 14 kDa (65%), 3 kDa (28%) and 0.2 kDa (7%) (Tomaszewska and Mozia 2002). Salinity effects were tested using artificially prepared seawater at various salinity levels (0, 1%, 2%, and 4% (expressed as wt.% of salt) following the method by Kester et al. (1967). The effects of the environmental factors on the surface tension measurement as well as on the  $\gamma-\ln[C]$  ( $C$  is the dispersant concentration) correlations were evaluated by measuring the  $\gamma-\ln[C]$  curves under various pH, salinity and DOM levels.

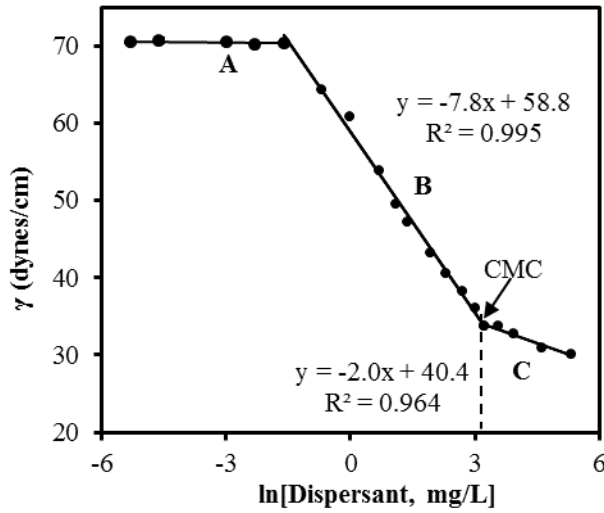
In marine oil spill studies, mixed sediment-seawater systems are often encountered (Zhao et al. 2015). To determine the effects of possible sediment exudates, surface tension was also measured using sediment amended seawater. The sediment amended seawater was prepared as follows: first, mix seawater with the sediment at a sediment/seawater ratio of 16 g / 40 mL on a rotator at 50 rpm for 48 hours; then separate the solid and liquid by centrifugation ( $\times 1359$  g for 5 minutes) and collect the supernatant. The sediment amended seawater (i.e., the supernatant) had a salinity of 3.5 wt.%, pH 7.0, a DOM concentration of 1.3 mg/L as TOC.

### **2.1.1.3. Analytical methods**

A Du Noüy Tensiometer (CSC scientific 70535 series, Fairfax, Virginia) was used to determine the surface tension of the dispersant solutions. The Du Noüy ring method (Tuckermann 2007) has been commonly used to measure the surface tension of solutions. The details on the measuring principle and procedure can be found elsewhere (Lunkenheimer and Wantke 1981, Noüy 1925). Briefly, a platinum ring, which is linked with a balance arm, is slowly lifted from the surface of a liquid, then the force required to break the surface (overcome the surface tension) is measured. To this end, each 20 mL of a dispersant solution was added in 60 $\times$ 15 mm glass petri dishes. The samples were kept still in the dishes for 30 min to assure the system equilibrium was achieved, i.e., the chemical potential at the interface is equal to that of the bulk solution (Eastoe and Dalton 2000). The tensiometer was calibrated on a daily basis, and all measurements were performed in duplicate and at 25 $\pm$ 1 °C. A Dohrmann Phoenix 8000 TOC Analyzer (Tekmar Dohrmann, Cincinnati, OH, USA) was used to analyze DOM and Corexit EC9500A as total organic carbon (TOC).

### **2.1.2. Analysis of dispersant samples**

**Figure 5** shows the change of surface tension as a function of  $\ln[\text{dispersant}]$ . The general trend was similar to the correlation of surface tension vs dispersant concentration as in **Figure 4**. When the dispersant concentration is lower than 0.2 mg/L (or  $\ln C < -1.6$ ) (Region A), the dispersant had little effect on surface tension; however, in Region B where the dispersant is  $> 0.2$  mg/L but  $< \text{CMC}$  (23.5 mg/L), the surface tension decreased sharply and linearly with increasing dispersant concentration with a slope ( $k$ ) of -7.8; the linear correlation remains in region C (dispersant  $> \text{CMC}$ ) but with a much lower slope ( $k = -2.0$ ).



**Figure 5. Correlation between equilibrium surface tension and ln[Corexit EC9500A] in seawater.** Experimental conditions: Temperature = 25±1 °C; pH = 7.9; salinity = 3.15 %; DOM = 0.2 mg/L.

The resulting correlation equations are as follows:

$$\gamma = -7.8 \cdot \ln(C) + 58.8, R^2 = 0.995, p < 0.001 \quad (0.2 \text{ mg/L} < C < 23.5 \text{ mg/L}) \quad (1)$$

$$\gamma = -2.0 \cdot \ln(C) + 40.4, R^2 = 0.964, p = 0.003 \quad (C > 23.5 \text{ mg/L}) \quad (2)$$

where  $C$  is the dispersant concentration (mg/L),  $R^2$  is the coefficient of determination, and  $p$  is the significance level of the fitted slope.

According to the Gibbs equation (Adamson 2001, Li et al. 2013a), the change in the surface tension with surfactant activity is described by

$$-d\gamma = RT \sum_i \Gamma_i d(\ln a_i) \quad (3)$$

where  $\Gamma_i$  is the surface excess of component  $i$ ,  $a_i$  is the activity of the component in the aqueous phase,  $R$  is the universal gas constant, and  $T$  is temperature (K).

When the concentration is below the CMC value, the activity can be approximated with the concentration for nonionic surfactants (Li et al. 2013a). Thus, the Gibbs equation can be written as

$$\frac{d\gamma}{d(\ln C_i)} = -RT \sum_i \Gamma_i \quad (4)$$

where  $C_i$  is the surfactant concentration,  $d\gamma/d(\ln C_i)$  is the slope of the  $\gamma$ - $\ln C_i$  curves.

In accord with the Gibb's equation, **Figure 5** indicates that there exist three distinct levels of surface excess of the dispersant with three different slopes that correspond to the three regions. The observation agrees with the reported correlations in various surfactant systems (Lopez-Cervantes et al. 2013, Reichert and Walker 2013, Simister et al. 1992).

The observed  $\gamma\text{-ln}[C]$  curve mimics an S-shaped adsorption isotherm (Gong et al., 2014). In the low concentration range (Region A), the dispersant components prefer to partition into the solution phase more than the interface, which can be attributed to the enhanced dissolution effect of the mixed surfactants and co-solvents. As a result, a very flat slope was evident. In Region B, aggregates of the surfactants are formed (Gong et al. 2014) and the partition becomes increasingly more favorable toward the interface, resulting in the sharp change of  $d\gamma\text{-ln}[C]$ . At dispersant concentrations near or above the CMC (Region C), micelles (mainly the neutral surfactants) are formed, and the surfactants prefer to partition into the micelles than accumulate on the interface (Li et al. 2013a, Menger et al. 2009). Consequently, the slope of the  $d\gamma\text{-ln}[C]$  line is abruptly leveled. It is also noteworthy that the CMC value (578 mg/L) for the anionic surfactant (DOSS) (Yehia 1992) is much higher than those for the non-ionic surfactants (e.g., 23 mg/L for Tween 85 and 14 mg/L for Tween 80). Namely, no micelles of the anionic surfactants are likely formed under the experimental conditions. Therefore, the much reduced slope in Region C than in Region B is attributed to the formation of micelles of the non-ionic surfactants.

The findings indicate that despite being a complex mixture of surfactants and solvents, Corexit EC9500A behaves like a lumped or combined “surfactant”. Though the lumped CMC value reflects the collective effect of the surfactants and co-solvents, the mixture CMC for the dispersant was nearly the same as that (23 mg/L) of Tween 85, slightly higher than that (14 mg/L) of Tween 80, but much lower than that (578 mg/L) of DOSS (Gong et al. 2014), suggesting that Tween 85 plays a predominant role in the mixed micelles (Ahn et al. 2010), which can be attributed to its much larger size, special molecular structure (i.e., polyethoxylated sorbitan esters), and possibly high fraction in the dispersant.

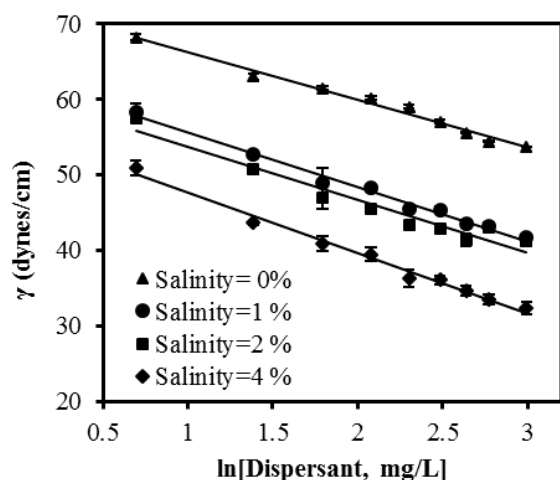
The correlation curve (Equation 1) can be used to conveniently determine the concentration of Corexit EC9500A in the concentration range from  $> 0.5$  to  $< 23$  mg/L by simply measuring the surface tension using a simple and low-cost interfacial Tensiometer. The detection limit may be lowered if the correlation line in Region A is determined accurately, which may require a more sophisticated Tensiometer. When the dispersant concentration is above the CMC, Equation 2 can be used, or, alternatively, the solution can be diluted to the concentration window that is suitable for Equation 1.

The  $\gamma\text{-ln}[C]$  correlation in Region B was highly reproducible; experimental results showed that the relative standard deviation was within 3% from 5 replicate measurements. Based on 10 replicate measurements of blank and Corexit EC9500A samples (Harris 2010), the detection limit with Equation 2 was determined at 0.5 mg/L.

## 2.1.3. Effects of environmental factors on surface tension analysis

### 2.1.3.1. Salinity

Figure 6 shows that the solution salinity can significantly decrease surface tension of the dispersant solution. The effect is more significant when the salinity was increased from 0 to 1%. This phenomenon can be interpreted by the increased surfactant adsorption onto the air/water interface with the increase of electrolyte concentration (Xu et al. 2013), known as the “salting out” effect (Prosser and Franses 2001). Similar findings were also reported by Persson et al. (2003), who studied the correlation between surface tension concentration of surfactant DOSS at various NaCl concentrations. Therefore, proper standard curves will need to be developed to assure the consistent salinity between samples and the standards. It is noteworthy that despite the different levels of surface tension at different salinities, the correlation lines appear parallel to each other, i.e., they have nearly the same slope. Therefore, the same standard curve may be scaled for measuring  $\gamma$  at various salinities by correcting the difference in the intercept.



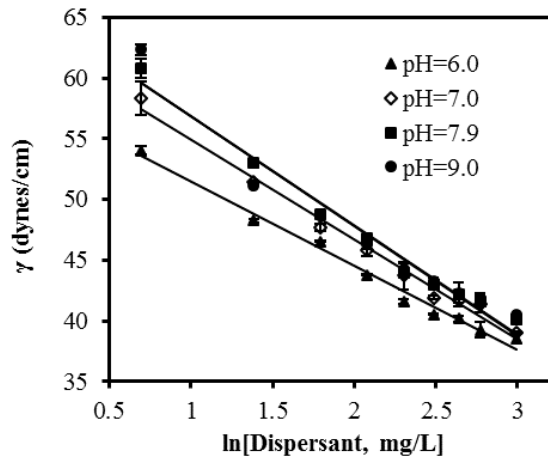
**Figure 6. Correlation between equilibrium surface tension and ln[Corexit EC9500A].**

Experimental conditions: Corexit EC9500A concentration = 2 to 20 mg/L in seawater; salinities = 0, 1%, 2%, and 4%; temperature =  $25 \pm 1$  °C. Data are plotted as mean of duplicates, and error bars indicate standard error range.

### 2.1.3.2. pH

Figure 7 shows that the  $\gamma$  -ln[C] correlation remained statistically unchanged ( $p > 0.05$ ) when the solution pH was raised from 7.9 to 9.0; however, the surface tension dropped significantly as the pH was lowered from 7.9 to 6.0.

The anionic surfactant, i.e., DOSS, of Corexit EC9500A undergoes increasing protonation as pH decreases (Underberg and Lingeman 1983). Though fully deprotonated DOSS is rather hydrophilic (Yates and von Wandruszka 1999), the protonation at lower pH renders the hydrophilic heads of DOSS less polar. As a result, more surfactant molecules migrate to the surface, resulting in decreased surface tension at lower pH. Figure 7 also indicates that the pH effect is more profound at lower dispersant concentrations.

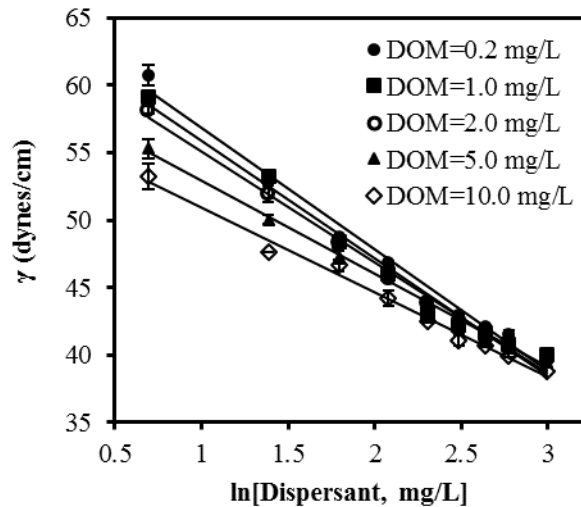


**Figure 7. Correlation between equilibrium surface tension and ln[Corexit EC9500A].**

Corexit EC9500A concentration = 2 to 20 mg/L in seawater, temperature is  $25 \pm 1$  °C, salinity = 3.15 %, DOM = 0.2 mg/L, pH = 6.0, 7.0, 7.9 and 9.0.

### 2.1.3.3. DOM

**Figure 8** shows that the presence of DOM at 5 mg/L as TOC significantly decreased the surface tension, and the effect was more evident at lower dispersant concentrations ( $< 2$  mg/L).



**Figure 8. Equilibrium surface tension against ln[Corexit EC9500A] at various DOM levels (measured as TOC).**

Corexit EC9500A concentration = 2 to 20 mg/L in seawater, temperature =  $25 \pm 1$  °C, pH =  $7.9 \pm 0.5$ , salinity = 3.15 %.

Due to the amphiphilic characteristics of some components in DOM, such as humic acid, DOM can affect both the surfactant activity and the surface excess (or accumulation) (Yates and von Wandruszka 1999). The Szyskowski equation (Aumann et al. 2010, von Szyskowski 1908) is often used to describe the effects of organic compounds, such as carboxylic acids, alcohols and esters, on the surface tension of aqueous solutions.

$$\gamma = \gamma_0 - \Gamma_{max} RT \ln \left( 1 + \frac{c}{\beta} \right) \quad (5)$$

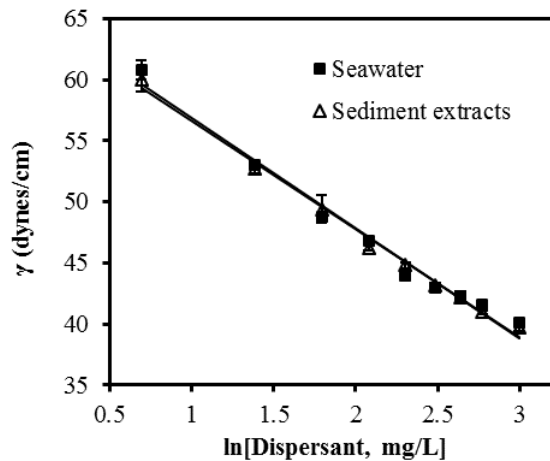
where  $\gamma$  and  $\gamma_0$  are surface tension for solution and pure water, respectively,  $\Gamma_{max}$  is the maximum surface excess,  $c$  is the solute (DOM) concentration, and  $\beta$  is the inverse Langmuir adsorption coefficient.

This equation predicts that increasing DOM decreases surface tension of a solution. Lee and Hildemann (2013) measured surface tension of humic acid solutions at 20 °C, and obtained the  $\Gamma_{max}$  and  $\beta$  values by fitting the experimental surface tension data over a range of solute concentrations, where  $\Gamma_{max} = 2.93 \pm 0.35 \times 10^{-6} \text{ mol/m}^2$ ,  $\beta = 966 \pm 267 \times 10^{-3} \text{ g/kg}$ . At low DOM concentrations, DOM affects the surface tension mainly by altering the surface excess of surfactants; at elevated DOM concentrations, DOM may reduce both surface excess and the activity of surfactants, resulting in a lower  $\gamma$ .

#### 2.1.3.4. Soluble components from marine sediment

In sediment-water systems, it has been challenging to measure dispersant concentration due to interference from the soluble components from the sediment. **Figure 9** shows effects of sediment extracts on the surface tension. Compared with the seawater, the salinity of sediment amended seawater increased from 3.15 to 3.50 ‰, DOM increased from 0.2 mg/L to 1.3 mg/L, but pH decreased from 7.9 to about 7.0. It is evident from **Figure 9** that the effect of the sediment extracts on the surface tension measurement was statistically insignificant ( $p > 0.05$ ) despite the variations of the water-chemistry conditions.

The surface tension measurements will not be affected when the changes in salinity, DOM and pH are within the following limits: salinity change  $< 0.3 \text{ ‰}$ , DOM  $< 1.3 \text{ mg/L}$  as TOC, and  $7.0 \leq \text{pH} \leq 9.0$ . Separate  $\gamma$ - $\ln[C]$  correlation equations will need to be established or corrected when changes in the water quality parameters exceed these criteria.



**Figure 9. Correlation of equilibrium surface tension with  $\ln[\text{Corexit EC9500A}]$  in seawater and sediment extracts.**

Corexit EC9500A concentration = 2 to 20 mg/L, temperature =  $25 \pm 1 \text{ °C}$ , pH =  $7.9 \pm 0.5$ , salinity = 3.15 ‰.

#### 2.1.4. Accuracy of the method

To confirm the accuracy of this surface tension-based method, the same Corexit EC9500A solutions at the dispersant concentrations of 1, 5, 10, 15, and 20 mg/L were analyzed by this method and also by direct TOC analysis. **Table 3** gives the resulting dispersant concentration obtained independently with the two methods. The results show that the differences in the mean concentrations obtained by the two methods are statistically insignificant ( $p < 0.05$ ) except for the case of 1 mg/L, and in all cases, the measurement errors were within 3.5% from the true values. Between the two methods, the relative standard deviation of the surface tension based method ranged from 2% to 5%, compared to from 4% to 53% for the TOC-based method, indicating that the new the method is of higher precision. At 1 mg/L, the TOC method became unstable, while the surface tension method remained robust. The fluctuation for the TOC method can be attributed to: 1) accumulation of the dispersant components at the water-air interface, which affects the consistency in sampling of the water for TOC analysis but not for the surface tension measurement, 2) adsorption of the surfactants on the sampling devices and TOC analyzer, and 3) incomplete catalytic conversion of the organic carbon by the UV-persulfate based TOC analyzer. Indeed, we observed long and gradual tails of the TOC evolution curve, suggesting that some of the components in Corexit EC9500A are more resistant to the UV-persulfate oxidation.

**Table 3. Comparison of Corexit EC9500A concentrations in seawater measured by TOC analysis and by the surface tension based method**

Corexit EC9500A concentration (mg/L)	1	5	10	15	20
Measured by surface tension (mg/L)	0.98±0.05	5.16±0.14	9.65±0.15	15.40±0.24	20.06±0.39
Relative standard deviation (%)	5	3	2	2	2
Measured by TOC (mg/L)	0.81±0.43	5.42±0.55	9.14±0.92	15.09±0.55	20.51±2.12
Relative standard deviation (%)	53	10	10	4	10

#### 2.1.5. Conclusions

This work proposed and tested a new method to determine the Corexit EC9500A concentration in seawater by measuring the surface tension of dispersant solutions and by using the linear correlation between surface tension and  $\ln$ [dispersant concentration]. Compared to conventional methods, which often target a fraction of the dispersant components, this method is not only simple, fast, economical and viable, but also measures the collective effect of the dispersant as a whole. The most-suitable dispersant concentration range is 0.5 to 23.5 mg/L. However, a dispersant of lower or higher concentrations than the optimum window may be accommodated by use of separate standard  $\gamma - \ln[C]$  lines and/or through proper concentration or dilution of the samples. Small changes in solution salinity (< 0.3%), pH (7.0–9.0), and DOM (< 1.5 mg/L as TOC) had negligible effects on the surface tension measurements, and thus, the correlation equations. Though the method is most sensitive to salinity changes, the correlation lines appear parallel to each other at various salinity levels, and thus, the correlation equation at one salinity level can be scaled to others by correcting the Y-axis intercept. In case of radical changes in water chemistry and environmental conditions, separate correlation curves can be readily constructed in accord with the target sample conditions. Because effects of extracts from typical marine sediments were negligible, the method may be directly applied to seawater-sediment systems. The method accuracy was

confirmed by comparing with the TOC analysis. Though the method was demonstrated using Corexit EC9500A as the prototype oil dispersant, the method may be extended to other oil dispersants and surfactants. This new analytical method provides a convenient and useful alternative means for researchers and practitioners for quantitative analysis of complex oil dispersants and surfactants in aquatic systems.

## **2.2. A New Technique for Determining Critical Micelle Concentrations of Surfactants and Oil Dispersants via UV Absorbance of Pyrene**

Various methods have been used to determine CMC, such as tensiometry, conductometry, calorimetry, and viscometry (Chatterjee et al. 2001, Cirin et al. 2012, Ghosh and Moulik 1998, Moulik and Ghosh 1997). In general, these methods are based on direct measurements of the solution properties, and the advantages or limitations of these methods have been well documented. Some indirect methods have also been developed by measuring the fluorescence of selected probe molecules (Majhi et al. 1999), where pyrene has been widely used as the fluorescent probe molecule (Kalyanasundaram and Thomas 1977).

Over the last few years, researchers have attempted to use the UV absorption of probe molecules to conveniently determine CMCs. Ray and co-workers first used UV absorption of pyrene to determine the CMCs of both ionic and non-ionic surfactants, and they found the absorbance against surfactant concentration for all the major UV spectral peaks of pyrene to be sigmoidal in nature, and accordingly the Sigmoidal-Boltzmann equation (SBE) can be employed to evaluate CMCs of various surfactants (Ray et al. 2006). Recently, researchers from the same institute employed curcumin, a widespread natural medicinal product, to determine CMCs of surfactants using its UV absorption (Mondal and Ghosh 2012). In addition, Tanhaei et al. (Tanhaei et al. 2013) also used the UV spectroscopic method with pyrene as the probe to determine the CMC of single and mixed surfactants systems.

The most important components in oil dispersants are surfactant molecules for their amphipathic characteristics and ability to lower the surface tension (Fu et al. 2014, Gong et al. 2014b). Oil dispersants contain both ionic and nonionic surfactants. Because nonionic surfactants generally exhibit much lower CMCs than ionic surfactants (Zoller 2008), the observed CMCs for oil dispersants are often governed by the nonionic surfactants. Theoretically, the combined CMC of an oil dispersant can be determined by the same methods as surfactants do. However, the heterogeneity and solvent effects, especially at high concentrations of oil dispersants, can breach the applicability of the conventional methods.

Compared to other methods, the approach by measuring the UV absorption of probe molecules has been shown to be reliable and convenient. Yet the underlying mechanism for this method remains in the black-box stage. In addition, we found the baseline fluctuation of the UV spectra and the associated uncertainty in the pyrene probe analysis can impede the accuracy of the method especially at elevated concentrations of surfactants. To overcome this problem and in search of a more reliable way to interpret the spectra toward more accurate CMC determination, we revised the pyrene UV-absorption method by using the absorption peak differences rather than the absorbance of the major UV spectral peaks, and we proposed a two-step strategy for determination of CMCs. In addition, this work explored the underlying mechanism for the method. Last, we demonstrated the robustness of the method by measuring CMCs for six model surfactants and two oil dispersants.



## **2.2.1. Methods for critical micelle concentration measurements**

### **2.2.1.1. Materials**

Pyrene solids (purity >98%) and methanol (HPLC grade) were purchased from Alfa Aesar (Ward Hill, Massachusetts). Acetonitrile (HPLC grade) was purchased from EMD Millipore Corporation (Billerica, Massachusetts). Two model Corexit dispersants EC9500A and EC9527A were acquired through the courtesy of Nalco Company (Naperville, Illinois). Polyoxyethylene sorbitan monooleate (Tween 80), polyoxyethylene sorbitan trioleate (Tween 85), DOSS, decyltrimethylammonium bromide (C<sub>10</sub>TAB) were purchased from Fisher Scientific (Fair Lawn, New Jersey). SDS and hexadecyltrimethylammonium bromide (C<sub>16</sub>TAB) were obtained from Sigma-Aldrich (St. Louis, Missouri). Deionized water was used for preparation of all samples and mobile phases.

### **2.2.1.2. Measurements**

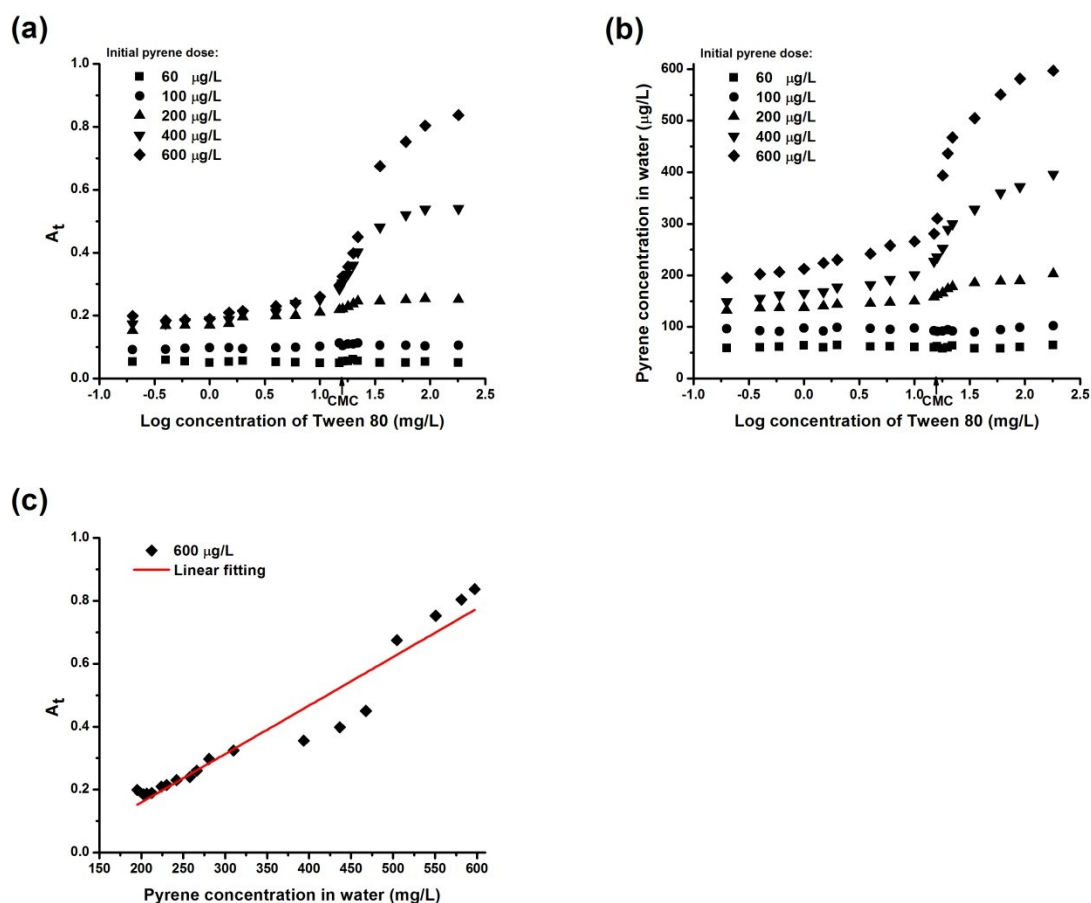
A stock solution of pyrene (0.3 g/L) was prepared in a methanol solution. Triplicate surfactant or dispersant solutions of varying concentrations from below to above the respective CMC values were prepared with deionized water and shaken for 1 h to completely dissolve or disperse the surfactants or dispersants. Known amounts of the pyrene stock solution were added into duplicate surfactant or dispersant solutions (a control was prepared in parallel without pyrene). In all cases, the methanol content was < 0.2 % (v/v), which will not affect the UV-spectra and aggregation behaviors of amphiphiles (confirmed through control tests). The mixtures were then shaken for 2 h to maximally dissolve pyrene in the surfactant or dispersant systems. After centrifuging for 10 min at 3 000 rpm to remove the insoluble solids, the pyrene-saturated supernatants were collected for subsequent analysis. The centrifugation had no effect on the concentration of the surfactants.

UV absorbance was measured by a HP 8453 UV-Vis spectrophotometer using a 1×1 cm quartz cell (Hewlett Packard, California). The spectra were recorded in the 200–400 nm wavelength range. The UV spectra of pyrene in surfactant and dispersant solutions were corrected by subtracting the background absorbance of the controls. To compare the results, the CMC values were also determined by the tensiometry method using a Du Noüy Tensiometer. The aqueous pyrene concentration was determined by a HP 1100 HPLC (Hewlett Packard, California) equipped with a UV detector (240 nm) and a Zorbax SB-C18 column (150 × 468 mm), using the mobile phase of 70% acetonitrile, 30% water, and 0.1% phosphoric acid. All data were measured at the room temperature (22±1 °C). All measurements were made in duplicate and the mean values were reported.

## **2.2.2. Methodological mechanism of the new method**

Though previous researchers have successfully used the UV absorption of probe molecules to determine the CMC (Mondal and Ghosh 2012, Ray et al. 2006, Tanhaei et al. 2013), the mechanistic aspects for this method have not been addressed. A close inspection of the related literature reveals that the reported concentration of the probe compounds in the UV absorption measurements is much higher than their solubility. Ray et al. (2006) and Tanhaei et al. (2013) used 2 μM (404 μg/L) of pyrene, which is about 3 times of the pyrene solubility (135 μg/L); Mondal and Ghosh (2012) employed 9.1 μM (3,352 μg/L) of curcumin, which also far exceeds its water solubility of 11 μg/L at pH 5.0 (Tonnesen et al. 2002). In the presence of the supersaturated probe chemicals, the UV absorbance increases sharply with increasing concentration of surfactants. For instance, the total absorbance of curcumin increased from 0.17 to 0.65 (almost 4 times) when the concentration of SDS increased from 0.25 to 15 mM (Mondal and Ghosh 2012). Numerous studies have shown that surfactants can enhance the aqueous solubility of pyrene (Edwards et al. 1991, Zhu and Feng 2003, Zhu and Chiou 2001). The remarkable rise in UV absorbance of the probe molecules is likely associated with the surfactant-enhanced solubility of the probe chemical.

To test this postulate, we repeated the Rays' experiments by adding various doses of pyrene from below to above its solubility in the presence of a prototype surfactant Tween 80. At the pyrene doses of 60 and 100  $\mu\text{g/L}$ , which are below the solubility (135  $\mu\text{g/L}$ ), the sum of the UV absorbance of all the major peaks ( $A_t$ ) exhibited no changes when the Tween 80 concentration was varied from below to above the CMC ( $\sim 16 \text{ mg/L}$ ) (**Figure 10a**). This observation indicates that the surfactant itself would not significantly affect the intensity of UV absorption of pyrene. However, when the pyrene dose was above its solubility (200, 400 and 600  $\mu\text{g/L}$ ), the  $A_t$  value sharply increased when Tween 80 concentration is above the CMC (**Figure 10a**), and the higher the pyrene dose, the greater the  $A_t$  changes. **Figure 10b** provides direct evidence that the dissolved pyrene in the surfactant solution also displays similar patterns. Taken together, **Figure 10c** exemplifies a strong correlation between the UV absorbance and the aqueous pyrene concentration with increasing Tween 80 concentration (correlation coefficient,  $r^2 = 0.936$ ; initial pyrene dose, 600  $\mu\text{g/L}$ ). The surfactant-enhanced solubility of the probe chemical is a prerequisite or key mechanism in enhanced UV absorbance in the determination of CMCs of surfactants.



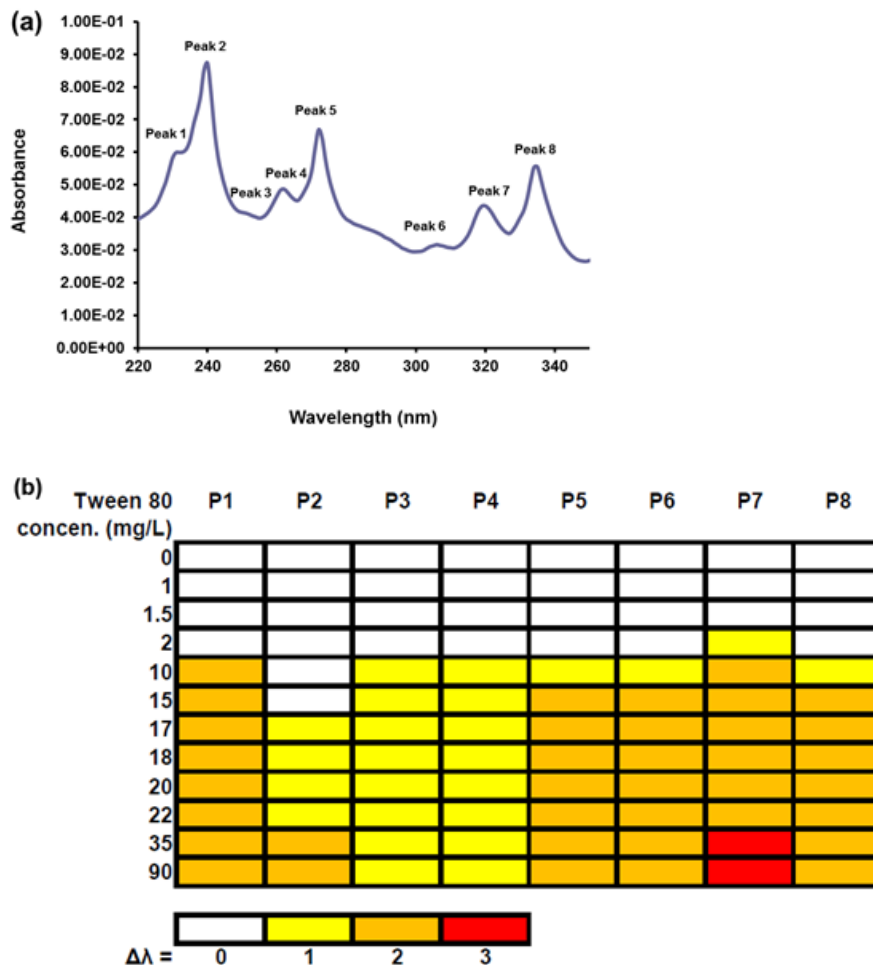
**Figure 10. Relationship between UV absorption and aqueous concentration of pyrene in Tween 80 solution.**

(a) plot of  $A_t$  (sum of UV absorbance of all the major peaks) against log Tween 80 concentration, (b) plot of pyrene concentration in water against log Tween 80 concentration, and (c) correlating  $A_t$  and pyrene concentration in water. The initial pyrene doses were 60, 100, 200, 400 and 600  $\mu\text{g/L}$ .

### 2.2.3. The red shift of maximum absorption wavelength as an indicator of CMC

When surfactant micelles are formed, pyrene molecules are likely to be incorporated into the palisade layer of the micelles, which will enhance the aqueous solubility of pyrene (Masrat et al. 2013). It is well known that the characteristics of UV absorption spectra of aromatic nuclei are related to the polarity of the medium. As pyrene is incorporated into the micelles, which are less polar than the aqueous phase, the UV absorption spectra of pyrene are expected to shift (An and Carraway 2002, An 2001). In our work, clear red shifts of the UV spectra were observed (**Figure 11**). Recent investigations revealed that the interactions between  $\pi$  electron clouds of aromatic molecules and the hydrophilic head groups of surfactants can lead to the red shift of UV spectra (Zheng and Zhao 2006). Besides the medium properties, the UV spectra are also related to the  $\pi$  electron distortions of the aromatic nuclei. Because the  $\pi$  electrons of pyrene interact with surfactant monomers differently than with the surfactant micelles, the red shift of UV spectra may serve as a viable indicator for the formation of micelles.

**Figure 11a** shows that there are a total of eight peaks (P1–P8), at 231(w), 240 (s), 252 (w), 260 (w), 272 (s), 306 (w), 319 (s) and 335 (s) nm in the UV absorption spectra of pyrene in water (s = strong, w = weak). Increasing the surfactant concentration from below to above CMC progressively increased the red shifts for all peaks. Taking Tween 80 solution as an example, at concentration of 10 mg/L, P1 and P3–P8 all showed red shift (**Figure 11b**), which is below the reported CMC (~16 mg/L). The pre-micellation red shifts can be attributed to the formation of the surfactant aggregates at the concentration below the CMC (Hadjiivanova and Diamant 2009). The interactions between these pre-micelles and pyrene result in the red shifts. A closer examination of the UV spectra reveals that the red shift for the strongest UV absorbance peak (P2) occurred only at the surfactant concentration  $\geq 17$  mg/L. This strong peak is ascribed to pyrene molecules that are located at the palisade layer of the micelles, and accordingly, the red shift of this peak is attributed to the close interactions between the surfactant head groups and the  $\pi$  electron clouds of pyrene (Zheng and Zhao 2006). Defining the corresponding wavelength as  $\lambda_{\max}$ , then the red shift of  $\lambda_{\max}$  indicates the formation of micelles. The extent of the red shift of  $\lambda_{\max}$  reflects the strength of the interactions between surfactant heads and  $\pi$  electrons of pyrene (Zheng and Zhao 2006). For instance, under otherwise identical conditions, we observed the largest red shift of  $\lambda_{\max}$  was 3 nm with a Tween 85 solution, while the red shift was only 1 nm in anionic surfactant solutions (DOSS and SDS). Thus, the nonionic Tween 85 micelles exert much stronger interactions with the pyrene  $\pi$  electrons than the ionic surfactant micelles.



**Figure 11. UV spectrum and red shift.**

(a) UV absorption spectrum of pyrene in water. (b) Red shift of UV absorption peaks of pyrene in Tween 80 solution (P stands for Peak). Measurements were carried out at room temperature ( $22 \pm 1$  °C). The initial pyrene doses were  $600 \mu\text{g/L}$ .  $\Delta\lambda$  = peak wavelength differences compared with the peak wavelengths in water without Tween 80.

#### 2.2.4. Determination of critical micelle concentration by various methods

Based on the  $\lambda_{\text{max}}$  red shift, we conveniently located the range of the CMCs for eight common surfactants/dispersants: Tween 80 (CMC=15–17 mg/L), Tween 85 (10–14 mg/L), DOSS (1–1.2 g/L), SDS (2–2.5 g/L),  $\text{C}_{10}\text{TAB}$  (15–20 g/L),  $\text{C}_{16}\text{TAB}$  (325–350 mg/L), Corexit EC9500A (15–20 mg/L) and Corexit EC9527A (20–30 mg/L). The results agree with those measured by other more sophisticated approaches (Table 4). This method provides a quick and adequate estimate of the CMC range, which, if desired, can facilitate more accurate measurement in a targeted manner.

Conventionally, the CMC is determined based on the UV absorption peak (Mondal and Ghosh 2012, Ray et al. 2006, Tanhaei et al. 2013), where the centroid of the sigmoid is regarded as the CMC (Mondal and Ghosh 2012, Ray et al. 2006). Generally, a typical plot of  $A_t$  against  $\log(\text{surfactant concentration})$  can be divided into 3 sections (Figure 10a). The first section is below the CMC, where the absorbance gradually increases with increasing surfactant concentration, which is coupled with increasing pyrene solubility. The second section refers to the narrow inflection zone near the CMC, where the absorbance

risers sharply due to the formation of micelles. Afterwards, the curve enters into the third section, where the increase of absorbance turns gradual due to saturation of pyrene dissolution. Therefore, the CMC value should be located at the break point where the red shift of  $\lambda_{\max}$  occurs. The centroid of the sigmoid (in the second section) is generally higher than the true CMC (**Table 4**), though it is usually very close due to the narrowness of the inflection zone. The intersection point between the two linear regression lines below and above the CMC has been used to estimate the CMC value (Mukerjee and Mysels 1971).

In the actual analysis of pyrene UV-absorbance spectra, the baseline variation of the UV spectra has been a challenging problem when used for measuring CMCs, especially in the case of supersaturated surfactants of low solubility. **Figure 11a** shows the plot of  $A_i$  against (log concentration of Tween 85), where increased data scattering is evident at elevated surfactant concentrations ( $\log C > 1$ ). Tween 85 is a lipophilic surfactant and is sparingly soluble in water. Although it can be well dispersed in water, slight local heterogeneity in concentration distribution will affect the baseline of the UV spectra. Likewise, in the presence of supersaturated  $C_{16}TAB$ , the UV baseline of pyrene in  $C_{16}TAB$  solutions is unstable, and the UV absorption of pyrene even showed negative values at elevated concentrations (400 and 500 mg/L) of  $C_{16}TAB$  (**Figure 12b**). In this case, the peak values cannot be accurately estimated, leading to failure of the method. To overcome this problem, we compared three parameters—peak area, peak ratio and peak difference (i.e., the difference between the strongest absorbance and a selected weaker peak)—to estimate the CMC, and found that the peak difference is a more robust parameter to accurately determine the CMC despite the fluctuation of baseline.

Generally, the absorbance obeys the Beer-Lambert law, i.e., absorbance is proportional to the compound concentration in a given solution. However, in our observation the absorbance peak at  $\lambda_{\max}$  increases faster than other peaks with increasing surfactant concentration. **Figures 12c and 12d** show the correlations between the difference of P2 and P7 (P2–P7) to log (Tween 85) and log  $C_{16}TAB$  concentration, respectively. In both cases, two nearly perfect linear regressions with distinctively different slopes are observed below and above the CMC. The selection of P2 and P7 as the reference peaks is based on three key considerations: 1) P2 is the strongest peak, which gives the largest difference when compared with another peak, 2) the larger difference gives better resolution of the method, and 3) P7 is a weaker, stable and clearly measurable peak, and the value of (P2–P7) remains high at elevated concentrations of a surfactant.

Applying the peak difference (P2–P7) approach, we successfully determined the CMCs of two nonionic surfactants (Tween 80 and Tween 85), two anionic surfactants (DOSS and SDS), 2 cationic surfactants ( $C_{10}TAB$  and  $C_{16}TAB$ ) and two oil dispersants (Corexit EC9500A, and Corexit EC9527A), and the results are summarized in **Table 4**. To verify the data, **Table 4** also gives the CMCs estimated by the surface tension method. The plots of UV absorbance and surface tension against log surfactant/dispersant concentrations are provided in the supporting information of published paper (Fu et al. 2015). The CMCs measured by the peak difference method are in line with those obtained from the surface tension method and with the reported values (see **Table 4**) (Chakraborty and Moulik 2007, Chatterjee et al. 2001, Cirin et al. 2012, Diemand 2011, Ghosh 2001, Ghosh and Moulik 1998, Gong et al. 2014, Griffiths et al. 2004, Mondal and Ghosh 2012, Ray et al. 2006, Ribeiro et al. 2004, Steffy et al. 2011, Wan and Lee 1974)), indicating the general validity of this method.

For comparison, we also tested the methods by plotting the sum of the eight peaks against log (surfactant concentration). We found the peak sum method failed for Tween 85,  $C_{16}TAB$ , as well as the two oil dispersants due to the strong baseline fluctuations at elevated concentrations of the surfactants and dispersants.

**Table 4. CMCs of surfactants or dispersants obtained from different methods in this work and reported data from open publications**

	CMCs (mg/L) measured in this work				Reported CMCs (mg/L)				
	Measured by UV absorbance of pyrene			Surface tension method	UV absorbance	Fluorescence	Surface tension	Turbidity	Conductometry
	Peak sum	P2–P7							
Tween 80	25.11 <sup>a</sup>	16.13 <sup>b</sup>	16.24	14.00	11.79 [9]	17.07 [9]	13.1 [26]	/	/
Tween 85	NA <sup>c</sup>	NA	10.60 (CMC <sub>1</sub> ) 20.10 (CMC <sub>2</sub> )	10.00 (CMC <sub>1</sub> ) 24.32 (CMC <sub>2</sub> )	/	/	23 [19] 25.72 [5]	/	/
DOSS	13.58×10 <sup>2</sup>	9.86×10 <sup>2</sup>	10.88×10 <sup>2</sup>	10.00×10 <sup>2</sup>	/	/	12.09×10 <sup>2</sup> [4] 17.00×10 <sup>2</sup> [20]	/	/
SDS	25.04×10 <sup>2</sup>	23.15×10 <sup>2</sup>	19.04×10 <sup>2</sup>	18.20×10 <sup>2</sup>	20.44×10 <sup>2</sup> [8]	20.33×10 <sup>2</sup> [8]	23.07×10 <sup>2</sup> [21]	/	/
C <sub>10</sub> TAB	18.05×10 <sup>3</sup>	17.98×10 <sup>3</sup>	17.60×10 <sup>3</sup>	16.60×10 <sup>3</sup>	19.42×10 <sup>3</sup> [8]	/	/	/	18.39 × 10 <sup>3</sup> [22] 16.87 × 10 <sup>3</sup> [23]
C <sub>16</sub> TAB	NA	NA	33.86×10 <sup>1</sup>	34.70×10	34.62×10 [8]	31.71×10 [8]	/	/	34.99 × 10 <sup>1</sup> [22]
Corexit EC9500A	NA	NA	17.78	17.73	/	/	22.50 <sup>d</sup> [24]	20.22 <sup>d</sup> [25]	/
Corexit EC9527A	NA	NA	20.11	20.36	/	/	/	/	/

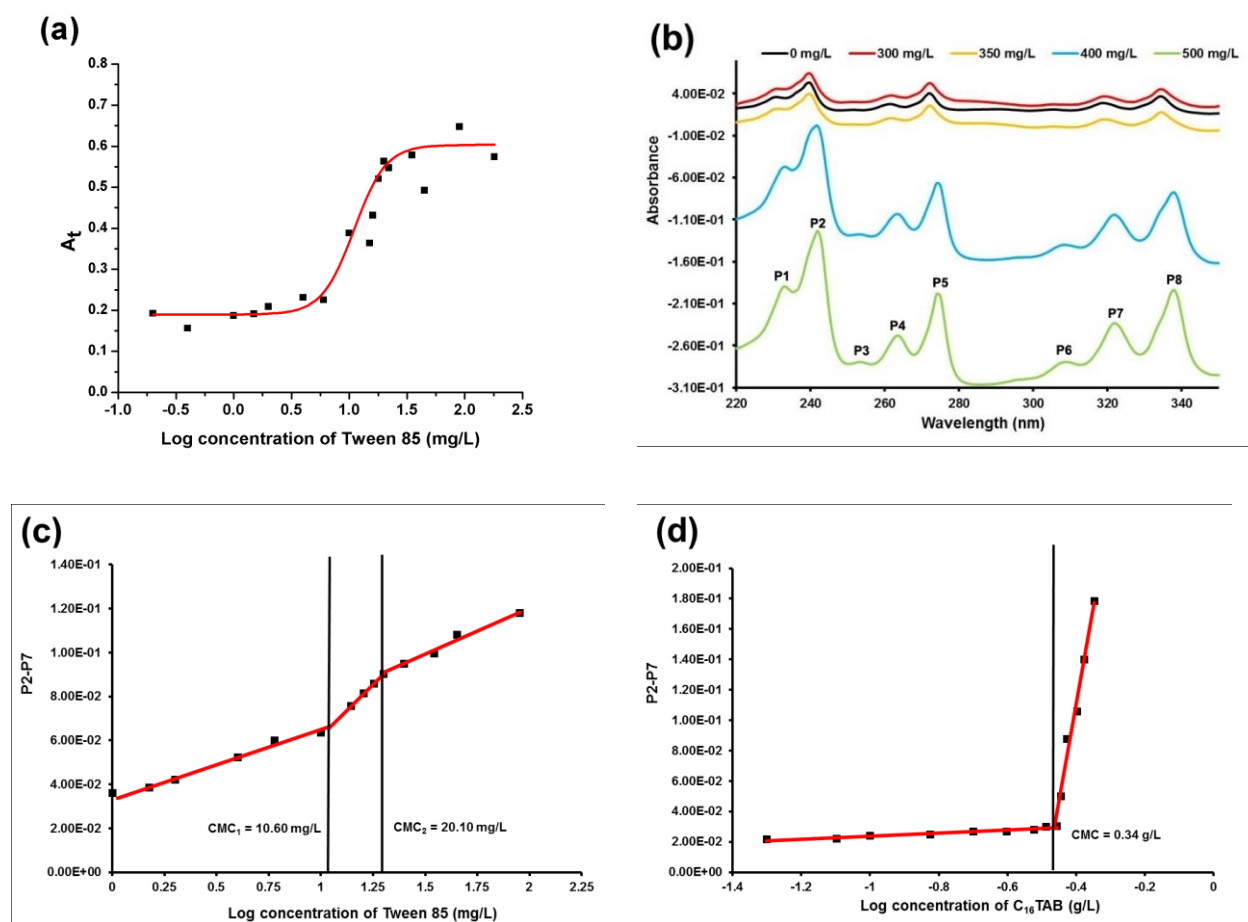
<sup>a</sup> Data were obtained by Sigmoid fitting

<sup>b</sup> Data were obtained by linear regressions

<sup>c</sup> NA, not applicable

<sup>d</sup> Data was obtained in seawater

Both the peak difference and the surface tension methods revealed two close, but distinct, CMC values for Tween 85 (Table 4). In fact, Tween 85 is an amphiphilic mixture including mono-, di- or trimester derivatives of polyoxyethylene-sorbitan, mono- or diester derivatives of polyoxyethylene-isorbitide, and other by-products (Borisov et al. 2011). Erdem and coworkers identified polyoxyethylene-sorbitan monooleate and polyoxyethylene-sorbitan dioleate as the two major components of Tween 85 (Solak Erdem et al. 2014), which account for the two CMC values observed in this work. Likewise, oil dispersants are mixtures of anionic and nonionic surfactants and solvents. However, only one distinctive CMC value was obtained for both of the oil dispersants in the concentration range tested. The CMCs for dispersants were close to the CMCs of the nonionic surfactants and much lower than the anionic surfactants (Table 4), implying the CMCs of the dispersants are governed by the nonionic surfactants micelles and the CMCs are likely due to the mixed micelles of the surfactants. However, another higher CMC should be expected for the dispersants due to the formation of the anionic surfactant micelles at much higher concentrations. For example, Corexit EC9527A has a higher CMC of 382.9 mg/L (Singer et al. 1995), which is due to the formation of DOSS micelles. Because surfactants or dispersants at high concentrations ( $> 200$  mg/L) become less water miscible, the precision of the UV absorbance measurements becomes greatly compromised. Moreover, the presence of organic solvents in the dispersants can distort the UV spectral. Consequently, the UV absorbance-based peak difference method is not applicable for measuring the much higher CMCs of the dispersants.



**Figure 12. Correlations of UV absorbance with surfactant concentration.**

(a) Plot of  $A_t$  against log concentration of Tween 85. (b) UV spectra of pyrene at various concentrations of C16TAB. (c) Linear regressions of (P2–P7) against log concentration of Tween 85. (d) Linear regressions of (P2–P7) against log concentration of C16TAB. Measurements were carried out at  $22 \pm 1$  °C. The initial pyrene dose was  $600 \mu\text{g/L}$ .

## 2.2.5. Ratio of pyrene and surfactant molecules in micelles

As mentioned earlier, the enhanced pyrene dissolution is due to the incorporation of the probe chemical into the surfactant micelles. Based on the UV absorbance, we may calculate the ratio of pyrene to surfactant molecules in the micelles. To this end, the following assumptions are invoked: (1) the formation of aggregates does not change the total number of monomers of the surfactants, (2) the presence of a surfactant or dispersant below its CMC does not alter the solubility of pyrene, and (3) each micelle receives the same number of pyrene molecules. Consider an aqueous solution of a surfactant has a bulk concentration  $[S]$ , which is above the CMC, then the concentration of micelles,  $[M]$ , can be expressed as (Turro and Yekta 1978):

$$[M] = \frac{[S] - \text{CMC}}{N} \quad (5)$$

where  $N$  is the aggregation number of surfactant micelles. The number of pyrene ( $n$ ) partitioned into the micelles can be estimated via:

$$n = \frac{\Delta[Py]}{[M]} = \frac{[Py] - [Py]_{\text{CMC}}}{([S] - \text{CMC})/N} \quad (6)$$

where  $[Py]$  is the total pyrene concentration and  $[Py]_{\text{CMC}}$  is pyrene concentration at CMC. Thus, the ratio of pyrene to surfactant molecules in micelles ( $n/N$ ) is given by:

$$n/N = \frac{[Py] - [Py]_{\text{CMC}}}{[S] - \text{CMC}} \quad (7)$$

As the pyrene solubility remains the same before CMC,  $[Py]_{\text{CMC}}$  can be considered as the pyrene solubility  $[Py]_{\text{sol}}$  in water, which is  $0.667 \mu\text{mol/L}$ . In this work, the maximum pyrene concentration  $[Py]_{\text{max}}$  was  $2.97 \mu\text{mol/L}$ , where all the initial added pyrene molecules ( $600 \mu\text{g/L}$ ) were dissolved or dispersed in the surfactant solutions. Here, we employ the SBE to interpret the plot of P2–P7 ( $P$ ) to log surfactant concentration ( $\log [S]$ ) (Ray et al. 2006):

$$P = \frac{(P_i - P_f)}{1 + \exp\left(\frac{\log [S] - \log [S]_0}{\Delta \log [S]}\right)} + P_f \quad (8)$$

where  $P_i$  and  $P_f$  are the initial and final asymptotes of the sigmoid, respectively,  $\log [S]_0$  is the center of the sigmoid and  $\Delta \log [S]$  is the interval of the independent variable  $\log [S]$ . The  $n/N$  is supposed to be a constant parameter in the pyrene-surfactant system, and thus it can be estimated at a given surfactant concentration, which is above CMC. At the center of the sigmoid (4),  $n/N$  is given by

$$n/N = \frac{([Py]_{\text{max}} + [Py]_{\text{sol}})/2 - [Py]_{\text{sol}}}{10^{\log [S]_0} - \text{CMC}} = \frac{([Py]_{\text{max}} - [Py]_{\text{sol}})/2}{10^{\log [S]_0} - \text{CMC}} \quad (9)$$

Substituting the values of  $[Py]_{\text{max}}$  and  $[Py]_{\text{sol}}$  into Equation (9), we have

$$n/N = \frac{1.15}{10^{\log [S]_0} - \text{CMC}} \quad (10)$$

Using Equations (8) and (10), the  $n/N$  values in the pyrene-surfactant systems were calculated, including: Tween 80 ( $n/N = 0.16$ ), DOSS (0.0014), SDS (0.0018) and C<sub>10</sub>TAB (0.0046). Due to the prohibitive baseline fluctuation at high surfactant concentrations,  $\log [S]_0$  for C<sub>16</sub>TAB was not



measurable. Because the compositions in Tween 85, Corexit EC9500A and Corexit EC9527A are rather complex, the  $n/N$  cannot be obtained in these solutions. However, based on the reported values of  $N$  (61 for Tween 80 (Ullah et al. 2014), 35 for DOSS (Akbat et al. 2004), 60 for SDS (Gehlen and De Schryver 1993) and 40 for C<sub>10</sub>TAB (Evans et al. 1984)), the mean number of pyrene molecules in the micelles ( $n$ ) can be estimated: 9.76 for Tween 80, 0.049 for DOSS, 0.11 for SDS and 0.18 for C<sub>10</sub>TAB. Evidently, much more pyrene molecules are incorporated into the Tween 80 micelles, while lowest partitioning was observed for DOSS. The results indicate that nonionic surfactants are more efficient in increasing the solubility of pyrene, which may be due to the lower polarity of nonionic surfactants. In fact, many nonionic surfactants have been employed to remove the PAHs from contaminated soils or sediments (Peng et al. 2011).

## 2.2.6. Conclusions

A revised UV-based approach for measuring CMCs of an array of surfactants or oil dispersants was proposed and tested. Based on UV absorption analysis of a probe compound pyrene, we proposed two convenient and robust parameters for estimating CMCs for a wide range of surfactants and dispersants, namely using the critical red shift concentration corresponding to the strongest UV peak, and, for more accurate measurements, by means of the maximum measurable peak difference as a function of surfactant concentration. Though the conventional UV-based methods often fail to measure CMCs of low-solubility surfactants due to severe baseline fluctuation of the UV spectra, the proposed peak difference method eliminates the effect of baseline variation and provides a powerful alternative for various kinds of surfactants and oil dispersants. To facilitate most effective application of the method, we would propose a two-step strategy to determine CMCs: 1) roughly locate the CMC range by identifying the red shift of  $\lambda_{\max}$ , and 2) further identify the CMC graphically by plotting (P2–P7) against log surfactant or dispersant concentration. This work also provides evidence that the fundamental principle of the UV-based methods is the surfactant-enhanced solubility of the probe compound. Additionally, this work demonstrated an approach to estimate the ratio of pyrene and surfactant molecules in micelles based on the UV absorbance data in various surfactant-probe systems, which further reveals the ability of various surfactants in dissolution of pyrene (or other PAHs).

### **3. Effects of Dispersant on Sorption and Desorption and Transport of Oil and Oil Components**

#### **3.1. Effects of Oil Dispersant and Oil on Sorption and Desorption of Phenanthrene with Gulf Coast Marine Sediments**

PAHs are important pollutants associated with oil spills; they are of great concern due to their toxicity, mutagenicity, carcinogenicity, and persistency (Nam et al. 2008). For instance, the *DwH* oil contained ~3.9% PAHs by weight, and the *DwH* oil spill released  $\sim 2.1 \times 10^7$  kg of PAHs into the Gulf of Mexico (Reddy et al. 2012b).

Sorption and desorption affect the transport, physical and biological availabilities, toxicity, and ultimate fate of PAHs in the environment (Johnson et al. 2008). In the marine environment, suspended particulate matter (SPM) is a major transport medium for pollutants (Voice and Weber Jr 1983, Wu and Gschwend 1986). Because of their hydrophobic nature, PAHs can be strongly sorbed to SPM and accumulate in bottom or coastal sediments through SPM-facilitated transport and settling (Yang et al. 2005), which can greatly alter the weathering rate and environmental fate of PAHs (Gearing et al. 1980).

Sediment organic matter (SOM) is the key component for sorption of hydrophobic compounds (Braidai et al. 2001, White and Pignatello 1999). In addition to sorption, the extent and rate of desorption are also important factors in controlling physical and biological availabilities of sorbed contaminants (Pignatello and Xing 1995). Yet, it remains unknown how oil dispersants affect such interactions between sediment particles and persistent oil components such as PAHs.

Due to the amphiphilic nature of surfactants, dispersants can cause contrasting effects on the sorption of PAHs by sediments (Cheng and Wong 2006, Pan et al. 2009, Zhang and He 2011). On one hand, a surfactant can increase the apparent solubility of PAHs through its hydrophobic tail which reduces sorption and favors desorption of PAHs. On the other hand, the sorption of surfactant on sediments enhances the partitioning of additional PAHs onto the immobilized surfactant. The overall effects of a dispersant would depend on the extent of these contrasting factors. Cheng and Wong (2006) observed that desorption of phenanthrene and pyrene from soil was enhanced in the presence of a nonionic surfactant (Tween 80) at concentrations higher than the CMC, however, no significant desorption enhancement was evident in the surfactant concentration range of 0–7.5 mg/L. Pan et al. (2009) reported that the presence of 4.3 mg/L of an anionic surfactant increased sediment sorption of perfluorooctane sulfonate.

The overall goal of this part of study was to investigate effects of a model oil dispersant (Corexit EC9500A) on the distribution of a model PAH (phenanthrene) in a sediment-seawater system. The specific objectives were to: 1) investigate sorption and desorption behaviors of Corexit EC9500A with two types of representative Gulf Coast marine sediments; 2) determine effects and mechanisms of the dispersant on sorption and desorption isotherms and kinetics of phenanthrene; and 3) evaluate effects of WAO and DWAO on sediment sorption of phenanthrene.

### 3.1.1. Materials and methods for phenanthrene sorption and desorption

#### 3.1.1.1. Materials

Two marine sediments (0–30 cm) were collected at Grand Bay, Alabama in December 2010. The latitudes and longitudes of the two sites were (30.37926, 88.30684) and (30.37873, 88.30679), respectively. The sampling sites sit in the neighborhood with some sites affected by the *DwH* oil spill, such as Bayou La Batre and Dauphin Island. The sediments correspond to the loamy sand and sandy loam based on the USDA Soil Taxonomy used for soil classification. Seawater samples were collected from the top 30 cm of the water column from the same area. The seawater was first filtered through 0.45  $\mu\text{m}$  membrane filters to remove suspended solids, and then sterilized at 121  $^{\circ}\text{C}$  for 35 minutes via autoclaving. Sediment analysis was performed by the Soil Testing Laboratory at Auburn University. **Table 5** gives salient properties of the sediments.

All chemicals used in this study were of analytical or higher grade.  $^{14}\text{C}$ -radiolabeled phenanthrene (in methanol) with a specific activity of 52.0 mCi/mmol (99.5% purity) was purchased from Moravek Biochemicals, Inc. Nonradioactive phenanthrene and dichloromethane were purchased from Alfa Aesar. Sodium sulfate ( $\text{Na}_2\text{SO}_4$ ) was obtained from Fisher Scientific. A surrogate LSC was used. According to the manufacturer, the oil is physically, chemically, and toxicologically similar to the Macondo well crude oil in Mississippi Canyon Block 252.

**Table 5. Salient physical and chemical properties of marine sediments used in this work**

<b>Sample</b>	<b>Nitrogen<sup>a</sup> (%)</b>	<b>Carbon<sup>a</sup> (%)</b>	<b>Sulfur<sup>a</sup> (%)</b>	<b>SOM<sup>b</sup> (%)</b>	<b>pH<sup>c</sup></b>	<b>Cation Exchange Capacity (meq/100g)</b>					<b>Sand<sup>d</sup> (%)</b>	<b>Silt<sup>d</sup> (%)</b>	<b>Clay<sup>d</sup> (%)</b>	<b>Textural Class<sup>e</sup></b>
Loamy Sand	0.07	0.43	0.210	0.7	7.00	21.21					85.0	5.0	10.0	Loamy Sand
Sandy Loam	0.15	1.58	0.682	2.7	7.38	37.38					56.3	31.3	12.5	Sandy Loam
<b>Sample</b>	<b>Ca (mg/kg)</b>	<b>K</b>	<b>Mg</b>	<b>P</b>	<b>Al</b>	<b>Cd</b>	<b>Cr</b>	<b>Cu</b>	<b>Fe</b>	<b>Mn</b>	<b>Na</b>	<b>Ni</b>	<b>Pb</b>	<b>Zn</b>
Loamy Sand	301	177	536	11	60	0.1	0.1	5	241	35	3068	0.1	1	4
Sandy Loam	780	336	988	8	119	0.3	0.1	11	701	65	5057	0.4	2	9

<sup>a</sup> Total carbon, nitrogen and sulfur contents were determined following the combustion method (Kirsten 1979).

<sup>b</sup> SOM was obtained based on the empirical relationship: SOM = 1.72×TOC (Davies, 1974).

<sup>c</sup> Sediment pH was measured on a 1:1 sediment:water mixture via the Reference Soil Test Methods (UGA, 1983).

<sup>d</sup> Categorized based on USDA-definition.

<sup>e</sup> Sediment texture was conducted following the hydrometer method (Bouyoucos 1962).

Note: Metal contents were measured per EPA method 3050B. Soil calcium, magnesium, potassium and sodium were first extracted per the Mehlich 1 procedure, filtered through a #1 qualitative filter paper, and then determined by a Varian Vista-MPX Radial Spectrometer.

### **3.1.1.2. Sorption and desorption of Corexit EC9500A by sediment**

Batch experiments were conducted in duplicate to determine dispersant sorption isotherms with sandy loam using 43-mL glass vials with Teflon-lined caps. Each vial was first filled with 0.21 g of sandy loam mixed with 2 mL of seawater, and then filled with 40 mL of dispersant solutions, resulting in initial dispersant concentrations from 0 to 1080 mg/L. The mixtures were then equilibrated on an end-to-end rotator at 30 rpm kept at  $21 \pm 1$  °C for 5 days. Then, the solids were separated from aqueous solution by centrifuging at 3000 rpm for 10 minutes, and aliquots (40 mL each) of the supernatants were pipetted out for surface tension analysis. The dispersant concentration was then determined based on the surface tension. Control tests conducted without the sediments showed that the loss of dispersant due to sorption to the vial walls and septa was < 5% in all cases. Dispersant uptake by the sediment (mg/g) was calculated based on the difference in initial and final aqueous dispersant concentrations.

To test sorption reversibility of the dispersant, desorption isotherm tests were carried out. Following the sorption equilibrium, 99% of the supernatant was replaced with an equal volume of dispersant-free seawater. To assure equal background compositions, the sediment-amended replacement seawater was first amended with the same sediment by mixing the sediment with seawater at the same sediment-to-water ratio as in sorption isotherm tests. The vials were then re-equilibrated for 7 days, and desorption isotherms were then obtained in the same manner.

### **3.1.1.3. Effects of dispersant on sorption and desorption kinetics of phenanthrene**

A stock solution of nonradioactive phenanthrene was prepared at 1.4 g/L in methanol. The  $^{14}\text{C}$ -radiolabeled phenanthrene was diluted 10 times using methanol. The two solutions were then mixed at a volume ratio of 1:9, which was then diluted with seawater to a phenanthrene concentration of 630  $\mu\text{g/L}$ .

Batch phenanthrene sorption kinetic tests were conducted in duplicate in 43-mL glass tubes with Teflon-lined caps. First, a known mass of sterilized sediments (1.05 g of loamy sand or 0.21 g of sandy loam) was mixed with 2 mL of seawater in each vial. The phenanthrene sorption was then initiated by adding 40 mL of the phenanthrene solution to each sediment-seawater suspension, which resulted in an initial phenanthrene concentration of 600  $\mu\text{g/L}$ . Nearly zero headspace was maintained in the vials to minimize volatilization loss of phenanthrene. The volume fraction of methanol in all cases was < 0.1% to avoid co-solvent effect. The vials were then sealed and rotated on an end-to-end rotator operated at 60 rpm in an incubator at  $21 \pm 1$  °C. After the predetermined time intervals, vials were sacrificially centrifuged at 3000 rpm for 10 minutes to separate the solids from the solution. After 5 minutes, 1 mL of each supernatant was sampled and added to 10 mL of Ecoscint cocktail (National diagnostics, Atlanta, GA, USA) for liquid scintillation counting. To determine the dispersant effect, the kinetic tests were also carried out in the presence of 18 mg/L of Corexit EC9500A. Control experiments carried out without sediments showed that phenanthrene loss was consistently < 4%.

Following the sorption equilibrium, phenanthrene desorption tests were initiated by replacing 99% of the supernatant with an equal volume of sediment-amended seawater. The vials were then mixed and sacrificially sampled in the same manner as in the sorption tests. To evaluate effects of the dispersant on the desorption rate and extent, four experimental scenarios were evaluated: 1) Phenanthrene was pre-sorbed onto the sediments without dispersant, then subjected to desorption without dispersant; 2) Sorption was the same as in scenario (1), but desorption was conducted with dispersant; 3) Phenanthrene was pre-sorbed on the sediments with dispersant, then subjected to desorption without dispersant; and (4) Sorption was the same as in scenario (3), but desorption with dispersant.

### 3.1.1.4. Effect of dispersant on sorption and desorption isotherms of phenanthrene

Sorption isotherm tests were conducted with an equilibration time of 5 days and a range of initial phenanthrene concentrations (24–864 µg/L). Isotherms were constructed in the presence of 0, 18, and 180 mg/L of the dispersant. Control tests without the sediments showed that the loss in phenanthrene and the dispersant was < 4%. Following the sorption equilibrium tests, desorption isotherms were obtained by replacing 99% of each supernatant with an equal volume of the replacement fluid, and re-equilibrating the systems for 7 days. To test effects of the dispersant on sorption reversibility, the equilibrium tests were carried out according to the aforementioned four scenarios.

To confirm mass balance, phenanthrene in the sediment phase was extracted with hot methanol (1.05 g loamy sand in 50 mL methanol, and 0.21 g sandy loam in 40 mL methanol) at 70 °C for 4 hours. Mass balance results showed that the overall error was < 5%.

### 3.1.1.5. Dual-mode sorption equilibrium and kinetic models

As a natural adsorbent, SOM is the key component for sorption of hydrophobic compounds. The dual-mode model considers that SOM consists of a soft or rubbery domain and a condensed or glassy domain. It is assumed that sorption of PAHs on SOM results from a combination of solid-phase dissolution (partitioning) in the rubbery domain and adsorption (or hole-filling) in the glassy domain of SOM (Pignatello 1998, Pignatello and Xing 1995, Xing et al. 1996). For a single solute, the dual-mode isotherm model is given as follows:

$$q_e = K_D C_e + \frac{bQC_e}{1 + bC_e} \quad (11)$$

where  $q_e$  is the equilibrium uptake,  $C_e$  the solute concentration in solution,  $K_D$  the partition coefficient between the solution and the dissolution domain of SOM (including sorbed dispersant aggregates), and  $b$  and  $Q$  are the Langmuir affinity and capacity coefficients, respectively (Pignatello and Xing 1995). It is assumed that the uptake of the dispersant on sediments adds an additional domain of partitioning. As a result, the first term in Equation 11 includes phenanthrene partitioning in both immobilized dispersant and the rubbery domain of SOM. The model parameters ( $K_D$ ,  $b$  and  $Q$ ) were acquired through fitting the model to the corresponding experimental isotherms.

The dual-mode radial diffusion model was used to simulate the sorption kinetic data. The governing equation is (Zhao et al. 2002a):

$$\frac{\partial q_D}{\partial t} = D_a \left( \frac{\partial^2 q_D}{\partial r^2} + \frac{2}{R} \frac{\partial q_D}{\partial r} \right) \quad (12)$$

where  $q_D$  is the uptake in the dissolution domain,  $r$  is the radial coordinate,  $t$  is time, and  $D_a$  is the apparent diffusivity defined by

$$D_a = D_D \left( 1 + \frac{bQ/K_D}{[1+(b/K_D)q_D]^2} \right) \quad (13)$$

where  $D_D$  is the diffusivity in the dissolution domain. The equation was solved using the Crank-Nicolson finite difference method under the batch experimental initial and boundary conditions. The value of

$D_D/r_0^2$  was obtained by fitting the model to the experimental kinetic data.

### **3.1.1.6. Effects of WAO and DWAO on sorption kinetics of phenanthrene**

WAO and DWAO were prepared with the surrogate oil following the protocol (Singer et al. 2000). The procedure represents a compromise that balances the need to prepare environmentally realistic media with the requirement for media of highly repeatable compositions (Singer et al. 2000). WAO was prepared in 2200 mL glass aspirator bottles containing a hose bib fitted with silicon tubing and clamp at the bottom of the vessels. Each bottle was filled with 1760 mL of seawater, leaving a 20% headspace. Crude oil was carefully added at the volume ratio of 1:200 to the seawater surface, and the mixture was sealed and magnetically stirred for 18 hours. The stir plate was adjusted to obtain an oil vortex of 25% of the total volume of seawater. The mixture was then allowed to gravity-settle for six hours. Then, the WAO fraction was collected in glass vials with Teflon lined caps from the bottom without disturbance of the oil-seawater surface, allowing no headspace in the vials. DWAO was prepared following the same protocol except that the dispersant was added to the oil-seawater mixture at a dispersant:oil volume ratio of 1:20.

Petroleum hydrocarbons in the aqueous phase were extracted using dichloromethane in three consecutive steps (10 mL solution with 2 mL dichloromethane in each step) (Ramachandran et al. 2004). The extracts were then passed through 0.3 g anhydrous granular sodium sulfate loaded in a Pasteur pipette to remove moisture (Saeed et al. 2011), and then blown to dryness under a stream of nitrogen gas. The dried extracts were re-dissolved in 0.2 mL of dichloromethane (DCM) for GC-MS analysis.

### **3.1.1.7. Chemical analysis**

Petroleum hydrocarbons in WAO and DWAO were analyzed using a GCT Premier time-of-flight (TOF) mass spectrometer operated in the splitless mode. A DB-5 fused silica capillary column (length 30 m; inner diameter 0.25  $\mu\text{m}$ ; film thickness 0.25  $\mu\text{m}$ ) was used to separate the analytes. The GC oven temperature was programmed as follows: 80  $^{\circ}\text{C}$  (hold for 3 mins), ramp to 160  $^{\circ}\text{C}$  at 10  $^{\circ}\text{C}/\text{min}$ , ramp to 280  $^{\circ}\text{C}$  at 4  $^{\circ}\text{C}/\text{min}$ , and ramp to 300  $^{\circ}\text{C}$  at 20  $^{\circ}\text{C}/\text{min}$  (hold for 2 mins). Helium was used as the carrier gas (flow rate = 1.0 mL/min), and sample injection volume was 3  $\mu\text{L}$ . The system was operated in the total ion current mode, and the chemical compounds were identified through high probability matching using the NIST spectral library.

$\text{SO}_4^{2-}$ ,  $\text{Cl}^-$  and  $\text{NO}_3^-$  were analyzed using a Dionex ion chromatography system (Dionex, Sunnyvale, CA, USA) equipped with an AS14 column, with a detection limit of 0.2, 0.2, and 0.1 mg/L, respectively.

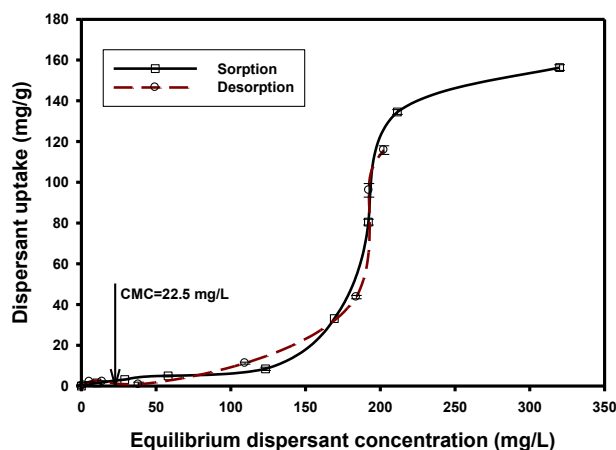
## **3.1.2. Sorption and desorption of Corexit EC9500A**

The CMC of Tween 85 was measured to be 23 mg/L, which is higher than that (14 mg/L) of Tween 80, but much lower than that (578 mg/L) of DOSS. Therefore, the Tween 85 plays a predominant role in the mixed micelles (Ahn et al. 2010). While both nonionic surfactants tend to partition into anionic surfactant micelles or semimicelles, Tween 80 is more prone to interact with the anionic surfactant due to its smaller molecular size (Zhao et al. 2005). The interaction of nonionic surfactants with the anionic surfactant decreases the repulsive forces among the ionic heads of the anionic surfactant, and the hydrophobic interactions of the alkyl chains of anionic and nonionic surfactants facilitate formation of mixed micelles at a much lower concentration than the CMC of DOSS (Zhao et al. 2005).

**Figure 13** presents sorption and the corresponding desorption isotherms of the dispersant with sandy loam. The sorption isotherm exhibits the characteristic S-shape, indicative of transition of monomeric uptake to formation of dispersant hemimicelles or admicelles on the sediment surface (Ko et al. 1998a). At dispersant concentration < 123 mg/L (designated as region 1), low (< 8.4 mg/g) but steadily growing dispersant uptake was observed. In the dispersant concentration range from 123 to 211 mg/L (denoted as region 2), the sorption capacity increased sharply from 8.4 to 134.5 mg/g. At elevated dispersant concentrations (> 211 mg/L) (region 3), a sorption plateau (~156.3 mg/g) was reached.

In the low concentration region 1, the dispersant was adsorbed as monomers. Sorption of DOSS is not favored due to electrostatic repulsions between the anionic headgroups and the negatively charged sediment surface, which results from deprotonation of the SOM functional groups (e.g., carboxyls and hydroxyls) (Shen 1999) at the prevailing pH. Sorption of the dispersants results from hydrogen bonding between the hydrophobic surfactant tails and SOM (Zhang and Zhu 2010). In region 2, the surfactant concentration is sufficiently high to offset the electrostatic repulsion, as such, sorbed surfactant monomers begin to aggregate and form hemimicelles/admicelles presumably through lateral interactions of the hydrophobic tails (Ko et al. 1998b). A sorption plateau (~156.3 mg/g) was reached at elevated dispersant concentrations (> 211 mg/L), owing to elevated electrostatic repulsion, saturation of surface coverage, and/or the attainment of a constant surfactant monomer concentration in the aqueous phase (Ko et al. 1998b).

**Figure 13** also shows that the desorption isotherm nearly coincides with the sorption isotherm (the difference was statistically insignificant at the 95% confidence level), indicating that the dispersant sorption was nearly reversible. The observation also excludes the possibility of irreversible deformation of SOM and precipitation of DOSS with mineral ions from the sediment such as  $\text{Ca}^{2+}$  and  $\text{Mg}^{2+}$  (Zhang and Zhu 2010).



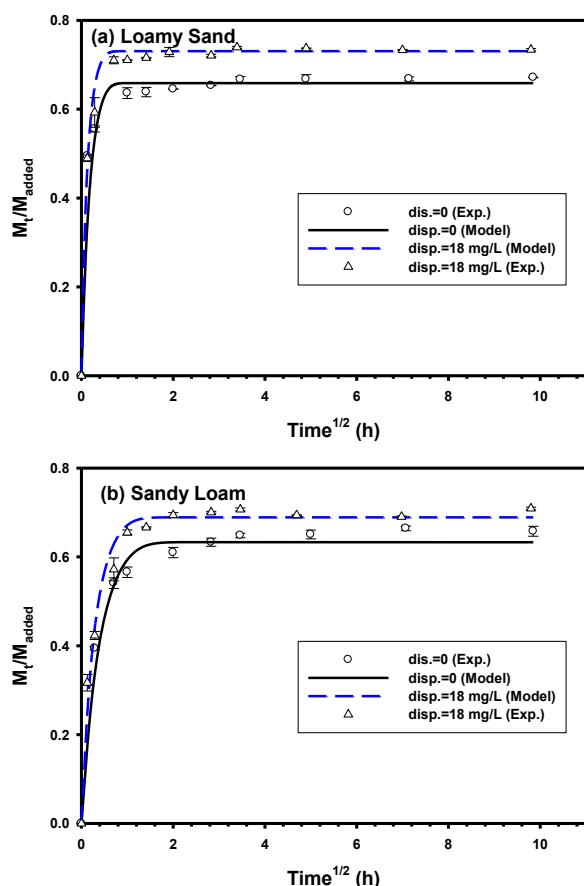
**Figure 13. Sorption and desorption isotherms of Corexit EC9500A.**

Experimental conditions: sandy loam = 0.21 g, dispersant initial concentration = 0–1080 mg/L, solution volume = 42 mL, and pH = 6.7–7.4. Data are plotted as mean of duplicates, and error bars indicate standard deviation from the mean.



### 3.1.3. Effects of dispersant on sorption and desorption kinetics of phenanthrene

Figure 14 shows phenanthrene sorption kinetics with the two sediments in the absence or presence of 18 mg/L of Corexit EC9500A. In the absence of the dispersant, loamy sand removed 67% of phenanthrene at equilibrium within 96 hours (Figure 14a). The presence of the dispersant increased the phenanthrene uptake by 7%. Likewise, the dispersant increased phenanthrene uptake from 66% to 71% for sandy loam after 96 hours (Figure 14b). Based on the t-tests, the differences between the equilibrium phenanthrene uptakes with and without dispersant for both sediments are statistically significant with a  $p$  value of  $< 0.05$  at the 0.05 level of significance.



**Figure 14. Sorption kinetics of phenanthrene onto (a) loamy sand and (b) sandy loam sediments.** Experimental conditions: initial phenanthrene = 600  $\mu\text{g/L}$ , Corexit EC9500A = 0 or 18 mg/L, pH = 7.4-7.9, loamy sand = 1.05 g, sandy loam = 0.21 g, and solution volume = 42 mL.  $M_t$ : phenanthrene mass uptake at time  $t$ , and  $M_{\text{added}}$ : total mass in the system. Symbols: experimental data, lines: dual-mode model fittings. Data are plotted as mean of duplicates; error bars indicate standard deviation from the mean.

The dispersant can affect phenanthrene uptake by sediments in two ways (Park and Jaffe 1993, Yuan et al. 2007): First, sediment sorbed dispersant provides additional sorption capacity. Second, the dispersant increases the solubility of phenanthrene in the aqueous phase, which diminishes the thermodynamic driving force for phenanthrene diffusion and sorption. The overall effect depends on the extent of these two contrasting factors. In the presence of 18 mg/L dispersant, considering the strong

sorption of the dispersant on sediments (**Figure 13**) and the weak solubilization of phenanthrene, the phenanthrene uptake was enhanced.

The equilibrium phenanthrene distribution coefficient ( $K_d$ ) between the sediment phase and the aqueous phase was determined to be 81 mL/g for loamy sand and 388 mL/g for sandy loam in the absence of the dispersant. The dispersant increased the  $K_d$  values to 114 and 490 mL/g, respectively. The greater  $K_d$  value for sandy loam results from its higher SOM content (2.7%) than loamy sand (0.7%).

To estimate the relative contribution of the sorbed dispersant to overall phenanthrene uptake,  $K_d$  is split into two terms (Lu and Zhu 2012):

$$K_d = \frac{q_e}{C_e} = K_{oc}f_{oc} + K_{df}Q_{df} \quad (14)$$

where  $K_{oc}$  is the sediment organic carbon-normalized distribution coefficient,  $f_{oc}$  is the mass fraction of sediment organic carbon, which is calculated based on SOM fraction ( $f_{om} = 1.72 \times f_{oc}$ ),  $K_{df}$  is the dispersant-normalized distribution coefficient, and  $Q_{df}$  is the mass fraction of the sorbed dispersant, which was estimated to be 1.5 mg/g from dispersant sorption isotherm (**Figure 13**). For sandy loam,  $K_{df}$  was calculated to be 67.6 mL/mg, which was 2.7 times greater than  $K_{oc}$  for the sediment (24.7 mL/mg).

Based on the sorption equilibrium parameters (**Table 6**), the diffusion rate parameter ( $D_D/r_0^2$ ) was obtained (**Table 7**) by fitting the dual-mode kinetic model to the sorption kinetic data with and without dispersant (**Figure 14**). Considering a mean radius ( $r_0$ ) of 457.5  $\mu\text{m}$ , the diffusivity  $D_D$  was calculated to be  $1.7 \times 10^{-7}$  and  $2.3 \times 10^{-8}$   $\text{m}^2/\text{h}$  for loamy sand and sandy loam, respectively, without dispersant. At 18 mg/L of the dispersant,  $D_D$  was escalated by 12% (to  $1.9 \times 10^{-7}$ ) and by 35% (to  $3.1 \times 10^{-8}$   $\text{m}^2/\text{h}$ ) for loamy sand and sandy loam, respectively (The differences between the  $D_D$  values with and without dispersant are statistically significant with a  $p$  value of 0.01 and 0.0002, respectively, at the 0.05 level of significance). Evidently, the remarkable increment in the  $D_D$  value suggests that the sorbed dispersant offers not only greater sorption affinity, but less mass transfer resistance. The dispersant-enhanced mass transfer rate of phenanthrene in SOM can be attributed to the partial softening or swelling of the more rigid SOM domains upon sorption of the dispersant (Jonker et al. 2003).

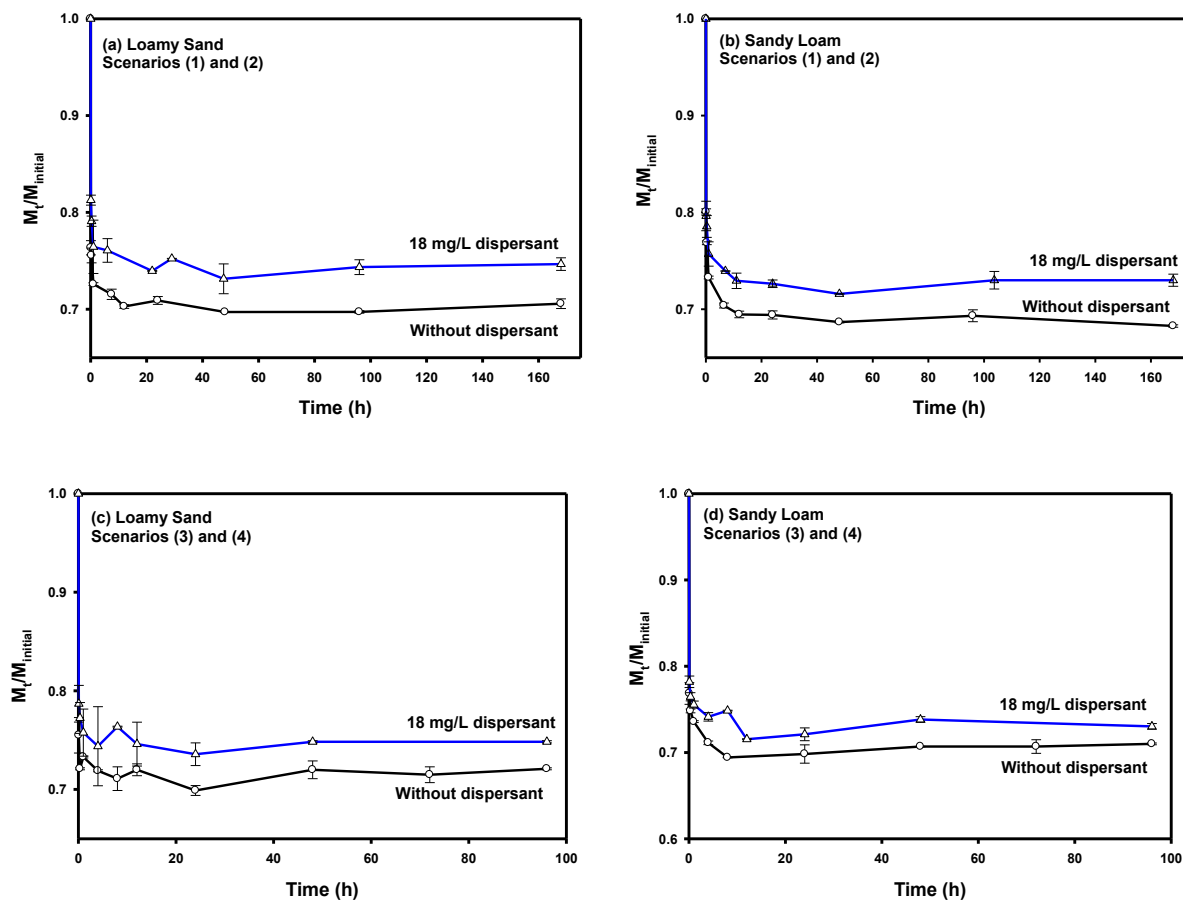
**Table 6. Equilibrium sorption parameters for phenanthrene onto loamy sand and sandy loam sediments in the absence or presence of various concentrations of the dispersant.**

Sample	Corexit EC9500A (mg/L)	Dual-mode Isotherm Model		
		$K_D$ (mL/g)	$b$ (mL/ $\mu\text{g}$ )	$Q$ ( $\mu\text{g/g}$ )
Loamy Sand	0	42.1 $\pm$ 8.6	4.6 $\pm$ 1.4	16.2 $\pm$ 6.5
	18	52.8 $\pm$ 1.4	4.6 $\pm$ 1.4	16.2 $\pm$ 6.5
	180	190.6 $\pm$ 2.7	4.6 $\pm$ 1.4	16.2 $\pm$ 6.5
Sandy Loam	0	312.4 $\pm$ 27.3	26.7 $\pm$ 2.3	10.2 $\pm$ 8.2
	18	374.8 $\pm$ 6.3	26.7 $\pm$ 2.3	10.2 $\pm$ 8.2
	180	1058.1 $\pm$ 20.0	26.7 $\pm$ 2.3	10.2 $\pm$ 8.2

**Table 7. The best-fitted values of phenanthrene diffusivities and the corresponding mean weighted square error (MWSE) in the absence or presence of the dispersant.**

Sample	Corexit EC9500A (mg/L)	$D_D/r_0^2$ (1/h)	$D_D$ (m <sup>2</sup> /h)	MWSE
Loamy Sand	0	0.8±0.010	$(1.7±0.02)×10^{-7}$	0.0008
	18	0.9±0.005	$(1.9±0.01)×10^{-7}$	0.0010
Sandy Loam	0	0.11±0.0005	$(2.3±0.01)×10^{-8}$	0.002
	18	0.15±0.00005	$(3.1±0.001)×10^{-8}$	0.001

**Figures 15a and b** show desorption kinetics of phenanthrene from loamy sand and sandy loam under scenarios (1) and (2). For both sediments, the kinetic profiles agreed with the commonly cited biphasic process: rapid initial (8 hours) desorption from more easily accessible sites, followed by slow desorption due to slow diffusion through the micropores of SOM (Pavlostathis and Mathavan 1992, Pignatello and Xing 1995, Sahoo and Smith 1997). Desorption equilibrium was reached in ~2 days, compared to ~4 hours for sorption equilibrium (**Figure 14**). At equilibrium, 29% of phenanthrene on loamy sand was desorbed, compared to 32% for sandy loam. The presence of the dispersant (18 mg/L) during desorption hindered phenanthrene desorption by 4% for loamy sand and 5% for sandy loam ( $p$  value  $< 0.04$  at the 0.05 level of significance). **Figures 15c and 15d** depict desorption kinetics of phenanthrene under scenarios (3) and (4). Again, the dispersant during desorption hindered phenanthrene desorption by 3% and 2% for loamy sand and sandy loam, respectively ( $p$  value  $< 0.02$  at the 0.05 level of significance).

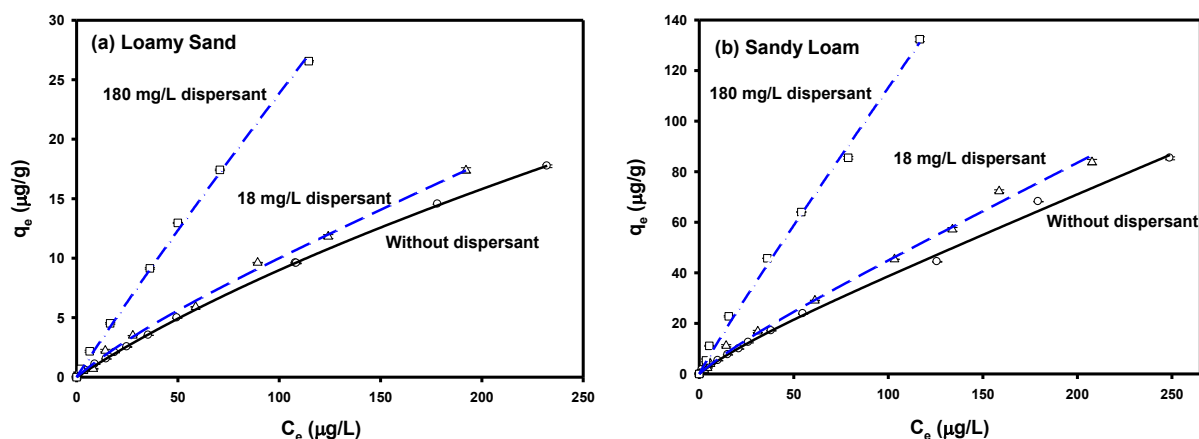


**Figure 15. Desorption kinetics of phenanthrene from (a) loamy sand and (b) sandy loam sediments.**

Scenarios (1) and (2): Phenanthrene was pre-sorbed without dispersant, then subjected to desorption in the absence (1) or presence (2) of 18 mg/L of Corexit EC9500A. Scenarios (3) and (4): Phenanthrene was pre-sorbed with 18 mg/L of the dispersant present, then subjected to desorption in the absence (3) or presence (4) of 18 mg/L of Corexit EC9500A. Experimental conditions: loamy sand = 1.05 g, sandy loam = 0.21 g, solution volume = 42 mL, and pH = 7.3–7.5.  $M_t$ : phenanthrene mass sorbed at time  $t$ ,  $M_{t_{initial}}$ : the initial phenanthrene mass in the sediments.

### 3.1.4. Effects of dispersant on sorption and desorption isotherms of phenanthrene

Figure 16 shows phenanthrene sorption isotherms by the sediments in the presence of 0, 18, and 180 mg/L of Corexit EC9500A, respectively. The results confirmed that increasing the dispersant concentration progressively increases phenanthrene uptake for both sediments. The adsorption of the dispersant on the sediments adds a strong hydrophobic sink, resulting in the enhanced adsorption affinity and capacity for phenanthrene.



**Figure 16. Effects of Corexit EC9500A on sorption isotherms of phenanthrene.**

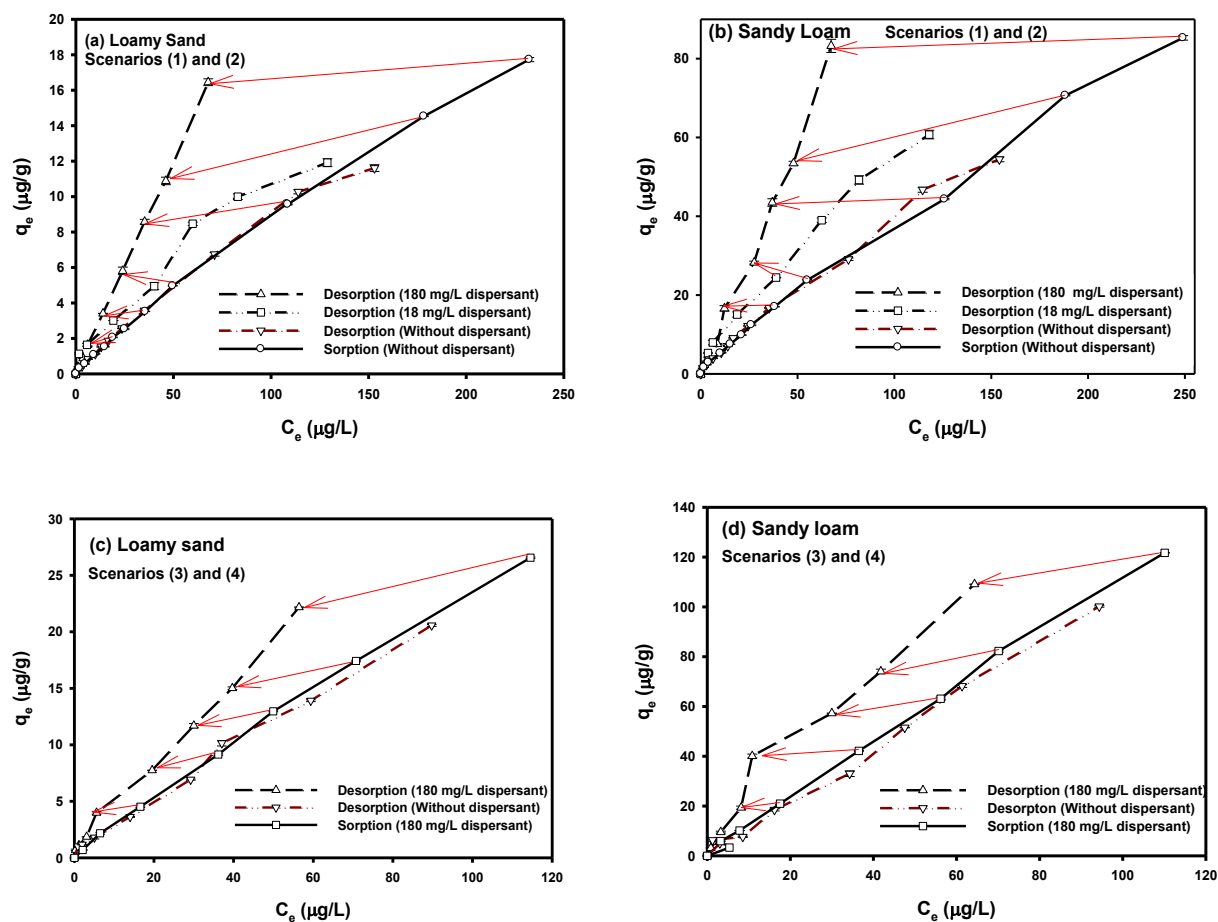
(a) loamy sand and (b) sandy loam. Experimental conditions: loamy sand = 1.05 g, sandy loam = 0.21 g, initial phenanthrene concentration = 12–864 µg/L, solution volume = 42 mL, total dispersant = 0, 18 and 180 mg/L, pH = 6.8–7.7, and equilibrium time = 5 days. Symbols: experimental data, Lines: dual-mode equilibrium model fittings.

The dual-mode isotherm model (Equation 11) was able to adequately simulate the isotherm data. **Table 8** gives the best-fitted model parameters ( $K_D$ ,  $b$  and  $Q$ ). For loamy sand,  $K_D$  increased from 42.1 to 52.8, and 190.6 mL/g in the presence of 18 and 180 mg/L of the dispersant, respectively. For sandy loam,  $K_D$  escalated from 312.4 to 374.8 and 1058.1 mL/g, respectively. Between the two sediments, sandy loam contains not only much higher SOM, but possesses nearly two times greater cation exchange capacity (CEC) (**Table 5**). As both SOM and CEC favor surfactant uptake (Wang and Keller 2008), sandy loam offered much greater phenanthrene sorption capacity. The findings confirm that the sorbed dispersant added an additional domain of partitioning, resulting in enhanced phenanthrene uptake by the sediments.

**Table 8. Equilibrium sorption parameters for phenanthrene onto loamy sand and sandy loam sediments in the absence or presence of various concentrations of the dispersant.**

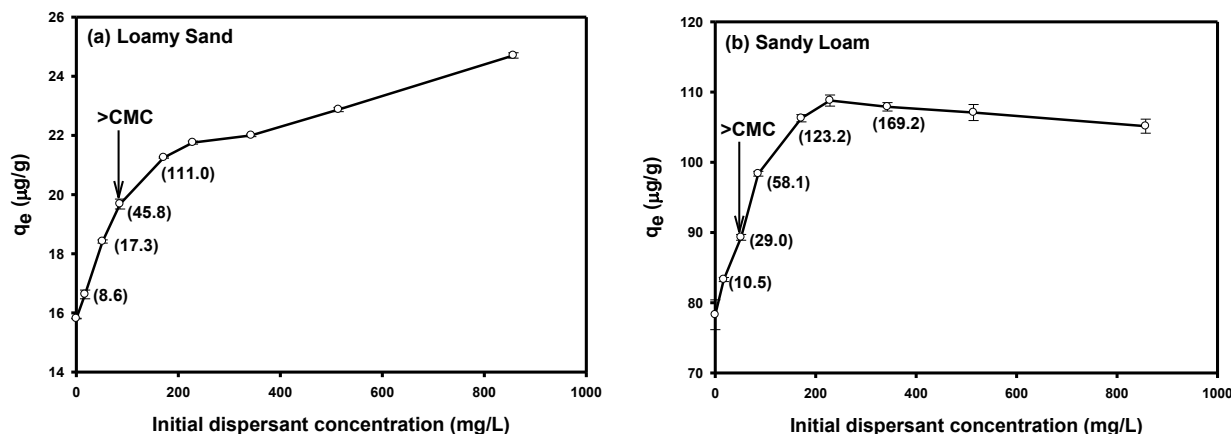
Sample	Corexit EC9500A (mg/L)	Dual-mode Isotherm Model		
		$K_D$ (mL/g)	$b$ (mL/µg)	$Q$ (µg/g)
Loamy Sand	0	42.1±8.6	4.6±1.4	16.2±6.5
	18	52.8±1.4	4.6±1.4	16.2±6.5
	180	190.6±2.7	4.6±1.4	16.2±6.5
Sandy Loam	0	312.4±27.3	26.7±2.3	10.2±8.2
	18	374.8±6.3	26.7±2.3	10.2±8.2
	180	1058.1±20.0	26.7±2.3	10.2±8.2

**Figure 17** shows desorption isotherms of phenanthrene from the two sediments under the four scenarios. Overall, phenanthrene sorption was fully reversible in the absence of the dispersant during desorption. The presence of the dispersant during sorption increased phenanthrene sorption capacity, but did not induce hysteresis. However, the presence of the dispersant (18 or 180 mg/L) during desorption caused remarkable sorption hysteresis and the extent of sorption irreversibility increases with increasing dispersant concentration. The dispersant-induced hysteresis is attributed to the elevated hydrophobicity and added sorption capacity-affinity due to sorption of the dispersant (Rodríguez-Cruz et al. 2005). Zhang and Zhu (2010) reported that Tween 80 at 852 mg/L desorbed 38% and 39%, respectively, less phenanthrene and pyrene from a PAH-contaminated soil than plain water.



**Figure 17. Effects of Corexit EC9500A on desorption hysteresis of phenanthrene on sediments.** Lines with arrows indicate the corresponding points from the sorption isotherm to the desorption isotherm. Scenarios (1) and (2): Phenanthrene sorption was carried out without dispersant, but desorption with various initial concentrations of Corexit EC9500A (0, 18 or 180 mg/L). Scenarios (3) and (4): Phenanthrene sorption was carried out with 180 mg/L of dispersant, but desorption without or with 180 mg/L of Corexit EC9500A. Experimental conditions: loamy sand = 1.05 g, sandy loam = 0.21 g, initial phenanthrene = 12–864  $\mu\text{g/L}$ , pH = 6.8–7.7, and solution volume = 42 mL.

**Figure 18** shows equilibrium phenanthrene uptake by the sediments in the presence of various concentrations of the dispersant. For loamy sand, phenanthrene uptake increased nearly linearly from 15.8 to 21.8  $\mu\text{g/g}$  when the dispersant concentration increased from 0 to 230 mg/L. Further increase of the dispersant concentration to 860 mg/L resulted in a steady, though lesser, increase in phenanthrene sorption (24.7  $\mu\text{g/g}$ ). The increment in phenanthrene uptake concurs with the sorption isotherm of the dispersant (**Figure 13**), and is associated with elevated uptake of the dispersant on the sediments. Taken together that the dispersant can boost both water solubility and sediment uptake of phenanthrene, **Figure 18a** indicates that in the low dispersant concentration range (0–230 mg/L), the dispersant more favors sorption enhancement; in the higher concentration range (230–860 mg/L), the sorption enhancement is largely offset by the solubility enhancement.



**Figure 18. Phenanthrene uptake by (a) loamy sand and (b) sandy loam sediments.**

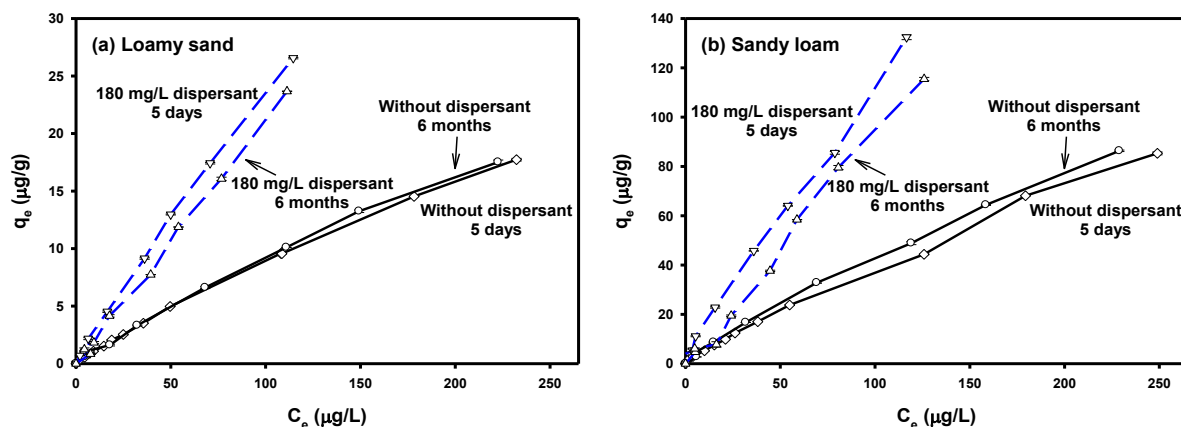
Experimental conditions: loamy sand = 1.05 g, sandy loam = 0.21 g, initial phenanthrene = 600  $\mu\text{g/L}$ , pH = 6.8–7.4, and solution volume = 42 mL. Numbers in brackets refer to the corresponding equilibrium dispersant concentration, arrows indicate the points where the equilibrium concentration may exceed CMC, and  $q_e$  denotes equilibrium uptake. Corexit EC9500A was used as the model dispersant.

It is noteworthy that the apparent CMC value (22.5 mg/L) was exceeded at the initial dispersant concentration of 86 mg/L and higher. Yet, the slope (proportionality) of the  $q_e$  against dispersant dosage remained nearly the same over the concentration range of 0–230 mg/L (**Figure 18a**). This observation can be attributed to: 1) the surfactants of the dispersant were not equally sorbed by the sediment (e.g., Tween 85 is likely more preferably sorbed than the more soluble Tween 80 and DOSS), resulting an elevated CMC value; 2) micelles were not fully developed (i.e., only associates were formed); and/or 3) the number of the aqueous micelles was not enough to outweigh the sink effect of the sorbed surfactants. However, further increasing the dispersant concentration to above 230 mg/L diminished the percentage uptake of the dispersant, resulting in the reduced distribution coefficient (i.e., the smaller slope of the uptake curve) (**Figure 18a**).

For the sandy loam sediment, the effect of the dispersant on phenanthrene sorption was concentration-dependent. The dispersant displayed a sharp increase in phenanthrene sorption in the dispersant concentration range of 0–230 mg/L (**Figure 18b**). The uptake reached a maximum (108.8  $\mu\text{g/g}$ ) at a dispersant level of 230 mg/L followed by decreased uptake to 105.1  $\mu\text{g/g}$  when the dispersant was further increased to 860 mg/L. Again, the sharply enhanced phenanthrene uptake in the low dispersant concentration range is attributed to the dispersant being more favorably sorbed by the sediment. This is evident by comparing the magnitude of the two contrasting effects of the dispersant: increasing the dispersant concentration from 18 to 180 mg/L increases the solubility of phenanthrene by 2.4 times, but

also increases the sediment uptake of the dispersant by 4.6 times. However, at elevated dispersant concentrations (343–860 mg/L), a decreasing trend in phenanthrene uptake was observed. The decrease in phenanthrene uptake can be attributed to: 1) partial leaching of SOM from the sediment at elevated dispersant concentrations (though SOM leaching by seawater without dispersant was negligible), resulting in reduced sediment uptake of both phenanthrene and the dispersant; and 2) formation of micelles, causing more phenanthrene to partition in the solution.

**Figure 19** shows that in the absence of the dispersant, the phenanthrene sorption capacity for both sediments slightly increased after 6 months of aging. The aging effect is attributed to mass transfer limitations through extremely narrow and tortuous paths or in condensed matrix structure of SOM (Pignatello and Xing 1995). However, in the presence of the dispersant, the sorption capacity of phenanthrene slightly decreased after 6 months of aging, although the overall sorption capacity remained much higher than that without dispersant. The capacity drop is probably associated with dispersant-facilitated partial leaching of SOM, and partial dissolution of sorbed dispersant molecules resulting from, for example, dissolution of mineral cations (e.g.,  $\text{Ca}^{2+}$ ) from the sediments (Yang et al. 2006b).



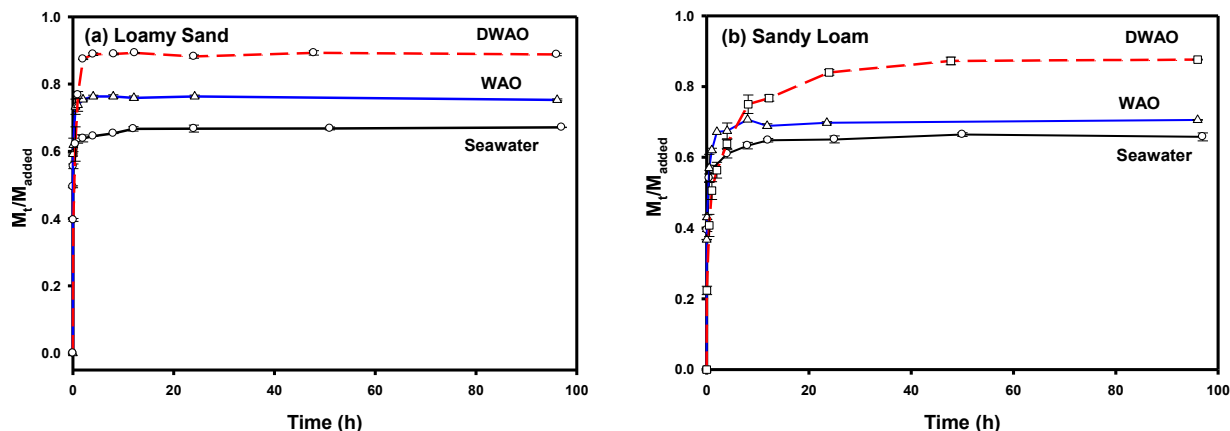
**Figure 19. Effects of aging time on phenanthrene uptake.**

(a) loamy sand and (b) sandy loam. Experimental conditions: loamy sand = 1.05 g, sandy loam = 0.21 g, initial phenanthrene concentration = 12–864  $\mu\text{g/L}$ , Corexit EC9500A = 0 or 180 mg/L, pH = 6.6–7.7, and contact time = 5 days to 6 months. Data are plotted as mean of duplicates, and error bars indicate standard deviation from the mean.

### 3.1.5. Effects of WAO and DWAO on sediment sorption of phenanthrene

**Figure 20a** shows that the equilibrium uptake of phenanthrene on loamy sand reached 67% without oil, 75% with WAO, and 89% with DWAO ( $p$  value < 0.001 at the 0.05 level of significance). The presence of WAO or DWAO increased the  $K_d$  values from 81 mL/g for plain sediment to 120 mL/g with WAO and 324 mL/g with DWAO. Likewise, **Figure 20b** shows that WAO and DWAO increased the equilibrium phenanthrene uptake on sandy loam by 5% and 22%, respectively ( $p$  value < 0.05 at the 0.05 level of significance); and the  $K_d$  values from 388 to 490 (with WAO) and 1467 mL/g (with DWAO).

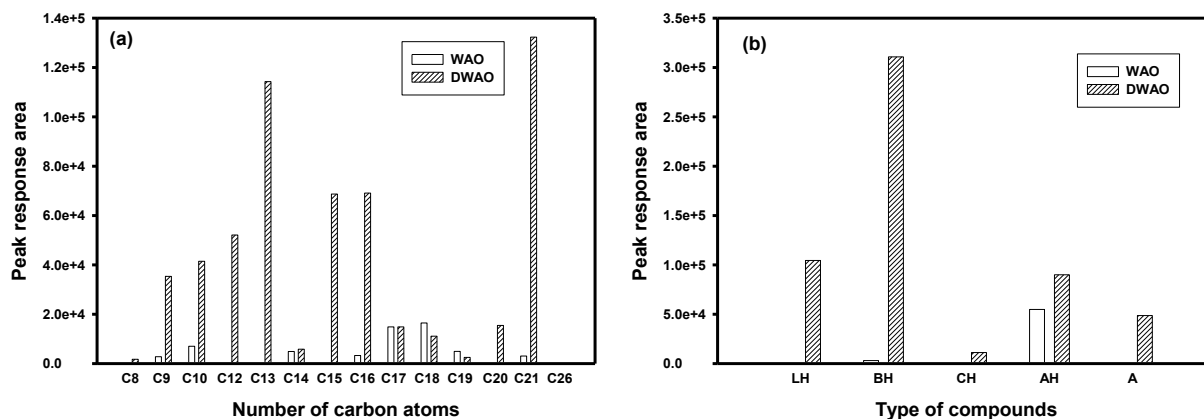




**Figure 20. Effects of WAO and DWAO on sorption kinetics of phenanthrene.**

(a) loamy sand and (b) sandy loam. Experimental conditions: loamy sand = 1.05 g, sandy loam = 0.21 g, initial phenanthrene = 600  $\mu\text{g/L}$ , solution volume = 42 mL, and pH = 6.7–7.4. WAO was prepared at an oil-to-seawater volume ratio of 1:200, resulting in a WAO of 7.8 mg/L as TOC. DWAO was prepared at a dispersant-to-oil-to-seawater volume ratio of 1:20:4000, resulting in a DWAO of 42 mg/L as TOC.  $M_t$ : phenanthrene mass uptake at time  $t$ , and  $M_{\text{added}}$ : total mass in the system.

**Figure 21a** shows the distribution of the hydrocarbons in WAO and DWAO based on the number of carbon atoms. The presence of the dispersant increased the fractions of C8-10, C12-16, C20, C21, and C26 hydrocarbons. **Figure 21b** presents the distribution of the hydrocarbons based on the type of the compounds, i.e., linear aliphatic hydrocarbons (LH), branched aliphatic hydrocarbons (BH), cyclic aliphatic hydrocarbons (CH), aromatic hydrocarbons (AH), and alkenes (A). The dispersant greatly increased the amounts of LH, BH, CH, AH, and alkenes. As would be expected, more hydrocarbons are found in the dissolved phase in the system with added dispersant.



**Figure 21. GC-MS analysis of WAO and DWAO.**

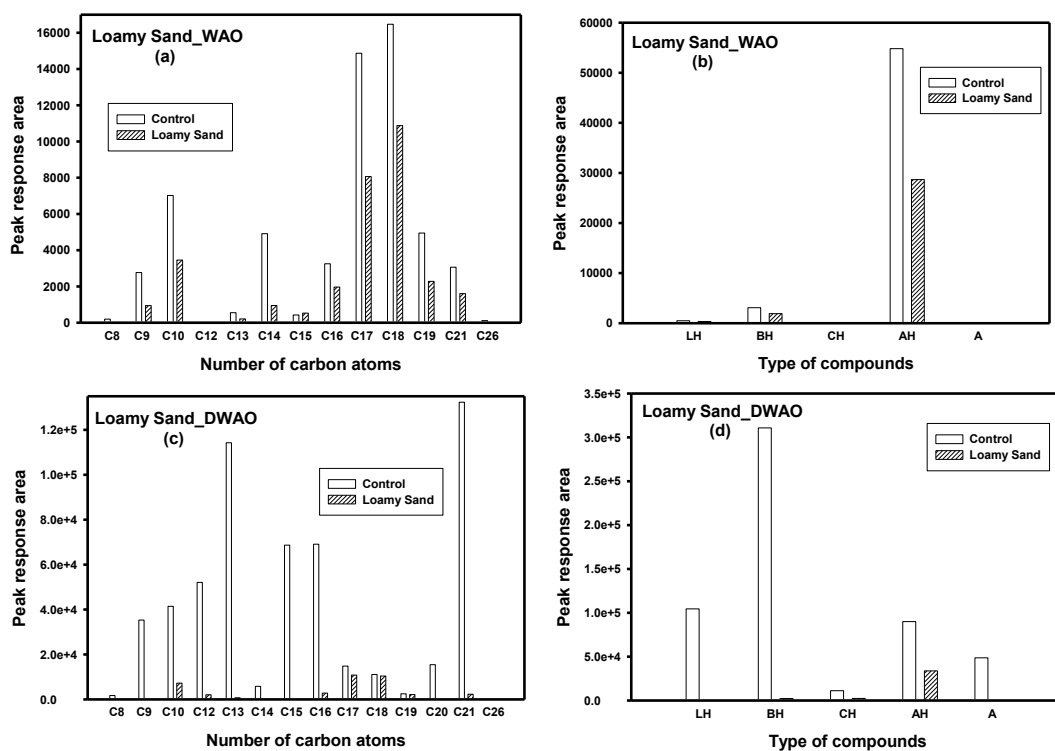
(a) As a function of the number of carbon atoms, and (b) as a function of the type of chemical compounds. LH: linear aliphatic hydrocarbons; BH: branched aliphatic hydrocarbons; CH: cyclic aliphatic hydrocarbons; AH: aromatic hydrocarbons; and A: alkenes.

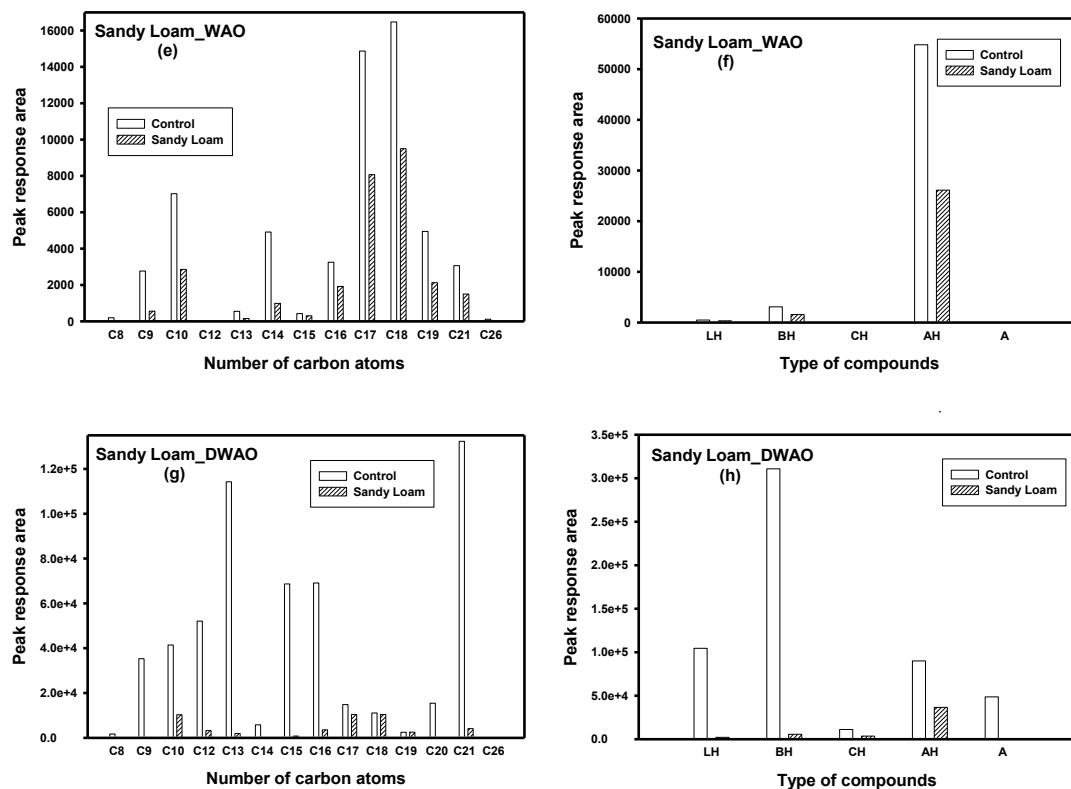
**Figure 22** shows hydrocarbon distributions of WAO and DWAO in the aqueous phase before and after sorption to the sediments. For WAO, the fractions C8-10, C13-14, C16-19, C21, and C26 were remarkably removed by both sediments (**Figures 22a** and **e**). In terms of types of hydrocarbons, loamy sand removed 30% of LH, 38% of BH, 48% of AH, and 81% of alkenes (**Figure 22b**), whereas sandy

loam removed 33%, 49%, 52%, and 65%, respectively (**Figure 22f**). Evidently, sorption of LH, BH, AH, and alkenes is responsible for enhanced phenanthrene uptake by the sediments in the presence of WAO.

**Figures 22d** and **22h** reveal that both sediments removed nearly all of LH, BH, and alkenes, loamy sand removed 79% of CH and 63% of AH, and sandy loam removed 68% of CH and 59% of AH. Therefore, the further enhanced phenanthrene uptake is attributed to elevated uptake of LH, BH, AH, CH, and alkenes along with the dispersant in the presence of DWAO.

The WAO-facilitated phenanthrene sorption is attributed to the “plasticizing” effect of oil hydrocarbons on the structure and properties of SOM, i.e., the sorption of WAO may swell SOM and convert part of glassy SOM to a more rubbery polymer, making the hydrophobic interior sorption sites more accessible for phenanthrene (Jonker et al. 2003). In addition, the uptake of WAO renders the sediment surface more hydrophobic and affords additional sorption pools for phenanthrene. The presence of the dispersant further enhances the effect of WAO. On the one hand, the dispersant causes dispersion or dissolution of more oil hydrocarbons in the solution, which in turn results in transferring more hydrocarbons to the sediment-SOM phase. On the other hand, the sorption of dispersant onto sediments provides more sorption sites for oil hydrocarbons and PAHs, bestowing additional sorption capacity for phenanthrene.





**Figure 22. Hydrocarbon compositions of WAO and DWAO.**

WAO and DWAO were prepared in the same manner as in Figure 21. Control: no sediment adsorption; Loamy sand and sandy loam: after adsorption by the respective sediments.

### 3.1.6. Conclusions

This section of study investigated effects of oil and Corexit EC9500A on sorption and desorption of a model PAH with two representative Gulf Coast marine sediments. The primary findings are summarized as follows:

- 1) The dispersant poses two contrasting effects on the distribution of phenanthrene. On the one hand, it increases the aqueous solubility, which tends to reduce sediment sorption of the PAH. On the other hand, sediment sorption of the dispersant provides additional partitioning capacity for the PAH. Overall, increasing the concentration of the dispersant increases sediment uptake of the PAH.
- 2) The dispersant itself is subject to sorption to sediments with an S-shaped isotherm, likely indicative of transition from monomeric uptake in the low concentration region to formation of hemimicelles and admicelles at elevated concentrations. Yet, the sorption was reversible throughout the concentration range examined.
- 3) Batch sorption kinetic tests showed that the presence of the dispersant at 18 mg/L enhanced the sediment uptake of phenanthrene by up to 7%. The sorbed dispersant serves as a more effective sorbent for phenanthrene than native SOM with a 2.7-times greater distribution coefficient than  $K_{oc}$ .
- 4) Equilibrium sorption data reveal that the presence of the dispersant during sorption progressively

increases phenanthrene sorption capacity for both sediments. The presence of the dispersant during desorption resulted in remarkable sorption hysteresis.

- 5) The dual-mode isotherm and kinetic models were able to adequately simulate phenanthrene sorption isotherms and kinetic data for both sediments in the presence of various concentrations of the dispersant.
- 6) The presence of WAO and DWAO increases phenanthrene uptake of loamy sand by 8% and 22%, respectively, and that of sandy loam by 5% and 22%. The enhanced phenanthrene uptake by the sediments is attributed to elevated uptake of various classes of oil hydrocarbons such as LH, BH, AH, CH and alkenes along with the dispersant.

The results are important for understanding the roles of oil dispersants on environmental distribution, fate, and transport of spilled oil and persistent oil components in marine water-sediment systems.

### **3.2. Effects of Oil Dispersant on Solubilization, Sorption, and Desorption of Polycyclic Aromatic Hydrocarbons in Sediment-Seawater Systems**

Crude oil is a mixture of more than 17,000 hydrocarbon compounds with varying volatility, solubility and toxicity (Sammarco et al. 2013). The light molecular weight hydrocarbons are relatively more soluble in water, such as PAHs, monoaromatic hydrocarbons, phenols and nitrogen- and sulfur-containing heterocyclic compounds, which are often of priority concern due to their high mobility and toxicity (Gong et al. 2014). After an oil spill, these compounds may be elevated in the marine environment. For example, during and after the *DWH* oil spill, elevated concentrations of PAHs and alkylated PAHs were detected, including naphthalene, 1-methylnaphthalene, phenanthrene, pyrene, chrysene, and benzo(a)pyrene in the Gulf of Mexico. During the accident, up to 0.13 mg/L of naphthalene and 0.34 mg/L of pyrene were detected on the sea surface near the site, and 1.22 mg/L and 0.02 mg/L, respectively, near the wellhead. The alkylated naphthalene concentration reached 0.71 mg/L in the surface water and 32.1 mg/L near the wellhead (Diercks et al. 2010).

Oil dispersants are designed to disperse oil in the water column, enhance biodegradation and mitigate the impacts on near-shore ecosystems (Kujawinski et al. 2011). Surfactants are known to affect sorption of PAHs by soil and sediment, but little is known on the effects of oil dispersants. In water-sediment systems, surfactant molecules can exist as micelles, monomers, hemimicelles and admicelles, depending on the surfactant concentration. Partitioning of oil or PAHs into surfactant micelles or monomers can increase the apparent solubility, thereby dispersing or solubilizing more oil-PAHs in the water column. On the other hand, the surfactants can also be adsorbed on the particles to form hemimicelles or admicelles, providing additional capacity to adsorb PAHs (Ko et al. 1998b). Gong et al. (2014b) reported that Corexit EC9500A enhanced uptake of phenanthrene onto a sandy loam sediment.

The presence of oil or dispersed oil may alter the distribution of PAHs in sediment-water systems. Walter et al. (2000) investigated distribution of 9 PAHs in an oil-contaminated soil system and observed that more PAHs were distributed in the adsorbed oil and liquid oil phases than in the aqueous phase. However, there has been little information available on the effects of oil dispersants and dispersed oil.

During the *DWH* oil spill,  $\sim 2.91 \times 10^6$  L Corexit EC9500A was applied at the 1500 m deep wellhead (Kujawinski et al. 2011). The deepwater conditions are characterized by high pressure ( $\sim 16$  MPa), low temperature ( $\sim 4$  °C), little or no light, constant salinity (3.5%), and sluggish currents ( $< 0.25$  knots)

(Glover and Smith 2003). However, there has been no information available on sorption and desorption behaviors of oil dispersant and PAHs under such conditions.

The overall goal of this study was to investigate effects of a model oil dispersant (Corexit EC9500A) on the solubilization, sorption and desorption of two model parent PAHs (naphthalene and pyrene) and one alkylated PAH (1-methylnaphthalene) in sediment-seawater systems. The specific objectives were to: 1) investigate effects of the dispersant on solubilization of the PAHs; 2) examine sediment sorption and desorption behaviors of the dispersant under surface water and deepwater conditions; 3) determine the effects of the dispersant and dispersed oil on sediment sorption and desorption of the PAHs and elucidate the underlying mechanisms; and 4) test the PAH-sediment interactions under deepwater conditions in the presence of the dispersant.

### **3.2.1. Materials and methods for solubilization, sorption and desorption of polycyclic aromatic hydrocarbons**

#### **3.2.1.1. Materials**

All chemicals were of analytical grade or higher. Naphthalene, 1-methylnaphthalene, and pyrene were purchased from Alfa Aesar.  $^{14}\text{C}$ -radiolabeled naphthalene (specific activity: 52 mCi/mmol) and pyrene (60 mCi/mmol) were purchased from Moravek Biochemicals, Inc..

Seawater was collected at Grand Bay, Alabama (N30.38, W88.31), and treated with the same methods as shown in Section 3.1.1.1. The salient properties of the treated seawater include: pH = 8.88, dissolved organic carbon (DOC) = 0.43 mg/L, salinity = 3.2 ‰,  $\text{Cl}^-$  = 18.55 g/L,  $\text{NO}_3^-$  = 2.55 g/L and  $\text{SO}_4^{2-}$  = 4.25 g/L. Two marine sediments, a loamy sand and a sandy loam, were the same as used in previous studies, the salient properties of the sediments are shown in **Table 5**.

#### **3.2.1.2. Dispersant-enhanced solubilization of PAHs**

The apparent solubility of PAHs in seawater was measured in the presence of various concentrations of the dispersant based on the procedure by Zhao et al. (2005). Individual solutions of a supersaturated PAH were prepared by mixing 0.1 g of a PAH with 43 mL of seawater containing 0 to 200 mg/L of the dispersant. After being mixed for 3 days, the vials were centrifuged at 3000 rpm (1509  $g \times$  force) for 10 minutes and 10 mL of the supernatants were carefully sampled and diluted with 1.0 mL of methanol. And the PAH concentration was then quantified via HPLC (HP Series 1100) equipped with a UV detector and a Zorbax SB-C18 column (150 $\times$ 468 mm). The mobile phase consisted of 80% acetonitrile, 19.9% water, and 0.1% phosphoric acid. The operating flow rate was set at 1.0 mL/min at 40 °C with an optimal wavelength of 254 nm.

#### **3.2.1.3. Effects of dispersant on sorption and desorption of PAHs**

Stock solutions for individual PAHs were prepared at 1 g/L in methanol. To facilitate PAH analysis,  $^{14}\text{C}$ -radiolabeled PAHs were added into the stock solutions (1:50 v/v) before use. Sorption kinetic tests of PAHs with the two sediments were carried out in 44 mL glass vials fitted with Teflon-lined septa. PAH-laden seawater solutions were prepared by injecting 0.6 mL (for naphthalene or 1-methylnaphthalene) or 0.06 mL (for pyrene) of a PAH stock solution in 1000 mL of the seawater and then mixed for 12 hours in dark. To test the dispersant effects, Corexit EC9500A was added before mixing to give a dispersant concentration of 18 mg/L. The methanol content was < 0.1 vol.% to avoid co-solvent effect. PAH sorption was initiated by mixing a PAH solution with a sediment of known mass.

Following the kinetic tests, sorption isotherm tests were carried out at the same solid:solution ratio and in a broader range of initial PAH concentrations. The sorption equilibrium was reached in 3 days. The sorption isotherms were then obtained by measuring the equilibrium PAH distributions. To acquire the corresponding desorption isotherms, the vials were centrifuged at 3000 rpm for 10 minutes and then 96% to 99% of the supernatant was replaced with an equal volume of sediment-amended seawater to start the desorption tests. The sediment-amended seawater was prepared by mixing the sediment and seawater at the same solid:solution ratio as in the equilibrium tests to maintain the same background compositions. To test the dispersant effects, 18 or 180 mg/L of the dispersant was added in the solutions at the beginning of desorption. The vials were then re-equilibrated for 3 days under rotating to get the desorption isotherms.

To test the dispersant effects under deepwater conditions, equilibrium sorption experiments were conducted in 200 mL high-pressure stainless-steel reactors (Huihua Special Instruments, Tianjin, China) at the same solid:solution ratio as in the isotherm tests. NaCl was added to increase the salinity of seawater from 3.2‰ to 3.5‰. The reactor pressure was kept at  $16 \pm 0.5$  MPa and the reactors were then equilibrated for 3 days under rotating in an incubator set at 4 °C. The dispersant dosage was 0–5000 mg/L for naphthalene and 1-methylnaphthalene, and 0–350 mg/L for pyrene.

#### **3.2.1.4. Effects of WAO and DWAO on sorption of PAHs**

WAO and DWAO were prepared following the procedures described in Section 3.1.1.6. Equilibrium sorption tests were then carried out in the presence of WAO or DWAO following the same experimental procedure.

#### **3.2.2. Dispersant-facilitated solubilization of PAHs**

**Figure 23** shows solubilization of the three model PAHs as a function of the dispersant dosage. The apparent solubility for each PAH nearly linearly increased with increasing dispersant concentration from 0 to 200 mg/L. The apparent CMC of Corexit EC9500A was determined to be 22.5 mg/L in seawater. It is noteworthy that the dispersant enhanced the PAH solubility even at submicelle (< CMC) concentrations. At 18 mg/L, the dispersant increased the solubility by 5%, 11% and 44% for naphthalene, 1-methylnaphthalene and pyrene, respectively; at the point of CMC, the solubility enhancements were 7%, 12% and 71%, which were further increased to 27%, 59% and 660%, respectively, at 200 mg/L of the dispersant. Evidently, the formation of stable micelles turned the monomeric solvent solubilization into the more effective micellar solubilization.

The observed solubility enhancement in the submicelle concentrations of the dispersant contrasts those in pure surfactant systems. For example, Edwards et al. (1991) reported that individual pure surfactants had negligible effect on solubilization of the PAHs at < CMC, and they observed an abrupt solubility enhancement at CMC. Likewise, Mohamed and Mahfoodh (2006) reported the solubility of naphthalene remained constant when the concentration of an anionic surfactant (SDS) was < CMC. However, when SDS was mixed with a nonionic surfactant Tween 80, enhanced solubilization at < CMC was evident for both naphthalene and pyrene. The researchers attributed the observation in part to the much lowered CMC of the mixed micelles than that of single SDS and to the synergistic surfactant–surfactant interaction occurring within the solubilization sites. Lippold et al. (2008) reported a slight solubility enhancement of pyrene at submicellar concentrations of SDS and attributed it to the formation of pre-micellar aggregates. Yet, the submicellar solubilization was overshadowed by the sharp solubility rise upon micellar solubilization at CMC.

**Figure 23** reveals the important roles of the synergistic effects of the solvent-surfactants mixture at both submicellar and micellar concentrations. Corexit EC9500A contains one anionic, three nonionic surfactants and three solvents (**Table 1**). In general, nonionic surfactants are more effective in solubilizing hydrophobic hydrocarbons than anionic surfactants (Mohamed and Mahfoodh, 2006) due to the lower CMC for the former. However, nonionic surfactants are poorly soluble, which would confine the formation of micelles and dispersion of PAHs or oil. Mixing with anionic surfactants and solvents promotes solubilization of the nonionic surfactants, and the interactions between the nonionic and anionic surfactants decrease the repulsive forces among the ionic heads, facilitating formation of more and denser micelles at an overall lower CMC (Zhao et al. 2005). Tokuoka et al. (1995) concluded that the effective solubilization area and the radius of mixed micelles are larger than those of pure surfactant micelles. Kamil and Siddiqui (2013) asserted that solubilization of PAHs commenced at the surfactant CMC and was proportional to the concentration of surfactant in micelles.

Indeed, the CMC value of Corexit EC9500A is higher than that for Tween 80 (14 mg/L), and nearly the same as for Tween 85 (23 mg/L), but much lower than that for DOSS (578 mg/L), indicating that the Tween surfactants are the predominant ingredients in the dispersant. The unusual solubility enhancement at dispersant < CMC is attributed to the interactions between the different surfactants and the solvents, which facilitated the formation of aggregates and mixed micelles below the overall CMC. Martino and Kaler (1995) reported that propylene glycol decreases the value of the Hamaker constant by replacing the water molecules in the lamellar phase. As a result, the lamellar stability is lowered, and the inter-bilayer and intra-aggregate interactions between nonionic and anionic surfactants promote the formation of mixed micelles.

**Figure 23** also reveals that the dispersant was much more effective in solubilizing more hydrophobic PAHs. This is consistent with the results by Mohamed and Mahfoodh (2006), who studied solubilization of naphthalene and pyrene by SDS-Tween 80 mixed surfactants. For relatively less hydrophobic PAHs such as naphthalene, the solubilization occurs at the mixed micelle-water interface, and the synergistic effects of the mixed surfactants and solvents are virtually absent due to the very weak interactions between the hydrophilic groups of the two surfactants. In contrast, pyrene is most likely solubilized in the micellar cores, which makes better use of the synergistic effects. (Gao et al. 2002) stated that SDS molecules in SDS-Tween 80 binary micelles have more restricted motional freedom, and thus a more rigid microenvironment for pyrene, than in SDS self-aggregated micelles. Conventionally, the effectiveness of a surfactant to solubilize a given solubilizate is quantified in terms of molar solubilization ratio (MSR), which reflects the slope of the solubility enhancement lines (**Figure 23**) at surfactant > CMC (Srivastava and Ismail 2014). In this work, the lack of the exact molecular compositions of the dispersant prohibited from obtaining the MSR values. Consequently, we adopted an alternative approach by quantifying the PAH partitioning between micelles and water (Zhou and Zhu 2005). At dispersant  $\geq$  CMC, the micelle-water partition coefficient,  $K_{mic}$  (L/g), is defined on a mass concentration basis as:

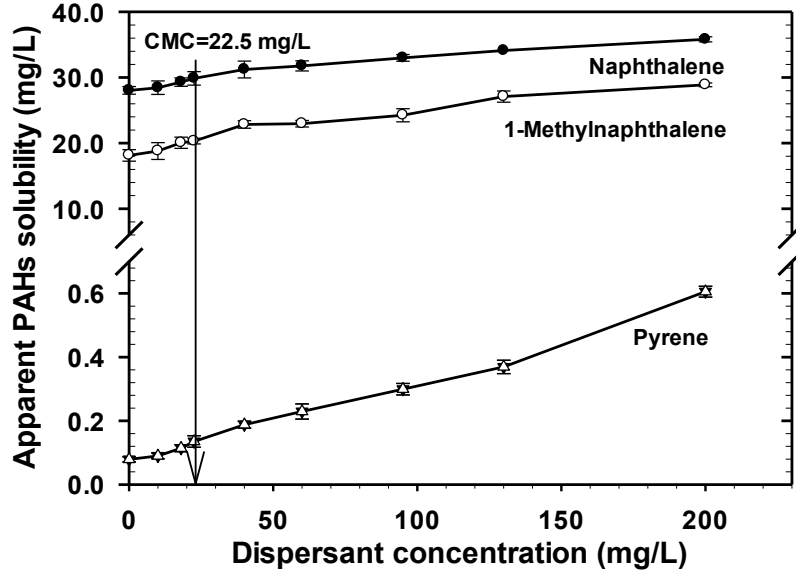
$$K_{mic} = \frac{S_{mic}}{S_w C_{mic}} = \frac{S - S_{CMC}}{S_w (C_{dis} - C_{CMC})} \quad (15)$$

where  $S_{mic}$  (g/L) is the concentration of a PAH in the micelles,  $S_w$  (g/L) is the PAH solubility in seawater free of dispersant,  $C_{mic}$  (g/L) is the concentration of dispersant in the form of micelles, and  $S$  and  $S_{CMC}$  are the apparent solubility of the PAH at a dispersant concentration of  $C_{dis}$  (g/L) and at the critical micelle concentration ( $C_{CMC}$ ), respectively.

In the submicellar range, we define a pseudo-partition parameter  $K_S$  (L/g) as:

$$K_S = \frac{S_S}{S_w C_{dis}} = \frac{S - S_w}{S_w C_{dis}} \quad (16)$$

where  $S_S$  (g/L) is the concentration of a PAH solubilized through solvents and surfactant monomers or aggregates at  $< CMC$ .



**Figure 23. Apparent solubility of three model PAHs.**  
Dispersant: Corexit EC9500A.

**Table 9** lists the  $K_{mic}$  and  $K_S$  values based on linear regression fittings. The more hydrophobic PAHs have larger  $K_{mic}$  and  $K_S$  values, implying the greater sensitivity to the dispersant. This trend agrees with the previous observations with pure anionic surfactants or nonionic surfactants (Ko et al., 1998; Mohamed and Mahfoodh, 2006; Zhou and Zhu, 2005).

**Table 9. Parameters for the solubilization of three PAHs**

	$K_S$ (L/g) ( $R^2$ )	$K_{mic}$ (L/g) ( $R^2$ )	$\log K_{ow}$
Naphthalene	2.46 (0.93)	1.14 (0.97)	3.36
1-methylnaphthalene	5.81 (0.95)	2.54 (0.94)	3.87
Pyrene	24.18 (0.93)	32.24 (0.98)	5.18

With the three PAHs, we observed a good linear correlation between  $K_{mic}$  (and  $K_S$ ) and  $K_{ow}$  as follows (though more PAHs should be tested to validate the equations):

$$K_{mic} = 0.0002K_{ow} + 0.8272 \quad (R^2 = 0.99) \quad (17)$$

$$K_S = 0.0001K_{ow} + 3.4431 \quad (R^2 = 0.99) \quad (18)$$



### 3.2.3. Effects of dispersant on sorption and desorption of PAHs

**Figure 24** shows the sorption kinetics of the three PAHs on the two marine sediments with or without the dispersant. In all cases, rapid initial sorption rate was observed, and equilibrium was reached within 24 hours. The presence of 18 mg/L of the dispersant increased the equilibrium naphthalene uptake from 53.0% to 55.9% for sandy loam, and from 44.2% to 47.5% for loamy sand. Likewise, the dispersant increased the 1-methylnaphthalene uptake from 52.3% to 57.5% and pyrene uptake from 74.3% to 85.3% by loamy sand. In all cases, the *t*-test *p* values are <0.05 at the 0.05 level of significance. Evidently, the dispersant facilitated sorption of more PAHs to the sediments.

The dual-mode kinetic model was able to adequately interpret the sorption kinetic data (**Figure 24**). And based on the sorption isotherm parameters (**Table 10**), the diffusion parameter ( $D_D/r_0^2$ ) was obtained by fitting the model to the experimental data. In all cases, the presence of the dispersant increased the diffusivity, which can be attributed to the dispersant softening of SOM and the added sinks of sorbed hemimicelles and admicelles (Pignatello 1998).

In a dispersant-free system, the PAH distribution coefficient ( $K_d$ , L/g) is defined as:

$$K_d = \frac{q_e}{C_e} \quad (19)$$

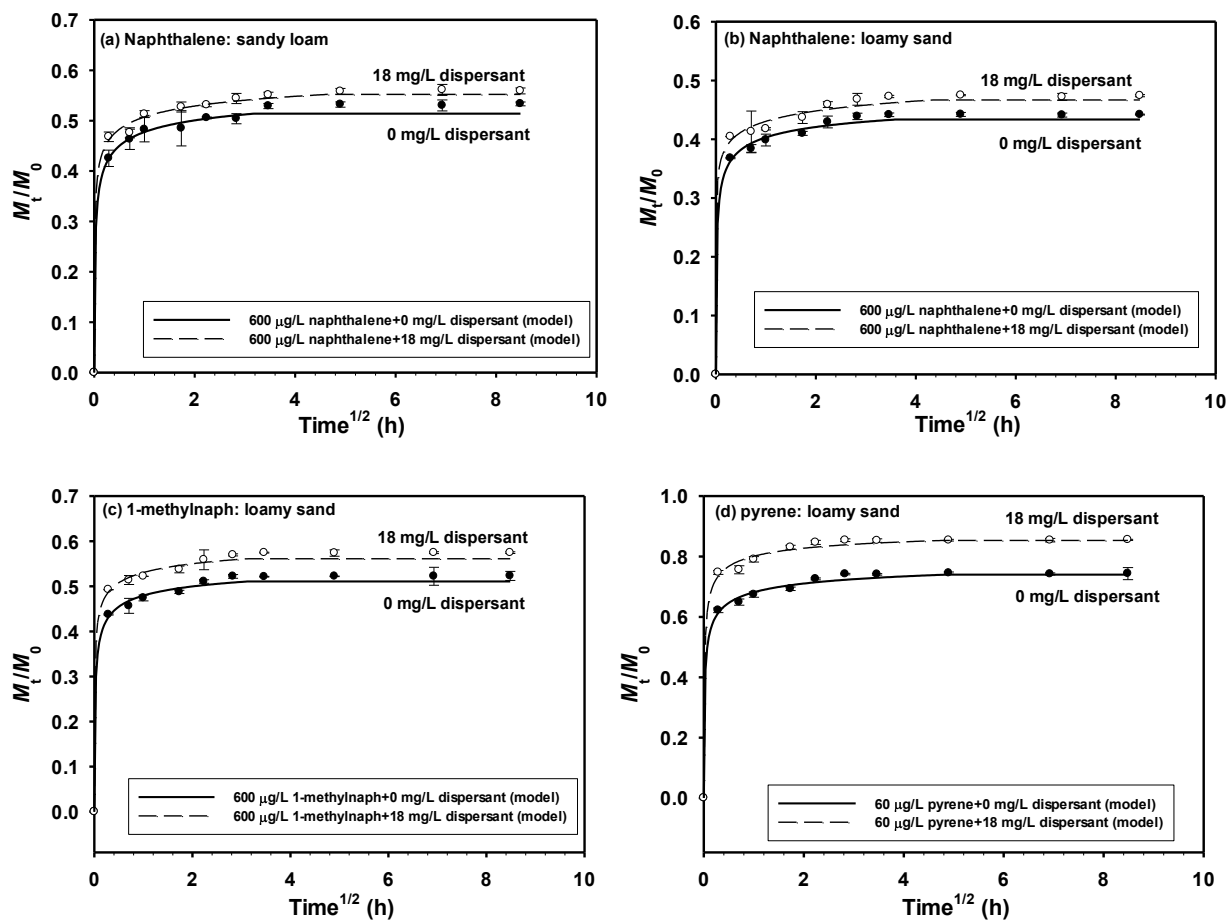
where  $q_e$  (mg/g) and  $C_e$  (mg/L) are PAH concentrations in the sediment and water phase, respectively. Accordingly, the sediment organic carbon-normalized distribution coefficient ( $K_{oc}$ , L/g) is given by:

$$K_{oc} = \frac{K_d}{f_{oc}} \quad (20)$$

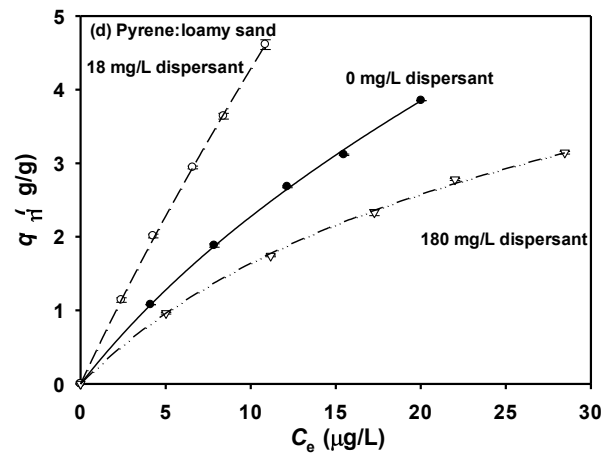
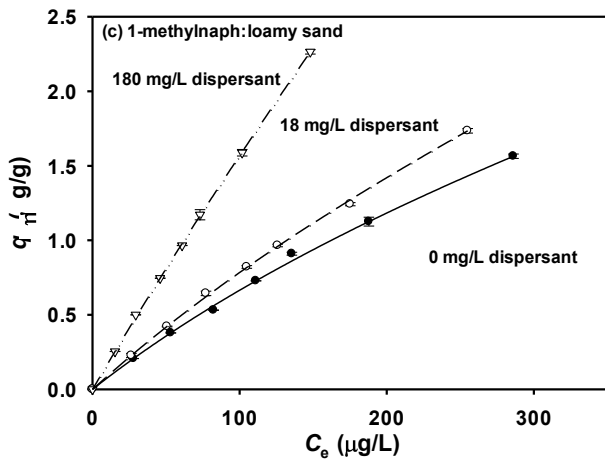
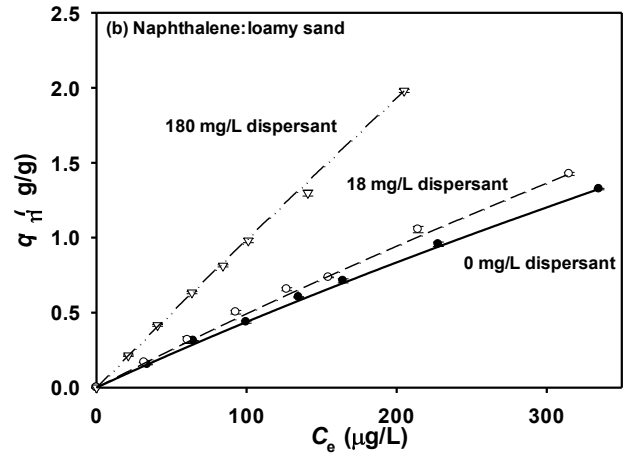
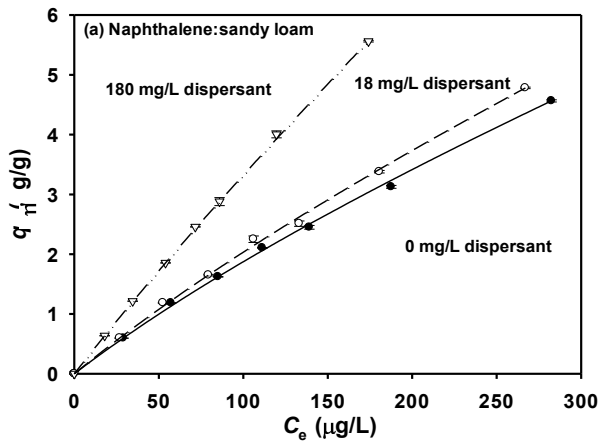
$$f_{om} = 1.72 \times f_{oc} \quad (21)$$

where  $f_{oc}$  and  $f_{om}$  are fractions of organic carbon and organic matter in sediment.  $K_d$  was taken as the mean based on the sorption isotherm data (**Figure 25**) and the values are given in **Table 10**.

**Figure 25** shows the PAH sorption isotherms at various concentrations of the dispersant. For all PAHs, sandy loam (SOM = 2.7%) exhibited greater sorption capacity than loamy sand (SOM = 0.7%). The dual-mode model nicely simulated the isotherms in all cases. Based on the model premises, the Langmuir term was set as constant at various dispersant concentrations, i.e., the dispersant effect on the PAH uptake is affected by the fitted  $K_D$  values (**Table 10**). The dispersant at 18 mg/L increased the uptake of all PAHs, e.g. it increased  $K_D$  for naphthalene by 22% with loamy sand and 238% for pyrene (**Table 10**). Further increasing the dispersant to 180 mg/L further increased  $K_D$  for naphthalene and 1-methylnaphthalene, but diminished sorption of pyrene, indicating that the dispersant effect is dependent on hydrophobicity of the PAHs. For more hydrophobic PAHs, the dispersant more profoundly enhances the PAH uptake at low dispersant dosages, but the solubilization effect of the dispersant outweighs the adsolubilization effect at elevated dispersant concentrations.



**Figure 24. Sorption kinetics of PAHs onto (a) sandy loam and (b, c, d) loamy sand sediments.** Corexit EC9500A = 0 or 18 mg/L.  $M_t$ : PAH mass uptake at time  $t$ , and  $M_0$ : total mass in the system. Symbols: Experimental data; Lines: Dual-mode model simulations.



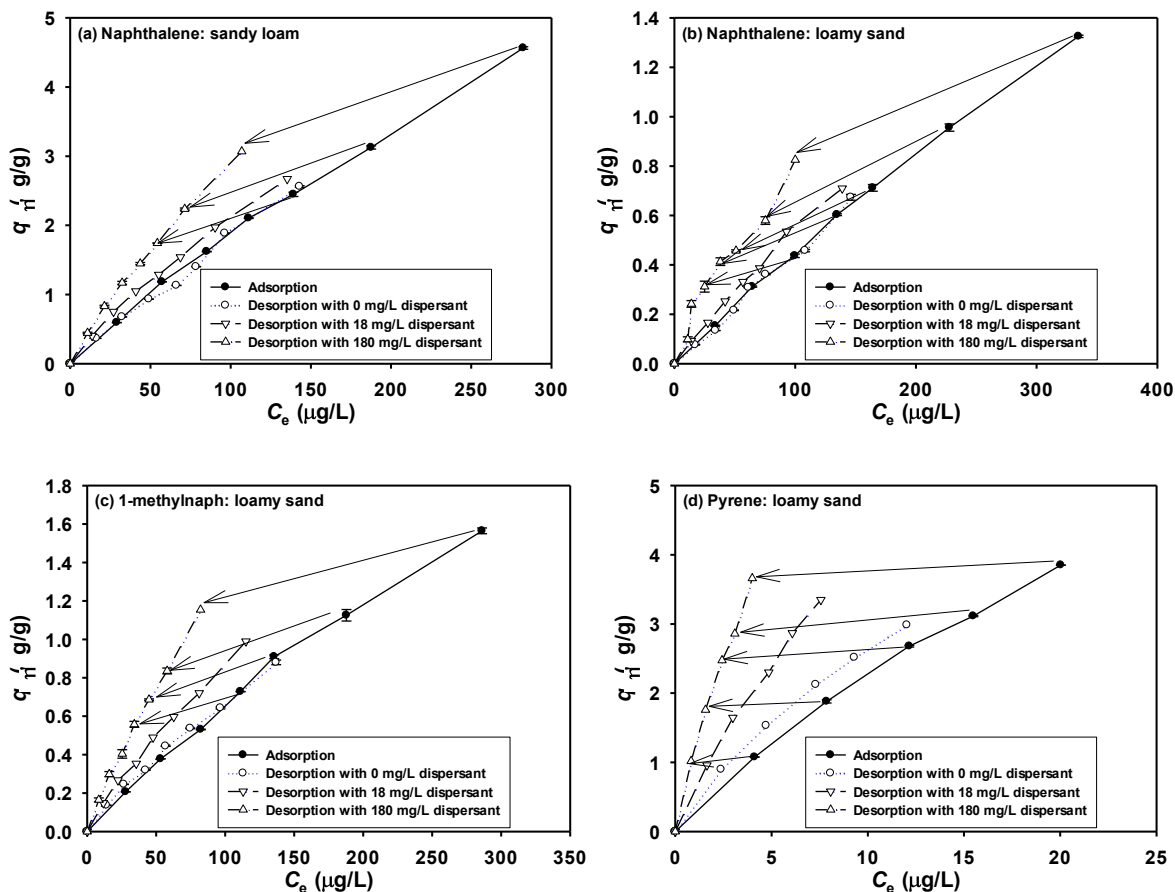
**Figure 25. Sorption isotherms of PAHs with (a) sandy loam, and (b, c, d) loamy sand sediments.** Corexit EC9500A = 0, 18 or 180 mg/L. Symbols: Experimental data; Lines: Dual-mode model simulations.  $q_e$ : Solid phase concentration of a PAH, and  $C_e$ : aqueous phase concentration of a PAH at equilibrium.

**Table 10. Equilibrium sorption parameters for PAHs onto sediments in the absence and presence of dispersant Corexit EC9500A**

PAHs	Soil	Initial dispersant (mg/L)	$K_D$ (mL/g)	$b$ (mL/mg)	$Q$ ( $\mu$ g/g)	$K_d$ or $K_d^o$ (mL/g)	$D_D/r_0^2$ (1/h)	$K_{oc}$ (mL/g)	$q_{dis}$ (mg/g)
Naphthalene	Sandy loam	0	10.80	3.56	3.02	18.5 $\pm$ 1.8	0.81		
		18	12.40	3.56	3.02	20.3 $\pm$ 1.8	0.98		
		180	28.90	3.56	3.02	34.0 $\pm$ 1.2			
Naphthalene	Loamy sand	0	2.49	1.40	1.54	4.2 $\pm$ 0.4	1.33	1032 $\pm$ 98	0.00
		18	3.03	1.40	1.54	5.0 $\pm$ 0.3	1.53		0.09
		180	7.98	1.40	1.54	9.8 $\pm$ 0.3			0.85
1-methylnaph	Loamy sand	0	2.56	2.80	1.87	6.1 $\pm$ 0.9	0.23	1498 $\pm$ 221	0.00
		18	3.75	2.80	1.87	7.2 $\pm$ 0.7	0.38		0.09
		180	11.60	2.80	1.87	16.1 $\pm$ 0.6			0.85
Pyrene	Loamy sand	0	84.50	48.35	4.38	222.9 $\pm$ 28.1	0.09	54769 $\pm$ 6880	0.00
		18	285.60	48.35	4.38	450.0 $\pm$ 22.5	0.13		0.62
		180	21.3	48.35	4.38	143.7 $\pm$ 31.2			4.58

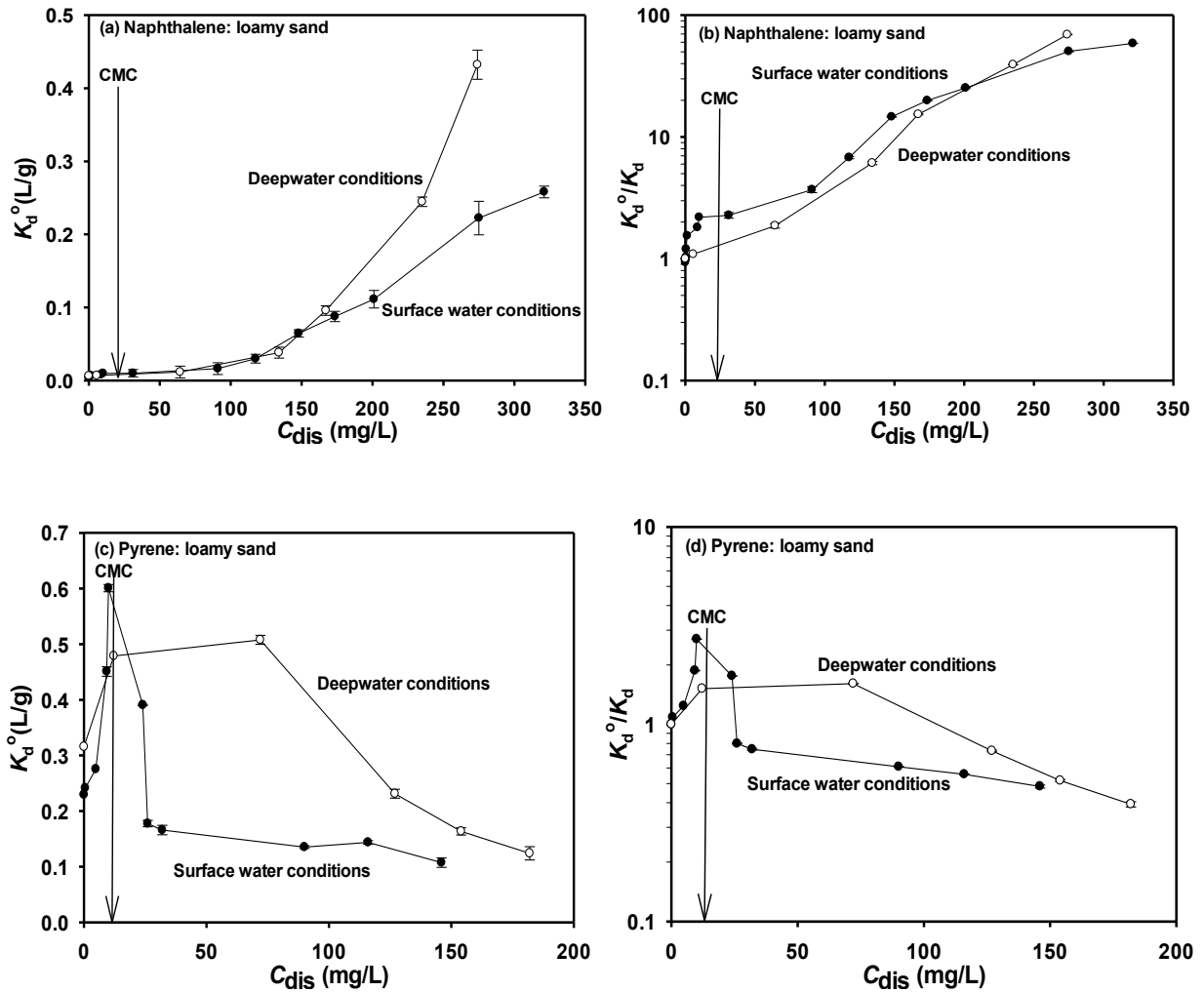
Note:  $K_d$  and  $K_d^o$  are calculated as mean $\pm$ standard deviation based on the experimental isotherm data (Figure 25).

**Figure 26** plots the sorption and desorption isotherms of each PAH at 0, 18 and 180 mg/L of the dispersant. In the absence of the dispersant, the sorption of naphthalene and 1-methylnaphthalene was fully reversible, though a modest but significant hysteresis was observed for pyrene. Notably, the presence of the dispersant induced a phenomenal sorption hysteresis for all cases, and the higher the dispersant concentration, the more the sorption irreversibility. The dispersant-facilitated hysteresis is attributed to the uptake of the dispersant and the dispersant adsolubilization of the PAHs. Zhang and Zhu (2010) reported that Tween 80 inhibited desorption of PAHs from soil and they attributed it to elevated hydrophobicity of soil.



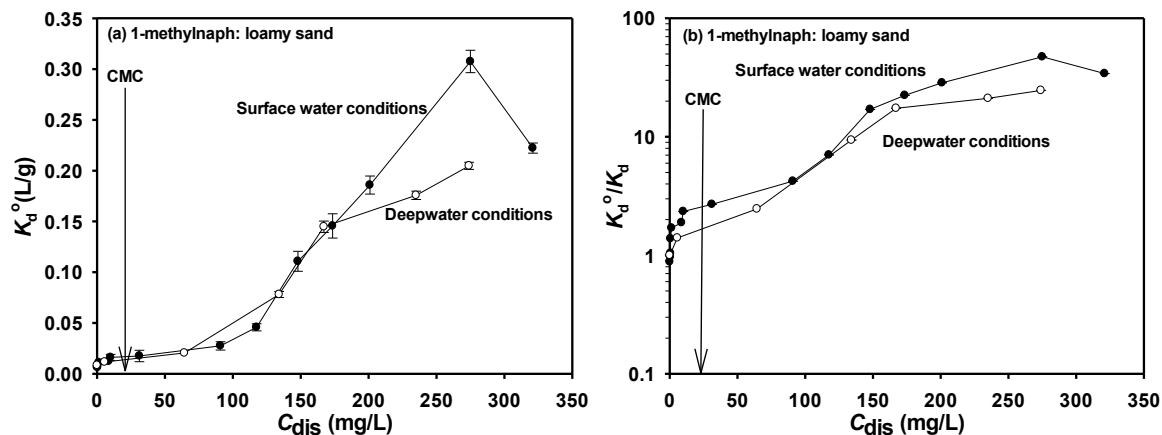
**Figure 26. Sorption and desorption isotherms of PAHs.**  
 (a) sandy loam and (b, c, d) loamy sand sediments. Corexit EC9500A = 0, 18 or 180 mg/L.

**Figure 27 and 28** compare the  $K_d^o$  and  $K_d^o/K_d$  to  $C_{dis}$  curves for the PAHs under the surface and deepwater conditions (16 MPa, 4 °C, salinity = 3.5 wt.%). For the less hydrophobic PAHs (naphthalene and 1-methylnaphthalen), the dispersant enhanced the PAH uptake to a lesser extent (i.e., a lower  $K_d^o/K_d$ ) under the deepwater conditions, though  $K_d^o$  increased steadily with increasing dispersant uptake. For pyrene, a much broader peaking profile was evident under the deepwater conditions.



**Figure 27. Equilibrium distribution coefficients of PAHs.**

(a, c) The apparent soil-water distribution coefficients ( $K_d^o$ ) of naphthalene and pyrene. (b, d)  $K_d^o / K_d$  for naphthalene and pyrene as a function of equilibrium Corexit EC9500A concentration under surface and deepwater conditions.



**Figure 28. Equilibrium distribution coefficients of 1-methylnaphthalene.**

(a) The apparent soil-water distribution coefficients ( $K_d^o$ ) of and (b)  $K_d^o / K_d$  as a function of equilibrium Corexit EC9500A concentration under surface and deepwater conditions.

Under the deepwater conditions, the solubility of naphthalene, 1-methylnaphthalene and pyrene dropped by 44.2%, 45.3% and 63.3%, respectively. The deepwater conditions also diminished the dispersant solubilization effectiveness. For instance, in the presence of 200 mg/L of the dispersant, the dispersant-facilitated solubility for the three PAHs decreased by 50.7%, 56.9% and 72.8%, respectively. Such solvent-driven process resulted in higher overall PAH uptake (i.e., higher  $K_d$ ) at lower temperature (He et al. 1995, Zhang et al. 2009). Then, the diminished dispersant effect (lower  $K_d^o / K_d$ ) under the deepwater conditions is attributed to the lowered dispersant uptake and heightened  $K_{oc}$ .

The salting-out effect plays an insignificant role in lessening the solubilization effect of the dispersant than temperature and pressure. Of the latter, temperature exerts more effects on the solubility than pressure (Oliveria et al. 2009). The surfactant CMC is remarkably heightened at the deepwater temperature, and the temperature effect is enlarged under saline conditions (Schick 1963). For instance, lowering temperature from 25 to 5 °C in a 0.6 M NaCl solution increased the CMC for n-dodecanol by 61% (Schick, 1963). Higher salt concentration lowers the CMC, but to a lesser extent. On the other hand, pressure was reported to be an important factor governing the formation and characteristics of surfactant micelles, and smaller micelles are formed under elevated pressure (Innocente et al. 2009), which diminishes the dispersant solubilization of PAHs.

### 3.2.4. Effects of WAO and DWAO on sorption of PAHs

Figure 29 shows that the presence of WAO and DWAO increases the uptake for all three PAHs on the sediment. The equilibrium uptakes of naphthalene, 1-methylnaphthalene and pyrene were enhanced by 3.2%, 5.5% and 8.6%, respectively in the presence of WAO, and 14.1%, 19.2% and 15.3% by DWAO. Gong et al. (2014) reported that the Corexit EC9500A greatly enhanced the solubility of various petroleum hydrocarbons. As a result, the sediment will take up more of these dispersed hydrocarbons when exposed to DWAO than WAO, resulting in more hydrophobic sorption sites for PAHs. In addition, the petroleum components can act as a “plasticizer” for SOM that can soften the glassy domain of SOM, facilitating accessibility of the sorption sites (Jonker et al. 2003). Moreover, the dispersant and the petroleum components may interact synergistically on the sediment surface, facilitating formation of more and larger hemimicelles or admicelles.

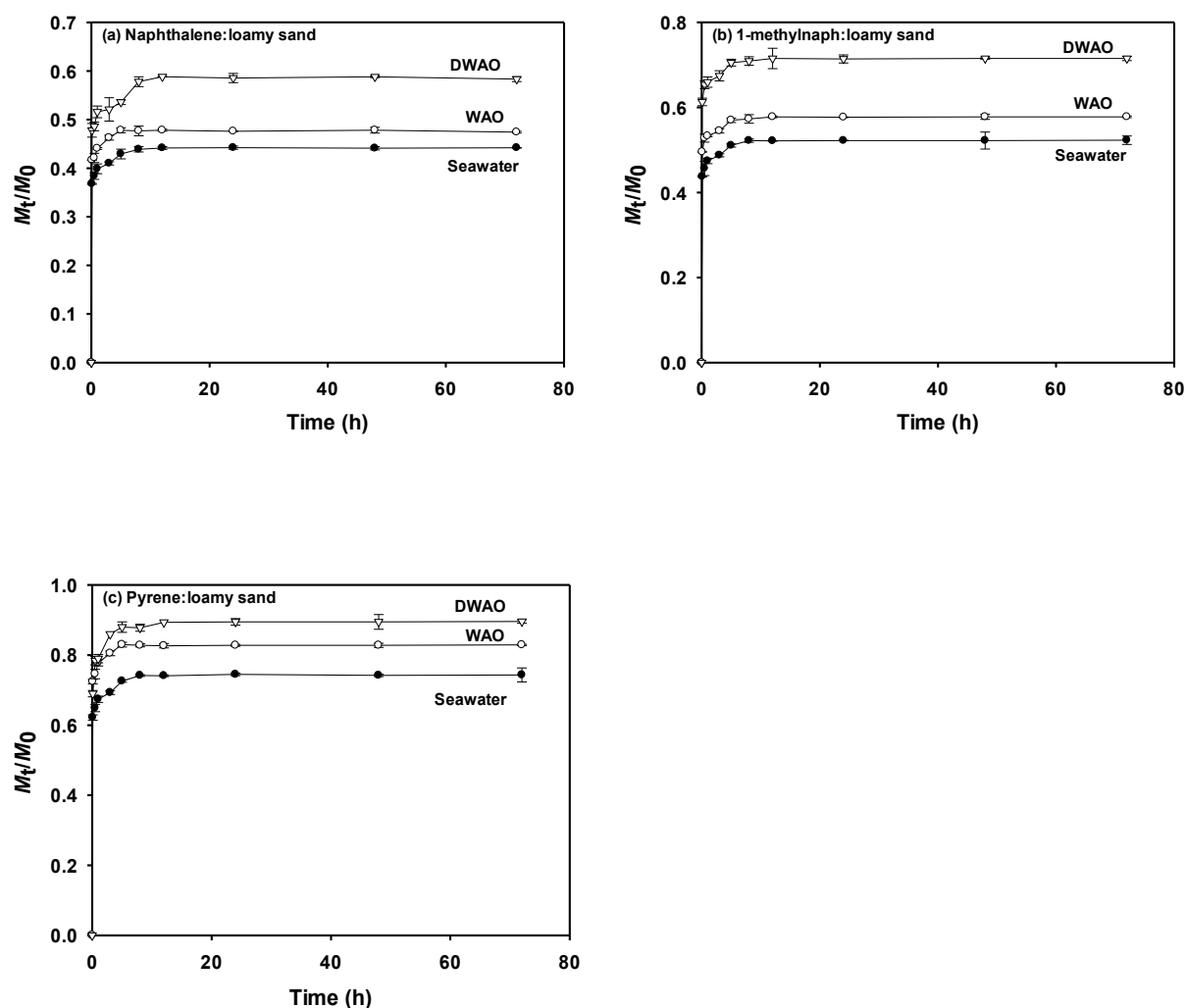


Figure 29. Effects of WAO and DWAO on sorption kinetics of PAHs onto a loamy sand sediment.  $M_t$ : Mass of PAH adsorbed at time  $t$ , and  $M_0$ : Total mass of PAH in the system.



### 3.2.5. Conclusions

This study investigated effects of a prototype oil dispersant on solubilization, sorption and desorption of three model PAHs with two representative Gulf Coast marine sediments under surface water and deepwater conditions. The primary findings are summarized as follows:

- 1) The dispersant can linearly enhance the solubilities of PAHs. While pure surfactants enhance PAH solubilization primarily in the above-CMC concentration range, the dispersant effectively enhanced PAH solubilization in both sub- and above-micellar concentrations. Partitioning of PAHs to the dispersant micelles and aggregates correlates well with the  $K_{ow}$  values of the PAHs.
- 2) The dispersant enhanced both the sorption extent and rate of the PAHs for both sediments. The sorbed dispersant provides additional adsorption capacity for PAHs, and the presence of the dispersant during desorption of PAHs rendered remarkable hysteresis for the PAHs. The PAH sorption to the sorbed dispersant was the key reason for enhanced PAH uptake and hysteresis.
- 3) The dual-mode models were able to adequately simulate the sorption isotherms and kinetics in the presence of various concentrations of the dispersant, and the dispersant-enhanced PAH uptake can be quantified by the linear partition parameter  $K_D$ .
- 4) For more soluble PAHs, the uptake increases linearly with increasing dispersant concentration over a broader dispersant concentration range, while for less soluble PAHs,  $K_d^0/K_d$  peaked at  $< CMC$ , and a “wash off” of sorbed PAHs occurred at slightly above CMC.
- 5) The deepwater conditions diminished the dispersant effect on solubilization, resulting in much lowered PAH solubility, and thus enhanced uptake of PAHs, despite lowered dispersant uptake.
- 6) The presence of WAO and more so DWAO markedly enhanced the uptake of PAHs due to the elevated uptake of oil hydrocarbons and the dispersant.

The findings can help us better understand the roles of oil dispersants on environmental distribution, fate, and transport of oil dispersants, spilled oil and persistent oil components. In particular, the results indicate that the use of dispersants can not only disperse more oil into the water column, but also transfer more oil to the sediment phase, which may end up in sea bottom or travel to near-shore areas. The dispersant or WAO facilitated sorption of oil to sediment particles may alter the transport pathways and affect the biological and chemical availabilities of the adsorbed oil components. Moreover, such effects of dispersants are quite different under the deepwater conditions.

### 3.3. Effects of Oil Dispersants on Desorption of Aged Oil Components from Jimmy Bay Sediment

The petroleum hydrocarbons that were released into the marine environment are subjected to several natural processes, including evaporation of the light crude oil components into air, dissolution of crude oil components, dispersion of crude oil due to natural wave action and chemical dispersants, degradation including biodegradation and chemical degradation (for example, photodegradation and ozonation), and sorption onto suspended particulate matter (SPM), and sediments ((Fu et al. 2014, Liu et al. 2012b, Yin et al. 2015a). The petroleum hydrocarbons in the aqueous phase (i.e, in the water column) underwent a faster attenuation than those associated with the solid phase due to several factors, which include a higher

evaporation and dissolution rate and higher biological availability. However, the petroleum hydrocarbons associated with the solid phase (i.e, adsorbed on sediments, salt marsh and/or SPM) are more resistant to natural weathering processes and thus persistent (Tansel et al. 2011, Yin et al. 2015b).

The persistence of sediment-sorbed oil components may pose an increased health risks to humans and the marine ecosystem (Liu et al. 2012b, Yin et al. 2015a). Boehm et al. (2016) reported the distribution of spilled oil and the weathering process acting on that spilled oil following the *DwH* oil spill. However, the fate of oil sorbed on sediments or other solid media after long-term weathering process has not been well studied, and the effect of oil dispersants on the desorption of the persistent oil fractions from sediment remains unknown. Therefore, there is a need to determine the quantity and availability of aged oil in sediment and to uncover the fate of the residual oil and the effect of the oil dispersant on the desorption rate of the residual oil in sediment.

This study investigated the residual oil components in sediment from Bay Jimmy, Louisiana. The oil in the sediment samples had been aged for five years following the *DwH* oil spill. The overall goal of this study was to determine the residual oil content, compositions and desorption rate of the sediment-sorbed oil and the effect of dispersant-seawater-sediment interactions on the oil desorption process. The specific objectives were to: 1) understand the distribution and abundance of oil residuals in the sediment to see what fractions of petroleum hydrocarbons are more recalcitrant to natural weathering as well as their abundance; 2) study the solubilization and adsolubilization effect of a model oil dispersant on the oil residuals; and 3) determine the ultimate desorption rate and extent via successive desorption tests.

### **3.3.1. Materials and methods**

#### **3.3.1.1. Materials**

The sediment was collected from Bay Jimmy, Louisiana, in March 2015, about five years after the 2010 *DwH* oil spill. The wet sediment samples (water content = 46 wt.%) were well mixed, sieved through a standard mesh of 2 mm openings, and then sealed in the glass bottle and stored in a refrigerator at 4 °C. Seawater was collected from the top 30 cm of the water column from the Grand Bay area, Alabama, in October 2014, and treated with the same procedures as described in Section 3.1.1.1.

All chemicals and organic solvents used in this study were of analytical or higher grade. Hexane was purchased from Fisher Scientific (Fair Lawn, New Jersey), and dichloromethane (DCM) from Alfa Aesar (Ward Hill, MA, USA). Silica gel (60–200 µm) was acquired from Sigma-Aldrich (St. Louis, Missouri) and was activated before each use. A standard reagent consisting of the 16 EPA listed PAHs specified in EPA Method 610 and a standard of *n*-alkanes mixtures (C9–C40) were purchased from Supelco (Bellefonte, PA, USA).

#### **3.3.1.2. Extraction of sediment**

Extraction of various oil components from the contaminated sediment was conducted according to a modified protocol of Wang and Fingas (1997). Briefly, each 2 g of a sediment sample was sequentially extracted by 30 mL of DCM and hexane (1:1 volume ratio) mixture in a batch setting for 24 h at room temperature. Upon separation of the solid via centrifugation (5000 rpm, 10 min), the sediment was further extracted using 30 mL of DCM twice consecutively. Afterwards, the extracts were combined, and passed through a column filled with anhydrous Na<sub>2</sub>SO<sub>4</sub> to remove moisture. The solvent was then concentrated under nitrogen purging to 10 mL for further analysis.

The extract was then passed through a column packed with 3 g anhydrous sodium sulfate topped with 3 g activated silica gel and supported by a layer of glass wool at the bottom. The column retained oil hydrocarbons were then fractionated through the following solvent elution processes. First, the column was eluted with 12 mL of hexane, and the eluted fraction was labeled as F1, and half of F1 was used to analyze the saturated hydrocarbons (*n*-alkanes). Then, the column was further eluted using a 15 mL of a mixture of hexane and dichloromethane (volume ratio = 1:1) to get fraction F2, half of which was used to analyze parent and alkylated PAHs. Lastly, half F1 and half F2 were combined (labeled as F3), and F3 was analyzed for TPHs (Wang and Fingas 1997, Yim et al. 2011).

The total TPHs in the samples were analyzed using GC-FID (Agilent 6890 Series GC System) equipped with a DB5 column (30 m × 0.25 mm, 0.25 μm film thickness). The injection volume was 1 μL with a split ratio of 20. The programmed column temperature was ramped from 40 to 280 °C at a rate of 8 °C min<sup>-1</sup> and held at 280 °C for 60 min (Liu et al., 2012b). *n*-alkanes (C9–C40) and PAHs (the 16 parent PAHs specified in EPA Method 610 and the corresponding alkylated PAHs) were analyzed using GC-MS (Agilent 7890A GC coupled with the 5975C Series MS). The analytical method was optimized and the selected ion monitoring (SIM) mode was set up based on the previous reports and the NIST library in GC-MS (Liu et al. 2012b, Wang et al. 2007). A DB-EUPAH column (length 20 m; inner diameter 0.18 mm; film thickness 0.14 μm) was used to separate the analytes. The front inlet temperature was set at 250 °C. The GC oven temperature was programmed as follows: 50 °C (hold for 0.8 min), ramp to 180 °C at 40 °C min<sup>-1</sup>, ramp to 230 °C at 7 °C min<sup>-1</sup> (hold for 0.5 min), and ramp to 335 °C at 15 °C min<sup>-1</sup> (hold for 5 min). The sample injection volume was 2 μL. Standard curves were developed for each PAH using the EPA Method 610 and the alkylated homologues were quantified according to a standard method using straight baseline integration of various levels alkylated PAHs (Wang et al. 2007).

### **3.3.1.3. Desorption tests**

Desorption rate and extent of oil components from the sediment were tested using plain seawater and in the presence of dispersants Corexit EC9500A and SPC 1000, respectively. SPC 1000 is an EPA reviewed, NCP listed water based dispersant. It has been included in the NCP Product Schedule for use as a dispersant for oil spills (Jacob and Bergman 2001). Dispersit SPC 1000 is a unique aqueous composition with highly effective emulsifiers, surfactants and a water-soluble coupling solvent. SPC 1000 contains no petroleum solvents. Dispersit SPC 1000 has an overall effectiveness of 73%, almost 50% better than the EPA requirement and it is considered less toxic than the dominant petroleum based dispersants (Jacob and Bergman 2001). For each desorption batch test, 2 g of the wet sediment was mixed with 40 mL sterilized seawater in the presence of 0 or 18 of a dispersant in a 43 mL amber glass vial sealed with Teflon-lined cap, where almost no headspace was left to minimize volatilization loss of the oil compounds. The vials were tightly sealed and rotated on an end-to-end rotator (60 rpm, 25 °C) in the dark. At predetermined time intervals, the vials were sacrificially sampled and extracted by DCM three times (40 mL solution with 10 mL DCM in each extraction). The extracts were combined and cleaned up by passing through an anhydrous sodium sulfate column, then concentrated under a gentle nitrogen blow to around 5 mL.

Successive dilution desorption tests were also conducted to determine the maximal desorbable oil components in the aged sediment. Following each desorption equilibrium (which was reached in ~4 days), the vials were centrifuged and supernatants pipetted out, and replaced with either seawater only or seawater containing 18 mg/L of SPC 1000. At predetermined time intervals, the vials were sacrificially sampled, and the supernatants were extracted and analyzed for the remaining oil components in the aqueous phase. The successive desorption tests were repeated three times.

### 3.3.2. Results and discussion

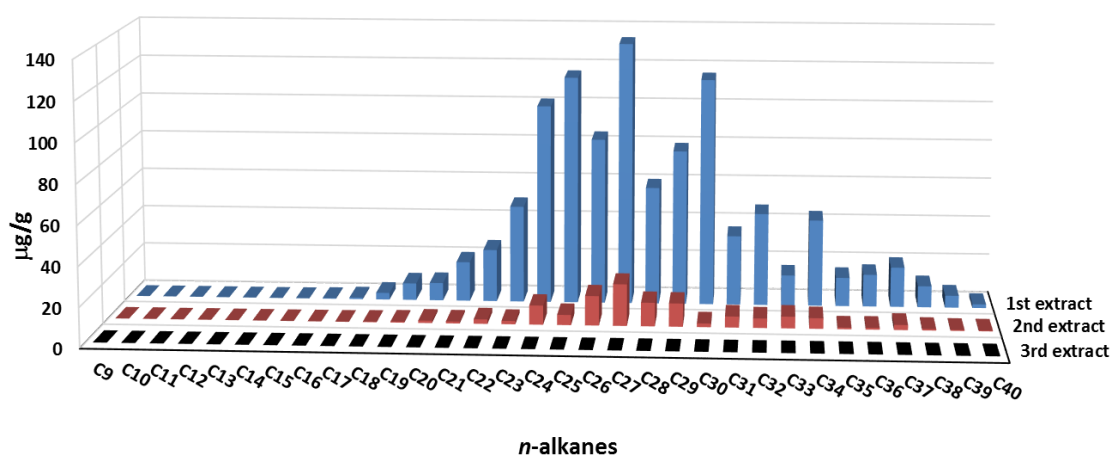
#### 3.3.2.1. Residual oil components in five-year aged sediment

The concentration of TPHs in the 5-year aged sediment was determined to be 2.310 mg/g-sediment prior to the desorption experiments (**Table 11**). It was shown that 2.029 mg/g-sediment of TPHs (87.7 wt.%) of the TPHs was extracted in the first extraction, 97.9 wt.% recovery was achieved in the first two extractions, and the third extraction recovered 2.1 wt.% of the TPHs. It should be noted that while the extraction method was valid for less aged sediment samples (Wang and Fingas 1997, Yim et al. 2011), it may recover less TPHs from the 5 year aged sediment samples. Therefore, the total recovery may be envisioned as somewhat operationally defied.

**Table 11. TPHs concentration in the sediment via sequential extraction**

Extraction	Concentration (mg/g-sediment)			Extraction efficiency (%)
	Sample 1	Sample 2	Mean	
1 <sup>st</sup>	2.005	2.053	2.029	87.7
2 <sup>nd</sup>	0.251	0.223	0.237	10.2
3 <sup>rd</sup>	0.056	0.041	0.0485	2.1

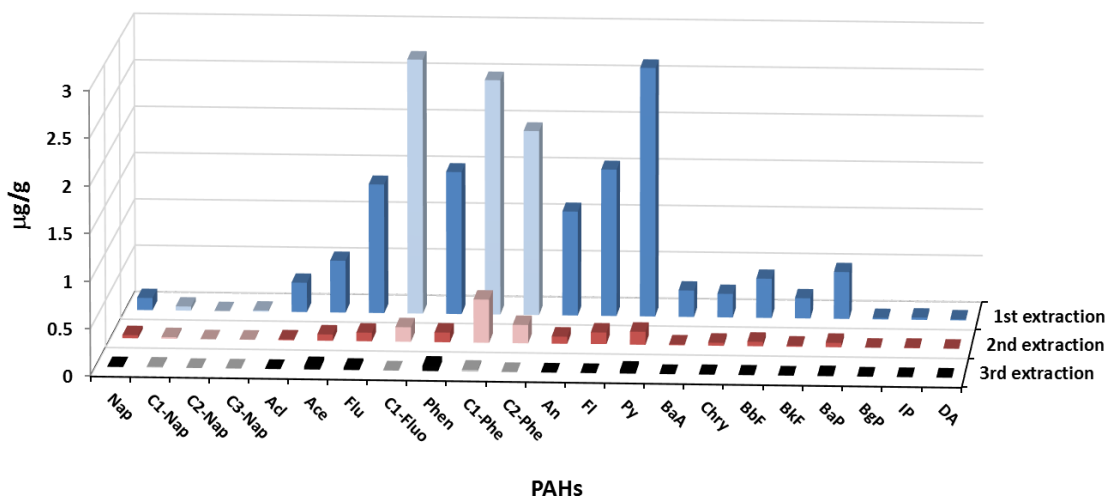
The total extractable *n*-alkanes concentration in the sediment was determined to be 1.141 mg/g-sediment (**Figure 30**). Nearly all the *n*-alkanes (99.2%) were extracted in the first two extractions. After 5 years of weathering following the *DwH* oil spill, the concentration of residual alkanes with LMW (C9–C20) was relatively low (2.21% of total *n*-alkanes). The concentration of HMW *n*-alkanes (C31–C40) accounted for 21.18% of total *n*-alkanes. The MMW (C21–C30) *n*-alkanes made up the largest percentage (76.61% of total *n*-alkanes), which is consistent with the oil compositions in the crude oil and is attributed to their higher adsorbability and lower physical and biological availabilities. C27 was the most abundant *n*-alkane, which alone constituted 13.70% of the total *n*-alkanes. The carbon preference index (CPI) represents the relative abundance of odd-numbered *n*-alkanes to that of even-numbered ones (Ehrhardt and Petrick 1993). The CPI of the sediments was equal to 0.97, which was quite close to the reported CPI value of 1 for MC252 crude oil (Liu et al. 2012b).



**Figure 30. Distributions of *n*-alkanes in the sediment.**

The concentration of total parent PAHs in the sediment was measured to be 11.934  $\mu\text{g/g}$ -sediment, with 10.973, 0.793 and 0.168  $\mu\text{g/g}$  being recovered in each extraction (**Figure 31**). After 5 years of weathering, pyrene was the most abundant PAH in the sediment, representing 23.7% of the total parent PAHs, followed by fluoranthene, phenanthrene and fluorene, which account for 14.2%, 14.1%, and 12.5% of the total parent PAHs, respectively. The 3-ring and 4-ring PAHs dominated the parent PAHs, accounting for 44.8% and 42.8% of the total parent PAHs, respectively, while 2-ring, 5-ring, and 6-ring PAHs contributed 1.4%, 10.5%, and 0.5%, respectively.

The concentration of total alkylated PAHs was 8.110  $\mu\text{g/g}$ -sediment, which is 2.4 times of the corresponding parent PAHs. The first two extractions were able to recover 99.7% of the total alkylated PAHs from the sediment. The 3-ring alkylated PAHs (C1-fluorene, C-phenanthrene and C2-phenanthrene) were the most abundant alkylated PAHs, which compose up to 99.0% of the total alkylated PAHs.



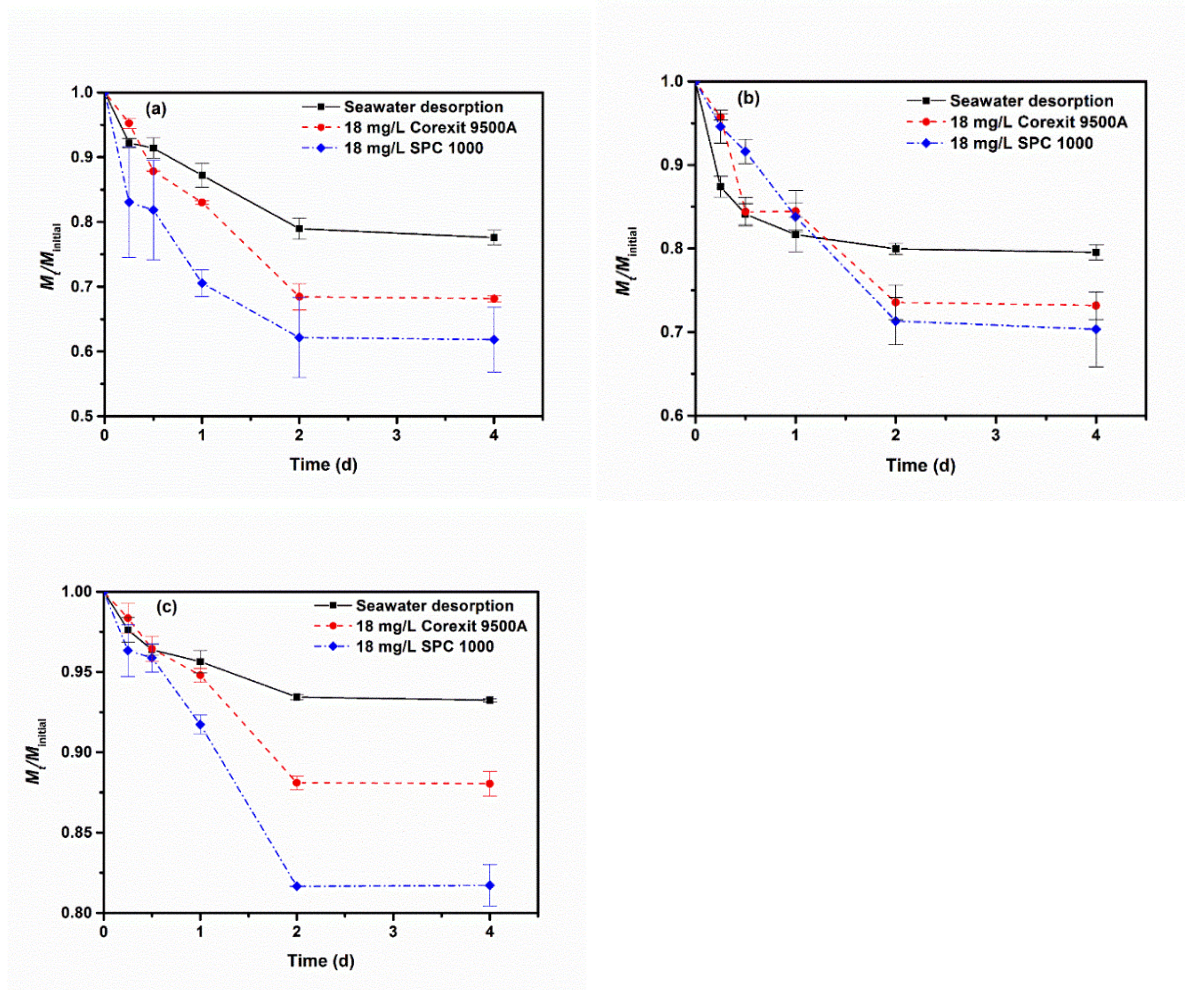
**Figure 31. Distributions of PAHs in sediment.**

PAHs were extracted via sequential extractions using DCM-hexane. Nap: Naphthalene, C1-Nap: C1-Naphthalene, C2-Nap: C2-Naphthalene, C3-Nap: C3-Naphthalene, Ad: Acenaphthylene, Ace: Acenaphthene, Flu: Fluorene, C1-Flu: C1-Fluorene, Phen: Phenanthrene, C1-Phe: C1-Phenanthrene, C2-Phe: C2-Phenanthrene, An: Anthracene, Fl: Fluoranthene, Py: Pyrene, BaA: Benz(a)anthracene, Chry: Chrysene, BbF: Benzo(b)fluoranthene, BkF: Benzo(k)fluoranthene, BaP: Benzo(a)pyrene, BgP: Benzo(g,h,i)perylene, IP: Indeno(1,2,3-cd)pyrene, DA: Dibenzo(a,h)anthracene.

### 3.3.2.2. Effects of oil dispersants on the desorption kinetics of aged oil

**Figure 32** shows the desorption kinetics of TPHs, *n*-alkanes and PAHs from the Jimmy Bay sediment with or without Corexit EC9500A or SPC 1000. In all cases, faster desorption was observed in the first two days, and became extremely slow thereafter, and the presence of a dispersant accelerated the desorption rate and extent. Generally, the amount of oil components desorbed followed the sequence of: SPC 1000 > Corexit EC9500A > no dispersant. In the absence of a dispersant, the final concentration of TPHs in seawater amounted to 34.7 mg/L; in the presence of 18 mg/L SPC 1000 or Corexit EC9500A, the final aqueous concentration was increased to 59.1 and 49.4 mg/L, respectively. For *n*-alkanes, the final concentration was 22.5, 22.2 and 16.0 mg/L, respectively, in the presence of SPC 1000 or Corexit EC9500A and in the absence of the dispersants; and for PAHs, the final concentration was 73.8, 48.3 and 27.3  $\mu\text{g/L}$ , respectively. The results reveal that both of the dispersants can promote the desorption of oil components from the aged sediment, and SPC 1000 appeared more effective than Corexit EC9500A.

Moreover, the dispersants were more effective toward PAHs than *n*-alkanes.

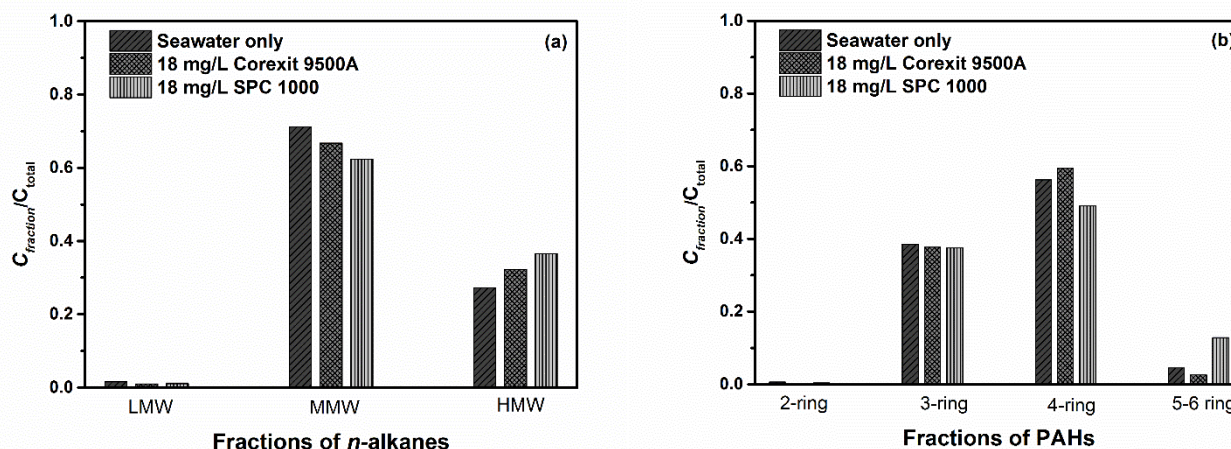


**Figure 32. Desorption kinetics of TPHs (a), *n*-alkanes (b) and parent PAHs (c).**

Experimental conditions: pH = 7.6–8.1, salinity = 3.15%, Corexit EC9500A = 18 mg/L, SPC 1000 = 18 mg/L, and temperature =  $25 \pm 0.2$  °C.  $M_t$ : mass remaining in sediment at time  $t$ ,  $M_{initial}$ : total initial mass of TPHs, *n*-alkanes or parent PAHs.



**Figure 33** presents the relative concentrations of various fractions of *n*-alkanes and PAHs desorbed into seawater from the sediment after 4 days of the desorption tests. It is evident that most desorbed fractions of the oil compounds were MMW and HMW *n*-alkanes and PAHs of 3-4 rings. Furthermore, the oil dispersants were more effective in enhancing desorption of more hydrophobic *n*-alkanes.

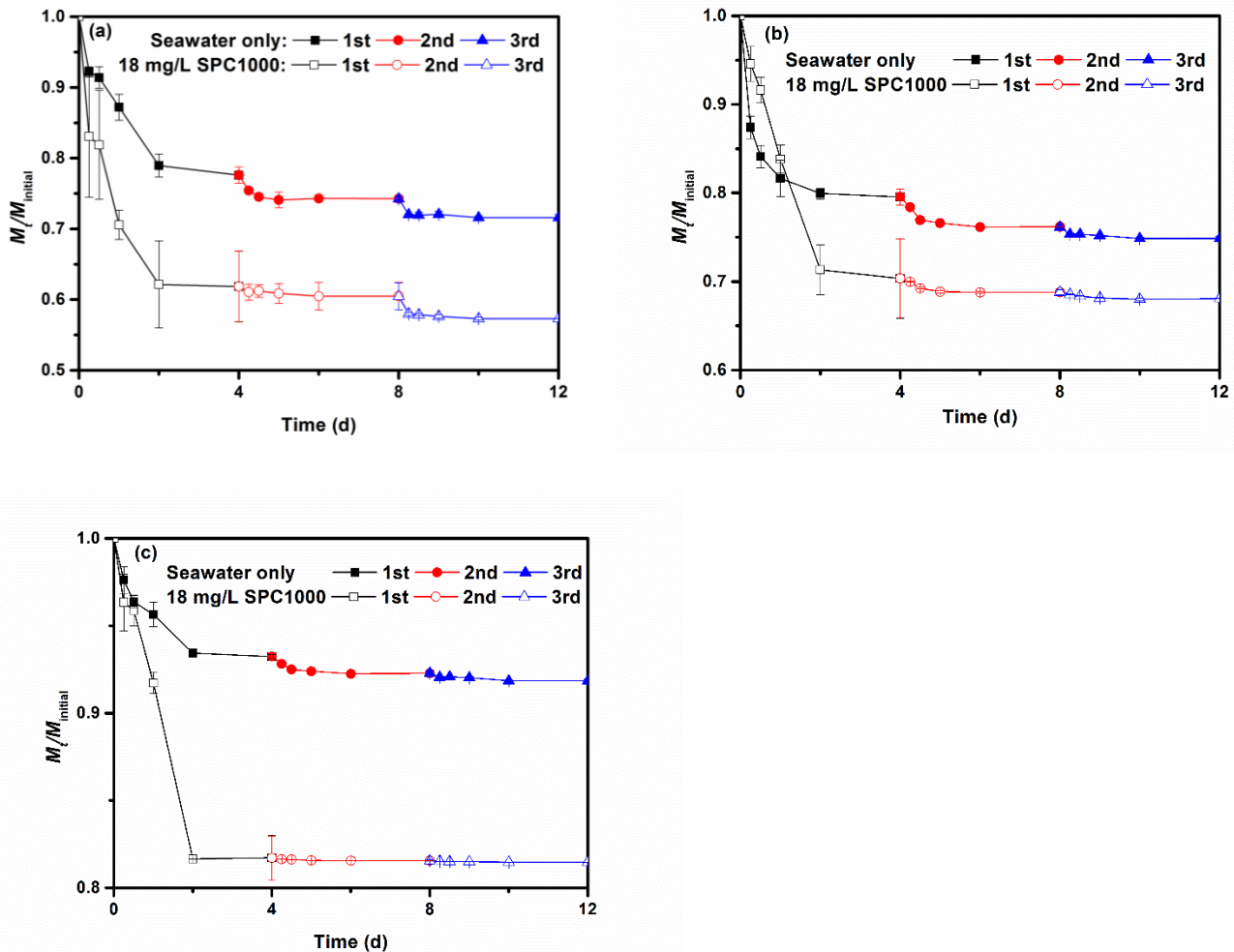


**Figure 33. Different fractions of *n*-alkanes and PAHs desorbed.**

(a) Relative concentrations of different fractions of *n*-alkanes (a), and (b) different fractions of PAHs desorbed into seawater with or without dispersant. Experimental conditions: pH = 7.6-8.1, salinity = 3.15%, Corexit EC9500A = 18 mg/L, SPC 1000 = 18 mg/L, temperature =  $25 \pm 0.2$  °C, desorption time = 4 days.  $C_{\text{fraction}}$ : Concentration of a given fraction of alkanes or PAHs that are desorbed into seawater,  $C_{\text{total}}$ : total *n*-alkanes or PAHs in seawater.

### 3.3.2.3. Successive desorption kinetics

**Figure 34** shows the successive desorption kinetics of TPHs, *n*-alkanes and PAHs from the Jimmy Bay sediment with or without 18 mg/L SPC 1000 over 3 consecutive desorption runs. Each desorption cycle lasted for 4 days. After the 3 desorption runs, the desorption rate became extremely slow. In the absence of the dispersant, the final concentrations of TPHs, *n*-alkanes and parent PAHs in the seawater solution were 44.6, 18.9 and 0.033 mg/L, respectively. In contrast, in the presence of 18 mg/L SPC 1000, the final concentrations of TPHs, *n*-alkanes and parent PAHs were increased to 66.2, 24.9 and 0.075 mg/L, respectively. Notably, most of the oil components were desorbed in the first desorption cycle, and the dispersant was most effective in the initial desorption stage. The results indicate that after the three successive desorption runs, there remained 71.6% of TPHs, 74.8% of *n*-alkanes, and 91.9% of PAHs in the sediment when the sediment was subjected to seawater desorption without dispersant; the residual TPHs, *n*-alkanes and parent PAHs were lowered to 57.3%, 68.1%, and 81.4%, respectively, when the sediment was subjected to 18 mg/L of SPC 1000. Evidently, the oil components adsorbed in this domain of SOM are much more resistant to desorption and much less available for chemical or biochemical transformations under the normal sediment-seawater environmental conditions.



**Figure 34. Successive desorption kinetics of various oil components.**

(a) TPHs, (b) *n*-alkanes, and (c) parent PAHs with or without dispersant. Experimental conditions: pH = 7.6–8.1, salinity = 3.15‰, SPC 1000 = 18 mg/L, temperature = 25±0.2 °C.

### 3.3.3. Conclusions

Five years after the *DwH* oil spill, significant amounts of oil components remained in the affected Bay Jimmy sediment. The content of TPHs was 2.310 mg/g-sediment, of which the total *n*-alkanes accounted for ~50% (1.141 mg/g-sediment). C27 was the most abundant *n*-alkane, and the MMW *n*-alkanes (C21–C30) made up 76.61% of the total *n*-alkanes. The total parent and alkylated PAHs were 11.934 and 8.110 µg/g-sediment, respectively, in which the 3-ring and 4-ring accounted for more than 80% of the total PAHs. The presence of the oil dispersant greatly accelerated the desorption rate and extent of the sediment sorbed oil residuals, and SPC 1000 was more effective than Corexit EC9500A. After three successive desorption runs, there remained 74.8% of *n*-alkanes, 71.6% of TPHs, and 91.9% of PAHs in the sediment when the sediment was only subjected to seawater desorption; while the presence of 18 mg/L of SPC 1000 lowered the residual TPHs, *n*-alkanes and parent PAHs to 68.1%, 57.3%, and 81.4%, respectively. The residual oil components may exist in the sediment-seawater system for prolonged period



of time, which may continue to desorb slowly but may not pose significant toxic effect because of its extremely desorption rate and physical and biological availabilities. Lastly, it should be noted that although the majority of the oil components are believed to be associated with the *DwH* oil spill based on the analysis of the oil components and prior sediment monitoring data, other sources (e.g., boating, natural seepage) may also contribute to the TPHs in the sediment.

### 3.4. Formation of Marine Snow and Its Effect on Oil Transport

Marine snow (MS) is a class of organic and inorganic particles or aggregates (operationally defined as those  $\geq 0.5$  mm) naturally formed in the ocean, consisting of minerals, detritus, bacteria mucus or extracellular polymeric substance (EPS), phytoplankton, and zooplankton feces (Alldredge and Silver 1988, Passow et al. 2012). Marine snow is ubiquitous in the ocean, and has an important role in the downward transport of materials and energy by gravitational settling (Lombard et al. 2013). Marine snow can be an important food source for organisms living in the aphotic zone (Newell et al. 2005). Though the exact formation mechanism of MS remains unclear, it is believed that both physico-chemical processes (e.g., coagulation and flocculation) and microbial processes are involved (Alldredge and Silver 1988).

During the *DwH* oil spill,  $\sim 2.1$  million gallons (7.9 million liters) of chemical dispersants were applied at the sea surface and near the 1,500 m deep wellhead in response to this unprecedented oil release (Kujawinski et al. 2011). In May 2010, shortly after the onset of the *DwH* oil spill, oil-associated marine snow (marine oil snow, MOS) of very large floc size ( $> 1$  cm) was observed at the surface in the vicinity of the spilled oil slicks near the oil platform (Passow et al. 2012). During the spill, a continuous oil plume was reported, which was “more than 35 kilometers in length, at approximately 1100 meters depth that persisted for months without substantial biodegradation” (Camilli et al. 2010). Though the mechanism of plume formation is complex and largely unknown, the following factors have been cited to play a role: the interplay of gas and oil in multiphase flow, preferential solubility of each oil constituent, and potential gas hydrate formation (Camilli et al. 2010, Johansen 2003). However, the role of oil, oil dispersants and dispersed oil in the oil plume formation or formation of MOS has not been addressed.

We hypothesized that oil and oil dispersants interacted with SPM, and thus impacted the formation of MOS. Furthermore, we hypothesized that MOS played an important role in transporting oil components in different environmental compartments (e.g., from the water column to the sea bottom) (Lehr et al. 2010). Many investigations have indicated that oil, dispersant components, minerals, and biologically-derived solids accumulated on the seafloor as a result of the *DwH* oil spill (Liu et al. 2012b, Steffy et al. 2013). Researchers observed that some brown flocculent (likely MOS) induced widespread signs of stress for seafloor coral colonies following the *DwH* incident (White et al. 2012). Yet, the role of MOS in the material transport process remains unexplored.

The most important factors that can affect formation of MOS include the hydrodynamic conditions, collision rate of suspended mineral particles, biologically-derived mucus and biopolymer, interactions of oil components with SPM, particle coagulation and flocculation characteristics, and interactions of oil components with microorganisms (Passow et al. 2012). In addition, based on our recent work (Gong et al. 2014a, Gong et al. 2014b), oil dispersants can significantly facilitate uptake of oil components on sediment particles, and dispersed oil is likely more easily adsorbed by SPM. However, detailed information remains lacking on how oil and dispersants impact the formation rate and characteristics of MOS. Moreover, it is not clear whether or how MOS facilitates uptake and transport of important oil components.

The overall goal of this part of work was to investigate the effects of oil and oil dispersants on the formation of MOS. The specific objectives were to: 1) investigate the formation of artificial marine snow through roller table experiments in the presence of oil and a prototype oil dispersant (Corexit EC9500A); 2) evaluate the role of natural suspended solids, especially indigenous microorganisms, in the formation of MOS; 3) characterize physical properties (number, size, and sinking or rising velocity) of MOS; and 4) elucidate the underlying mechanism of SPM formation and its implication to the fate and transport of spilled oil.

### 3.4.1. Materials and methods for marine snow formation and analysis

#### 3.4.1.1 Materials

Seawater samples were collected from the top water column (30 cm) at Grand Bay, Alabama (as described in Section 2.1.1.1). The water contained approximately 34.2 mg/L of suspended solids (SS). Surrogate LSC acquired from BP was used in the experiments. All chemicals used in this study were of analytical or higher grade and obtained from Sigma-Aldrich or Fisher Scientific.

#### 3.4.1.2. Roller table experiments

Roller table experiments were conducted using 755 RMV Jar Mills and 250 mL Boston round glass bottles. Experiments were designed to test MS and MOS formation under seven scenarios: I) untreated seawater only; II) untreated seawater + oil; III) untreated seawater + dispersant; IV) untreated seawater + oil and dispersant; V) micro-filtered seawater + oil; VI) sterilized seawater only; and VII) sterilized seawater + oil. The doses of oil and dispersant were set at 0.06% (v/v, oil/seawater) and 1:20 (dispersant/oil), respectively. In selected cases, microfiltration was exercised using 0.45  $\mu\text{m}$  cellulose nitrate membranes to remove the SPM from the seawater, and seawater sterilization was carried out by autoclaving the seawater at 121  $^{\circ}\text{C}$  for 35 min. In each scenario, the bottles were incubated for 28 days at room temperature ( $22 \pm 1$   $^{\circ}\text{C}$ ) at a rotation speed of 20 rpm. On a daily bases, the bottles were removed from the roller tables and placed up-right to record the morphology and motion of the MS-MOS flocs through photographic imaging and video recording with a Canon EOS 600D camera and a Digital IXUS 80 IS camera (Tokyo, Japan). All tests were carried out in duplicate.

#### 3.4.1.3. Characterization of marine snow particles

Six parameters were used to characterize the MS-MOS particles, i.e., particle number ( $N$ ), mean diameter ( $D_m$ , mm), aspect ratio ( $R_a$ ), vertical inclination angle ( $A_v$ ,  $^{\circ}$ ), total volume ( $TV$ ,  $\text{mm}^3$ ), and mean sinking or rising velocity ( $V_{ms}$  or  $V_{mr}$ , mm/s).  $N$  and  $D_m$  were obtained by analyzing the photographs of marine snow particles using the Image-Pro Plus 6.0 software (Media Cybernetics, Inc.).  $D_m$  is defined as the average particle size measured at 2 degree intervals and passing through the particle's centroid.  $R_a$  is the ratio between the major and minor axes of the equivalent ellipse of a particle.  $A_v$  is the angle between the major axis and the vertical axis.

$TV$  is calculated from the identical spherical volume using following equation:

$$TV = N \times \frac{4}{3} \times \pi \times \left(\frac{D_m}{2}\right)^3 \quad (22)$$

$V_{ms}$  and  $V_{mr}$  were estimated by analyzing particles' videos using the Leawo Video Converter software and the Adobe After Effects CS4 software). When  $N$  is  $\leq 30$ ,  $V_{ms}$  and  $V_{mr}$  were measured by taking the average velocity of individual particle velocities. However, when  $N$  is  $> 30$ ,  $V_{ms}$  and  $V_{mr}$  were determined based on the particle size distribution assuming a linear relationship between velocity and particle size (Passow et al. 2012):

$$V_{ms} = V_{smax} - \frac{(D_{msmax}^2 - D_{msmean}^2) \times (V_{smax} - V_{smin})}{D_{msmax}^2 - D_{msmin}^2} \quad (23)$$

$$V_{mr} = V_{rmin} + \frac{(D_{mrmax}^2 - D_{mrmean}^2) \times (V_{rmax} - V_{rmin})}{D_{mrmax}^2 - D_{mrmin}^2} \quad (24)$$

where  $V_{smax}/V_{rmax}$  and  $V_{smin}/V_{rmin}$  are the maximum and minimum sinking/rising velocities of the sinking/rising particles (mm/s), respectively;  $D_{msmean}/D_{mrmean}$ ,  $D_{msmax}/D_{mrmax}$  and  $D_{msmin}/D_{mrmin}$  are the mean, maximum and minimum  $D_m$  of the sinking or rising particles (mm), respectively.

#### 3.4.1.4. Total bacteria counting and determination of extracellular polymeric substance

The total bacteria numbers (TBN) in cases I-IV (with untreated seawater) after predetermined incubation times (0, 2, 14, and 28 days) were estimated following the fluorochrome staining method (Kepner and Pratt 1994). In addition, EPS in Cases I-IV incubated for 0, 2, 14, and 28 days were extracted and determined through the gravimetric method. More details on the methods for quantifying TBN and EPS can be found in other literature (Fu et al. 2014).

#### 3.4.1.5. Analytical methods

Seawater DOC was measured using a Dohrmann Phoenix 8000 TOC Analyzer. Suspended solids (SS) and salinity were determined gravimetrically (Echaniz and Vignatti 2011): filter 250 mL of the seawater with a 0.45  $\mu\text{m}$  fiberglass membrane, and dry the solids on the membrane at 105  $^{\circ}\text{C}$  for  $\sim 4$  h to get the weight of SS; evaporate the filtered seawater to dryness, and weigh the dry solid residual to get the salinity. *n*-Alkanes (C9–C40) in the aqueous phase and in MS-MOS were determined according to the method described in Section 3.3.1. The seawater, MS or MOS samples were first extracted with dichloromethane/*n*-hexane (1:1, v/v), concentrated and then analyzed by GC-MS.

### 3.4.2. Formation of MS and MOS

**Table 12** summarizes the observations on the MS and MOS formation during the roller table experiments for the aforementioned seven cases. In Case I, the suspended particles in the raw water gradually aggregated over the experimental period. Though aggregates were observed with a maximum  $D_m$  of 0.48 mm, the size is slightly smaller than the threshold of 0.5 mm (Alldredge and Silver 1988, Thornton 2002). As such, MS was barely formed in Case I.

In Case II, the presence of oil greatly sped up particle aggregation, and MS flocs ( $>0.5$  mm) were formed in 2 days (**Table 12**). At Day 6, the largest  $D_m$  (2.10 mm) and lowest  $N$  ( $19 \pm 3$ ) were obtained (**Figures 35, 2a, 2b**). The formed MS flocs appeared relatively elongated, though largely irregular, and showed a high  $R_a$  (2.73),  $A_v$  ( $87.52^{\circ}$ ) and  $V_{ms}$  (15.76 mm/s) (**Table 12** and **Figures 36c–e**). From Day 4 to Day 6, the flocs number remained stable at approximately 22 flocs. From Day 6 on, some oil droplets were formed and the oil droplets became incorporated into the MS flocs and smaller SPM seeds, resulting in more fine strip-like particles ( $N > 70$ ) with a relatively bigger head of oil droplet (approximately 0.5 mm in diameter) and a mineral tail (1–2 mm in length) (**Figure 35**). The MS and MOS particles formed

during the initial stage ( $\leq 6$  d) tended to settle by gravity, whereas those strips with sufficient oil incorporated were lighter than water, and thus, ascended at a relatively high  $V_{mr}$  (9.34 mm/s) and with small  $A_v$  (29–41°) (**Figures 36d, 36e**). From Day 16 to 18, an interesting phenomenon was observed—a large oil droplet of approximately 2 mm in diameter was incorporated into a floc and further became interwoven with several flocs to form a large star-like MOS (**Figure 35**). After Day 19, with the dissipation of the oil droplet, this large MOS was gradually broken up.

The addition of the dispersant (Case III) resulted in rapid formation of MS in one day (**Table 12**). The resulting flocs were generally smaller with a lower  $R_a$  (2.26),  $A_v$  (57–71°) and  $V_{ms}$  (14.81 mm/s) than those in Case II (**Figures 35, 36c–e**). On Day 3, the largest  $D_m$  (1.65 mm) and lowest  $N$  ( $19 \pm 2$ ) were observed. The flocs were then split into smaller ones gradually. On Day 12, the particle number grew to  $75 \pm 2$ , and subsequently, the MS flocs slowly re-aggregated (**Figures 35, 36a, 36b**).

In the presence of both dispersant and oil (Case IV), the natural suspended particles aggregated rapidly to form large flocs within two days (**Table 12**). At Day 4, the largest flocs ( $D_m = 1.55$  mm) were formed and the liquid appeared translucent with a sandy color (**Figures 35, 36b**). After Day 4, these large flocs were broken into many smaller ones with the incorporation of oil droplets. The formed oil droplets in Case IV were mostly less than 0.1 mm, which were much smaller than those in Case II. It is noteworthy that from Day 3 on, the previously sinking flocs gradually began to rise due to the incorporation of oil droplets or oil components of lower density. On Day 28, only a few small particles sank (**Figure 36**), while most MOS either floated at the surface or suspended in the water column. Compared with Cases II and III, more and smaller flocs ( $N = 190 \pm 10$ ,  $D_m = 0.58$ – $0.98$  mm) were formed in the presence of the dispersed oil at the end of incubation, and these flocs were also more roundish ( $R_a = 1.57$ – $1.85$ ) with a slower  $V_{ms}$  or  $V_{mr}$  (2.14 and 2.93 mm/s, respectively) (**Figure 36**).

No MS was generated in the micro-filtrated seawater even in the presence of oil (Case V) (**Table 12**). The particle aggregation in sterilized seawater (Cases VI and VII) was quite slow compared with Cases I–IV and no MS was formed (**Table 12**).

**Table 12. Observations of marine snow formation during roller table experiments**

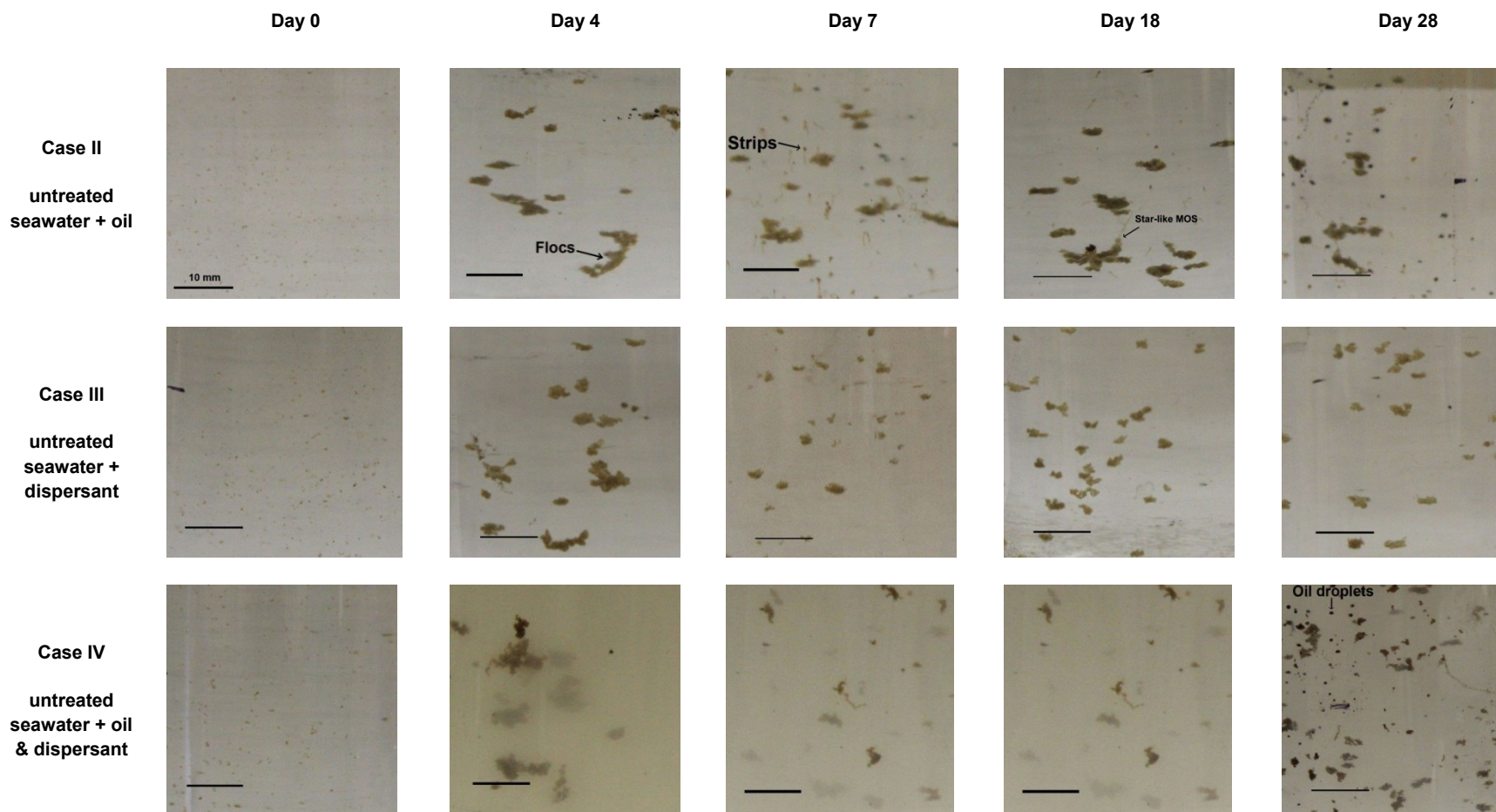
Case	Formation of MS <sup>a</sup>	Aggregates type	Maximum $D_m$	Sinking behavior	Rising behavior
I: untreated seawater only	No	/	0.48 mm (day 25)	7.68 mm/s <sup>c</sup> (day 28)	No
II: untreated seawater+oil	Yes (day 2 <sup>b</sup> )	Flocs, strips (day 6)	2.10 mm (day 6)	15.76 mm/s (day 9)	Day 6 <sup>d</sup> , 9.34 mm/s (day 14)
III: untreated seawater+ dispersant	Yes (day 1)	Flocs	1.65 mm (day 3)	14.81 mm/s (day 3)	No
IV: untreated seawater+oil & dispersant	Yes (day 2)	Flocs	1.55 mm (day 4)	5.90 mm/s (day 2)	Day 3, 4.98 mm/s (day 19)
V: micro-filtered seawater+oil	No	/	/	/	/
VI: sterilized seawater only	No	/	0.34 mm (day 26)	3.61 mm/s (day 28)	No
VII: sterilized seawater+oil	No	/	0.39 mm (day 12)	3.14 mm/s (day 28)	No

<sup>a</sup> A  $D_m$  of >0.5 mm indicates formation of MS

<sup>b</sup> Appearance time

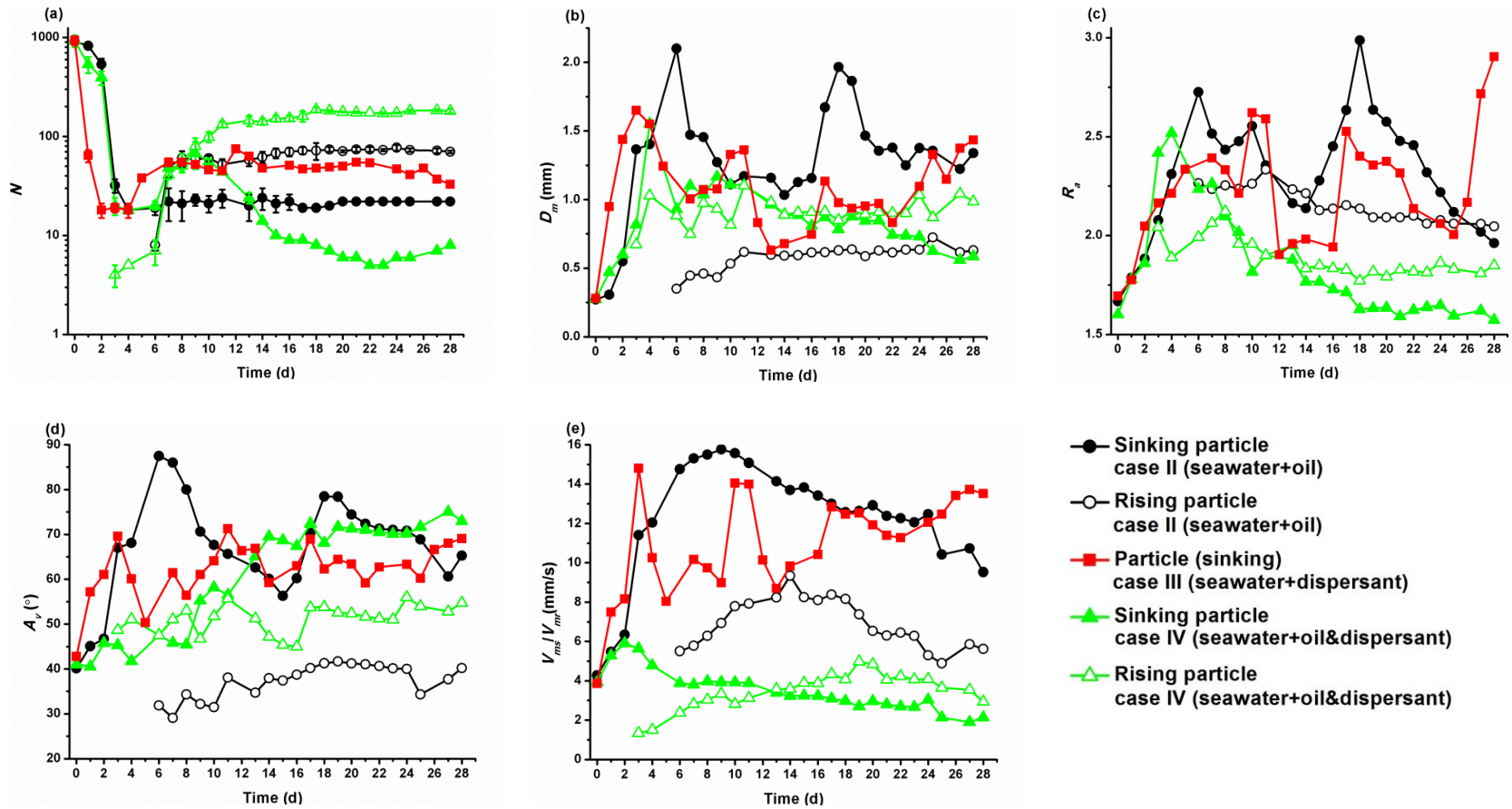
<sup>c</sup> Maximum  $V_{ms}$  Or  $V_{mf}$

<sup>d</sup> Time of first appearance



**Figure 35. Morphological changes of particle aggregates.**

In Cases II-IV during 28-day roller table experiments. Case II: seawater only; Case III: seawater + LSC oil (0.06%, v/v); and Case IV: seawater + LSC oil (0.06%, v/v) + Corexit EC9500A (dispersant to oil ratio = 1:20). All bottles (250 mL) were incubated at room temperature ( $22 \pm 1$  °C) at a rotation speed of 20 rpm. Scale bar = 10 mm.



**Figure 36. Changes of particle parameters.**

In Cases II-IV during 28-day roller table experiments: (a) particle number ( $N$ ), (b) mean diameter ( $D_m$ ), (c) aspect ratio ( $R_a$ ), (d) vertical inclination angle ( $A_v$ ), and (e) mean sinking and rising velocity ( $V_{ms}$  and  $V_{mr}$ ).



### 3.4.3. Formation mechanism of MOS and effects of oil and dispersant

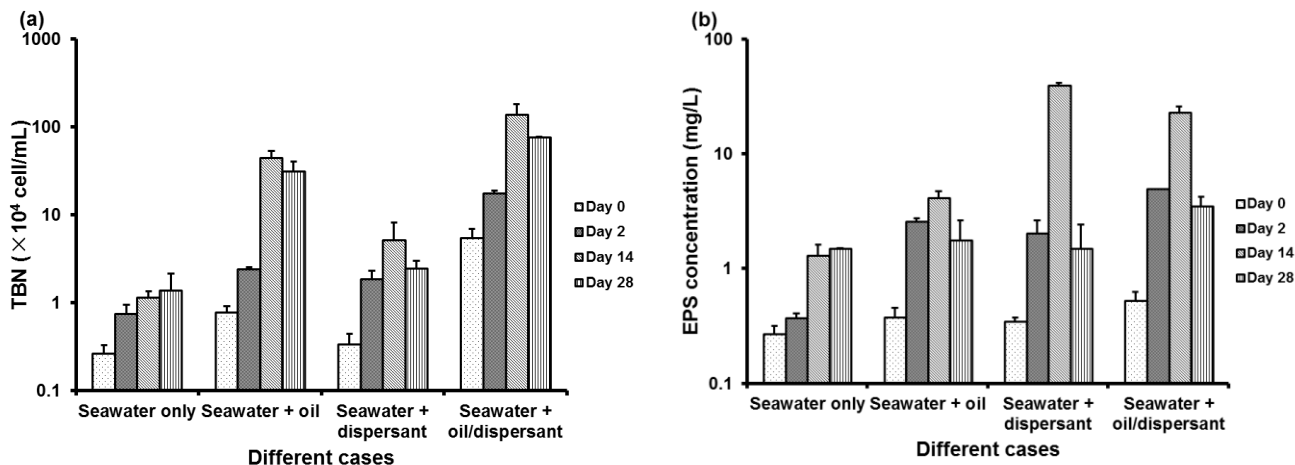
It is known that turbulence is necessary to induce suspension and collision of the particles (Tooby et al. 1977). Based on our preliminary work and work by others, the roller table approach provided sufficient rotational turbulence, which kept the particles in suspension, increased the collision rate between suspended particles and facilitated the particle aggregation (Kjørboe 1997), while simulating conditions near the sea surface.

No MS or aggregates were formed under the particle-free conditions even in the presence of oil (Case V, **Table 12**), indicating that the particulate matter was essential for the formation of MS. The lack of sufficient particulate matter may account for the reported observation that there was no MOS formed in situ in the deepwater oil plumes following the 2010 *DwH* oil spill (Passow et al. 2012), i.e., the plumes are likely composed of mostly dispersed oil droplets.

As most particles in marine systems carry net negative charges, the classical Derjaguin–Landau–Verwey–Overbeek (DLVO) theory can be used to interpret the collision and adhesion of these like-charged particles (Liss et al. 2004). According to this theory, the forces governing the particle interactions are the van der Waals attraction (WA) and the electrostatic repulsion (ER) (Logan 2012). When the collision energy overcomes the primary maximum energy barrier to reach the primary minimum, or alternatively, falls in the secondary minimum domain, the particles will aggregate or flocculate. In this work, the breakup of the initially formed large MS and MOS flocs suggested that the flocculation was at least partially reversible, i.e., the secondary minimum was an important mechanism in the formation of MS and MOS.

The experimental results also revealed that the indigenous microbes play a critical role in the particle aggregation and formation of MS and MOS. Of the seven cases, the lowest particle aggregation rate (particle number reduction/time) was found in Cases VI and VII (9.6 and 21.8 d<sup>-1</sup>, respectively), where the seawater was sterilized. This observation reveals that the bacteria activity plays a critical role in the formation of MS. In fact, bacteria are known to produce “sticky” matter, i.e., EPS, which can be incorporated in the suspended particles to form mucus matrices that facilitate particle aggregation and MS formation (Passow et al. 2012). Liu et al. (2010) demonstrated that although bacteria themselves are net-negatively charged, EPS played crucial roles in the aggregation of sewage sludge by contributing to the overall attractive energy based on the extended DLVO theory. Likewise, the bacteria-facilitated formation of MS-MOS is attributed to the EPS-facilitated aggregation and/or bridging effects. **Figure 37** shows that both TBN and EPS in Cases I–IV rapidly increased with the particle aggregation from Day 1 to 14, indicating the important role of EPS in the MS and MOS formation process.





**Figure 37. Changes in total bacterial number and extracellular polymeric substances.**

(a) total bacterial number (TBN), and (b) extracellular polymeric substances (EPS) concentrations in Cases I-IV at days 0, 2, 14 and 28, respectively.

The much enhanced MS-MOS formation in Cases II-IV (**Table 12**) indicated the important role of oil and the dispersant. Dissolved or dispersed oil hydrocarbons in aqueous solutions can compress the diffuse layer surrounding the particles and reduce the repulsive energy, and thus, promoting the aggregation of particles (Mittal 2000). In addition, the incorporation of the oil and dispersant hydrocarbons can enhance the hydrophobic interactions between SPMs, leading to the accelerated aggregation rates (Wilén et al. 2003). Such a snowballing effect continues until a dynamic steady state is reached, where the particle growth is counterbalanced by the shearing forces.

The results also indicate the importance of the interactions between oil and indigenous bacteria and EPS in promoting the formation of MOS. In the initial 4 days,  $N$  in Case II was reduced from  $912 \pm 28$  to  $18 \pm 3$  with an aggregation rate of  $223.5 \text{ d}^{-1}$  (**Figure 36a**). Several factors are responsible for the effect. First, the dissolved and dispersed oil hydrocarbons enhanced the bacteria growth by serving as additional carbon and energy sources, which in turn resulted in the production of more EPS. For instance, TBN and EPS in Case II at Day 2 were  $2.38 \pm 0.14 \times 10^4$  cells/mL and  $2.59 \pm 0.17$  mg/L, respectively, which were 3.2- and 7-fold higher than those in Case I (**Figure 37**). Second, the bio-surfactants present in EPS produced by bacteria can emulsify the oil to increase bioavailability of the hydrocarbons (McGenity 2014) and enhance interactions between the hydrocarbons and suspended particles. This is supported by the observation that fine oil droplets were formed in Case II from Day 6 on till Day 28 (50–60 oil droplets at Day 28). However, in Case VII without the bacteria, only a few oil droplets were discernable in the end of the incubation. Section 3.4.4 gives the distribution of  $n$ -alkanes in aqueous and MS or MOS phases.

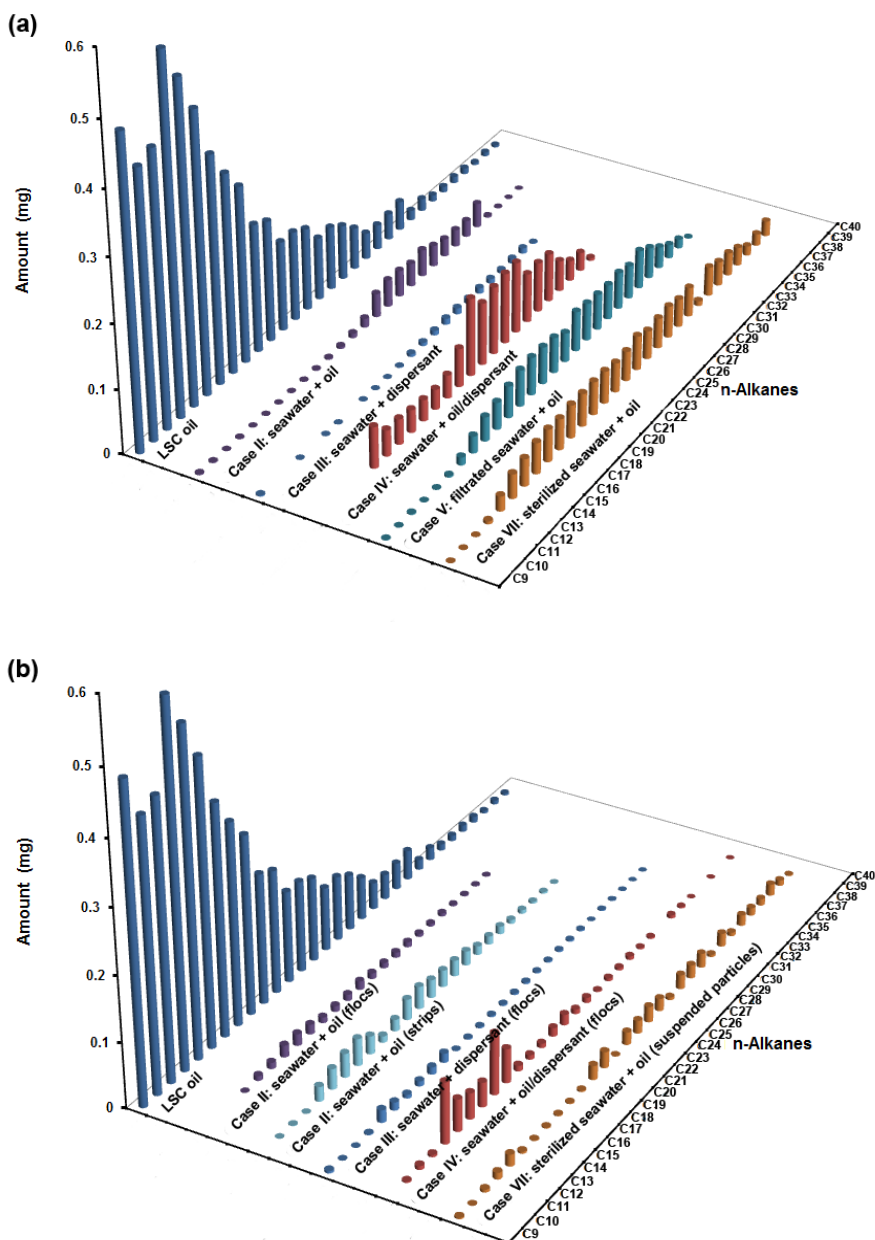
Case III reveals that the dispersant alone was able to accelerate the formation of MS (**Table 12**). The  $N$  value was reduced from  $934 \pm 99$  to  $18 \pm 4$  in the first 2 days with an aggregation rate of  $458 \text{ d}^{-1}$  (**Figure 36a**), which was even faster than the oil-facilitated MOS formation (Case II). Corexit EC9500A consists of both nonionic and anionic surfactants, and organic solvent (including kerosene) (Hayworth and Clement 2012). Therefore, the aforementioned oil-facilitated aggregation mechanisms remain operative due to the presence of hydrophobic tails and kerosene. Moreover, the uptake of the surfactants renders the particle surface more hydrophobic, promoting the attractive hydrophobic interactions between particles (Hu and Dai 2003). Surfactants also promote the adsorption of hydrocarbons and EPS by suspended particles (Besra et al. 2004, Gong et al. 2014b). Furthermore, the dispersant components are biodegradable and may serve as carbon and energy sources that stimulate the microbial activities (Garcia et al. 2009). **Figure 37** shows that the dispersant greatly elevated the TBN and especially EPS levels. At

Day 14, TBN in Case III increased by 15.3-fold compared with the initial level, while TBN in Case I increased by only 4.3-fold; At Day 14, the EPS content in Cases III increased by 115.0-fold, compared to only 4.8- and 11.0-fold respectively for Cases I and II.

Interestingly, the combination of oil and the dispersant (Case IV) did not show an additive or synergistic effect in terms of aggregation rate. In the first 3 days,  $N$  in Case IV was reduced from  $925 \pm 126$  to  $23 \pm 4$  with an aggregation rate of  $301 \text{ d}^{-1}$  (**Figure 36a**), which is between those in Cases II (oil only) and III (dispersant only). This is possible because the interactions between oil and the dispersant prevent either oil or the dispersant from fully exerting its individual role. Compared with Cases II and III, the flocs in Case IV were more abundant in number but relatively smaller in size. After the 28-day incubation, most of the flocs in the presence of the dispersed oil showed positive or neutral buoyancy while those formed in the presence of oil alone or dispersant alone all sank (**Figure 36**). The different characteristics of flocs resulted from the incorporation of different types and amounts of oil components. The application of a chemical dispersant to an oil slick increases the formation of much smaller oil droplets and disperses much more oil in the water column, compared to naturally or mechanically dispersed oil (Khelifa et al. 2008). These fine oil droplets not only facilitate formation of more MOS flocs, but resulted in much higher oil content in the resulting MOS. On Day 28, approximately 200 small oil droplets ( $< 0.1 \text{ mm}$ ) were observed in Case IV (**Figure 35**) and much more were incorporated into the MOS flocs. On the other hand, the co-adsorbed dispersant molecules may orient themselves in the head-out fashion, which acts as a repulsive energy barrier, confining further growth of the MOS.

### 3.4.4. Distribution of *n*-alkanes in aqueous and MS and MOS phases

The amounts of *n*-alkanes in seawater and MS and MOS particles were determined after the 28-day incubation. **Figure 36** summarizes the results. The concentration of total *n*-alkanes (C9–C40) in the LSC oil was 34.61 mg/mL and the oil mass added in each bottle was 5.19 mg. The raw seawater (Case I) and sterilized seawater (Case VI) contained 0.05 and 0.06 mg of total *n*-alkanes, respectively. The addition of the dispersant (Case III) elevated the content to 0.09 mg (**Figure 38a**), which accounts for the petroleum composition in Corexit EC9500A (Hayworth and Clement 2012).



**Figure 38. Mass distributions of *n*-alkanes in seawater (a) and in particle aggregates (b).** C9–C40 *n*-alkanes were extracted following the 28-day roller table experiments. The amount of *n*-alkanes in LSC oil was determined in 0.15 mL of the crude oil, which was the amount added in each testing bottle.

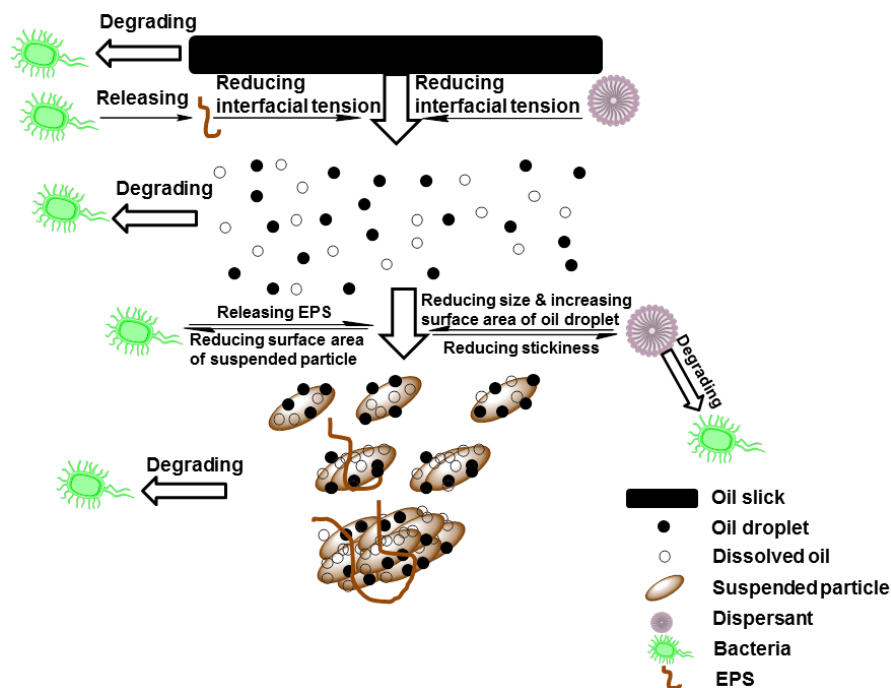
In Case II, the total mass of *n*-alkanes dissolved in seawater was 0.40 mg, i.e., 7.7% of the total mass of *n*-alkanes added. The application of the dispersant to the oil (Case IV) escalated the dissolved *n*-alkanes to 1.25 mg. In addition, relatively high levels of *n*-alkanes were detected in Cases V (0.98 mg) and VII (1.06 mg), where oil was added in micro-filtered and sterilized seawater, respectively.

Total *n*-alkanes in the natural suspended particles without addition of oil or dispersant were very low, 0.001 and 0.002 mg in Cases I and VI, respectively. In the presence of the dispersant (Case III), 0.11 mg of *n*-alkanes was detected in the formed MS (**Figure 38b**). MOS flocs in the oil-dispersant system (Case IV) contained nearly three times more *n*-alkanes (0.48 mg) than in the oil-only system (Case II, 0.17 mg). However, more *n*-alkanes (0.42 mg) were detected in the “strips” (Case II) where rather distinctive oil droplets were incorporated in the particles (**Figure 38**). The addition of oil in sterilized seawater (Case VII) resulted in 0.34 mg of *n*-alkanes in the suspended solids.

Of the *n*-alkanes, the LMWHs species (C9–C18) tended to partition more favorably in the MS and MOS particles than in the aqueous phase. The LMW *n*-alkanes in the MS and MOS flocs of Cases II-IV were 0.08, 0.07 and 0.38 mg, respectively, accounting for 7.9%, 39.9% and 22.1% of the total *n*-alkanes in seawater and the MS and MOS; whereas the LMW *n*-alkanes in the aqueous phase were only 0.8%, 1.4% and 14.4%, respectively (**Figure 38**). However, for sterilized seawater (Case VII), the solid-retained mass of LMW *n*-alkanes was 4.1%, while leaving 24.2% in the aqueous phase. In the natural seawater without oil or dispersant (Cases I and VI), the LMW *n*-alkanes were low in both the aqueous and particle phases (0-3.8%).

### 3.4.5. MS-MOS-facilitated uptake and transport of oil hydrocarbons

The Crude oil contains approximately 81 vol.% *n*-alkanes and 19 vol.% aromatics (Wang et al. 2003). Therefore, it is of great significance to evaluate the transport of alkanes during the formation of MOS. Both dispersed oil droplets and dissolved oil can interact with SPMs and become associated with MS-MOS. Consequently, MS-MOS can affect the transport and fate of the oil components (**Figure 39**).



**Figure 39. Schematic diagram on the fate and transport of oil during formation of marine oil snow.**

The dispersant and bacterial activity greatly impact the formation, oil content, and fundamental properties (e.g., size, shape and density) of MS and MOS. The chemical dispersant reduces the interfacial tension between the oil and seawater, and hence promotes the formation of oil droplets (Lessard and Demarco 2000). When the dispersant concentration exceeds its CMC (22.5 mg/L) micelles will be formed, which results in more oil dispersed in the water column and transfers more oil in MS and MOS (Zhu and Chiou 2001). In this work, the dispersant dose was 32 mg/L. Therefore, micelles are expected in the systems. In fact, the dispersant increased the total “dissolved” *n*-alkanes in Case IV by 191% than in Case II (excluding *n*-alkanes from the dispersant). With respect to uptake of oil hydrocarbons on particle aggregates or MS-MOS, the dispersant can exert a number of competing effects. First, the dispersant molecules reduce the stickiness of oil droplets and inhibit their adhesion to particles (Lessard and Demarco 2000). On the other hand, the dispersant generate more and smaller oil droplets (Khelifa et al. 2008), which are favorable for incorporating more oil into the particles. Furthermore, the surfactant molecules can form hemimicelles at the particle surface, which also promote uptake of more hydrocarbons (Portet-Koltalo et al. 2013). Conversely, interactions between hydrocarbons and aqueous dispersant micelles and molecules tend to disperse more oil in the aqueous phase. In our case, the dispersant increased the total *n*-alkanes adsorbed on the MS-MOS flocs by 1.23-fold, suggesting a net positive effect of the dispersant on the incorporation of more hydrocarbons into the MOS.

The biosurfactants from indigenous bacteria can also facilitate oil dispersion and dissolution in a similar fashion (McGenity 2014). The bacteria could take up and degrade oil hydrocarbons dispersed or

dissolved in the aqueous phase (**Figure 39**). The presence of indigenous bacteria (Case II) reduced the aqueous *n*-alkanes from 1.06 mg (Case VII) to 0.40 mg, indicating remarkable bio-uptake and biodegradation of the hydrocarbons. Our findings also suggested that the indigenous microbes in seawater rather than those from the oil played the major roles in degrading the hydrocarbons. In terms of facilitating oil-particle interactions and formation of MS-MOS, bacteria can play a number of important roles. First, the bacteria-produced EPS enhances transferring more oil into the EPS matrix (Zhang et al. 2011b), and the bio-dispersed oil droplets are also in favor of interacting with the solid particles. On the other hand, bacteria increase the aggregation of particles that may reduce the particle surface area and hinder the interactions between the particles and oil droplets. Lastly, biodegradation of oil hydrocarbons reduces the concentration and species distribution of the oil hydrocarbons in both the aqueous and particle phases. The biodegradation effect was manifested by the observation that the *n*-alkanes level in particles without indigenous bacteria (Case VII) was 2-fold higher than that in Case II where the bacteria were active.

Effects of chemical dispersants on biodegradation of petroleum hydrocarbons have been studied for decades. It is generally agreed that chemical dispersants increase bioavailability of oil slicks and accelerates biodegradation of oil. **Figure 38** shows that *n*-alkanes in both the aqueous phase and the particles are approximately 3-fold higher in Case IV (with dispersant) than in Case II (without dispersant). This is because the effect of the dispersant on oil dispersion and dissolution is more apparent than its enhancement on the biodegradation of oil.

It is known that LMW hydrocarbons are more prone to oil weathering such as evaporation, dissolution and biodegradation (Leahy and Colwell 1990, Liu et al. 2012b), Strong biodegradation of the LMW oil fraction was evident from the observation that the aqueous content of LMW *n*-alkanes (0.8% of the total *n*-alkanes sum in seawater and particle aggregates) in Case II (with bacteria) was much lower than (24.2%) in Case VII (without bacteria). **Figure 38** shows that the LMW *n*-alkanes content in MOS (Cases II and IV) is higher than that in the aqueous phase, which can be attributed to incorporation of the dispersed oil droplets into the MOS. In contrast, no conspicuous incorporation of oil droplets was observed in Case VII (without bacteria), resulting in the low LMW *n*-alkanes percentage (4.1%) in the particles.

### 3.4.6. Environmental Significance and Implications

The experimental results provide compelling evidence about the critical roles of active bacteria, oil and oil dispersants in the formation of MS-MOS in the marine environment. The information is valuable for aiding our understanding of the mechanisms of MS-MOS formation and MOS-facilitated transport of oil hydrocarbons, which has been largely ignored in estimating oil budget following major oil spills, such as the 2010 *DWH* oil spill. In this context, the key environmental implications are inferred and briefed as follows:

- 1) MS-MOS is more favorably formed in the upper mixed layer (25–200 m), where abundant active microorganisms, suspended matter and sufficient turbulence coexist.
- 2) Indigenous bacteria are the essential and primary facilitator for the MS-MOS formation, while bacteria from the crude oil exert little or no effect.
- 3) Oil dispersants, dispersed oil droplets and dissolved oil greatly facilitate the formation of MS-MOS by stimulating the bacterial activities (more EPS production), enhancing oil-particles interactions, and promoting effective particle aggregations.
- 4) The oil dispersant results in much more and smaller MOS and transfers more LMW oil in MOS, which

enhances the buoyancy, i.e., incorporation of oil and dispersant in the particles inhibits sinking of MS-MOS or reverse the transport direction. Increasing the MOS residence time in the water column may promote the oil degradation in the euphotic zone and alleviate the impact of MOS on the benthos ecosystem. On the other hand, the MOS-facilitated oil transport may partially account for the reported oil accumulation at the seafloor following the *DWH* oil spill, while the observed deepwater oil plumes are less likely to be associated with MS-MOS.

- 5) Dispersants alone may stimulate the formation of MS through stimulating EPS-producing bacteria activities, which warrants further investigation.

### **3.5. Effects of Oil Dispersant on Settling Performance of Suspended Sediment Particles and Vertical Transport of Oil Contaminants**

During the 2010 *DwH* oil spill incident, approximately 2.1 million gallons (7.9 million liters) of chemical dispersants were applied at the sea surface and near the 1,500 m deep wellhead (Kujawinski et al. 2011). Application of oil dispersants can result in elevated concentrations of oil droplets and oil hydrocarbons in the water column. For example, the volatile aromatic hydrocarbons in a water column oil plume during the *DwH* oil spill reached 139  $\mu\text{g/L}$  (Hazen et al. 2010). The high oil droplet concentration is favorable for the formation of oil sediment aggregates (OSAs) (Gong et al. 2014a), which can not only alter the settling behavior of the particles, but also facilitate distribution and transport of important oil compounds that are associated with the aggregates. Guyomarch et al. (1999) found that the presence of the chemical dispersant, Inipol IP90, enhanced the formation of OSAs, and approximately 80% of oil was entrained in the OSAs, which subsequently settled down to the bottom of the tank during wave tank experiments. Recent work also showed that the presence of Corexit EC9500A promotes the formation of marine oil snow (MOS) and sorption of oil components onto MOS (Fu et al. 2014).

Oil contaminants can strongly interact with suspended sediment particles. For example, significant portions of PAHs can be adsorbed on, or incorporated in, the OSAs. Consequently, the formation of OSAs and subsequent particle settling and transport in the marine environment can alter the distribution, transport and environmental fate of PAHs and other important oil components (Bouloubassi et al. 2006, Zuijdgeest and Huettel 2012). For instance, adsorption of PAHs onto sediment particles may mitigate the peak concentration of PAHs in the water column by transferring significant amounts of PAHs into the sediment phase; on the other hand, the PAHs present in OSAs can be transported to the sea bottom, to the surface, or to nearshore areas via particle-facilitated transport process.

In addition, as PAHs persist much longer in the sediment phase than at the sea surface (Harayama et al. 1999), sediment adsorption may prolong the life time of PAHs in the ecosystems. Recent studies have shown that oil dispersants can enhance sorption of PAHs by sediment and induce sorption hysteresis (Gong et al. 2014b, Zhao et al. 2015). Though a wealth of information on the adsorption of oil components onto sediments has been reported (Guo et al. 2007, Tremblay et al. 2005, Zhao et al. 2015), little is known about effects of dispersants or dispersed oil on the transport of fine sediment particles and how such particle-facilitated oil transport affects the fluxes and fate of oil components (Allan et al. 2012). As oil spills often occur in, or can reach, nearshore and estuarine zones, where the concentration of suspended sediment particles is usually high (NRC 2005a), the oil-particle interactions may play even more profound roles in these more ecologically sensitive areas even though dispersants are not allowed to be directly applied to nearshore areas in the United States.

Environmental conditions, such as pH, salinity, temperature, and DOM are known to affect settling of suspended particles. Kretzschmar et al. (1998) investigated influence of pH and humic acid on the

coagulation of kaolinite by the dynamic light scattering technique, and observed that at  $\text{pH} < 5.8$  the interparticle attractive forces predominate the suspension system, resulting in destabilization of the particles (i.e., the colloidal dispersion no longer remains suspended). Humic acid was reported to render a suspension system more stable due to the combination of electrostatic and steric stabilization effects (Heil and Sposito 1993a, Heil and Sposito 1993b, Kretzschmar et al. 1993). However, knowledge has been lacking on the effects of such environmental parameters in the presence of oil dispersants, especially, how oil dispersants affect the settling properties of suspended particles under various environmental conditions.

The overall goal of this study was to systematically investigate effects of three model oil dispersants (Corexit EC9527A, Corexit EC9500A, and SPC 1000) on the settling behaviors of sediment particles and how such dispersant-particle interactions affect distribution and transport of key oil components. The specific objectives were to: 1) determine the settling kinetics of representative sediment particles in the presence of the model dispersants; 2) elucidate the mechanisms underlying the particle-dispersant interactions; 3) test the dispersant effects under various environmental conditions, such as pH, salinity, DOM, and temperature; and 4) explore how dispersant-facilitated particle sedimentation affects distribution and transport of important oil components in sediment-water systems.

### **3.5.1. Materials and methods for sediment settling tests**

#### **3.5.1.1. Materials**

The key compositions of the Corexit dispersants, such as Tween 85, Tween 80, DOSS and 2-butoxyethanol, were purchased from VWR Corporation.

A surrogate LSC oil was obtained by courtesy of BP in Houston. The oil was artificially weathered according to the evaporation method by Sorial et al. (2004). Briefly, air was bubbled up from the bottom of a graduated cylinder filled with 1.0 L of crude oil at a constant air flow rate of  $\sim 2$  L/min. The volume and weight of crude oil remaining in the cylinder was recorded as a function of time. After 10 days of the weathering process, the oil mass diminished from 807 to 608.5 g (by 24.6 wt.%), and the density of the oil increased from 0.807 to 0.834  $\text{g}/\text{cm}^3$ . The WAO and DWAO were prepared with the procedure shown in Section 3.1.1.6.

Seawater was collected from Grand Bay, Alabama. More information about the sampling site and treating procedures is shown in Section 3.1.1.1. Three model sediments, referred to as GB, OS and EIWR were collected, respectively, from Grand Bay, Alabama (N30.37873, W88.30679), the Ocean Springs National Seashore Park, Mississippi (N30.39772, W88.79175), and the Elmer's Island Wildlife Refuge (EIWR), Louisiana (N29.17764, W90.07401). The salient physical and chemical properties of the sediments were tested by the Soil Testing Laboratory at Auburn University; the details on the analytical methods have been described elsewhere (Gong et al. 2012). Table 13 gives the physicochemical characteristics of the sediment samples.



**Table 13. Physicochemical characteristics of sediment samples**

Sample name	pH	SOM %	CEC Meq/100g	Zeta potential mV	Taxonomy	Sand %	Silt %	Clay %
GB	6.0	3.1	19.6	-14.1	Sandy Loam	56.5	33.5	10.0
OS	6.4	1.6	6.6	-15.3	Loamy Sand	81.6	15.3	3.2
EIWR	7.9	0.8	8.9	-16.1	Sand	87.2	11.5	1.3

Sample name	Ca mg/kg	K mg/kg	Mg mg/kg	Na mg/kg	Al mg/kg	Zn mg/kg	Fe mg/kg	Mn mg/kg	B mg/kg	P mg/kg
GB	767.6	646.6	1209.3	16701.5	204.0	17.2	191.7	18.6	9.2	15.7
OS	441.9	182.7	314.5	4118.4	87.7	5.2	73.1	3.9	3.23	9.1
EIWR	1140.6	247.5	309.2	3894.0	54.0	3.4	232.0	34.0	2.9	61.5

### 3.5.1.2. Effects of dispersants on sediment settling

The settling rate of the sediment particles was tested in 480-mL amber bottles with PTFE lined caps. First, each bottle was filled with 300 mL seawater, and then a known mass (1.2 to 4.2 g, depending on the sediment type) of a sediment was added into the seawater (the sediment mass was adjusted to achieve an equal initial turbidity of  $180 \pm 24$  NTU for the suspensions). The sediment-seawater suspensions were then thoroughly mixed by hand shaking. Upon addition of a known concentration (up to 20 mg/L) of a dispersant, the bottles were placed on an orbital shaker (Excella E5 Platform Shaker, New Brunswick scientific, New Jersey) operated at 200 rpm for 12 hours, and then at 50 rpm for 10 minutes to allow complete contacts between the dispersant molecules and sediment particles. The fully mixed suspensions were then allowed to stand still to initiate quiescent gravity settling of the particles. At predetermined times, samples (4 mL each) were taken from the center (6 cm from the surface) of the suspensions, and then measured for the turbidity change over time.

It should be noted that it took about 15 seconds to obtain a stable turbidity reading. In addition to the three dispersants, the effects of key individual dispersant components, including three surfactants (Tween 80, Tween 85, DOSS) and one solvent (2-butoxyethanol) were also tested to assess their individual effects on the settling performance. In all cases, control tests were carried out without dispersant but under otherwise identical conditions. To assure data quality, all experiments were conducted in duplicate. In all figures, data were plotted as mean of duplicates and error bars were calculated as standard deviation to indicate data reproducibility.

Gordon (1970) showed that the suspended particles are numerically most abundant at the size (diameter) of  $< 7 \mu\text{m}$  in the ocean. For the sediment particles involved, it takes  $\sim 40$  min for the  $7\text{-}\mu\text{m}$  particles to settle from surface to below the sampling point ( $\sim 6$  cm) (See Section 3.5.1.3). Therefore, the 40-min sedimentation efficiency ( $R_{40}$ ) was used to compare settling rates of particles under various conditions.

$$R_{40} = \frac{\text{Turbidity at 40 min } (T_{40})}{\text{Initial Turbidity } (T_0)} \quad (24)$$

Assuming the density of all suspended particles is uniform and does not change, the particle size was calculated according to Stokes' law:

$$V = \frac{2(\rho_p - \rho_f)}{9\mu} gR^2 \quad (25)$$

where  $V$  is the settling velocity of sediment particle (m/s),  $g$  is the gravitational acceleration (9.8

$m/s^2$ ),  $\rho_p$  is the density of the particles,  $\rho_f$  is the density of the seawater, and  $\mu$  is the dynamic viscosity ( $9.594 \times 10^{-4}$  kg/m·s).  $R$  is the radius of the sediment particle (m).

From the calculation, the particles with diameter larger than 82  $\mu\text{m}$  will settle from the surface layer to below the sampling point (depth of 6 cm) within 15 seconds. And the particles with a diameter of 7  $\mu\text{m}$  take ~40 min for the particles to settle from the surface layer to below the sampling point.

### **3.5.1.3. Effects of environmental factors, WAO and DWAO on settling of sediment particles**

The effect of pH was evaluated by comparing the particle settling rates in the pH range of 4 to 9.2, where pH was adjusted using dilute (0.5 M) NaOH or HCl solutions. The effect of salinity was tested by using synthetic solutions containing 0 to 3.5 wt.% NaCl (in this case deionized water was used). To test the effect of DOM, a commercial humic acid (Fluka, Switzerland) was added to the seawater to achieve a DOM concentration of 10 mg/L as TOC. The effect of temperature was tested at 4 °C simulating the deepwater temperature and 25 °C for surface water temperature (Liu et al., 2012b). All the experiments were carried out in the presence or absence of a dispersant (Corexit EC9527A). To assess effects of WAO and DWAO on sediment settling, the batch settling experiments were also conducted using 300 mL of the WAO or DWAO solution.

### **3.5.1.4. Effects of dispersant on sorption and transport of oil and PAHs**

Adsorption kinetic tests of two model PAHs (phenanthrene and pyrene) by sediment was carried out to evaluate the adsorption rate and sediment-facilitated transport of oil compounds. The tests were carried out using 480-mL amber glass bottles capped with Teflon-lined septa. First, 3.6 g sediment (OS) was mixed with 300 mL seawater in each bottle, and then an aliquot of the Corexit EC9527A solution was added to reach a dispersant concentration of 10 mg/L. Then, the sorption was initiated by adding an aliquot of the PAH stock solutions into the sediment-seawater suspensions, which resulted in an initial phenanthrene concentration of 600  $\mu\text{g/L}$  or pyrene concentration of 40  $\mu\text{g/L}$ . The bottles were mixed on an orbital shaker operated at 200 rpm. At predetermine times, samples (3 mL each) were withdrawn from the bottles and centrifuged at 3000 rpm ( $1359 \times g$ ) for 5 minutes to separate the solids from the solution. The supernatant was then mixed with methanol (v/v = 1:1), and the mixture was filtered through a 0.2  $\mu\text{m}$  Anopore syringe filter (Whatman® Anotop 10). The filtrate was analyzed for the PAHs. The addition of methanol prevents PAHs sorption on the filter. For comparison, the same tests were also carried out without dispersant.

The effects of oil dispersants on sediment-facilitated transport of crude oil and PAHs from water column to bottom sediment were tested through the same batch settling test procedure. Briefly, 60  $\mu\text{L}$  of the oil sample was added in 300 mL sediment-seawater mixture in 480 mL-amber glass bottles. Then, an aliquot of the Corexit EC9527A stock solution was added to achieve a dispersant concentration of 10 mg/L, or a dispersant-to-oil ratio (DOR) of 1:20. Then the bottles were mixed on an orbital shaker for 12 hours and settled for 8 hours. The remaining surface oil, settled sediment, and the water column were separated as follows: first ~90% water was pipette-sampled from the water column; then, the mixture was frozen, which allowed the surface oil phase to be collected with dichloromethane; the remaining sediment phase was then obtained upon thawing the mixture. The water column and sediment samples were extracted three times using dichloromethane (Zhang et al. 2010), and the TPHs, PAHs and *n*-alkanes in the extracts were determined using GC-FID or GC-MS (Section 3.3.1.2). Control tests indicated that the liquid-liquid extraction recovered > 95% of the oil compounds in water, and > 90% in the sediment phase.

### 3.5.1.5. Analytical methods

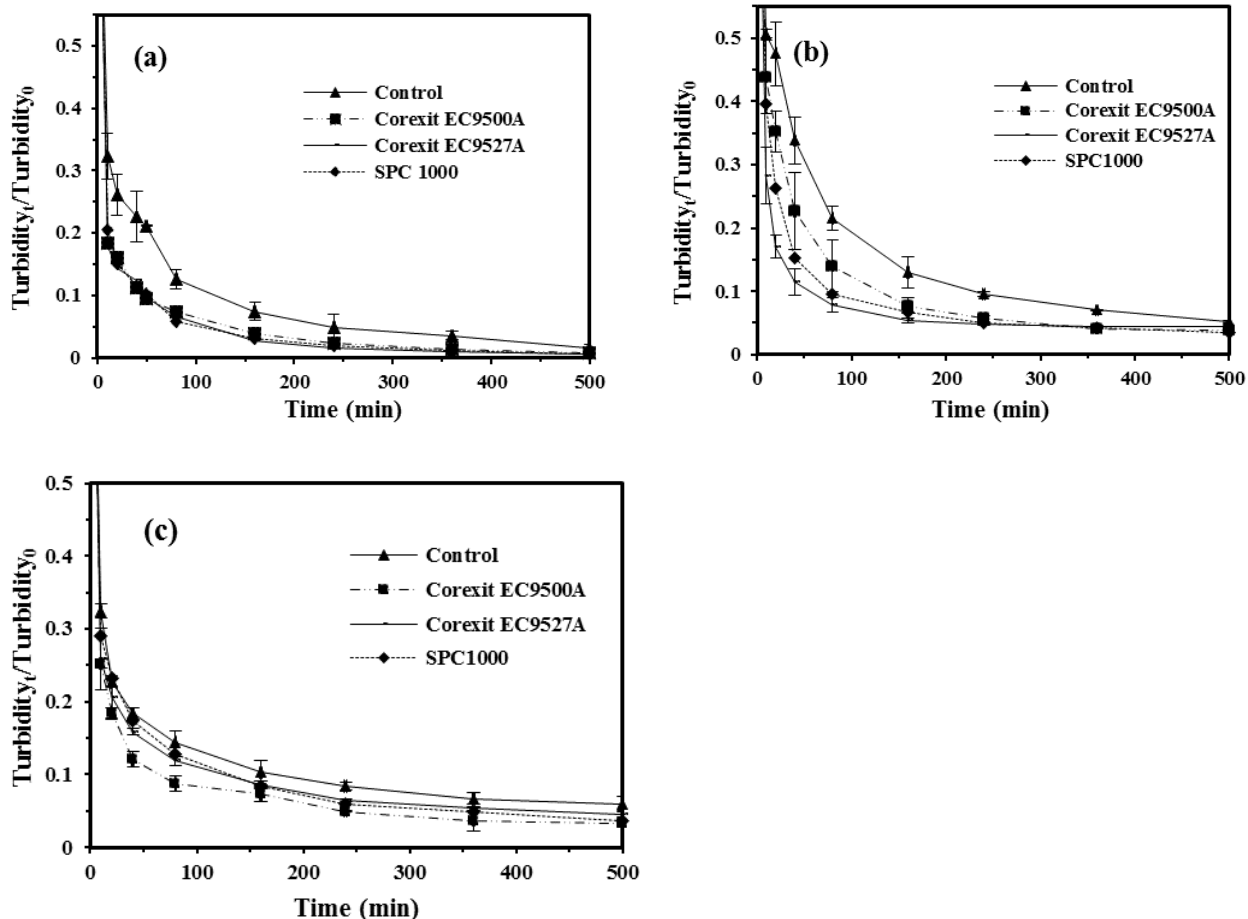
The turbidity of the sediment suspensions was measured using a HACH 2100N Turbidimeter, with a detection limit of 0.5 NTU. The hydrodynamic diameter and zeta potential of suspended particles were determined by dynamic light scattering (DLS) (Zetasizer Nano ZS, Malvern Instruments Ltd.) at 25 °C. TOC was measured by a Tekmar Dohrmann Pheonix 8000 UV-Persulfate TOC analyzer. Phenanthrene and pyrene in seawater were quantified using an HPLC system. More information about the analysis methods are shown in Section 3.2.1.2.

### 3.5.2. Effect of dispersants on sediment settling

**Figure 40** presents the settling kinetics of the three sediments in the presence of the three model dispersants. **Figure 40a** and **b** show that all three dispersants accelerated the settling rates of GB and OS sediments significantly ( $p < 0.05$ ). For GB, the effects for the three dispersants were nearly equal, where the  $R_{40}$  increased from 77.4% to ca. 88.3% in the presence of dispersants (**Figure 40a**). However, the effects of dispersants on OS varied slightly, although the steady state turbidity levels were about the same (**Figure 40b**). The presence of Corexit EC9500A, Corexit EC9527A and SPC 1000 increased the  $R_{40}$  from 66.2% (as control) to 83.3%, 88.5%, and 84.7%, respectively. Corexit EC9527A appeared to be most effective on enhancing the settling velocity of the particles, followed by Corexit EC9500A (a sister product). However, as **Figure 40c** shows, the effect of Corexit EC9500A was more profound than Corexit EC9527A and SPC 1000 on enhancing the settling rate of EIWR sediment particles. Among the three sediments, the EIWR sediment displayed the fastest settling rate than the other sediments in the absence of dispersant (the  $R_{40}$  values are 77.4%, 66.2%, 81.6% for GB, OS, EIWR sediments, respectively).

**Table 13** shows that GB is classified as sandy loam, OS as loamy sand, EIWR as sand. The SOM, silt and clay contents in sediments follow the sequence of: GB > OS > EIWR, which agree with the notion that the initial turbidity of sediments is primarily due to suspended silt and clay particles.

Surfactants (the major dispersant components) can be adsorbed on sediment particles through hydrophobic interactions between the surfactant tail and SOM or through electrostatic interactions between the surfactant heads and the mineral functional groups of sediments. The adsorption is more favored with smaller particles or larger surface area and/or higher sediment SOM content (Jones-Hughes and Turner 2005). Based on particle size, GB and OS are expected to take up more dispersants than EIWR; on the other hand, based on the SOM content and the actual sediment dosage in the mixtures, the total SOM in the OS system was the highest (0.192 g/L), followed by GB (0.124 g/L) and then EIWR (0.112 g/L). The fact that the dispersants showed the most effect on the settling of OS and least on EIWR indicates that SOM content is the most critical parameter governing the dispersant effect.



**Figure 40. Effects of oil dispersants on the settling kinetics of marine sediments.**

(a) GB at 4 g/L, (b) OS at 12 g/L, and (c) EIWR at 14 g/L. Experimental conditions: initial turbidity =  $180 \pm 24$  NTU in all cases, Corexit EC9527A = 5 mg/L, pH =  $7.0 \pm 0.5$ , temperature =  $25 \pm 1$  °C.

The settling velocity distribution of suspended sediment at various dispersant concentrations was calculated based on the sampling depth (6 cm) and settling time, and the corresponding size distribution of suspended sediment particles was calculated according to Stokes' law (Equation 25), and is shown in **Figure 41**. The results indicate that the addition of the dispersant enhanced aggregation of the fine particles, e.g., the percentage of particles with  $r < 2.9$   $\mu\text{m}$  decreased from 22.6% to 12.4% for GB sediment, 33.8% to 11.5% for OS sediment, 18.4% to 15.9% for EIWR sediment in the presence of Corexit EC9527A at 5 mg/L.

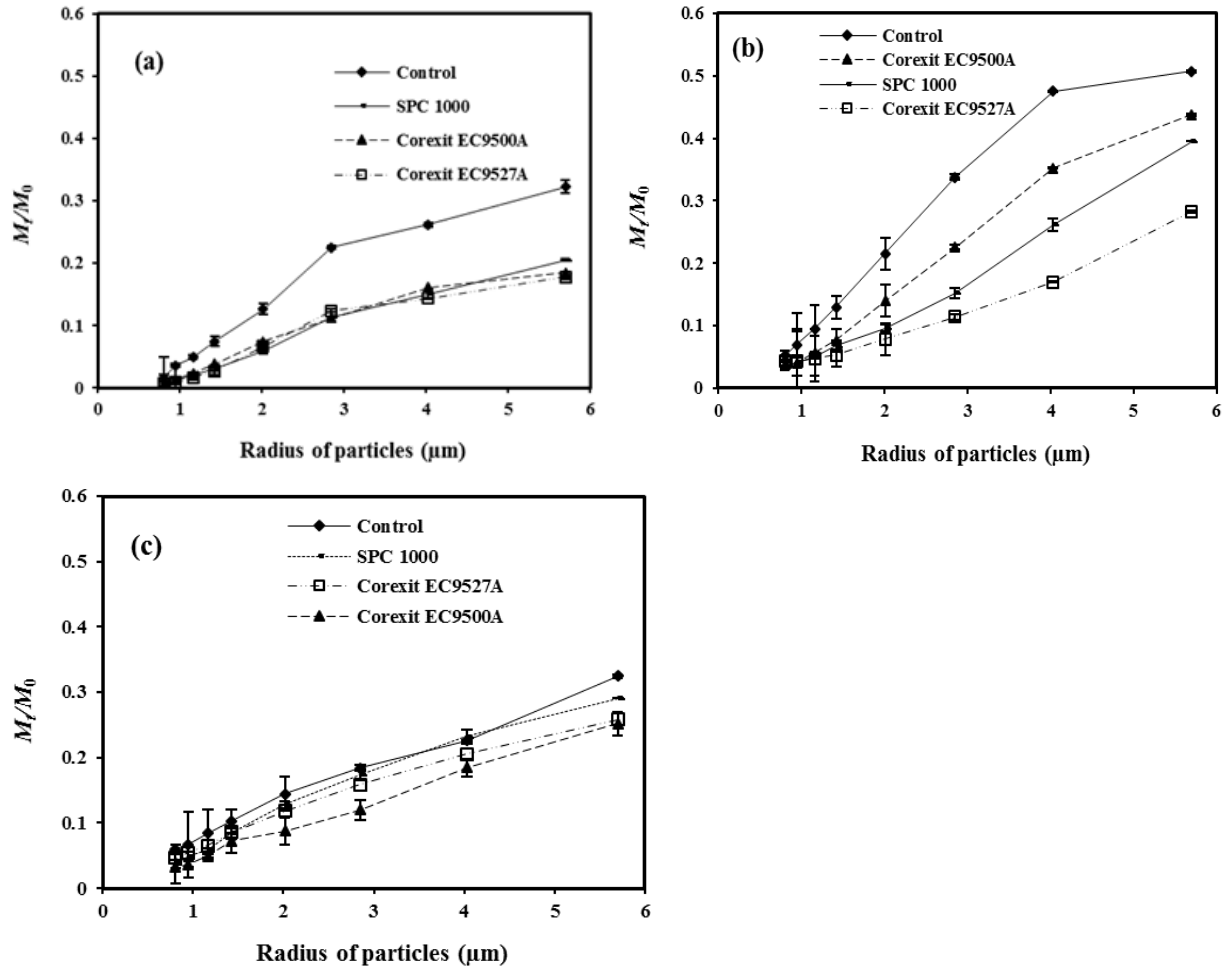


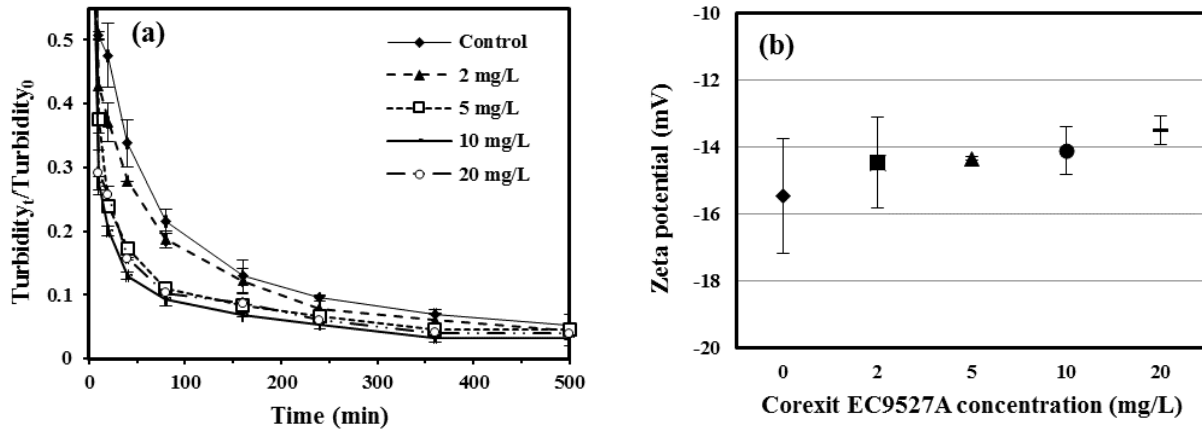
Figure 41. Effects of oil dispersants on particle size distribution of marine sediments. (a) GB at 4 g/L, (b) OS at 12 g/L, and (c) EIWR at 14 g/L.  $M_0$  is the total mass of all particles, and  $M_i$  refers to the mass of particles with radius less than the corresponding x-axis value.

As the most salient dispersant effects were observed for the OS sediment with Corexit EC9527A, more detailed investigation was carried out with OS and Corexit EC9527A subsequently to further explore the mechanisms on the dispersant-accelerated settling of suspended sediment particles.

**Figure 42** shows effects of various levels of Corexit EC9527A on the settling of the sediment particles. The presence of 2 and 5 mg/L of the dispersant increased  $R_{40}$  from 66.2% to 72.1% and 82.8%, respectively. However, further increasing the dispersant concentration to 20 mg/L showed insignificant additional effect. The observation indicates that the 10 mg/L dispersant concentration represents a saturation level showing the maximum effect.

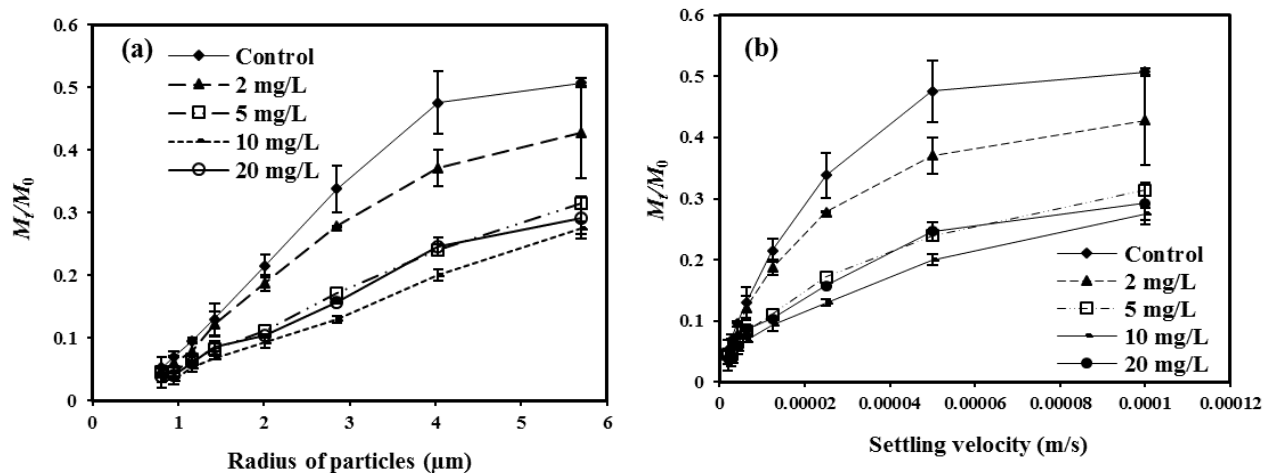
**Figure 42b** shows that increasing the dispersant concentration from 0 to 20 mg/L modestly suppressed the zeta potential of the particles from -15.5 to -13.5 mV ( $p < 0.05$ ), indicating that the decrease in the surface potential played a minor but significant role (Hunter 2013). **Figure 43** shows the size and settling velocity distributions of suspended particles as a function of the dispersant concentration, and the data indicate that increasing the dispersant concentration up to 10 mg/L progressively enhanced aggregation of the fine particles, e.g., in the presence of 2 and 10 mg/L of Corexit EC9527A, the percentage of particles with  $r < 2.9 \mu\text{m}$  decreased from 33.8% to 27.9% and 13.0%, and that for particles with  $v < 0.00005 \text{ m/s}$

decreased from 47.5% to 37.1% and 20.0%, respectively.



**Figure 42. Settling kinetics of OS sediment particles and zeta potential of sediment.**

(a) In the presence of various concentrations of Corexit EC9527A, and (b) zeta potential of the sediment suspension. Experimental conditions: OS sediment = 12 g/L, seawater volume = 300 mL, pH = 7.3±0.3.

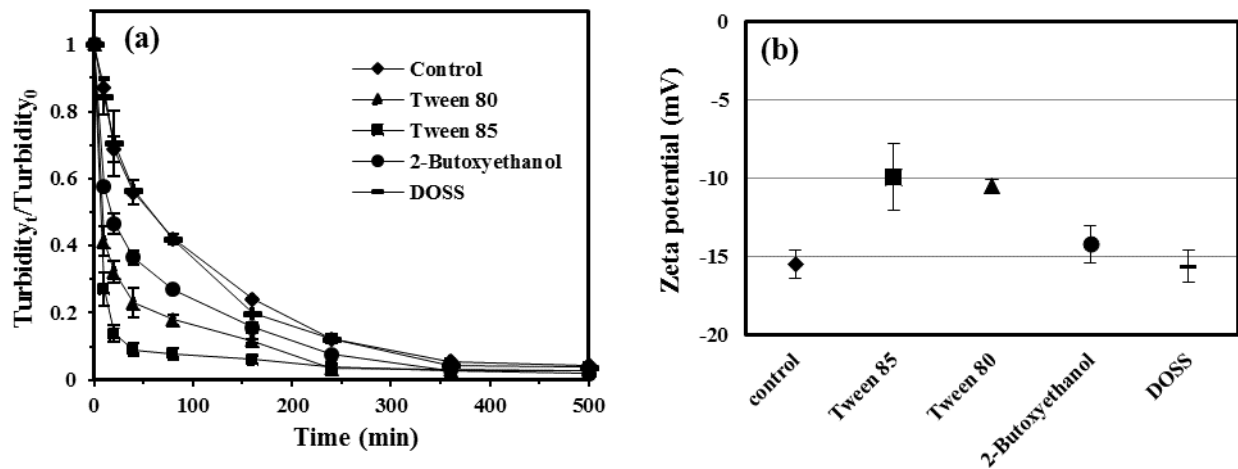


**Figure 43. Distributions of particle size (a) and settling velocity (b) of sediment particles.**

Suspended sediment particles: OS; Corexit EC9527A = 0–20 mg/L.  $M_0$  is the total mass of all particles, and  $M_i$  refers to the mass of particles with radius or settling velocity less than the corresponding x-axis value.

Corexit EC9527A is a mixture of both anionic (35%) and nonionic (48%) surfactants in solvent (Bruheim et al. 1999). It contains the same surfactants as Corexit EC9500A, and a solvent 2-butoxyethanol, which is not an ingredient in Corexit EC9500A (Gong et al. 2014b, Zhao et al. 2015). **Figure 44a** shows the individual effects of the three key surfactants (Tween 80, Tween 85, and DOSS) of the Corexit dispersants and the solvent (2-butoxyethanol) on the settling performance of the sediment particles. The nonionic surfactants, i.e., Tween 85 and Tween 80, enhanced particle settling the most, while the anionic surfactant DOSS had negligible effect on particle settling. Between the two nonionic surfactants, Tween 85 has three hydrophobic tails (three C18 tails) per molecule, and Tween 80 has only one hydrophobic tail per molecule with the same chain length (C18) (Cirin et al. 2012, Mahdi et al. 2011). Consequently, Tween 85 offers higher affinity for SOM, and thus, was found more effective in enhancing

the particle aggregation. 2-butoxyethanol was also able to accelerate the settling velocity, though to a lesser extent than the non-ionic surfactants, which partially explains the greater effect of EC9527A over EC9500A. **Figure 44b** shows that the presence of the two nonionic surfactants suppressed the zeta potential by  $\sim 5$  mV, while DOSS exhibited a negligible effect.



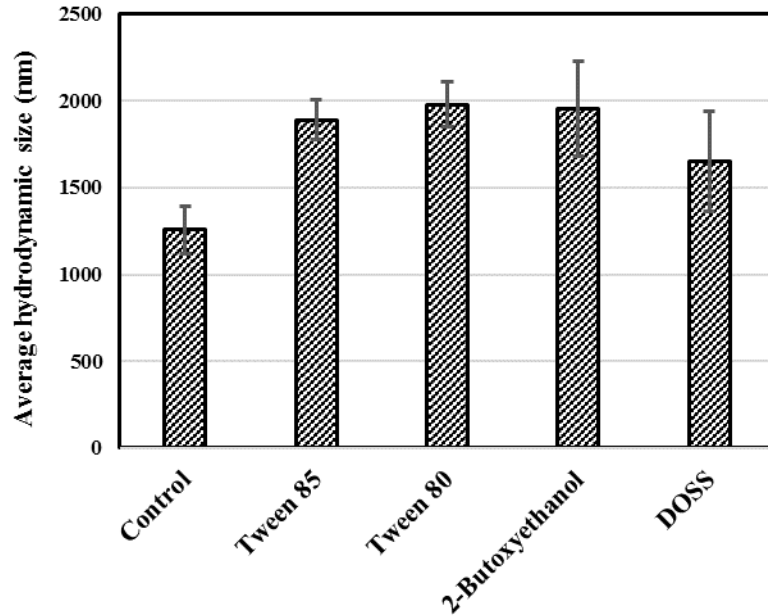
**Figure 44. Effects of dispersant components on settling and zeta potential of sediment particles.** (a) Settling kinetics of OS sediment in the presence of individual key dispersant components, and (b) effects of individual dispersant components on zeta potential of sediment suspension. Experimental conditions: sediment dosage = 15 g/L, dispersant components = 10 mg/L, pH = 7.3 $\pm$ 0.2.

Both Tween 80 and Tween 85 contain hydrophilic ethylene glycol heads and hydrophobic alkyl tails. These amphiphilic molecules can bind with sediment minerals and SOM through electrostatic and hydrophobic interactions (Joshi et al. 2008, Shen et al. 2011, Zhou et al. 2011), and can act as a bridging agent to facilitate flocculation of fine particles. In addition, the adsorbed nonionic surfactant layer on charged particles may shield the surface electrical potential and thus diminish the electrostatic repulsion between the particles, both being conducive to particle aggregation. Rufier et al. (2011) studied the effect of surfactants on hydrophobically end-capped poly(ethylene oxide) self-assembled aggregates by using small-angle neutron scattering (SANS), and found that the addition of a nonionic surfactant increased the aggregation. 2-butoxyethanol ( $\text{CH}_3(\text{CH}_2)_3\text{O}(\text{CH}_2)_2\text{OH}$ ) behaves as an alcohol that lowers the surface tension and reduces the surface charge of particles (Kline and Kaler 1994). It was reported that increasing 2-butoxyethanol concentration could convert the strong interparticle repulsive force to hard sphere attractive force (Kline and Kaler 1994). The observation indicates that the enhanced settling by the Corexit dispersants is primarily attributed to the effects of the nonionic surfactants along with the solvent, whereas the anionic surfactant DOSS tends to maintain the same surface potential due to its negative heads.

To test effects of the dispersant components on aggregation of the finer sediment particles, the hydrodynamic size of the suspended particles of  $<10 \mu\text{m}$  was monitored using the Malvern Zetasizer. The suspended particles were obtained by taking the supernatant from a sediment-seawater mixture after 80 min of gravity settling (initial OS = 15 g/L). **Figure 45** shows the effects of various dispersant components (10 mg/L) on the hydrodynamic diameter of the particles when the particles were mixed with the dispersant components for 12 h.

**Figure 45** shows that the presence of Tween 85, Tween 80, and 2-butoxyethanol increased the average hydrodynamic particle size from 1.26 (control) to 1.89, 1.98, and 1.96  $\mu\text{m}$ , respectively, which is consistent with the zeta potential profile (**Figure 45**). However, although DOSS had little effect on the

zeta potential (**Figure 45**), it also increased the average hydrodynamic size of the sediment particles, though to a lesser extent. This can be due to the opposing effects of the tail and head of DOSS: though the surfactant chain tends to bridge the fine particles (Gupta et al. 2014), the charged head tends to resist the aggregation of the particles.



**Figure 45. Effects of dispersant components on particle size.**

Average hydrodynamic particle size of suspended particles in the presence of various key dispersant components. Dispersant components concentration was 10 mg/L. Experimental pH =  $7.3 \pm 0.3$ .

The comparison of **Figure 45** and **Figure 46** reveals that despite the modestly increased hydrodynamic particle size, DOSS did not significantly promote the settling rate, suggesting that the aggregates associated with DOSS are more loose and fluffy (i.e., of lower density). Likewise, although the presence of 2-butoxyethanol increased the hydrodynamic size to that comparable to Tween 85 or Tween 80, the particle settling was not as significantly enhanced as by the surfactants (**Figure 45a**). In fact, the solvent barely altered the zeta potential (**Figure 45b**). This observation indicates that the hydrodynamic size alone may not reflect the settleability, other factors such as the density and shapes of the aggregates should also be taken into account.



The settling velocity ( $v$ ) of fine sediment particles is dependent on the balance between the drag and gravitational forces on the particles as depicted by Equation 26 (Khelifa and Hill 2006).

$$v = \left( \frac{4}{3} \theta \cdot g \cdot C_d^{-1} \cdot \frac{\Delta\rho}{\rho_w} \cdot D \right)^{0.5} \quad (26)$$

where  $\theta$  is the dimensionless particle-shape factor,  $g$  is the gravitational acceleration ( $\text{m/s}^2$ ),  $C_d$  is the dimensionless drag coefficient,  $\Delta\rho$  is the effective density of the particle, or excess density ( $\rho_p - \rho_w$ ) with  $\rho_p$  and  $\rho_w$  being the densities of the particle and solution ( $\text{kg/m}^3$ ), respectively, and  $D$  is the equivalent spherical diameter of the particle (m).  $C_d$  can be determined by the empirical correlation equation:

$$C_d = \frac{24}{Re} (1 + 0.15 Re^{0.687}) \quad (27)$$

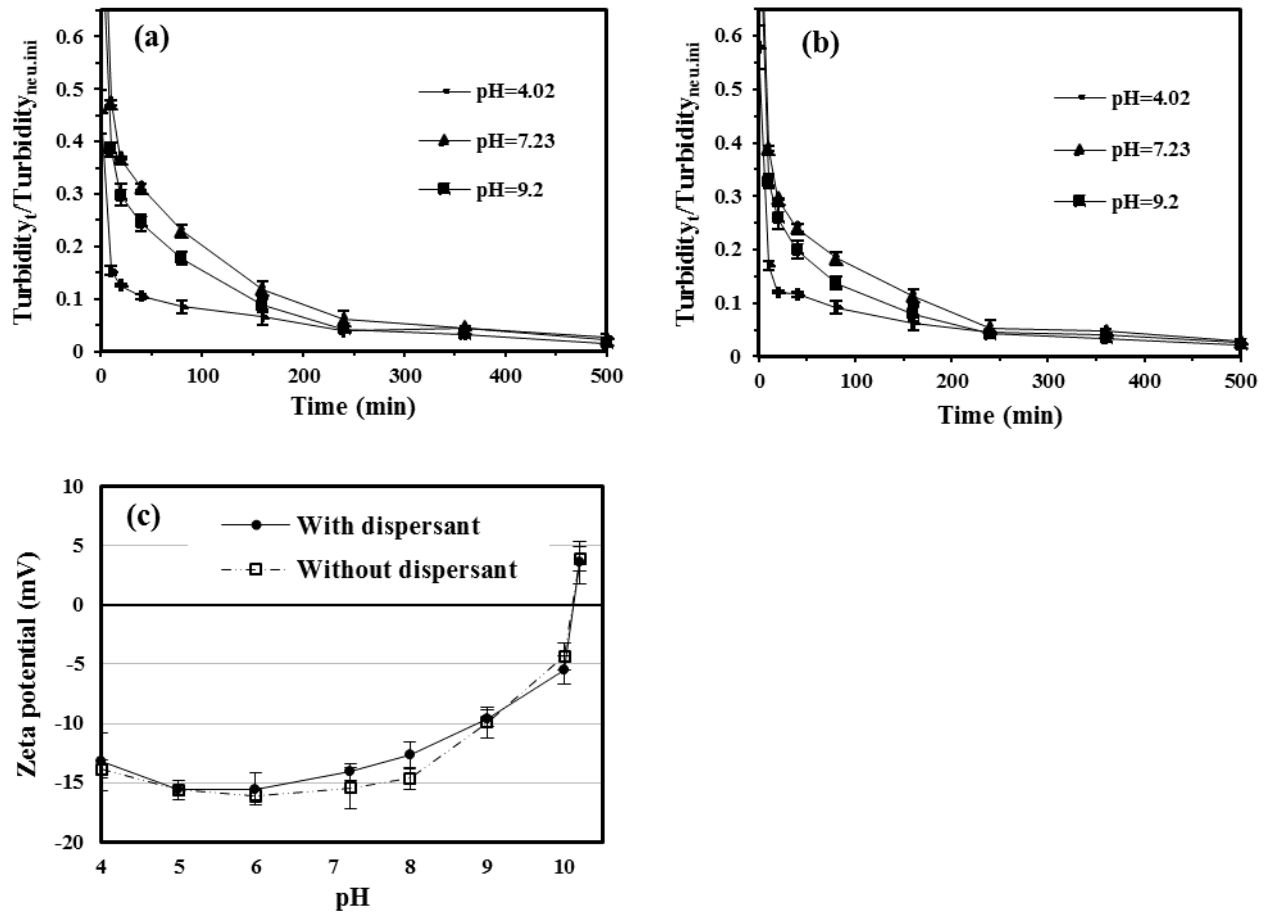
where  $Re$  is the Reynolds number.

Equation 26 and 27 are in accord with the classic Stokes law, where the size and density of particles govern the settling velocity (Khelifa and Hill 2006). The dispersant components may not increase the density of the particles; rather, they can promote the aggregation of small particles through interparticle bridging and/or by lowering the interparticle repulsive electrical double-layer forces. Given the rather negative zeta potential and coating of the bulky surfactant molecules on the particle surface, the particle aggregation falls into the unfavorable collision domain, i.e., the aggregation is due to the secondary energy minimum according to the DLVO theory (Redman et al. 2004, Shen et al. 2007). Therefore, formation of the dispersant-associated aggregates is likely to be reversible.

### 3.5.3. Effects of dispersant under various environmental conditions

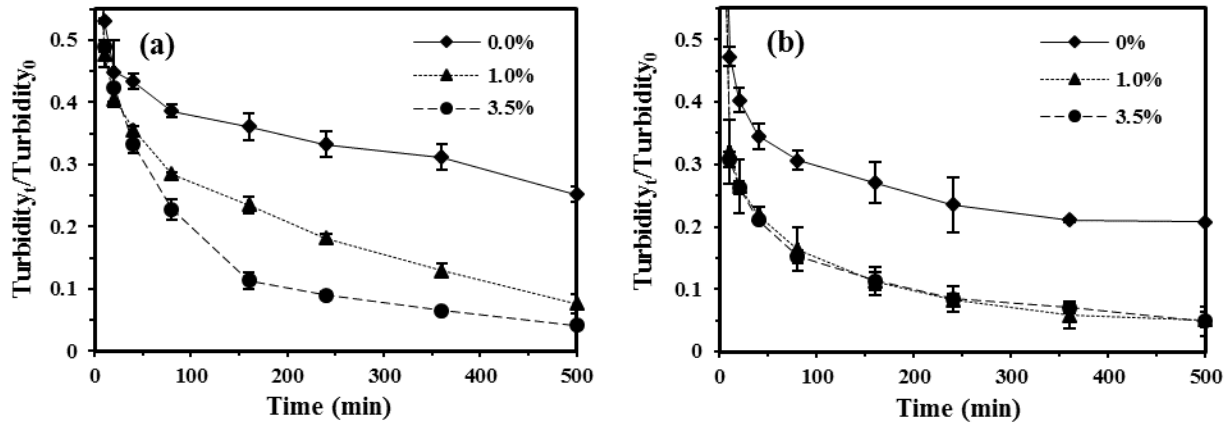
**Figure 46** shows the settling kinetics and zeta potential of sediment particles as a function of pH with or without dispersant. The results show that regardless of the dispersant, the fastest particle settling was observed at the acidic pH 4.02 ( $R_{40} = 88.4\%$  with dispersant and  $89.5\%$  without dispersant), whereas the slowest settling was at pH 7.23 ( $R_{40} = 75.9\%$  and  $68.8\%$ , respectively). The dispersant increased  $R_{40}$  from  $68.7\%$  to  $75.9\%$  at pH 7.23 and from  $75.5\%$  to  $80.0\%$  at pH 9.2, but had little effect at pH 4.02. **Figure 46 c** shows that the dispersant had negligible effect on the zeta potential in the broad pH range except at pH 7 and 8, indicating that the zeta potential is important to the settling performance of sediment at neutral pH, but not the only factor that alters the aggregation and settling performance of sediment particles.

The seawater and sediment contain high concentrations of metal ions, e.g.  $\text{Mg}^{2+}$  and  $\text{Ca}^{2+}$  concentration are 1250 and 360 mg/L in the seawater, 314.5 and 441.9 mg/kg in the OS sediment. As pH rises, more precipitates of metal hydroxides and carbonates will form, resulting in lowered zeta potential. For instance, based on the Visual MINTEQ (version 3.1) calculation,  $\text{Mg}^{2+}$  becomes oversaturated at pH  $> 10$ , where the solid mineral brucite  $\text{Mg}(\text{OH})_2(\text{s})$  is formed. The dramatic drop in soluble metal concentrations at pH  $> 10$  was confirmed by directly analyzing the soluble metal concentrations. Consequently, the unusually high pH of the point of zero charge ( $\text{pH}_{\text{pzc}}$ ) shown in **Figure 46c** may not indicate the true value for the sediment (Yukselen and Kaya 2003). The high metal concentrations can also be responsible for the weakened effect of the dispersant on the zeta potential.



**Figure 46. Influences of pH on settling kinetics and zeta potential of OS sediment.** (a) Settling kinetics without dispersant, (b) settling with Corexit EC9527A, and (c) zeta potential of the sediment particles as a function of pH. Experimental conditions: Corexit EC9527A = 10 mg/L, sediment (OS) = 12 g/L.

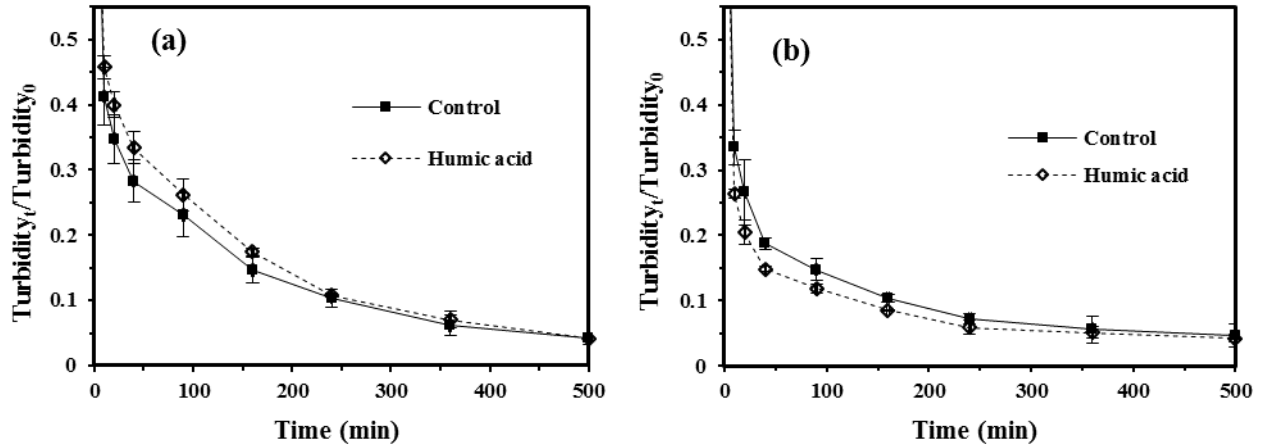
**Figure 47** confirms that increasing electrolyte (NaCl) concentration greatly accelerates particle aggregation and increases the settling velocity of suspended solids in the absence of dispersant ( $R_{40} = 56.6\%$ ,  $64.4\%$  and  $66.8\%$  at 0, 1.0, and 3.5 wt.% of NaCl, respectively). However, the electrolyte effects differed notably in the presence of the dispersant. First, the presence of NaCl and the dispersant synergistically enhanced the settling and increased  $R_{40}$  to  $79.0\%$  even at 1.0 wt.% of NaCl, which is in accord with the double-layer theory. Second, further increasing the salt to 3.5 wt.% showed negligible further effect, indicating that the dispersant molecules shielded some of the negative sites on the sediment particles from interacting with counter ions in the solution, i.e., the dispersant may alleviate the ionic strength effect.



**Figure 47. Settling kinetics of OS sediment particles at various NaCl concentrations in the absence (a) or presence (b) of dispersant Corexit EC9527A.**

Experimental conditions: OS sediment = 12 g/L, Corexit EC9527A = 10 mg/L, pH =  $7.3 \pm 0.2$ .

**Figure 48** shows that the presence of humic acid decreased the settling rate ( $R_{40}$ ) from 71.7% to 66.6%. However, the presence of humic acid accelerated the  $R_{40}$  from 78.6% to 83.1% in the presence of dispersant. Humic acid has strong affinity to the surface of clay and metal oxide particles (Tombacz et al. 2004), the sorption of humic acid renders a more negatively charged particle surface, and thus stronger repulsive forces and greater particle stability (Furukawa et al. 2009, Kretzschmar et al. 1997). However, the presence of dispersant and humic acid synergistically accelerated the settling rate, which can be due to the increased uptake of dispersant on sediment with sorbed humic acid (Alila et al. 2007). The elevated dispersant on sediment in turn masked the electrical potential from the dissociated organic acid functional groups, resulting in elevated aggregation of the sediment particles.

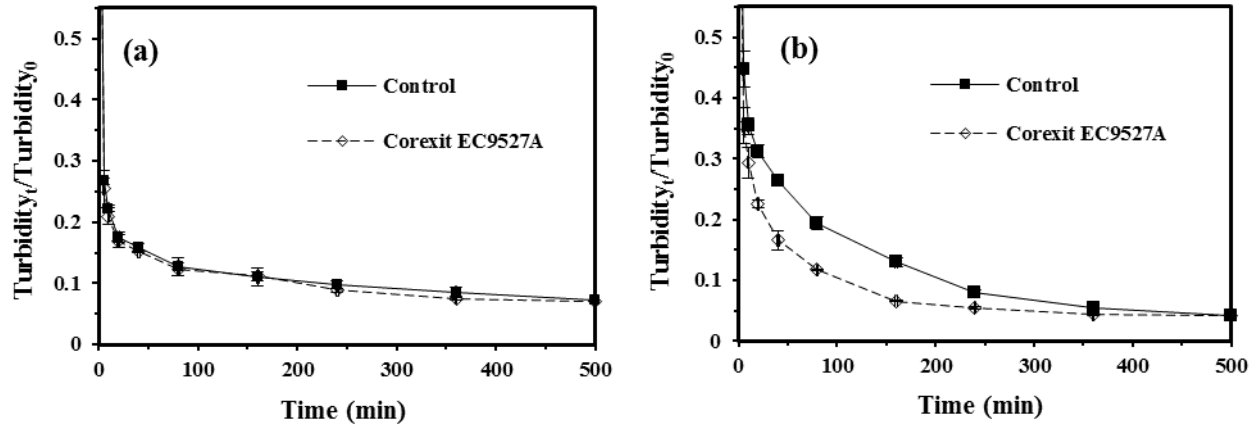


**Figure 48. Effects of humic acid on settling of OS sediment.**

Particle settling kinetics with humic acid in the absence (a) or presence (b) of dispersant Corexit EC9527A.

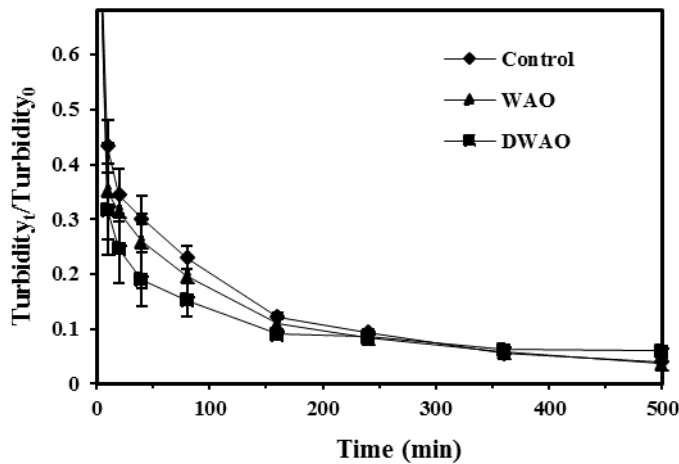
Experimental conditions: OS sediment = 12 g/L, Corexit EC9527A = 10 mg/L, pH = 7.3±0.2, temperature = 25±1 °C.

Seawater temperature varies widely from surface to bottom. **Figure 49** compares the dispersant effects at 4 and 25 °C, representing bottom and surface seawater temperatures. The dispersant shows negligible effect on altering settling of the sediment at 4 °C, but increased  $R_{40}$  from 73.6% to 83.4% at 25 °C. The hindered dispersant effects at 4 °C can be primarily attributed to the reduced adsorption of non-ionic surfactants by sediment. Increasing temperature increasingly desolvates the head group, rendering it less hydrophilic and more compact, and thus increases the surface activity and saturation adsorption values (Paria and Khilar 2004). Zhao et al. (2015) reported that the adsorption of dispersant (Corexit EC9500A) by marine sediment at 4 °C was much lower than at 21 °C.



**Figure 49. Effects of temperature on settling kinetics of sediment particles.** (a) 4 °C, and (b) 25 °C with or without dispersant. Experimental conditions: sediment (OS) = 12 g/L, Corexit EC9527A = 10 mg/L, pH 7.3±0.2.

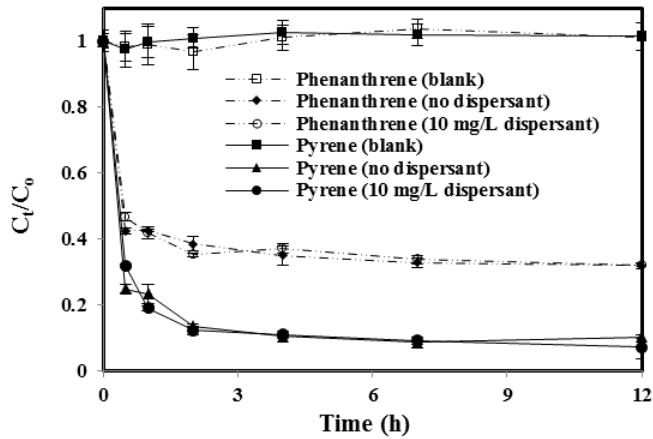
**Figure 50** shows effects of WAO and DWAO on the settleability of the sediment particles. The presence of WAO increased  $R_{40}$  from 70.0% to 74.1%, and the addition of DWAO increased  $R_{40}$  from 70.0% to 81.0%. The very subtle effect of WAO is associated with the very limited solubility of oil (< 2 mg/L), whereas the much pronounced impact of DWAO is attributed to: 1) with the dispersant, much more oil was dispersed, and thus much more oil was adsorbed on the particles, and 2) DWAO and elevated oil uptake can facilitate the formation of OSAs (Wang et al. 2013c). The final turbidity for the suspension with DWAO appeared slightly higher, which can be attributed to the distributed oil droplets and some oiled-particles that are lighter and less settable. Fu et al. (2014) studied the effects of oil and dispersant Corexit EC9500A on formation of MOS, and found that both the dispersant and oil promoted the formation of MOS. The researchers also observed that dispersant may facilitate sorption of oil components onto MOS (Xue et al. 2015), which in turn promotes further aggregation and facilitates transport of the oil components.



**Figure 50. Effects of WAO and DWAO on settling of OS sediment particles.**  
 Experimental conditions: sediment (OS) = 12 g/L, pH = 7.3±0.2, temperature = 25±1 °C.

### 3.5.4. Effect of dispersant on sediment-facilitated distribution and transport of oil components

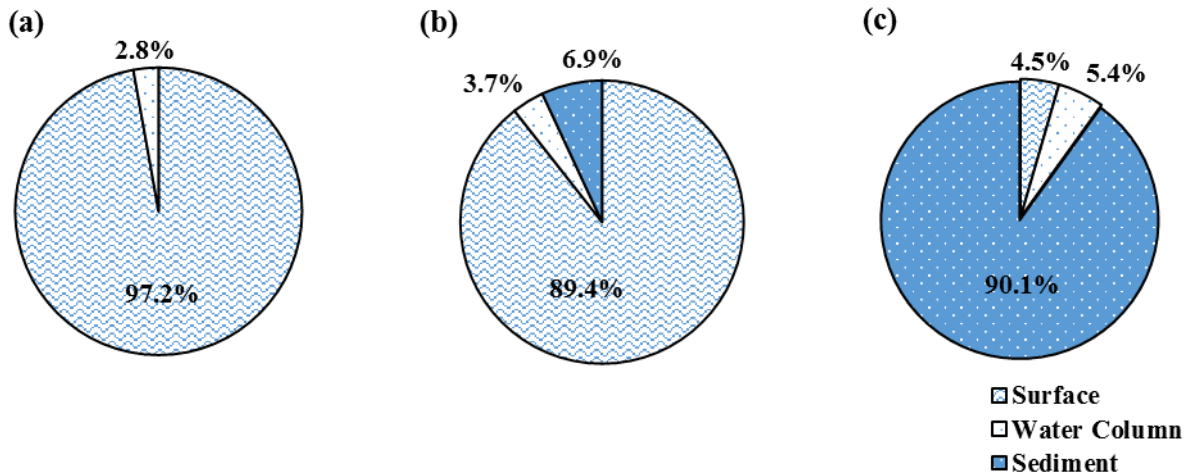
PAHs and other oil components are subject to sorption to sediment particles. For instance, **Figure 51** shows that the OS sediment particles can rapidly adsorb both phenanthrene and pyrene. Given that the dispersant enhances settling of suspended particles, the dispersant would also facilitate the vertical transport of sediment-associated oil components to the seafloor.



**Figure 51. Sorption kinetics of phenanthrene and pyrene.**

Experimental conditions: initial phenanthrene = 600  $\mu\text{g/L}$ , initial pyrene = 40  $\mu\text{g/L}$ , Corexit EC9527A = 0 or 10 mg/L, sediment (OS) = 12 g/L, pH = 7.0–7.5, temperature =  $25 \pm 1$   $^{\circ}\text{C}$ . Control tests were carried out without sediment.

**Figure 52** shows the equilibrium distributions of oil (as TPHs). In the presence of the dispersant, oil in the sediment phase was increased from 6.9% (no dispersant) to 90.1%, which reveals that oil dispersion can dramatically promote partitioning of oil into the sediment phase. The sediment-facilitated transport of dispersed oil may partially account for the oil in the bottom sediment observed following the *DWH* oil spill (White et al. 2012). Interestingly, the oil content in the water column was increased only modestly from 3.7% to 5.4%, compared with 2.8% without dispersant and sediment. This observation clearly reveals that when sufficient sediment is present, the primary role of the dispersant is to facilitate transferring oil from the water surface to the sediment phase rather than in the water column. Furthermore, it might be conceived that in some circumstances dispersants and selected sediment particles may be applied simultaneously as a rapid and emergency approach to mitigate impacts of oil spill.



**Figure 52. TPH distributions on seawater surface, in seawater column or sediment.**

In the following systems: (a) Seawater and oil, (b) seawater, oil and sediment without dispersant, and (c) seawater, oil and sediment with dispersant. Experimental conditions: sediment (OS) = 12 g/L, Corexit EC9527A = 10 mg/L, pH = 7.3±0.2, oil dosage = 60 µL oil in 300 mL seawater for all the cases.

Oil dispersants are known to facilitate formation of small oil-surfactant aggregates, thereby dispersing more oil into the water column (Paris et al. 2012). Gong et al. (2014b) reported that dispersant not only enhances dissolution, but also promotes sediment uptake of oil components. Payne et al. (1989) proposed an equation to characterize the loss rate of free oil droplets due to collision and adherence to SPM.

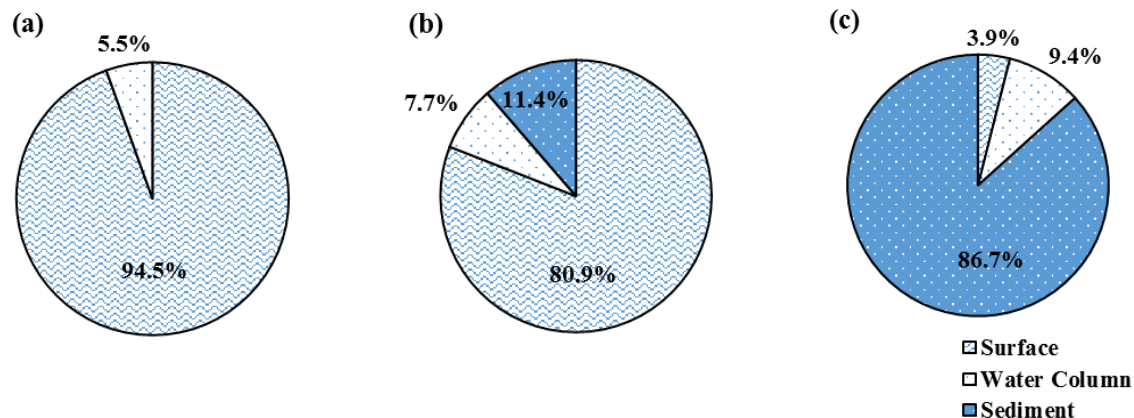
$$dC/dt = -1.3\alpha[\varepsilon/\nu]^{1/2}CxS \quad (28)$$

where  $C$  = concentration of oil droplets (mg/L),  $S$  = concentration of SPM (mg/L),  $\alpha$  = SPM “shape, size, and sticking” coefficient,  $\varepsilon$  = the energy dissipation rate (per mass of fluid), and  $\nu$  = the kinematic viscosity of the water.

From Equation 28, the removal of the dispersed oil droplets from the water column by sediment is primarily attributed to the high sediment concentration (12 g/L). Furthermore, taking into account the dynamic particle aggregation, the initially sorbed oil droplets and dispersant molecules create an even more favorable condition for attracting more oil from the water column, resulting in the formation of even larger oil-sediment aggregates (Bandara et al. 2011).



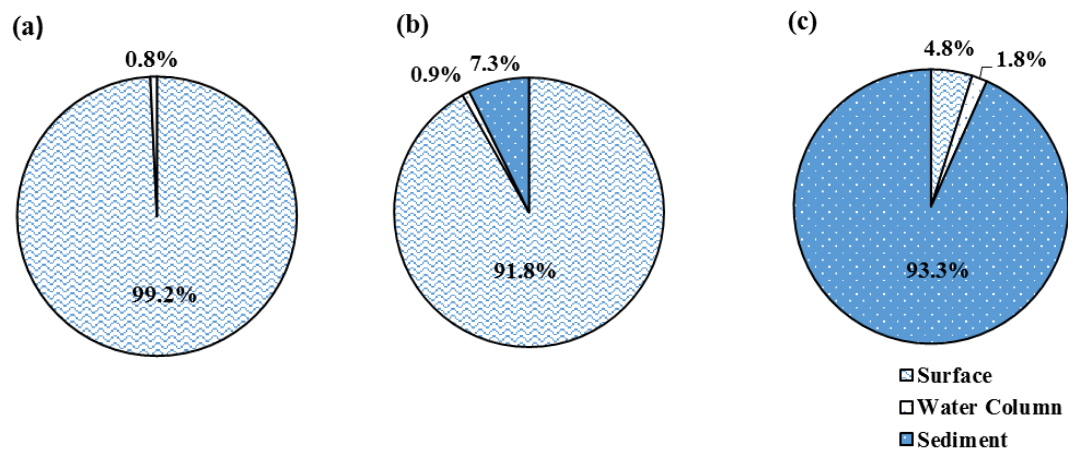
**Figure 53** shows that the presence of dispersant increased the total PAHs content in the sediment phase from 11.4% to 86.7%, and the PAHs concentration in the water column from 7.7% to 9.4%, which is consistent with the distributions of TPHs. Similar dispersant-facilitated sediment uptake was also observed for the oil alkanes.



**Figure 53. Total PAHs distributions on seawater surface, in seawater column or sediment.**

In the following systems: (a) seawater and oil, (b) seawater, oil and sediment without dispersant, and (c) seawater, oil and sediment with dispersant. Experimental conditions: sediment (OS) concentration = 12 g/L, Corexit EC9527A = 10 mg/L, pH = 7.3±0.2, oil dosage = 60 µL oil in 300 mL seawater for all the cases.

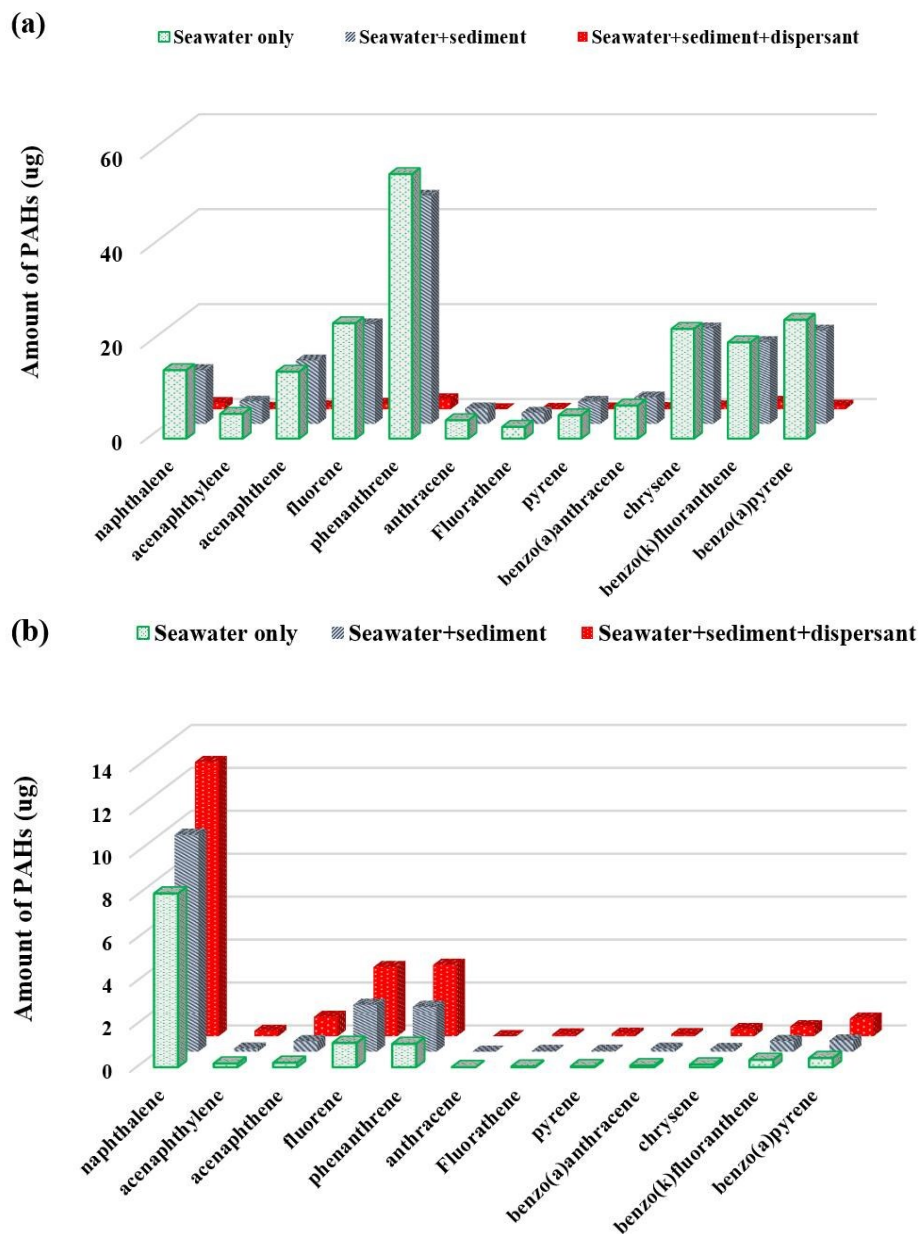
**Figure 54** shows that the presence of the dispersant increased alkanes in the sediment phase from 7.3% to 93.3%. In light of the extremely low solubility of alkanes, the dispersant-facilitated formation of fine oil droplets is critical for the substantial sediment uptake of alkanes.



**Figure 54. Total alkanes distributions on seawater surface, in seawater column or sediment.**

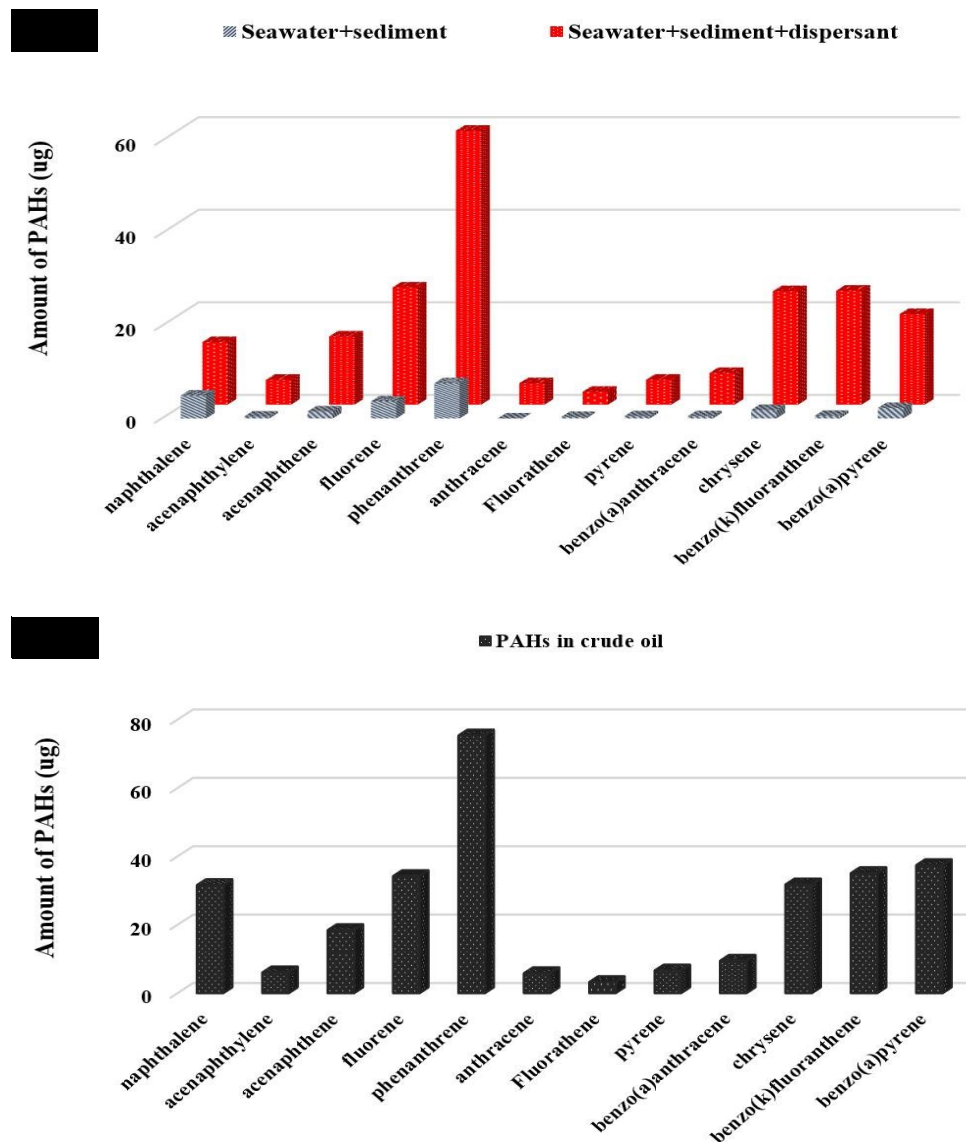
In the following systems: (a) seawater and oil, (b) seawater, oil and sediment without dispersant, and (c) seawater, oil and sediment with dispersant. Experimental conditions: sediment (OS) concentration = 12 g/L, Corexit EC9527A = 10 mg/L, pH = 7.3±0.2, oil dosage = 60 µL oil in 300 mL seawater for all the cases.

Figures 55 and 56 show the mass distributions of 12 PAHs of the oil in the three phases (surface oil, water column and sediment). Evidently, the surface oil phase was nearly depleted in the presence of the dispersant and sediment (Figure 55a). In the water column, naphthalene stood out as the most dominant PAH (Figure 55b), which can be attributed to its higher solubility (or weaker interactions with the sediment and dispersant); in addition, significant amounts of fluorene and phenanthrene were also detected in the water column, which can be attributed to their relatively lower adsorbability and higher concentrations in the crude oil. In the sediment phase, only small amounts of PAHs (mainly naphthalene, fluorene, and phenanthrene) were detected in the absence of dispersant, while the sediment uptake was dramatically increased for all PAHs in proportion to the distribution of PAHs in the crude oil.



**Figure 55. Mass distributions of PAHs on seawater surface (a) and in seawater column (b).** In the following systems: seawater and oil; seawater, oil and sediment without dispersant; and seawater, oil and sediment with dispersant. Experimental conditions: sediment (OS) concentration = 12 g/L, Corexit EC9527A = 10 mg/L, pH = 7.3±0.2, oil dosage = 60 µL oil in 300 mL seawater for all the cases.

The experimental results reveal the following findings: 1) in the absence of the dispersant, most oil PAHs prefers to stay in the surface oil phase; 2) the presence of the dispersant splits the PAHs from the bulk oil phase and PAHs in the dispersed oil droplets are more prone to sediment adsorption (Kim et al. 2013); and 3) the dispersant-facilitated adsorption is likely more effectively for the larger and more hydrophobic PAHs, which are inherently lipophilic.



**Figure 56. Mass distributions of various PAHs in sediment (a) and PAHs in crude oil (b).** Experimental conditions: sediment (OS) concentration = 12 g/L, Corexit EC9527A = 10 mg/L, pH = 7.3±0.2, oil dosage = 60 µL oil in 300 mL seawater for cases in (a).

### 3.5.5. Conclusions

This study investigated the effects of oil dispersants on the settling behavior of suspended sediment particles as well as on the distribution and transport of oil components in sediment-seawater systems, and explored the effects of dispersants under various environmental conditions. Major findings are summarized as follows:

- 1) All three model dispersants were able to accelerate the settling velocity of suspended sediment particles, with the Corexit dispersants being more effective than the SPC 1000 dispersant. The nonionic surfactants (Tween 80 and Tween 85) in the dispersants are the most effective ingredients for enhancing aggregation and settling of sediment particles. The dispersant effects are profound for sediment particles of higher SOM content and smaller size.
- 2) The dispersant enhanced the particle settling more profoundly at alkaline or neutral pH, but had little effect at pH 4.02. The dispersant-enhanced particle settling was further boosted in the presence of electrolytes. Though humic acid alone decreased the sediment settling rate, combining the dispersant with humic acid showed synergistic acceleration of the settling velocity. The dispersant effect on sediment settling was insignificant at the simulated deepwater temperature (4 °C). The presence of WAO and DWAO increased  $R_{40}$  from 70.0% to 74.1% and 81.0%, respectively.
- 3) The presence of oil dispersant in sediment-seawater systems greatly increased the formation of oil-mineral aggregates and facilitated transferring of surface oil to the sediment phase. In the presence of 10 mg/L of Corexit EC9527A, the TPHs mass percentage in the sediment phase was increased from 6.9% (without dispersant) to 90.1%, and that increased from 11.4% to 86.7% for PAHs.

The findings will advance our understanding of the role of oil dispersants in the formation of oil-sediment aggregates and in the sediment-facilitated transport of oil and PAHs in the marine environment.

## 4. Effects of Dispersant on Photodegradation of Oil and Oil Components

### 4.1 Effects of Dispersant on UV-Facilitated Photodegradation of Oil PAHs in Seawater

In the marine environment, PAHs undergo a number of physical and chemical processes, such as dissolution and volatilization (Liu et al. 2012b), adsorption (Yang et al. 2005), bioaccumulation (Baumard et al. 1998), biodegradation (Baumard et al. 1998), and photodegradation (D'Auria et al. 2009). Volatilization and photodegradation are important processes affecting the environmental fate and transport of PAHs. Because PAHs can strongly absorb light in the ultraviolet region, photochemical reactions are considered a major abiotic mechanism in degrading PAHs (Shemer and Linden 2007). Zhang et al. (2008) found that benzo[a]pyrene can be photo-degraded in the presence of TiO<sub>2</sub>. Beltran et al. (1995) studied the direct UV-photolysis of fluorene, phenanthrene, and acenaphthene, and found that the PAHs were completely degraded within 20 min. An and Carraway (2002) reported that direct UV-photolysis of phenanthrene and pyrene followed a first-order rate law.

Three primary mechanisms have been proposed for photodegradation of PAHs: 1) direct photoionization or photolysis; 2) energy transfer from an excited PAH triplet state to molecular oxygen; and 3) charge or electron transfer from an excited singlet or triplet PAH state to molecular oxygen (Fasnacht and Blough 2002, Fasnacht and Blough 2003). Fasnacht and Blough (2003) examined the role of oxygen, photoionization, and PAH cation radicals in the photodegradation of nine PAHs, and concluded that the photodegradation proceeded primarily through reaction of O<sub>2</sub> with both excited singlet and triplet states of the PAHs.

DOM such as humic acid, ionic strength (IS) or salinity, and pH are known to impact photodegradation of PAHs (Clark et al. 2007, Xia et al. 2009). DOM can influence photodegradation of PAHs in two contrasting ways: accelerating the reaction by stimulating production of hydroxyl radicals or inhibiting the degradation due to the competition of the matrix components for absorption of the radiation (Fasnacht and Blough 2002, Xia et al. 2009). De Bruyn et al. (2012) observed that the photodegradation rate of phenanthrene decreased by a factor of 5 in the presence of 10 mg/L of humic acid as TOC. In contrast, Fasnacht and Blough's (2002) reported that photodegradation of anthracene increased by 70% by 5 mg/L of Suwannee River fulvic acid. Clark et al. (2007) reported that photodegradation of pyrene doubled as IS increased from 0.001 to 0.1 M.

Corexit EC9500A consists of three nonionic surfactants, namely, Span 80, Tween 80, and Tween 85, an anionic surfactant, DOSS, and a mixture of organic solvents (Gong et al. 2014b, Scelfo and Tjeerdema 1991). Researchers have investigated effects of individual surfactants on photo-degradation of PAHs. An and Carraway (2002) observed enhanced pyrene photolysis and retarded phenanthrene photolysis in a micellar ammonium perfluorooctanoate solution relative to water. Sigman et al. (1998) reported that photodegradation of pyrene was inhibited in Brij35 micellar media, where the photolysis quantum yield was halved. However, little is known on the effects of oil dispersants on the photodegradation kinetics, mechanisms, and pathways of PAHs. Moreover, the influences of other factors such as IS, humic acid, pH, and temperature on PAHs degradation in the presence of oil dispersant have not yet been explored.

The overall goal of this study was to determine effects of a stereotype oil dispersant (Corexit EC9500A) on the volatilization and photochemical degradation rates of pyrene in seawater. The specific objectives were to: 1) investigate effects of the dispersant on the volatilization rate of pyrene in seawater; 2) compare dispersant effects on photodegradation of pyrene under UV and sunlight irradiations; 3) formulate an integrated model to simulate effects of the dispersant on the overall dissipation

(volatilization and photodegradation) rate of pyrene; 4) elucidate the mechanisms and pathways of pyrene photodegradation in the presence of the dispersant; and 5) examine effects of IS (or salinity), HA, pH, and temperature on photodegradation of pyrene in dispersant solutions.

#### 4.1.1. Materials and methods for pyrene photodegradation under UV light

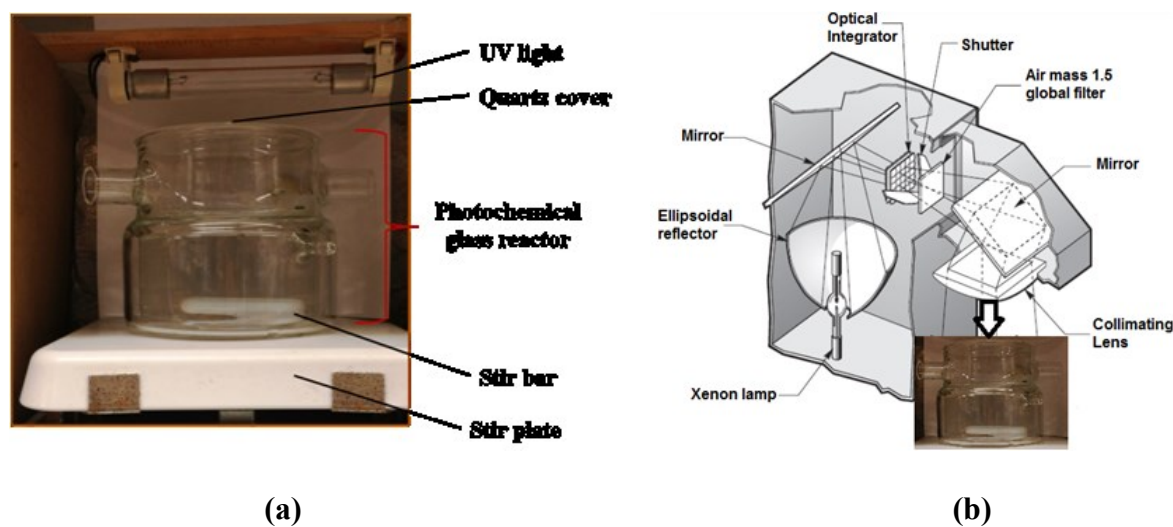
##### 4.1.1.1. Materials and chemicals

Seawater samples were collected from the top water column (30 cm) at Grand Bay, Alabama, and the treating process and properties are described in Section 2.1.1.1.

All chemicals used in this study were of analytical grade or higher. 1,4-benzoquinone and tert-butanol, were purchased from Alfa Aesar (Ward Hill, Maryland). Humic acid (sodium salt, 50~60% as humic acid) was procured from Acros Organics (Morris Plains, New Jersey).

##### 4.1.1.2. Experimental apparatus

Batch degradation kinetic tests were carried out in a well-controlled glass photo-reactor with a surface area of 78 cm<sup>2</sup> and a volume of 650 mL. Two types of light sources were employed: (a) UV irradiation using a 4W UV lamp operated at a wavelength of 253.7 nm; and (b) simulated sunlight using an Oriel Sol1A solar simulator with an additional air mass 1.5 global filter installed in the radiation beam to match the spectrum of the 450 W Xenon lamp with the typical solar spectrum. The light intensity was determined to be 7.7 and 257.7 W/m<sup>2</sup> for UV light and sunlight, respectively, by an optical power meter Model 1916-R. The total UV irradiation intensity was designed to be equal for both light sources, though the UV intensity in the sunlight represents the sum of UVA, UVB, and UVC (wavelength 100–400 nm), whereas the UV light is fixed at 253.7 nm. The light dose is also in accord with the actual solar irradiation (208 W/m<sup>2</sup>) in the Grand Bay area. **Figure 57** shows the schematic of the experimental set-up. Before each experiment, the lamps were warmed up for 15 min to ensure stable output. A quartz plate was used as the cover without blocking the light.



**Figure 57. A schematic of the experimental set-up.**  
(a) reactor under UV light, and (b) reactor under simulated sunlight.

#### **4.1.1.3. Effects of dispersant on volatilization and photodegradation of pyrene**

Batch kinetic tests were carried out with the reactor open to the atmosphere under UV or solar irradiation. In each batch, the reactor was filled with 300 mL of a seawater solution (pyrene = 60 µg/L), and stirred with a magnetic stirrer (300 rpm) to simulate ocean wave actions and maintain uniform pyrene distribution. Control tests (carried out in a closed system in dark) indicated that pyrene loss due to sorption to the reactor walls was negligible. To determine the volatilization rate of pyrene, parallel tests were carried out in dark under otherwise identical conditions. To explore the net photodegradation rates, kinetic tests were also conducted under UV or sunlight with the reactor sealed (no volatilization). During the tests, 1 mL each of the solution was sampled at predetermined times and analyzed for pyrene remaining. To investigate the effects of the dispersant, the tests were conducted in the presence of 0, 18, and 180 mg/L of Corexit EC9500A. All experiments were conducted in duplicate at 22±1 °C.

The formation of oxidative species, such as singlet oxygen ( $^1\text{O}_2$ ), superoxide ( $\text{O}_2^{\cdot-}$ ), and hydroxyl radicals ( $\cdot\text{OH}$ ), and their roles in the pyrene degradation processes were investigated in the absence and presence of 18 mg/L of Corexit EC9500A. The following scavengers were used to quench these radicals, turt-butanol (221 mg/L) for  $\cdot\text{OH}$ ,  $\text{NaN}_3$  (200 mg/L) for  $^1\text{O}_2$  and  $\cdot\text{OH}$ , and 1,4-benzoquinone (161 mg/L) for  $\text{O}_2^{\cdot-}$ .

#### **4.1.1.4. Photodegradation pathways of pyrene with or without dispersant**

During the pyrene photodegradation process, samples (10 mL each) were collected from the reactor and transferred into glass separation funnels. The intermediate products with or without the dispersant were then extracted using dichloromethane consecutively for three times (3 mL dichloromethane in each step). The extracts were then passed through a Pasteur pipette containing granular sodium sulfate anhydride (1 g) to remove any moisture, concentrated to a volume of 0.1 mL under a stream of nitrogen gas, and then analyzed by GC-MS.

#### **4.1.1.5. Effects of solution chemistry and temperature**

Effects of IS, humic acid, pH, and temperature were investigated through similar kinetic experiments with 18 mg/L of the dispersant. To test the IS effect, IS of the reaction solution was varied from 0.01, 0.7, to 1.2 M. NaCl was added to increase the original seawater IS (0.7 M) to 1.2 M, whereas DI water was added to dilute it down to 0.01 M. To examine the pH effect, the initial solution pH was adjusted to 5 and 8 using 0.1 M HCl (final pH dropped to 4.8 and 7.8, respectively). To probe the humic acid effect, the photodegradation tests were conducted in the presence of various humic acid concentrations (0, 5.5, and 22 mg/L as TOC). To investigate the temperature effect, the experiments were carried out at 10 and 22 °C, which represent the lowest and highest seawater temperatures in the Grand Bay area.

#### **4.1.1.6. Analytical methods**

UV spectra of various solutions were obtained using a Hewlett Packard 8453 UV-visible spectrophotometer with a 1×1 cm quartz cell. Humic acid concentrations were determined as TOC by a TOC analyzer. Pyrene concentration was determined using an HPLC system. More information about the analysis methods are in Section 3.2.1.2.

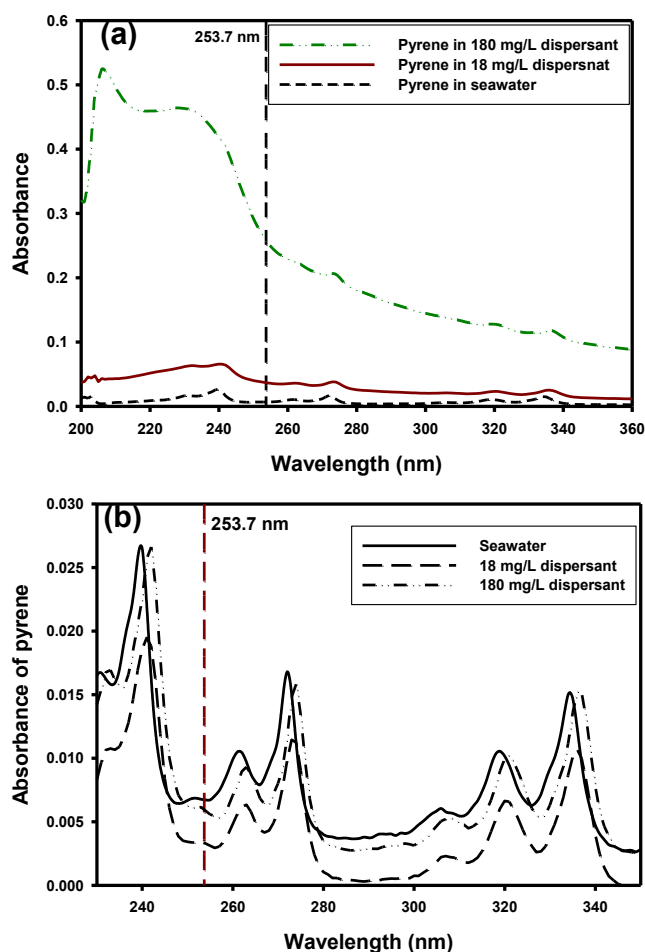
Reaction intermediates were determined using an Agilent 7890A GC coupled with the 5975C series mass spectrometry. A DB-EUPAH column (length = 20 m, inner diameter = 0.18 mm, film thickness = 0.14 µm) was used with helium as the carrier gas at a flow rate of 0.9 mL/min. Sample injection volume was 2.0 µL. The inlet temperature was set at 250 °C, and the oven temperature was programmed as follows: 50 °C hold for 1 min, and ramped at 5 °C /min to 300 °C (hold for 5 min). The scan range was



from 50 to 550 m/z (mass to charge ratio).

#### 4.1.2. UV-spectroscopic studies of pyrene in dispersant solutions

UV spectroscopy provides useful information on the solubilization characteristics of compounds in solutions (Riegelman et al. 1958). **Figure 58** shows the corrected UV-vis absorption spectra of pyrene in seawater with various concentrations of Corexit EC9500A. **Figure 58a** indicates that increasing the dispersant concentration progressively enhances the UV absorption of the solution. **Figure 58b** compares the effects of the dispersant. The peaks in dispersant solutions were notably lowered and red-shifted compared to those in seawater. The CMC of Corexit EC9500A is 22.5 mg/L (Gong et al. 2014b). At 180 mg/L of the dispersant, dispersant micelles are formed. The peak difference indicates that pyrene in the dispersant solutions is more polar than in seawater (An and Carraway 2002). **Figure 58b** also shows that the dispersant decreases the UV absorbance at 254 nm, suggesting that the dispersant competes with pyrene for UV irradiation.



**Figure 58. UV-vis absorption spectra of pyrene.**

In seawater, or a monomeric dispersant solution (Corexit EC9500A = 18 mg/L) or a micellar dispersant solution (180 mg/L). (a) Spectra were corrected by subtracting seawater background absorbance; (b) Spectra in seawater were corrected by subtracting seawater background absorbance, and spectra in dispersant solutions were corrected by subtracting background dispersant-seawater absorbance. Pyrene concentration = 60  $\mu\text{g/L}$ .



### 4.1.3. Effects of dispersant on photodegradation of pyrene under UV and sunlight

Direct photolysis and photosensitized degradation of a trace chemical in well-mixed aqueous systems can be described by the first-order rate law (Kawaguchi 1993, Zepp and Schlotzhauer 1979):

$$\ln(C_t / C_0) = -kt \quad (29)$$

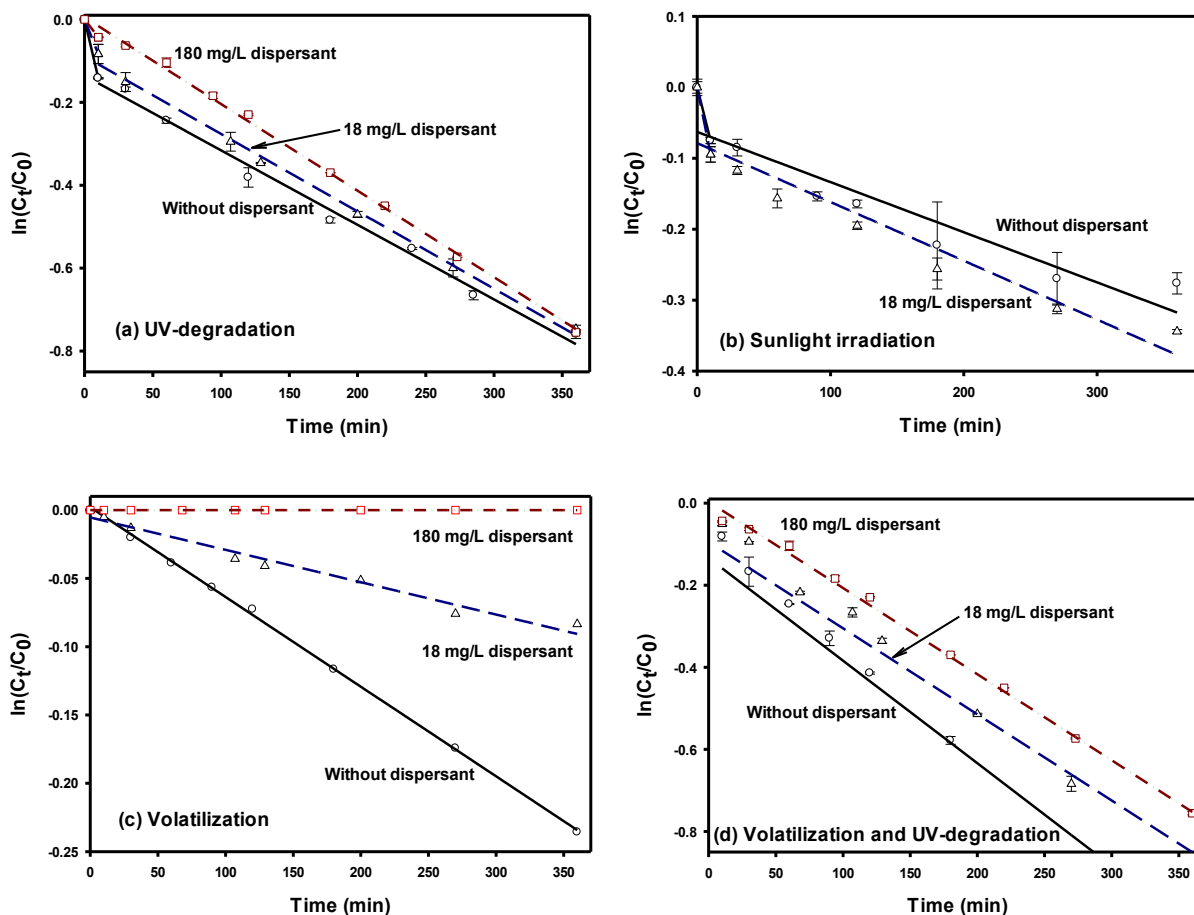
where  $C_0$  and  $C_t$  are the reactant concentrations at irradiation time 0 and  $t$ , respectively, and  $k$  is the first-order rate constant, which was obtained by fitting Equation 29 to the corresponding experimental data (Figure 59).

Figures 58a and 58b display an unusual two-stage kinetic profile, i.e., a much faster rate in the first 10 min (the induction period) followed by a slower rate. Accordingly, the first-order kinetic model was applied to the two stages separately.

Table 14 gives the resultant kinetic parameters. The UV-degradation rate constant in stage 1 ( $k_1 = 0.0142 \text{ min}^{-1}$ ) decreased to  $0.0018 \text{ min}^{-1}$  (by a factor of 7.9) in stage 2. Likewise, the sunlight-mediated rate constant in stage 1 was 10.7 times greater than in stage 2. The two-stage degradation kinetics suggests that different degradation mechanisms were operative. During the induction period, direct photolysis played a more prevalent role; while the electron transfers from excited pyrene species to oxygen became the controlling mechanism thereafter (see Section 4.1.5 for details).

Under UV irradiation, the 18 mg/L dispersant suppressed  $k_1$  from  $0.0142$  to  $0.0083 \text{ min}^{-1}$  (by 41.5%) due to the dispersant competition for UV irradiation at 253.7 nm (Figure 59). In contrast, the dispersant increased  $k_2$  from  $0.0018$  to  $0.0019 \text{ min}^{-1}$  (by 5.5%) for UV and from  $0.0007$  to  $0.0008 \text{ min}^{-1}$  (by 14.3%) for sunlight. Based on the t-tests, the differences are statistically significant ( $p < 0.05$ , level of significance = 0.05).

An effective photodegradation process requires that the emission spectra of the source light overlap with the absorption spectra of the target compounds (Mill et al. 1981). The higher pyrene degradation rate under UV irradiation than sunlight can be attributed to the more compatible emission spectra of UV at 253.7 nm.



**Figure 59. First-order kinetic plots of pyrene dissipation.**

(a) under UV-degradation, (b) under simulated sunlight irradiation, (c) by volatilization only and (d) through combined volatilization and UV-degradation, in seawater and in a monomeric dispersant solution (Corexit EC9500A = 18 mg/L) and micellar dispersant solution (Corexit EC9500A = 180 mg/L). Experimental conditions: initial pyrene = 60 µg/L, solution pH = 7.6–8.3, temperature = 22 °C. Data plotted as mean of duplicates and error bars indicate data reproducibility.

**Table 14. First-order photodegradation rate constants for pyrene in the absence or presence of Corexit EC9500A under UV and sunlight irradiations**

Corexit EC9500A (mg/L)	UV irradiation				Sunlight irradiation			
	0–10 min		10–360 min		0–10 min		10–360 min	
	$k_1$ (min <sup>-1</sup> )	$R^2$	$k_2$ (min <sup>-1</sup> )	$R^2$	$k_1$ (min <sup>-1</sup> )	$R^2$	$k_2$ (min <sup>-1</sup> )	$R^2$
0	$(1.42 \pm 0.01) \times 10^{-2}$	1	$(1.80 \pm 0.01) \times 10^{-3}$	0.991	$(7.50 \pm 0.44) \times 10^{-3}$	1	$(7.0 \pm 0.2) \times 10^{-4}$	0.930
18	$(8.30 \pm 0.02) \times 10^{-3}$	1	$(1.90 \pm 0.02) \times 10^{-3}$	0.996	$(9.50 \pm 1.10) \times 10^{-3}$	1	$(8.0 \pm 0.1) \times 10^{-4}$	0.973

**Note:**  $k_1$  and  $k_2$  (min<sup>-1</sup>): UV-degradation rate constant in stage 1 and stage 2, respectively;  $R^2$ : coefficient of

determination,  $R^2 = 1 - \frac{\sum (y_i - y_{i(\text{predict})})^2}{\sum (y_i - \bar{y})^2}$ , where  $y_i$  and  $y_{i(\text{predict})}$  are observed data and model values, respectively, and

$\bar{y}$  is the mean of the observed data.

#### 4.1.4. Effects of dispersant on volatilization and photodegradation of pyrene

**Figure 59c** shows that the volatilization rate of pyrene decreased with increasing dispersant concentration. At 360 min, 21% of pyrene volatilized without dispersant. The dispersant at 18 and 180 mg/L reduced the volatilization to 8% and 0, respectively. **Figure 59d** indicates that the combined volatilization and UV-degradation rate diminished with increasing dispersant concentration. After 360 min, pyrene remaining in seawater increased from 33% without dispersant to 41% and 47% with 18 and 180 mg/L of the dispersant, respectively.

**Figures 59a** and **59c** show that both photodegradation rate and volatilization rate from 10 to 360 min can be well interpreted by first-order kinetic models. **Table 15** gives the rate constants. The reaction rate constant was escalated from  $0.0018 \text{ min}^{-1}$  (without dispersant) to  $0.0019 \text{ min}^{-1}$  (by 5.5%) and  $0.0021 \text{ min}^{-1}$  (by 16.7%) with 18 and 180 mg/L of the dispersant, respectively ( $p = 0.047$  and  $0.02$ , respectively, at 0.05 level of significance). The presence of 18 and 180 mg/L of the dispersant reduced the volatilization rate constant ( $k_v$ ) from  $0.0007$  to  $0.0002$  and  $0 \text{ min}^{-1}$ , respectively. Equilibrium dissolution tests revealed that increasing the dispersant concentration from 0 to 18 and 180 mg/L enhanced the pyrene solubility by 9% and 22%, respectively.

**Table 15. First-order rate constants for pyrene volatilization and/or UV-mediated photodegradation with or without Corexit EC9500A.**

Corexit EC9500A (mg/L)	Volatilization		UV-mediated photodegradation (10-360 min)		Volatilization and photodegradation
	$k_v \text{ (min}^{-1}\text{)}$	$R^2$	$k \text{ (min}^{-1}\text{)}$	$R^2$	$(k_v+k) \text{ (min}^{-1}\text{)}$
0	$(7.0 \pm 0.1) \times 10^{-4}$	0.999	$(1.80 \pm 0.01) \times 10^{-3}$	0.991	0.0025
18	$(2.0 \pm 0.2) \times 10^{-4}$	0.973	$(1.90 \pm 0.02) \times 10^{-3}$	0.996	0.0021
180	0	0.999	$(2.10 \pm 0.04) \times 10^{-3}$	0.997	0.0021

**Note:**  $k_v \text{ (min}^{-1}\text{)}$ : volatilization rate constant.

Based on individual first-order rate models for volatilization and UV-photodegradation, an integrated first-order kinetic model is formulated as follows:

$$\frac{dC}{dt} = (k_v + k)C \quad (30)$$

The model was able to adequately predict the pyrene dissipation rate that includes both volatilization and photodegradation in the presence of various concentrations of the dispersant (**Figure 59d**). While the dispersant reduces pyrene volatilization, it increases pyrene UV-photodegradation. These contrasting effects decreased the overall pyrene dissipation rate constant from  $0.0025 \text{ min}^{-1}$  (no dispersant) to  $0.0021 \text{ min}^{-1}$  with 18 or 180 mg/L of the dispersant.

#### 4.1.5. Roles of radicals, photodegradation mechanisms, and effects of dispersant

UV irradiation is known to produce various reactive oxygen species (ROS), including  $^1\text{O}_2$ ,  $\text{O}_2^{\cdot-}$ , and  $\cdot\text{OH}$  (Xu et al. 2008). Yet effects of oil dispersants on the production of the radicals have been unknown. The role of each radical in pyrene photodegradation with or without Corexit EC9500A was investigated using three selective radical scavengers, i.e., tert-butanol for selectively quenching  $\cdot\text{OH}$ , azide for  $^1\text{O}_2$  and  $\cdot\text{OH}$  (Xu et al. 2008), and 1,4-benzoquinone for  $\text{O}_2^{\cdot-}$  (Stylidi et al. 2004).

**Table 16** presents pyrene photodegradation rate constants and enunciates the relative contributions of the radicals. Evidently, tert-butanol or NaN<sub>3</sub> did not affect the photodegradation rate regardless of the dispersant, indicating that ·OH and <sup>1</sup>O<sub>2</sub> are not responsible for pyrene photodegradation.

**Table 16. Contributions of radicals ( $\cdot\text{OH}$ ,  $^1\text{O}_2$  and  $\text{O}_2^{\cdot-}$ ) to pyrene photodegradation with or without Corexit EC9500A**

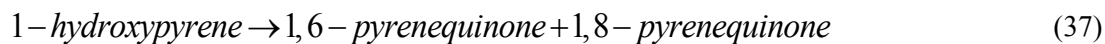
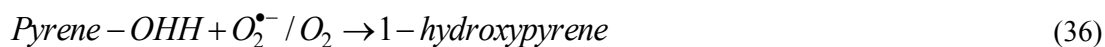
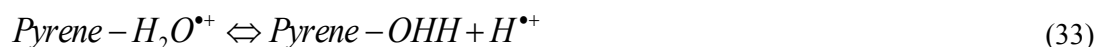
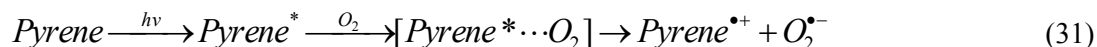
Dispersant concentration (mg/L)	First-order rate constants ( $\text{min}^{-1}$ )					$\cdot\text{OH}$ and $^1\text{O}_2$ contribution to pyrene photodegradation rate ( $\text{min}^{-1}$ )	$\text{O}_2^{\cdot-}$ contribution to pyrene photodegradation rate ( $\text{min}^{-1}$ )	Percentage contribution of $\text{O}_2^{\cdot-}$ to pyrene degradation rate
	$k$	$k_{\text{TB}}$	$k_A$	$k_B$	$k-k_A$			
0	$(1.80 \pm 0.01) \times 10^{-3}$	$(1.80 \pm 0.01) \times 10^{-3}$	$(1.80 \pm 0.01) \times 10^{-3}$	$(1.0 \pm 0.1) \times 10^{-4}$	0	0.0017	94%	
18	$(1.90 \pm 0.02) \times 10^{-3}$	$(1.90 \pm 0.02) \times 10^{-3}$	$(1.90 \pm 0.02) \times 10^{-3}$	$0 \pm 1.1 \times 10^{-5}$	0	0.0019	100%	

**Note:**  $k_{\text{TB}}$ ,  $k_A$  and  $k_B$  ( $\text{min}^{-1}$ ): UV-degradation rate constants in the presence of tert-butanol (221 mg/L), azide (200 mg/L), and 1,4-benzoquinone (161 mg/L), respectively.

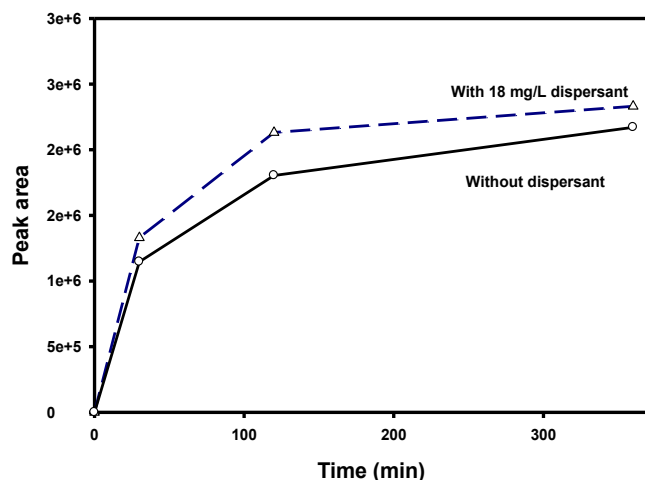
When quenched with 1,4-benzoquinone, the photodegradation rate was decreased from 0.0018 to 0.0001 min<sup>-1</sup> (without dispersant) and from 0.0019 to 0 min<sup>-1</sup> (with dispersant) (**Table 16**). This observation indicates that O<sub>2</sub><sup>•-</sup> has a predominant role in the photodegradation process. The rate constant due to O<sub>2</sub><sup>•-</sup> was 0.0017 min<sup>-1</sup> without dispersant and 0.0019 min<sup>-1</sup> with dispersant, i.e., O<sub>2</sub><sup>•-</sup> accounted for 94% and 100% of the overall photodegradation (**Table 16**). It is noteworthy that the dispersant boosted the O<sub>2</sub><sup>•-</sup> generation, enhancing the O<sub>2</sub><sup>•-</sup>-facilitated photodegradation.

Two possible mechanisms have been proposed for the oxidative photodegradation of pyrene (Sigman et al. 1998): 1) electron transfer, and 2) singlet molecular oxygen addition. The fact that O<sub>2</sub><sup>•-</sup> plays a predominant role indicates that electron transfer from an excited singlet and/or triplet state of pyrene to a molecular oxygen is the main degradation mechanism (Fasnacht and Blough 2002).

1-hydroxypyrene was observed to be the major intermediate regardless of the dispersant, which agrees with observations by others for non-dispersant systems (Clark et al. 2007, Sigman et al. 1998, Wen et al. 2003). Reactions 31 to 37 provides the reaction pathways with or without dispersant. UV irradiation converts ground-state pyrene to excited-state pyrene (pyrene\*), which is quenched by O<sub>2</sub> to produce [Pyrene\*...O<sub>2</sub>] complexes. The complexes are then excited to yield pyrene cation and O<sub>2</sub><sup>•-</sup> radicals (Reaction 31). The water trapping step of the pyrene cations (Reaction 32) and the subsequent deprotonation (Reaction 33) give rise to hydroxypyrenyl radicals along with protons. Reaction 34 depicts the acid-base equilibrium involving the hydroperoxyl radical (pK<sub>a</sub> = 4.4–4.8) (Sigman et al. 1998), which is fully dissociated in our reaction systems (pH 7.6–8.3). Pyrene is then directly degraded by O<sub>2</sub><sup>•-</sup> radicals (Reaction 35). Reaction 36 shows a possible but less important route where hydroxypyrenyl radical is oxidized by O<sub>2</sub><sup>•-</sup> and/or O<sub>2</sub>. Given the predominant role of O<sub>2</sub><sup>•-</sup>, Reaction 35 is the rate-determining-step. The product 1-hydroxypyrene is further photo-chemically oxidized to yield 1,6- and 1,8-pyrenequinones (Reaction 37).



In the presence of the dispersant, more intermediate 1-hydroxypyrene was observed (**Figure 60**), for example, at 120 min, 1-hydroxypyrene was 16.7% higher in the 18 mg/L dispersant system. The results indicate that the dispersant-enhanced photodegradation of pyrene is due to increased ability of the medium to support charge separation (Reaction 31) and enhanced generation of O<sub>2</sub><sup>•-</sup> radicals.



**Figure 60. Production of intermediate 1-hydroxypyrene.**

Production of 1-hydroxypyrene was quantified as GC-MS peak area during photodegradation of pyrene in the presence and absence of Corexit EC9500A. Experimental conditions: initial pyrene = 60  $\mu\text{g/L}$ , initial dispersant = 18  $\text{mg/L}$ , pH = 7.6–8.3, temperature = 22  $^{\circ}\text{C}$ .

The change of the photodegradation rate associated with the oil dispersant can be expressed as follows (Xia et al. 2009):

$$dr = dA + dC + dO \quad (38)$$

where  $dr$  ( $\text{min}^{-1}$ ) is the net change of photodegradation rate,  $dA$  is the rate change due to dispersant-facilitated production of active species (i.e.,  $\text{O}_2^{\cdot-}$  radicals),  $dC$  is the rate change due to competition of the dispersant with pyrene for the photon and energy, and  $dO$  is the change caused by other mechanisms (e.g., Reaction 31).

The fact that  $\text{O}_2^{\cdot-}$  was fully responsible for pyrene photodegradation with dispersant indicates that the presence of the dispersant resulted in more  $\text{O}_2^{\cdot-}$  radicals. The 18  $\text{mg/L}$  dispersant increased the rate constant due to the  $\text{O}_2^{\cdot-}$  route ( $k-k_B$ ) by 0.0002  $\text{min}^{-1}$  (Table 16), and the overall rate constant ( $k$ ) by 0.0001  $\text{min}^{-1}$ . The discrepancy can be attributed to the photon and energy competition effects of the dispersant, i.e., the dispersant also competes for the effective radiation energy with pyrene (Figure 58b). At 18  $\text{mg/L}$  of the dispersant, the fraction of light absorbed by pyrene was measured to be only 0.11 (Figure 58a). GC-MS analysis revealed that Corexit EC9500A was decomposed at least partially during the photodegradation process and many by-products from the dispersant were observed, such as oleic acid, methyl oleate, and ethyl 2-ethylhexyl ester fumaric acid.

At concentrations higher than the CMC value, the dispersant can further enhance the photodegradation through the “cage effect”, i.e., the accumulation of pyrene in the micelles, which results in a higher local concentration, and thus a faster degradation rate (Chu and Jia 2009, Zhang et al. 2011c). The resultant degradation intermediates tend to reside in the nonaqueous “cage” due to the similar hydrophobic properties. The incident photons are then effectively absorbed by the concentrated pyrene and intermediate molecules.

#### 4.1.6. Effects of environmental factors on photodegradation of pyrene in dispersant solutions

The photodegradation kinetics in the presence of 18 mg/L of Corexit EC9500A was tested as a function of IS, humic acid, pH, and temperature. The first-order rate constants after 10 min were obtained through the linear regression  $\ln(C_t/C_0)$  to  $t$ , and are listed in **Table 17**.

**Table 17. First-order rate constants for pyrene photodegradation in 18 mg/L dispersant solutions as a function of IS, humic acid, pH, and temperature**

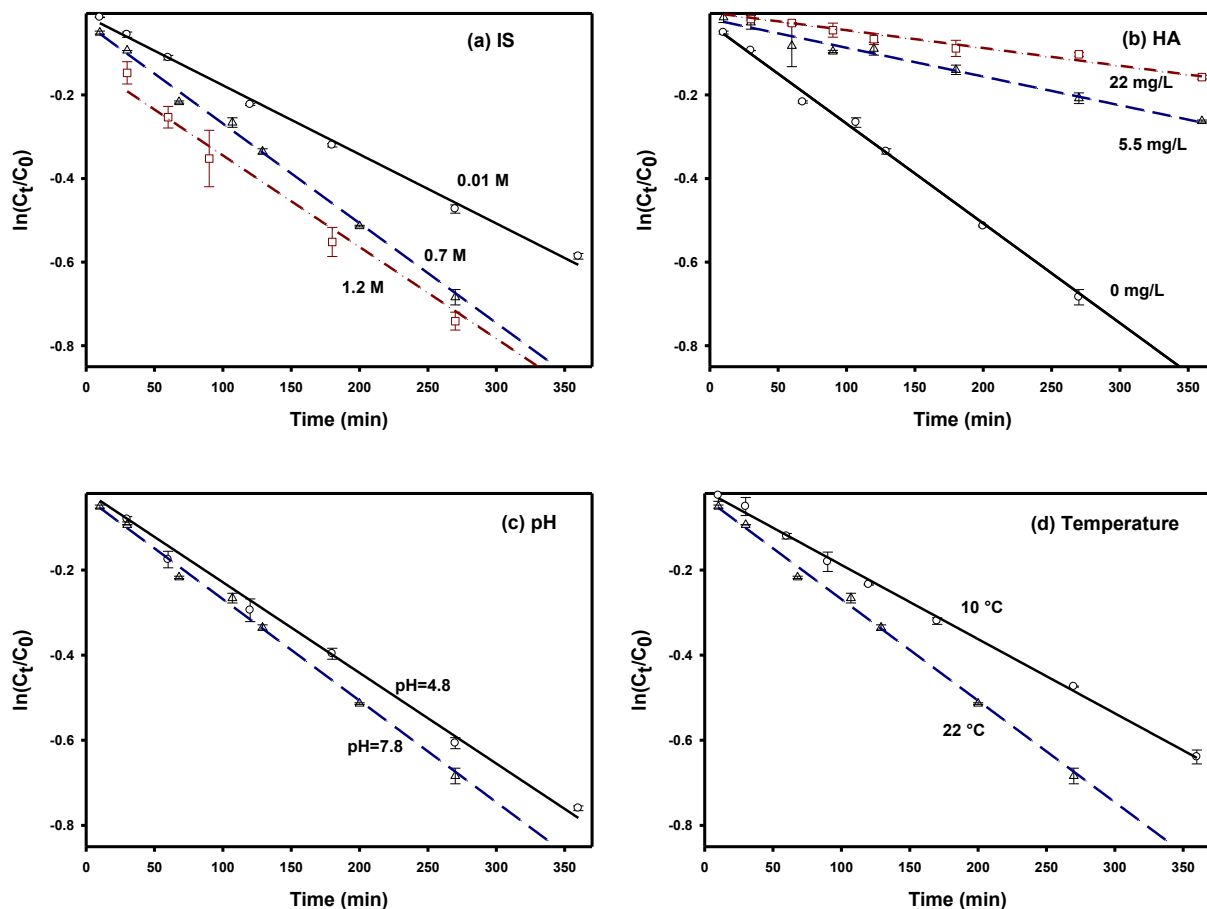
Initial pyrene concentration ( $\mu\text{g/L}$ )	Solution medium in 18 mg/L dispersant solution		$k$ ( $\text{min}^{-1}$ ) (10-360 min)	$R^2$
60	IS (M)	0.01	$(1.70 \pm 0.04) \times 10^{-3}$	0.996
60		0.7	$(1.90 \pm 0.02) \times 10^{-3}$	0.996
60		1.2	$(2.20 \pm 0.10) \times 10^{-3}$	0.986
60	Humic acid (mg/L)	0	$(1.90 \pm 0.02) \times 10^{-3}$	0.996
60		5.5	$(0.70 \pm 0.04) \times 10^{-3}$	0.976
60		22.0	$(0.40 \pm 0.03) \times 10^{-3}$	0.964
60	pH	4.8	$(1.70 \pm 0.08) \times 10^{-3}$	0.990
60		7.8	$(1.90 \pm 0.02) \times 10^{-3}$	0.996
60	Temperature ( $^{\circ}\text{C}$ )	10	$(1.70 \pm 0.03) \times 10^{-3}$	0.998
60		22	$(1.90 \pm 0.02) \times 10^{-3}$	0.996

##### 4.1.6.1. Effects of IS

**Figure 61** shows effects of IS on pyrene photodegradation in dispersant solutions. The rate constant increased from  $0.0017$  to  $0.0019 \text{ min}^{-1}$  as the IS increased from  $0.01$  to  $0.7 \text{ M}$ . Further increasing IS to  $1.2 \text{ M}$  boosted the rate to  $0.0022 \text{ min}^{-1}$  ( $p = 0.046$  and  $0.043$ , respectively).

The solution property can affect the electron transfer by controlling the diffusion rate and by establishing the microscopic environment of the solvent cage, within which the electron transfer between two species takes place (Clark and Hoffman 1997). For diffusion-controlled reactions, increasing IS increases the rate for two like-charged ions diffusing together, but decreases the rate for oppositely charged ions (Clark and Hoffman 1997), and may have little effect if one of the reactants is neutral. Because Reaction 35 is the rate-determining step, and the reactants include a neutral species (Pyrene), the reaction is less likely diffusion-controlled. Hence, the positive IS effect here can be attributed to: 1) the solvent cage effect, i.e., elevated IS reduces the solvent cage, resulting in more effective collisions between the reactants; and 2) the salting-out effect of pyrene, i.e., elevated IS can increase the local concentration of pyrene, resulting in a faster degradation rate.





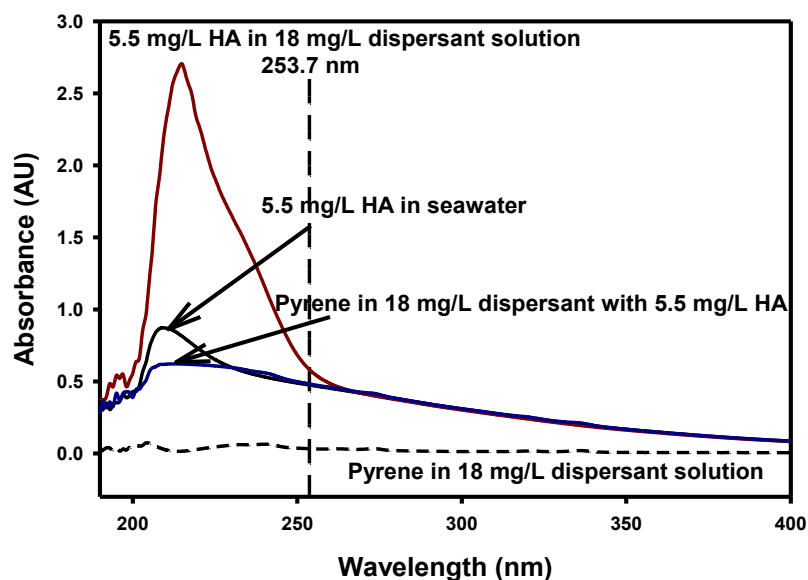
**Figure 61. Effects of environmental conditions on photodegradation of pyrene with dispersant.** Effects of (a) IS, (b) humic acid, (c) pH, and (d) temperature on photodegradation of pyrene in 18 mg/L Corexit EC9500A solutions. Experimental condition: initial pyrene = 60  $\mu\text{g/L}$ . Data plotted as mean of duplicates and error bars indicate data reproducibility.

#### 4.1.6.2. Effects of humic acid

**Figure 61b** shows the pyrene degradation kinetic data at various concentrations of humic acid (0, 5.5 and 22.0 mg/L as TOC). As the humic acid concentration increased from 0 to 5.5 and 22 mg/L, the rate constant decreased from 0.0019 to 0.0007 and 0.0004  $\text{min}^{-1}$ , respectively.

Humic acid can inhibit the photodegradation in several ways. First, humic acid competitively absorbs UV light. DOM is known to be major light absorbing species in surface waters, with a well-established absorption spectrum in the range of 200–450 nm (Boyle et al. 2009). **Figure 62** shows the relative UV absorbance of pyrene and humic acid in seawater and the dispersant solutions. The highest absorbance was observed in the solution containing 5.5 mg/L of humic acid and 18 mg/L of the dispersant, which indicates the strong light absorbing ability of humic acid and the dispersant over the wavelength range of 200–260 nm. However, when pyrene is present in the same system, the absorbance sharply reduced, suggesting that complexation of pyrene with the dispersant and humic acid lowered the energy absorbance. Comparing the absorbance spectra reveals that humic acid is more competitive than pyrene in absorbing light, thereby inhibiting pyrene photodegradation. In addition, humic acid may quench photochemically produced reactive species (Frimmel 1994), i.e., the excited pyrene and  $\text{O}_2^{\cdot-}$ . Lastly, sorption of

pyrene within the complex humic acid matrix (Simpson et al. 2004) may shield it from oxygen and photodegradation. On the other hand, humic acid can act as a photosensitizer to induce generation of radical species and promote PAHs degradation (Wang et al. 1995). In this study, the inhibitive effects outweighed the promoting effects.



**Figure 62. Absorption spectra of humic acid and pyrene.**

HA = 5.5 mg/L, pyrene = 60  $\mu\text{g/L}$  in 18 mg/L Corexit EC9500A solutions. The spectra were corrected by subtracting seawater background absorbance.

#### 4.1.6.3. Effects of pH and temperature

**Figure 61c** shows that decreasing pH from 7.8 to 4.8 did not significantly affect the photodegradation rate in the dispersant solution ( $p = 0.123$ ). This is consistent with the fact that the hydroperoxyl radical is largely deprotonated in the pH range.

**Figure 61d** shows that decreasing temperature from 22  $^{\circ}\text{C}$  to 10  $^{\circ}\text{C}$  decreased the rate constant from 0.0019 to 0.0017  $\text{min}^{-1}$  ( $p = 0.037$ ). Higher temperature accelerates the molecular collision rate, and the change in interatomic interactions weakens the chemical bonds, resulting in faster reaction rates. However, the observed rate enhancement is much lower than that predicted per the classic Arrhenius equation, which can be attributed to: 1) interactions between pyrene and the dispersant, and 2) competition of the dispersant with pyrene for UV at 253.7 nm. The activation energy for the photolysis is provided by light energy, rather than systematic thermal energy (Li et al. 2013b). Therefore, the influence of temperature on the photolysis rate is limited.

#### 4.1.7. Conclusions

This study investigated effects of a model oil dispersant on volatilization and photochemical degradation of pyrene in the seawater. The primary findings are summarized below.

- 1) Both UV and simulated sunlight irradiations effectively degrade pyrene with or without the dispersant, though UV irradiation is more efficient. The photodegradation followed a two-stage, first-order kinetics, i.e., a much faster initial degradation rate followed by a slower degradation rate thereafter (10–360 min).
- 2) The presence of 18 and 180 mg/L of the dispersant reduced or ceased pyrene volatilization.
- 3) The dispersant enhances UV-mediated photodegradation of pyrene. At 18 and 180 mg/L, the dispersant increased the rate constant by 5.5% and 16.7%, respectively, compared to that without dispersant.
- 4) Based on the individual volatilization and photodegradation kinetics, an integrated first-order kinetic model was formulated, which adequately predicts the overall dissipation of pyrene in seawater with various concentrations of the dispersant.
- 5) Superoxide radicals play a predominant role in pyrene photodegradation with 1-hydroxypyrene being the main intermediate, indicating that pyrene photodegradation proceeds through electron transfer from excited pyrene to oxygen. The dispersant boosted the  $O_2^-$  generation, leading to enhanced pyrene photodegradation.
- 6) The pyrene photodegradation rate in 18 mg/L dispersant solution increased by 29% when IS was increased from 0.01 to 1.2 M, and decreased by 63% and 79% in the presence of 5.5 and 22 mg/L of humic acid, respectively. Decreasing temperature from 22 to 10 °C lowered the reaction rate by 10.5%. The effect of solution pH in the range of 4.8–7.8 was insignificant.

#### 4.2. Effects of Oil Dispersant on Simulated Sunlight-Facilitated Photodegradation of Oil PAHs in Seawater

PAHs are important components in crude oil, for instance, the Macondo well oil contains ca. 3.9% of PAHs (by weight) (Reddy et al. 2012a). The PAHs are known to be toxic, carcinogenic, and mutagenic. Sixteen of the parent PAHs have been listed as priority pollutants by the EPA (Cai et al. 2016, US EPA 2014). Typically, crude oil contains much more alkylated PAHs than the parent PAHs (Liu et al. 2012b). More-alkylated PAHs are more likely to accumulate in plant and animal systems (Brandt et al. 2002), and show stronger carcinogenic potency (Slaga et al. 1980). However, information on the degradation of alkylated PAHs is much less than that for parent PAHs. Therefore, it is of great significance to evaluate the weathering of both parent and alkylated PAHs in the marine environment. Anthracene and its alkylated derivative, 9,10-dimethylanthracene (9,10-DMA), are of high abundance in crude oil and have been commonly detected in the oil affected ecosystems (Allan et al. 2012).

Photodegradation is a major abiotic process affecting spill oil attenuation. It has significant implications to redox cycling, transport, and degradation of oil components (Fu et al. 2014, Nicodem et al. 2001). Though there is a significant body of knowledge on the photochemical degradation of PAHs in natural waters, information has been lacking on the photodegradation behaviors and mechanisms of dispersed PAHs (Fasnacht and Blough 2002). Oil dispersants are known to alter the physico-chemical properties of PAHs, such as distribution of PAHs in the water column, size of the oil droplets, light

absorbance, quantum yield, and production of ROS (Gong et al. 2015). Though these changes are likely to impact photolysis of PAHs, no information has been available on the effects of oil dispersants on the photodegradation of PAHs and alkylated PAHs by solar light and on the underlying mechanisms.

The overall goal of this study was to examine the effects of oil dispersants on the photodegradation of PAHs (anthracene and 9,10-DMA) in seawater under simulated solar light. The specific objectives were to: 1) investigate the effects of three model dispersants, i.e., Corexit EC9500A, Corexit EC9527A and SPC 1000, on photodegradation of the two model PAHs; 2) identify the key dispersant components that affect the photodegradation rate of PAHs; 3) evaluate effect of DO on the photolysis of PAHs and verify the key reactive oxygen species in the presence of oil dispersants; and 4) elucidate the photodegradation mechanisms in the presence of oil dispersants.

## **4.2.1. Materials and methods**

### **4.2.1.1. Materials and experimental apparatus**

The following chemicals (analytical grade or higher) were used as received: anthracene, 9,10-DMA, superoxide dismutase. The individual dispersant compositions were obtained from either Fisher Scientific or Sigma-Aldrich, including Tween 85, Span 80, DOSS, kerosene, and 2-butoxyethanol for the Corexit dispersants; and polyethylene glycol monooleate, dipropylene glycol monomethyl ether, and cocamide diethanolamine (DEA) for SPC 1000.

Seawater samples were collected from the top water column (30 cm) at the Grand Bay site, Alabama, and the treating process and properties are described in Section 2.1.1.1

**Figure 57b** shows the photodegradation setup, the detailed information about the light simulator can be found in Section 4.1.1.2. The light intensity in this study was set at  $85 \pm 0.5$  mW/cm<sup>2</sup>. A sealed glass photo-reactor with a working volume of 250 mL was used in the experiments, including a quartz cover to allow the vertical transport of the solar light, and a water circulating coating to keep the reactor at constant temperature (25 °C).

### **4.2.1.2. Effects of dispersants on photodegradation of PAHs**

Batch photodegradation kinetic tests were carried out to evaluate the effects of dispersants. Stock solutions of anthracene and 9,10-DMA (each at 0.3 g/L) were prepared separately by dissolving a known amount of a PAH in methanol. In each batch test, 250 mL of filtered seawater was added in the photo-reactor, followed by adding an aliquot of the PAH stock solution and a dispersant (or dispersant components), which gave an initial PAH concentration of 30 µg/L and dispersant (or dispersant components) concentration of 18 mg/L. The solution was mixed for 30 min by magnetic stirring in the sealed photo-reactor. Then, the photodegradation was initiated by irradiating the reactor under simulated solar light. At predetermined time intervals, samples were withdrawn for determining the PAHs remaining in the solution or reaction intermediates. Control experiments were conducted in dark but under otherwise identical conditions.

To investigate effects of oil dispersants on the vertical distribution of PAHs in the water column, a 250 mL anthracene solution of 30 µg/L was mixed with a dispersant or dispersant component in the photo-reactor for 30 min in dark. Then, each 1 mL sample was withdrawn at various depths and mixed with methanol for analysis of the PAHs concentration.

#### **4.2.1.3. Roles of dissolved oxygen and radicals in photodegradation of PAHs**

To investigate the effects of dissolved oxygen (DO), the photodegradation tests were also carried out with seawater that was purged with nitrogen for 1 h. The roles of radicals, i.e.  $^1\text{O}_2$ ,  $\text{O}_2^{\cdot-}$ , and  $\cdot\text{OH}$  radicals, in PAH photodegradation were evaluated by using selective radical scavengers. Specifically, tert-butanol at 221 mg/L was used for quenching  $\cdot\text{OH}$ , sodium azide at 200 mg/L for  $^1\text{O}_2$  and  $\cdot\text{O}_2^{\cdot-}$  (Gong et al. 2015), and superoxide dismutase at 14 mg/L for  $\text{O}_2^{\cdot-}$  (Diaz et al. 2004, Ryu and Choi 2004).

#### **4.2.1.4. Analytical methods**

Anthracene and 9,10-DMA in seawater were quantified using HPLC, the wavelength of UV detector was 254 nm, which afforded a detection limit of 0.5  $\mu\text{g/L}$  for both PAHs. More information about the HPLC analysis method is provided in Section 3.2.1.2.

To determine the photodegradation intermediates, each 100 mL of solution samples were withdrawn from the photo-reactor at various reaction times, and extracted using 5 mL dichloromethane consecutively for 3 times, then the extracts were dried by sodium sulfate anhydrous ( $\text{Na}_2\text{SO}_4$ ) and concentrated to 0.5 mL under a gentle stream of  $\text{N}_2$  gas. The concentrated extracts were then analyzed by GC-MS by the methods in Section 4.1.1.6.

UV-Vis absorption spectroscopic study and fluorescence analysis of the PAH solutions were performed using a UV-Vis SpectraMax M2 plate reader (Molecular Devices, Sunnyvale, California, USA) with a 1-cm path quartz cuvette. The excitation wavelength of anthracene and 9,10-DMA are 366 and 375 nm, respectively, and the emissions were recorded in the range of 360 to 550 nm for the fluorescence analyses.

## 4.2.2. Effects of dispersants on PAHs photolysis

Figure 63 shows effects of Corexit EC9500A on photodegradation of anthracene and 9,10-DMA under simulated sunlight. The control tests indicated that the loss of anthracene or 9,10-DMA was < 4% without light, and the dispersant did not react with the PAHs. The presence of Corexit EC9500A remarkably promoted photodegradation of both PAHs. The presence of 18 mg/L of the dispersant shortened the complete removal time from 300 to 120 min for anthracene and from 80 to 15 min for 9,10-DMA. Between the two PAHs, the alkylated counterpart (9,10-DMA) was more vulnerable to photolysis than the parent anthracene. This observation is consistent with other studies where increasing alkyl-substitution of PAHs gives faster photooxidation rates (Khairy and Lohmann 2012, Lima et al. 2005, Naspinski et al. 2008) and it can be attributed to the benzyl hydrogen activation of 9,10-DMA where the alkyl group acts as the electron donating group (Radding et al. 1976). The results also indicate that the dispersant enhanced the photodegradation of the alkylated PAH more effectively than the parent PAH. More details on the mechanisms of dispersant facilitated photodegradation will be discussed in Section 4.2.3.

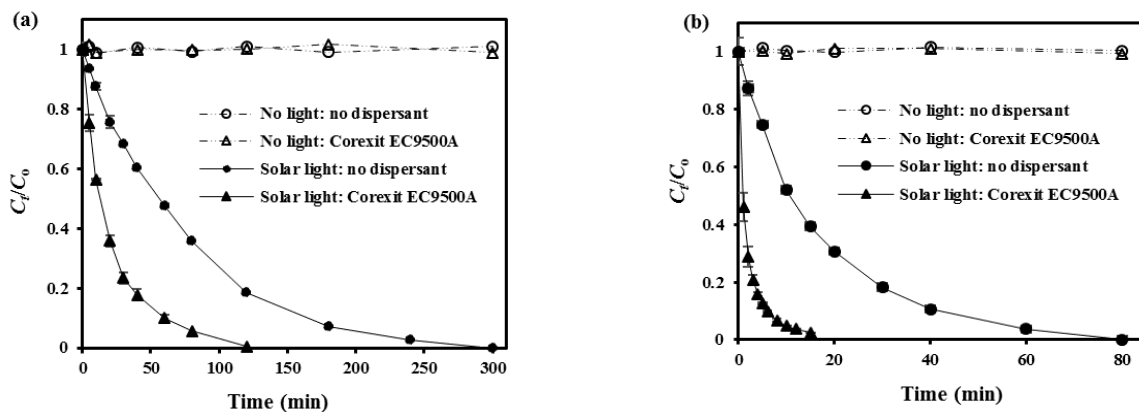
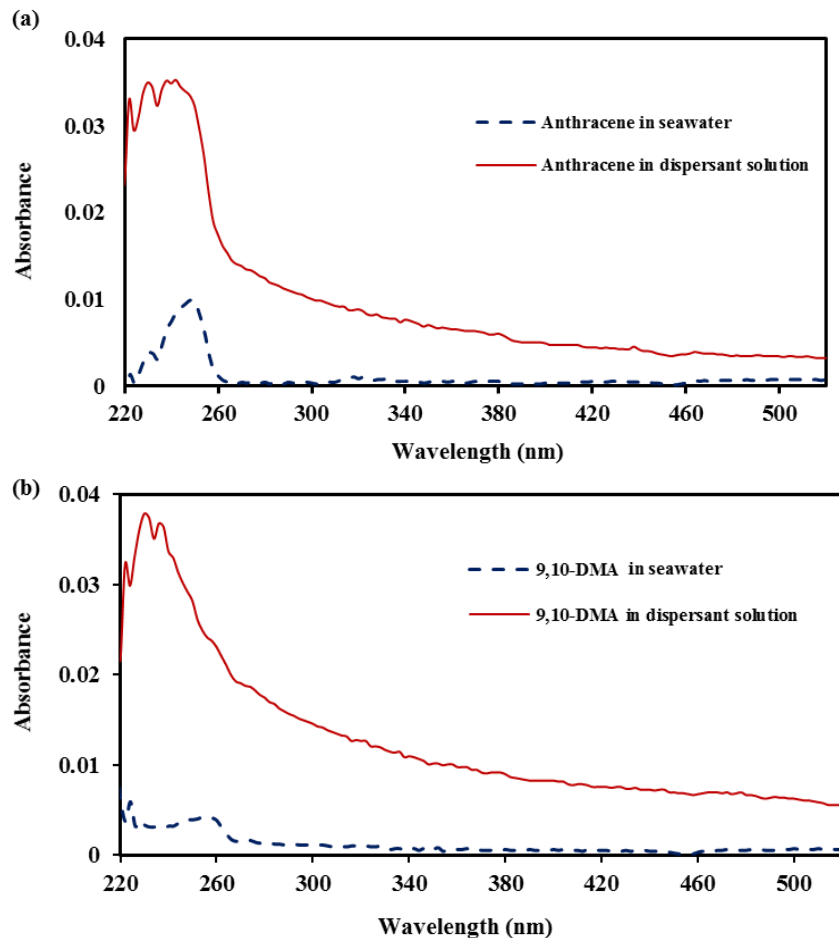


Figure 63. Effects of Corexit EC9500A on photodegradation of anthracene (a) and 9,10-DMA (b) in seawater.

Experimental conditions: Corexit EC9500A = 18 mg/L, initial anthracene or 9,10-DMA = 30  $\mu\text{g/L}$ , pH =  $7.8 \pm 0.2$ , temperature =  $25 \pm 0.2$   $^{\circ}\text{C}$ .

**Figure 64** shows the corrected UV-Vis absorbance spectra of anthracene and 9,10-DMA in plain seawater or in Corexit EC9500A seawater solution. The maximum absorbance for anthracene and 9,10-DMA occurred at 248 nm and 255 nm, respectively, in seawater. The maximum absorbance for anthracene and 9,10-DMA occurred at 248 nm and 255 nm, respectively, in seawater. The absorbance of solar irradiation of solution (PAHs with dispersant) dramatically enhanced, especially in the UV region (< 400 nm). Although UV light only accounts for a small fraction (~5%) of sunlight, UV irradiation is much more energetic than visible light (Jeong et al. 2003). Therefore, enhanced UV absorbance contributes in part to the accelerated photodegradation rate.

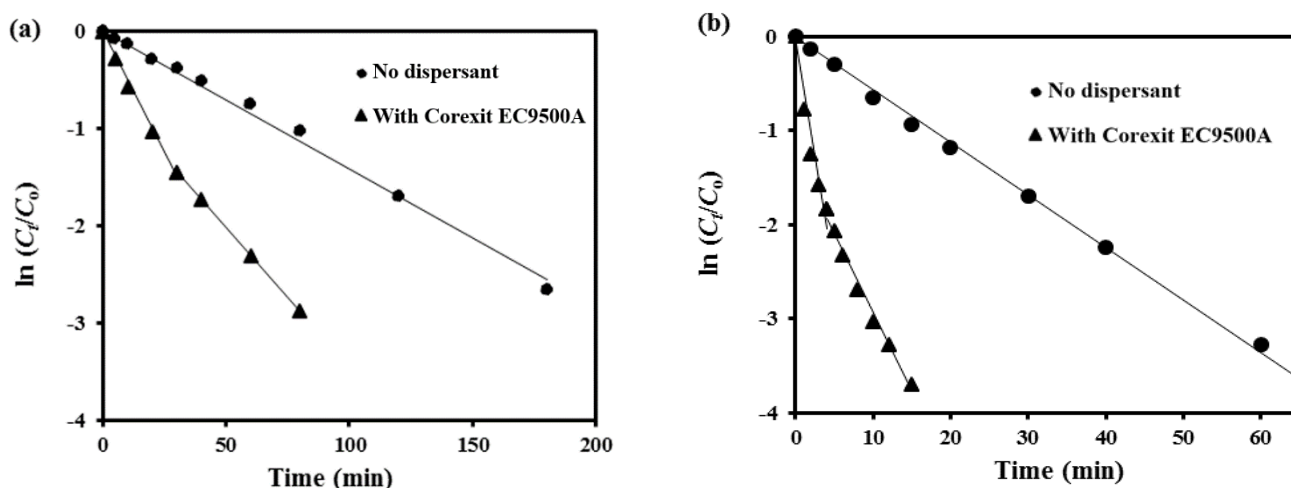


**Figure 64. UV-Vis absorption spectra of anthracene (a) and 9,10-DMA (b).**

In seawater and Corexit EC9500A seawater solutions. Spectra were corrected by subtracting the absorbance spectra of seawater. Experimental conditions: anthracene or 9,10-DMA = 30  $\mu\text{g/L}$ , Corexit EC9500A = 18 mg/L.

**Figure 65** shows the linearized plots of the kinetic data in accord with the rate model. For both PAHs, the first-order kinetic model was able to adequately ( $R^2 > 0.99$ ) describe the photolysis process when no dispersant was present. However, the presence of the dispersant (18 mg/L) induced a two-stage degradation kinetic profile for both PAHs, i.e. a faster initial degradation rate (with a steeper slope) followed by a later slower rate. Nonetheless, the first-order model was able to be separately interpreted the kinetic data over the two stages. **Table 18** gives the best fitted  $k$  values. It is noteworthy that the presence of Corexit EC9500A increased the  $k$  values by a factor of 3.8 and 9.1, respectively, for anthracene and 9,10-DMA in the initial stage, and by 2.2 and 3.0 in the second stage. Similar two-stage profiles have been observed by Gong et al. (2015). The photodegradation rate of pyrene under UV light was 7.9 times faster at initial stage (first 10 min) than that at second stage (10-360 min). They claimed that the two stage degradation kinetics are due to the more prevalent role of direct photolysis in the initial stages, and dominant role of electron transfer from excited pyrene species to oxygen in the second stages (Gong et al. 2015). However, the two-stage degradation kinetics of PAHs can also be attributed to: 1) some photodegradation byproducts are produced and act as internal light absorbers, thus weakening the light intensity that is available for the target PAHs, or act as quenchers for the radicals (Chu and Kwan 2002); and 2) the effective dispersant components that accelerate PAHs degradation are photodegraded in the initial stage.

Considering that 77% of anthracene and 84% of 9,10-DMA were degraded in the initial stage, the  $k$  values of the initial stage were used to compare the enhanced photolysis rates hereafter in this part.



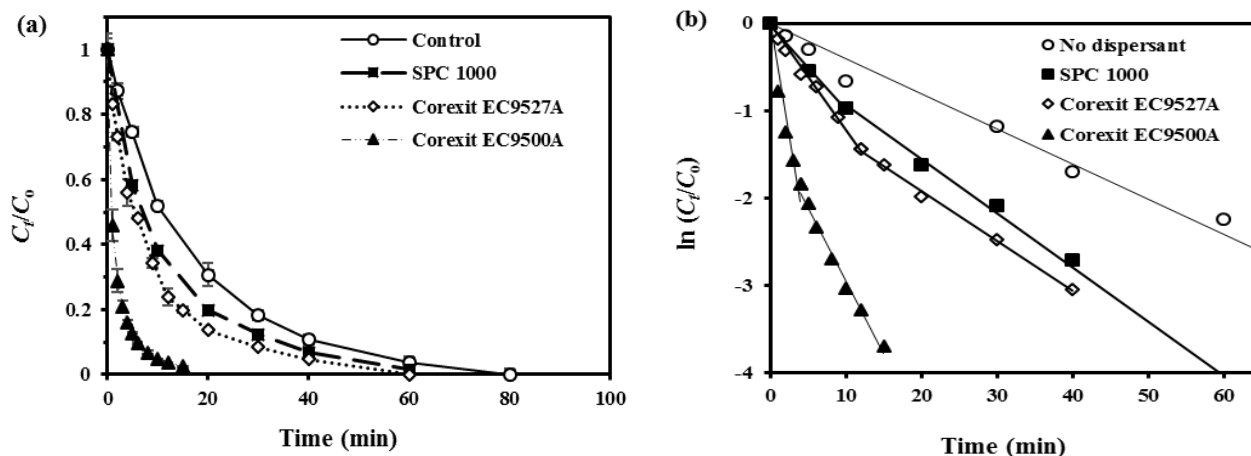
**Figure 65. Fitting the first-order kinetic model to the experimental rate data.** (a) Anthracene, and (b) 9,10-DMA, in the absence or presence of 18 mg/L of Corexit EC9500A.

**Table 18. The first-order photodegradation rate constants ( $k$ ) of anthracene and 9,10-DMA under solar irradiation.**

PAHs	No dispersant		With Corexit EC9500A (18 mg/L)			
	$k$ ( $\text{min}^{-1}$ )	$R^2$	Initial stage		Second stage	
			$k$ ( $\text{min}^{-1}$ )	$R^2$	$k$ ( $\text{min}^{-1}$ )	$R^2$
<b>Anthracene</b>	0.013	0.99	0.050	0.99	0.029	1.00
<b>9,10-DMA</b>	0.056	1.00	0.511	0.92	0.167	0.99



Using 9,10-DMA as a model PAH, the effects of two other dispersants, i.e. Corexit EC9527A and SPC 1000, on the photodegradation rate were further studied. **Figure 66** compares the effects of the three different oil dispersants. Evidently, all three dispersants accelerated the photodegradation rate of 9,10-DMA, and the effectiveness follows the order of: Corexit EC9500A >> Corexit EC9527A > SPC 1000. Like Corexit EC9500A, Corexit EC9527A showed a higher initial photolysis rate ( $k_1 = 0.122 \text{ min}^{-1}$ ) and a lower rate ( $k_2 = 0.057 \text{ min}^{-1}$ ) in the second stage (after 12 min), and the  $k_2$  was comparable to the photolysis rate without dispersant ( $0.056 \text{ min}^{-1}$ ); for SPC 1000, however, a straight constant rate ( $0.062 \text{ min}^{-1}$ ) was observed. The different behaviors of the three dispersants are attributed to their different formulas and effective compositions (see Section 4.2.3).



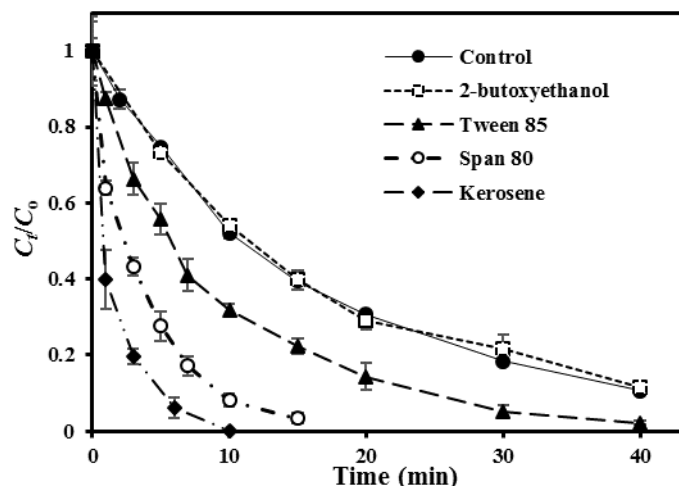
**Figure 66. Effects of model oil dispersants on photodegradation of 9,10-DMA in seawater.**

(a) Degradation kinetics with or without dispersants, and (b) the linearized first-order kinetic plots of the kinetic data. Experimental conditions: dispersant dosage = 18 mg/L, initial 9,10-DMA = 30  $\mu\text{g/L}$ , pH =  $7.8 \pm 0.2$ , temperature =  $25 \pm 0.2$   $^\circ\text{C}$ .

### 4.2.3. Effects of individual dispersant components on PAH photolysis

Oil dispersants contain various surfactants and organic solvents (Fu et al. 2015, Hayworth and Clement 2012). Therefore, it is important to understand the effects of key individual dispersant components on the photochemical reactions. Again, using 9,10-DMA as a model PAH, the effects of primary individual component of Corexit dispersants on the PAH degradation were investigated.

**Figure 67** shows the photodegradation rates of 9,10-DMA in the presence of 5 key Corexit dispersant components, including Tween 85, Span 80, kerosene and 2-butoxyethanol (each at 18 mg/L). **Table 19** gives the best-fitted  $k$  values in the initial stage. Tween 85, Span 80 and kerosene all accelerated the photolysis rate by a factor of 1.8, 4.3 and 8.8, respectively, while 2-butoxyethanol showed negligible effect on the photodegradation rate. As the nonionic surfactants (Tween 85 and Span 80) account for nearly 50% of the dispersant (Bruheim et al. 1999), Tween 85 and Span 80 can be the critical contributors to the enhanced photolysis rate.

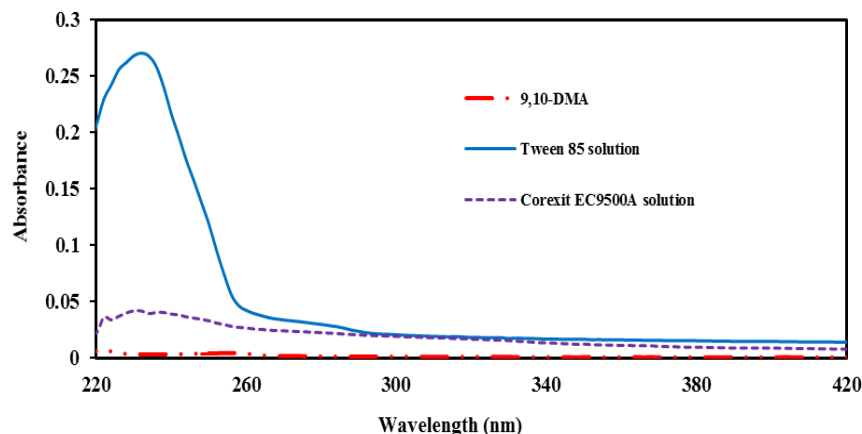


**Figure 67. Effects of dispersant components on photodegradation of 9,10-DMA in seawater.** Experimental conditions: dispersant component concentration = 18 mg/L, initial 9,10-DMA = 30  $\mu\text{g/L}$ , pH =  $7.8 \pm 0.2$ , temperature =  $25 \pm 0.2$   $^{\circ}\text{C}$ .

**Table 19. Best-fitted first-order photodegradation rate constants ( $k_1$ ) of anthracene in the presence of individual dispersant components under solar irradiation**

	Control	2-butoxyethanol	Tween 85	Span 80	Kerosene
$k_1$ ( $\text{min}^{-1}$ )	0.056	0.055	0.098	0.239	0.493
$R^2$	1.00	0.98	0.99	0.97	0.95

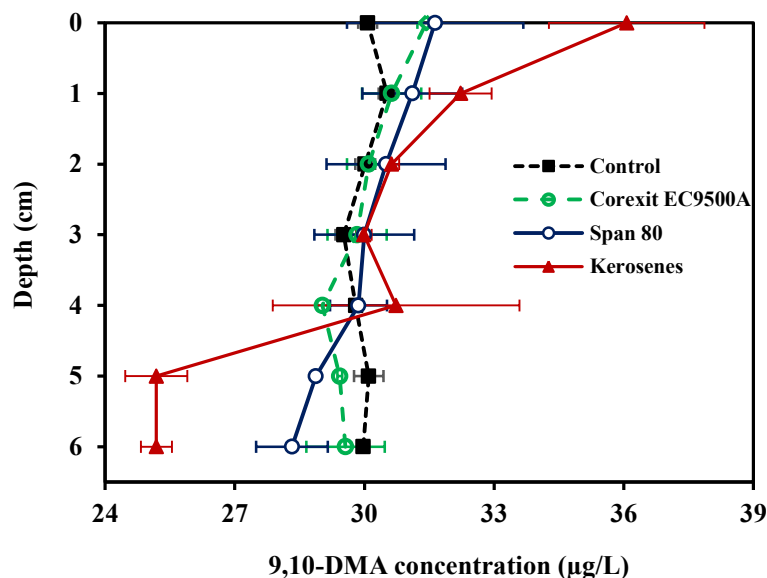
**Figure 68** shows that Tween 85 exhibited a strong peak in the UVC range (< 260 nm), much stronger than that for the dispersant as a whole, which can be attributed to the abundance of electron-rich double bonds in the molecular structure of Tween 85 (Erdem et al. 2014). The absorbed solar energy on Tween 85 may lead to the formation of primary and secondary reactive species, e.g.  $^1\text{O}_2$  (Wenk et al. 2011), and/or transfer energy to PAHs, and thus induce the photosensitized degradation. The other tested dispersant components showed less strong peak than Tween 85 in seawater.



**Figure 68. UV-Vis absorption spectra of 9,10-DMA, Tween 85, and Corexit EC9500A in seawater.** Spectra were corrected by subtracting the absorption spectra of seawater. Experimental conditions: Corexit EC9500A or Tween 85 = 18 mg/L, 9,10-DMA = 30  $\mu\text{g/L}$ .

Span 80 is a nonionic surfactant with a low hydrophilic-lipophilic balance (HLB) value (4.3) (Ruckmani et al. 2000), which can be only partially dissolved or dispersed in water (Barbetta and Cameron 2004). 9,10-DMA is highly hydrophobic ( $\log K_{ow} = 5.69$ ) and it can favorably partition and accumulate in the hydrophobic phase of Span 80. Furthermore, the density of Span 80 (0.99 g/mL) is lower than that of the seawater (1.03 g/mL). Consequently, Span 80 may stratify in the water column with more surfactant in the upper part; namely, Span 80 may entrain and enrich more 9,10-DMA in the upper layer of the solution, which is favorable for absorbing light. Likewise, kerosene is also hydrophobic solvent ( $\log K_{ow} = 3.7\text{--}8.0$ ), with an even lower density (0.80 g/mL), and thus, kerosene will pose even greater floating effect than Span 80 on the 9,10-DMA enrichment despite its small fraction in the dispersant.

**Figure 69** shows the vertical distribution of 9,10-DMA in the photo-reactor water column in the presence of the dispersant (18 mg/L) or with the same concentration of each individual components. Evidently, kerosene displayed the strongest floating effect on the PAH, which enriched the PAH concentration in the top layer by  $\sim 20\%$  compared to that in the control (plain seawater). Span 80 alone caused slightly more PAH stratification than the dispersant as a whole, enriched the surface PAH concentration by  $\sim 5.4\%$  and  $\sim 4.8\%$ , respectively. Therefore, the surface enrichment of PAHs facilitated by the light hydrophobic components is partially responsible for the dispersant-enhanced photodegradation. It should be noted, though, that the enrichment effect was less significant for the dispersant than for the individual components; this is because the dispersant was formulated in a way to achieve maximal water dispersibility of the hydrophobic compounds.

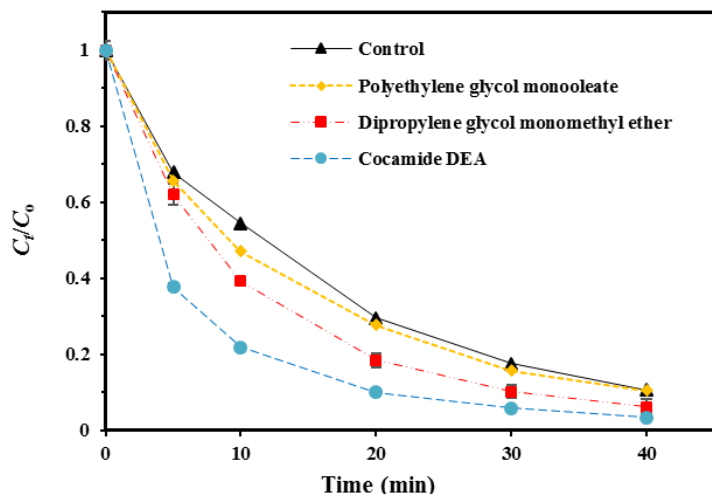


**Figure 69. Vertical distribution of 9,10-DMA concentration in the photo-reactor.**

In the absence or presence of Corexit EC9500A or individual Corexit dispersant components. Experimental conditions: Corexit EC9500A or dispersant components = 18 mg/L, 9,10-DMA = 30 µg/L.

The dispersant components of Corexit EC9527A are similar to those of Corexit EC9500A but with a unique organic solvent (2-butoxyethanol) (**Table 1**). The 2-butoxyethanol had negligible effect on the photolysis of 9,10-DMA (as shown in **Figure 67**); this may partially interpret the weaker effect of Corexit EC9527A than Corexit EC9500A on enhancing the photolysis rate of 9,10-DMA.

For comparison, the effects of three most abundant SPC 1000 components (polyethylene glycol monooleate, dipropylene glycol monomethyl ether, and cocamide DEA) on the photodegradation of 9,10-DMA were tested at the identical conditions (**Figure 70**). Polyethylene glycol monooleate did not affect the photolysis rate of 9,10-DMA; dipropylene glycol monomethyl ether and cocamide DEA enhanced the photolysis rate ( $k_1$ ) from 0.056 to 0.068 and 0.094  $\text{min}^{-1}$ , respectively. Dipropylene glycol monomethyl ether and cocamide DEA only amount to < 19% of the total SPC 1000 content (Jacob and Bergman 2001), but the polyethylene glycol monooleate and water comprise ca. 36% and 20% of total SPC 1000 content (Jacob and Bergman 2001). Therefore, the SPC 1000 was less effective than Corexit dispersants on accelerating the photolysis of PAHs.



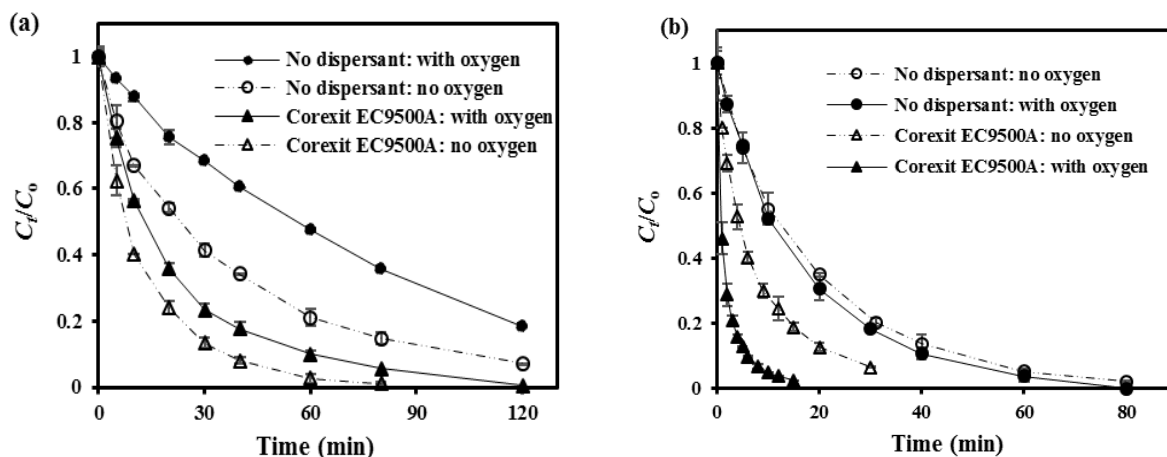
**Figure 70. Effects of key components of SPC 1000 on photodegradation of 9,10-DMA in seawater.** Experimental conditions: dispersant component concentration = 18 mg/L, initial 9,10-DMA = 30 µg/L, pH = 7.8±0.2, temperature = 25±0.2 °C.  $C_0$ : Initial concentration of 9,10-DMA,  $C_t$ : Concentration at time  $t$ .

#### 4.2.4. Chemical mechanisms of dispersant-enhanced PAH photolysis

In addition to the above physical mechanisms (change PAHs distribution in water), the dispersant may chemically enhance the photodegradation rate of PAHs. As is well known, photochemical change may involve both direct and indirect (sensitized) photolysis. In direct photolysis, a substrate absorbs the solar quanta “directly”, followed by degradation of the excited state (Zepp 1979). Organic chemicals that are structurally composed of chromophoric moieties, e.g. aromatics, conjugated C=C, or ketones, which can absorb light at wavelengths present in solar irradiation, and are susceptible to direct photolysis (Schwarzenbach et al. 2003). Direct photolysis has been known to be the dominant pathway for PAHs photodegradation in natural waters (Fasnacht and Blough 2002, Miller and Olejnik 2001). Indirect photolysis of PAHs involves the excitation of photosensitizers, e.g., colored DOM or nitrate, resulting in production of reactive species, e.g., free radicals and triplet excited DOM ( $^3\text{DOM}^\bullet$ ) (Lam et al. 2003).

DO plays an important role in photodegradation of PAHs as DO can react with excited PAHs directly or form ROS, leading to indirect photolysis of PAHs (Miller and Olejnik 2001); on the other hand, molecular oxygen can also act as a quencher for the singlet and triplet states, leading to inhibition on photolysis (Lehto et al. 2000).

To investigate the underlying photodegradation mechanisms in the presence of Corexit EC9500A, a series of tests were carried out to examine the roles of DO and various radicals in the photolysis of the PAHs. **Figure 71** profiles the effects of DO on the photodegradation of anthracene and 9,10-DMA under solar light. **Table 20** presents the photodegradation rate constants. For anthracene, the depletion of DO (< 0.1 mg/L) remarkably increased the photodegradation rate regardless of the dispersant. For instance, removal of DO increased the  $k$  value from 0.013 to 0.023  $\text{min}^{-1}$  in the absence of Corexit EC9500A, and from 0.050 to 0.070  $\text{min}^{-1}$  in the presence of Corexit EC9500A. In contrast, DO showed the opposite effect on the photolysis of 9,10-DMA. In the absence of Corexit EC9500A, the removal of DO did not significantly alter the photolysis rate of 9,10-DMA; the removal of DO decreased the  $k$  value from 0.511 to 0.144  $\text{min}^{-1}$  in the presence of Corexit EC9500A.



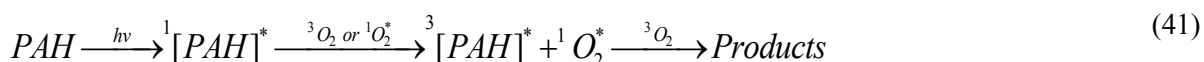
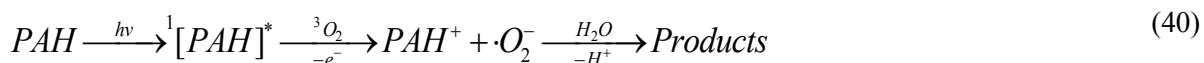
**Figure 71. Effects of DO on photodegradation of anthracene (a) and 9,10-DMA (b).**

Experimental conditions: Corexit EC9500A = 0 or 18 mg/L, initial anthracene or 9,10-DMA = 30  $\mu\text{g/L}$ , pH =  $8.0 \pm 0.3$ , temperature =  $25 \pm 0.2$   $^\circ\text{C}$ .

**Table 20. First-order rate constants ( $k_1$ ) in the initial stage of anthracene and 9,10-DMA photodegradation with or without DO**

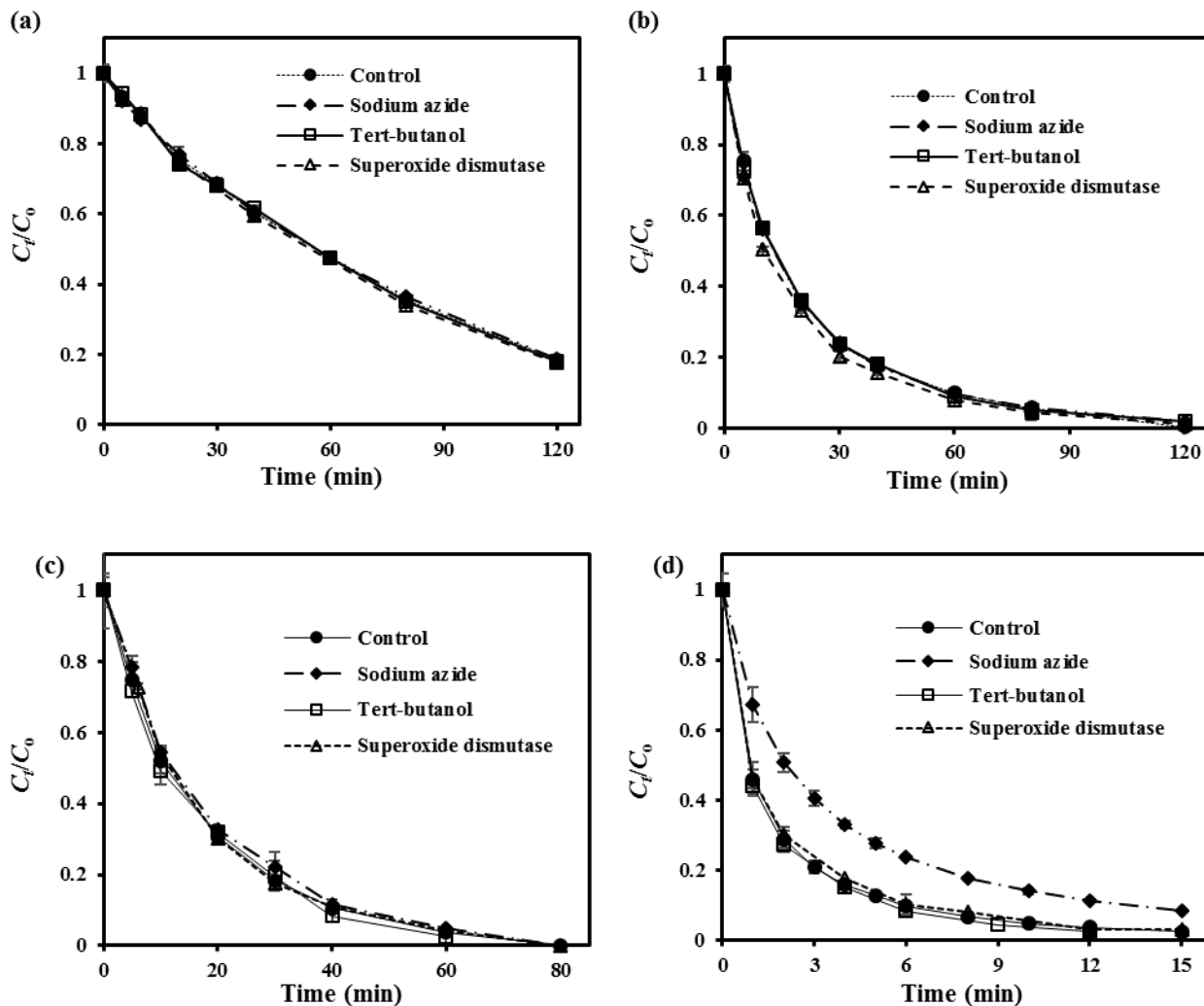
PAHs	Dispersants	With DO		Without DO	
		$k_1$ ( $\text{min}^{-1}$ )	$R^2$	$k_1$ ( $\text{min}^{-1}$ )	$R^2$
Anthracene	No dispersant	0.013	0.99	0.023	0.97
	With dispersant	0.050	0.99	0.070	0.97
9,10-DMA	No dispersant	0.056	1.00	0.049	1.00
	With dispersant	0.511	0.92	0.144	0.97

The opposite effects of DO on the photodegradation of the parent and alkylated PAHs indicate that different degradation mechanisms are operative and the dispersant has different roles in the two reaction systems. Photolysis of PAHs in the aqueous phase can take place through different pathways without and with DO: 1) direct photochemical ionization at the initial reaction step followed by oxidation of the formed PAH radical cations (Reaction 39); 2) formation of PAH radical cations via electron transfer to oxygen due to quenching of excited singlet PAH ( $^1[\text{PAH}]^*$ ), followed by photooxidation of PAHs radical cations (Reaction 40); and/or 3) formation of excited singlet and triplet PAH ( $^3[\text{PAH}]^*$ ), followed by the reaction of excited triplet state PAH with oxygen by transferring energy to molecular oxygen (Reaction 41) (Fasnacht and Blough 2003, Kahan and Donaldson 2007). In the absence of DO, the photolysis of anthracene and 9,10-DMA undergoes the direct ionization process (Reaction 39).



In the presence of DO, the molecular oxygen quenches the singlet and triplet states (Reactions 40 and 41), and thus contributes to the decay of any excited state that has a long lifetime (Lehto et al. 2000). The life time of triplet PAHs is exceedingly long ( $> 100 \mu\text{s}$ ) (Dabestani and Ivanov 1999) and the quenching rate of triplet PAHs (e.g., phenanthrene, anthracene and chrysene) by oxygen is quite high ( $\geq 10^{10} \text{ M}^{-1} \text{ s}^{-1}$ ) (Abdel-Shafi and Wilkinson 2000). For anthracene, deoxygenation greatly increased the photolysis rate (**Figure 71a**), indicating that the excited triplet state anthracene during direct ionization was vulnerable to quenching by molecular oxygen. The presence of Corexit EC9500A mitigated the quenching effect for the following reasons: 1) the dispersant induced production of other reactive species, resulting in enhanced indirect photolysis mechanism that overweighs the quenching effect; and 2) some DO was consumed by reacting with the dispersant components (Andrews et al. 2000). For 9,10-DMA, DO had negligible effect on the photolysis rate in the absence of Corexit EC9500A (**Figure 71b**), indicating that the photolysis process was probably due to the direct photolysis and the electron transfer from triplet excited organic matter, rather than the production of ROS (e.g.,  $^1\text{O}_2$  or/and  $\bullet\text{O}_2^-$ ). However, in the presence of Corexit EC9500A, DO remarkably increased the photolysis rate of 9,10-DMA (**Figure 71b**), which can be due to the increased formation of ROS. The structure of 9,10-DMA leads to its higher reactivity than anthracene, because the alkyl bond of 9,10-DMA acts as electron donating group, which makes the 9,10-DMA be more prone to be oxidized than anthracene (Gandra et al. 2009). During the photolysis process, the reactive species that involve in the degradation of 9,10-DMA may have much weaker effects on anthracene.

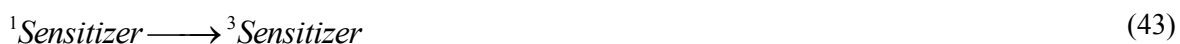
The roles of various free radicals were further investigated by applying three selective radical scavengers, i.e., tert-butanol for quenching  $\bullet\text{OH}$ , azide for  $^1\text{O}_2$  and  $\bullet\text{OH}$ , and superoxide dismutase for  $\bullet\text{O}_2^-$ . **Figure 72** presents the photodegradation rates of anthracene and 9,10-DMA in the presence of each of the radical scavengers. Evidently, the quenching of  $^1\text{O}_2$ ,  $\bullet\text{OH}$ , and  $\bullet\text{O}_2^-$  radicals did not alter the photolysis rates of anthracene regardless of the dispersant, indicating that these radicals had negligible contribution to the anthracene photodegradation process. For 9,10-DMA, the presence of tert-butanol and superoxide dismutase did not significantly change the photolysis rates regardless of Corexit EC9500A; however, the presence of azide decreased the rate constant from 0.511 and 0.278  $\text{min}^{-1}$  in the presence of Corexit EC9500A, but had no effect in the absence of Corexit EC9500A. This observation indicated that the radicals  $\bullet\text{OH}$  and  $\bullet\text{O}_2^-$  played negligible roles in the photodegradation of 9,10-DMA in all cases, but the  $^1\text{O}_2$  played an important role in the photolysis process in the presence of the dispersant. The results reveal that Corexit EC9500A boosted the formation of  $^1\text{O}_2$  from  $\text{O}_2$ , which enhanced photodegradation of 9,10-DMA. Comparing with 9,10-DMA, the higher stability of anthracene makes it less likely to be oxidized by  $^1\text{O}_2$ .



**Figure 72. Effects of radical scavengers on photolysis of anthracene and 9,10-DMA.**

(a) Photolysis of anthracene without dispersant, (b) photolysis of anthracene with Corexit EC9500A, (c) photolysis of 9,10-DMA without dispersant, and (d) photolysis of 9,10-DMA with Corexit EC9500A. Experimental conditions: Corexit EC9500A = 18 mg/L, initial 9,10-DMA or anthracene = 30  $\mu\text{g/L}$ , pH =  $8.0 \pm 0.3$ , temperature =  $25 \pm 0.2$  °C.

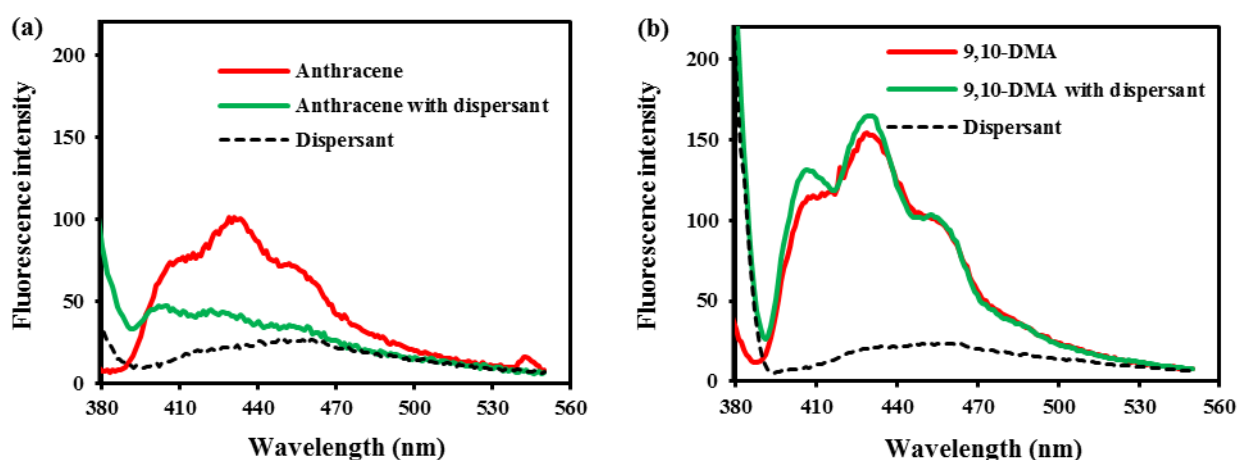
Figure 72 shows that ROS did not significantly contribute to the PAH degradation in the absence of the dispersant. Therefore, it is more likely that the dispersant components themselves act as the photosensitizers. Energy is transferred from the excited sensitizers to the ground state oxygen and raises its energy status, resulting in the production of  $^1\text{O}_2$  (Reactions 42 and 43) (Foote and Wexler 1964). Due to the high activity of 9,10-DMA (Gandra et al. 2009), the elevated  $^1\text{O}_2$  concentration had a more profound effect on the photolysis of 9,10-DMA than anthracene.





Due to the relatively low radical production rate and the sinks of photochemically generated radicals, i.e.  $\bullet\text{OH}$ ,  $^1\text{O}_2$ , and  $\bullet\text{O}_2^-$ , in natural waters (Fasnacht and Blough 2002), the contribution of indirect PAHs photolysis is lower than direct photolysis even in the presence of dispersant.

The fluorescence of PAHs can be quenched when PAHs are associated with DOM, and thus, measuring fluorescence spectra can distinguish the DOM-associated PAHs and freely dissolved PAHs (Gauthier et al. 1986, Raber et al. 1998). **Figure 73** profiles the fluorescence spectra of anthracene and 9,10-DMA in the absence or presence of Corexit EC9500A. Evidently, the dispersant dramatically quenched the fluorescence intensity of anthracene (peaked at the emission wavelength of 430 nm), but showed negligible effect on 9,10-DMA, indicating that more anthracene is associated with the dispersant than 9,10-DMA. Therefore, the energy captured by the dispersant molecules may directly transfer to anthracene and accelerate its photolysis process, while for the case of 9,10-DMA, it is more likely transferred to oxygen to form  $^1\text{O}_2$ , which also explains the different roles of DO in the photodegradation of anthracene and 9,10-DMA.



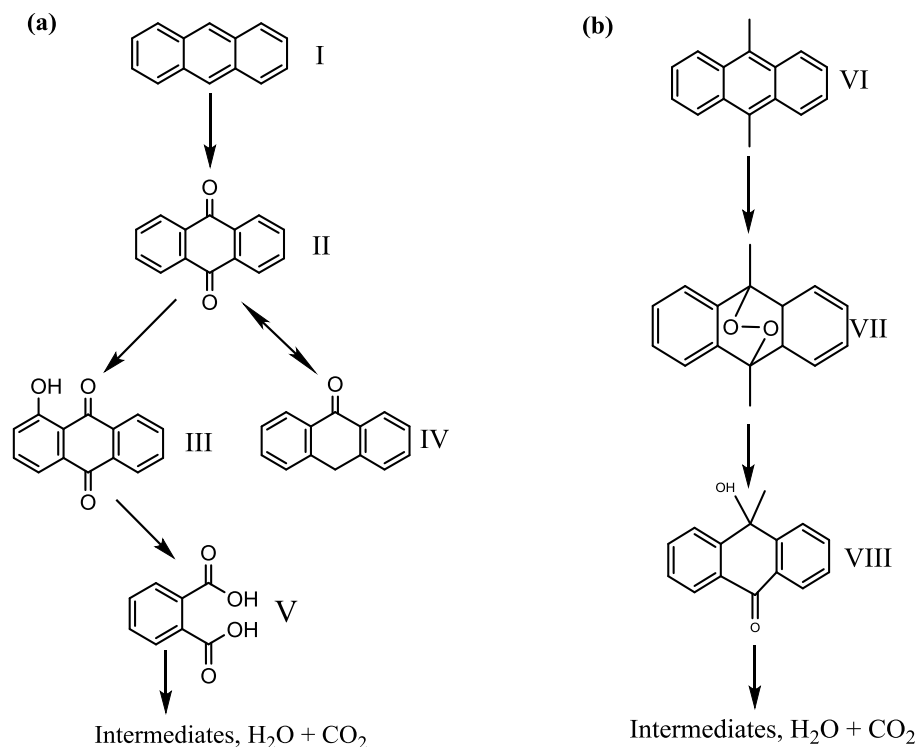
**Figure 73. Fluorescence spectra of anthracene (a) and 9,10-DMA (b).**

Experimental conditions: Corexit EC9500A = 0 or 18 mg/L, anthracene or 9,10-DMA = 30  $\mu\text{g/L}$ , pH =  $8.0 \pm 0.3$ , temperature =  $25 \pm 0.2$   $^{\circ}\text{C}$ .

#### 4.2.5. Photodegradation pathways of anthracene and 9,10-DMA

9,10-anthraquinone (Product II), 1-hydroxy-9,10-anthraquinone (Product III), phthalic acid (Product V) and trace amount of anthrone (Product IV) were detected by GC-MS during the photolysis of anthracene, but only one anthrone derivative (Product VII) was found during the photolysis of 9,10-DMA. Based on the mechanistic studies and intermediates identified by GC-MS, the photolysis pathways of anthracene and 9,10-DMA are proposed in **Figure 74**. 9,10-anthraquinone, as a major intermediate, can be produced from the excited anthracene via an endoperoxide intermediate (Librando et al. 2014). The 9,10-anthraquinone can act as a photosensitizer, and itself will be involved in the formation 1-hydroxy-9,10-anthraquinone or anthrone during the photooxidation process. However, the conversion of 9,10-anthraquinone to anthrone is a reversible reaction (Theurich et al. 1997); the anthrone will finally undergo to degradation via converting to 9,10-anthraquinone. The photooxidation of 1-hydroxy-9,10-anthraquinone yielded phthalic acid, and underwent the further mineralization (produce  $\text{H}_2\text{O}$  and  $\text{CO}_2$ ). For 9,10-DMA, the solar irradiation induced the excitation of 9,10-DMA, followed by the addition of oxygen to 9,10-DMA to yield the endoperoxides (Product VII) (Aksnes and Vagstad 1979). This reaction is more favorable in the system with dispersant, where dispersant promoted the formation of  $^1\text{O}_2$ , which is prone to react with 9,10-DMA. The formed endoperoxides can further convert to the anthrone derivative,

then involved in further photodegradation and mineralization (Miller and Olejnik 2001). Our study showed that the photolysis of anthracene and 9,10-DMA can undergo without DO (**Figure 71**), the oxygen in the observed intermediates may come from water, probably via a cation radical intermediate (Reaction 41) (Mill et al. 1981).



**Figure 74. Proposed photodegradation pathways.**

(a) Photodegradation of anthracene, and (b) photodegradation of 9,10-DMA in seawater under sunlight.

It is noteworthy that the same PAH photodegradation byproducts were detected in the presence and absence of Corexit EC9500A. Therefore, the presence of dispersant may only affect the photolysis rate; that is, it did not alter the photodegradation pathway.

#### 4.2.6. Conclusions

This work studied the effects of model oil dispersants on the photodegradation of two model PAHs (anthracene and 9,10-DMA) in seawater. The key findings are as follows:

- 1) The tested dispersants, i.e. Corexit EC9500A, Corexit EC9527A and SPC 1000, markedly promoted the photolysis rate of the PAHs. The accelerating effects follow the order of: Corexit EC9500A >> Corexit EC9527A > SPC 1000.
- 2) In the presence of dispersant, the photodegradation rate follows a two-stage, first-order kinetic law, with a faster initial photolysis rate; while in the absence of dispersant, the photolysis rate obeys the classic first-order rate law with one constant rate constant. Corexit EC9500A increased the photolysis rate (*k*) of anthracene and 9,10-DMA by a factor of 3.8 and 9.1, respectively.
- 3) The dispersant components (Tween 85, Span 80, and kerosene) were found to be the critical dispersant components that promote the photolysis rate of the PAHs. Tween 85 enhanced the UV absorbance,

and kerosene and span 80 enriched the surface PAH concentration. As a result, photolysis rate was enhanced.

- 4) Chemically, DO acts as a quencher for the excited states of the organics, thus hindering the photolysis of anthracene. Conversely, DO is involved in the formation ROS (e.g.,  $^1\text{O}_2$ ) in the presence of oil dispersants, which is beneficial to the photolysis of 9,10-DMA. More anthracene is associated with dispersant than 9,10-DMA, which is favorable to directly transfer of energy to anthracene, while the energy is more likely transferred to oxygen to form  $^1\text{O}_2$  in the case of 9,10-DMA.
- 5) Oil dispersants accelerated the photolysis rates of anthracene and 9,10-DMA but did not change their degradation pathways.

The results provide useful information for understanding the roles of oil dispersants on the environmental weathering of persistent oil components in the marine environment.

### **4.3. A Mechanistic Investigation into Sunlight-Facilitated Photodegradation of Pyrene in Seawater with Oil Dispersants**

Photodegradation is known to be a major abiotic process that affects petroleum weathering and has significant implications in the redox cycling, transport, and degradation of oil components (Nicodem et al. 2001, Zafiriou et al. 1984). Large quantities of applied oil dispersants may have great impacts on the photodegradation of oil because of the strong chemical and physical interactions among the dispersant and oil components. Unfortunately, there is little information on the effects of oil dispersants on photodegradation of oil components under solar irradiation and on the action mechanisms.

Typically, the main components in oil are hydrocarbons, including alkanes and aromatics (e.g., PAHs) (Liu et al. 2012b). Compared with alkanes, PAHs often pose a greater ecological threat due to their higher toxicity, mutagenicity, carcinogenicity, and persistency (Nam et al. 2008). PAHs can pose both short- and long-term impacts on the marine ecosystems (Liu et al. 2012b, Reddy et al. 2012b). Therefore, it is critical to evaluate weathering rate and extent of PAHs in the marine environment to guide the long-term risk assessment and remediation or restoration efforts.

The overarching goal of this research was to gauge the effects of model oil dispersants on photochemical degradation of representative PAHs in the presence of sunlight. Using pyrene as the prototype PAH and Corexit EC9500A, Corexit EC9527A and Dispersit SPC 1000 as model dispersants, this work aimed to: 1) determine the rate and extent of photodegradation of pyrene in Gulf coast seawater under simulated solar irradiation in the presence of different types and concentrations of oil dispersants; 2) elucidate the underlying action mechanisms of key individual dispersant components on the photodegradation effectiveness; 3) identify the key ROS, the photodegradation pathway, and intermediate products; and 4) examine photochemical weathering rate of oil dispersants and the degradation by-products derived from dispersant components under solar irradiation. The information will help us better understand dispersant effects on the photochemical weathering of oil and environmental fate of applied oil dispersants in the Gulf of Mexico ecosystem.

### **4.3.1. Materials and methods for PAHs photodegradation experiments**

#### **4.3.1.1. Materials and experimental apparatuses**

Seawater samples were collected from the top 30 cm of the water column of Grand Bay, Alabama, and the treating process and properties are described in elsewhere (Fu et al. 2014a). The chemicals (analytical grade or higher) were used as received. The photodegradation set up is described in Section 4.1.1.1.

#### **4.3.1.2. Experimental procedure**

A stock solution of pyrene (0.3 g/L) was prepared in methanol, which was shaken overnight to assure complete dissolution. Then, a 300 mL pyrene solution (60 µg/L) was prepared by diluting the stock solution in 300 mL of seawater, of which 250 mL was used for batch photodegradation kinetic tests. Before each test, the lamp was warmed up for ~30 min. The photodegradation was initiated by exposing the pyrene solution to sunlight or UV light under the aforementioned conditions, during which the reactor remained sealed and the solution was gently stirred (300 rpm) with a 1-inch magnetic bar. At predetermined times, 1 mL samples were taken for determination of pyrene concentration or 10 mL samples were taken for analysis of degradation products. To investigate the effects of dissolved oxygen (DO), before the experiment, DO-free seawater was obtained by purging the seawater using pure nitrogen for 30 minutes. To evaluate the effects of dispersants, individual dispersant components, and radical scavengers, the photodegradation tests were carried out in the presence of known concentrations of the chemicals. Control tests were conducted without light irradiation. Each experiment was conducted in duplicate at 22±1 °C. The vertical distribution of pyrene in the water column was tested by the method shown in Section 4.2.1.2.

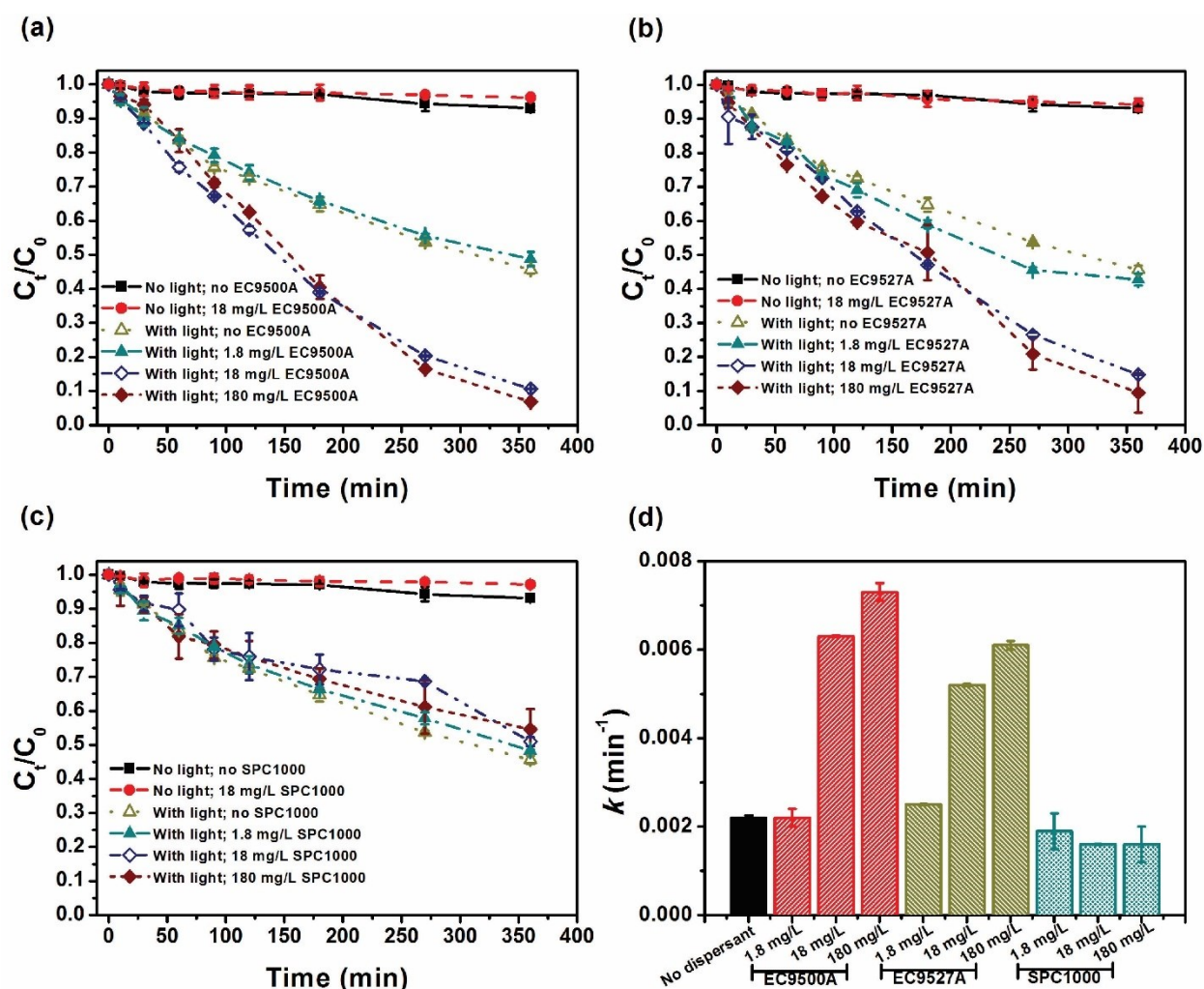
#### **4.3.1.3. Analytical methods**

UV spectra (200–400 nm) of various solutions and fluorescence measurements were conducted on a SpectraMax M2 plate reader. The excitation wavelength of pyrene was set at 335 nm and the emission spectra were recorded in the wavelength range of 350–550 nm. More details are shown in Section 4.2.1.4.

Pyrene concentration was determined using HPLC, and the photodegradation products were analyzed using GC-MS system. More details are shown in Section 3.2.1.2 and 4.1.1.6.

### 4.3.2. Effects of oil dispersants on pyrene photodegradation

Figure 75 shows the photodegradation kinetics of pyrene in the presence of the oil dispersants. The control tests indicated that mass loss of pyrene was < 7% after 6 h in the reactor system without solar irradiation. Under the solar irradiation, 54% of pyrene was photodegraded in 6 h in the absence of any dispersant. Figures 74a–c show that increasing the Corexit dispersant concentration progressively promoted photodegradation of pyrene, while SPC 1000 slightly inhibited the reaction rate. For instance, in the presence of 18 mg/L of a dispersant, the 6-h pyrene removal reached 89% for Corexit EC9500A, 85% for Corexit EC9527A, and 49% for SPC 1000, compared to 55% without dispersant. The first-order kinetic model was employed to fit the kinetic data (Clark et al. 2007, Zepp and Schlotzhauer 1979). Figure 75d compares the best-fitted rate constants, which clearly indicates that both Corexit dispersants increased the reaction rate. For example, increasing EC9500A from 1.8 to 180 mg/L increased the photodegradation rate constant by 232% from  $(2.2 \pm 0.0) \times 10^{-3}$  to  $(7.3 \pm 0.2) \times 10^{-3} \text{ min}^{-1}$ . In contrast, increasing SPC 1000 from 1.8 to 180 mg/L decreased the rate constant by approximately 16%.



**Figure 75. Effects of various dispersants on photodegradation of pyrene in seawater.**

Photodegradation under simulated sunlight in the presence of: (a) Corexit EC9500A, (b) Corexit EC9527A and (c) Dispersit SPC 1000; and (d) the best-fitted first-order reaction rate constants.

Experimental conditions: light intensity =  $100 \text{ mW/cm}^2$ , initial pyrene concentration =  $60 \text{ } \mu\text{g/L}$ , solution volume =  $250 \text{ mL}$ , temperature =  $22 \pm 1 \text{ } ^\circ\text{C}$ .

### 4.3.3. Mechanisms of dispersant effects

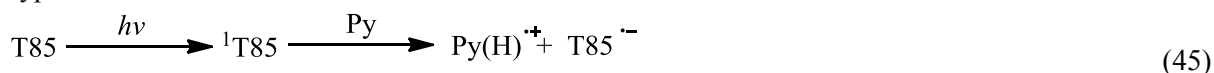
Because oil dispersants are a mixture of surfactants and organic solvents (Hayworth and Prabakhar Clement 2012), understanding the effects of individual dispersant components would help elucidate the collective dispersant effects on the photodegradation. **Table 1** summarizes the compositions of Corexit EC9500A and EC9527A. To identify the most critical components that affect the pyrene photodegradation, photodegradation kinetic data of pyrene were collected in the presence of 18 mg/L of each individual component. **Figure 76a** compares the first-order rate constants in the presence of the Corexit dispersants or their individual components against the benchmark rate constant ( $k_0$ ) measured in seawater only. Evidently, the non-ionic surfactants Span 80 and Tween 85 stood out as the most effective promoting components. Span 80 and Tween 85 accelerated pyrene photodegradation by 17.5 and 2.3 folds, respectively. The other surfactants, i.e., DOSS and Tween 80, and the solvents di(propylene glycol)butyl ether, BE and propylene glycol showed little or slightly inhibitory effects on the photodegradation. Because kerosene alone is insoluble in water, it was excluded from the tests.

Span 80 is an oil-soluble surfactant with a very low hydrophilic-lipophilic balance value (4.3), and it is sparingly dissolved and dispersed in water (Barbetta and Cameron 2004). Because its density (0.99 g/mL) is slightly lower than that of the seawater (1.02–1.03 g/mL), it tends to suspend in the upper layer of the water column. On the other hand, due to the hydrophobic nature, pyrene molecules are favorably partitioned in the Span 80 aggregates. Consequently, more pyrene is entrained in the upper layer as more Span 80 is enriched there, resulting in greater exposure to the light and enhanced photodegradation. **Figure 76b** shows the vertical concentration distributions of pyrene in the presence of the dispersants or each individual component. The pyrene concentration on the surface was ~18% higher than in the bottom layer in the presence of Span 80. A similar concentration profile was observed when Corexit EC9500A and EC9527A were present, though to a lesser extent, while the concentration gradient appeared flat in the presence of other components (i.e., Tween 85, Tween 80, DOSS, BE, DBE, and PG). Addition of water-miscible solvents such as DBE and/or water-soluble surfactants such as Tween 80 alleviated the concentration gradients due to lowered surface tension and solubility enhancement of Span 80 by the additives (especially Tween 80) (**Figure 76b**). From the photochemical reaction aspect, the reaction rates were suppressed in the presence of these additives (**Figure 76c**) in accord with the vertical concentration distributions.

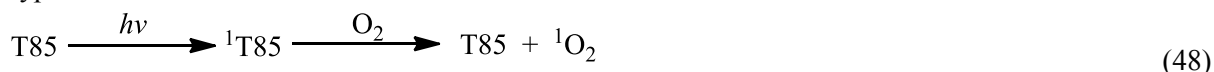
Unlike Span 80, Tween 85 is water-soluble, with a hydrophilic-lipophilic balance of 11.0, and its density (1.028 g/mL) is about the same as that of the seawater. Hence, the concentration stratification effect is insignificant. Instead, Tween 85 was found to exhibit remarkably strong UV absorbance (**Figure 76d**), which is due to the large number of electron-rich double bonds of Tween 85 (Solak Erdem et al. 2014). Moreover, the CMC of Tween 85 in seawater was determined to be around 18 mg/L, indicating micelles or semi-micelles were formed under the experimental conditions (Hadgiivanova and Diamant 2009, Jensen et al. 2013). The  $I_1/I_3$  ratio of pyrene fluorescence in Tween 85 solution was lower compared with that in seawater (**Figure 77a**), but much higher than in the hydrocarbon solvents range (0.57–0.61). Thus, it is sensible that pyrene molecules partitioned into the micelles and concentrated near the polar head groups of the surfactants (Basu Ray et al. 2006). The red shift of the UV absorption spectra of pyrene indicated a strong interaction between the  $\pi$  electron cloud of pyrene and the hydrophilic head groups of surfactants (**Figure 77b**) (Fornasiero and Grieser 1990, Fu et al. 2015). Therefore, under solar irradiation, Tween 85 can facilitate absorption of UV light, which is the most powerful energy source for the photodegradation, and the enriched UV energy is then transferred to pyrene molecules around the hydrophilic head groups, resulting in enhanced pyrene photodegradation.

In the photosensitization process, Tween 85 acts as a sensitizer, and it undergoes following two types of reactions:

Type I:

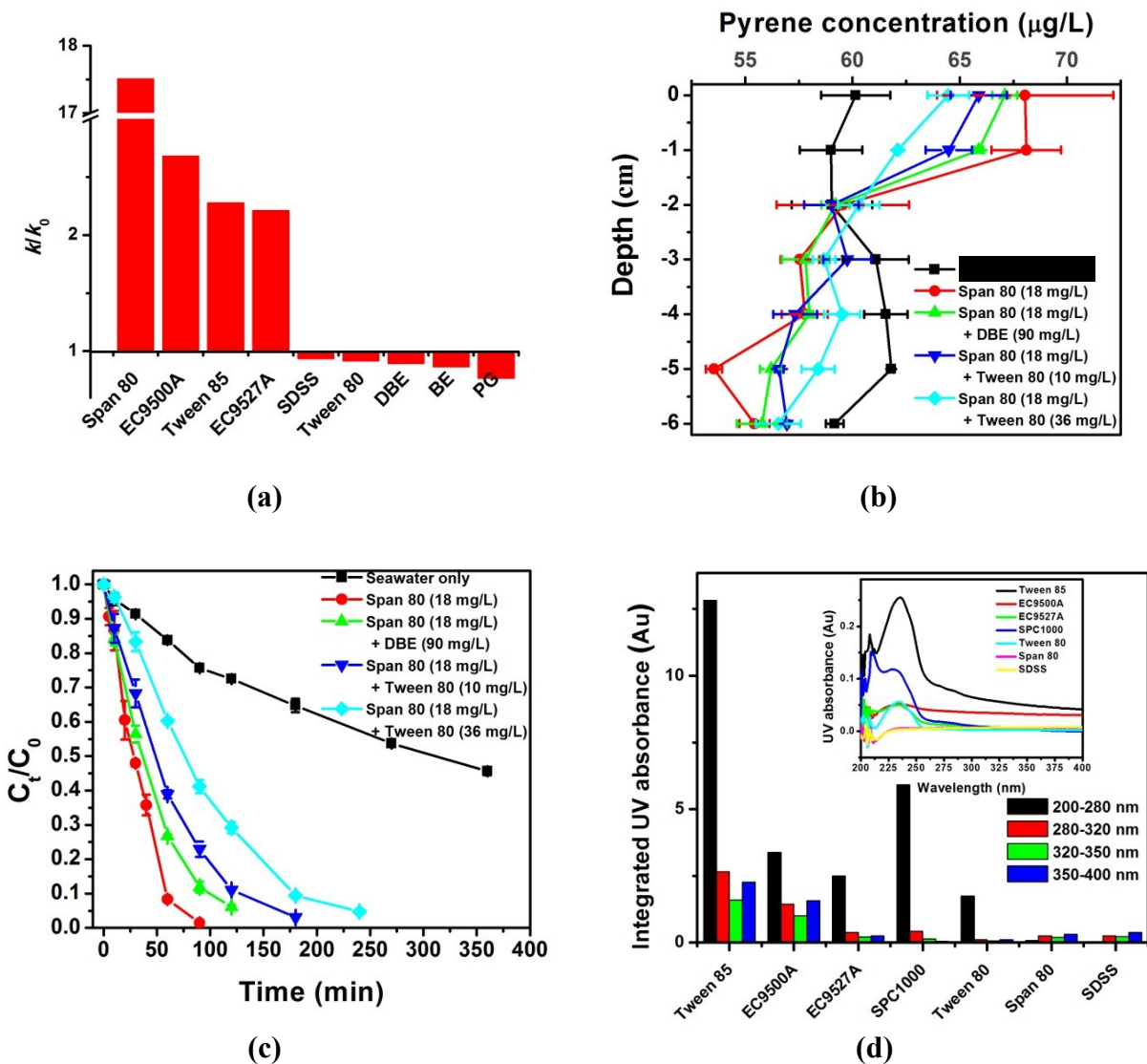


Type II:



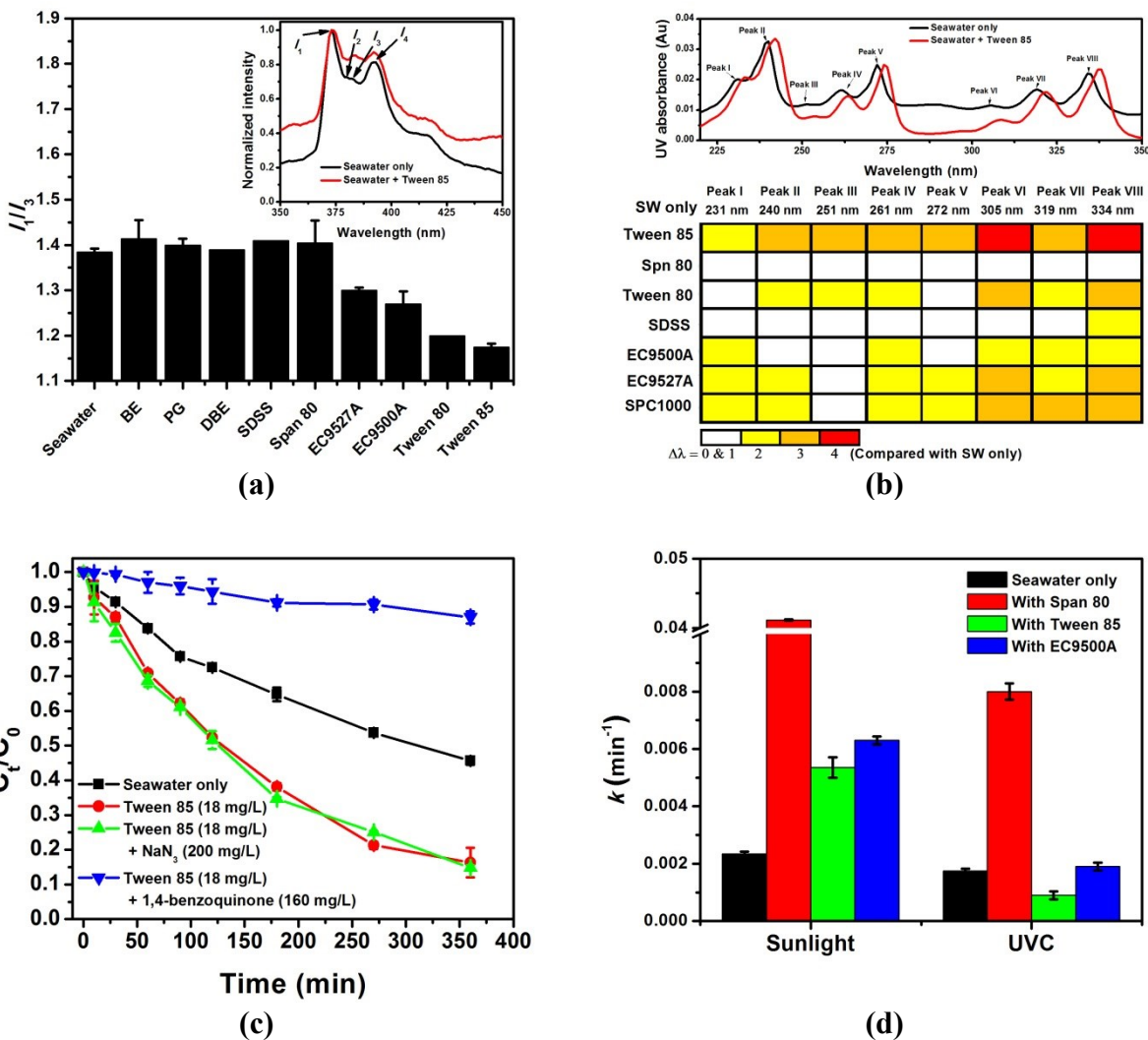
In the Type I reactions, excited Tween 85 ( ${}^1\text{T85}$ ) reacts directly with pyrene (Py), yielding one pyrene radical cation ( $\text{Py(H)}^{\bullet+}$ ) and one Tween 85 radical anion ( $\text{T85}^{\bullet-}$ ) for each electron transferred. In the presence of oxygen ( $\text{O}_2$ ),  $\text{Py(H)}^{\bullet+}$  can be further oxidized to oxygenated products, whereas  $\text{T85}^{\bullet-}$  can transfer the extra electron to  $\text{O}_2$  to produce the superoxide radical anion ( $\text{O}_2^{\bullet-}$ ), which also regenerates the original T85. In the Type II reactions,  ${}^1\text{T85}$  transfers its excess energy to ground-state  $\text{O}_2$ , producing excited state singlet oxygen ( ${}^1\text{O}_2$ ) and regenerating the ground-state T85.  ${}^1\text{O}_2$  then oxidizes Py to its oxidized products. The addition of  $\text{NaN}_3$  (a  ${}^1\text{O}_2$  scavenger) did not affect the pyrene photodegradation rate in the presence of Tween 85, while the presence of 1,4-benzoquinone (a  $\text{O}_2^{\bullet-}$  scavenger) significantly inhibited the reaction (**Figure 77c**). This observation indicates that the enhanced pyrene photodegradation by Tween 85 is attributed to the Type I photosensitization process.

However, the photosensitization between Tween 85 and pyrene is confined to a certain wavelength range. Because of the surfactant's strong preference for UVC (**Figure 76d**), and as the simulated sunlight contained no UVC, we employed a 254-nm UVC light to compare the effects of Span 80 and Tween 85. Though Span 80 strongly enhanced the pyrene photodegradation under the UVC irradiation, Tween 85 actually significantly inhibited the photodegradation. Consequently, the dispersant EC9500A only slightly (8.6%) increased the reaction rate under UVC due to the antagonistic effects of the two surfactants (**Figure 77d**). This observation suggests that some specific photons in the UVA or UVB range of sunlight may play important roles in the energy transfer and the photosensitization process. Many studies have indicated the light wavelength-dependence of a photosensitizer, i.e., a photosensitizer can only absorb a certain wavelength of electromagnetic radiation and transfer it to other molecules (Ullman and Baumann 1968, Vankayala et al. 2013).



**Figure 76. Mechanistic investigation on dispersants facilitated pyrene photodegradation.** (a) Comparison of the first-order photodegradation rate constants ( $k$ ) of pyrene in the presence of Corexit EC9500A and its individual components ( $k_0$ : rate constant in seawater only); (b) Vertical distribution of pyrene in the photoreactor; (c) Pyrene photodegradation kinetics in the presence of Span 80 or its mixtures with DBE or Tween 80; (d) UV absorption of three model dispersants and their key individual components. The concentrations of dispersants and individual components were 18 mg/L, and the initial pyrene concentration was 60  $\mu\text{g/L}$  in all cases. DBE stands for di(propylene glycol)butyl ether and PG is short for propylene glycol.

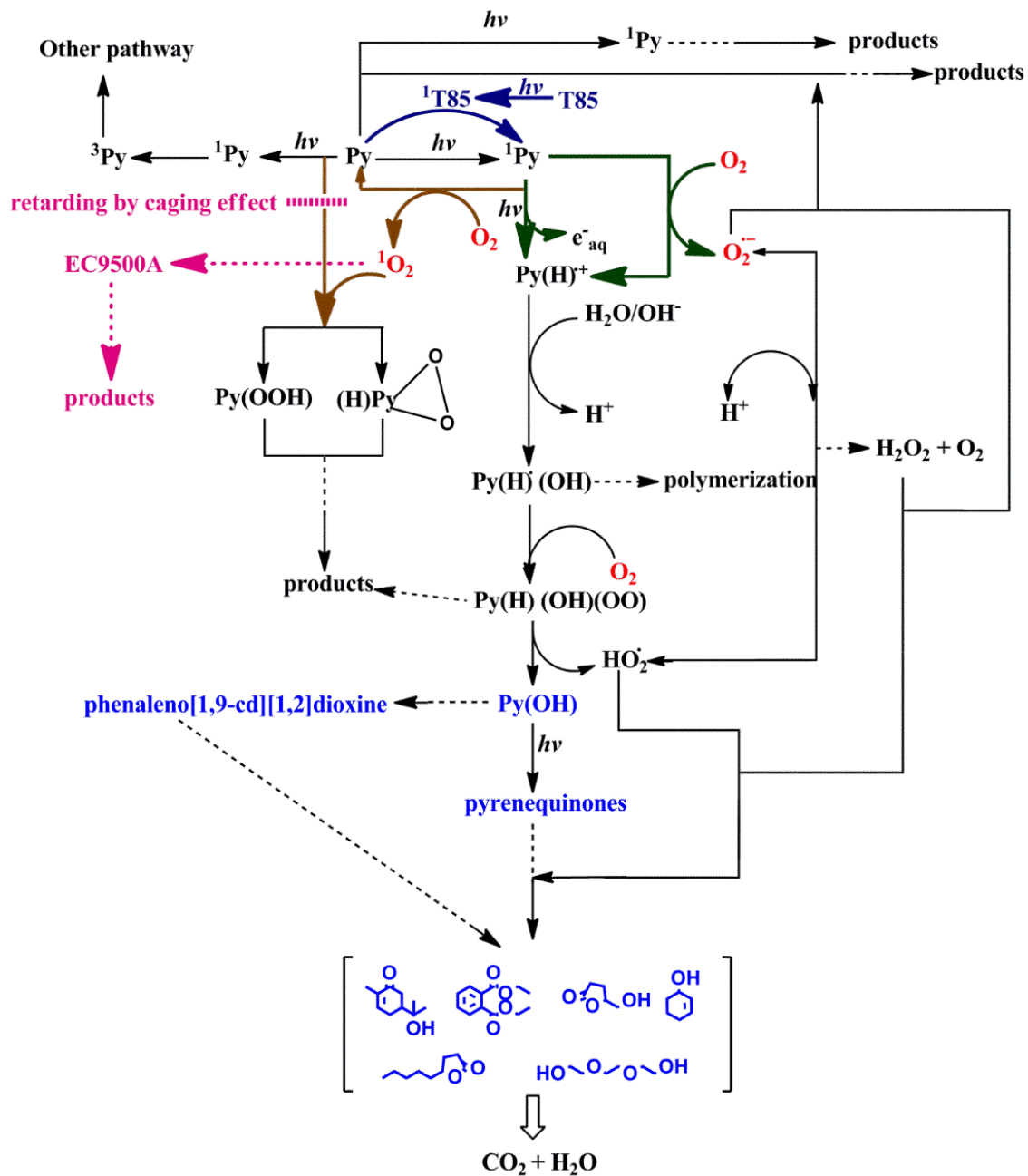




**Figure 77. Mechanistic investigation on dispersants facilitated pyrene photodegradation.** (a) Pyrene fluorescence peak ratios ( $I_1/I_3$ ); (b) UV absorption spectra in the presence of dispersants and their individual components in reference to UV spectra in seawater (SW); (c) Pyrene photodegradation kinetics in the presence of Tween 85 and two radical scavengers ( $\text{NaN}_3$  or 1,4-benzoquinone); (d) Comparison of pyrene photodegradation rates under simulated sunlight or UVC (254 nm) irradiations. The concentrations of dispersants and individual components were 18 mg/L, and the initial pyrene concentration was 60  $\mu\text{g/L}$  in all cases.

#### 4.3.4. Effects of dispersants on pyrene photodegradation pathway

**Figure 78** proposes the possible photodegradation pathway of pyrene based on the experimental results on the available reactive species and intermediate products. Several reactive species may be involved in the photodegradation, including triplet pyrene ( $^3\text{Py}$ ),  $\bullet\text{OH}$ ,  $^1\text{O}_2$ , and  $\text{O}_2^{\bullet-}$  (Braun et al. 1991, Miller and Olejnik 2001, Murov et al. 1993). To identify the roles of DO and the various reactive species and effects of Corexit EC9500A, pyrene photodegradation kinetic tests were carried out with or without DO and with various selective radical scavengers. **Table 21** summarizes the results. Based on the first-order rate constants, the photodegradation rate was reduced by 64.6% when DO was purged out from the seawater and in the absence of the dispersant; the reaction rate without DO was lowered by 70.7% in the presence of 18 mg/L Corexit EC9500A, indicating the crucial role of DO. Oxygen molecules not only directly react with excited pyrene, they are also essential in forming reactive oxygen species (e.g.  $^1\text{O}_2$ ,  $\text{O}_2^{\bullet-}$ , and  $\text{HO}_2^{\bullet}$ ) to indirectly oxidize pyrene (Miller and Olejnik 2001). With DO, the dispersant promotes generation of more ROS, and thus enhances the photodegradation. Without DO, the dispersant inhibits the reaction. Specifically,  $^3\text{Py}$  contributed  $\sim 10\%$  to the overall photodegradation of pyrene regardless of the dispersant, which agrees with the observation by Sigman et al. (1998);  $\bullet\text{OH}$  showed almost no effect on the photodegradation; while  $^1\text{O}_2$  and  $\text{O}_2^{\bullet-}$  played critical roles (in the absence of dispersant, the degradation rates were inhibited by 21.5% and 58.5% respectively by the respective radical scavengers).  $^1\text{O}_2$  is formed when  $\text{O}_2$  reacts with an excited pyrene molecule.  $^1\text{O}_2$  can then attack a pyrene molecule in the ground state, resulting in endoperoxides and hydroperoxides.  $\text{O}_2^{\bullet-}$  is formed due to electron transfer from excited pyrene to oxygen, and is much less reactive (Legrini et al. 1993). However,  $\text{O}_2^{\bullet-}$  can transform into  $\text{HO}_2^{\bullet}$  or  $\text{H}_2\text{O}_2$  that can effectively promote pyrene decomposition. The addition of Corexit EC9500A inhibits the  $^1\text{O}_2$  pathway, but enhances the role of  $\text{O}_2^{\bullet-}$ , which can be interpreted as follows: 1) changes in pyrene distribution (i.e., partition into Span 80 phase and incorporation into surfactant aggregates or micelles) may show a caging effect that hinders the encountering between oxygen and excited pyrene molecules; 2) some organic components in Corexit EC9500A may compete for  $^1\text{O}_2$ ; and 3) the photosensitization enabled by Tween 85 facilitates the solvated electron transfer to oxygen, yielding more  $\text{O}_2^{\bullet-}$  (Equation 46).



**Figure 78. Proposed pathway of pyrene photodegradation in seawater.**  
With or without oil dispersant (Corexit EC9500A) under simulated solar irradiation.

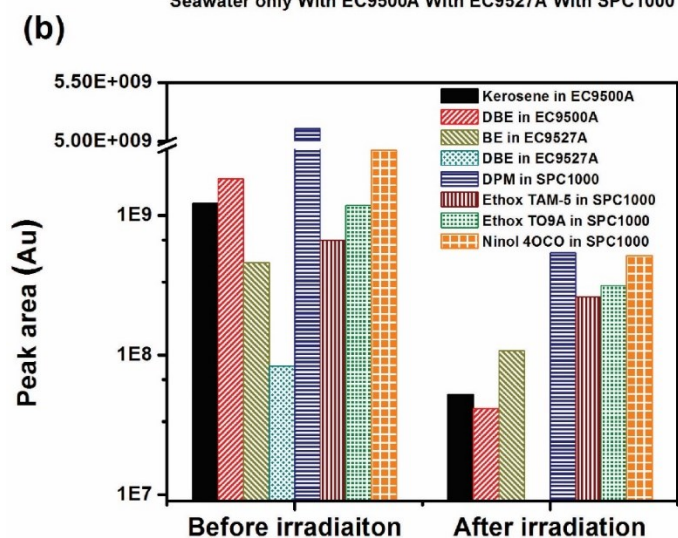
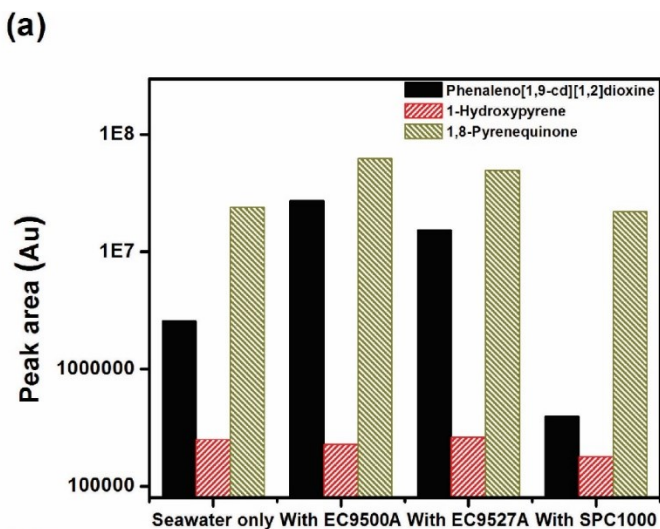
**Table 21. Contributions of different reactive species to photodegradation of pyrene under simulated solar irradiation.**

Treatment	Scavenging radical	Without Corexit EC9500A		With Corexit EC9500A	
		$k^a$ (min <sup>-1</sup> )	% Inhibition <sup>b</sup>	$k$ (min <sup>-1</sup> )	% Inhibition <sup>b</sup>
Seawater		0.0022		0.0063	
DO-free Seawater		0.00077	64.6%	0.0018	70.7%
Seawater + 1.2 mM HgCl <sub>2</sub>	<sup>3</sup> Py	0.0020	9.2%	0.0056	11.2%
Seawater + 220 mg/L <i>t</i> -C <sub>4</sub> H <sub>9</sub> OH	•OH	0.0022	0	0.0064	0
Seawater + 200 mg/L NaN <sub>3</sub>	•OH & <sup>1</sup> O <sub>2</sub>	0.0017	21.5%	0.0063	0
Seawater + 160 mg/L 1,4-benzoquinone	O <sub>2</sub> <sup>•-</sup>	0.0009	58.5%	0.0002	96.8%

<sup>a</sup> First-order kinetic rate constant; initial pyrene and EC9500A concentrations were 60 µg/L and 18 mg/L, respectively.

<sup>b</sup> Inhibition was calculated based on controls without radical scavengers.

The pyrene photodegradation products were identified by GC-MS. No new intermediate products of pyrene photodegradation were observed in the presence of any of the 3 dispersants, suggesting the dispersants did not create new pathways. However, concentrations of polyaromatic intermediates, i.e., phenaleno[1,9-cd][1,2]dioxine, 1-hydroxypyrene, and 1,8-pyrenequinone, were elevated remarkably in the presence of Corexit EC9500A or EC9527A, while the concentrations were slightly lowered by SPC 1000, compared to those in the seawater (**Figure 79a**). This observation is consistent with the kinetic data of pyrene photodegradation. It is well-known that 1-hydroxypyrene can be rapidly generated in pyrene photodegradation via the following two steps: 1) generation of hydroxypyrenyl radicals by water tapping, and 2) subsequent hydrogen atom abstraction by molecular oxygen (Clark et al. 2007, Sigman et al. 1998). The resulting 1-hydroxypyrene can undergo similar photochemical oxidation as pyrene to give pyrenequinones, and the quantum yield for photolysis of 1-hydroxypyrene is generally higher than that of pyrene (Sigman et al. 1998). The structure of phenaleno[1,9-cd][1,2]dioxine was deduced based on the mass spectrum, which may have resulted from oxidation of 1-hydroxypyrene via ring-cleavage and subsequent endoperoxidation. In addition, the following smaller organic molecules derived from pyrene were also detected, including diethyl phthalate, 8-hydroxycarvotanacetone, 5-pentyldihydrofuran-2(3H)-one, 5-hydroxymethyl-dihydrofuran-2-one, triethylene glycol, and 2-cyclohexen-1-ol, which can be further oxidized to carbon dioxide.

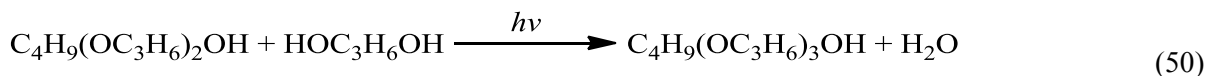


**Figure 79. Photodegradation products expressed as peak areas from GC-MS chromatograms.**

(a) polycyclic aromatic intermediates derived from pyrene, and (b) residual individual components of dispersants before and after solar irradiation.

#### 4.3.5. Photochemical stability of dispersants

There has been little information available on photochemical decomposition of oil dispersants in the marine environment. Based on a literature search, only two studies reported photodegradation of two individual solvents (i.e., BE and PG) and one anionic surfactant (DOSS) in Corexit dispersants (Batchu et al. 2014, Kover et al. 2014). Based on our GC-MS analysis, a number of degradation products derived from the Corexit dispersants were detected, including 2-ethylhexan-1-ol and bis(2-ethylhexyl) maleate from DOSS, isosorbide and oleic acid from Tween 80 or Tween 85. Of particular interest is the detection of 1-((1-((1-butoxypropan-2-yl)oxy)propan-2-yl)oxy)propan-2-ol, which may be generated via the dehydration reaction between PG and DBE:



The compositions of SPC 1000 are quite complex, including 4 nonionic surfactants (Ethox TO9A, Ethox TAM-5, Ninol 4OCO, and Tergitol 15-S-5), one anionic surfactant (Petronate HL), an organic solvent (DPM) and water (Jacob and Bergman 2001). After the photodegradation, several amides and N-(2-hydroxyethyl)dodecanamide from Ninol 4OCO, secondary alcohols from Ethox TAM-5, tallow amines from Ethox TAM-5, thiols from Petronate HL, and oleic and eicosenoic acids from Ethox TO9A were detected. These results indicate that the dispersant components were quite labile to photochemical weathering under solar irradiation.

Some residual dispersant components were also detected, including BE, several aliphatic hydrocarbons in kerosene, DBE, N,N-bis(2-hydroxyethyl)dodecanamide in Ninol 4OCO, DPM, polyoxyethylene tallow amine in Ethox TAM-5, and 2-hydroxyethyl oleate in Ethox TO9A. As dispersants can be broken down rapidly in seawater, the individual components BE, DBE, PG and DOSS have been used as indicators to determine the spreading of dispersed oil and Corexit dispersants (Hayworth and Prabakhar Clement 2012, Kujawinski et al. 2011, OSAT 2010). Based on these indicator components, Corexit EC9500A appeared most prone to the photochemical decomposition, with an average degradation of 96.7%, compared to 88.3% for Corexit EC9527A and 76.5% for SPC 1000 upon the 6-h solar irradiation (**Figure 79b**). Mechanistically, the photochemical stability of the 3 dispersants was consistent with their ability to absorb UV light in the range of 280–400 nm (**Figure 76d**).

#### **4.3.6. Conclusions**

This work investigated effects of three model oil dispersants and their individual components on photochemical weathering of a prototype PAH, and elucidated the underlying physical and photochemical mechanisms. The information is valuable for aiding in our understanding of photochemical weathering of petroleum PAHs. As dispersant use has evolved into a major response strategy in coping with oil spills, this information may also facilitate reckoning the photochemical weathering rate and extent of dispersed oil and oil dispersants, leading to sounder assessment of the ecological impacts on the marine ecosystem. In addition to the physical dispersion effect, accelerated photodegradation of larger oil compounds by the Corexit dispersants may also enhance the dissolution and decomposition of persistent oil compounds, alleviating the chemical toxicity and promoting biodegradation of oil and restoration of impacted ecosystems. However, cautions should be exercised that the effects of oil dispersants may vary with different surfactant compositions.

## 5. Photocatalytic Degradation of PAHs by Engineered Catalysts

### 5.1. Photodegradation of Oil PAHs by Co-Deposited Titanate Nanotubes

Catalytic photodegradation of organic compounds including oil PAHs using solar irradiation has elicited great interest in recent years (Schneider et al. 2014), and photodegradation of oil or oil components (especially persistent oil PAHs) by engineered catalysts is a promising technique for oil removal from contaminated water.

Traditionally, TiO<sub>2</sub>-based materials have been the most widely used photocatalysts, and have been found effective in a variety of environmentally related uses, such as solar-driven hydrogen production, and photocatalytic decomposition and adsorption of inorganic contaminants (Chen and Burda 2008, Chen and Mao 2007, Liu et al. 2013c, Pelaez et al. 2012, Tan et al. 2014). Although TiO<sub>2</sub> can effectively utilize UV light, its large band gaps limit its optical absorption in the solar spectrum, which consists of UV, visible and infrared (IR) radiations with a relative energy distribution of ~5%, 43% and 55%, respectively (Chen et al. 2015b, Shankar et al. 2015). As a result, a great deal of effort has been devoted to improving the visible light absorption of TiO<sub>2</sub>. Though nanoscale TiO<sub>2</sub> has shown to offer improved catalytic activity, the slow sedimentation characteristics limit the separation from water and reuse of the spent catalyst (Liu et al. 2013a).

Of various modifications, one-dimensional titanate nanotubes (TNTs) synthesized by hydrothermal treatment of TiO<sub>2</sub> have gained significant attention in recent years (Liu et al. 2013a, Liu et al. 2013c, Wang et al. 2013b, Xiong et al. 2011b). TNTs can serve as excellent adsorbents for heavy metals owing to their high specific area, great ion-exchange properties, easy solid-liquid separation and abundant functional groups. However, TNTs have been found to be poor photocatalysts despite their high surface area and crystalline structure due to the rapid electron-hole recombination rate upon excitation under illumination (Kim et al. 2012, Lee et al. 2007, Yu et al. 2006a). Therefore, researchers have studied various approaches to inhibit the electron-hole recombination, including calcination (Lin et al. 2008, Yu et al. 2006a), H<sub>2</sub>O<sub>2</sub> treatment (Khan et al. 2006), acid treatment (Chen et al. 2015a), and surface modification using non-metals such as C, F and P (Kim et al. 2012, Liu et al. 2012a) or metals such as Fe, Cu, Pd, and W (Chen et al. 2013, Grandcolas et al. 2013, Liu et al. 2015b). Of these approaches, metal doping appears very promising. An appropriate metal dopant can not only inhibit the recombination of electron-hole pairs, but also facilitate absorption of visible light by narrowing the absorption band gaps. Cobalt is one of the commonly used dopant for modifying TiO<sub>2</sub>, and cobalt oxides have narrower band gaps (e.g., ~2.4 eV for CoO and 2.19 eV for Co<sub>3</sub>O<sub>4</sub>) (Dahl et al. 2014, Marin et al. 2013). For instance, cobalt oxide-TiO<sub>2</sub> composites showed improved photo-activity for organic compounds and H<sub>2</sub> production rates than plain TiO<sub>2</sub> (Dai et al. 2013, Wang et al. 2013d, Zhang et al. 2012). However, cobalt as a potential dopant for TNTs has not been studied.

PAHs are produced during incomplete combustion of fossil fuels and are an important component of crude oil (Gong et al. 2014a, Zhao et al. 2015). Due to their toxic, mutagenic, and carcinogenic properties, PAHs represent a major environmental concern associated with oil spills, discharge, and seepage, and thus, have been classified as the priority pollutants by US EPA (Nam et al. 2008). In addition, PAHs (e.g. phenanthrene, anthracene, and pyrene) are rather persistent to photodegradation under solar light (Wen et al. 2002). PAHs can absorb light in the UV regions, and then be transformed into excited PAH molecules and photo-oxidized (Kou et al. 2008). Phenanthrene is one of the most commonly detected PAHs, consisting of three fused benzene rings, it is fairly resistant to natural photodegradation, and thus, has been often used as a prototype PAH for photolysis studies (Jia et al. 2012, Sirisaksoontorn et al. 2009, Wangl et al. 1995).

In this section, we prepared and characterized a new type of photocatalyst, referred to as cobalt-deposited titanate nanotubes (Co-TNTs). The overall goal of this work was to develop and test the Co-TNTs for efficient photodegradation of PAHs under solar light. The specific objectives were to: 1) develop an optimized hydrothermal-calcination method for preparing the desired catalyst; 2) test the effectiveness of the catalyst for phenanthrene photodegradation; and 3) elucidate the mechanisms for enhanced photocatalytic activity by characterizing the morphology, crystal phases and compositions of Co-TNTs.

### 5.1.1. Synthesis of Co-deposited TNTs and material characterization methods

Co-TNTs were synthesized through a one-step hydrothermal method. In brief, 0.1, 0.2, 0.4, or 0.6 g  $\text{CoCl}_2 \cdot 6\text{H}_2\text{O}$  was mixed with 1.2 g of the  $\text{TiO}_2$  nanoparticles in a beaker with 20 mL DI water. The mixtures were magnetically stirred for 30 min and sonicated using a Branson 1510R-MTH sonicator (70W, 42 KHZ) for another 30 min. Then, a NaOH solution (prepared with 29 g NaOH in 47 mL DI water) was added dropwise into each mixture for about 5 min, and then sonicated for another 60 min. Afterwards, each mixture was transferred into a Teflon reactor with stainless steel coating, and then purged with pure  $\text{N}_2$  for 10 min to remove dissolved oxygen. Then the reactors were heated at 150 °C for 48 h to complete the hydrothermal reaction. The resulting blue precipitates were separated and washed with DI water until the rinse water became neutral and then oven-dried at 80 °C for 4 h. The as-prepared materials are denoted as Co-TNTs for typographical convenience.

The Co loadings on Co-TNTs were determined according to EPA Method 3050B (EPA 1996). Briefly, 0.2 g each of the materials was dispersed into 20 mL of concentrated nitric acid (65%) and shaken for 24 h, and the resulting solution was diluted 10 times and then analyzed for Co via inductively coupled plasma-optical emission spectroscopy (ICP-OES, 710-ES, Varian). Subsequently, the Co-TNTs were calcined at 400, 600, or 800 °C in a muffle furnace for 3 h, and the resultant catalysts are denoted as Co-TNTs-xxx (xxx indicates the calcination temperature). The photocatalytic activities of the materials prepared with different Co loadings and calcination temperatures were then tested to optimize the recipe. For comparison, neat TNTs were also synthesized following the traditional hydrothermal method without Co loading (Chen et al. 2002, Xiong et al. 2010), where 1.2 g  $\text{TiO}_2$  (P25) and 10 M NaOH were mixed and heated at 130 °C for 72 h. In selected cases, the TNTs were calcined at 600 °C for 3 h, and the calcined TNTs are designated as TNTs-600.

The morphology of material was analyzed using Tecnai30 FEG transmission electron microscopy (TEM, FEI) operated at 300 kV, and energy dispersive spectra (EDS) of the materials were obtained at the same time. The surface morphology was imaged using a scanning electron microscope (SEM) (FEI XL30F, Philips) operated at 20 kV. The crystal phase of the sample was obtained by means of a Bruker D2 phaser X-ray diffractometer using  $\text{Cu } K\alpha$  radiation ( $\lambda = 1.5418 \text{ \AA}$ ) at a scan rate ( $2\theta$ ) of 4°/min. AXIS-Ultra X-ray photoelectron spectroscopy (XPS, Kratos) analysis was performed to determine the elemental composition and oxidation state of materials using  $\text{Al } K\alpha$  X-ray at 15 kV and 15 mA. The standard C 1s peak (Binding energy,  $E_b = 284.80 \text{ eV}$ ) was used to eliminate the static charge effects. Fourier transform infrared spectroscopy (FTIR) (Tensor 27 analysis was carried out to obtain the functional groups, operated with a scanning range of 4000–400  $\text{cm}^{-1}$  and resolution of 4  $\text{cm}^{-1}$  through the KBr pellet method. The Brunauer-Emmett-Teller (BET) surface area was measured on an ASAP 2010 BET surface area analyzer (Micromeritics) using nitrogen in the relative pressure range of 0.06–0.20. Pore size distribution was obtained following the Barret-Joyner-Halender method. Nitrogen adsorption volumes at the relative pressure of 0.99 were used to determine the pore volumes and the average pore diameters. UV-visible diffuse reflectance absorption spectra (UV-DRS) of the materials were obtained using a UV-2400 spectrophotometer (Shimadzu).  $\text{BaSO}_4$  powder was used as the reference at all energies (100% reflectance) and the reflectance measurements were converted to absorption spectra using the Kubelka-Munk function. The sedimentation rate tests of the materials were evaluated following the UV



absorbance of the particle suspensions using a UV-vis spectrophotometer (UV1800, Shimadzu) (the particles were first dispersed in DI water with sonication) (Liu et al. 2013a).

### 5.1.2. Photocatalytic degradation methods

The experimental setup for the photodegradation of phenanthrene was the same as that shown in **Figure 57b**. Photocatalytic degradation kinetic tests were carried out with various materials under the simulated solar light. Specifically, 200  $\mu\text{g/L}$  of phenanthrene and 1.0 g/L of a given material were loaded in the photo-reactor. The mixture was stirred for 2 h in dark to reach the phenanthrene adsorption equilibrium. Afterwards, the reactor was subjected to the solar irradiation. Water samples (1 mL each) were taken at predetermined times and immediately centrifuged at 8000 rpm (6400 g-force) for 10 min. The supernatant was then mixed with methanol at 1:1 (v/v) ratio, and then analyzed for phenanthrene using HPLC. The eluate was analyzed with a UV diode array detector at 254 nm. The detection limit for phenanthrene was  $\sim 1 \mu\text{g/L}$ . More information about the HPLC analysis method are in Section 3.2.1.2. Control tests were conducted in the absence of any catalysts but under otherwise identical conditions.

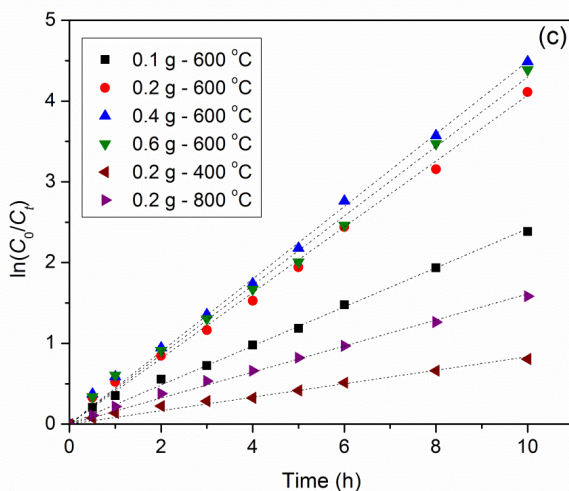
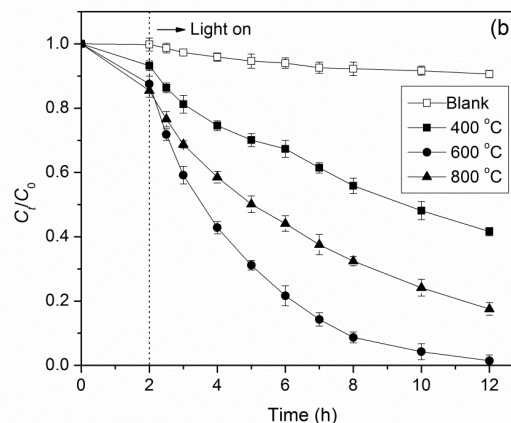
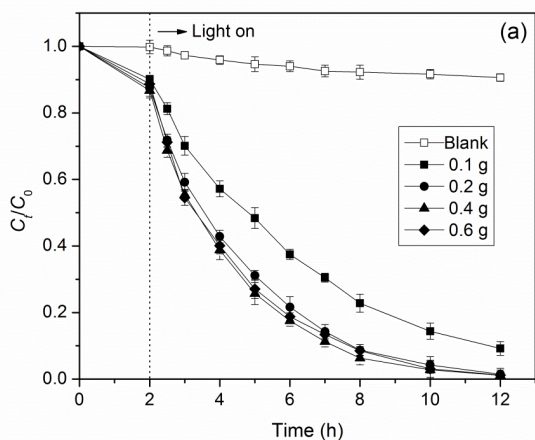
To determine the degradation intermediates, samples (100 mL each) were collected at 1, 3, and 6 h. Following centrifugation, each sample was extracted using 10 mL dichloromethane in 125 mL separatory funnels. The organic phase was collected and treated with anhydrous  $\text{Na}_2\text{SO}_4$  to remove any water. Upon filtering with 0.22  $\mu\text{m}$  PTFE membrane, the solvent was analyzed for various organic compounds using a GC-MS system, more information about the GC-MS analysis are shown in Section 4.1.1.6.

Based on the screening tests, Co-TNTs-600, the most active catalyst prepared with 2.26 wt.% of Co loading and at a calcination temperature of 600  $^\circ\text{C}$ , was further tested for reusability. After an adsorption-photocatalysis cycle, the catalyst was recovered by filtering the suspension using a 0.22  $\mu\text{m}$  PTFE membrane, and then reused by repeating the same adsorption-photodegradation cycle. Separate tests indicate that air-drying the catalyst had no effect on its catalytic activity.

The production of  $\bullet\text{OH}$  by various Ti-based materials was measured following the photoluminescence (PL) technique using terephthalic acid as the probe molecule. As terephthalic acid reacts with  $\bullet\text{OH}$ , 2-hydroxyterephthalic acid will form with a high fluorescent, and the fluorescence intensity is proportional to the amount of  $\bullet\text{OH}$ . In each test, 0.2 g of a material was dispersed in a mixture of 0.5 mmol terephthalic acid and 2 mmol NaOH with a total volume of 200 mL in the photo-reactor. After 2-h illumination under the solar light, samples were taken and micro-filtered. The PL spectra were then obtained on a fluorescence spectrophotometer at an excitation wavelength of 425 nm.

### 5.1.3. Photocatalytic activity of Co-deposited TNTs under different synthesis conditions

**Figure 80** shows photocatalytic degradation of phenanthrene by Co-doped TNTs prepared with various cobalt loadings and/or at different calcination temperatures. **Figure 80a** shows that increasing the initial  $\text{CoCl}_2 \cdot 6\text{H}_2\text{O}$  dosage from 0.1 to 0.2 g in the hydrothermal reaction enhanced the first-order rate constant ( $k_1$ ) from 0.24 to 0.39  $\text{h}^{-1}$ . However, further increasing the cobalt dosage from 0.2 to 0.6 g only modestly affected the  $k_1$  value (0.39 to 0.43  $\text{h}^{-1}$ ), with nearly the same final phenanthrene removal of > 98%. At the initial  $\text{CoCl}_2 \cdot 6\text{H}_2\text{O}$  concentrations of 0.1, 0.2, 0.4 and 0.6 g, the Co loadings were (wt%): 1.13, 2.26, 2.68 and 2.81, respectively. Doubling the initial  $\text{CoCl}_2 \cdot 6\text{H}_2\text{O}$  from 0.1 to 0.2 g also doubled the Co loading, resulting in 62.5% increase in  $k_1$ . However, further increasing  $\text{CoCl}_2 \cdot 6\text{H}_2\text{O}$  from 0.2 to 0.6 g resulted in only 0.55 wt% increase in Co loading, and thus, only modest enhancement in the photocatalytic activity.



**Figure 80. Photocatalytic degradation of phenanthrene by Co-deposited TNTs.**

(a) Co-deposited TNTs synthesized at different Co loadings (but fixed calcination temperature of 600 °C), and (b) at various calcination temperatures (but identical Co loading of 2.26%); (c) linearized plots of the first-order model fittings to the kinetic data. Experimental conditions: initial phenanthrene = 200 µg/L, material dosage = 1.0 g/L, pH = 7.0±0.2, temperature = 25±0.2 °C.

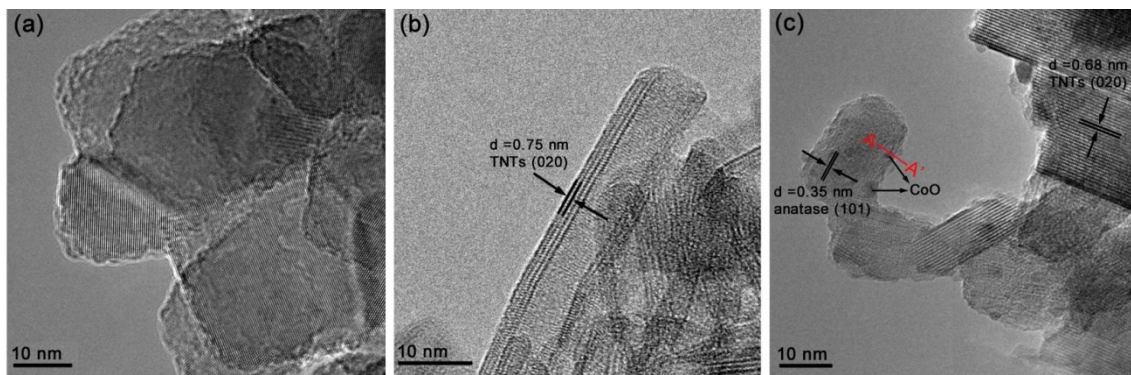
It is noteworthy that increasing the cobalt dosage from 0.4 to 0.6 g slightly decreased the rate constant from 0.43 to 0.41 h<sup>-1</sup>, suggesting that there is a limiting value for the Co loading. At lower Co loadings, the deposited Co acts as electron traps that inhibit the recombination of the photo-generated electron-hole pairs; however, when the Co loading dosage exceeds the limit, excessive CoO crystals may facilitate recombination of the electron-hole pairs, thus reducing photocatalytic activity. Similar results have been reported by previous studies on Cu-deposited titanate nanotubes and Mn-doped titanium nanosheets (Doong et al. 2013, Lu et al. 2015). The much further gain in photo-activity can also be due to lowered accessibility of the Co sites upon calcination. Based on **Figure 80a**, the optimal initial CoCl<sub>2</sub>·6H<sub>2</sub>O dosage was set at 0.2 g.

Increasing the calcination temperature from 400 to 600 °C dramatically increased the  $k_1$  value from 0.083 to 0.39 h<sup>-1</sup> (by a factor of 4.7). However, the rate was lowered to 0.16 h<sup>-1</sup> when it was calcined at 800 °C. Calcination temperature is highly related to the crystallinity of materials. Previous studies indicated that increasing the calcination temperature from 400 to 600 °C enhances the crystalline phase of anatase, yet higher temperatures (> 700 °C) would cause the formation of rutile, a much weaker photocatalyst than anatase (Lee et al. 2007, Yu et al. 2006b). Considering both photocatalytic activity and cost effectiveness, Co-TNTs-600 synthesized with a Co loading 2.26 wt%) and a calcination temperature of 600 °C was chosen as the optimal photocatalyst, which was then fully characterized and studied to elucidate the underlying mechanisms for the enhanced photocatalytic activity.

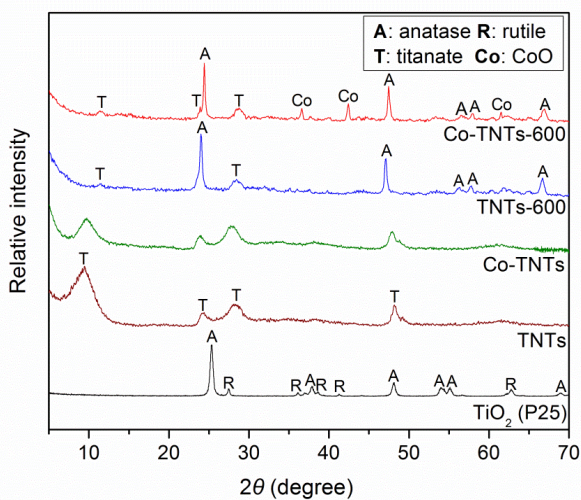
#### 5.1.4. Morphology, crystal phases and compositions of Co-deposited TNTs

**Figure 81** shows TEM images of TiO<sub>2</sub>, TNTs and Co-TNTs-600. The precursor TiO<sub>2</sub> is present as aggregated particles with a primary particle size range of 20–50 nm (**Figure 81a**). Upon the hydrothermal treatment, TiO<sub>2</sub> was transformed into TNTs, which appear as multilayer (4–5 layers) nanotubes, with an inner diameter of ~4.5 nm and outer diameter of ~9 nm (**Figure 81b**) (Xiong et al. 2010). The interlayer distance of the nanotubes is 0.75 nm, which is assigned to the crystal plane of titanate (200) (Chen et al. 2002). When Co-TNTs were calcinated at 600 °C, the TNTs were broken into shorter nanotubes with an interlayer distance of 0.68 nm (020) (**Figure 81c**), indicating the high-temperature calcination partly damaged the tubular structure and shrank the interlayer distance. In addition, nanoparticles (10–30 nm) with a crystal distance of 0.35 nm were formed, which is in accordance with the crystal plane of anatase (101) (Zhang et al. 2011a). Furthermore, the calcination resulted in some 2–5 nm nanoparticles (nanodots) (**Figure 81c**), which were further confirmed to be CoO through XRD and XPS analyses. In addition, EDS line-scan of Co-TNTs-600 through section A–A' (**Figure 81d**) shows that the main elements of the new material are Na, O, Ti, and Co, indicating successful Co deposition.

**Figure 82** presents the XRD patterns for the materials. The pristine TiO<sub>2</sub> is a mixture of anatase and rutile, which was completely transformed to titanate upon the hydrothermal treatment. The peaks at 10°, 24°, 28° and 48° are all ascribed to sodium titanate (Liu et al. 2013c, Sun and Li 2003). The resulting titanate nanotubes are a kind of tri-titanate with a chemical formula of Na<sub>x</sub>H<sub>2-x</sub>Ti<sub>3</sub>O<sub>7</sub> ( $x$  depends on the sodium content) and a skeletal structure of layered corrugated ribbons formed through edge-sharing of triple [TiO<sub>6</sub>] octahedrons with H<sup>+</sup> and Na<sup>+</sup> located in interlayers (Liu et al. 2013a, Liu et al. 2013c, Xiong et al. 2011a). The peak at 10° represents the interlayer distance of TNTs (0.75 nm as shown in **Figure 81b**) (Liu et al. 2013c, Sun and Li 2003). The XRD patterns for Co-TNTs nearly resemble those of TNTs, indicating that cobalt is loaded as Co<sup>2+</sup> ions without forming of crystalline Co oxides during the hydrothermal process. Therefore, during the hydrothermal process, Co<sup>2+</sup> substituted for interlayer Na<sup>+</sup> without changing the basic titanate skeleton. When TNTs are calcinated at 600 °C (TNTs-600), titanate partially transformed into anatase (peaks at ~25°, 47°, 55°, 58°, and 67° JCPDS 21-1272) (Choi and Yong 2014), whereas part of the titanate phase remains as evidenced by the peaks at 10° and 28°. However, the interlayer peak at 10° is greatly weakened due to the damage of the tubular structure. For Co-TNTs-600, besides the crystal phases of titanate and anatase, a CoO crystal phase arises, as reflected by the peaks at 36.5°, 42.4° and 61.5° (JCPDS 75-0393) (Qiao et al. 2009, Zheng et al. 2013). In the calcination process, interlayered Co<sup>2+</sup> will transform into CoO and stably intercropped in titanate or formed anatase, which is important for its role in the photocatalytic reactions. The interlayer peak was also observed, though significantly weakened and shifted from 9.5° to 11.3°, which is attributed to the breakage of the tubular and layered structure in the calcination process (**Figure 81c**).



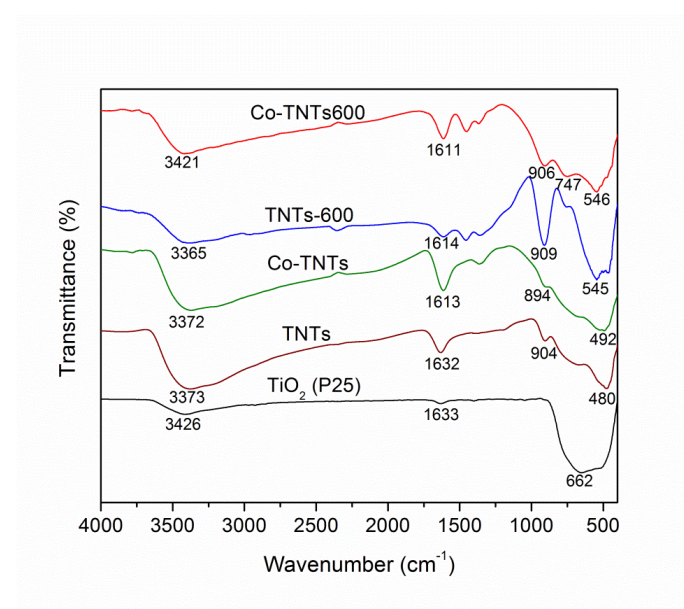
**Figure 81. TEM images of (a) TiO<sub>2</sub> (P25), (b) TNTs, (c) Co-TNTs-600, and (d) EDS spectra of Co-TNTs-600.**



**Figure 82. XRD patterns of various Ti-based materials.**



**Figure 83** compares the FTIR spectra for the typical Ti-based materials. For  $\text{TiO}_2$ , the absorption bands at 662, 1633, and 3462  $\text{cm}^{-1}$  are attributed to O–H, H–O–H, and Ti–O bonding vibrations (Park and Kang 2005). Upon the hydrothermal reaction, two new bands at 480 and 904  $\text{cm}^{-1}$  are observed, which are assigned to the  $[\text{TiO}_6]$  octahedron and the four-coordinated Ti–O stretching vibrations, respectively (Liu et al. 2013a, Liu et al. 2013c, Xiong et al. 2011a). Like the XRD data, the FTIR spectra for TNTs and Co-TNTs are rather alike though the Ti–O band is shifted from 904 to 894  $\text{cm}^{-1}$ , which reflects the formation of Ti–O–Co. The FTIR data for TNTs and Co-TNTs confirm the incorporation of  $\text{Co}^{2+}$  ions, and the basic skeleton of the  $[\text{TiO}_6]$  octahedron remains intact during the hydrothermal treatment of TNTs. However, when calcined at 600 °C (TNTs-600), the  $[\text{TiO}_6]$  octahedron band shifted to 545  $\text{cm}^{-1}$ , indicating the transition of titanate to  $\text{TiO}_2$  (anatase). For Co-TNTs-600, the new band at 747  $\text{cm}^{-1}$  indicates the vibration of  $\text{Co}^{2+}$  in the tetrahedral hole (i.e., Co–O) (Lin et al. 2003), indicating conversion of  $\text{Co}^{2+}$  ions into CoO.



**Figure 83. FTIR spectra of various Ti-based materials.**

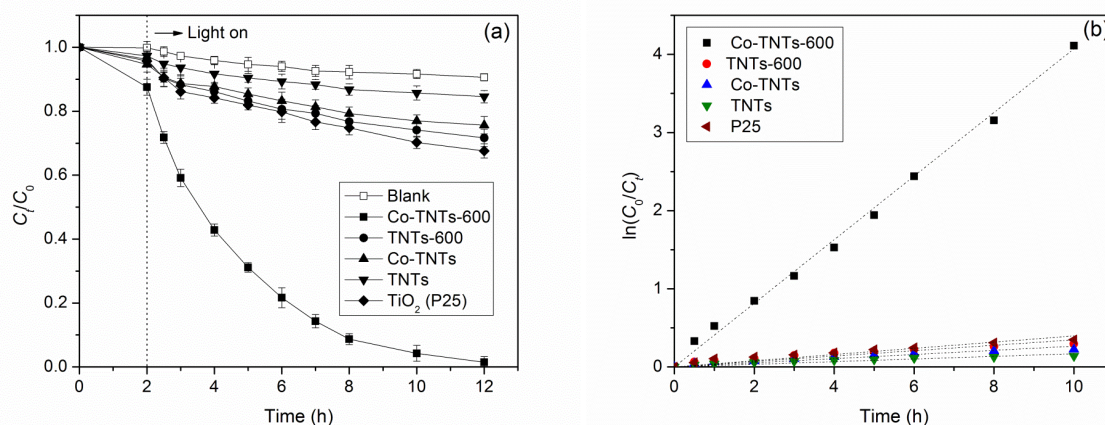
**Table 22** presents the BET surface area, total pore volume and average pore diameter of P25, TNTs and Co-TNTs-600. Compared to TNTs (Liu et al. 2013a, Tian et al. 2014, Xiong et al. 2011a), the  $\text{N}_2$ -based BET surface area and total pore volume of Co-TNTs-600 are decreased from 272.3  $\text{m}^2 \text{g}^{-1}$  and 1.26  $\text{cm}^3 \text{g}^{-1}$  for TNTs to 72.5  $\text{m}^2 \text{g}^{-1}$  and 0.26  $\text{cm}^3 \text{g}^{-1}$ , respectively, which is due to the collapse of layered tubular structure of TNTs at the calcination temperature. However, the BET surface area and total pore volume of Co-TNTs-600 are still larger than those of P25.

**Table 22. Salient physical parameters of  $\text{TiO}_2$ , TNTs, and Co-TNTs-600**

Material	BET surface area ( $\text{m}^2 \text{g}^{-1}$ )	Single point total pore volume ( $\text{cm}^3 \text{g}^{-1}$ )	Average pore diameter (nm)
$\text{TiO}_2$ (P25)	46.9	0.18	15.5
TNTs	272.3	1.26	18.5
Co-TNTs-600	72.5	0.26	8.3

### 5.1.5. Photocatalytic degradation of phenanthrene by Co-deposited TNTs

**Figure 84** compares photocatalytic degradation kinetics of phenanthrene by Co-TNTs-600 and other Ti-based materials. In the absence of photodegradation (initial 2 h), Co-TNTs-600 adsorbed 12.5% of phenanthrene (i.e.,  $C_t/C_0 = 0.875$ ), whereas the other materials adsorbed <6%. The maximum Langmuir capacity was determined to be 25.8  $\mu\text{g/g}$ . Generally, adsorption of phenanthrene is attributed to hydrophobic effects and  $\pi-\pi$  interactions (Chen et al. 2007b). Co-TNTs-600 is rather hydrophilic due to the abundant surface  $-\text{OH}$  groups and inorganic skeleton; hence, it cannot favorably adsorb hydrophobic compounds.

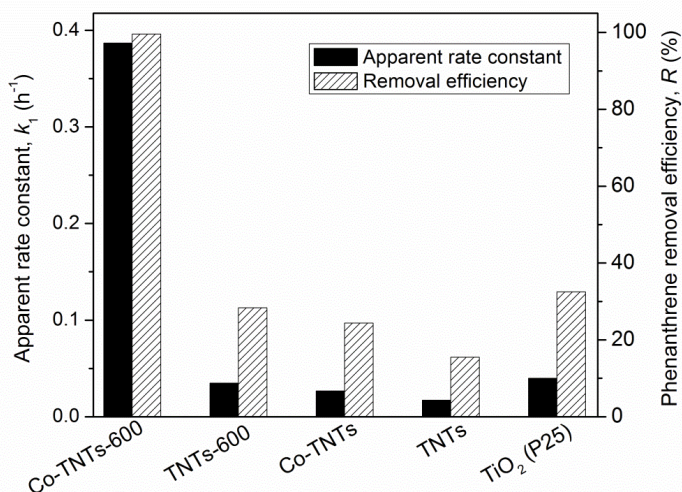


**Figure 84. Photocatalytic degradation of phenanthrene by various Ti-based materials.**

(a) Photodegradation kinetics, and (b) linearized first-order model fitting to the kinetic data.

Experimental conditions: initial phenanthrene = 200  $\mu\text{g/L}$ , material dosage = 1.0 g/L, pH =  $7.0 \pm 0.2$ , temperature =  $25 \pm 0.2$  °C.  $C_0$  and  $C_t$  are phenanthrene concentrations at time 0 and t, respectively.

**Figure 85** compares the  $k_1$  values and removal efficiencies ( $R$ ) for photocatalytic degradation of phenanthrene by different titanium materials. TNTs showed extremely low photocatalytic activity, with a low  $k_1$  of  $0.017 \text{ h}^{-1}$  and with a phenanthrene removal of 15.5% at 12 h, which is even lower than that of the precursor  $\text{TiO}_2$  (28.4%). The calcinated TNTs (TNTs-600) increased the removal to 32.5%, whereas depositing Co on TNTs (Co-TNTs, without calcination) increased the removal to 24.4%. However, when Co-deposition and calcination were combined (Co-TNTs-600), the  $k_1$  value was increased to  $0.39 \text{ h}^{-1}$  and the removal to 98.6%. The rate constant is  $\sim 23$  times that of TNTs and  $\sim 10$  times of P25.



**Figure 85. Apparent rate constants ( $k_1$ ) and removal efficiencies ( $R$ ).**

Values of  $k_1$  and  $R$  for photocatalytic degradation of phenanthrene by various Ti-based materials.

Despite the highest specific surface area, TNTs showed the lowest photocatalytic activity, which can be attributed to crushing of the  $\text{TiO}_2$  crystalline, resulting in a high recombination rate of electron-hole pairs after excitation (Kim et al. 2012, Lee et al. 2007, Yu et al. 2006a). Upon incorporation of  $\text{Co}^{2+}$  (Co-TNTs), the recombination rate of electron-hole pairs is modestly curbed, resulting in the modest activity increase. The calcination of TNTs (TNTs-600) recovered some of the anatase crystalline (**Figure 82**), resulting in a reactivity close to the precursor  $\text{TiO}_2$ .  $\text{TiO}_2$  and TNTs-600 mainly absorb the UV fraction of the solar light, whereas Co-deposited TNTs facilitate absorption of visible light. Therefore, the combination of Co-deposition, calcination and crystallization resulted in the dramatic synergistic effect of Co-TNTs-600. Upon calcination, the  $\text{Co}^{2+}$  ions in TNTs are transformed to Co oxides, which act as electron transfer mediator, inhibiting the hole-electron recombination in the photocatalytic process. In addition, the conversion of titanate anatase crystalline in the calcination process further impedes the electron-hole recombination.

One downside for conventional  $\text{TiO}_2$  (especially nano- $\text{TiO}_2$ ) has been related to poor separation from solutions, which limits its use in water treatment and also prevents from effective recovery of the catalyst. We found that after 180 min of gravity sedimentation, 77.1% of Co-TNTs-600 settled, compared to 64.1% for TNTs and only 0.5% for P25. Over 94% removal of Co-TNTs-600 was achieved in 357 min of sedimentation. For material reuse, the 12-h phenanthrene removal drops gradually and remains at 87.2% after 6 cycles of operations. Also, the bleeding of Co from the catalyst totaled at only 4.20% in the 6 runs (2.87% in the first 2 runs), which could be lowered to  $< 0.3\%$  had Co-TNTs-600 been pre-rinsed.

### 5.1.6. Mechanisms for enhanced photocatalytic activity of Co-TNTs-600

Figure 86 displays the DRS UV-vis spectra of TNTs and Co-TNTs-600. Based on the data, the optical energy gaps for the materials are calculated using Equation (51) (Feng et al. 2015):

$$\alpha h\nu = A(h\nu - E_g)^{n/2} \quad (51)$$

in which  $\alpha$ ,  $h$ ,  $\nu$ ,  $A$  and  $E_g$  represent the absorption coefficient, Planck constant, photon frequency, proportionality constant and band gap, respectively; and  $n$  is a constant depending on the optical transition type of a semiconductor ( $n = 1$  for direct absorption;  $n = 4$  for indirect absorption), and  $n = 4$  for the titanate materials in this study.

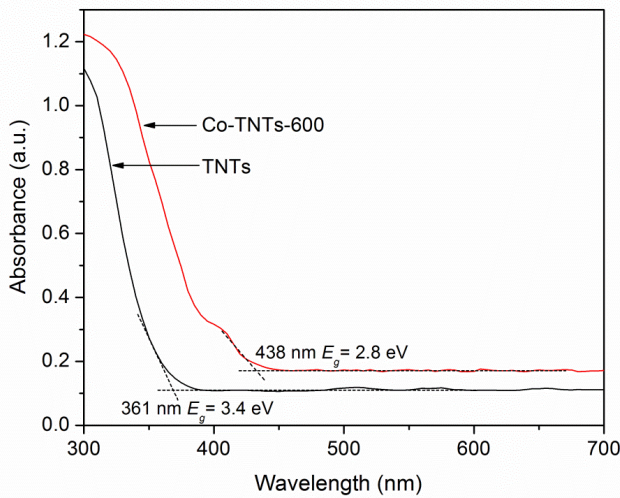
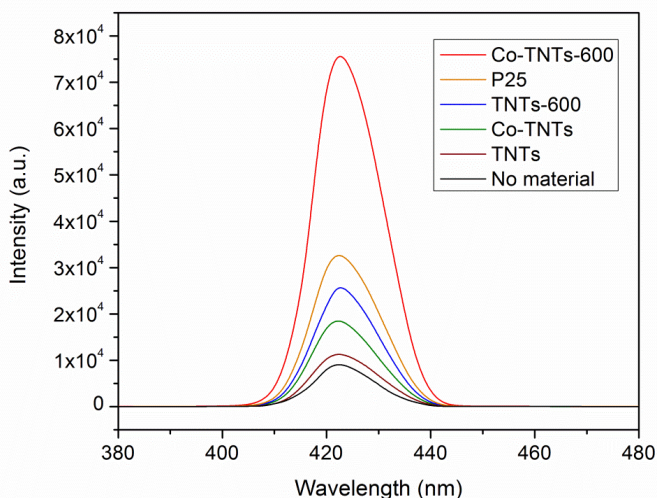


Figure 86. DRS UV-vis spectra of TNTs and Co-TNTs-600.

Compared to TNTs, the absorption edge of Co-TNTs-600 shifts to visible region (from 361 to 438 nm), indicating the photo-effect under visible light is enhanced for Co-TNTs-600. The absorbance peak at ca. 430 nm for Co-TNTs-600 can be attributed to the attachment of CoO (Zheng et al. 2013). The resulting  $E_g$  for Co-TNTs-600 is 2.8 eV, compared to 3.4 eV for TNTs and 3.2 eV for P25 (Chen and Burda 2008). Therefore, a new e-donor level is formed in Co-TNTs-600, which facilitates the transfer of the photo-generated electrons, thereby inhibiting the recombination of the electron-hole pairs.

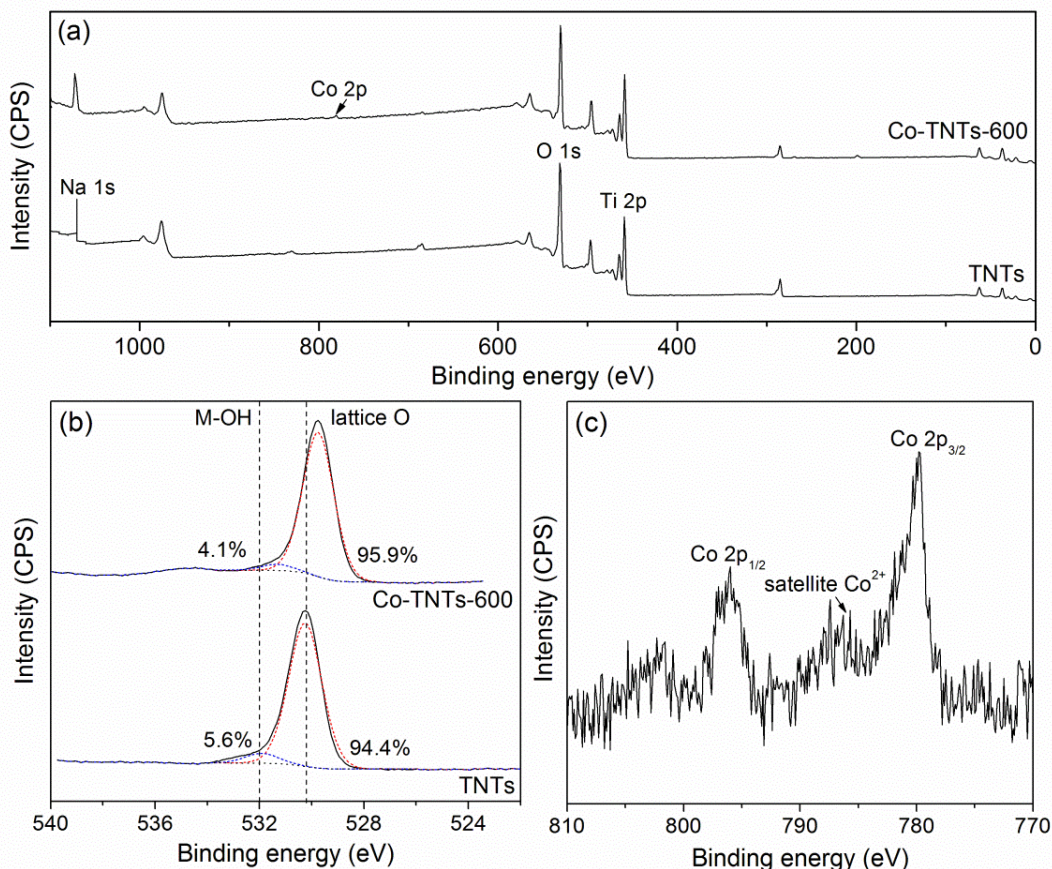


**Figure 87** shows PL spectra of terephthalic acid, which reflects the production of  $\bullet\text{OH}$  under solar irradiation. The fluorescence intensity at 425 nm for the materials follows the sequence of: Co-TNTs-600 >> P25 > TNTs-600 > Co-TNTs > TNTs, which is consistent with that of the apparent rate constant ( $k_1$ ) for phenanthrene degradation (**Figure 84** and **Table 22**). Therefore, enhanced production of the  $\bullet\text{OH}$  radicals accounts for the enhanced photodegradation of phenanthrene by Co-TNTs-600.



**Figure 87. PL spectra of various Ti-based materials under solar irradiation.**

XPS analysis further demonstrates the role of Co in the photocatalysis. As shown in **Figure 88**, the main elements for TNTs are Na (12.3%), Ti (23.4%) and O (64.3%), with a chemical formula of  $\text{Na}_{1.58}\text{H}_{0.42}\text{Ti}_3\text{O}_7 \cdot 1.24\text{H}_2\text{O}$  based on the basic structure of tri-titanate and interlayered  $\text{H}^+/\text{Na}^+$ . For Co-TNTs-600, a Co 2p peak emerges in the XPS survey spectra (**Figure 88a**). The Na content decreases from 12.3% for TNTs to 10.6% for Co-TNTs-600, which is due to the ion exchange of  $\text{Co}^{2+}$  with  $\text{Na}^+$  in the hydrothermal process. The atomic percentage of Co is determined at 1.7% (2.66 wt.%) by XPS, which is consistent with the Co loading dosage obtained from the EPA method (2.26 wt.%), indicating a relatively low Co-deposition can greatly enhance the photocatalytic activity of TNTs. For the high resolution of O 1s (**Figure 88b**), the peaks at ca. 532 eV and 530 eV are assigned to the oxygen from the surface hydroxyl groups and the material lattice, respectively (Ou et al. 2008). For TNTs, the oxygen compositions can include O from the surface Ti-OH ( $E_b \approx 532$  eV) and the crystal lattice [Ti-O<sub>6</sub>] ( $E_b \approx 530$  eV) (Liu et al. 2013c). The lattice O in Co-TNTs-600 is 95.9%, compared to 94.4% for TNTs, indicating transition of titanate to  $\text{TiO}_2$  (also see **Figure 82**), as the content of hydroxyl groups in TNTs is higher than that in  $\text{TiO}_2$  due to the hydrothermal treatment (Chen et al. 2002, Liu et al. 2013c, Xiong et al. 2010). In addition, the formation of CoO also leads to the increase of lattice O. For high resolution of Co 2p (**Figure 88c**), the peaks at ca. 796 and 780 eV represent the Co 2p<sub>1/2</sub> and 2p<sub>2/3</sub> orbits, respectively (Konova et al. 2006, Wang et al. 2010). Specifically, the peak at 780 eV is assigned to  $\text{Co}^{2+}$ , indicating the formation of CoO after calcination (Konova et al. 2006). Moreover, there is a satellite  $\text{Co}^{2+}$  peak at ca. 786 eV, which belongs to Co-O-Ti ( $\text{Co}^{2+}$  in the interlayers of TNTs) (de la Pena O'Shea et al. 2011). The resulting CoO accepts the electrons excited by titanate and  $\text{TiO}_2$  under visible light, thus inhibiting the recombination of electron-hole pairs.

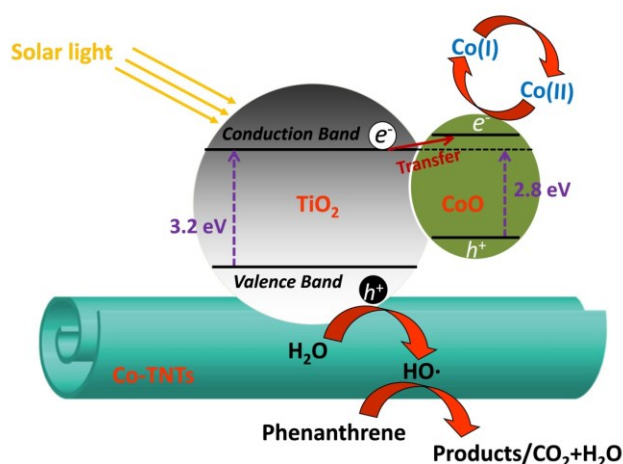
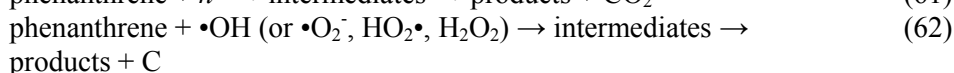
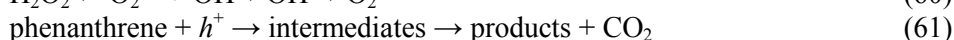


**Figure 88. XPS spectra of TNTs and Co-TNTs-600.**

(a) Survey, (b) high resolution of O 1s, and (c) Co 2p.

**Figure 89** illustrates the key mechanisms for the enhanced photocatalytic activity of Co-TNTs-600, and Equations 52–62 depict the photocatalytic reactions during photocatalytic of phenanthrene. Under illumination of solar light, anatase, TNTs and CoO all can generate a conduction band ( $e^-$ , electrons) and a valence band ( $h^+$ , holes) (Equations 52–53). Because the pristine TNTs and  $\text{TiO}_2$  are weakly responsive to visible light, the production of the ROS, e.g.,  $\cdot\text{OH}$ ,  $\cdot\text{O}_2^-$ ,  $\text{HO}_2\cdot$ ,  $\text{H}_2\text{O}_2$ , will be limited. In addition, the excited electron-hole pairs are prone to recombination for TNTs due to the loss of the crystalline phases. For Co-TNTs-600, however, photo-generated electrons are transferred by CoO coupled with a reduction of  $\text{Co}^{2+}$  to  $\text{Co}^+$  (Equations 54–55), thus inhibiting the recombination of electron-hole pairs. Previous studies also confirmed this kind of electron transfer function by doped or deposited metal oxides, such as CuO,  $\text{Mn}_x\text{O}_y$ ,  $\text{Fe}_2\text{O}_3$  and so on. Dah et al. summarized the mechanisms of all kind of doping or depositing-metals (including Co) for enhancing photocatalytic activity of  $\text{TiO}_2$ . The electrons can reduce  $\text{O}_2$  molecule to  $\cdot\text{O}_2^-$ , and then produce  $\text{HO}_2\cdot$  (Equations 56–57). In the meanwhile, the holes can oxidize  $\text{H}_2\text{O}$  molecules into the ROS, primarily  $\cdot\text{OH}$  (Equations 58–60) (**Figure 87**), which are responsible for phenanthrene degradation (Equations 61–62) (Jia et al. 2012, Linsebigler et al. 1995, Tian et al. 2014, Wen et al. 2002, Zhang et al. 2015). The cobalt deposition also shifts the light absorption edge to the visible light range and narrows down the energy gap to 2.8 eV, which means there is a new electron

acceptor formed (in CoO) acting as photo-generated electrons transfer medium, and therefore, more visible light is absorbed by the new catalyst for photodegradation. Moreover, the rise in anatase crystallinity promotes production of more electron-hole pairs under visible light and further impedes the electron-hole recombination.



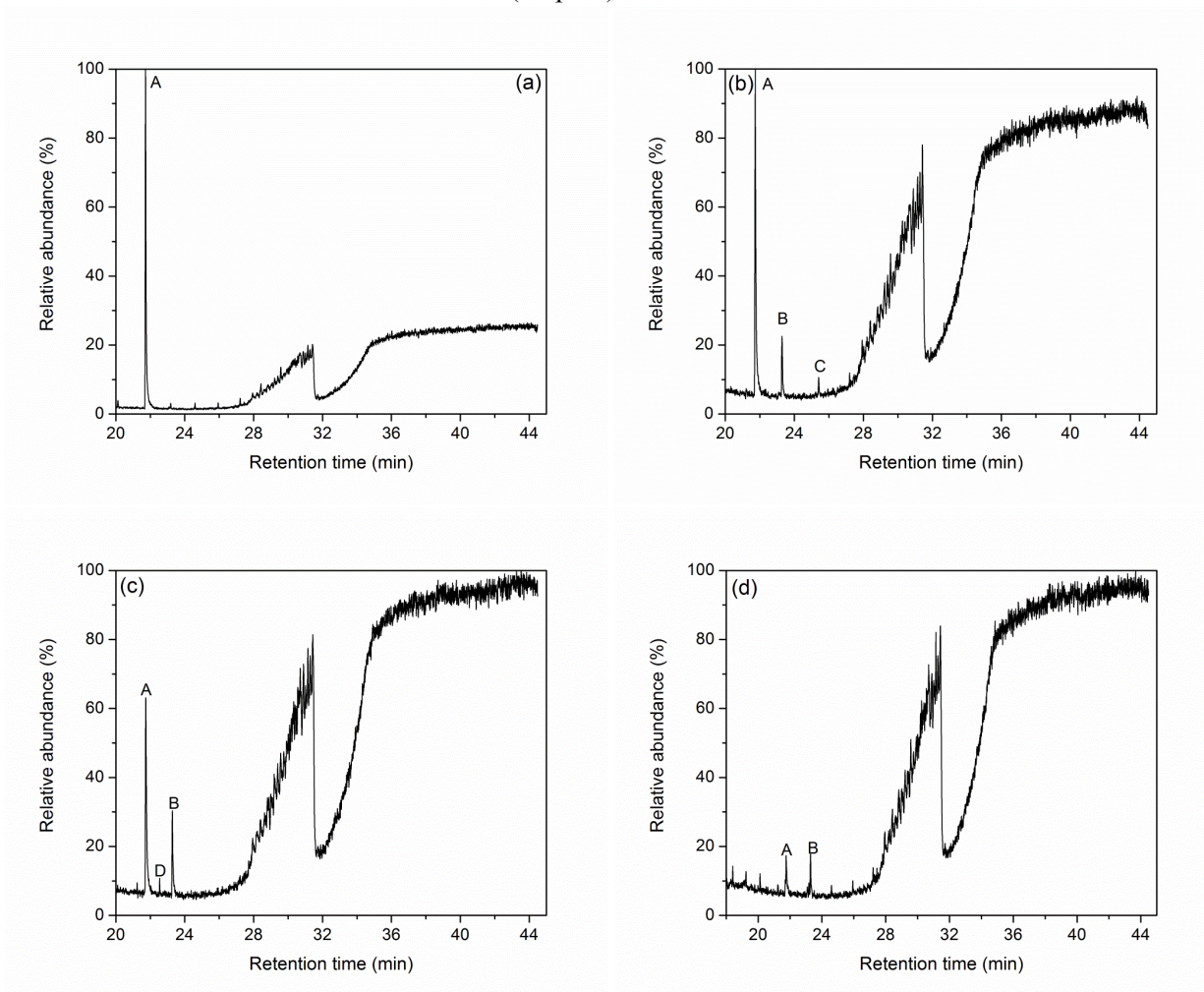
**Figure 89. Schematic illustration of enhanced photocatalytic activity of Co-TNTs-600.**

Note that at the nanoscale, TNTs appear as spirally curled sheets.

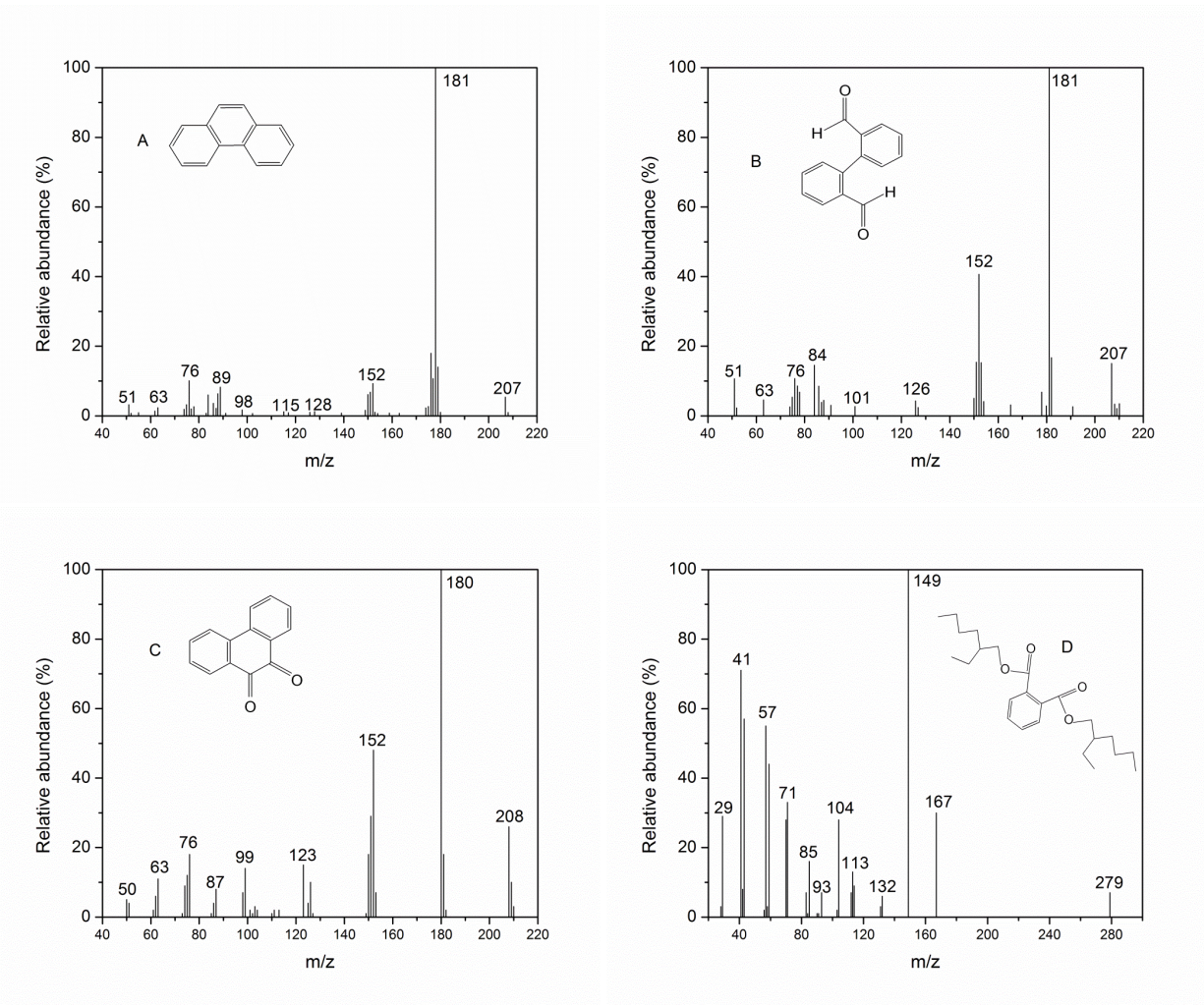
**Figures 90** and **91** show the total ion chromatograms and the MS spectra of phenanthrene and its photodegradation byproducts at various reaction times, and **Figure 89** depicts the phenanthrene degradation pathway in the photocatalytic process using Co-TNTs-600. After 1 h of photo-degradation (**Figure 90b**), two main peaks were identified as (1,1-biphenyl)-2,2-dicarboxaldehyde (B) and 9,10-phenanthrenedione (C) (**Figure 91**). 9,10-phenanthrenedione was formed through ketonization of the hydroxylated benzene ring of phenanthrene (Steps 1-2-3 in **Figure 92**), and (1,1-biphenyl)-2,2-dicarboxaldehyde was produced via ring-opening of 9,10-phenanthrenedione (Step 4). The results are consistent with those reported by others (Jia et al. 2012, Kou et al. 2009, Woo et al. 2009). At 3 h (**Figure 90c**), 9,10-phenanthrenedione disappeared, while a new peak assigned to bis(2-ethylhexyl) phthalate (D) arose, indicating continued benzene ring opening and subsequent alkylation by some photo-activated alkanes ( $\cdot\text{R}$ ) (Steps 6-8) (Jia et al. 2012, Wen et al. 2002). At 6 h (**Figure 90d**), Product D disappeared, whereas 93% of initial phenanthrene and 27% of (1,1-biphenyl)-2,2-dicarboxaldehyde 1 h were degraded.



In the later stage, the phthalates would be further oxidized into smaller organic compounds, such as cyclohexanols, alkanolic acids, alkenes, alkanes, and alcohols (Step 9) (Jia et al. 2012, Kou et al. 2009), which are then mineralized to CO<sub>2</sub> and H<sub>2</sub>O (Step 10).



**Figure 90. Total ion chromatograms of phenanthrene and degradation byproducts.** (a) to time 0, (b) at 1 h, (c) at 3 h, and (d) at 6 h of photocatalysis using Co-TNTs-600.



**Figure 91. Mass spectra of phenanthrene and degradation byproducts.**  
 During photocatalysis phenanthrene using Co-TNTs-600.

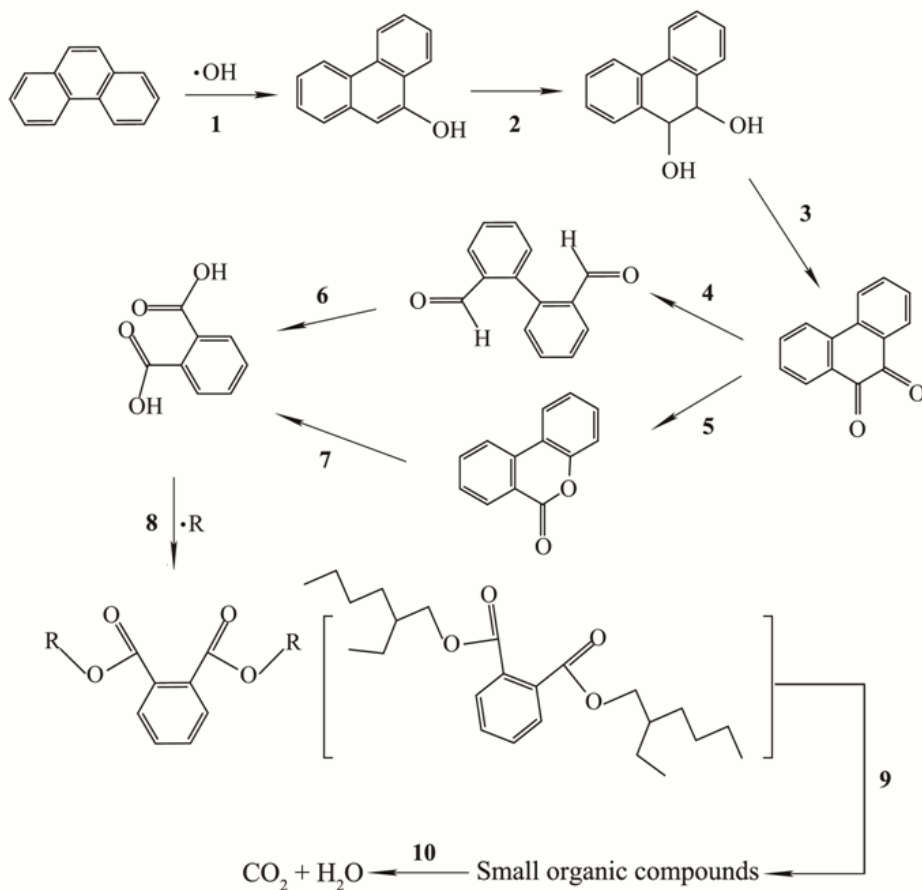


Figure 92. Proposed degradation pathway of phenanthrene by Co-TNTs-600 under solar light.

### 5.1.7. Conclusions

In this study, we developed and tested a new class of cobalt-deposited TNTs for enhanced photocatalytic degradation of oil PAH, phenanthrene, under solar light. Co-TNTs were successfully synthesized through a two-step process: hydrothermal treatment of commercial P25 as the Ti precursor, followed by calcination at 600 °C.  $\text{Co}^{2+}$  ions are incorporated in TNTs in the hydrothermal reaction, which are further transformed into CoO in the calcination process. The optimized catalyst (Co-TNTs-600) was prepared at 2.26% Co loading and a calcination temperature of 600 °C. TEM, XRD, FTIR and XPS characterizations indicate that Co-TNTs-600 is a nano-composite consisting of titanate, anatase and CoO. Co-TNTs-600 exhibited high photocatalytic activity for degradation of phenanthrene under solar light, with a 98.6% removal rate in 12 h at dosage of 1 g/L. The first-order kinetic model is able to adequately interpret the kinetic data, and the apparent rate constant was determined to be  $0.39 \text{ h}^{-1}$ , which is  $\sim 23$  times higher than that of TNTs and  $\sim 10$  times that of P25. The combination of Co-deposition, calcination and crystallization resulted in the dramatic synergistic effect of Co-TNTs-600. UV-vis DRS spectra of Co-TNTs-600 suggest that the absorption edge of Co-TNTs-600 shifts to the visible light region compared to P25 and un-calcined TNTs, and Co-TNTs-600 gives a much narrower optical energy gap of 2.8 eV, compared to 3.4 eV for TNTs and 3.2 eV for P25, indicating much improved sensitivity to visible light. The CoO nanoparticles in Co-TNTs-600 can not only facilitate effective utilization of visible light for production of electron-hole pairs, but also serve as an electron transfer mediator that inhibits

recombination of the pairs. Likewise, the increased crystallinity of anatase resulting from the calcination process promotes production of more electron-hole pairs and further impedes the electron-hole recombination. Co-TNTs-600 can be efficiently separated via gravity-settling and then reused in multiple runs. Despite the much greater catalytic activity of Co-TNTs-600, the photodegradation pathway for phenanthrene appears similar to that for other photocatalysts. (1,1-biphenyl)-2,2-dicarboxaldehyde and 9,10-phenanthrene-9,10-dione are the primary intermediates, both of which are expected to be completely mineralized.

Overall, Co-TNTs-600 appears to be an efficient photocatalyst for degradation of persistent oil PAHs under solar light.

## 5.2. Photodegradation of Oil PAHs by Pt-Deposited Titanate Nanotubes

As mentioned in Section 5.1, photocatalytic degradation of persistent oil PAHs using Ti-based materials is promising. Considering the weak photocatalytic activity of TiO<sub>2</sub> and titanate under solar-visible light, researchers have been consistently attempting to modify Ti-based photocatalysts so as to enhance the photo-efficiency under visible light through hindering the recombination of electron-hole pairs and narrowing down the band gaps (Doong et al. 2013, Liu et al. 2015a, Sung-Suh et al. 2004, Veldurthi et al. 2015, Zhao et al. 2016a). To this end, various noble metals, e.g., Pt, Au and Ag, have been used as dopants, facilitating production of ROS and absorption of visible light (Malato et al. 2009, Pan et al. 2016). Pt is one of the most used dopants for modifying TiO<sub>2</sub> and titanate (Liu et al. 2011). Pt can provide the highest Schottky Barrier among the metal species, facilitating the electron capturing and extending the electron-hole pair separation life time (Li and Li 2002). Meanwhile, incorporation of Pt into TiO<sub>2</sub> was reported to decrease the band gaps of TiO<sub>2</sub> and enhance visible light absorption (Li and Li 2002). Previous studies revealed that Pt(0)-doped TiO<sub>2</sub> displayed faster photocatalytic oxidation rate of *o*-cresol than TiO<sub>2</sub> (P25) under UV irradiation (Chen et al. 2007a), and Pt(IV)-modified TiO<sub>2</sub> was more active than TiO<sub>2</sub> (P25) for photodegradation of 4-chlorophenol (Burgeth and Kisch 2002). However, the effects of Pt(0) or Pt(IV) on titanate nanotubes have not been reported.

In this section, we developed and evaluated a new type of platinum-deposited TNTs (Pt-TNTs) for photocatalytic degradation of oil PAHs under solar irradiation. The specific objectives were to: 1) synthesize the desired Pt-TNTs nanomaterial and optimize the preparation conditions; 2) characterize the new composite material; 3) evaluate the effectiveness of the photocatalysts by testing photodegradation of phenanthrene (as a model PAH); and 4) elucidate the underlying mechanisms and roles of Pt based on the material characterization, contribution of visible irradiation to the reactivity, and production of ROS.

### 5.2.1. Synthesis of Pt-deposited TNTs

Pt-deposited TNTs were synthesized through a three-step method, i.e., hydrothermal conversion of TiO<sub>2</sub> to TNTs and subsequent Pt deposition and calcination. Briefly, 1.2 g TiO<sub>2</sub> powder was dispersed in 20 mL DI water, magnetically stirred for 20 min, and then sonicated using a Branson 1510R-MTH sonicator (70W, 42 KHZ) for another 20 min (solution A). Meanwhile, a 15 M NaOH solution was prepared by dissolving 29 g NaOH in 47 mL DI water (solution B). Then, solutions A and B were mixed and sonicated for 60 min, and the mixture was then transferred into a Teflon reactor with stainless steel coating and heated at 130 °C for 72 h. The resulting white precipitates (TNTs) were washed with DI water till pH ≈ 10, then dispersed in 10 mL ethanol and oven-dried at 80 °C for 4 h. Pt was then deposited on TNTs by mixing 1 g of TNTs with 40 mL of a H<sub>2</sub>PtCl<sub>6</sub> solution at various Pt concentrations (12.5, 25, 125 and 250 mg/L as Pt). The mixture was shaken at pH 3 for 4 h, when Pt(IV) was completely adsorbed on TNTs, the mixture was then purged with N<sub>2</sub> for 20 min to remove dissolved oxygen, and subsequently, 10 mL of a fresh NaBH<sub>4</sub> solution (0.8 g/L) was added into the flask dropwise under vacuum and shaking

(200 rpm) on a flat-top shaker. The resulting materials (gray to black depending on Pt dosage) were then washed with DI water and methanol consecutively (3 times each), and oven-dried at 80 °C for 4 h. The catalyst is denoted by Pt(0)-TNTs for typographical convenience. For comparison, Pt(IV) loaded TNTs, i.e., Pt(IV)-TNTs, were prepared following the same procedure but without the NaBH<sub>4</sub> reduction step. The materials were then calcined at 400, 600 or 800 °C, respectively, for 2 h in a muffle furnace, and the resulting materials were referred to as Pt(0)-TNTs-xxx or Pt(IV)-TNTs-xxx (where xxx indicates the calcination temperatures). For comparison, neat TNTs (without Pt) were prepared under the same conditions and calcined at 600 °C.

Characterization methods for materials are described in Section 5.1.1.

## 5.2.2. Experimental methods

Photocatalysis experiments were carried out in a similar manner to that presented in Section 5.1.2. The photocatalytic kinetic tests were conducted under the following conditions: solution volume = 200 mL, initial phenanthrene = 200 µg/L, catalyst dosage = 0.04 g. The solution pH was adjusted to ~7.0 using diluted HCl or NaOH solutions. The mixture was first stirred in dark for 2 h to allow for phenanthrene adsorption equilibrium. Subsequently, photodegradation was initiated by exposing the reactor to the simulated solar light. At predetermined time intervals, 1 mL sample was taken, and then centrifuged at 6000 rpm (5434×g force) for 3 min to remove the solids, and the supernatant was then mixed with methanol (1:1 v/v) and filtered through a 0.22 µm PTFE syringe filter (Millipore) (addition of methanol minimizes retention of phenanthrene by the filter). Section 5.1.2 describes the method for phenanthrene measurement.

To evaluate the photocatalytic activity of Pt(0)-TNTs-600 and Pt(IV)-TNTs-600 under only visible light, a UV cut-off filter (Institute of Electric Light Source) was applied on top of the photo-reactor to remove irradiation with wavelength < 420 nm. To test the reusability of spent catalysts, the spent material from the batch kinetic tests was recovered by filtering through a 0.22 µm PTFE membrane, air-dried, and then reused in another batch of phenanthrene photodegradation. The tests were repeated 6 times. Separate tests showed that the air-drying did not alter the photocatalytic activity.

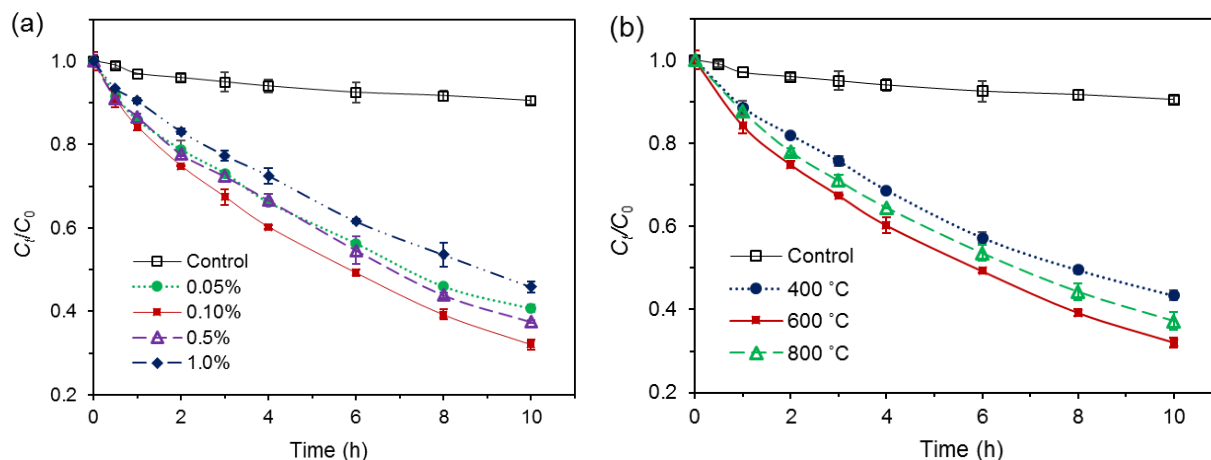
## 5.2.3. Photocatalytic activity of Pt(0)-TNTs prepared under various conditions

The photocatalytic activity of Pt(0)-TNTs prepared with different Pt loadings (0.05–1.0 wt.%, with a fixed calcination temperature of 600 °C) and calcination temperatures (400, 600 and 800 °C, with a fixed Pt loading of 0.1 wt.%) were evaluated in terms of the phenanthrene degradation rate under simulated solar light. The first-order kinetic model was used to interpret the phenanthrene degradation kinetic data. **Figure 93** shows the photodegradation kinetics. Increasing the Pt dosage from 0.05 to 0.1 wt.% increased the apparent rate constant ( $k_1$ ) from 0.10 to 0.12 h<sup>-1</sup> (**Figure 93a**). However, further increasing Pt dosage to 0.5 and 1.0 wt.% decreased the  $k_1$  to 0.10 and 0.08 h<sup>-1</sup>. Consequently, the optimum Pt loading was set at 0.1 wt.%. Generally, Pt at lower dosages acts as an electron trap to inhibit the recombination of photo-induced electron-hole pairs; however, an excessive amount of Pt on the TNTs may act as a recombination center for electron-hole pairs or block the active sites (Ou and Lo 2007).

**Figure 93b** shows that increasing the calcination temperature from 400 to 600 °C increased the  $k_1$  value from 0.09 to 0.12 h<sup>-1</sup>; however, further increasing the calcination temperature to 800 °C lowered the rate constant to 0.10 h<sup>-1</sup>. The calcination temperature can affect the morphology and structure of TNTs. There are two types of dehydration during calcination: 1) dehydration of intralayered –OH groups, which occurs at lower calcination temperature and has little effect on the nanotube length; and 2) dehydration of interlayered –OH groups, which occurs at higher temperature and will induce the change of the crystalline form and damage of the tubular structure (Lee et al. 2007). The increase in calcination



temperature leads to the crystallization of anatase, which exhibits much higher photocatalytic activity than uncalcined TNTs (Lee et al. 2007, Yu et al. 2006b). However, too high a temperature ( $> 700\text{ }^{\circ}\text{C}$ ) will decrease the specific surface area of TNTs and convert anatase into rutile, which is a weaker photocatalyst than anatase (Lee et al. 2007, Yu et al. 2006b). Consequently, the optimum calcination temperature was set at  $600\text{ }^{\circ}\text{C}$ , which is consistent with the finding by Lee et al (2007). Based on the observations, Pt(0)-TNTs-600 prepared with a Pt dosage of 0.1 wt.% and calcination temperature of  $600\text{ }^{\circ}\text{C}$  was further characterized and tested.

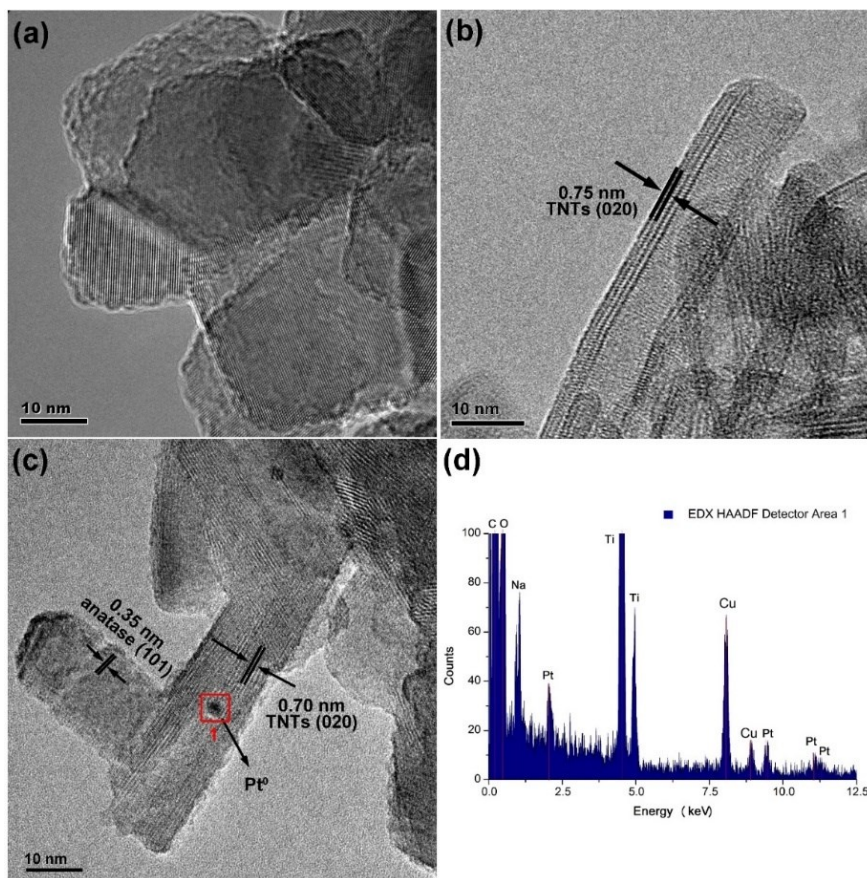


**Figure 93. Photocatalytic degradation of phenanthrene by various Pt(0)-TNTs.**

(a) Pt(0)-TNTs prepared at different Pt loadings, and (b) at various calcination temperatures. Experimental conditions: initial phenanthrene =  $200\text{ }\mu\text{g/L}$ , material dosage =  $0.2\text{ g/L}$ , pH =  $7.0\pm 0.2$ , temperature =  $25\pm 0.2\text{ }^{\circ}\text{C}$ .

#### 5.2.4. Morphology, crystal phases and compositions of Pt-deposited TNTs

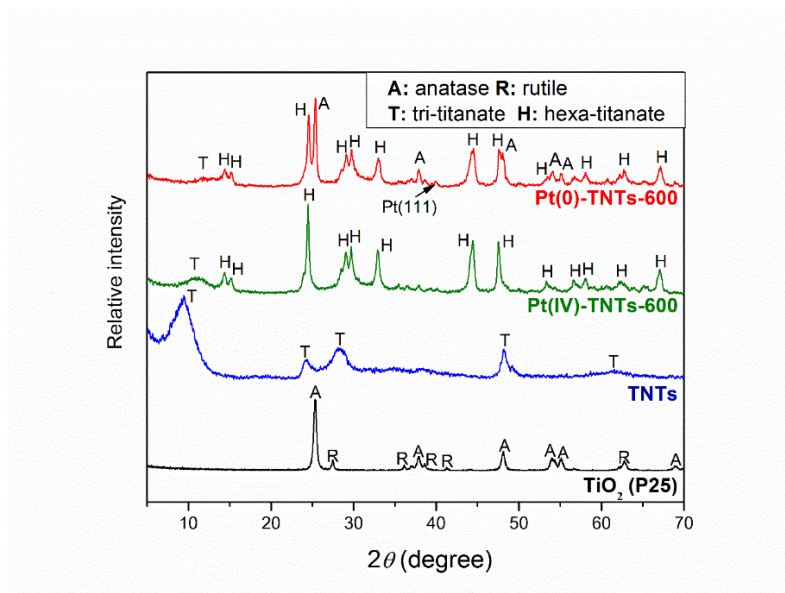
Figure 94 presents TEM images Pt(0)-TNTs-600 and the precursor materials.  $\text{TiO}_2$  (P25) was observed as agglomerated particles with a mean size of  $20\text{--}50\text{ nm}$  (Figure 94a), and TNTs obtained from the hydrothermal treatment were multilayered (4–5 layers) nanotubes with an inner diameter of  $\sim 4.5\text{ nm}$  and outer diameter of  $\sim 9\text{ nm}$  (Xiong et al. 2010). The interlayer distance of pristine TNTs was  $\sim 0.75\text{ nm}$ , which is assigned to the crystal plane of tri-titanate (020) (Figure 94b) (Chen et al. 2002). Upon calcination at  $600\text{ }^{\circ}\text{C}$ , the tubular structure was partially broken into shorter nanotubes as well as nanoparticles and nanorods (Figure 94c), with a slightly reduced interlayer distance of  $\sim 0.7\text{ nm}$ , which is assigned to crystal plane (020) of hexa-titanate (confirmed later by XRD) (Cai et al. 2015, Yang et al. 2011a). However, the facets of titanate (020) reveal that part of the TNTs survived the calcination process (Zhao et al. 2016a). The formation of nanoparticles and nanorods with a crystal distance of  $0.35\text{ nm}$  is attributed to the facets of anatase (101), indicating that TNTs were partially converted to  $\text{TiO}_2$  (anatase) (Figure 94c) (Cai et al. 2015). Figure 94c reveals some dark dots with a diameter of  $\sim 2\text{ nm}$  on Pt(0)-TNTs-600; these are ascribed to metallic Pt(0) based on the EDS scan (Figure 94d). Moreover, the EDS spectra also reveal that the main elements of Pt(0)-TNTs-600 are Na, O, Ti and Pt, indicating that Pt was successfully deposited on TNTs, which was further confirmed by XRD and XPS analyses.



**Figure 94.** TEM images of (a)  $\text{TiO}_2$  (P25), (b) TNTs, and (c) Pt(0)-TNTs-600; and (d) EDX spectra of Pt(0)-TNTs-600.

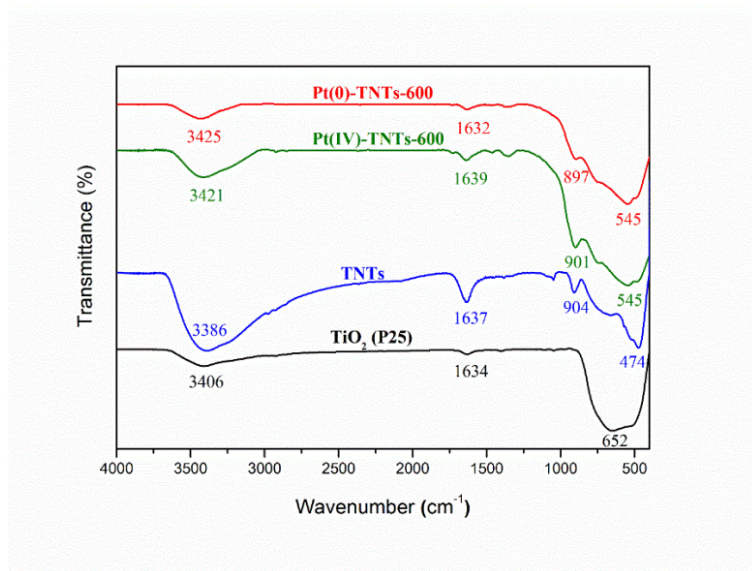
**Figure 95** presents XRD patterns for various Ti-based nanomaterials. The hydrothermal treatment completely converted  $\text{TiO}_2$  (P25, a mixture of anatase and rutile) into titanate (TNTs), which is evidenced by the diffraction peaks at ca.  $10^\circ$ ,  $24^\circ$ ,  $28^\circ$ ,  $48^\circ$  and  $62^\circ$  (Liu et al. 2013b, Sun and Li 2003). Moreover, the resulting titanate is a sodium tri-titanate composed of the edge-sharing triple  $[\text{TiO}_6]$  octahedrons with  $\text{H}^+/\text{Na}^+$  located in the interlayers, and the chemical formula  $\text{Na}_x\text{H}_{2-x}\text{Ti}_3\text{O}_7$  ( $x$  depends on the sodium content) (Liu et al. 2013a, Liu et al. 2013b, Xiong et al. 2011a, Zhao et al. 2016a). The peak at  $10^\circ$  represents the interlayer distance of TNTs (0.75 nm as shown in **Figure 94b**) (Liu et al. 2013b, Sun and Li 2003). Evidently, both Pt(0)-TNTs-600 and Pt(IV)-TNTs-600 show good crystallinity, though with different crystalline phases than neat TNTs. Though both materials showed a sodium hexa-titanate ( $\text{Na}_2\text{Ti}_6\text{O}_{13}$ ) crystalline phase, only Pt(0)-TNTs-600 displayed the anatase crystal. The hexa-titanate is represented by a framework enclosing tunnel structures formed by corner- and edge-shared  $[\text{TiO}_6]$  octahedra, while the tri-titanate ( $\text{Na}_2\text{Ti}_3\text{O}_7$ ) is formed with the zigzag ribbon structures consisting of edge-shared  $[\text{TiO}_6]$  octahedra (Inoue et al. 1991). During calcination of TNTs, tri-titanate with high sodium content is inclined to be converted to hexa-titanate, but decreasing the sodium content favors conversion to anatase (Lee et al. 2007). During the synthesis of Pt(0)-TNTs-600, the washing step that after the reduction of Pt(IV) to Pt(0) removed part of the  $\text{Na}^+$  ions that were sorbed on TNTs (9.6 wt.% for Pt(0)-TNTs-600 and 13.1 wt.% for Pt(IV)-TNTs-600 measured by XPS). The lower sodium content of Pt(0)-TNTs-600 resulted in formation of anatase, and the high sodium content in Pt(IV)-TNTs-600 just led to the conversion of tri-titanate to hexa-titanate. In addition, the Pt(111) peak, which belongs to Pt(0), was observed for Pt(0)-TNTs-600, though very weak due to the low Pt loading (0.1 wt.%). The interlayer

peaks ( $2\theta \approx 10^\circ$ ) of tri-titanate (020) were greatly diminished for both Pt(0)-TNTs-600 and Pt(IV)-TNTs-600, indicating calcination greatly altered the interlayers of TNTs.



**Figure 95. XRD patterns of various Ti-based materials.**

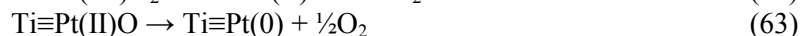
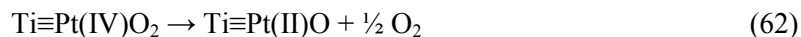
**Figure 96** displays the FTIR spectra of four Ti-based nanomaterials. The absorption bands of  $\text{TiO}_2$  at 652, 1634, and 3406  $\text{cm}^{-1}$  are assigned to Ti–O, H–O–H (bound water molecule), and O–H bonding vibrations (Park and Kang 2005). For TNTs, the bands at 474 and 904  $\text{cm}^{-1}$  are attributed to the  $[\text{TiO}_6]$  octahedron and four-coordinate Ti–O stretching vibrations of titanate (Liu et al. 2013a, Liu et al. 2013b, Xiong et al. 2011a). The FTIR spectra of Pt(0)-TNTs-600 and Pt(IV)-TNTs-600 are similar to those of TNTs except the Ti–O band is shifted from 904 to 897  $\text{cm}^{-1}$  for Pt(0)-TNTs-600 due to interaction of Pt with the Ti–O band and formation of Ti–O–Pt (Zhao et al. 2016a). Moreover, the calcination shifted the  $[\text{TiO}_6]$  octahedron band from 474 to 545  $\text{cm}^{-1}$  for both materials, which is attributed to the conversion of tri-titanate to anatase or hexa-titanate (Zhao et al. 2016a).



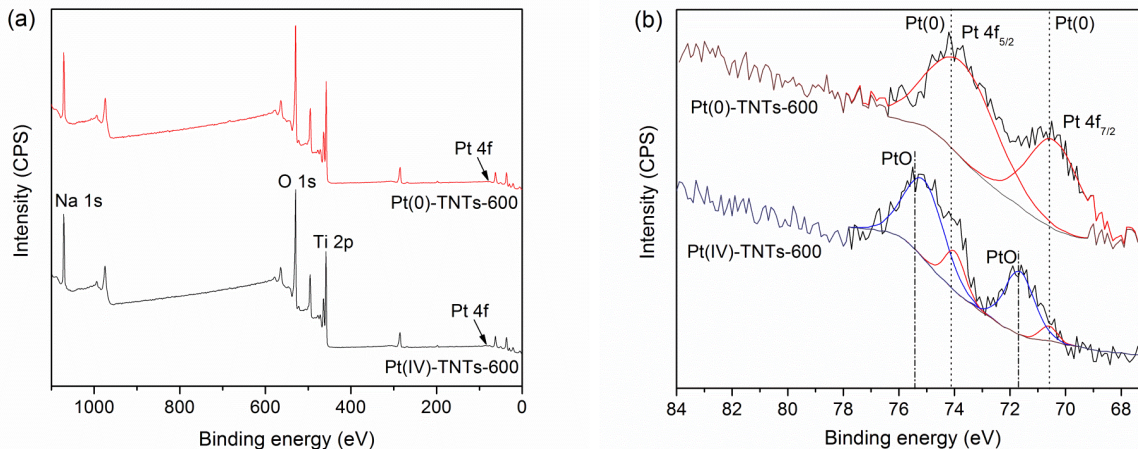
**Figure 96. FTIR spectra of various Ti-based materials.**



The XPS survey spectra (**Figure 97a**) indicate that the main elements for the both Pt-TNTs are Na, Ti, O, Pt and Cl (**Table 23**). The calculated surface Pt loading based on the XPS results is 0.11 wt.% for Pt(0)-TNTs-600 and 0.14 wt.% for Pt(IV)-TNTs-600; this is consistent with the designed Pt content (0.1 wt.%). In the high resolution spectra for Pt(0)-TNTs-600 (**Figure 97b**), the peaks at 70.6 (Pt 4f<sub>7/2</sub>) and 74.1 eV (Pt 4f<sub>5/2</sub>) are due to Pt(0) (Kuribayashi and Kitamura 2001, Wang et al. 2005). For Pt(IV)-TNTs-600, two new peaks at 71.7 and 75.4 eV, which are attributed to Pt(II) from PtO, were observed in addition to the Pt(0) peaks (Kuribayashi and Kitamura 2001, Wang et al. 2005); yet no peaks for Pt(IV) were observed, which indicates that Pt(IV) was converted to Pt(II) and Pt(0) during the calcination process (Ghita et al. 2012, Jin et al. 2003). The following reactions may describe the thermal decomposition of Pt(IV)-TNTs at 600 °C (Ghita et al. 2012, Jin et al. 2003):



where “Ti≡” represents the TNTs supporting the deposited Pt.



**Figure 97. XPS spectra.**

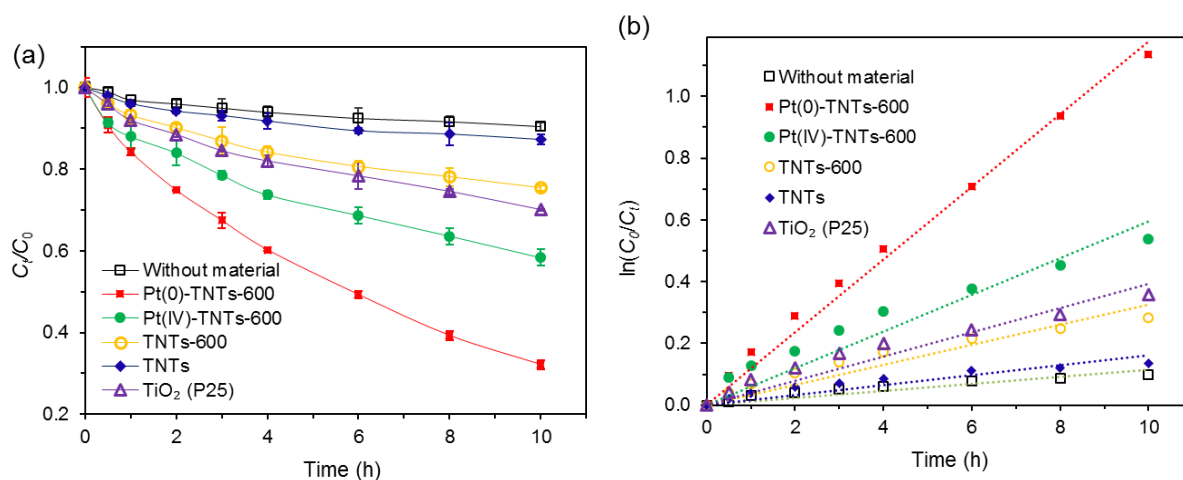
(a) XPS survey spectra and (b) high resolution spectra of Pt 4f for Pt(0)-TNTs-600 and Pt(IV)-TNTs-600.

**Table 23. Elemental weight percentages in Pt(0)-TNTs-600 and Pt(IV)-TNTs-600**

Material	Elemental percentage (wt.%)				
	Na	O	Ti	Pt	Cl
Pt(0)-TNTs-600	9.6	45.3	43.2	0.11	1.8
Pt(IV)-TNTs-600	13.1	44.8	39.9	0.14	2.0

## 5.2.5. Photocatalytic degradation of phenanthrene by various Ti-based materials

**Figure 98** shows the photocatalytic degradation of phenanthrene by various Ti-based nanomaterials, including the precursor  $\text{TiO}_2$ , neat TNTs, Pt(0)-TNTs, TNTs calcined at 600 °C without Pt (TNTs-600), Pt(0)-TNTs-600 and Pt(IV)-TNTs-600. Pristine  $\text{TiO}_2$  is a well-known photocatalyst under UV light, but insensitive to visible light. As a result, only 30% phenanthrene at 10 h ( $k_1 = 0.04 \text{ h}^{-1}$ ) was degraded under solar light, which contains ~5% UV. Neat TNTs showed the lowest photocatalytic activity ( $k_1 = 0.02 \text{ h}^{-1}$ ) due to rapid recombination of the electron-hole pairs (Kim et al. 2012, Lee et al. 2007, Yu et al. 2006a, Zhao et al. 2016a). The uncalcined Pt(0)-TNTs showed little improvement of the photo-activity. Calcined TNTs without Pt (TNTs-600) displayed a 50% greater photocatalytic activity than TNTs ( $k_1 = 0.03 \text{ h}^{-1}$ ), due to formation of anatase or hexa-titanate (Lee et al. 2007, Yu et al. 2006b, Zhao et al. 2016a). Pt(0)-TNTs-600 showed the highest activity, with a  $k_1$  value being 3 times of that for  $\text{TiO}_2$  and 6 times of TNTs under solar light. Pt(IV)-TNTs-600 also exhibited high photo-activity, though the  $k_1$  value was only half that for Pt(0)-TNTs-600, suggesting that Pt(0) is photochemically more effective than Pt(II).



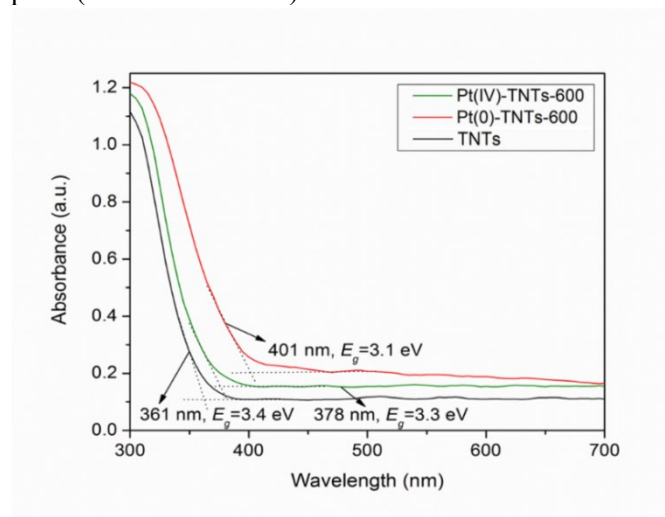
**Figure 98. Photocatalytic degradation of phenanthrene.**

(a) Photocatalytic degradation kinetics of phenanthrene by various Ti-based materials, and (b) linearized pseudo first-order model fittings of the kinetic data. Experimental conditions: initial phenanthrene = 200  $\mu\text{g/L}$ , material dosage = 0.2 g/L, pH = 7.0 $\pm$ 0.2, temperature = 25 $\pm$ 0.2 °C.

Pt(0)-TNTs-600 also can be more easily separated by gravity from water than, while the commercial  $\text{TiO}_2$  particles were almost un-settleable. For instance, after gravitational settling for 8 h, 91.5% of Pt(0)-TNTs-600 was removed, compared to 79.5% for TNTs, and only 4.4% for the commercial  $\text{TiO}_2$ . The good sedimentation performance is attributed to the tubular structure, higher density, and large aggregated particle size (Liu et al. 2013a, Zhao et al. 2016a), and it greatly eases recovery and reuse of the spent photocatalyst. For material reuse over 6 cycles for phenanthrene photodegradation by Pt(0)-TNTs-600, the 24-h phenanthrene degradation showed only a slight drop (~3.7%) after the first run, and remained identical thereafter. The observation indicates that the photodegradation process completely regenerates the catalyst, granting it long-lasting photocatalytic activity. In addition, no Pt leaching was detected over the 6 cycles of operations, indicating high physico-chemical stability of the catalyst.

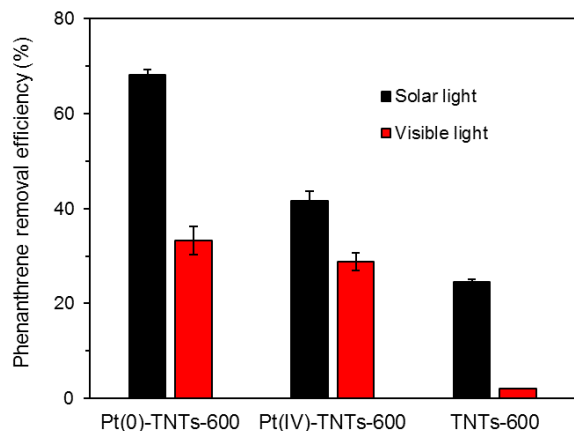
## 5.2.6. Mechanisms for enhanced photocatalytic activity of Pt-deposited TNTs

**Figure 99** presents the DRS UV-vis spectra of TNTs, Pt(0)-TNTs-600 and Pt(IV)-TNTs-600. The optical energy gaps ( $E_g$ ) of the tested materials were calculated following the Kubelka-Munk method (Feng et al. 2015, Zhao et al. 2016a). The absorption edges of both Pt(0)-TNTs-600 and Pt(IV)-TNTs-600 show a red shift to the visible light region compared to neat TNTs. A narrowed  $E_g$  was found for Pt(0)-TNTs-600 (3.1 eV) and Pt(IV)-TNTs-600 (3.3 eV), compared to 3.4 eV for TNTs. In addition, Pt(0)-TNTs-600 exhibited the highest absorbance in the visible light region, which is consistent with the good photocatalytic activity under visible light. The absorbance peak at 401 nm for Pt(0)-TNTs-600 can be attributed to the deposited Pt(0) in the band gap of TiO<sub>2</sub>, which derives a new electronic state below the band gap (Driessen and Grassian 1998). Therefore, incorporation of Pt in TNTs altered the  $e$ -donor levels, which facilitates the transfer of the photo-generated electrons and inhibit recombination of electron-hole pairs (Zhao et al. 2016a).



**Figure 99. DRS UV-vis spectra of TNTs, Pt(0)-TNTs-600 and Pt(IV)-TNTs-600.**

To verify the enhanced photocatalytic activity of the new catalysts under visible light, the degradation of phenanthrene under visible irradiation was compared with that under solar irradiation. **Figure 100** shows that the total phenanthrene degradation at 10 h under solar light was 24.6%, 41.7% and 68.1% in the presence of TNTs-600, Pt(IV)-TNTs-600 and Pt(0)-TNTs-600, respectively. Under the visible light only, almost no photodegradation of phenanthrene (< 3%) was observed with TNTs-600; in contrast, the visible irradiation contributed 68.1% and 48.9% to the total phenanthrene degraded in the presence of Pt(IV)-TNTs-600 and Pt(0)-TNTs-600, respectively. The much higher contribution of UV light for Pt(0)-TNTs-600 can be attributed to the more efficient utilization of UV by the anatase phase. For both cases, the Pt deposition dramatically enhanced the visible light activity of the nanomaterials, which agrees with the observed shift of DRS UV-vis spectra.

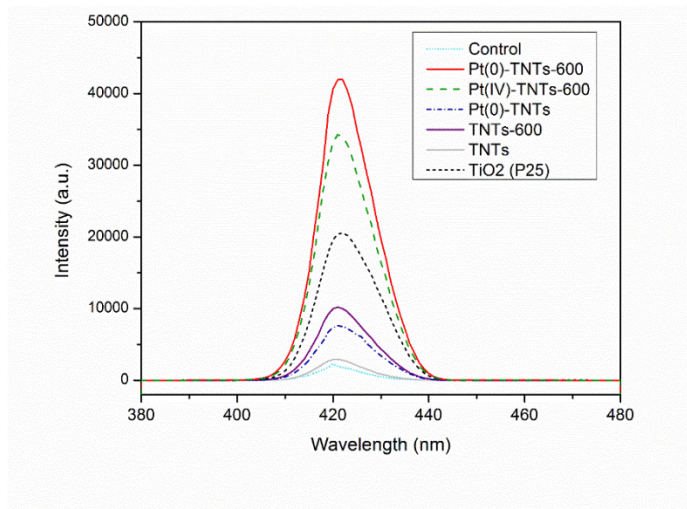


**Figure 100. Contributions of UV and visible irradiation to photocatalytic degradation of phenanthrene.**

Experimental conditions: initial phenanthrene = 200 µg/L, material dosage = 0.2 g/L, pH = 7.0±0.2, temperature = 25±0.2 °C).

Pt(0)-TNTs-600 far outperformed Pt(IV)-TNTs-600 in the phenanthrene photodegradation, which can be attributed to some fundamental differences in their functional compositions. First, Pt(0)-TNTs-600 contains both anatase and hexa-titanate, while Pt(IV)-TNTs-600 has only hexa-titanate. Anatase from tri-titanate promotes the production of more electron-hole pairs than hexa-titanate, resulting in greater quantum yield for Pt(0)-TNTs-600. Second, Pt(0) is an excellent conductor, which can more efficiently transfer photo-generated electrons than PtO. It is noteworthy that hexa-titanate has higher photocatalytic activity than tri-titanate due to the tunnel structures of [TiO<sub>6</sub>] octahedra, but weaker than TiO<sub>2</sub> (Inoue et al. 1991, Inoue et al. 1994). Formation of hexa-titanate is important for the enhanced photocatalytic activity of both Pt(0)-TNTs-600 and Pt(IV)-TNTs-600, because the tunnel structure is suitable for trapping Pt and accommodating the reaction between the active species (deposited Pt(0) and PtO) and Ti semiconductor (hexa-titanate structure). This situation can boost transfer of photo-excited electrons to sorbed phenanthrene on the catalyst (Inoue et al. 1991).

Production of ROS, (•OH), was determined to further elucidate the underlying mechanisms. **Figure 101** shows the PL spectra of terephthalic acid in the presence of various nanomaterials under solar irradiation, which indirectly shows the amount of •OH produced with the photocatalysts. The fluorescence intensity follows the order of: Pt(0)-TNTs-600 > Pt(IV)-TNTs-600 > TiO<sub>2</sub> (P25) > TNTs-600 > Pt(0)-TNTs > TNTs, which is consistent with the phenanthrene degradation rate. Evidently, •OH radicals play an important role in facilitating the photocatalytic degradation of phenanthrene for both Pt(0)-TNTs-600 and Pt(IV)-TNTs-600.

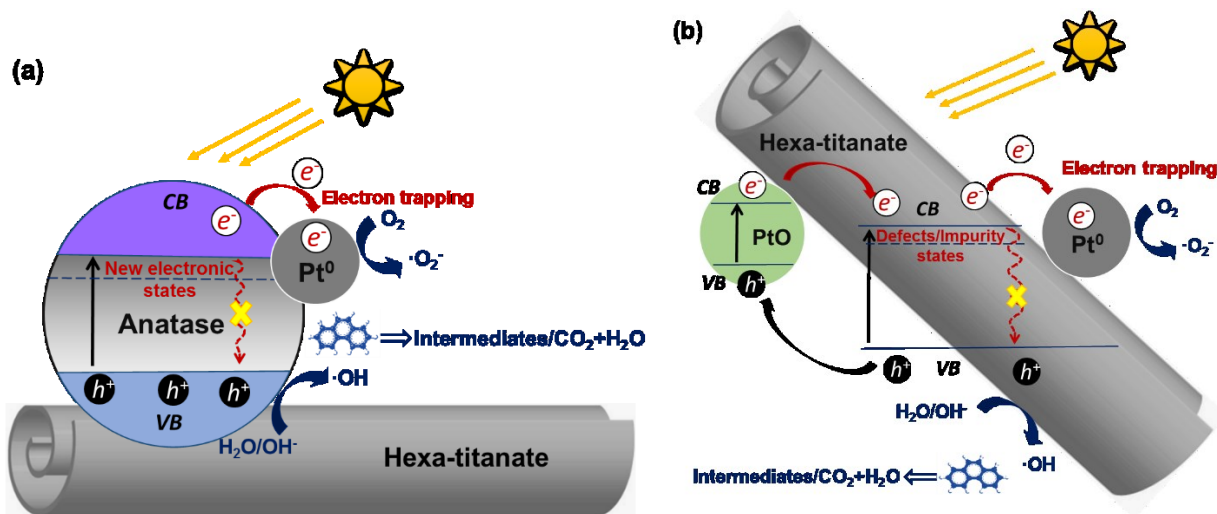
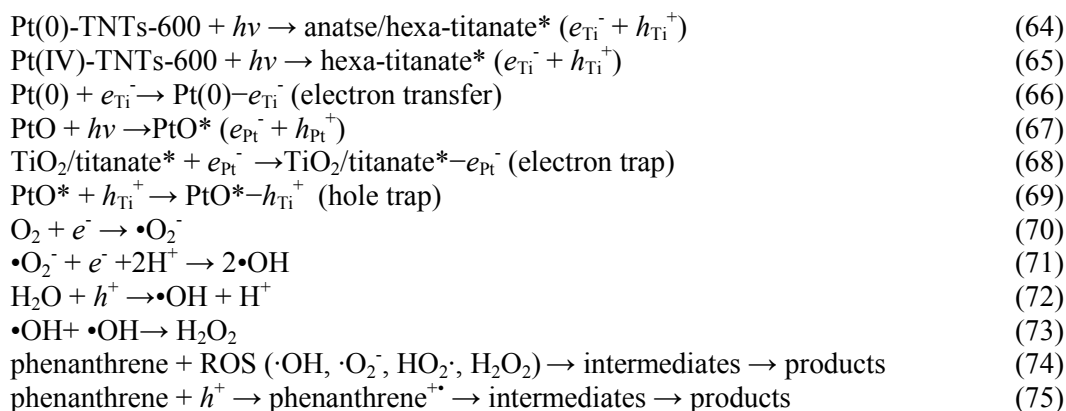


**Figure 101. PL spectra of various Ti-based materials under solar irradiation.**

Experimental conditions: material dosage = 0.2 g/L, pH = 7.0±0.2, temperature = 25±0.2 °C, no phenanthrene added.

**Figure 102** depicts the key mechanisms for the enhanced photocatalytic activity of Pt(0)-TNTs-600 and Pt(IV)-TNTs-600. Under solar irradiation, both TiO<sub>2</sub> (anatase) and TNTs (mainly hexa-titanate) can generate a conduction band ( $e^-$ , electrons) and a valence band ( $h^+$ , holes) (Equations 64 and 65). However, the pristine TiO<sub>2</sub> and titanate are not active under visible light due to their relatively high band gaps (Veldurthi et al. 2015, Zhao et al. 2016a). Moreover, the photo-generated electron-hole pairs on titanate are susceptible to recombination, resulting in a low photo-quantum yield (Li et al. 2015). In contrast, for Pt(0)-TNTs-600, the electrons can be immediately transferred to the deposited Pt metal upon excitation (Equation 66), thus inhibiting the electron-hole recombination; for Pt(IV)-TNTs-600, besides the Pt(0)-facilitated electron transfer, Pt in PtO can act as a photocatalysis center (Equation 67) (Hu et al. 2015), where electrons excited on the conduction band of PtO migrate to the conduction band of TiO<sub>2</sub> due to their conduction band offset (Equations 67 and 68), thus electron-hole recombination for both PtO and TiO<sub>2</sub> is suppressed due to electrons trapping on TiO<sub>2</sub> and holes on PtO (Equations 68 and 69) (Hu et al. 2015), resulting in enhanced photocatalytic activity. In addition, for both Pt(0)-TNTs-600 and Pt(IV)-TNTs-600, the deposited Pt lies in their band gaps, which may derive new electronic states below the band gaps (Driessen and Grassian 1998, Schierbaum et al. 1996), and thus extends the absorbance to the visible light region. The electrons can react with electron acceptors, e.g., O<sub>2</sub>, to form superoxide radicals ( $\bullet O_2^-$ ), and further to  $\bullet OH$  (Equations 70 and 71) (Driessen and Grassian 1998). The holes can oxidize water molecules and oxygen into ROS (e.g.,  $\bullet OH$  and H<sub>2</sub>O<sub>2</sub>) (Equations 72 and 73). These reactive species are responsible for degradation of phenanthrene (Equation 74). Meanwhile, phenanthrene can also be directly attacked by holes to produce the excited phenanthrene cation radical (phenanthrene<sup>+</sup>), which is further degraded via Equation 75 (Kou et al. 2009).





**Figure 102. Schematic illustration of enhanced photocatalytic activity.**  
 (a) Pt(0)-TNTs-600 and (b) Pt(IV)-TNTs-600.

## 5.2.7. Conclusions

In this section, we synthesized, characterized and tested a new class of Pt-deposited TNTs photocatalysts for highly efficient photocatalytic degradation of phenanthrene under solar light. The Pt-deposited TNTs were successfully synthesized via a simple three-step process: hydrothermal treatment of  $\text{TiO}_2$ , deposition of Pt, and calcination at  $600\text{ }^\circ\text{C}$ . The optimum Pt dosage was 0.1 wt.%, and calcination temperature was  $600\text{ }^\circ\text{C}$ . Both Pt(0)-TNTs-600 and Pt(IV)-TNTs-600 exhibited high photocatalytic activity for degradation of phenanthrene under solar light, with a first-order rate constant ( $k_1$ ) being 3 and 1.5 times of that of the parent  $\text{TiO}_2$ , respectively. Pt(0)-TNTs-600 outperformed Pt(IV)-TNTs-600 in catalyzing phenanthrene degradation. During the calcination process, tri-titanate was converted to anatase and hexa-titanate in Pt(0)-TNTs-600, but only hexa-titanate in Pt(IV)-TNTs-600. The extra anatase is photo-catalytically more active than hexa-titanate. Moreover, the calcination also converted Pt(IV) in Pt(IV)-TNTs-600 into PtO (primary) and Pt(0). For both materials, Pt(0) transfers the excited electrons, thereby inhibiting the electron-hole recombination; and for Pt(IV)-TNTs-600, PtO acts as an electron-hole

trap, which also inhibits the recombination of electron-hole pairs though less effective than Pt(0). DRS UV-vis spectra revealed that Pt(0)-TNTs-600 and Pt(IV)-TNTs-600 give a narrower optical energy gap of 3.1 and 3.3 eV, respectively, compared to 3.4 eV of TNTs, resulting in the much enhanced photocatalytic activity under visible light of these nanomaterials. Pt(0)-TNTs-600 can be separated through gravity-sedimentation, and reused in multiple cycles of operations without loss in the photocatalytic activity.

Overall, Pt(0)-TNTs-600 represents a significant step forward in development of novel photocatalysts for environmental cleanup uses, and the new material appears promising for more cost-effective photocatalytic degradation of persistent organic pollutants under solar light.

### 5.3. Photodegradation of Oil PAHs by SiO<sub>2</sub>/TiO<sub>2</sub> Composites

Silica aerogel is an effective adsorbent for petroleum hydrocarbons (Adebajo et al. 2003, Standeker et al. 2007, Wang et al. 2012), and it can float on water due to its mesoporous structure and low density. Considering the excellent photocatalytic activity of TiO<sub>2</sub> and good adsorptive performance of silica aerogel, depositing nano-TiO<sub>2</sub> onto silica aerogel may result in a highly efficient supported photocatalyst that can remove TPHs through initial adsorption and subsequent photocatalysis. In this section, a series of new composite materials, namely, silica aerogel supported TiO<sub>2</sub> (denoted as TiO<sub>2</sub>/SiO<sub>2</sub>), were synthesized through a sol-gel method, and these novel materials were found highly efficient for removing phenanthrene (and possibly other PAHs) via simultaneous adsorption and photocatalysis. Moreover, the synthetic materials can float on the water, which offer great convenience for in situ oil removal from contaminated water.

#### 5.3.1. Synthesis of SiO<sub>2</sub>/TiO<sub>2</sub>

The TiO<sub>2</sub>/SiO<sub>2</sub> composites were synthesized through a sol-gel method using silica aerogel (IC3120, 100 μm–1.2 mm, CARBOT Corporation) as a support. Specifically, the method included the following key steps: 1) 1.17 g of the silica aerogel was dispersed in 100 mL methanol and magnetically stirred for 10 min; 2) 5 mL of tetrabutyl titanate (TBOT, precursor of nano-TiO<sub>2</sub>) was added and continuously stirred for another 30 min; 3) Afterwards, a mixture of 0.26 mL DI water and 0.035 mL concentrated HNO<sub>3</sub> (15.9 M) was added in the mixture dropwise to start the hydrolysis, which lasted for another 2 h with stirring; 4) following the hydrolysis, the mixture was quickly heated to 265 °C to vent out the solvents; 5) After cooled to room temperature, the resulting material was washed with 40 mL menthol (>98%) 3 times to remove the residual organic compounds and finally dried at 80 °C for 4 h, the resultant composite material is referred to as TiO<sub>2</sub>/SiO<sub>2</sub>; and 6) TiO<sub>2</sub>/SiO<sub>2</sub> was calcinated at 400, 600 and 800 °C in a muffle furnace under atmospheric conditions, and the resulting materials are designated as TiO<sub>2</sub>/SiO<sub>2</sub>-400, TiO<sub>2</sub>/SiO<sub>2</sub>-600 and TiO<sub>2</sub>/SiO<sub>2</sub>-800, respectively.

TEM and XRD characterization methods were the same as those described in Section 5.1.1.

#### 5.3.2. Experimental methods: adsorption and photocatalysis

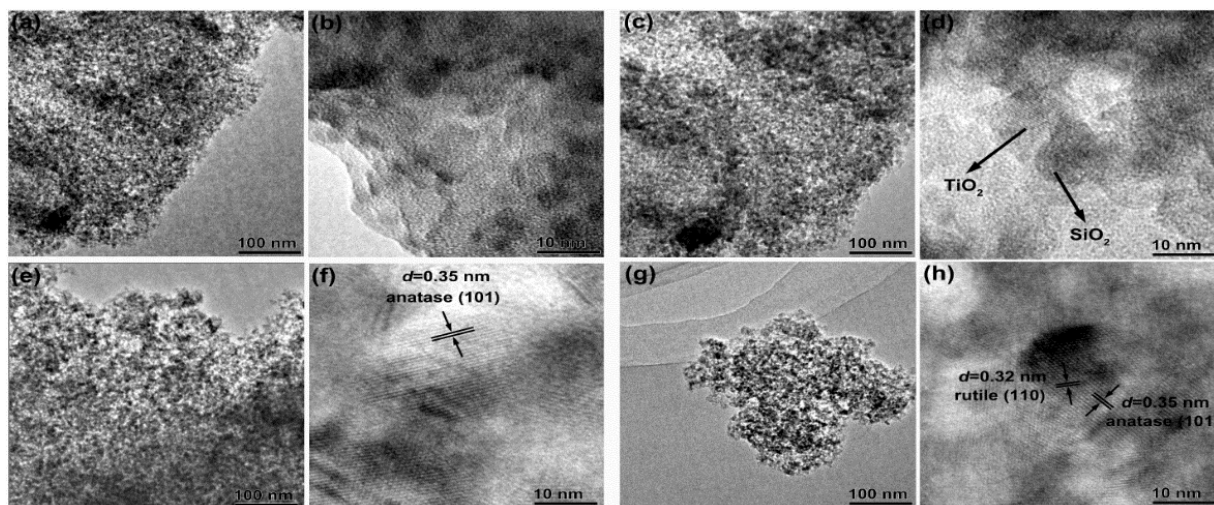
Adsorption kinetic tests were carried out in a brown glass bottle with 500 μg/L of phenanthrene (40 mL) and 0.5 g/L of the catalyst. The solution pH was adjusted to 7.0 ± 0.2 using diluted HCl and NaOH, and the mixture was shaken (200 rpm, 25±0.2 °C) in dark for 6 h. Samples were taken at the bottom of the bottle, and filtered through a 0.22 μm PTFE membrane. The concentration of phenanthrene was determined following the HPLC method as described in Section 3.2.1.2. For adsorption isotherms, the initial phenanthrene was varied from 50 to 500 μg/L with a fixed material dosage of 0.5 g/L at pH 7.0 ±

0.2. After the mixture was shaken for 4 h, samples were taken and the aqueous concentration of phenanthrene was determined after filtration of the samples. Phenanthrene was analyzed following the methods given in Section 5.1.2.

Kinetic tests were carried out to determine the removal of phenanthrene by the  $\text{TiO}_2/\text{SiO}_2$  composites due to adsorption during the initial 4 hours in dark and during the subsequent 6-hours photocatalysis under solar light. The kinetic tests used the same experimental setup as in **Figure 57** and followed similar experimental procedures as described in Section 5.1.2. At predetermined time intervals, samples were taken and membrane filtered by 0.22  $\mu\text{m}$  PTFE membrane to determine the phenanthrene concentration in the aqueous phase. At the same time, the solid particles were extracted using 3 mL of methanol for 24 h to determine the phenanthrene concentration in the solid-phase.

### 5.3.3. Characterization of $\text{TiO}_2/\text{SiO}_2$

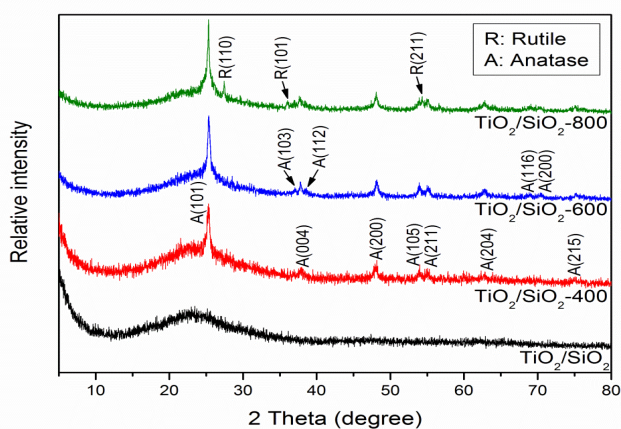
**Figure 103** shows the TEM and high resolution TEM (HRTM) images of  $\text{TiO}_2/\text{SiO}_2$  composites synthesized at the same initial Ti/Si weight ratio (1:1) but different calcination temperatures. In all cases the composite materials appear as aggregated nanoparticles. The uncalcined  $\text{TiO}_2/\text{SiO}_2$ , appear as scattered aggregates with ambiguous edges, and both  $\text{SiO}_2$  and  $\text{TiO}_2$  are amorphous as no crystal lattices were observed in the high resolution TEM (HRTEM) images (**Figures 102a** and **102b**). In contrast, the crystalline structure of  $\text{TiO}_2$  became increasingly evident as the calcination temperature was increased from 400 to 800  $^\circ\text{C}$  (**Figures 102d–102h**). For  $\text{TiO}_2/\text{SiO}_2$ -600, the interlayer distance of the formed nanoparticles was determined to be 0.35 nm, which is consistent with the crystal plane of anatase (101) (**Figure 103f**) (Xu et al. 2011, Zhao et al. 2016a). For  $\text{TiO}_2/\text{SiO}_2$ -800, both anatase (101) and rutile (110) crystal structures are observed (**Figure 103h**) (Xu et al. 2011). The TEM findings are in accordance with the XRD results (**Figure 104**).



**Figure 103. TEM and HRTEM images.**

(a, b, c, d): uncalcined  $\text{TiO}_2/\text{SiO}_2$ , (e, f):  $\text{TiO}_2/\text{SiO}_2$ -600, and (g, h):  $\text{TiO}_2/\text{SiO}_2$ -800.

**Figure 104** displays the XRD patterns of these TiO<sub>2</sub>/SiO<sub>2</sub> composites. There was no fine crystal phase observed without calcination. However, the crystallinity of TiO<sub>2</sub> became increasingly evident when the material was calcined at 400–800 °C. For TiO<sub>2</sub>/SiO<sub>2</sub>-400, the peaks at 25.3°, 37.8°, 48.1°, 53.9°, 55.0°, 62.8° and 75.1° are assigned to anatase, especially the crystal plane of A(101) (JCPDS 21-1272) (Hu et al. 2003, Huang et al. 2000). For TiO<sub>2</sub>/SiO<sub>2</sub>-600, several new peaks at 37.0°, 38.6°, 68.8° and 70.4° were observed, which are also ascribed to anatase (JCPDS 21-1272) and indicate better defined crystallinity of the anatase in TiO<sub>2</sub>/SiO<sub>2</sub>-600 (Hu et al. 2003, Huang et al. 2000). For TiO<sub>2</sub>/SiO<sub>2</sub>-800, the diffraction peak of A(101) became even sharper, and in addition, peaks for rutile phases (R(110), R(101) and R(211)) (JCPDS 21-1276) were observed (Hu et al. 2003, Huang et al. 2000). The enhanced crystallinity of TiO<sub>2</sub> gives improved photocatalytic activity, which agrees with our prior observation that higher calcination temperature gives the solids greater effectiveness to photo-degrade phenanthrene.



**Figure 104.** XRD patterns of various TiO<sub>2</sub>/SiO<sub>2</sub> composites.

### 5.3.4. Adsorption of phenanthrene by various TiO<sub>2</sub>/SiO<sub>2</sub> composite materials

**Figure 105** shows the adsorption kinetics of phenanthrene by various SiO<sub>2</sub>/TiO<sub>2</sub> composite materials. The pseudo-first-order and pseudo-second-order models are used to interpret the adsorption kinetic data (Ho and McKay 1998, 1999):

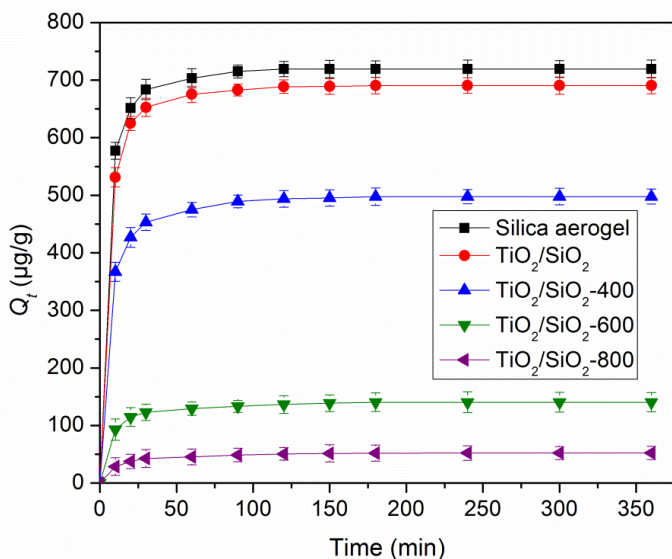
$$\text{Pseudo-first-order model: } q_t = q_e(1 - \exp(-k_1 t)) \quad (76)$$

$$\text{Pseudo-second-order model: } \frac{t}{q_t} = \frac{1}{k_2 q_e^2} + \frac{t}{q_e} \quad (77)$$

where  $q_t$  and  $q_e$  (μg/g) are the uptake of phenanthrene at time  $t$  (min) and equilibrium, respectively, and  $k_1$  (min<sup>-1</sup>) and  $k_2$  (g/(μg·min)) are the rate constants of the pseudo-first-order and pseudo-second-order kinetic models, respectively.

Rapid adsorption rates were observed for all the materials tested (**Figure 105**). Adsorption equilibrium was reached at 120 min for the plain silica aerogel, and within 180 min for all other TiO<sub>2</sub>/SiO<sub>2</sub> composite materials. At an initial phenanthrene concentration of 500 μg/L, the equilibrium uptake ( $q_e$ ) follows the order of: silica aerogel (719.4 μg/g) > TiO<sub>2</sub>/SiO<sub>2</sub> (690.6 μg/g) > TiO<sub>2</sub>/SiO<sub>2</sub>-400(497.8 μg/g) > TiO<sub>2</sub>/SiO<sub>2</sub>-600 (140.5 μg/g) > TiO<sub>2</sub>/SiO<sub>2</sub>-800 (52.2 μg/g), and the phenanthrene removal percentage: silica aerogel

(71.9%) > TiO<sub>2</sub>/SiO<sub>2</sub> (69.1%) > TiO<sub>2</sub>/SiO<sub>2</sub>-400 (49.7%) > TiO<sub>2</sub>/SiO<sub>2</sub>-600 (14.1%) > TiO<sub>2</sub>/SiO<sub>2</sub>-800 (5.2%). The pseudo-second-order kinetic model better describes the adsorption kinetic data ( $R^2 > 0.999$ ), suggesting that the rate-controlling step for adsorption is likely to be the initial diffusion and then interaction with the adsorbents (Ho and McKay 1999).



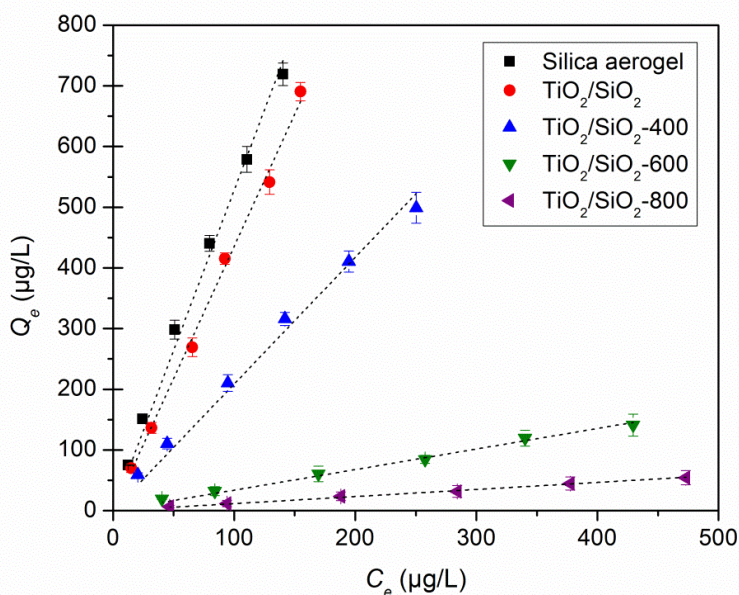
**Figure 105. Adsorption kinetics of phenanthrene by various SiO<sub>2</sub>/TiO<sub>2</sub> composite materials.**  
 Experimental conditions: Initial phenanthrene concentration = 500 µg/L, material dosage = 0.5 g/L, pH = 7.0±0.2, temperature = 25±0.2 °C.

**Table 24. Parameters of kinetic models for phenanthrene adsorption onto various SiO<sub>2</sub>/TiO<sub>2</sub> materials**

kinetic Model	Parameters	Adsorbent				
		SiO <sub>2</sub> aerogel	TiO <sub>2</sub> /SiO <sub>2</sub>	TiO <sub>2</sub> /SiO <sub>2</sub> -400	TiO <sub>2</sub> /SiO <sub>2</sub> -600	TiO <sub>2</sub> /SiO <sub>2</sub> -800
Pseudo-first-order	$q_{e,cal}^a$ (µg/g)	61.61	115.57	147.87	55.71	25.16
	$k_1$ (min <sup>-1</sup> )	0.0728	0.0700	0.0723	0.0638	0.0518
	$R^2$	0.7708	0.8656	0.9314	0.8887	0.9775
Pseudo-second-order	$q_{e,cal}$ (µg/g)	724.64	694.44	502.51	143.06	53.71
	$K_2$ (g/(mg·min))	0.0008	0.0007	0.0007	0.0013	0.0023
	$R^2$	1.0000	1.0000	1.0000	0.9999	0.9998

$q_{e,cal}$  refers to the equilibrium adsorption calculated from kinetic models.

**Figure 106** shows the adsorption isotherms of phenanthrene by various  $\text{SiO}_2/\text{TiO}_2$  composite materials. Linear, Langmuir and Freundlich isotherm models are tested to interpret the isotherm data, and **Table 24** lists the best-fitted model parameters. Consistent with the kinetic test results, the precursor, silica aerogel showed the highest adsorption capacity ( $Q_{max} = 4386.0 \mu\text{g/g}$ ) for phenanthrene, indicating the great efficiency of silica aerogel for removal of phenanthrene via adsorption. The linear model can well describe the adsorption of phenanthrene by all the materials ( $R^2 > 0.98$ ). Hydrophobic effect is considered the dominant mechanism for phenanthrene adsorption onto these inorganic materials (Fang et al. 2008, Lorphensri et al. 2006, Wang et al. 2001). The non-calcinated  $\text{TiO}_2/\text{SiO}_2$  also showed very high adsorption capacity, with a distribution coefficient ( $K_d$ ) of 4.36 L/g that is only slightly lower than that of silica aerogel (5.28 L/g). However, the adsorption capacity greatly decreased upon calcination, and the higher the calcination temperature, the lower the adsorption ( $K_d = 2.09, 0.34$  and  $0.12$  for  $\text{TiO}_2/\text{SiO}_2$ -400,  $\text{TiO}_2/\text{SiO}_2$ -600 and  $\text{TiO}_2/\text{SiO}_2$ -800, respectively). For  $\text{TiO}_2/\text{SiO}_2$ -800, the maximum Langmuir adsorption capacity is  $163.9 \mu\text{g/g}$ , which is only 3.7% of that for uncalcined  $\text{TiO}_2/\text{SiO}_2$ . However, as to be shown later on, the photocatalytic activity is enhanced due to the enhanced crystallinity at higher temperatures. In addition, while adsorption of PAHs on AC is often irreversible, the affinity towards the calcinated composite materials is lowered, which is in favor of the subsequent photodegradation.



**Figure 106. Adsorption isotherms of phenanthrene by various  $\text{SiO}_2/\text{TiO}_2$  composite materials.** Experimental conditions: Initial phenanthrene concentration = 50–500  $\mu\text{g/L}$ , material dosage = 0.5 g/L, pH =  $7.0 \pm 0.2$ , temperature =  $25 \pm 0.2$  °C.

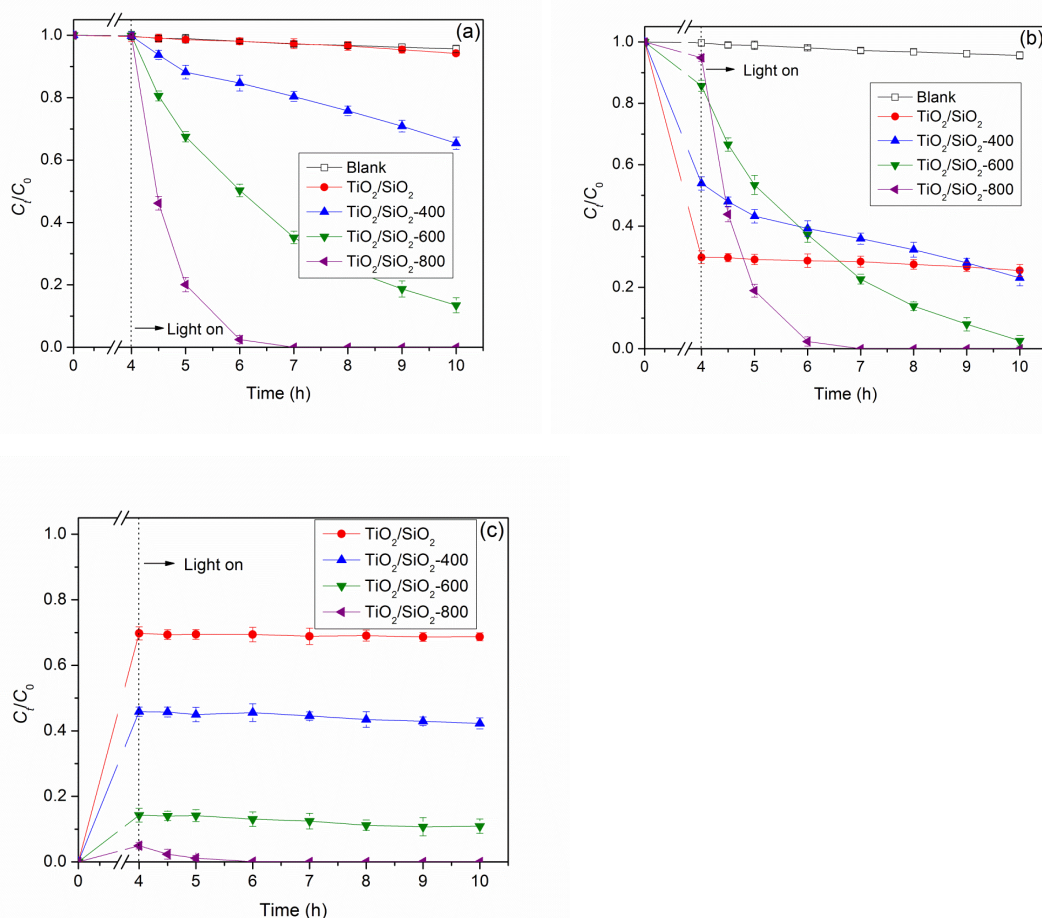


**Table 25. Parameters of isotherm models for phenanthrene adsorption onto various SiO<sub>2</sub>/TiO<sub>2</sub> materials**

Isotherm Model	Parameters	Adsorbent				
		SiO <sub>2</sub> aerogel	TiO <sub>2</sub> /SiO <sub>2</sub>	TiO <sub>2</sub> /SiO <sub>2</sub> -400	TiO <sub>2</sub> /SiO <sub>2</sub> -600	TiO <sub>2</sub> /SiO <sub>2</sub> -800
Linear	$K_d$ (L/g)	5.28	4.36	2.09	0.34	0.12
	$R^2$	0.9924	0.9959	0.9885	0.9913	0.9950
Langmuir	$Q_{max}$ (μg/g)	4385.97	3816.79	1015.23	256.73	163.94
	$b$ (L/μg)	0.0014	0.0012	0.0030	0.0019	0.0009
	$R^2$	0.9996	0.9987	0.9949	0.9873	0.9963
Freundlich	$K_F$ (μg/g·(L/μg) <sup>1/n</sup> )	7.74	4.79	4.32	0.76	0.19
	$n$	1.09	1.02	1.16	1.17	1.09
	$R^2$	0.9988	0.9975	0.9989	0.9953	0.9977

### 5.3.5. Photocatalysis of phenanthrene by various TiO<sub>2</sub>/SiO<sub>2</sub> composite materials

Figure 107a shows that during the photocatalysis process, the total phenanthrene concentration in the reactor system almost did not change in the presence of uncalcined TiO<sub>2</sub>/SiO<sub>2</sub>, while phenanthrene in the aqueous phase decreased by 70.2%, indicating that all the removal was due to adsorption, i.e. uncalcined TiO<sub>2</sub>/SiO<sub>2</sub> did not offer any photocatalytic activity under solar light. In contrast, the total phenanthrene concentration decreased by 35% and 88% in the presence of TiO<sub>2</sub>/SiO<sub>2</sub>-400 and TiO<sub>2</sub>/SiO<sub>2</sub>-600, respectively, in the end of the tests, indicating much enhanced photocatalytic activity due to calcination. However, phenanthrene adsorbed in the solid phase remained about the same, indicating the adsorption inhibited the photodegradation of phenanthrene (Figure 107c). The total removal efficiency for the aqueous phenanthrene by TiO<sub>2</sub>/SiO<sub>2</sub>-600 was 97.4% at 10 h, of which 86.5% was due to photodegradation and 10.9% to adsorption. TiO<sub>2</sub>/SiO<sub>2</sub>-800 was most effective (Figure 107b), and it was able to completely remove phenanthrene from water within 3 hours of photocatalysis, and the initially adsorbed phenanthrene (5.2% of total phenanthrene) was completely photodegraded after 3 hours of the photocatalysis.



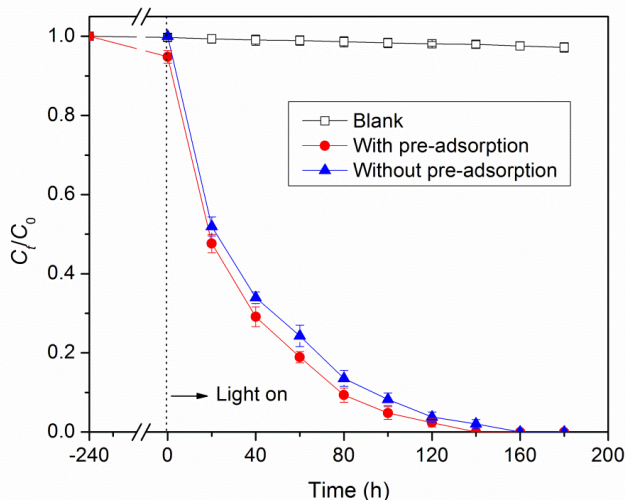
**Figure 107. Photocatalytic degradation of phenanthrene.**

Total phenanthrene (a), dissolved phenanthrene (b), and adsorbed phenanthrene (c) in the adsorption-photocatalysis system in the presence of various TiO<sub>2</sub>/SiO<sub>2</sub> composite materials. Experimental conditions: Initial phenanthrene concentration = 500 µg/L; material dosage = 0.5 g/L; pH = 7.0±0.2; temperature = 25±0.2 °C.



Therefore, the calcination temperature plays a critical role in the photocatalytic activity of the material. Strong adsorption may inhibit the photodegradation process. For the TiO<sub>2</sub>/SiO<sub>2</sub>-800 composite, both TiO<sub>2</sub> and SiO<sub>2</sub> are important for efficient removal of phenanthrene, where TiO<sub>2</sub> acts as the primary photocatalyst and silica serves as the support for nano-TiO<sub>2</sub>. As a weak adsorbent for phenanthrene, the silica support can facilitate the photodegradation by loosely adsorbing phenanthrene from solution to the surface of material, and at the same time act as an electron transfer medium.

To test the effect of the initial adsorption phase, the photodegradation tests were also carried out without the initial 4-h adsorption, i.e., the source solar light was turned on immediately after TiO<sub>2</sub>/SiO<sub>2</sub>-800 was added in the phenanthrene solution. **Figure 108** shows that the pre-adsorption process only slightly enhanced the removal of phenanthrene by TiO<sub>2</sub>/SiO<sub>2</sub>-800, with a slightly higher apparent rate constant ( $k_1 = 0.0298 \text{ min}^{-1}$  or  $0.0266 \text{ min}^{-1}$  with or without pre-adsorption), and 100% phenanthrene removal was achieved in 140 min with pre-adsorption and in 160 min without pre-adsorption. For both cases, phenanthrene was extracted from the material, and no adsorbed phenanthrene was detected at 140 and 160 min, respectively, indicating complete degradation of phenanthrene was achieved.

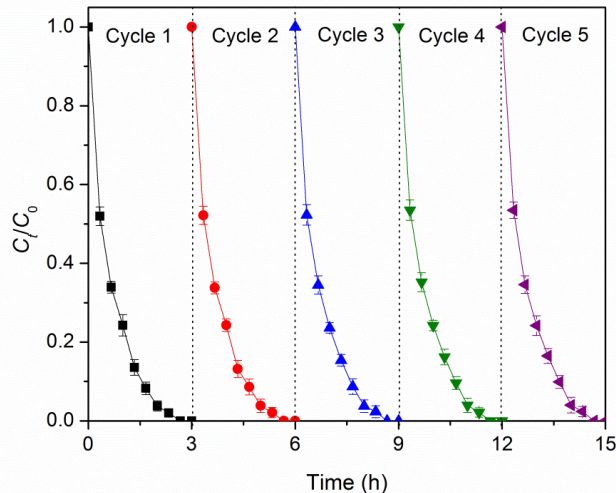


**Figure 108. Removal of phenanthrene by TiO<sub>2</sub>/SiO<sub>2</sub>-800 with and without pre-adsorption.**

Experimental conditions: Initial phenanthrene concentration = 500 µg/L; material dosage = 0.5 g/L; pH = 7.0±0.2; temperature = 25±0.2 °C.

### 5.3.6. Reusability of TiO<sub>2</sub>/SiO<sub>2</sub>-800

TiO<sub>2</sub>/SiO<sub>2</sub>-800 was reused in 5 consecutive cycles for removal of phenanthrene without pre-adsorption (**Figure 109**). The results indicate that 100% of phenanthrene was effectively removed after 5 cycles of repeated uses without significant rate drop, and no phenanthrene was adsorbed on material after extraction in each cycle, indicating the material can be reused in multiple cycles of operations.



**Figure 109. Reusability of TiO<sub>2</sub>/SiO<sub>2</sub>-800 for removal of phenanthrene over 5 consecutive cycles.** Experimental conditions: Initial phenanthrene concentration = 500 µg/L; material dosage = 0.5 g/L; pH = 7.0±0.2; temperature = 25±0.2 °C.

### 5.3.7. Conclusions

In this section, we prepared a new class of silica aerogel supported TiO<sub>2</sub> (TiO<sub>2</sub>/SiO<sub>2</sub>) composite materials through initial sol-gel method and subsequent calcination, and tested the materials for removal of phenanthrene through adsorption and photocatalysis. Anatase was formed at calcination temperature of 400 and 600 °C, while mixed crystal phases of anatase and rutile were found at 800 °C. All the TiO<sub>2</sub>/SiO<sub>2</sub> composite materials were able to rapidly adsorb phenanthrene, with equilibrium being reached within 180 min. Higher calcination temperature resulted in better crystallinity of TiO<sub>2</sub>, higher photocatalytic activity, and reduced the adsorption affinity of the material toward phenanthrene. TiO<sub>2</sub>/SiO<sub>2</sub>-800 showed minimal phenanthrene uptake (only 5.2% of total phenanthrene) but the strongest photocatalytic activity, and it was able to completely degrade phenanthrene within 3 h without any residual in the solid phase. For TiO<sub>2</sub>/SiO<sub>2</sub>-800, TiO<sub>2</sub> acts as the primary photocatalyst and silica serves as the support for nano-TiO<sub>2</sub>, which can facilitate accumulation and subsequent photodegradation of phenanthrene at the surface of the material by acting as a weak adsorbent as well as an electron transfer medium. The material can be repeatedly used in multiple cycles of operations without significant loss in its photocatalytic activity.

## 5.4. Removal of Oil Components by Activated Charcoal Supported Titanate Nanotubes through Adsorption and Photocatalysis

Conventional adsorbents (e.g., activated carbon) and emerging materials (e.g., carbon nanotubes [CNTs]) have been widely studied for removal of oil components including PAHs (Chen et al. 2008, Chen et al. 2007b, Garcia et al. 2004, Pan and Xing 2008, Wang et al. 2014, Wang et al. 2008, Wang et al. 2011, Yang et al. 2006a, Yang and Xing 2007, Zhao et al. 2014). In recent years, many researchers have reported that carbon nanomaterials (CNMs) can effectively adsorb PAHs (Chen et al. 2008, Chen et al. 2007b, Pan and Xing 2008, Wang et al. 2014, Wang et al. 2008, Wang et al. 2011, Yang et al. 2006a, Yang and Xing 2007, Zhao et al. 2014). For instance, single-walled and multi-walled CNTs were found to

offer 2–4 orders of magnitudes higher adsorption capacities for phenanthrene than fullerene (Yang et al. 2006a). In terms of adsorption mechanism, Chen et al. (2007b) proposed that the strong adsorption of nitroaromatics by CNTs was due to  $\pi$ - $\pi$  interactions between nitroaromatic molecules (electron acceptors) and the highly polarizable graphene sheets (electron donors). Though these emerging materials may offer improved performances than conventional activated charcoals (ACs), their much higher material cost prohibits their practical applications. Moreover, the potential nano-toxicity, and occupational and environmental health risks of CNMs remain under active investigations (Akhavan and Ghaderi 2010, Lam et al. 2006, Nel et al. 2006).

Both conventional and emerging carbonaceous adsorbents have been designed to adsorb and concentrate hydrophobic contaminants without chemical transformation. Often times, such adsorption-based technologies are limited by some key technical obstacles, such as regeneration and reusability of spent adsorbents and treatment of spent regenerant (Dąbrowski et al. 2005, Liu et al. 2013c). To facilitate “green” and cost-effective regeneration and reuse of the spent adsorbents, it has been desirable to develop composite materials that combine high adsorption capacity and reactivity. For instance, catalysts-modified CNMs have been shown to be able to adsorb and catalytically degrade organic compounds (Liu et al. 2013c, Parlett et al. 2013, Yang et al. 2011b), and the chemical transformation also regenerates the material.

Taking advantage of the high adsorption capacity of AC and photocatalytic activity of TNTs, we conceived a novel composite material, referred to as TNTs@AC, by depositing TNTs onto a common activated charcoal. The newly synthesized TNTs@AC is expected to show the following synergistic effects: 1) the high adsorption capacity of AC will concentrate the target organic pollutants onto the surface of TNTs@AC, facilitating the subsequent photocatalytic degradation; 2) the high photocatalytic activity of TNTs will facilitate effective degradation of the adsorbed pollutants, which also regenerates the spent TNTs@AC; 3) the hydrothermal treatment during the material synthesis may facilitate micro-AC coating on TNTs, and the AC-amended TNTs will enhance both the adsorption capacity and kinetics; and 4) AC on TNTs may serve as the electron shuttles and prevent recombination of the excited holes and electrons, and thus enhance the photodegradation efficacy.

As such, the overall goal of this section of study was to develop a novel bi-functional material that offers both high adsorption capacity and efficient photodegradation and regeneration for rapid and complete removal of oil PAHs (and possibly other trace organic contaminants) in water. Specifically, using phenanthrene as a model oil PAH, this work aimed to: 1) synthesize and characterize the desired TNTs@AC; 2) test the adsorption kinetics and capacity of TNTs@AC using phenanthrene as a model PAH; 3) examine the effects of various water chemistry conditions on adsorption, including pH, ionic strength and natural organic matters (NOMs); 4) evaluate the photo-degradation and regeneration efficiency and material reusability; and 5) elucidate the underlying mechanisms of the reaction of phenanthrene with TNTs@AC.

#### **5.4.1. Synthesis of TNTs@AC**

#### **5.4.2. Methods on adsorption and photocatalysis**

Phenanthrene adsorption kinetic experiments were carried out in the dark using brown glass vials (40 mL) with Teflon-lined caps. Adsorption kinetic tests were conducted at pH 7 with an initial concentration of phenanthrene of 500  $\mu\text{g/L}$  and TNTs@AC dosage of 0.5 g/L. The tests were initiated by adding TNTs@AC into the respective phenanthrene solutions and then the change in phenanthrene concentration was followed for 24 h while shaking at 200 rpm. At predetermined times, the vials were sacrificially sampled. After centrifuging at 8000 rpm (6400 g-force) for 5 min, the supernatants were sampled and analyzed for phenanthrene. For comparison, phenanthrene adsorption kinetics by original untreated AC

and hydrothermally-treated AC (AC-treated) were also tested. Adsorption isotherms were constructed in a similar fashion with an initial phenanthrene concentration of 50–1000 µg/L and a fixed TNTs@AC dosage of 0.5 g/L at pH 7, and the mixtures were equilibrated for 24 h while shaking. For comparison, adsorption isotherms by AC, AC-treated and TNTs were also obtained. To further investigate the adsorption behaviors of TNTs@AC at high phenanthrene concentrations, sequencing batch isotherm tests were conducted. After the adsorption reached equilibrium for initial phenanthrene concentration of 1000 µg/L, phenanthrene stock solution was further injected to increase the initial concentration by 400 µg/L each time. Phenanthrene concentration in solution at another round of equilibrium, and the sequencing batch tests lasted for 10 runs, i.e., up to 5000 µg/L for the cumulative initial phenanthrene concentration.

To test the effects of pH, the equilibrium tests were carried out at an initial phenanthrene concentration of 500 µg/L, a TNTs@AC dosage of 0.5 g/L, and final solution pH 3–11 (adjusted using dilute HCl and NaOH). To probe effects of ionic strength, the tests were carried out in the presence of 0–10 mM of NaCl and CaCl<sub>2</sub>. Likewise, effects of humic acid were tested by measuring equilibrium uptake of phenanthrene in the presence of 0–10 mg/L as TOC of LHA.

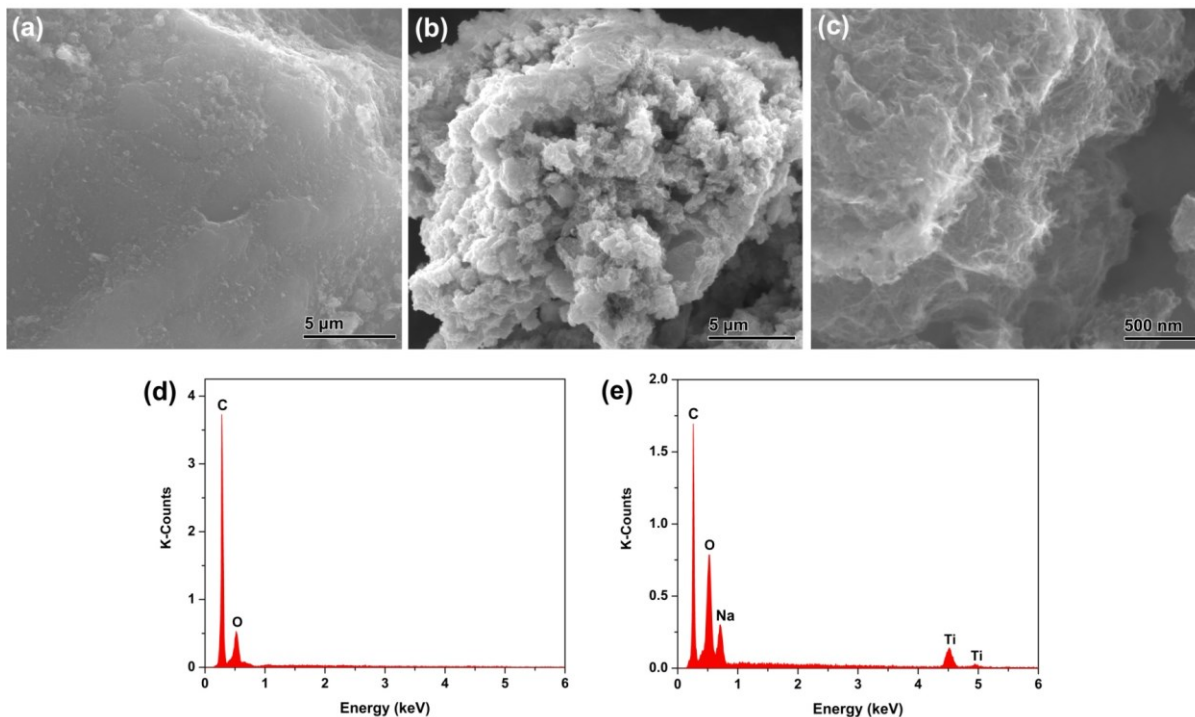
Regeneration of spent TNTs@AC was performed through photodegradation of phenanthrene adsorbed on TNTs@AC. Upon adsorption equilibrium, the mixture was left still for 1 h to allow the spent TNTs@AC to settle by gravity (>99% of TNTs@AC settled). Then, ~90% of the supernatant was removed, and the residual solid-liquid mixture was transferred into a glass photo-reactor with a quartz cover. The reactor was then placed under UV light (365 nm, 1.42 mW/cm<sup>2</sup>). After 60 min of UV irradiation, the liquid was decanted and the solid was extracted for remaining phenanthrene using 20 mL methanol at 80 °C for 4 h. (Karapanagioti et al. 1999) The regenerated TNTs@AC were then reused in another cycle to adsorb and degrade phenanthrene, and the adsorption-regeneration cycles were repeated 5 times to probe reusability of the material.

For batch tests on adsorption of oil components from DWAO by TNTs@AC, a series of glass vials with 40 mL DWAO (preparation method see Seciton 3.1.1.6) was used in the batch adsorption experiments. For adsorption kinetics, 0.025 or 0.05 g of TNTs@AC was added into each vial, and the adsorption was followed for different times (0–24 h) under rotating. Adsorption isotherm experiments were conducted in a similar manner with material dosage varying from 0.005 to 0.05 g and the adsorption lasted for 24 h. After adsorption under rotating, samples were taken and immediately centrifuged (8000 rpm, 5 min) to separate the material. The various oil components (TPHs, *n*-alkanes and PAHs) remaining in the aqueous phase were analyzed following our previous methods, which were also presented in Section 3.3.1.5 (Fu et al. 2014).

Regeneration of spent TNTs@AC was performed through photodegradation of oil organics in DWAO adsorbed on TNTs@AC under UV light. Upon adsorption equilibrium using 1.25g/L of TNTs@AC, the mixture was left still for 1 h to achieve the settling of > 99% spent TNTs@AC. After that, ~90% of the supernatant was removed, and the residual solid-liquid mixture was transferred into a glass photo-reactor with a quartz cover, which was then placed under UV light (365 nm, 1.42 mW/cm<sup>2</sup>) to start photo-degradation. The photo-reaction lasted for 4 hours and samples were taken every 1 hour. To quantify the residual oil components (TPHs, *n*-alkanes and PAHs) on the material phase after photo-degradation, TNTs@AC were separated and extracted using 10 mL DCM and then concentrated to 4 mL for further measurement.

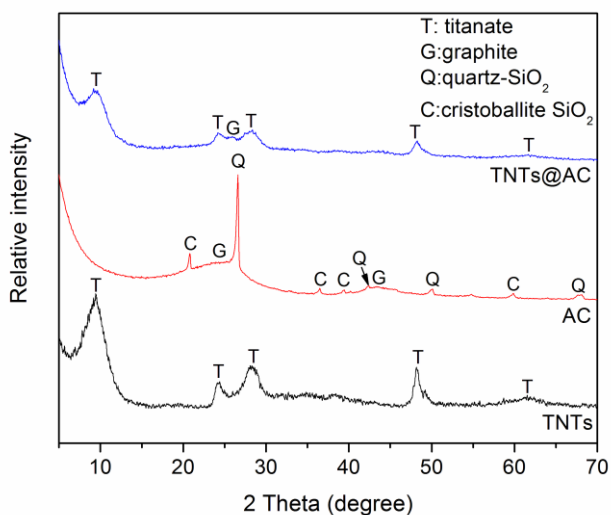
### 5.4.3. Characterizations of TNTs@AC

**Figure 110** presents the SEM images of the parent AC and TNTs@AC. While the surface of AC appeared bulky, flat and smooth (**Figure 110a**), the surface of TNTs@AC appeared rather rough and full of clusters of aggregates (**Figure 110b**). A close-up of the surface revealed that the needle-like TNTs formed an interweaved network spreading throughout the surface (**Figure 110c**). The length of the nanotubes stretched up to hundreds of nanometers. The EDS (**Figures 109d** and **109e**) reveal four major elements C, O, Na and Ti on the surface of TNTs@AC, indicating that TNTs were not just simply coated on AC, rather the nanotubes are intermingled with AC, i.e., some AC is also coated on TNTs.



**Figure 110.** SEM images of (a) AC and (b, c) TNTs@AC; EDS spectra of (d) AC and (e) TNTs@AC.

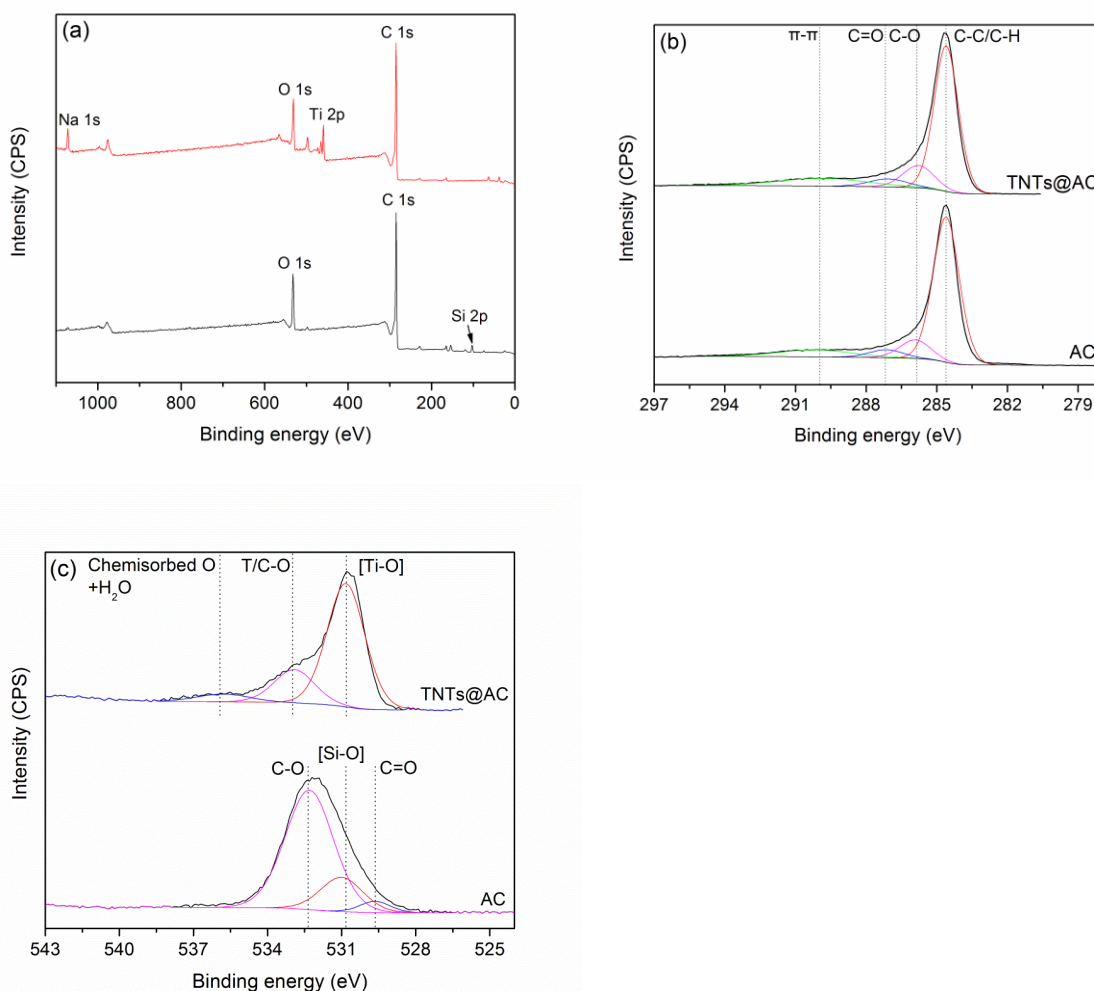
**Figure 111** displays the XRD patterns of neat TNTs, AC and TNTs@AC. For neat TNTs, the peak at 9.4°, 24.4°, 28.1°, 48.2° and 61.5° are all assigned to sodium tri-titanate (Liu et al. 2013c, Sun and Li 2003, Xiong et al. 2010), with a basic structure of  $\text{Na}_x\text{H}_{1-x}\text{Ti}_3\text{O}_7$  ( $x = 0-0.75$ , depending on the remaining sodium). The tri-titanate is composed of corrugated ribbons of triple edge-sharing  $[\text{TiO}_6]$  as a skeletal structure and  $\text{H}^+/\text{Na}^+$  located in interlayers (Chen et al. 2002, Liu et al. 2013c, Sun and Li 2003). In addition, the peak at 9.4° represents the interlayer distance (crystal plan (020)) of TNTs (Chen et al. 2002, Liu et al. 2013c, Sun and Li 2003). For AC, the two peaks at 26° and 43° are attributed to the diffractions of crystal planes of graphite (002) and (100), respectively (Hoang Anh et al. 2012, Quinones et al. 2014, Rey et al. 2012). For TNTs@AC, all the peaks observed for TNTs remained, and in addition, the graphite (002) peak was observed, confirming the SEM finding that AC is covered by TNTs with some AC coated on the surface TNTs.



**Figure 111.** XRD patterns of TNTs, AC and TNTs@AC.



**Figure 112** displays XPS spectra of AC and TNTs@AC, and 7.1% of Ti and 1.7% of Na are detected for TNTs@AC. 5.0% of Si in AC was from the impurities, quartz and cristoballite-SiO<sub>2</sub> as shown in XRD patterns (**Figure 110**). While after hydrothermal treatment in 10 M NaOH at 130 °C, the SiO<sub>2</sub> was dissolved in the high concentration NaOH and then washed away in the subsequent washing process. Based on the Na/Ti ratio and the general molecular formula of Na<sub>x</sub>H<sub>1-x</sub>Ti<sub>3</sub>O<sub>7</sub> for TNTs (Liu et al. 2013c, Sun and Li 2003), the compositions of the synthetic TNTs can be identified as Na<sub>0.7</sub>H<sub>1.3</sub>Ti<sub>3</sub>O<sub>7</sub>. Based on carbon content in AC (82.1%) and Ti mass added, the overall mass ratio of AC to TNTs in the composite material is ~1.7:1. The high resolution spectra of C 1s appeared similar before and after the hydrothermal treatment (**Figure 112b**), while the C atomic percent associated with the  $\pi$ - $\pi$  bond increased from 9.9% for AC to 13.0% for TNTs@AC (**Table 26**), indicating that TNTs@AC may offer stronger adsorption of aromatic organic compounds through  $\pi$ - $\pi$  interactions (Puziy et al. 2008). The high resolution spectra of O 1s (**Figure 112c**) reveal that the lattice O increased from 22.6% for AC (impurity [Si-O]) to 72.8% for TNTs@AC ([Ti-O<sub>6</sub>]) (**Table 26**) (Hoang Anh et al. 2012, Puziy et al. 2008, Yang et al. 2008), confirming accumulation of TNTs on AC. The O peak at 532.3 eV in TNTs@AC is assigned to Ti-O/C-O, which suggests formation of a linkage of C-O-Ti between TNTs and AC.



**Figure 112. XPS spectra of AC and TNTs@AC.**

(a) Survey XPS, (b) high resolution of C 1s, and (c) high resolution of O 1s.

**Table 26. Atomic percent of different compositions of C 1s and O 1s**

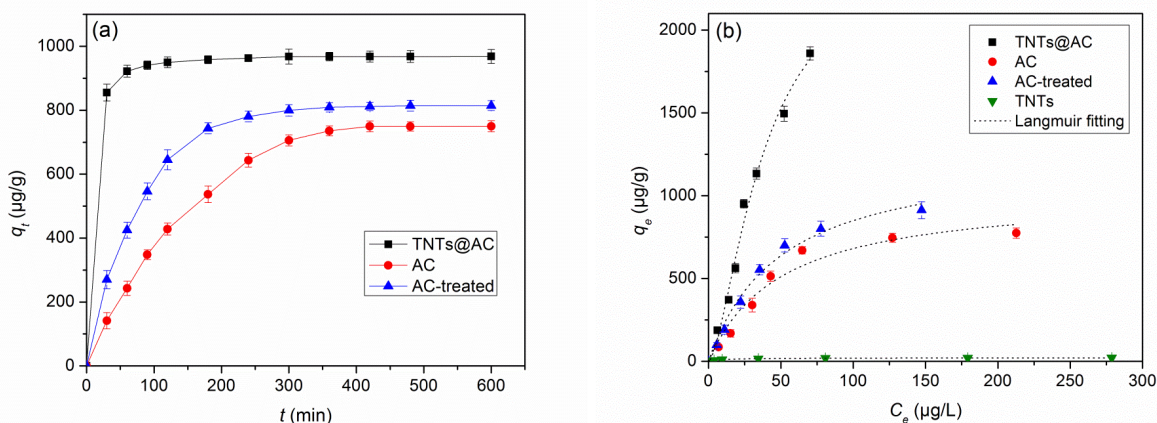
Region	AC		TNTs@AC		Assignment
	Position (eV)	At%	Position (eV)	At%	
C 1s	284.6	73.7	284.6	67.6	C-C/C-H
	285.9	11.1	285.8	13.4	C-O
	287.1	5.3	287.1	6.0	C=O
	290.1	9.9	289.8	13.0	$\pi$ - $\pi$
O 1s	529.7	4.5	-	-	C=O
	530.6	19.2	530.9	72.8	[Ti-O <sub>6</sub> ]/ [Si-O]
	532.3	76.3	532.9	21.0	Ti/C-O
	-	-	535.8	6.2	Chemisorbed O + H <sub>2</sub> O

#### 5.4.4. Adsorption of phenanthrene by TNTs@AC

**Figure 113a** shows adsorption kinetics of phenanthrene by TNTs@AC. TNTs@AC displayed rapid uptake rate. The adsorption equilibrium was reached in 180 min, with a high removal efficiency of 96.8% at equilibrium, and most (> 92%) of the adsorption capacity was filled in the first 60 min. In contrast, the parent AC showed much slower kinetics and lower phenanthrene capacity (74.9% removal at 600 min). Furthermore, the hydrothermally treated AC showed only slightly enhanced kinetics and equilibrium uptake compared to the original AC, and much lower capacity than TNTs@AC. These observations indicate that the TNTs has an important role in phenanthrene adsorption by providing more accessible reaction sites and added adsorption capacity. **Table 27** shows that the pseudo-second-order model best-fits the experimental kinetic data ( $R^2=1$ ) for TNTs@AC, whereas the intraparticle diffusion model performs worst, which differs from standard AC where film or intraparticle diffusion often controls the adsorption rate (Valderrama et al. 2008), suggesting that the rate-controlling step for TNTs@AC is due to chemical interactions (Ho and McKay 1999).

**Figure 113b** compares the adsorption isotherms of phenanthrene by TNTs@AC, parent AC, treated AC, and neat TNTs. Neat TNTs showed only negligible phenanthrene uptake (< 21  $\mu\text{g/g}$ ), whereas TNTs@AC offered the highest adsorption capacity. Both the dual-mode model and classic Langmuir model fit the isotherm data well for TNTs@AC (**Table 28**). The maximum Langmuir capacity for phenanthrene on TNTs@AC was 12.1 mg/g, which is  $\sim 11.5$  and 9.2 times higher than those of AC (1.1 mg/g) and AC-treated (1.3 mg/g), respectively. The better fit of the dual-mode model suggests that sorption of phenanthrene to TNTs@AC is attributed to combined adsorption on the AC surface and “hole-filling” or capillary condensation in the nanotubes, which mechanistically differs from the classic dual-mode adsorption model (Zhao et al. 2002b, Zhao et al. 2001a, Zhao et al. 2001b). The  $K_d$  value for TNTs@AC obtained from dual-mode model is as high as 16.6 L/g, which far exceeds that for the virgin AC (0.46 L/g). The adsorption capacity of TNTs@AC far exceeded the simple sum of those of neat TNTs and AC-treated. This unusual and novel finding reflects the synergy between AC and TNTs and is attributed to the different adsorption mechanisms. Based on the XPS spectra and the structures of TNTs@AC (shown in TEM images later), adsorption of phenanthrene is through, in addition to the standard hydrophobic interactions as for conventional AC, the enhanced  $\pi$ - $\pi$  interaction (Chingombe et al. 2005, Garcia et al. 2004, Pan and Xing 2008, Wang et al. 2011) and the hole-filling mechanism of the AC-coated TNTs on the surface.





**Figure 113. Phenanthrene adsorption kinetics and isotherms.**

(a) Adsorption kinetics and (b) isotherms of phenanthrene by AC, AC-treated, neat TNTs and TNTs@AC. Experimental conditions: For kinetics, initial phenanthrene = 500  $\mu\text{g/L}$ , material dosage = 0.5 g/L. For isotherms by TNTs@AC, initial phenanthrene = 500–1000  $\mu\text{g/L}$ , material dosage = 0.5 g/L, pH = 7.0; For isotherms by other materials, initial phenanthrene = 10–600  $\mu\text{g/L}$ , material dosage = 0.5 g/L, pH = 7.0.

**Table 27. Kinetic model parameters for adsorption of phenanthrene by TNTs@AC**

Model	Parameter	Material		
		TNTs@AC	AC	AC-treated
Pseudo-first-order model	$q_{e,cal}^a$ ( $\mu\text{g/g}$ )	175.93	778.99	570.74
	$k_1$ ( $\text{min}^{-1}$ )	0.0341	0.0064	0.0069
	$R^2$	0.9083	0.8850	0.7664
Pseudo-second-order model	$q_{e,cal}^a$ ( $\mu\text{g/g}$ )	970.87	925.93	884.96
	$k_2$ ( $\text{g}/(\mu\text{g}\cdot\text{min})$ )	$4.08 \times 10^{-4}$	$9.28 \times 10^{-6}$	$2.71 \times 10^{-5}$
	$R^2$	1.0000	0.9480	0.9913
Intraparticle diffusion model	$k_{int}$ ( $\mu\text{g}/(\text{g}\cdot\text{min}^{0.5})$ )	4.34	34.70	26.97
	$C$ ( $\mu\text{g/g}$ )	882.74	25.40	271.69
	$R^2$	0.6188	0.9137	0.7922
	$q_{e,exp}^b$ ( $\mu\text{g/g}$ )	968.42	749.68	814.38

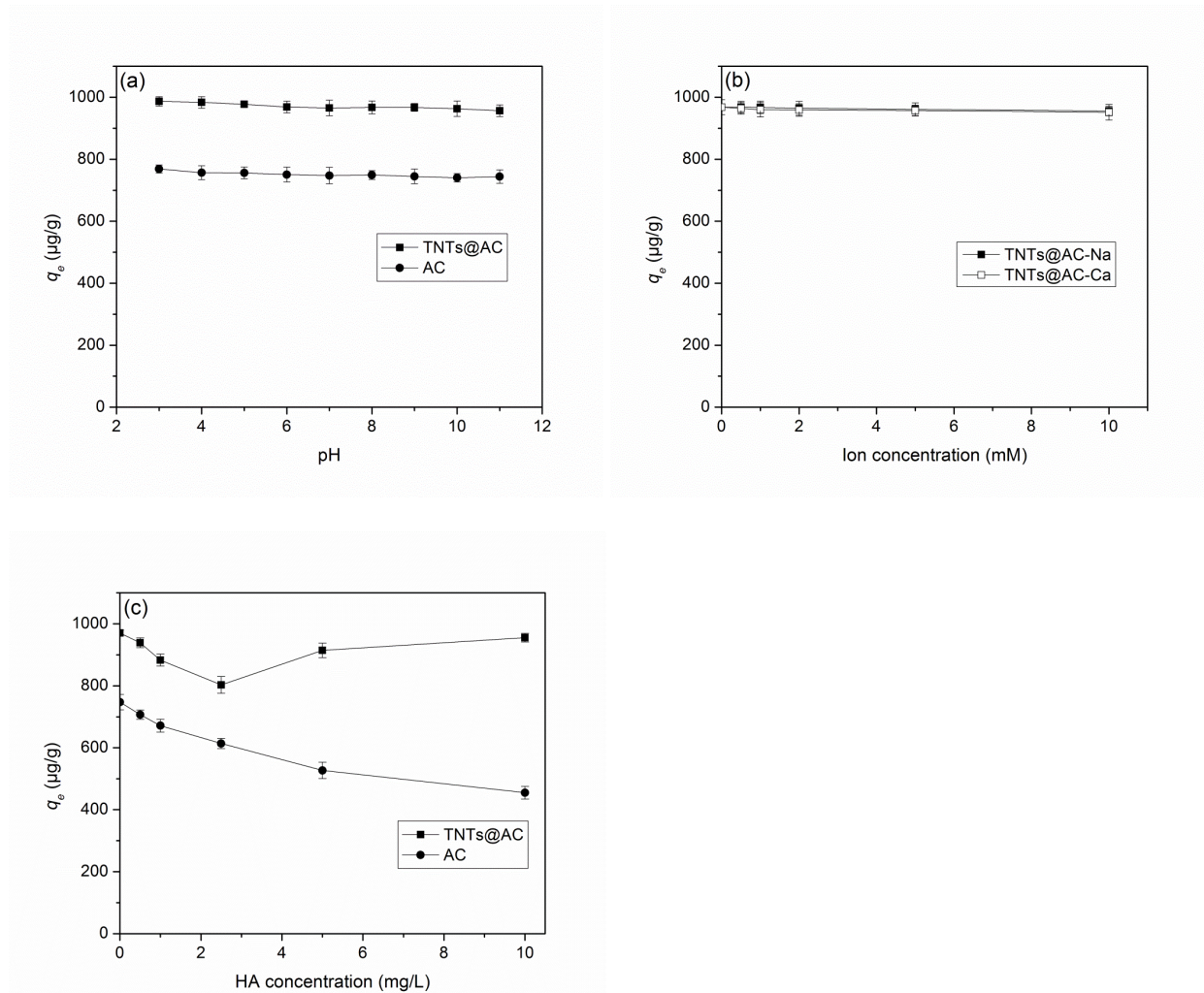
<sup>a</sup> Calculated adsorption capacity from kinetic models.

<sup>b</sup> Experimentally measured adsorption capacity from experiments.

**Table 28. Isotherm model parameters for adsorption of phenanthrene by AC, TNTs, and TNTs@AC**

Model	Parameter	Material			
		TNTs@AC	AC	AC-treated	TNTs
Linear model	$K_d$ (L/g)	28.8	4.9	7.8	0.1
	$R^2$	0.9591	0.4670	0.5869	0.1330
Langmuir model	$Q_{max}$ ( $\mu\text{g/g}$ )	12135.9	1052.6	1315.4	21.1
	$b$ (L/ $\mu\text{g}$ )	0.0029	0.0162	0.0165	0.1088
	$R^2$	0.9954	0.9475	0.9630	0.9973
Freundlich model	$K_F$ ( $\mu\text{g/g} \cdot (\text{L}/\mu\text{g})^{1/n}$ )	42.8	29.5	34.95	5.1
	$n$	1.10	1.48	1.40	3.60
	$R^2$	0.9803	0.9032	0.9454	0.9240
Dual-mode model	$K_d$ (L/g)	16.6	0.46	0.52	0.007
	$Q_L$ (mg/g)	1323.7	913.4	1162.3	20.2
	$b$ (L/mg)	0.018	0.023	0.022	0.112
	$R^2$	0.9916	0.9589	0.9869	0.9978

**Figure 114a** shows that TNTs@AC performed consistently well ( $> 950 \mu\text{g/g}$ ) over the broad pH range of 3–11. In addition, only 0.037% of Ti was dissolved into the solution even at pH 3, and no soluble Ti was detected in alkaline solutions, indicating the strong material stability of TNTs@AC (Bavykin et al. 2006, Wang et al. 2013a). **Figure 114b** displays that the presence of 10 mM NaCl and  $\text{CaCl}_2$  had statistically insignificant effect on phenanthrene uptake based on t tests ( $p > 0.05$ ). HA exhibited quite different effects on TNTs@AC and AC (**Figure 114c**). First, TNTs@AC was shown much more resistant to the organic fouling than the parent AC. Second, HA affects the adsorption capacity of AC and TNTs@AC in a quite different manner. When HA concentration was increased from 0 to 2.5 mg/L as TOC, phenanthrene uptake by TNTs@AC was decreased from 970.5 to 803.0  $\mu\text{g/g}$ ; however, when HA was further increased from 2.5 to 10 mg/L, the uptake bounced up to 955.4  $\mu\text{g/g}$ . In contrast, the uptake of phenanthrene by AC was progressively decreased from 747.4 to 455.2  $\mu\text{g/g}$  when HA was increased from 0 to 10 mg/L. The inhibitive effect on AC is consistent with the conventional notion that DOM can delay the adsorption of AC due to irreversible adsorption and clogging of the pores (also known as organic fouling or territorial binding) (Pignatello et al. 2006). For TNTs@AC, however, the much narrowed pore size and the modified surface characteristics exclude HA macromolecules from entering and clogging the pores, greatly mitigating organic fouling. The relatively minor suppression in the low HA concentration range ( $< 5 \text{ mg/L}$ ) can be attributed to competition of relatively smaller and hydrophobic HA molecules for the  $\pi$ - $\pi$  bonding sites and/or hydrophobic sites (Fujii et al. 2014, Yang et al. 2010). At elevated HA concentrations, the smaller adsorbable components of HA became increasingly aggregated through dispersive hydrophobic interactions and H-bonds (Chilom et al. 2009). Indeed, based on diffusion-ordered spectroscopic studies, it was shown that HA aggregates display diffusivities corresponding to average molecular weights  $> 66,000 \text{ Da}$  in concentrated solutions and 2500–6100 Da in less concentrated solutions (Simpson 2002). Because the experimental HA concentration is far below the reported critical micelle concentration of 5–10 g/L HA (Guetzloff and Rice 1994), no micelles are expected in the solution, though the aggregates are large enough to be excluded by the narrow pores of TNTs@AC. On the other hand, according to the “membrane model” (Wershaw 1994), surfactant-like HA molecules may form bilayer membranes coating on the TNTs, which, in turn, can facilitate ad-solubilization of phenanthrene.

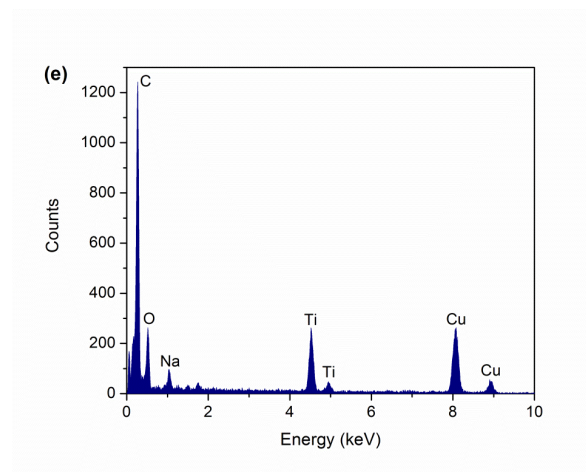
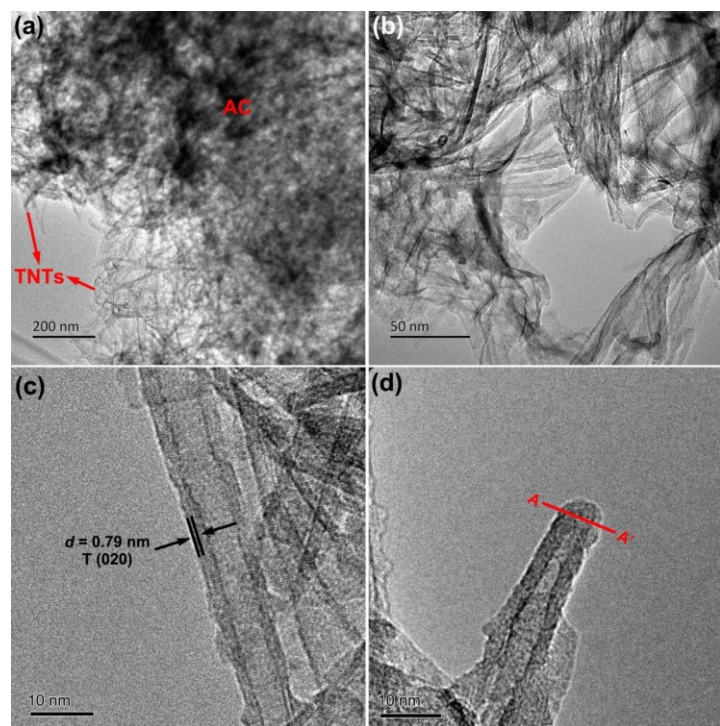


**Figure 114. Effects of environmental conditions.**

Effects of (a) pH, (b) ionic strength and (c) HA on equilibrium uptake of phenanthrene by by TNTs@AC. Experimental conditions: initial phenanthrene = 500  $\mu\text{g/L}$ , material dosage = 0.5 g/L; For (b) and (c), solution pH = 7.0.

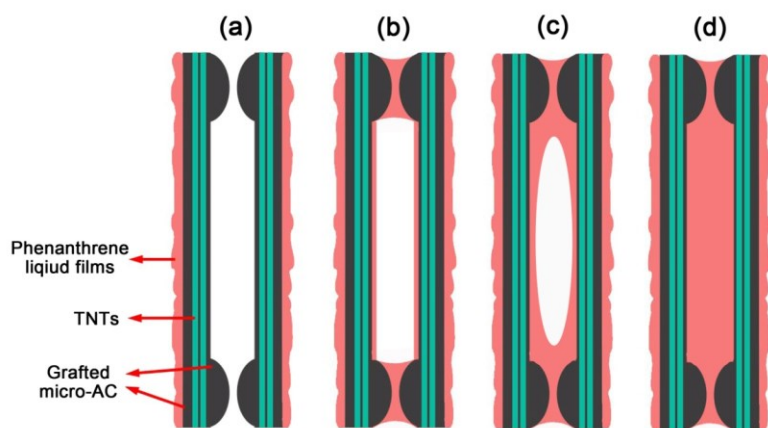
TEM and HRTEM images of TNTs@AC were then obtain to interpret the mechanisms on enhanced PAHs uptake by TNTs@AC. The substantially enhanced adsorption behavior of TNTs@AC is attributed to the much modified surface property, geometry and curvature, narrowed pore size, more confined pore space, and much enhanced capillary condensation inside the carbon-modified TNTs. **Figure 115** displays the TEM and HRTEM images of TNTs@AC. Consistent with the SEM images (**Figure 110**), TNTs are attached on scattered AC particles (**Figure 115a**). Due to the co-existence of AC in the hydrothermal process, the tubular structure of TNTs@AC appeared much contaminated and somewhat distorted compared to the neat TNTs, which are well-defined multilayered nanotubes (4–5 layers), with inner and outer diameters of 4.5 and 9 nm. The HRTEM also reveals some small patches on the coarse nanotubes or in the interlayer of TNTs (**Figures 114c** and **111d**), indicating partial coating of microscale AC on the nanotubes (also see prior characterization and discussion below). Moreover, the interlayer distance of neat TNTs is 0.75 nm (**Figure 115c**), which is assigned to the crystal plane (020) of titanate (Chen et al. 2002, Zhao et al. 2016a). In contrast, the interlayer distance increased to 0.79 nm for TNTs@AC, due to the

stretching by incorporated AC. Morphologically, though neat TNTs are open-ended, the nanotubes of TNTs@AC display a narrow ink-bottle structure with more carbon accumulated on the tube entry (**Figure 115d**). The EDS line-scan of section A–A' (**Figure 115e**) shows high carbon content on the TNTs walls, providing direct evidence of the carbon coating. Considering the inner diameter of TNTs is only 4.5 nm, the size incorporated micro-AC was extremely small ( $< 4$  nm), which was stripped from GAC in the hydrothermal process for material synthesis. Taken together, the making of TNTs@AC encompasses two critical features: 1) the hydrothermal treatment converts  $\text{TiO}_2$  into tubular TNTs that are attached on bulk AC particles; and 2) the treatment also facilitates micro-AC stripping from GAC and then coating/incorporation on the TNTs. As such, the resulting TNTs@AC adsorbs phenanthrene in dual modes, i.e., in addition to the standard adsorption by AC, the narrow ink-bottle shaped TNTs also facilitate much enhanced ‘bottle-filling’ or capillary condensation of phenanthrene.



**Figure 115.** (a, b) TEM of TNTs@AC, (c, d) HRTEM of single TNTs, and (e) EDS line spectra of TNTs walls.

**Figure 116** depicts the transition from adsorption to capillary condensation as a function of matric potential for carbon modified TNTs. Although AC is grafted on both the interior and exterior walls of the nanotubes, more AC is accumulated at the entrance (**Figure 115d**), forming a narrow throat at the open ends of the nanotubes and relatively larger, ellipsoidal cavity inside the nanotubes mimicking the ink-bottle pore geometry (Libby and Monson 2004). The carbon coating reduced most of the interior tube diameters to  $< 4$  nm, which is conducive to capillary condensation. Four steps can be discerned during the transition from adsorption to capillary-condensation (Tuller et al. 1999). At low concentrations, phenanthrene is adsorbed on the pore and slit walls following the classical Langmuir model (**Figure 116a**). With increasing matric potential, the adsorbed layer thickens to a point where the slits are filled up with liquid due to capillary condensation (**Figure 116b**). Further increasing the matric potential fills up the “belly” of the pore, resulting in a reduction in the radius of curvature of liquid-vapor interfaces and forming a circle or elongated oval-shaped interface (**Figure 116c**). Subsequently, the pore is completely filled up (**Figure 116d**).



**Figure 116. A conceptualized representation on the bottle-filling mechanism.**  
Note the transition from adsorption to capillary condensation for carbon modified TNTs.



### 5.4.5. Photo-regeneration of TNTs@AC and material reuse after phenanthrene adsorption

Figure 117 shows that almost no phenanthrene (< 4%) was eliminated in the photolysis process under UV irradiation without materials. However, the pre-concentrated phenanthrene on TNTs@AC was nearly completely (> 99%) under UV irradiation within 120 min for both loadings of phenanthrene (initial concentration of 200 or 500 µg/L). In comparison, only 9.2% ( $C_0 = 200$  µg/L) and 6.7% ( $C_0 = 500$  µg/L) of phenanthrene loaded on the parent AC was degraded under the identical UV irradiation, indicating excellent photocatalytic activity of TNTs grafted on AC. Compared to the precursor  $\text{TiO}_2$ , neat TNTs are known to show much weaker photocatalytic activity due to the easy recombination of electron-hole pairs (Lee et al. 2007, Liu et al. 2014a, Liu et al. 2015b). Yet previous work has shown that carbon doping or deposition can greatly enhance the photocatalytic activity of TNTs/ $\text{TiO}_2$ , because the carbon materials can act as an electron transfer mediator that inhibits the recombination of electron-hole pairs (Neville et al. 2013, Wu et al. 2009). Some of the grafted AC nanoparticles may act as carbon quantum dots, which have been known to be an effective photosensitizer of photocatalysts, i.e., activate the photocatalysts by absorbing ultraviolet or visible light and transferring the energy to adjacent molecules (Li et al. 2010, Yu et al. 2014, Zhang et al. 2013).

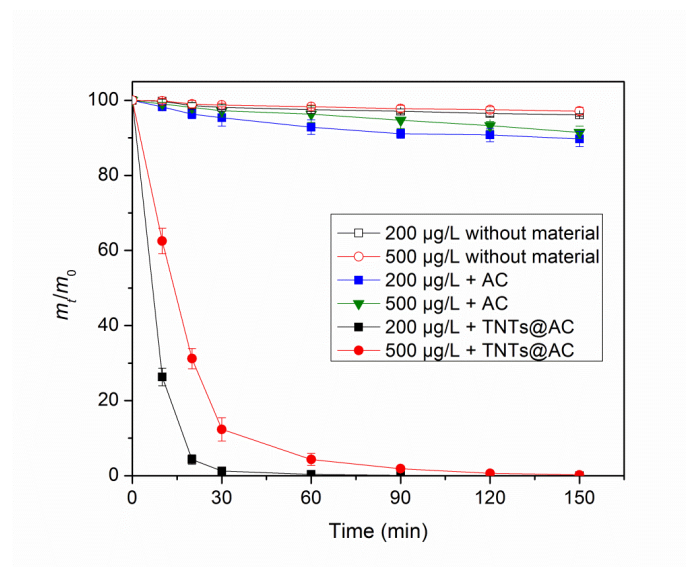
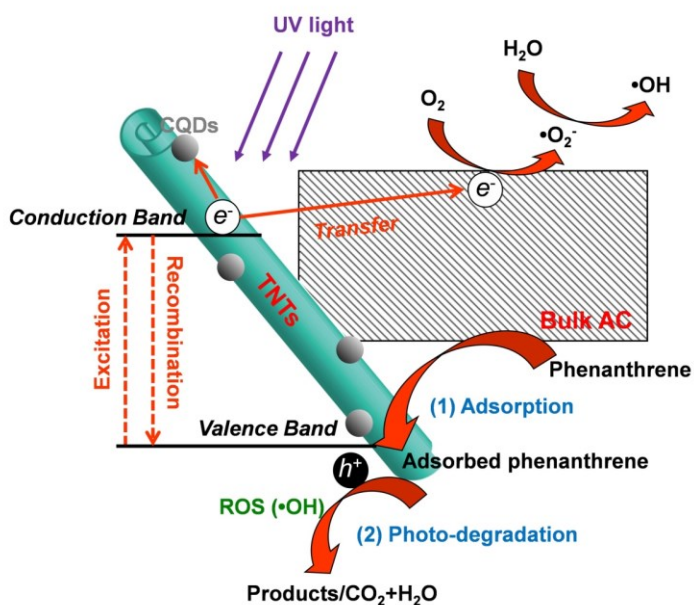
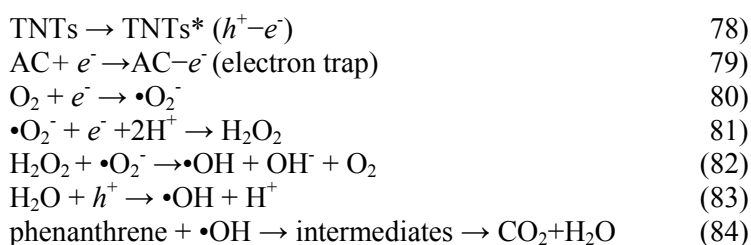


Figure 117. Photo-degradation of adsorbed phenanthrene by TNTs@AC.

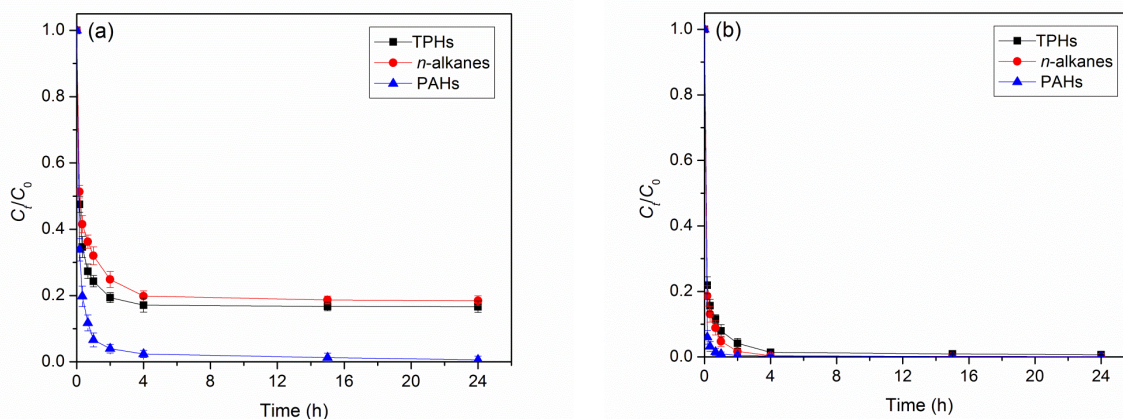
**Figure 118** summarizes the schematic and mechanisms of the two-step adsorption and photo-regeneration process and the synergistic effects of AC and TNTs. Phenanthrene is firstly adsorbed on TNTs@AC through adsorption and capillary condensation. TNTs, acting as the primary photocatalysis center, will be excited under UV light and generate a conduction band (electron,  $e^-$ ) and a valence band (hole,  $h^+$ ) (Equation 78). Then AC, especially the micro-AC grafted on TNTs, serves as electron mediator, which can transfer the  $e^-$  thus preventing recombination of the excited conduction band and the valence band (Equation 79). The quantization effect caused by the micro-AC facilitates utilization of UV light for electron escape from TNTs@AC and photocatalysis. Therefore, more electrons are accepted by  $O_2$  and  $H_2O$ , more ROS ( $\bullet O_2^-$  and  $\bullet OH$ ) are generated (Equations 80–82) (Woan et al. 2009, Xue et al. 2011), likewise, as more holes are used to oxidize  $H_2O$ , more  $\bullet OH$  radicals, which are the primary ROS in photocatalytic oxidation system, are produced (Equation 83) (as confirmed by PL spectra) (Wen et al. 2002, Zhang et al. 2011c). Consequently, trace levels of PAHs in water can be highly efficiently degraded (Equation 84).



**Figure 118. Schematic of a two-step adsorption-photodegradation process.** A two-step process for complete destruction of phenanthrene by TNTs@AC.

### 5.4.6. Adsorption and photodegradation of oil components in DWAO by TNTs@AC

**Figure 119** shows the adsorption kinetics of TPHs, *n*-alkanes and PAHs by TNTs@AC. Evidently, TNTs@AC was able to rapidly remove all the oil components from the DWAO at a low material dosage of 0.625 g/L. In all cases, the adsorption was completed or nearly completed within 4 h. **Figure 119a** shows that the final removal of TPHs, *n*-alkanes and PAHs amounted to 83.4%, 81.6% and 99.4% at 24 h, respectively. When the material dosage was increased to 1.25 g/L, nearly all (> 99.5%) of the oil components were depleted within 24 h (**Figure 119b**), indicating that TNTs@AC have an excellent adsorption affinity for oil hydrocarbons. The pseudo-first order and pseudo-second order models were employed to interpret the adsorption kinetic data (Ho and McKay 1998), and **Table 29** lists the best-fit model parameters. Evidently, the pseudo-second order model was more suitable for simulating the adsorption kinetics ( $R^2 \geq 0.9999$ ), and the model also well simulated the experimental equilibrium uptake ( $q_e$ ), suggesting that adsorption is likely to be the rate-controlling step (Ho and McKay 1999).



**Figure 119. Adsorption kinetics of TPHs, *n*-alkanes and PAHs in DWAO by TNTs@AC.** (a) with a material dosage of 0.625 g/L, and (b) 1.25 g/L. Experimental conditions: solution pH = 8.1, temperature =  $22 \pm 1$  °C, initial salinity = 2 wt.%, and dissolved organic matter (DOM) = 2.2 mg/L as TOC.

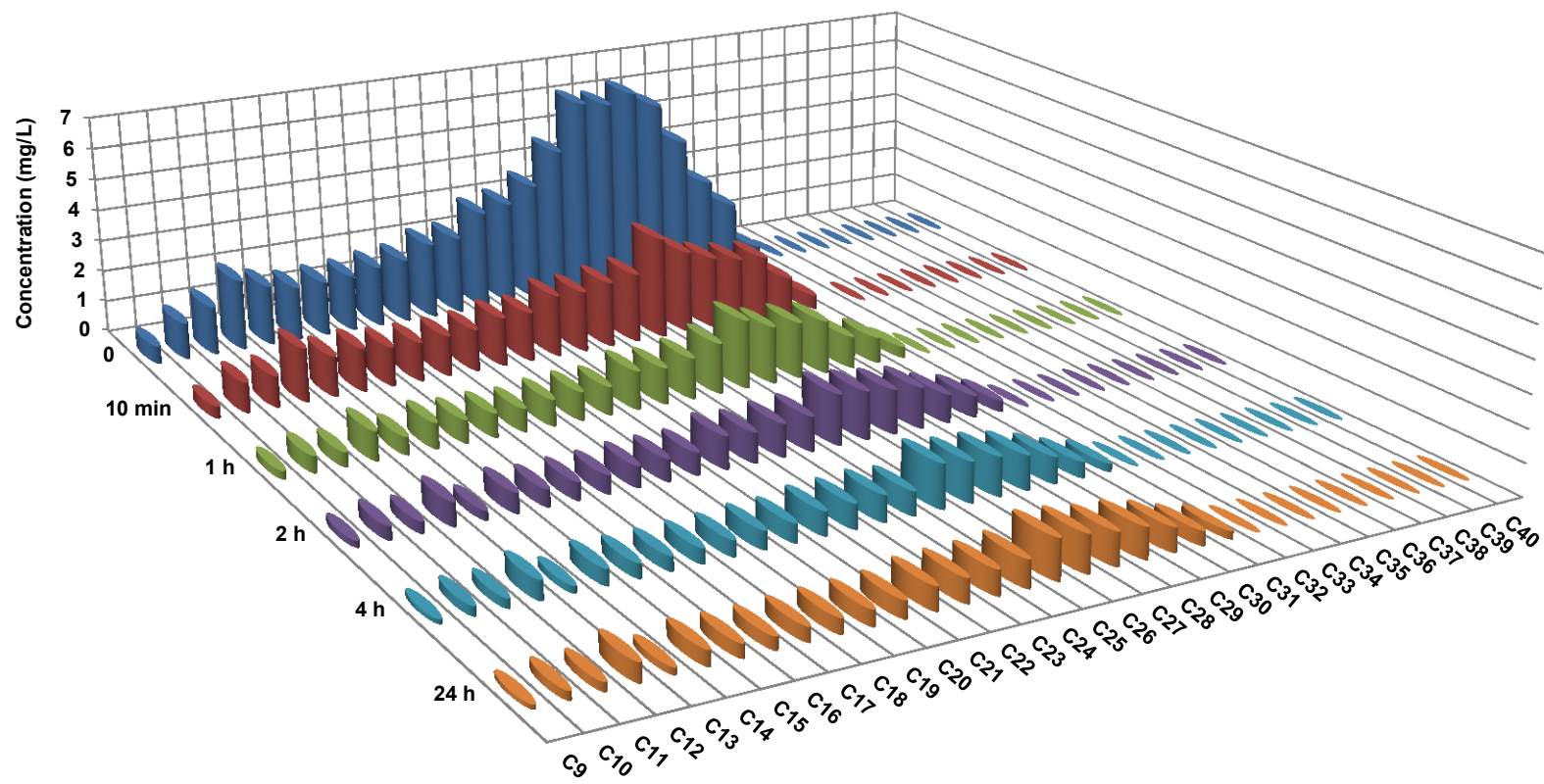
**Table 29. Kinetic parameters for adsorption of TPHs, *n*-alkanes and PAHs in DWAO by TNTs@AC**

Kinetic models	Parameters	Material dosage (g/L)					
		0.625			1.25		
		TPHs	<i>n</i> -alkanes	PAHs	TPHs	<i>n</i> -alkanes	PAHs
Pseudo-first order model	$k_1$ ( $\text{min}^{-1}$ )	0.71	2.78	0.82	0.89	0.79	0.69
	$q_e$ (mg/g)	17.63	28.66	0.09	34.49	26.46	0.99
	$R^2$	0.6765	0.8191	0.7794	0.7460	0.8278	0.8629
Pseudo-second order model	$k_2$ ( $\text{g}/(\text{mg}\cdot\text{min})$ )	0.15	0.47	48.46	0.07	0.08	2.68
	$q_e$ (mg/g)	119.8	57.21	2.70	197.39	93.76	5.39
	$R^2$	1.0000	1.0000	1.0000	1.0000	0.9999	1.0000



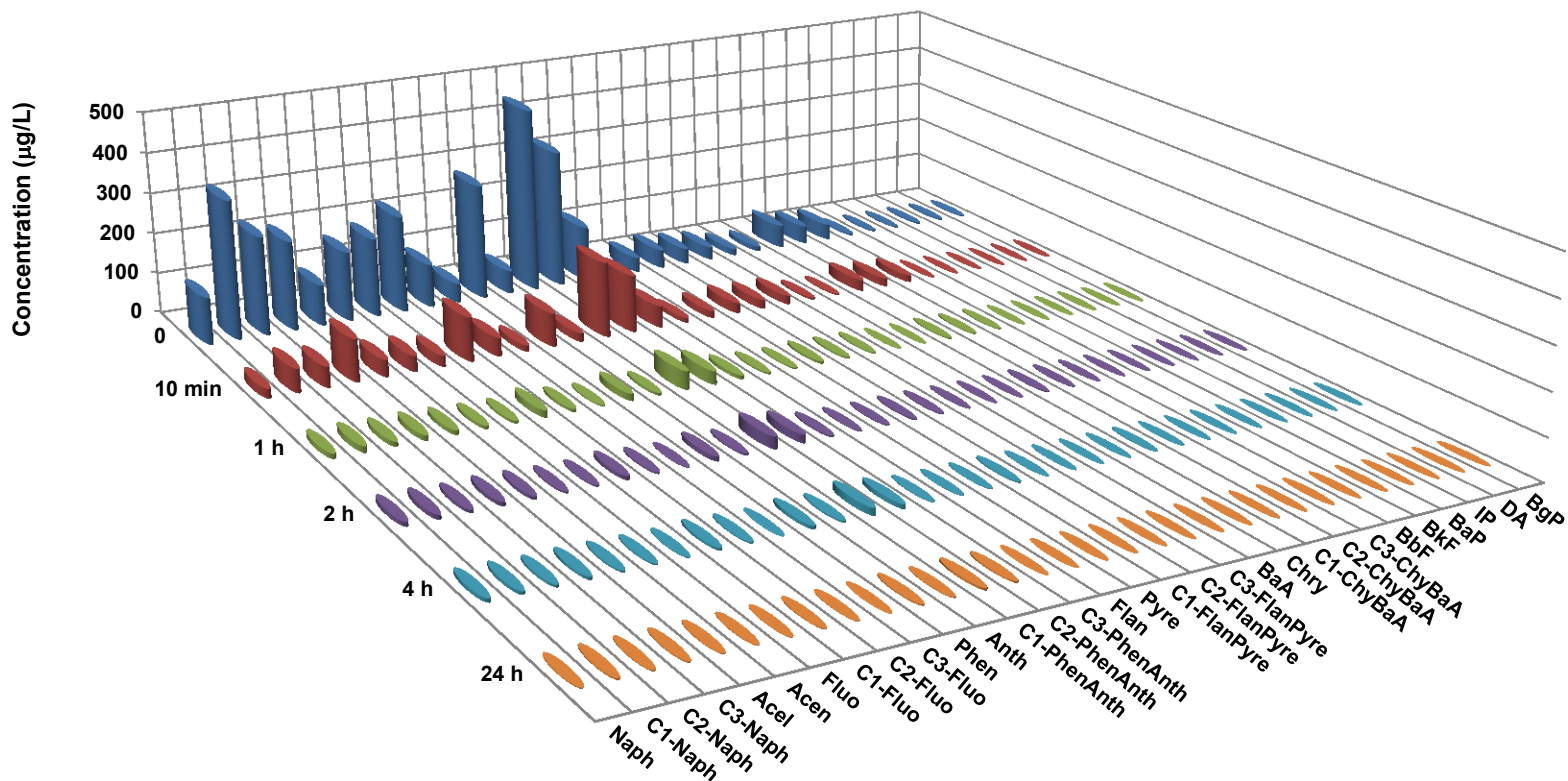
**Figure 120** displays the distribution of *n*-alkanes in the aqueous phase during the adsorption process at a material dosage of 0.625 g/L. The targeted *n*-alkanes (C9-C40) were grouped into lower molecular weight hydrocarbons (LMWHs, C9-C20), medium molecular weight hydrocarbons (MMWHs, C21-C30) and higher molecular weight hydrocarbons (HMWHs, C31-C40). The initial total concentration of *n*-alkanes was 71.5 mg/L, and two main peaks were centered in C24-C29 and C11-C13. The concentration of all *n*-alkanes gradually decreased as the adsorption proceeded, and the total *n*-alkanes removal was 49%, 80% and 82% at 10 min, 4 h and 24 h, respectively. However, the removal efficiency of LMWHs, MMWHs and HMWHs at 24 h was 79%, 82% and 91%, respectively, indicating that *n*-alkanes with longer carbon chains are more preferentially adsorbed, which can be attributed to their higher hydrophobicity.

**Figure 121** shows the distribution of PAHs during the adsorption at a material dosage of 0.625 g/L. The targeted 16 parent PAHs include naphthalene (Naph), acenaphthylene (Acel), acenaphthene (Acen), fluorene (Fluo), phenanthrene (Phen), anthracene (Anth), fluoranthene (Flan), pyrene (Pyre), benzo(a)anthracene (BaA), Chrysene (Chry), benzo(b)fluoranthene (BbF), benzo(k)fluoranthene (BkF), benzo(a)pyrene (BaP), Indeno(1,2,3-cd)pyrene (IP), dibenzo(a,h)anthracene (DA), and benzo(g,hi)perylene (BgP). In addition, primary alkylated PAHs were also targeted, including alkylated-Naph, alkylated-Fluo, alkylated-Phen, alkylated-Anth, alkylated-Flan, and alkylated-Pyre. The initial concentration of the total PAHs was 3.4 mg/L, including 1.0 mg/L of parent PAHs and 2.4 mg/L of alkylated PAHs. The 2-ring (e.g., Naph, Acen and Fluo) and 3-ring (e.g., Phen) PAHs were found to be the main components, while very low concentrations of >5-ring PAHs (< 0.4% of total PAHs) were detected in the DWAO. TNTs@AC were very effective at adsorbing PAHs. More than 90% of PAHs were removed within 1 h, and over 99% of both parent and alkylated PAHs were removed at 24 h, which is much higher than that for THPs (83%) and *n*-alkanes (82%). In addition, TNTs@AC preferred to adsorb parent PAHs over the corresponding alkylated PAHs, for example, 74% of the parent PAHs was adsorbed on TNTs@AC at 10 min compared with 63% for the alkylated PAHs.



**Figure 120. Distribution of *n*-alkanes in DWAO during adsorption by TNTs@AC.**

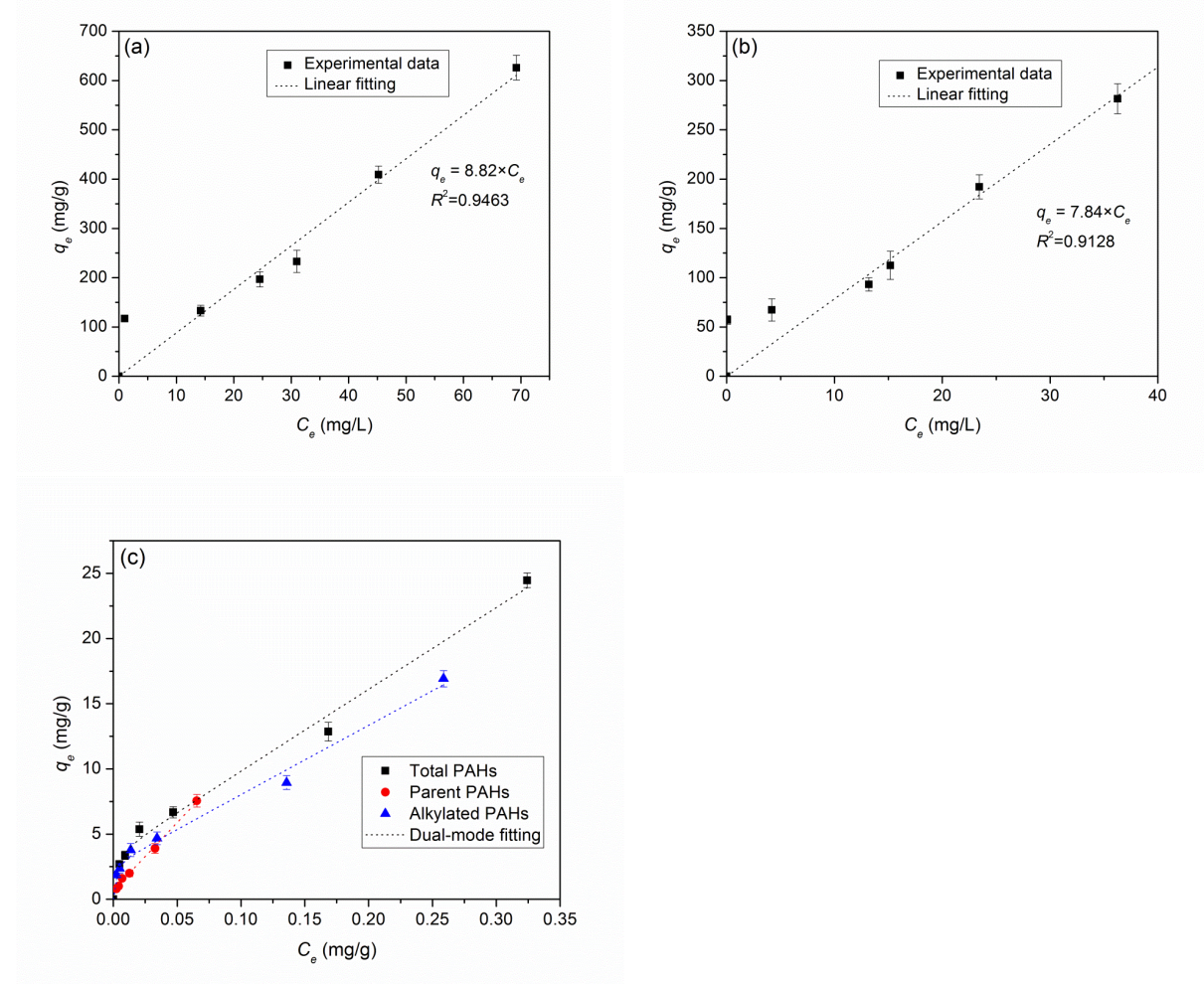
Experimental conditions: material dosage = 0.625 g/L, solution pH = 8.1, temperature = 22±1 °C, initial salinity = 2 wt.%, and dissolved organic matter (DOM) = 2.2 mg/L as TOC.



**Figure 121. Distribution of PAHs in DWAO during adsorption by TNTs@AC.**

Experimental conditions: material dosage = 0.625 g/L, solution pH = 8.1, temperature = 22±1 °C, initial salinity = 2 wt.%, and dissolved organic matter (DOM) = 2.2 mg/L as TOC.

**Figure 122** shows the adsorption isotherms of: (a) TPHs, (b) *n*-alkanes and (c) PAHs by TNTs@AC, and **Table 30** lists the best-fitted more parameters. The linear isotherm model was able to adequately interpret the adsorption equilibrium data for TPHs and *n*-alkanes (**Figures 121a** and **121b**), with a distribution coefficient ( $K_d$ ) of 8.8 and 7.8 L/g, respectively. However, the dual-mode isotherm model (Equation 11) was found more suitable for interpreting the adsorption of PAHs by TNTs@AC ( $R^2 > 0.99$ ). The results indicate that the uptake of PAHs by TNTs@AC was primarily due to partitioning; adsorption plays only a minor role. It is also noteworthy that the  $K_d$  values for PAHs are much higher than those for TPHs and *n*-alkanes, indicating TNTs@AC is more favorable toward PAHs than *n*-alkanes.



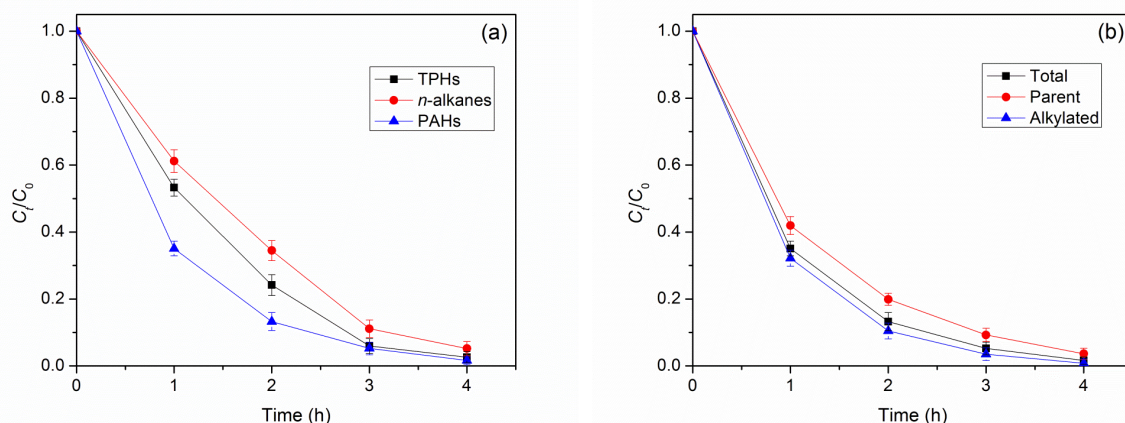
**Figure 122. Adsorption isotherms of: (a) TPHs, (b) *n*-alkanes and (c) PAHs in DWAO by TNTs@AC.** Experimental conditions: solution pH = 8.1, temperature =  $22 \pm 1$  °C, initial salinity = 2 wt.%, and DOM = 2.2 mg/L as TOC.

**Table 30. Isotherm parameters for adsorption of TPHs, *n*-alkanes and PAHs in DWAO by TNTs@AC**

Isotherm models	Parameters	TPHs	<i>n</i> -alkanes	PAHs		
				Total	Parent	Alkylated
Linear model	$K_d$ (L/g)	8.82	7.84	77.59	119.02	67.10
	$R^2$	0.9463	0.9128	0.8936	0.9569	0.8701
	$Q_{max}$ (mg/g)	657.89	272.48	25.28	9.45	16.76
Langmuir model	$b$ (L/mg)	0.03	0.10	14.59	34.13	23.31
	$R^2$	0.4591	0.6048	0.8038	0.6617	0.8235
	$K_F$ (mg/g*(L/mg) <sup>1/n</sup> )	88.78	79.62	35.68	41.41	24.80
Freundlich model	$n$	2.93	4.99	2.01	1.50	2.26
	$R^2$	0.6358	0.5855	0.9755	0.9849	0.9690
	$K_d$ (L/g)	7.57	6.05	62.53	103.36	52.99
Dual-Mode model	$Q_L$ (mg/g)	655.43	254.58	3.64	0.72	2.76
	$b$ (L/mg)	0.0031	0.0089	500.24	1964.94	849.94
	$R^2$	0.9367	0.9034	0.9935	0.9977	0.9925

#### 5.4.7. Photodegradation of adsorbed oil components by TNTs@AC

The highly efficient adsorption of oil components by TNTs@AC and the excellent photochemical activity of the AC-modified TNTs create a favorable condition to rapidly collect dispersed oil from contaminated water and then completely destroy it through subsequent photodegradation. **Figure 123** presents the photo-degradation kinetics of adsorbed TPHs, *n*-alkanes and PAHs on TNTs@AC. **Figure 123a** shows that 98.0%, 94.8%, and 98.4% of the pre-concentrated TPHs, *n*-alkanes and PAHs were degraded within 4 h, respectively. **Table 31** lists the best-fit model parameters when the pseudo first order model was used to interpret the photocatalytic kinetic data. The apparent rate constant ( $k_1$ ) follows the sequence of: PAHs (1.01 h<sup>-1</sup>) > TPHs (0.89 h<sup>-1</sup>) > *n*-alkanes (0.70 h<sup>-1</sup>), indicating that PAHs are more prone to the photocatalytic degradation. When PAHs and alkylated PAHs are compared, alkylated PAHs are more preferentially photodegraded (**Figure 123b**), with a higher  $k_1$  value of 1.17 h<sup>-1</sup>. Apparently, the ROS (e.g. •OH, •O<sub>2</sub><sup>-</sup> and <sup>1</sup>O<sub>2</sub>) produced in the photocatalytic reactions are more likely to attack the alkyl-groups in alkylated PAHs.



**Figure 123. Photodegradation kinetics of oil components.**

(a) Photodegradation of various oil components, and (b) various PAHs pre-concentrated on TNTs@AC. Experimental conditions: UV light intensity = 1.4 mW/cm<sup>2</sup>, solution pH = 8.1, temperature = 22±1 °C.

**Table 31. Parameters of first-order kinetic model for photocatalytic degradation of TPHs, *n*-alkanes and PAHs by TNTs@AC**

Parameters	TPHs	<i>n</i> -alkanes				PAHs		
		Total	LMWHs	MMWHs	HMWHs	Total	Parent	Alkylated
$k_1$ (h <sup>-1</sup> )	0.8852	0.7046	0.6771	0.7237	0.6250	1.0144	0.8168	1.1723
$R^2$	0.9751	0.9675	0.9543	0.9691	0.9904	0.9986	0.9984	0.9951

## 5.4.8. Conclusions

Separation and degradation of organic contaminants in water represents a major challenge in safeguarding human health. Conventional technologies such as adsorption and oxidation are often limited due to limited adsorption capacity, poor regeneration, and low degradation efficiency when used for treating oil contaminated water. For the first time, this work developed a novel composite material, TNTs@AC, through a simple hydrothermal process based on low-cost commercial AC and TiO<sub>2</sub>. As an adsorbent, TNTs@AC offers not only rapid adsorption, but also a high adsorption capacity for various oil hydrocarbons, thanks to the modified pore size distribution and formation of the high-capacity ink-bottle-shaped pores in the micro-AC modified TNTs. As a photocatalyst, TNTs@AC displayed superior photocatalytic activity over neat TNTs, owing to the AC-mediated electron transfer and enhanced generation of ROS. TNTs@AC performed well over a broad pH range and at high ionic strength and was highly resistant to organic fouling, which is a major drawback of conventional adsorbents. The high photocatalytic property allows for complete destruction of the adsorbed contaminants, which also regenerates the material and allows it to be used in multiple operations. Although oil components were tested as the target contaminants in this work, the two-step adsorption-photodegradation process may offer a novel solution to effectively concentrate and degraded a variety of other persistent micro-pollutants ranging from pharmaceuticals and personal care products, dyestuffs, and fluorinated organic chemicals. Therefore, TNTs@AC holds great potential to substantially advance current practices in treating spilled oil from water or seawater.



## 6. Ozonation of Oil and Oil Components and Effects of Dispersant

Ozone ( $O_3$ ) is a well-known strong oxidant ( $E^0=+2.07$  V) and relatively strong electrophile. Ozone is also an important natural gas in the atmosphere. It is the precursor of various transient secondary oxidant species, including hydroxyl ( $\bullet OH$ ), perhydroxyl ( $HO_2\bullet$ ), superoxide ( $O_2^{\bullet -}$ ), ozonide ( $O_3^{\bullet -}$ ) radicals, singlet oxygen ( $^1O_2$ ) and hydrogen peroxide ( $H_2O_2$ ) (Yu et al. 2007). In engineered processes, ozone has been widely used to degrade various organic compounds, ranging from PAHs (both parent and alkylated) (Chelme-Ayala et al. 2011, Lin et al. 2014, von Gunten 2003) to *n*-alkanes (Masten and Davies 1994, von Gunten 2003, Yu et al. 2007), in water treatment and soil remediation.

The two major pathways for ozone oxidation of *n*-alkanes and PAHs, are: 1) direct attack by  $O_3$  on the  $\sigma$ -bonding between C and H atoms via 1,3-dipolar insertion for alkanes and cycloaddition or electrophilic reaction for PAHs; and 2) indirect attack by the free radicals (primarily  $\bullet OH$ ) generated via reactive decomposition of ozone in aqueous solutions (Hellman and Hamilton 1974, Masten and Davies 1994, Zhao et al. 2011, Zhao et al. 2004).

Ozonation under atmospheric ozone is an important natural weathering process for petroleum hydrocarbons in marine systems. The ozonation rate and extent of spilled oil have not been studied so far. In addition, the effects of dispersants, natural organic matter, pH and temperature on the ozonation of oil remained unknown.

### 6.1. Effects of Dispersant on Ozonation of Oil PAHs by Surface-Level Ozone

Oil degradation by surface-level ozone is one of the important abiotic processes affecting the fate of oil in the Gulf coast, yet it has not been explored so far. Tropospheric ozone is produced by reaction of sunlight with air-borne hydrocarbons and nitrogen oxides. High levels of ozone have been widely detected at surface level along the Gulf coast. For example, based on the 2000–2002 monitoring data, the 8-hour ozone level in Alabama air ranged from 76 to 92 ppb, and the three-year average from 2004 to 2009 ranged from 63 to 86 ppb (ADEM, 2014). Ozone levels over an oil slick may be much greater due to the extensive evaporation of volatile hydrocarbons from spilled oil reaching the surface (Ryerson et al., 2011).

Elevated concentrations of alkylated PAHs were observed in the 2010 *DwH* oil spill, and the toxicity of alkylated PAHs is generally considered higher than that for the parent PAHs (Fallahtafti et al., 2012). To investigate the contribution of surface-level ozone oxidation to the weathering of spilled oil in seawater, three alkylated PAHs, which were detected during the *DwH* oil spill (Wade et al., 2011), were selected for ozonation tests, including 1-methylnaphthalene, 1-methylfluorene, and 9,10-DMA.

#### 6.1.1. Materials and methods

The ozonation experiments were carried out in a glass cylinder batch reactor ( $H \times D = 5 \text{ cm} \times 8 \text{ cm}$ ) with a flat quartz top. Two ports are connected to the Teflon tubes for gas flow and other two ports sealed by ground glass joints for sample collection. This reactor has a water cooling system and can be used for photodegradation or combined ozonation and photodegradation experiments. Ozone was generated from medical-grade oxygen using an A2Z Ozone Generator (Model HB5735B). Ozone gas flow through the surface of the solution was controlled at 8–15 mL/min by an Aalborg mass flow controller (Model GFC17). Ozone concentration was analyzed by a 2B Tech Ozone Monitor M106-L through measuring the ultra violet absorbance at 254 nm.

The PAH solutions were prepared by adding a target alkylated PAH in seawater at desired concentrations and mixed for 2 h before use. In each test, 250 mL of a solution in the presence or absence of the dispersant Corexit EC9500A was loaded in the reactor under constant magnetic stirring at 200 rpm, which gave an air-water interfacial surface area of 50 cm<sup>2</sup>. The reactor was always kept in dark to avoid photodegradation. To study the ozone dosage effects, the gas-phase inlet ozone concentration was varied from 86 to 300 µg/L. To investigate the dispersant effect, a Corexit EC9500A stock solution (10 g/L) was added into the mixture to yield a dispersant concentration ranging from 5 to 180 mg/L. To examine the contributions of direct ozone oxidation and indirect •OH oxidation, tert-butyl alcohol (10 mM) was employed as a scavenger which can inhibit the reaction between •OH and PAHs (Neta et al. 1988).

At predetermined times, each 1 mL of solution samples were collected in 2-mL amber glass vials with Teflon lined caps and analyzed by HPLC at the wavelength of 264 nm for the alkylated PAHs remaining in the aqueous phase. More information about the HPLC method has been described in Section 3.2.1.2. Separate control tests were carried out to determine the volatilization loss of the PAHs in the seawater solution under the same air-flow conditions but without ozone.

## 6.1.2. Oxidation of 1-methylnaphthalene by Surface-Level Ozone

### 6.1.2.1. Volatilization and ozonation of 1-methylnaphthalene

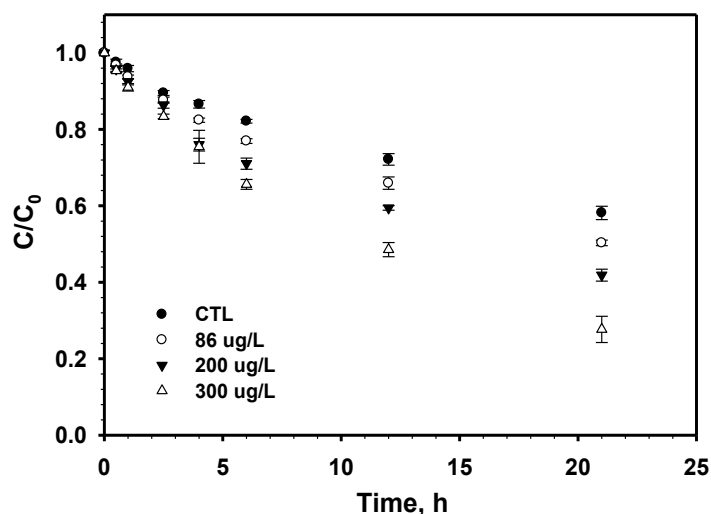
Volatilization is an important process affecting fate and transport of oil components. **Figure 124** profiles the volatilization and ozonation of 1-methylnaphthalene under the same gas flow rate but various ozone concentrations. At 21 h, 42% of 1-methylnaphthalene volatilized without ozone. The dissipation of the aqueous phase 1-methylnaphthalene was 50%, 59%, and 73% in the presence of ozone concentration at 86, 200 and 300 µg/L, respectively. The results indicate that both volatilization rate and overall dissipation rate from 0 to 21 h can be well interpreted by the first-order kinetic models. **Table 32** gives the respective rate constants. The following integrated first-order kinetic model was formulated, which was able to adequately predict the net ozonation rate:

$$\frac{dC}{dt} = kC = (k_v + k_o)C \quad (85)$$

$$k_o = k - k_v \quad (86)$$

where  $C$  is the reactant concentration at reaction time  $t$ ,  $k$  and  $k_v$  are the first-order rate constants of overall dissipation and volatilization, respectively, which were obtained by fitting Equation 85 to the corresponding experimental kinetic data,  $k_o$  is the ozonation rate constant.





**Figure 124. Volatilization and ozonation of 1-methylnaphthalene.**

Experimental conditions: initial 1-methylnaphthalene concentration = 500 µg/L, gas flow rate = 15 mL/min, temperature = 22±1 °C, initial pH = 8.3, salinity = 2%, and DOM = 2.2 mg/L as TOC.

**Table 32. First-order rate constants for 1-methylnaphthalene volatilization and ozonation**

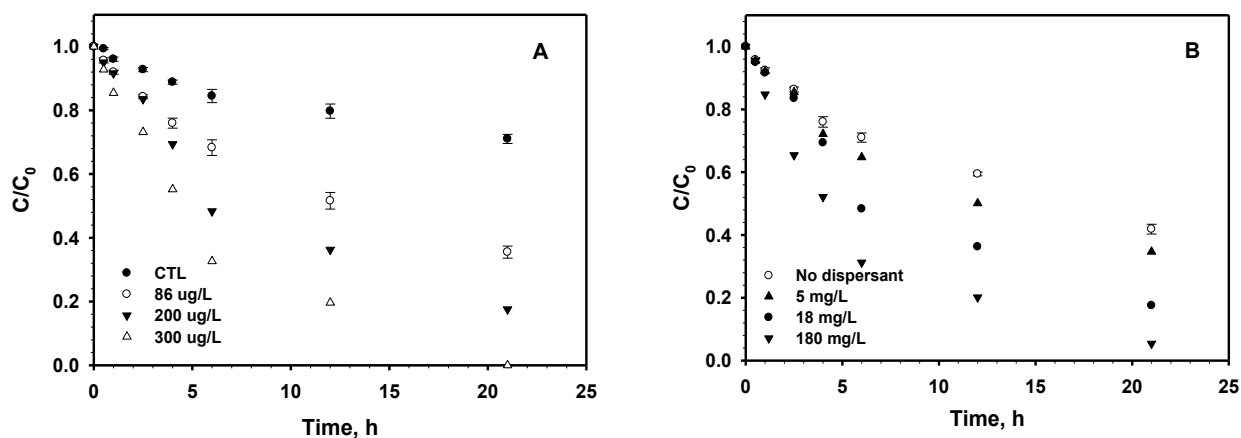
Ozone (µg/L)	Volatilization		Overall dissipation		Ozonation
	$k_v$ (h <sup>-1</sup> )	$R^2$	$k$ (h <sup>-1</sup> )	$R^2$	$k_o$ (h <sup>-1</sup> )
0	0.0249	0.99	0.0249	0.99	0
86	0.0249	0.99	0.0321	0.98	0.0072
200	0.0249	0.99	0.0432	0.96	0.0183
300	0.0249	0.99	0.0548	0.99	0.0299

The volatilization rate was calculated to be 0.0249 h<sup>-1</sup> under the air flow rate of 15 mL/min based on the experimental kinetic data. The ozonation rate was escalated from 0.0072 to 0.0183 h<sup>-1</sup> (by 1.5 times) and 0.0299 h<sup>-1</sup> (by 3 times) when the ozone concentration was increased from 86 µg/L to 200 µg/L and 300 µg/L, respectively. The ozonation and overall dissipation rates were significantly enhanced by increasing the ozone concentration. Both direct ozonation by O<sub>3</sub> via cycloaddition or electrophilic reaction and indirect attack by free radicals (primarily hydroxyl radical, •OH) are believed to be operative mechanisms (Ning et al. 2007a, 2007b). The relative contributions of direct ozone oxidation and •OH-facilitated indirect oxidation will be quantified later on in this work. The solution pH dropped from 8.3 to 7.5 during the reaction, which could be due to the accumulation of carboxylic acid and consumption of OH<sup>-</sup> (Li et al. 2014).

### 6.1.2.2. Dispersant effects on ozonation of alkylated PAHs

**Figure 125a** shows the volatilization and ozonation of 1-methylnaphthalene at various ozone concentrations in the presence of dispersant at 18 mg/L. **Table 33** gives the rate constants obtained by fitting Equation 85 to the experimental data. Compared to **Figure 124**, the presence of the dispersant reduced the volatilization from 42% to 29% at 21 h, i.e., the volatilization rate constant ( $k_v$ ) was reduced from 0.0249 h<sup>-1</sup> to 0.0208 h<sup>-1</sup>. On the other hand, the presence of the dispersant enhanced the ozonation of the PAH. At 21 h and in the presence of the dispersant, the overall dissipation of 1-methylnaphthalene reached 65%, 83% and 99% at the ozone concentrations of 86, 200 and 300 µg/L, respectively. Kinetically, the overall 1-methylnaphthalene dissipation rate constant ( $k$ ) increased from 0.0321 h<sup>-1</sup> to 0.0522 h<sup>-1</sup>, and the ozonation rate constant ( $k_o$ ) increased from 0.0072 h<sup>-1</sup> to 0.0314 h<sup>-1</sup> at the ozone concentration of 86 µg/L; in addition,  $k$  increased from 0.0432 h<sup>-1</sup> to 0.0859 h<sup>-1</sup> and from 0.0548 h<sup>-1</sup> to 0.1456 h<sup>-1</sup>, and  $k_o$  from 0.0183 h<sup>-1</sup> to 0.0651 h<sup>-1</sup> and from 0.0299 h<sup>-1</sup> to 0.1248 h<sup>-1</sup> at the ozone concentrations of 200 µg/L and 300 µg/L, respectively.

**Figure 125b** demonstrates the effect of dispersant concentration on the ozonation of 1-methylnaphthalene at the ozone concentration of 200 µg/L, which is designed to simulate the specific area of the high surface ozone level (ADEM, 2014). The overall 1-methylnaphthalene dissipation rate was increased with the increase of the dispersant concentration. For example, at an ozone concentration of 200 µg/L and in the absence of dispersant,  $k$  increased from 0.0432 h<sup>-1</sup> to 0.0542, 0.0859, 0.1418 h<sup>-1</sup> in the presence of the dispersant at 5, 18, and 180 mg/L, respectively, under otherwise identical conditions. The enhanced ozonation effect by the dispersant can be attributed to elevated production of free radicals in the presence of the dispersant, and thus the enhanced indirect ozonation.



**Figure 125. Dispersant effects on volatilization and ozonation of 1-methylnaphthalene.**

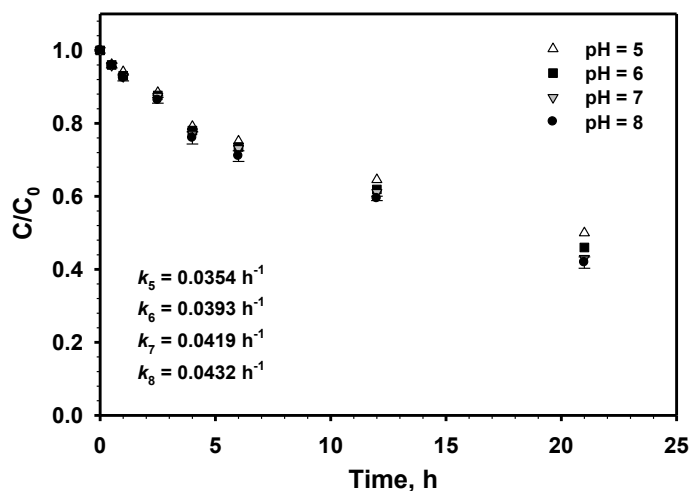
(a) At various ozone concentrations and a fixed dispersant concentration of 18 mg/L; (b) At various dispersant concentrations and a fixed ozone concentration of 200 µg/L. Experimental conditions: initial 1-methylnaphthalene concentration = 500 µg/L temperature = 22±1 °C, pH = 8.3, salinity = 2%.

**Table 33. First-order rate constants for 1-methylnaphthalene volatilization and ozonation in the presence of dispersant at 18 mg/L**

Ozone ( $\mu\text{g/L}$ )	Volatilization		Overall dissipation		Ozonation
	$k_v$ ( $\text{h}^{-1}$ )	$R^2$	$k$ ( $\text{h}^{-1}$ )	$R^2$	$k_o$ ( $\text{h}^{-1}$ )
0	0.0208	0.95	0.0208	0.95	0
86	0.0208	0.95	0.0522	0.98	0.0314
200	0.0208	0.95	0.0859	0.96	0.0651
300	0.0208	0.95	0.1456	0.97	0.1248

### 6.1.2.3. pH effects on the ozonation of 1-methylnaphthalene

Figure 126 shows the pH effects on the ozonation of 1-methylnaphthalene when the PAH solution was exposed to an air flow containing 200  $\mu\text{g/L}$  of ozone. The results indicate that decreasing pH from 8 to 5 only slightly inhibited the ozonation, and the overall PAH depletion decreased from 58% to 50% in the end of 21 h of reaction. The first-order removal rate constant ( $k$ ) (Figure 126) decreased from 0.0431  $\text{h}^{-1}$  at pH 8 to 0.0354  $\text{h}^{-1}$  at pH 5. Solution pH may affect both direct ozonation and radicals-facilitated indirect oxidation. Zhao et al. (2011) studied ozonation of cationic red X-GRL in aqueous solution and they claimed that increasing pH could enhance the hydroxyl radical generation, resulting in enhanced indirect ozonation but lower direct oxidation rate.



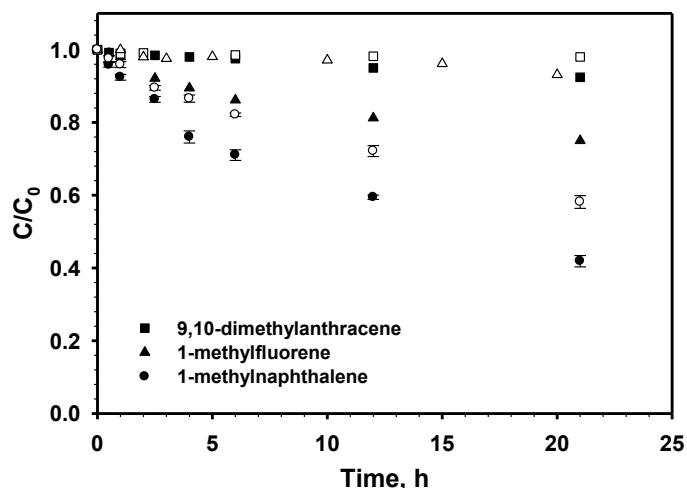
**Figure 126. Effects of pH on the ozonation of 1-methylnaphthalene.**

Experimental conditions: initial 1-methylnaphthalene concentration = 500  $\mu\text{g/L}$ , ozone concentration = 200  $\mu\text{g/L}$ , gas flow rate = 15 mL/min, temperature =  $22 \pm 1$   $^{\circ}\text{C}$ , salinity = 2%.

### 6.1.2.4. Comparison of three alkylated PAHs

Figure 127 shows the volatilization and ozonation kinetics of three alkylated PAHs, namely, 9,10-DMA, 1-methylfluorene and 1-methylnaphthalene. The initial concentrations of the PAHs were 40  $\mu\text{g/L}$ , 200  $\mu\text{g/L}$ , and 500  $\mu\text{g/L}$ , respectively, which is in accord with the solubility order of the PAHs in seawater. At 21 h, the volatilization loss was observed at 2%, 7%, and 42% for 9,10-DMA, 1-

methyfluorene and 1-methylnaphthalene under the air flow rate of 15 mL/min, respectively. In the presence of ozone (200 µg/L), the overall depletion of PAHs was increased to 8%, 25%, and 58% at 21 h. The results indicate that 9,10-DMA is not only less volatile, but more resistant to the surface level ozone oxidation than the other two PAHs, which may be due to its highly stable chemical structure, i.e., the three fused benzene rings. Therefore, the weathering rate of different oil components under surface level ozone may vary remarkably according to their chemical structure and stability. 1-methylfluorene and 1-methylnaphthalene were used in the further experiments to investigate the ozonation mechanism due to their significantly different volatilization rates and ozonation rates.



**Figure 127. Ozonation kinetics of three alkylated PAHs.**

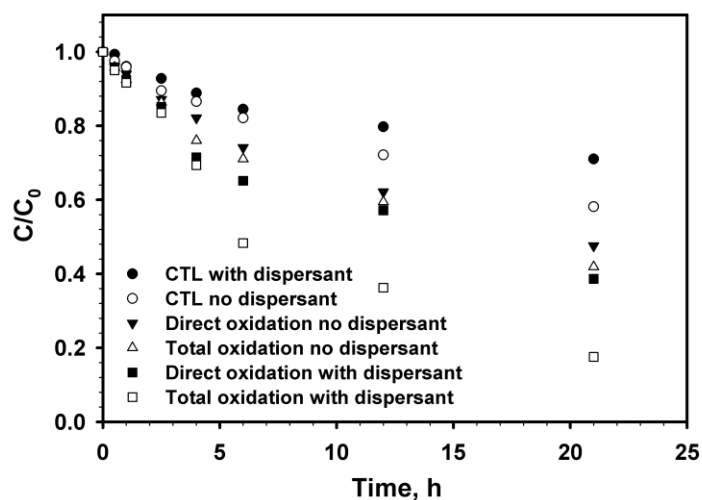
Experimental conditions: initial 9,10-DMA= 40 µg/L, initial 1-methylfluorene = 200 µg/L, initial 1-methylnaphthalene = 500 µg/L, ozone concentration = 200 µg/L, gas flow rate = 15 mL/min, temperature = 22±1 oC, initial pH = 8.3, salinity = 2%. Solid symbols are ozonation, blank symbols are volatilization correspondingly.

### 6.1.2.5 Ozonation mechanisms of 1-methylnaphthalene

**Figure 128** profiles the volatilization, direct ozonation and total oxidation rates of 1-methylnaphthalene in the absence and presence of the dispersant Corexit EC9500A (18 mg/L). The first-order volatilization rate constant ( $k_v$ ) was 0.0249 h<sup>-1</sup> in the absence of the dispersant and 0.0208 h<sup>-1</sup> in the presence of the dispersant. At 21 h, the overall depletion of 1-methylnaphthalene in the aqueous phase was 59% without the dispersant, of which direct ozonation accounted for 52%. The total dissipation and direct ozonation increased to 82% and 61% in the presence of the dispersant, respectively. To describe the dissipation rates involving volatilization, direct ozone oxidation ( $k_D$ ) and indirect radical oxidation ( $k_R$ ), a modified first-order kinetic model was proposed as follows:

$$\frac{dc}{dt} = -kC = (k_v + k_o)C = -(k_v + k_D + k_R)C \quad (87)$$

$$k_o = k'_D C_O + k'_R C_R \quad (88)$$



**Figure 128. Volatilization, direct ozonation and total oxidation of 1-methylnaphthalene.**

Experimental conditions: initial 1-methylnaphthalene concentration = 500  $\mu\text{g/L}$ , ozone = 200 ppb, gas flow rate = 15 mL/min, tert-Butyl alcohol = 10 mM, dispersant Corexit EC9500A = 0 or 18 mg/L, temperature =  $22 \pm 1$   $^{\circ}\text{C}$ , initial pH = 8.3, salinity = 2%.

**Table 34** gives the respective rate constants. Comparing the ozonation rate constants, the direct ozonation is the predominant ozonation mechanism in the absence of dispersant. However, the presence of the dispersant increased both direct ozonation rate ( $0.0208 \text{ h}^{-1}$ ) and indirect ozonation rate ( $0.0376 \text{ h}^{-1}$ ), in addition, the dispersant altered the contribution of the two oxidation mechanisms, i.e., indirect ozonation becomes the more important mechanism in the presence of the dispersant.

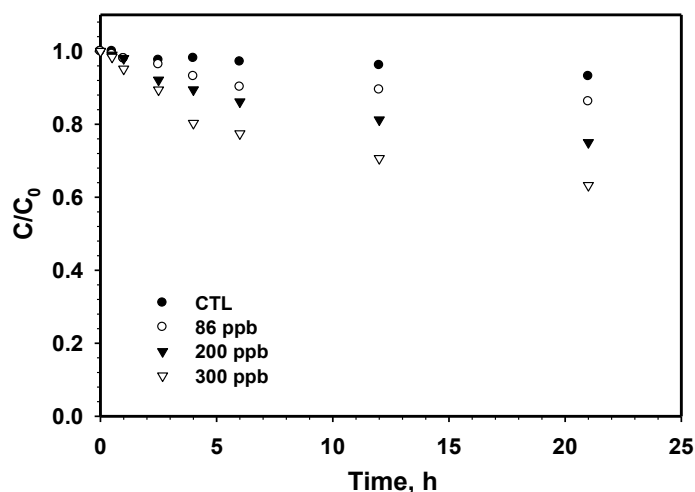
**Table 34. First-order rate constants for 1-methylnaphthalene volatilization and ozonation in the presence of 200 ppb ozone**

Dispersant (mg/L)	Volatilization		Direct ozonation		Indirect ozonation
	$k_v$ ( $\text{h}^{-1}$ )	$R^2$	$k_D$ ( $\text{h}^{-1}$ )	$R^2$	$k_R$ ( $\text{h}^{-1}$ )
0	0.0249	0.99	0.0128	0.95	0.0055
18	0.0208	0.99	0.0208	0.95	0.0376

### 6.1.3. Oxidation of 1-methylfluorene by Surface-Level Ozone

#### 6.1.3.1. Volatilization and ozonation of 1-methylfluorene

**Figure 129** shows the volatilization and ozonation of 1-methylfluorene under the same gas flow rate but at various ozone concentrations. At 21 h, 7% of 1-methylfluorene volatilized without ozone. The overall dissipation of the aqueous phase 1-methylfluorene was 15%, 25% and 35% when exposed to 86, 200 and 300 ppb of ozone, respectively. Both the volatilization rate and the overall dissipation rate from 0 to 21 h can be well interpreted by the first-order kinetic models (Equation 85). The best-fitted  $k_v$  value for 1-methylfluorene volatilization was  $0.0036 \text{ h}^{-1}$  under the air flow rate of 15 mL/min, which is much lower than that of 1-methylnaphthalene ( $0.0249 \text{ h}^{-1}$ ) due to the relatively stable structure of 1-methylfluorene. The ozonation rate was escalated from 0.0049 to  $0.0121 \text{ h}^{-1}$  (by 2.5 times) and  $0.0221 \text{ h}^{-1}$  (by 4 times) when the ozone concentration was increased from 86 ppb to 200 ppb and 300 ppb, respectively.



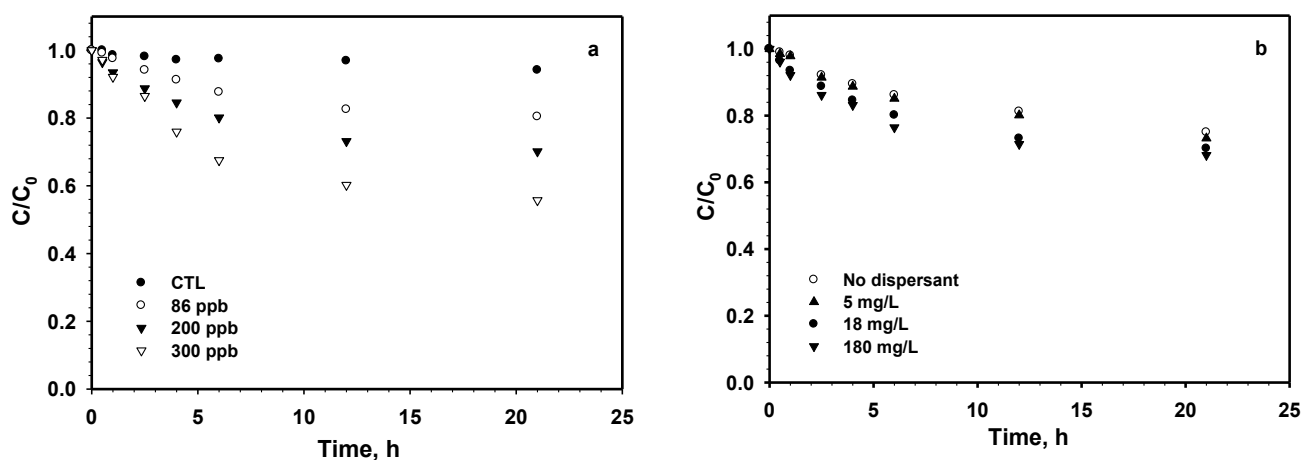
**Figure 129. Volatilization and ozonation of 1-methylfluorene.**

Experimental conditions: initial 1-methylfluorene concentration = 200  $\mu\text{g/L}$ , gas flow rate = 15 mL/min, temperature =  $22 \pm 1 \text{ }^\circ\text{C}$ , initial pH = 8.3, salinity = 2%, and DOM = 2.2 mg/L as TOC.

### 6.1.3.2. Dispersant effects on the ozonation of 1-methylfluorene

**Figure 130a** shows the volatilization and ozonation of 1-methylfluorene at various ozone concentrations in the presence of dispersant at 18 mg/L. **Table 35** gives the rate constants based on the first-order kinetic model (Equation 85). The dispersant had no significant effects on the volatilization loss, i.e., 6~7% at 21 h. Similar to the case of 1-methylnaphthalene, the ozonation rate of 1-methylfluorene was enhanced by the dispersant. At 21 h, the overall dissipation of 1-methylfluorene was 19%, 30%, and 45% when exposed to 86, 200, and 300 ppb of ozone, respectively. Kinetically, in the presence of 18 mg/L of the dispersant, the  $k_o$  value increased from 0.0049 h<sup>-1</sup> to 0.0092 h<sup>-1</sup> at the ozone concentration of 86 ppb; in addition,  $k_o$  increased from 0.0121 h<sup>-1</sup> to 0.0175 h<sup>-1</sup> and from 0.0221 h<sup>-1</sup> to 0.0310 h<sup>-1</sup> at the ozone concentration of 200 ppb and 300 ppb, respectively.

**Figure 130b** shows the effect of dispersant concentration on the ozonation of 1-methylfluorene at the ozone concentration of 200 ppb. The ozonation dissipation rate of 1-methylfluorene was increased with the increase of the dispersant concentration, e.g., the  $k_o$  value is 0.0121 h<sup>-1</sup> at 200 ppb ozone in the absence of dispersant was increased to 0.0133, 0.0175, 0.0195 h<sup>-1</sup> in the presence of dispersant at 5, 18, and 180 mg/L.



**Figure 130. Dispersant effects on the volatilization and ozonation of 1-methylfluorene.**

(a) At various ozone concentrations in the presence of 18 mg/L of the dispersant, and (b) at various dispersant concentrations with 200 ppb ozone. Experimental conditions: initial 1-methylfluorene concentration = 200 µg/L temperature = 22±1 °C, pH = 8.3, salinity = 2%, and DOM = 2.2 mg/L as TOC.

**Table 35. First-order rate constants for 1-methylnaphthalene volatilization and ozonation in the presence of dispersant at 18 mg/L**

Ozone (ppb)	Volatilization		Overall dissipation		Ozonation
	$k_v$ (h <sup>-1</sup> )	$R^2$	$k$ (h <sup>-1</sup> )	$R^2$	$k_o$ (h <sup>-1</sup> )
0	0.0036	0.90	0.0036	0.91	0
86	0.0036	0.90	0.0128	0.89	0.0092
200	0.0036	0.90	0.0211	0.92	0.0175
300	0.0036	0.90	0.0346	0.89	0.0310

### 6.1.3.3. pH effects on the ozonation of 1-methylfluorene

Figure 131 shows the pH effects on the ozonation of 1-methylfluorene at the ozone concentration of 200 ppb. The results indicate that decreasing pH from 8 to 5 only slightly inhibited the ozonation. The overall dissipation decreased from 25% to 17% when the solution pH decreased from 8 to 5 at 21 h. The  $k_o$  value shown in the figure decreased from 0.0121 h<sup>-1</sup> at pH 8 to 0.0062 h<sup>-1</sup> at pH 5. The solution pH could affect both direct ozone oxidation and indirect radical oxidation. Generally, direct oxidation is dominant in acidic solutions, whereas indirect oxidation contributes more in basic solutions (Tomiyasu et al. 1985, Zhao et al. 2006).

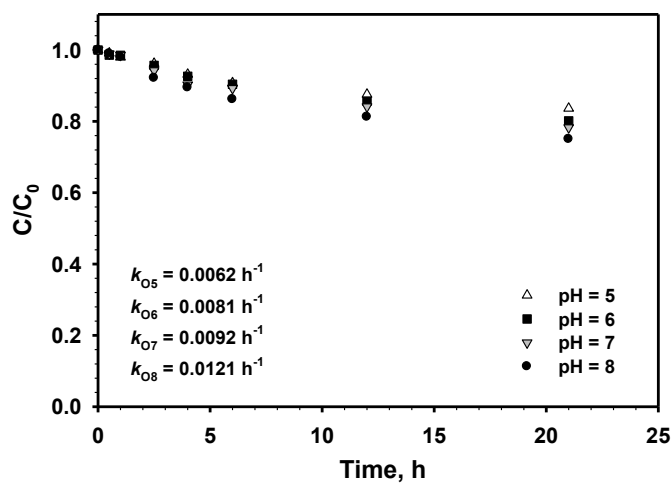


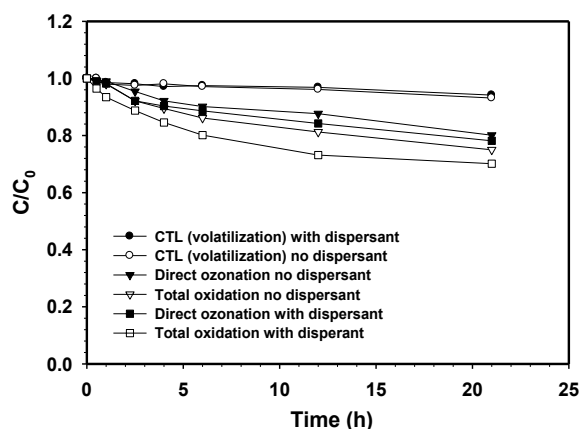
Figure 131. Effects of pH on the ozonation of 1-methylfluorene.

Experimental conditions: initial 1-methylfluorene concentration = 200 µg/L, ozone concentration = 200 ppb, gas flow rate = 15 mL/min, temperature = 22±1 °C, salinity = 2%, and DOM = 2.2 mg/L as TOC.



### 6.1.3.4. Ozonation mechanisms of 1-methylfluorene

**Figure 132** shows the volatilization, direct ozone oxidation and total ozonation rates of 1-methylfluorene in the absence or presence of the dispersant (18 mg/L). The volatilization rate constant ( $k_v$ ) of 1-methylfluorene was determined to be  $0.0036 \text{ h}^{-1}$ , which is much lower than that of 1-methylnaphthalene ( $0.0249 \text{ h}^{-1}$ ), and the presence of the dispersant only modestly affected the volatilization, which lowered the volatilization by ~6% to ~7% at 21 h. In the absence of the dispersant, the depletion of 1-methylfluorene by ozonation in the aqueous phase was 25% at 21 h, of which 20% was due to direct ozone oxidation. In the presence of the dispersant, the removal by ozonation and direct ozone oxidation increased to 30% and 22%, respectively.



**Figure 132. Volatilization, direct ozonation and total oxidation of 1-methylfluorene.**

Experimental conditions: initial 1-methylfluorene concentration = 200  $\mu\text{g/L}$ , ozone = 200 ppb, gas flow rate = 15 mL/min, tert-Butyl alcohol = 10 mM, dispersant Corexit EC9500A = 0 or 18 mg/L, temperature =  $22 \pm 1 \text{ }^\circ\text{C}$ , initial pH = 8.3, salinity = 2%.

Comparing the ozonation rate constants, the direct ozonation was the dominant ozonation mechanism in both cases (as shown in **Table 36**). The presence of the dispersant increased both direct ozonation rate ( $0.0097 \text{ h}^{-1}$ ) and indirect ozonation rate ( $0.0078 \text{ h}^{-1}$ ). This observation agrees with the ozonation of 1-methylnaphthalene.

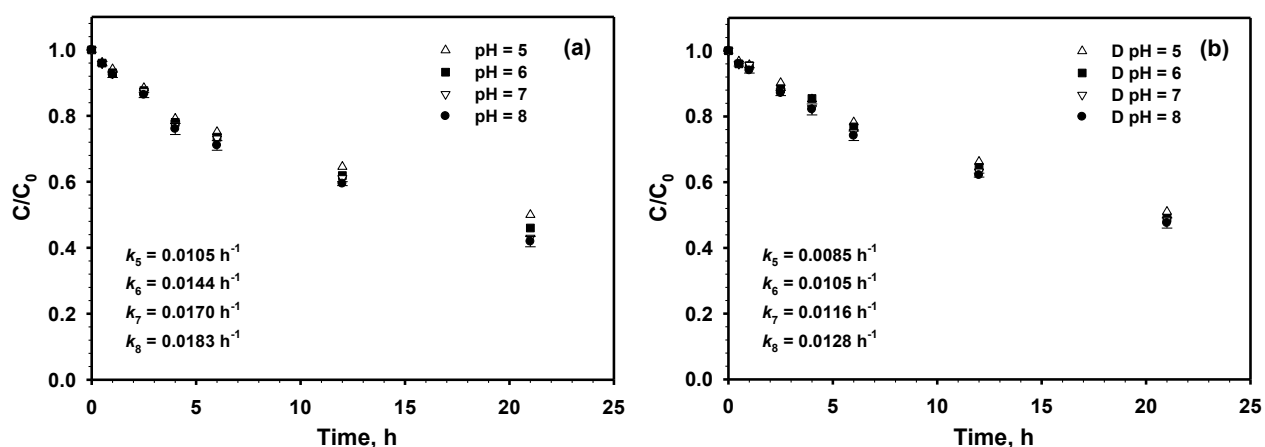
**Table 36. First-order rate constants for 1-methylfluorene ozonation (200 ppb ozone)**

Dispersant (mg/L)	Volatilization		Direct ozonation		Indirect ozonation
	$k_v \text{ (h}^{-1}\text{)}$	$R^2$	$k_D \text{ (h}^{-1}\text{)}$	$R^2$	$k_R \text{ (h}^{-1}\text{)}$
0	0.0036	0.90	0.0078	0.92	0.0043
18	0.0036	0.90	0.0097	0.90	0.0078

### 6.1.3.5. Effects of pH on direct and indirect ozonation of 1-methylnaphthalene

To investigate the effects of pH on the ozonation of alkylated PAHs, batch kinetic tests were conducted to study the pH effects on the direct oxidation rates of 1-methylnaphthalene at the 200 ppb level of ozone.

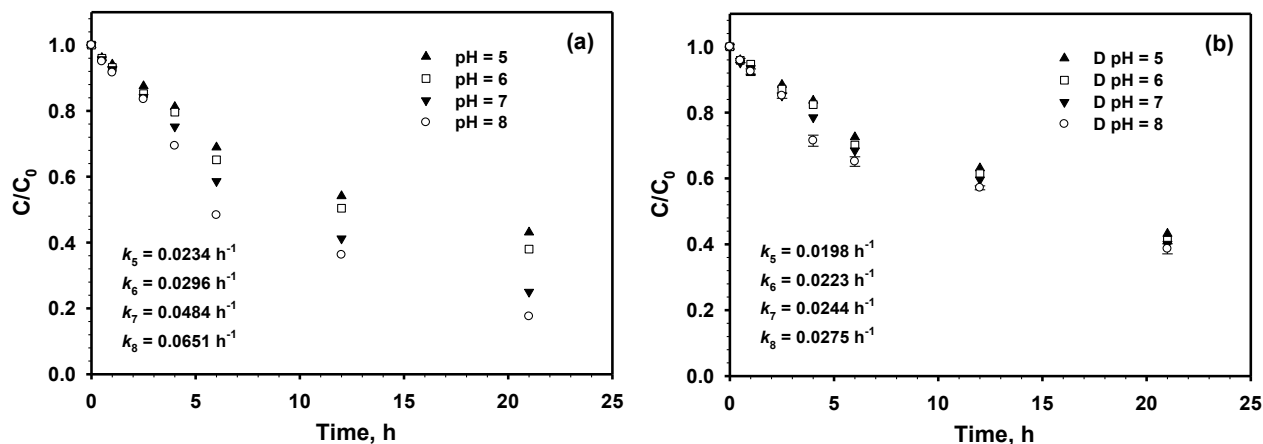
**Figure 133** shows the pH effects on the ozonation (**Figure 133a**) and direct ozonation (**Figure 133b**) of 1-methylfluorene under identical conditions. The  $k$  value in the Figure represents the oxidation rates based on the first-order kinetic model. The overall ozonation rate increased from 0.0105 to 0.0144, 0.0170 and 0.0183  $\text{h}^{-1}$  when the solution pH was increased from 5 to 6, 7 and 8, respectively, and the direct oxidation rate increased from 0.0085 to 0.0105, 0.0116 and 0.0128  $\text{h}^{-1}$ . The indirect oxidation rate was then calculated to be 0.0020, 0.0039, 0.0054 and 0.0055  $\text{h}^{-1}$  at pH 5, 6, 7 and 8, respectively. This observation indicates that both direct and indirect oxidation rates are enhanced when the solution pH is increased. Other researchers (Ning et al., 2007a) claimed that the increased overall ozonation rate is mainly due to the increasing influence on the indirect radical reaction with increasing pH.



**Figure 133. Volatilization and ozonation of 1-methylfluorene in the absence of dispersant.**

(a) Volatilization and overall ozonation, and (b) volatilization and direct ozonation. Experimental conditions: initial 1-methylnaphthalene concentration = 500  $\mu\text{g/L}$ , ozone = 200 ppb, gas flow rate = 15 mL/min, tert-Butyl alcohol = 10 mM, temperature =  $22 \pm 1$   $^\circ\text{C}$ , initial pH = 8.3, salinity = 2%.

To further study the effects of pH and dispersant, batch kinetic tests were conducted in the presence of 18 mg/L dispersant under otherwise identical conditions. **Figure 134** shows the kinetics of the overall ozonation and direct ozonation rates of 1-methylfluorene in the pH range 5 to 8.



**Figure 134. Volatilization and ozonation of 1-methylfluorene in the presence of dispersant.**

(a) Volatilization and overall ozonation, and (b) volatilization and direct ozonation of 1-methylfluorene in the presence of dispersant. Experimental conditions: initial 1-methylnaphthalene concentration = 500  $\mu\text{g/L}$ , ozone = 200 ppb, gas flow rate = 15 mL/min, tert-Butyl alcohol = 10 mM, dispersant Corexit EC9500A = 18 mg/L, temperature =  $22 \pm 1$   $^{\circ}\text{C}$ , initial pH = 8.3, salinity = 2%.

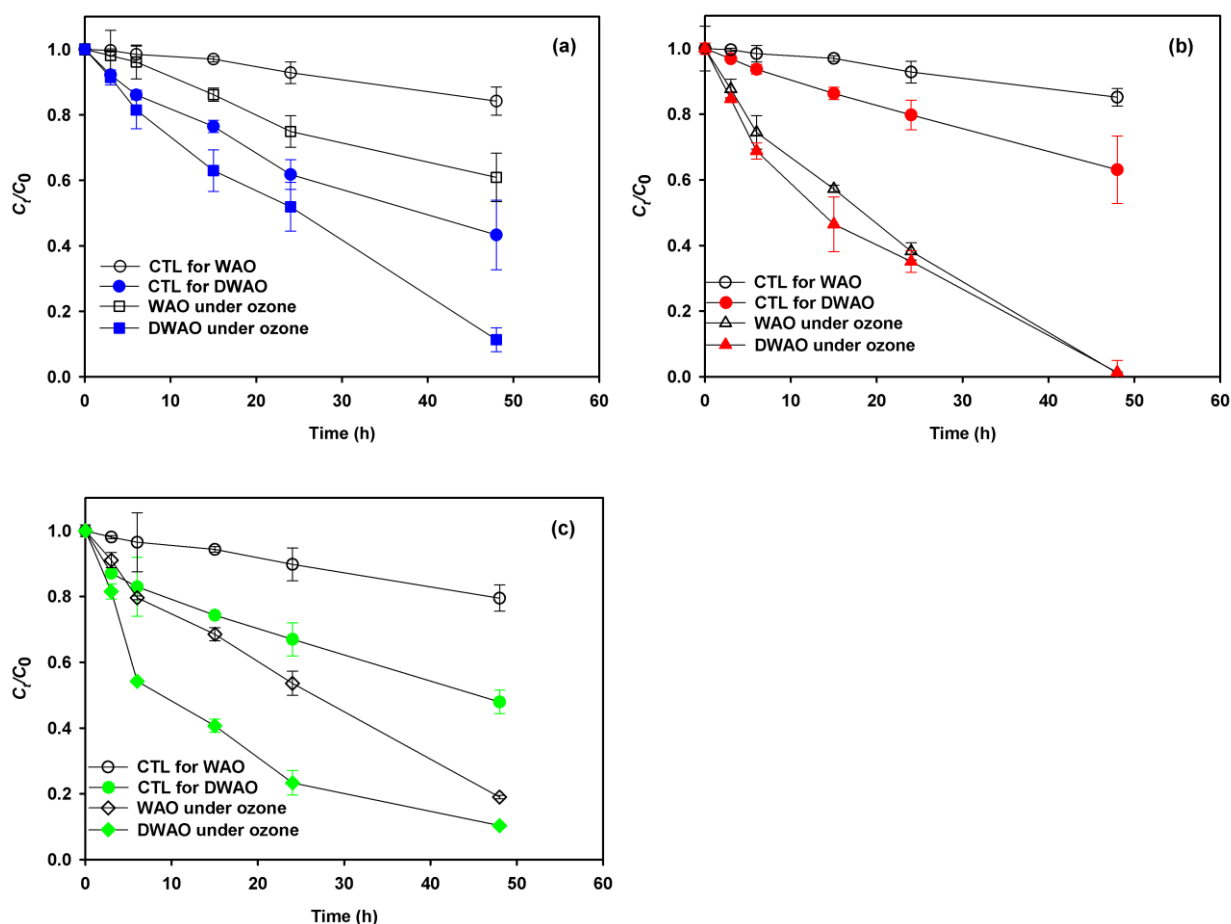
The overall oxidation rate ( $k$ ) increased from 0.0234 to 0.0296, 0.0484 and 0.0651  $\text{h}^{-1}$  when the solution pH was increased from 5 to 6, 7, and 8, respectively, and the direct oxidation rate increased from 0.0198 to 0.0223, 0.0244, 0.0275  $\text{h}^{-1}$ . Accordingly, the indirect oxidation rate was calculated to be 0.0036, 0.0073, 0.0240 and 0.0376  $\text{h}^{-1}$ . The solution pH could affect both direct ozone oxidation and indirect oxidation by radicals (Ning et al., 2007b). Direct oxidation is dominant in acidic solutions, whereas indirect oxidation contributes more in basic solutions (Tomiyasu et al., 1985; Zhao et al., 2006).

## 6.2. Effects of Dispersant on Ozonation of WAOs and DWAOs by Surface-Level Ozone

### 6.2.1. Effects of oil dispersant on ozone oxidation of DPHs in seawater

As shown above, volatilization and ozonation can be important processes affecting the fate and transport of PAHs or alkylated PAHs. Likewise, ozonation may also affect the transformation or weathering of DPHs by direct ozonation and/or the indirect reaction with free radicals (Stachelin and Hoigne 1985). The radicals are from the decomposition of ozone, which is initiated by the hydroxide ion or other trace substances (e.g., DOM). In the following work, the volatilization and ozonation of dissolved or dispersed oil components were tested. In all cases, the integrated first order kinetic model (Equation 87) was employed to interpret the ozonation kinetic data for TPHs,  $n$ -alkanes and Total PAHs (TPAHs) (Lin et al. 2014, Ning et al. 2015).

**Figure 135a** shows the volatilization and ozonation rates of TPHs under the atmospheric ozone level. At 48 h, the volatilization of TPHs in WAO and DWAO was 15.8% and 56.7% without ozone, respectively. In addition, the total depletion of the aqueous phase TPHs was 39.1% and 88.7% in the presence of 86 ppbv ozone in WAO and DWAO, respectively. **Figure 135b** shows the volatilization and ozonation of *n*-alkanes in WAO and DWAO in the presence of 86 ppbv ozone. **Figure 136** displays the distribution of *n*-alkanes in WAO and DWAO before and after the ozonation. Evidently, the dispersant Corexit EC9500A significantly increased the apparent solubility of *n*-alkanes (**Figure 136b**), especially for LMWHs (C10–C14) and HMWHs (C24–C29) *n*-alkanes, which is consistent with that reported by Zhao et al (2016c). **Figure 135c** shows the volatilization and ozonation rates of TPAHs in WAO and DWAO when exposed to 86 ppbv of atmospheric ozone. **Figure 137** displays the distributions of PAHs in WAO and DWAO before and after the ozonation. Similar to the distribution of *n*-alkanes, the presence of Corexit EC9500A significantly increased the solubility of PAHs in DWAO. **Figure 138** shows the volatilization and ozonation rates of parent PAHs and alkylated PAHs in WAO and DWAO when exposed to 86 ppbv of atmospheric ozone, and **Table 37** gives the corresponding rate constants.



**Figure 135. Volatilization and ozonation of oil components in WAO and DWAO solutions.** (a) TPHs, (b) *n*-alkanes, and (c) total PAHs in WAO and DWAO (Corexit EC9500A) solutions. Experimental conditions: initial TPHs, *n*-alkanes and TPAHs concentration in WAO = 0.371, 0.122 and 0.520 mg/L; initial TPHs, *n*-alkanes and TPAHs concentration in DWAO = 149.7, 79.3 and 6.21 mg/L; gas flow rate = 4 mL/min, temperature =  $22 \pm 1$  °C, volume of solution = 250 mL, solution pH =  $8.1 \pm 1$ , salinity = 2%. Symbols are experimental data plotted as mean of duplicates, and error bars refer to deviation from the mean to indicate data reproducibility.

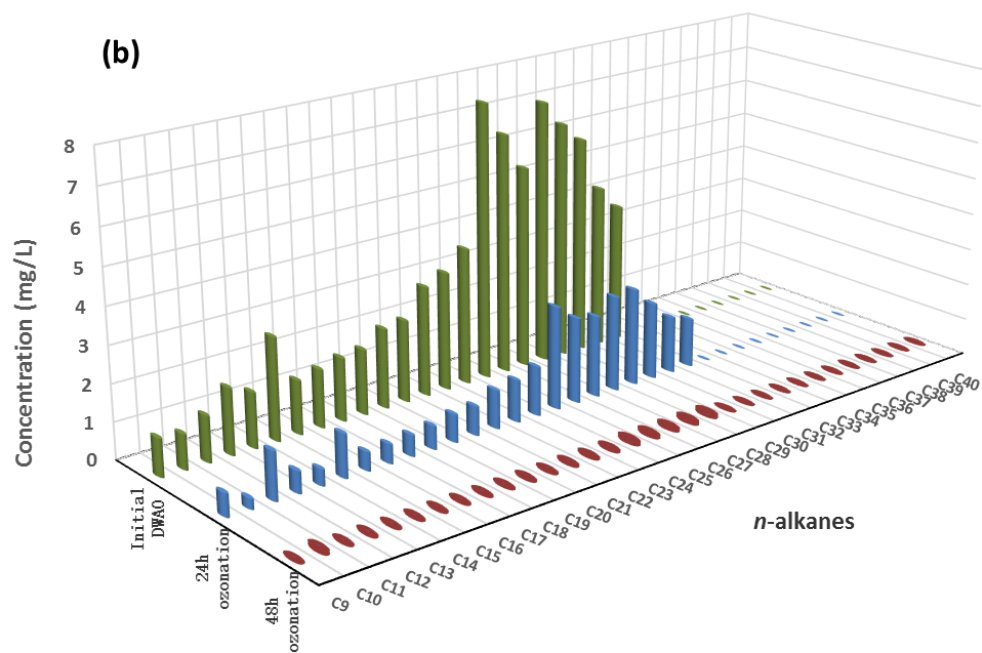
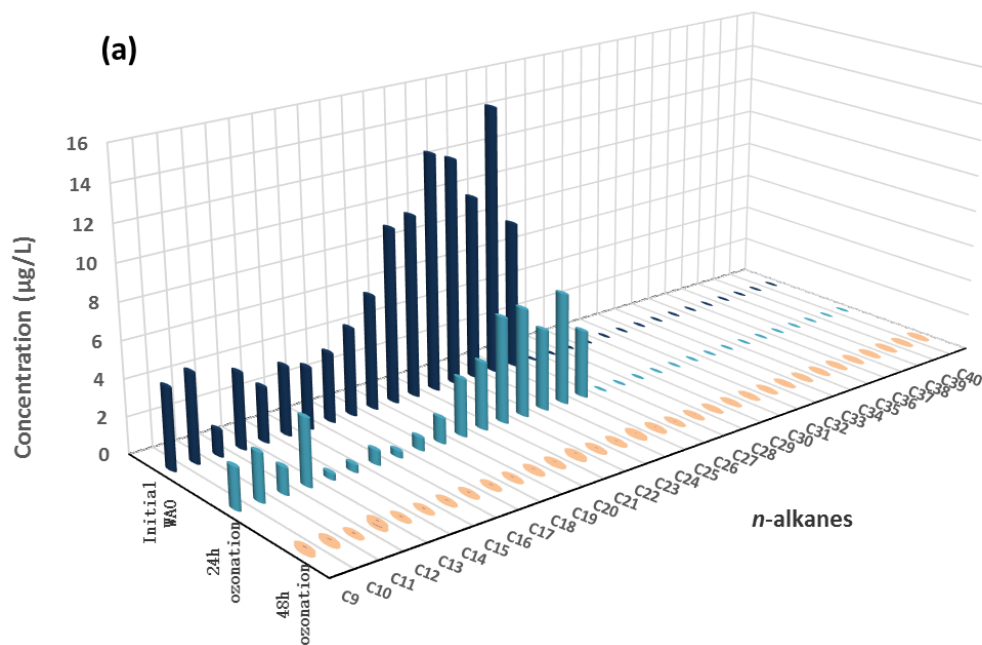


Figure 136. Distributions of  $n$ -alkanes in WAO (a) and DWAO (b) before and after ozonation.

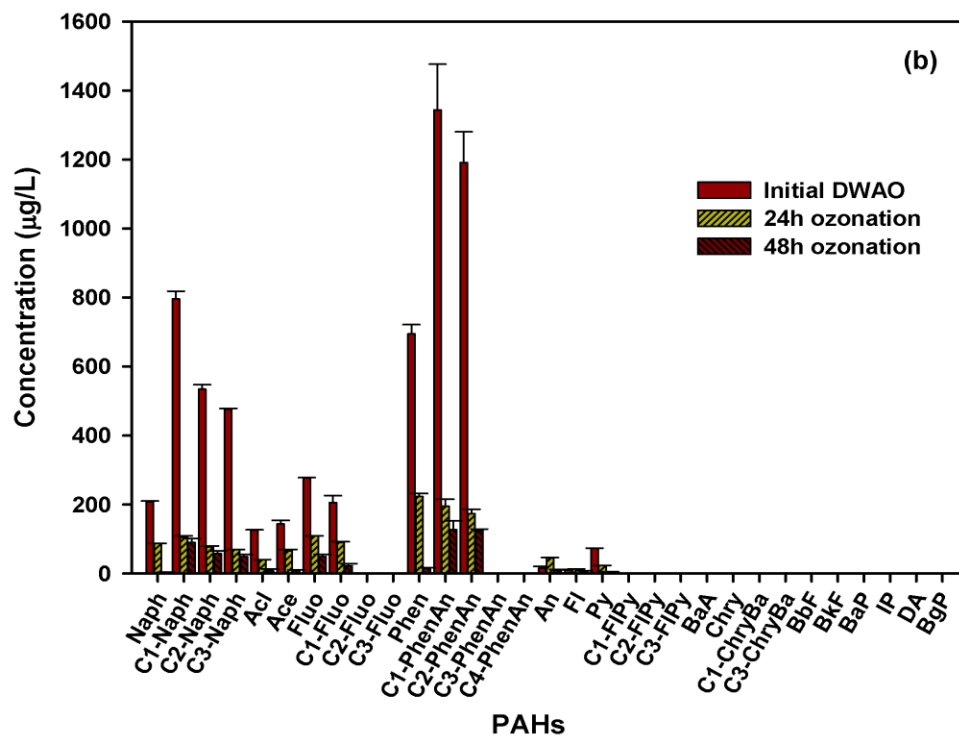
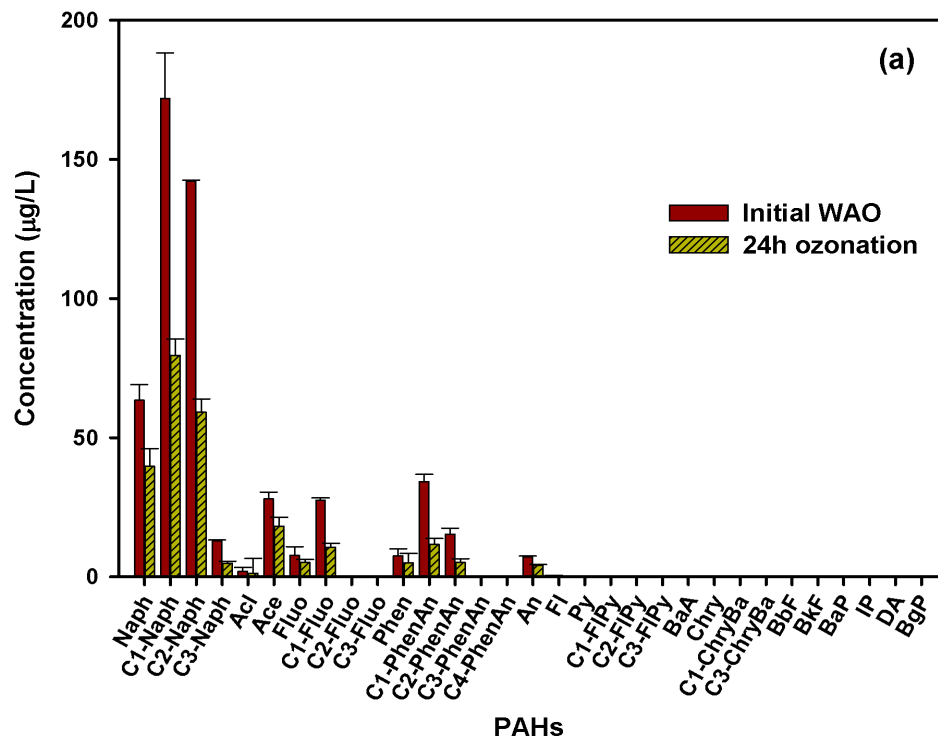
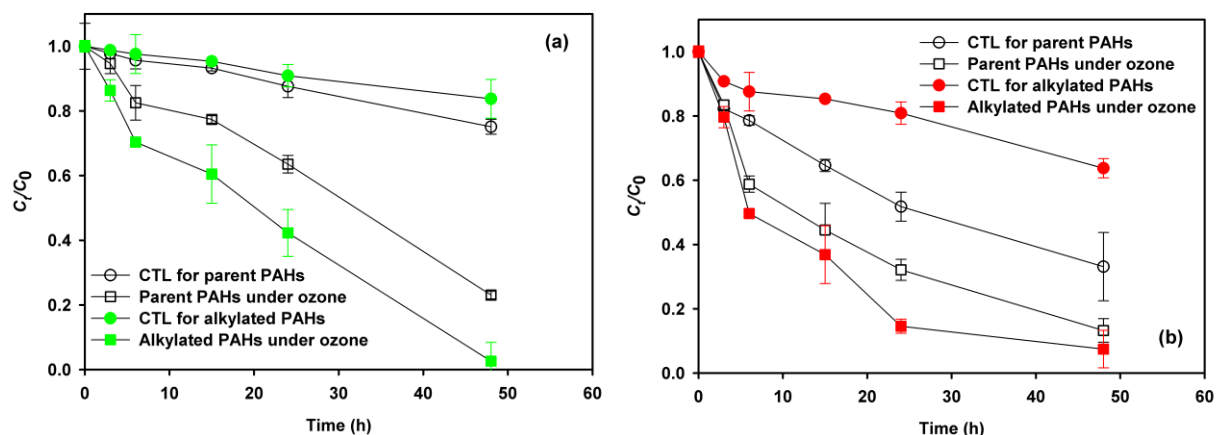


Figure 137. Distributions of PAHs in WAO (a) and DWAO (b) before and after ozonation.



**Figure 138. Volatilization and ozonation of parent PAHs and alkylated PAHs.**

(a) in WAO, and (b) in DWAO with Corexit EC9500A.

Accordingly, the first order kinetic model was applied to interpret the volatilization and total depletion rate data. **Table 37** gives the resultant kinetic parameters for volatilization and ozonation of TPHs, *n*-alkanes and Total PAHs in WAO and DWAO. Both volatilization and overall dissipation of TPHs, *n*-alkanes and Total PAHs can be adequately interpreted by the first-order kinetic model ( $R^2 > 0.96$ ). For WAO, the volatilization rate constant ( $k_v$ ) of TPHs, *n*-alkanes and Total PAHs was determined to be 0.0036, 0.0034 and 0.0046  $\text{h}^{-1}$ , respectively, under the air flow rate of 4 mL/min. And the ozonation rate constant ( $k_o$ ) was 0.0073, 0.0411 and 0.0245  $\text{h}^{-1}$ , respectively, when exposed to 86 ppbv of ozone. For DWAO, the volatilization rate of TPHs, *n*-alkanes and Total PAHs was 0.0177, 0.0095 and 0.0146  $\text{h}^{-1}$  under the air flow rate of 4 mL/min, respectively; and the ozonation rate was 0.016, 0.0415 and 0.0479  $\text{h}^{-1}$  with 86 ppbv ozone, respectively, when exposed to 86 ppbv of ozone.

**Table 37. First-order ozone oxidation rate constants for TPHs, *n*-alkanes and TPAHs in WAO and DWAO.**

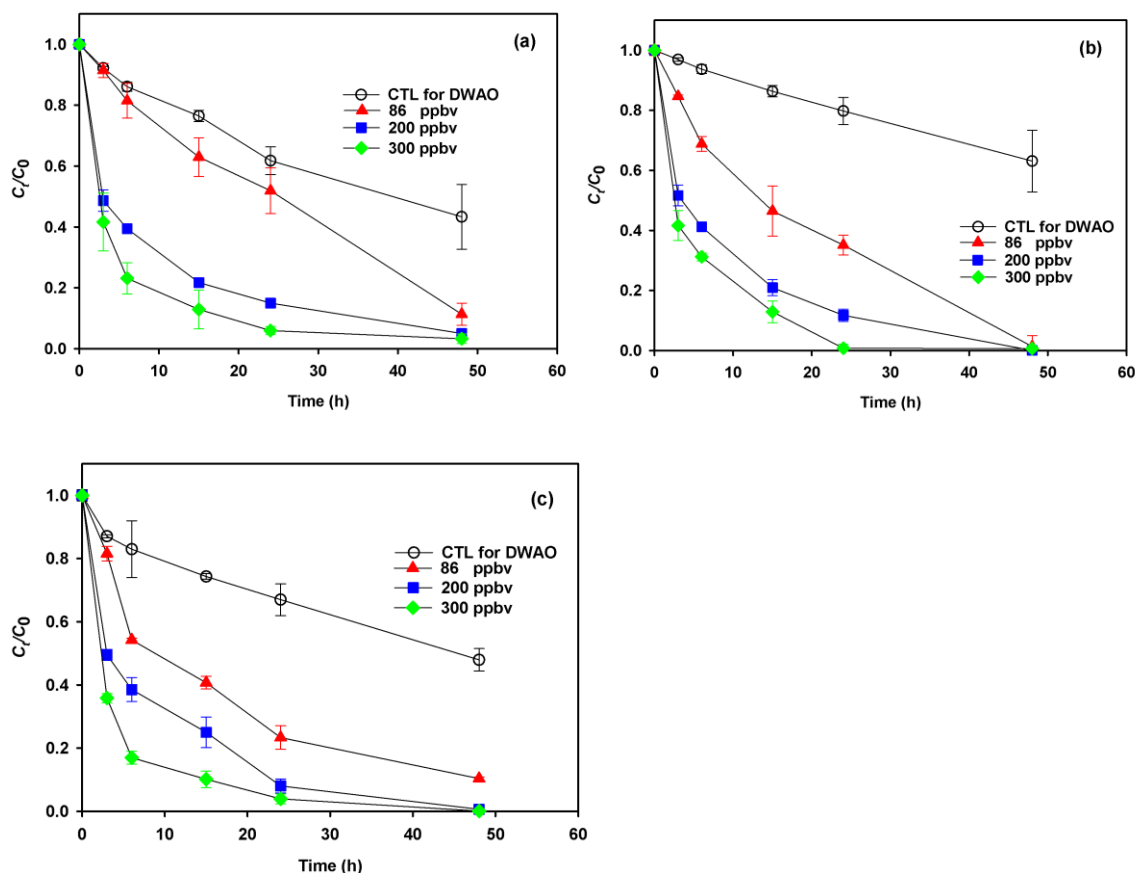
Type		Volatilization		Overall dissipation		Ozonation
		$k_v$ ( $\text{h}^{-1}$ )	$R^2$	$k$ ( $\text{h}^{-1}$ )	$R^2$	$k_o$ ( $\text{h}^{-1}$ )
TPHs	WAO	0.0036	0.9813	0.0109	0.9895	0.0073
	DWAO	0.0177	0.9920	0.0337	0.9752	0.0160
<i>n</i> -alkanes	WAO	0.0034	0.9856	0.0445	0.9742	0.0411
	DWAO	0.0095	0.9994	0.0510	0.9835	0.0415
TPAHs	WAO	0.0046	0.9919	0.0291	0.9809	0.0245
	DWAO	0.0146	0.9642	0.0625	0.9655	0.0479

Comparing WAO with DWAO, the ozonation was enhanced with addition of the dispersants. The dispersant Corexit EC9500A can affect the oxidation of TPHs, *n*-alkanes and TPAHs in two contrasting ways. On one hand, the dispersant can accelerate the degradation by lowering the surface tension which may reduce the gas transfer barrier between the ozone gas phase and the liquid phase, and thereby leading to an increase in the soluble ozone concentration in the water (Chu et al. 2006). On the other hand, the dispersant itself can consume ozone and free radicals resulting in reduced ozone degradation rate (Amat et al. 2007, Ikehata and El-Din 2004). The overall effect depends on the extent of these two contrasting factors. In this study, the promoting effects outweighed the inhibitive effects. The contributions of direct oxidation by ozone and  $\bullet\text{OH}$ -facilitated indirect oxidation are quantified in Section 6.2.3.

## 6.2.2. Influence of ozone concentration and water chemistry on ozonation of DPHs in DWAO

### 6.2.2.1. Effects of ozone concentration

Figure 139 shows the ozonation of TPHs, *n*-alkanes and PAHs in DWAO at a fixed gas flow rate of 4 mL/min and when exposed to various ozone concentrations (86, 200, and 300 ppbv). The initial concentrations of TPHs, *n*-alkanes and TPAHs were 149.7, 79.1, and 6.2 mg/L in DWAO, and accordingly, the removal rates of these oil compounds from the aqueous phase were 91.9%, 99.5% and 99.8% in the presence of 200 ppbv of ozone, respectively.



**Figure 139. Ozonation of oil components at various ozone concentrations.**

(a) TPHs, (b) *n*-alkanes and (c) TPAHs in DWAO (Corexit EC9500A). Experimental conditions: initial TPHs, *n*-alkanes and TPAHs concentration in DWAO = 149.7, 79.3 and 6.21 mg/L, gas flow rate = 4 mL/min, temperature =  $22 \pm 1$  °C, volume of solution = 250 mL, solution pH =  $8.1 \pm 1$ , salinity = 2%. Symbols: experimental data plotted as mean of duplicates; error bars refer to deviation from the mean to indicate data reproducibility.

Figure 139b shows the ozonation rate of *n*-alkanes in DWAO at a fixed gas flow rate of 4 mL/min and at ozone concentrations of 86, 200 and 300 ppbv. The overall removal rate of *n*-alkanes increased with increasing ozone concentration, and the  $k_o$  value increased from 0.0415 to  $0.2101 \text{ h}^{-1}$  when the ozone

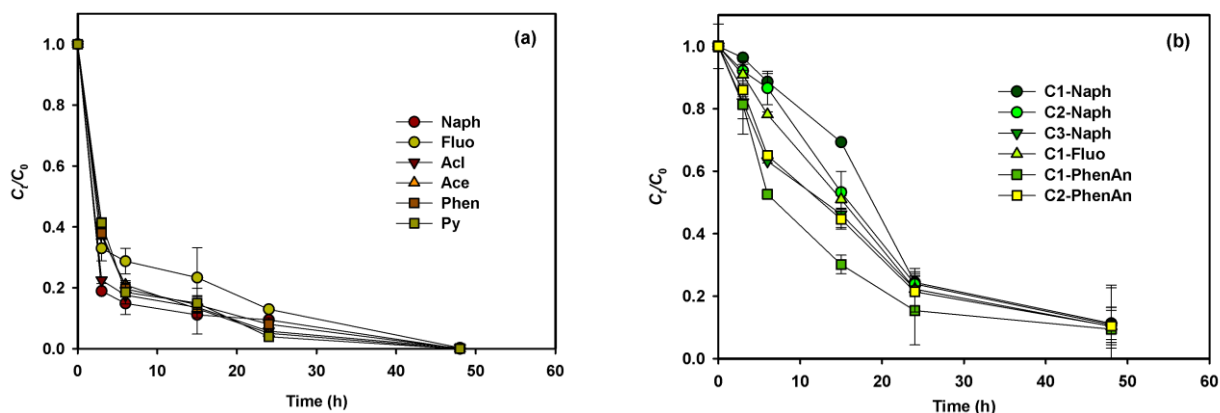


concentration was increased from 86 to 300 ppbv (**Table 38**). The concentration of *n*-alkanes of larger molecular weight (C24–C29) was higher, which was more difficult to degrade. Further tests are conducted to investigate the mechanisms for ozonation in Section 6.2.3.

**Table 38. First-order ozone oxidation rate constants for TPHs, *n*-alkanes and TPAHs in DWAO when exposed to various concentrations of atmospheric ozone**

Type	Ozone concentration	Volatilization		Overall dissipation		Ozonation
		$k_v$ ( $\text{h}^{-1}$ )	$R^2$	$k$ ( $\text{h}^{-1}$ )	$R^2$	$k_o$ ( $\text{h}^{-1}$ )
TPHs	86 ppbv	0.0177	0.9920	0.0337	0.9752	0.0160
	200 ppbv	0.0177	0.9920	0.1357	0.9189	0.118
	300 ppbv	0.0177	0.9920	0.2544	0.9727	0.2367
<i>n</i> -alkanes	86 ppbv	0.0095	0.9994	0.0510	0.9835	0.0415
	200 ppbv	0.0095	0.9994	0.1335	0.9542	0.124
	300 ppbv	0.0095	0.9994	0.2196	0.9721	0.2101
TPAHs	86 ppbv	0.0146	0.9642	0.0625	0.9655	0.0479
	200 ppbv	0.0146	0.9642	0.1381	0.9387	0.1235
	300 ppbv	0.0146	0.9642	0.3162	0.9840	0.3016

**Figure 140** shows the ozonation of typical parent PAHs and alkylated PAHs at an ozone concentration of 200 ppbv, and **Table 39** lists the corresponding rate constants for the degradation reaction. The degradation rates of the parent PAHs decreased with the increasing ring number. For example, the  $k$  value of naphthalene was  $0.4807 \text{ h}^{-1}$ , which was 1.68 times higher than that of phenanthrene ( $0.2863 \text{ h}^{-1}$ ) and 1.75 times that of pyrene.



**Figure 140. Ozonation of parent PAHs (a) and alkylated PAHs (b) in DWAO.**

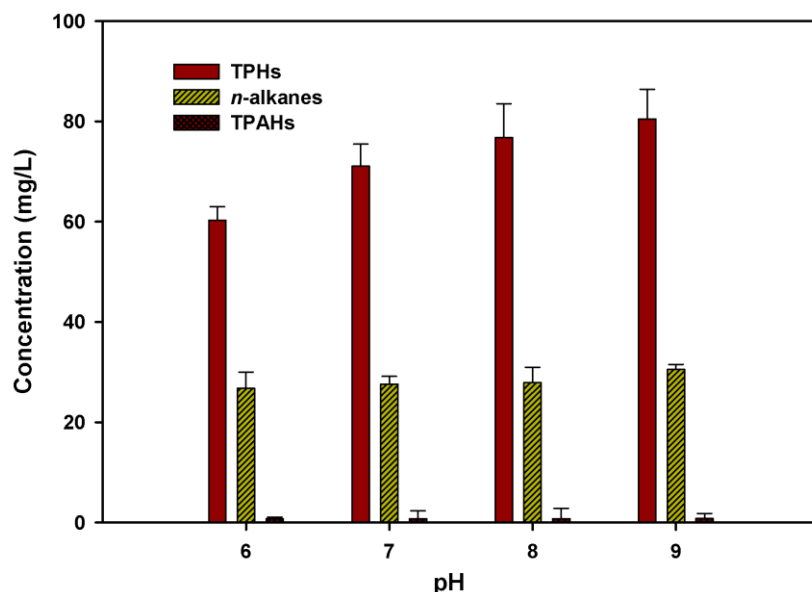
Experimental conditions: initial TPHs, *n*-alkanes and TPAHs concentration in DWAO (Corexit EC9500A) = 149.7, 79.3 and 6.21 mg/L, gas flow rate = 4 mL/min, ozone = 200 ppbv, temperature =  $22 \pm 1$  °C, volume of solution = 250 mL, solution pH =  $8.1 \pm 1$ , salinity = 2%.

**Table 39. First-order rate constants for various PAHs at an ozone concentration of 200 ppbv**

PAHs	Parameters $k$ ( $\text{h}^{-1}$ )	$R^2$
Naphthalene	0.4807	0.9530
Acenaphthylene	0.2485	0.8632
Acenaphthene	0.4168	0.9502
Fluorene	0.2870	0.9707
Phenanthrene	0.2863	0.9619
Pyrene	0.2751	0.9714

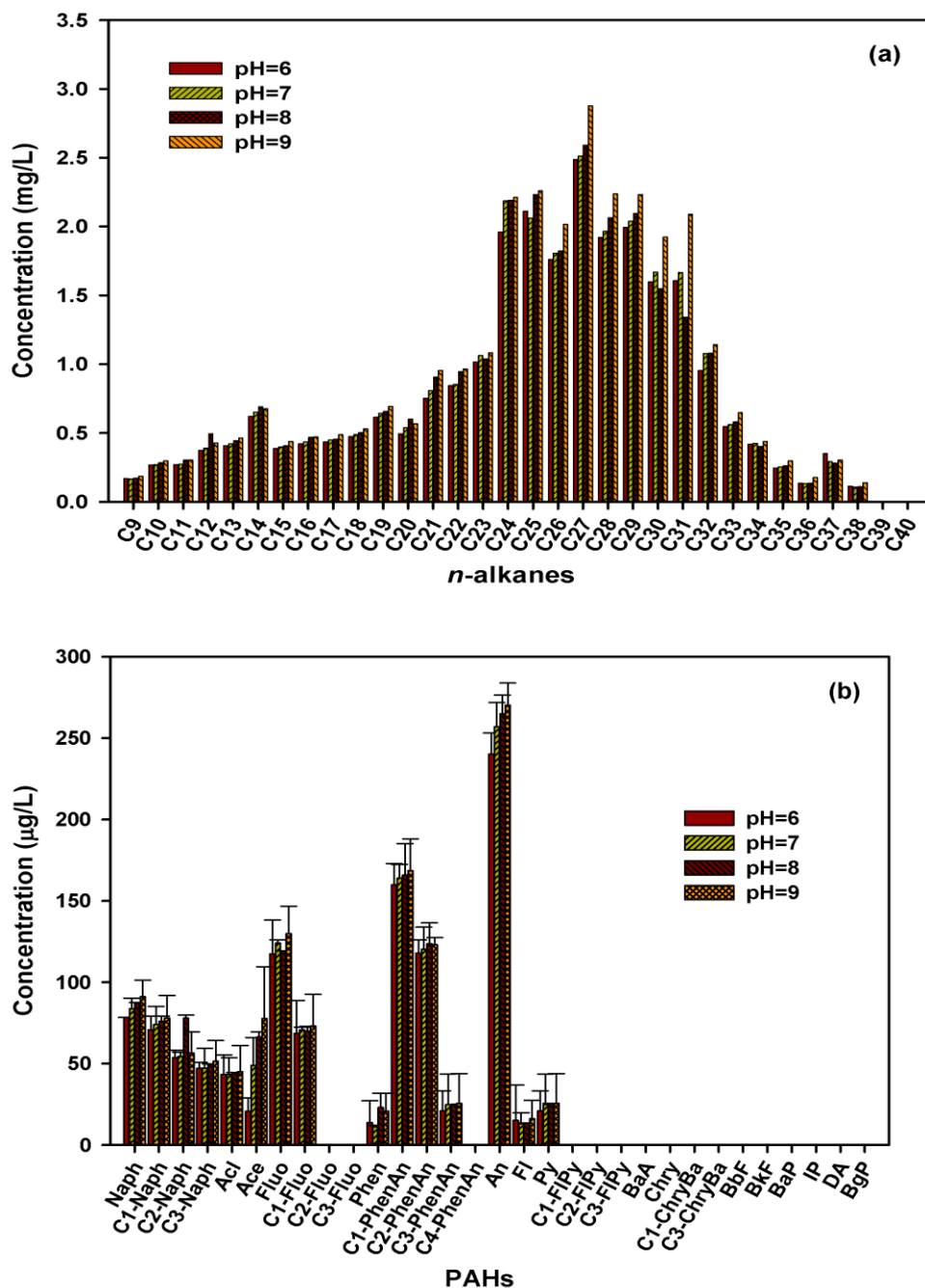
### 6.2.2.2. Effects of pH on the ozonation of DPHs in DWAO

**Figure 141** shows the pH effects on ozonation of TPHs, *n*-alkanes and TPAHs in DWAO at an ozone concentration of 86 ppbv. The overall dissipation rate of TPHs decreased only slightly from 93.3% to 92.6% when the solution pH was increased from 6 to 9 at 24 h, indicating fairly minor effects of pH in the tested pH range. **Figure 142** shows distribution of *n*-alkanes and PAHs after 24h ozonation at various pH. **Figure 143** profiles the ozonation of parent and alkylated PAHs at various pH levels. After 24 hours of ozonation, the final parent PAHs concentrations were 0.44, 0.48, 0.61, and 0.78 mg/L at pH of 6, 7, 8, and 9, respectively; and the final concentrations of alkylated PAHs were 0.48, 0.49, 0.71, and 0.77 mg/L. **Figure 142b** shows the distributions of parent and alkylated PAHs after ozonation, indicating that increasing pH inhibited ozonation of all the PAHs (2, 3, and 4 rings of PAHs) in DWAO.



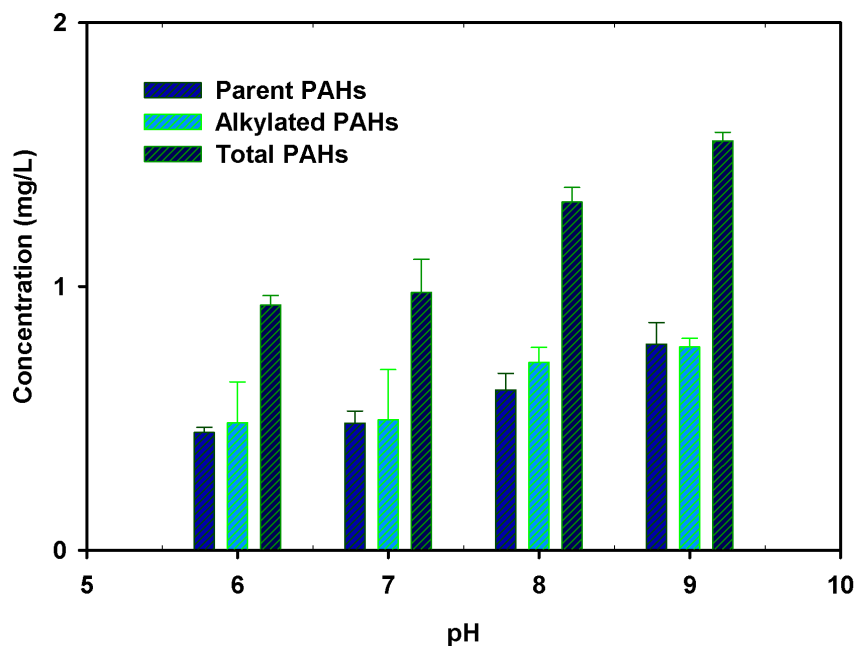
**Figure 141. Effects of pH on ozonation of TPHs, *n*-alkanes and total PAHs in DWAO.**

Experimental conditions: initial TPHs = 149.7 mg/L, *n*-alkanes = 79.3 mg/L, and TPAHs = 6.2 mg/L (in DWAO with Corexit EC9500A), gas flow rate = 4 mL/min, ozone = 86 ppbv, temperature = 22±1 °C, volume of solution = 250 mL, solution pH = 8.1±1, salinity = 2 wt.%. Symbols: experimental data plotted as mean of duplicates; lines linear regressions or First-order-type non-linear fittings; error bars refer to deviation from the mean to indicate data reproducibility.



**Figure 142. Distributions of *n*-alkanes (a) and PAHs (b) in DWAO after 24h ozonation.**

Experimental conditions: initial TPHs = 149.7 mg/L, *n*-alkanes = 79.3 mg/L, and TPAHs = 6.2 mg/L (in DWAO), gas flow rate = 4 mL/min, ozone = 86 ppbv, temperature = 22±1 °C, volume of solution = 250 mL, solution pH = 8.1±1, salinity = 2 wt.%.



**Figure 143. Effects of pH on ozonation of parent and alkylated PAHs in DWAO.**

Experimental conditions: initial TPHs = 149.7 mg/L, *n*-alkanes = 79.3 mg/L, and TPAHs = 6.2 mg/L (in DWAO with Corexit EC9500A), gas flow rate = 4 mL/min, ozone = 86 ppbv, temperature = 22±1 °C, volume of solution = 250 mL, solution pH = 8.1±1, salinity = 2 wt.%.

Solution pH significantly influences ozone decomposition in water. The pH may affect both direct oxidation by ozone and indirect oxidation by radicals. Zhao et al. (2011) studied the ozonation of cationic red X-GRL in water and they claimed that the increasing pH could enhance the indirect oxidation rate (i.e., increasing the hydroxyl radical concentration), but lower the direct oxidation rate. As pH increased, the ozone decomposition occurred via the following five-step chain reactions as shown in Equations 89 to 93 (Kasprzyk-Hordern et al. 2003). Though the alkaline environment can increase ozone decomposition to form more free radicals, and thus indirect ozonation of DPHs was favored at alkaline pH, direct ozonation was compromised to a greater extent than the gain in the indirect ozonation, resulting in a decrease in the overall DPHs degradation rate.



### 6.2.2.3. Effects of humic acid on the ozonation of DWAO

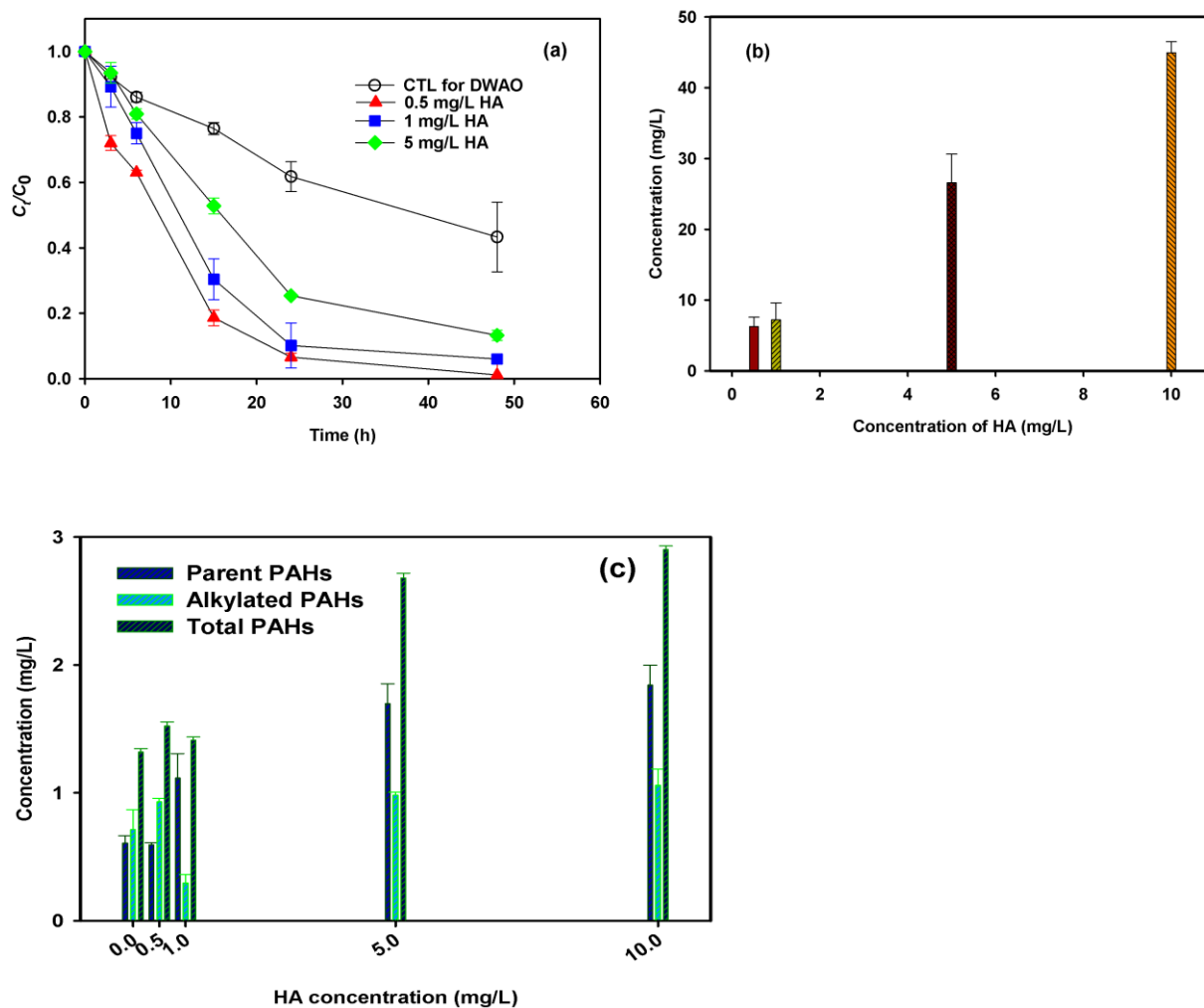
**Figure 144a** shows the volatilization and ozonation of TPHs in DWAO under a fixed gas flow rate of 4 mL/min and an ozone concentration of 86 ppbv but in the presence of different concentrations of humic acid. At 24 h, the volatilization loss of TPHs in DWAO was 38.2%, and the total depletion of the aqueous phase TPHs was 93.4%, 89.9%, and 74.6% in the presence of 0.5, 1, and 5 mg/L (as TOC) humic acid, respectively. **Table 40** presents the model-fitted first order rate constants for overall depletion, volatilization and ozonation of TPHs in DWAO. Both volatilization and overall dissipation of TPHs can be adequately interpreted by the first-order kinetic model ( $R^2 > 0.97$ ).

**Figure 144b** shows the volatilization and ozonation of *n*-alkanes of DWAO when different concentrations of humic acid were added. The total *n*-alkanes concentration in the aqueous phase after 24 h ozonation was 6.2, 7.2, 26.5, and 44.9 mg/L in the presence of 0.5, 1, 5, and 10 mg/L humic acid, respectively. Similar to TPHs, increasing humic acid concentration inhibited the ozonation of *n*-alkanes. The distributions of different segments of *n*-alkanes after 24 hours ozonation (**Figure 145a**) indicate that the inhibitive effect of humic acid is more evident on larger *n*-alkanes, in particular the fraction of HMWH (C25–C30), and the higher the humic acid concentration, the less HMW *n*-alkanes were degraded. Though the HMWHs in DWAO or WAO were expected to be converted into LMWHs in the ozonation process, the residual concentrations of LMWHs in the DWAO after the ozonation only slightly hanged with the addition of humic acid, indicating that humic acid had little effect on smaller *n*-alkanes.

**Figure 144c** profiles the ozonation of PAHs when various concentrations of humic acid were added. The total concentration of parent PAHs in the aqueous phase after 24 hours ozonation was 3.0, 8.9, 17.0, and 18.4 mg/L in the presence of 0.5, 1, 5, and 10 mg/L humic acid, respectively. Increasing humic acid concentration inhibited the degradation of PAHs. The inhibition mechanism is similar to that for TPHs and *n*-alkanes. **Figure 145b** shows the distributions of PAHs after 24h ozonation at various additional humic acid concentrations. More 3-ring PAHs (acenaphthene, fluorene and phenanthrene) remained after the ozonation at higher humic acid concentrations (5 or 10 mg/L), indicating degradation of these PAHs were inhibited to a greater extent by addition of humic acid.

The volatilization rate constant ( $k_v$ ) of TPHs in DWAO was calculated at  $0.0177 \text{ h}^{-1}$  under the air flow rate of 15 mL/min based on the kinetic data (**Table 40**). The overall dissipation rate constant ( $k$ ) decreased from  $0.0999$  to  $0.0499 \text{ h}^{-1}$  when the humic acid concentration was increased from 0.5 to 5 mg/L. Meanwhile, the ozonation rate constant ( $k_o$ ) decreased from 0.0822 to 0.0592, and  $0.0322 \text{ h}^{-1}$ , respectively, when 1 and 5 mg/L humic acid was added in the reactor. In all cases, the addition of humic acid inhibited the ozonation rate.

Researchers have claimed that humic acid can act as a promoter to convert the nonselective hydroxyl radicals into superoxide radicals (Staehelin and Hoigne 1985), inhibiting the indirect ozone oxidation of TPHs, *n*-alkanes and PAHs by hydroxyl radicals. Moreover, humic acid may compete for molecular ozone with TPHs, *n*-alkanes and PAHs in DWAO, inhibiting the direct ozonation rate.

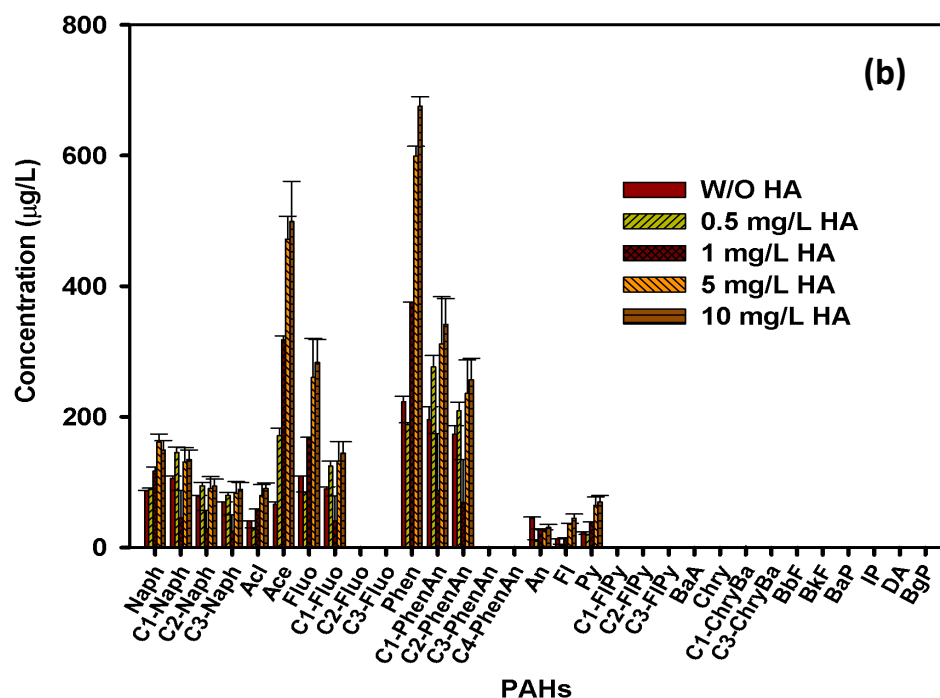
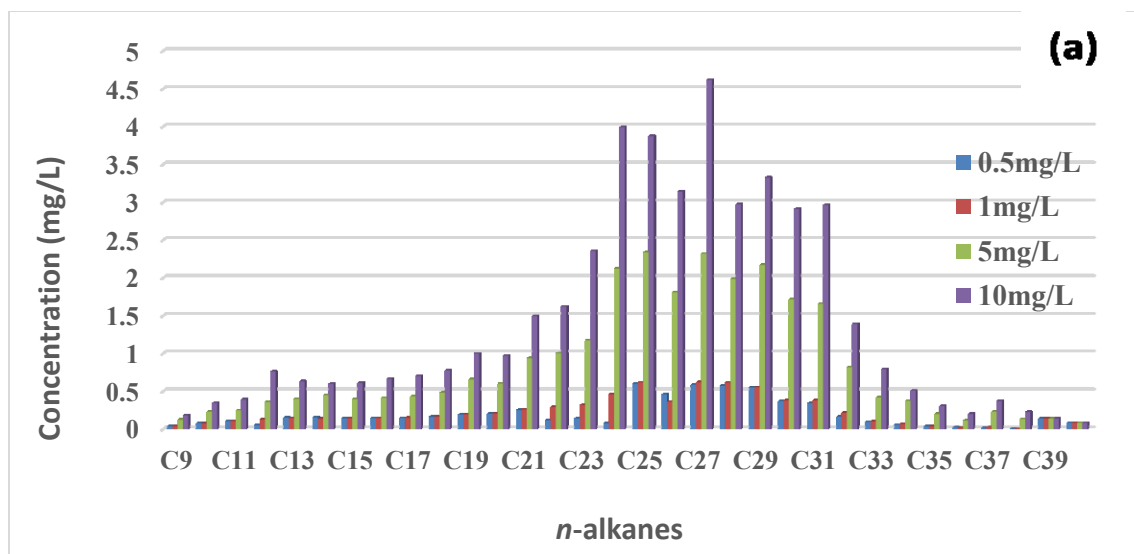


**Figure 144. Effects of humic acid on ozonation of oil components.**

(a) TPHs, (b) *n*-alkanes and (c) PAHs in DWAO (Corexit EC9500A) in the presence of various concentrations of humic acid (given as TOC). Experimental conditions: initial TPHs = 149.7 mg/L, *n*-alkanes = 79.3 mg/L, and TPAHs = 6.2 mg/L (in DWAO with Corexit EC9500A), gas flow rate = 4 mL/min, ozone = 86 ppbv, temperature = 22±1 °C, volume of solution = 250 mL, solution pH = 8.1±1, salinity = 2 wt.%.

**Table 40. First-order ozone oxidation rate constants for TPHs in DWAO in the presence of various concentrations of humic acid**

HA concentration	Volatilization		Overall dissipation		Ozonation
	$k_v$ ( $h^{-1}$ )	$R^2$	$k$ ( $h^{-1}$ )	$R^2$	$k_o$ ( $h^{-1}$ )
0.5 mg/L	0.0177	0.9920	0.0999	0.9853	0.0822
1 mg/L	0.0177	0.9920	0.0769	0.9701	0.0592
5 mg/L	0.0177	0.9920	0.0499	0.9757	0.0322



**Figure 145. Distributions of *n*-alkanes (a) and PAHs (b) in DWAO after 24 h ozonation.** Experimental conditions: initial TPHs = 149.7 mg/L, *n*-alkanes = 79.3 mg/L, and TPAHs = 6.2 mg/L (in DWAO with Corexit EC9500A), gas flow rate = 4 mL/min, ozone = 86 ppbv, temperature = 22±1 °C, volume of solution = 250 mL, solution pH = 8.1±1, salinity = 2 wt.%.



#### 6.2.2.4. Effects of salinity on the ozonation of DWAO

Figure 146a shows the effect of salinity on ozonation of TPHs in DWAO at the ozone concentration of 86 ppbv. The overall dissipation of TPHs at 24 h slightly increased from 48.1% to 53.7% when the solution salinity increased from 2% to 8%. Figure 146b profiles the effect of salinity on ozonation of *n*-alkanes in DWAO at the ozone concentration of 86 ppbv. Figure 147a shows the distributions of *n*-alkanes in DWAO after 24-h ozonation and at various salinity levels (2%, 5% and 8%). The overall dissipation of *n*-alkanes increased from 64.78% to 74.23% when the solution salinity increased from 2% to 8% at 24 h, which is consistent with the results on ozonation of TPHs. In addition, the concentration of LMWHs (especially C14) and HMWHs (especially C24–C32) decreased much more than other alkanes, when the solution salinity increased from 2% to 8%.

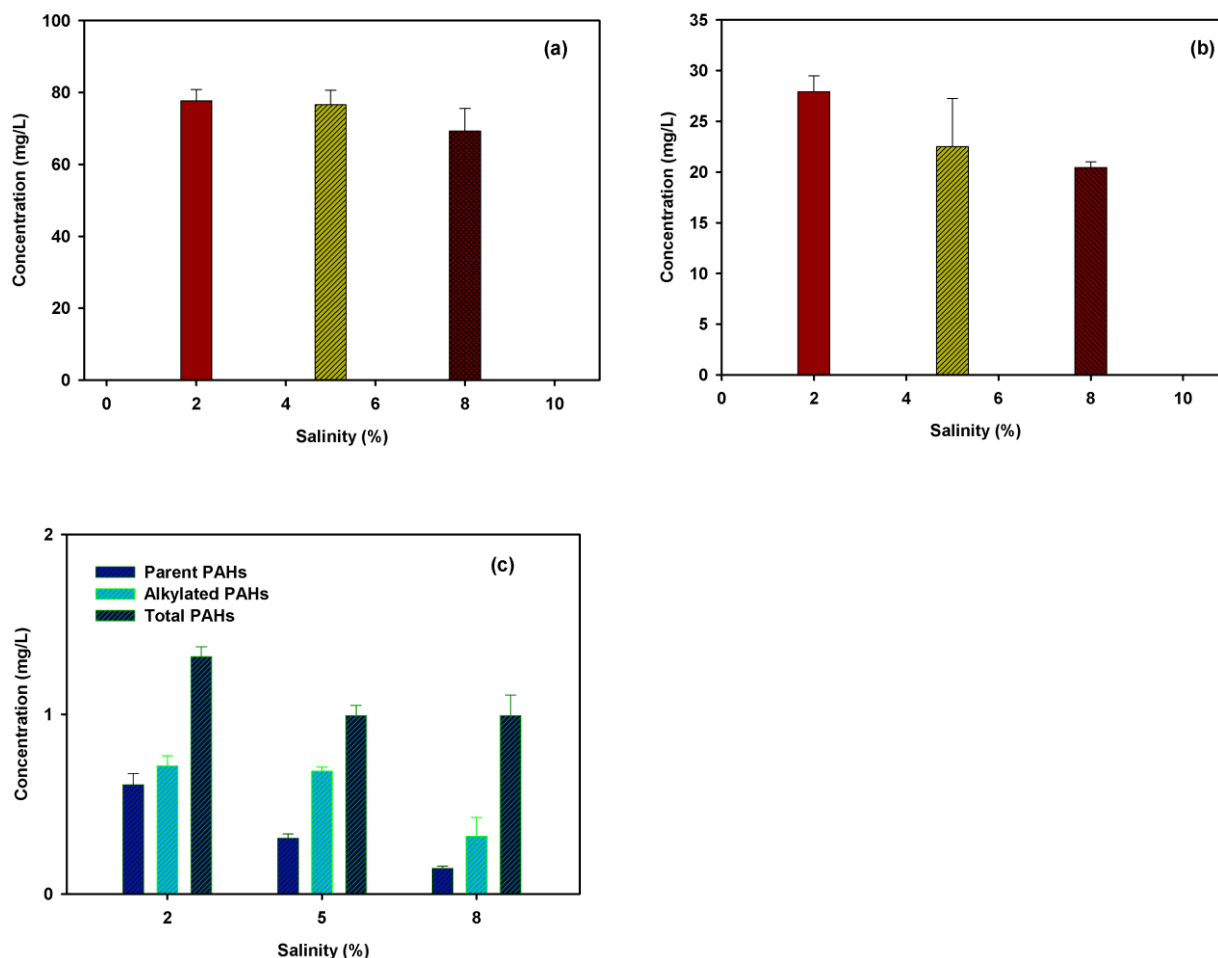
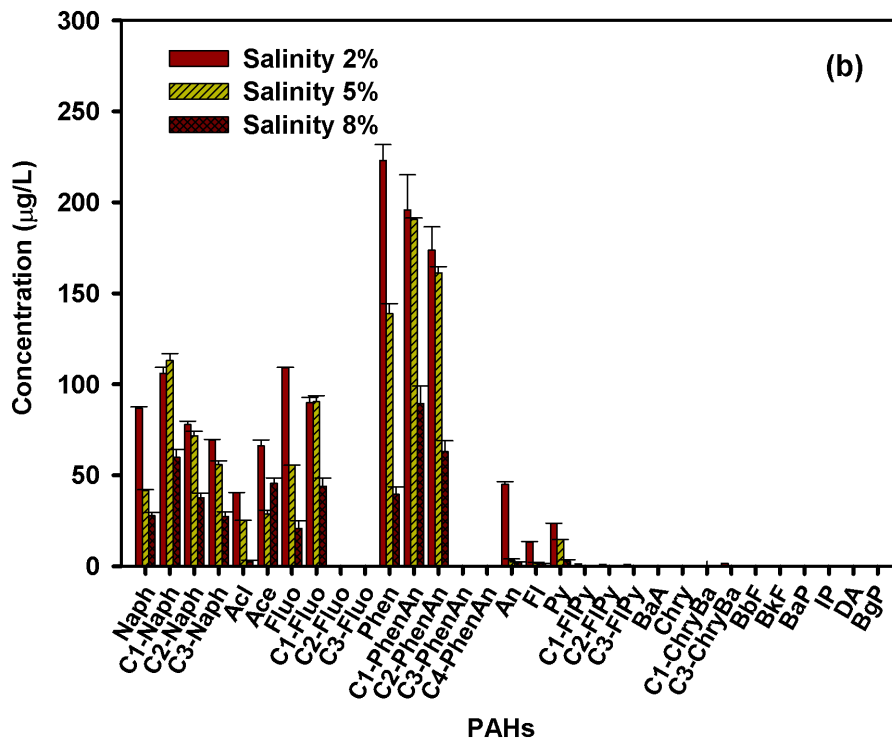
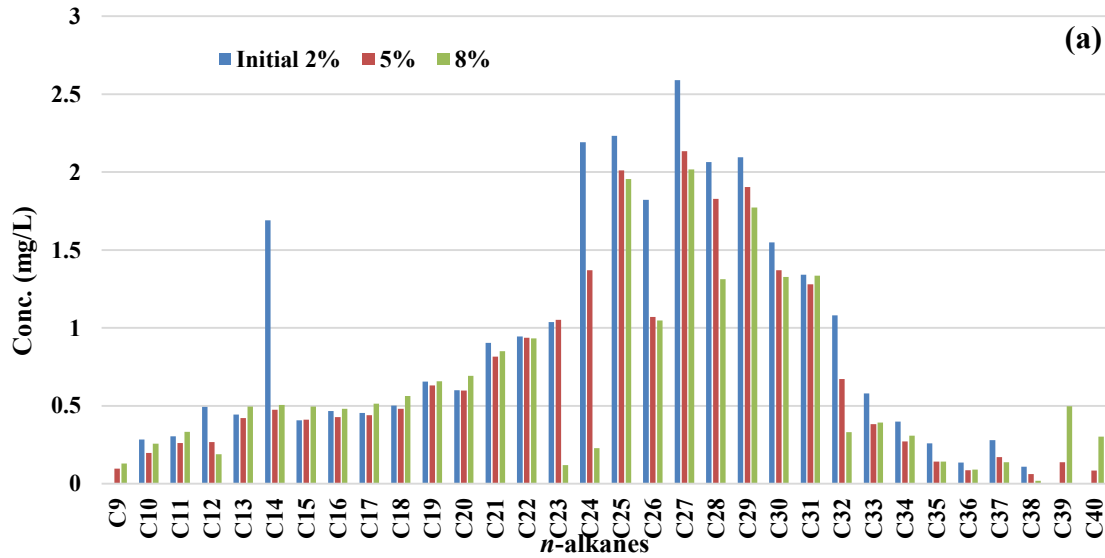


Figure 146. Ozonation of (a) TPHs, (b) *n*-alkanes and (c) PAHs at various salinity levels.

Experimental conditions: initial TPHs = 149.7 mg/L, *n*-alkanes = 79.3 mg/L, and TPAHs = 6.2 mg/L (in DWAO with Corexit EC9500A), gas flow rate = 4 mL/min, ozone = 86 ppbv, temperature = 22±1 °C, volume of solution = 250 mL, solution pH = 8.1±1.



**Figure 147. Distributions of *n*-alkanes (a) and PAHs (b) in DWAO after 24 h ozonation.**

Experimental conditions: initial TPHs = 149.7 mg/L, *n*-alkanes = 79.3 mg/L, and TPAHs = 6.2 mg/L (in DWAO with Corexit EC9500A), gas flow rate = 4 mL/min, ozone = 86 ppbv, temperature = 22±1 °C, volume of solution = 250 mL, solution pH = 8.1±1. Salinity is given in weight percent.

Salinity can enhance the ozone oxidation of oil components in the dispersant solutions through 1) the solvent cage effect, i.e., elevated salinity reduces the solvent cage, resulting in more effective collisions between the reactants; and 2) the salting-out effect of hydrophobic compounds, i.e., elevated salinity can increase the local concentration of DPHs at the water-air interface, resulting in a faster degradation rate. On the other hand, the sale at elevated concentrations may compete for the hydroxyl radicals with DPHs via the following reactions (pH = 8.1) (Muthukumar and Selvakumar 2004):



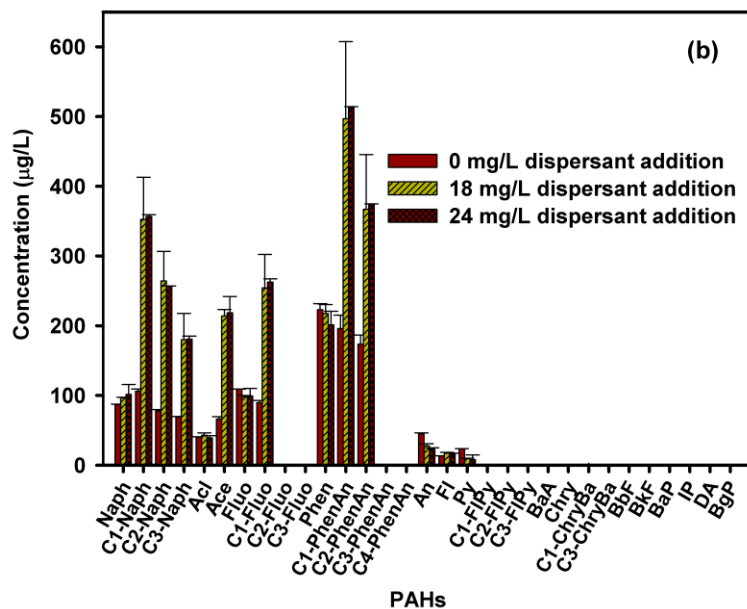
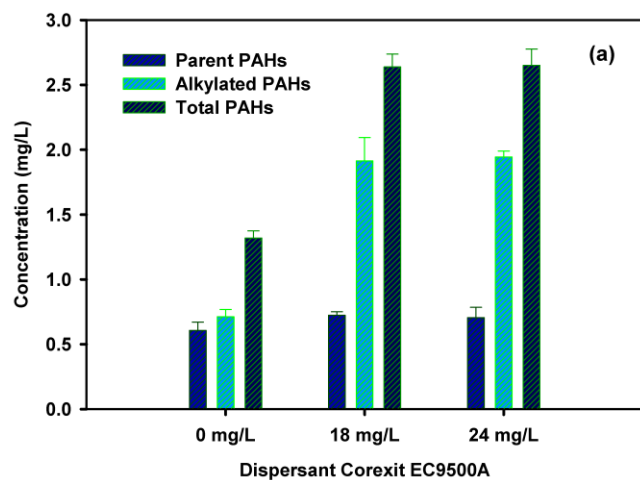
In this study, the promoting effects of salinity outweighed the inhibitive effects. However, because salinity in real seawater is a mixture of various salts, the overall effects can be more complex.

#### 6.2.2.5. Effects of dispersant concentration on ozonation of PAHs in DWAO

**Figure 148a** shows the ozonation of parent and alkylated PAHs in the presence of various concentrations of Corexit EC9500A. After 24 hours of ozonation, the final concentrations of parent PAHs were 0.61, 0.72 and 0.71 mg/L in the dispersant concentration of 0, 18, and 24 mg/L, respectively; and the final concentrations of alkylated PAHs were 0.71, 1.91 and 1.94 mg/L. Increasing the dispersant concentration from 0 to 24 mg/L inhibited the degradation of PAHs from 78.6% to 57.0% for total PAHs, from 54.8% to 47.4% for parent PAHs, and from 85.2% to 59.6% for alkylated PAHs.

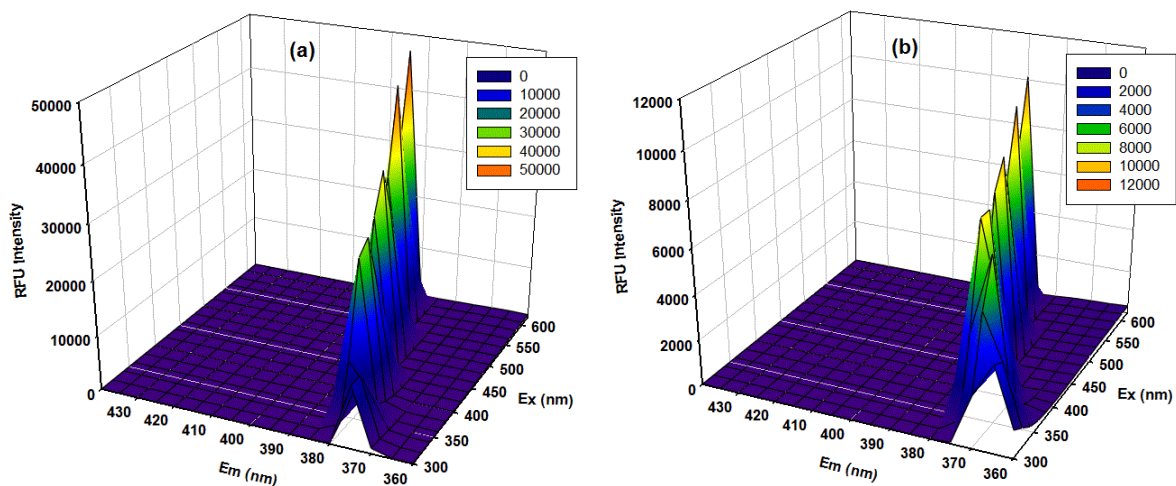
**Figure 148b** shows the distributions of parent and alkylated PAHs at various dispersant concentrations after 24 hours of ozonation. The parent PAHs, e.g. 2-ring PAHs (naphthalene), 3-ring PAHs (acenaphthylene, fluorene and anthracene) and 4-ring PAHs (fluoranthene and pyrene) in the aqueous phase were comparable. However, increasing the dispersant concentration from 0 to 18 mg/L inhibited degradation of 3-ring parent PAHs (acenaphthene) and all alkylated PAHs, though further increasing the dispersant concentration from 18 to 24 mg/L showed no further effect. Like DOM, the dispersant components can compete for molecular ozone with PAHs in DWAO-I, thereby inhibiting direct ozonation.

To acquire further insight into the role of the dispersant in the ozonation process, excitation-emission matrix (EEM) fluorescence spectra for DWAO were obtained, which can provide useful information for identification and quantification of PAHs in the system. **Figure 149** shows the fluorescence EEM spectra of DWAO with or without 18 mg/L of the dispersant after 24 hours of ozonation. The peaks at Ex/Em of (350–450)/(360–400) nm are assigned to aromatic compounds in the mixture, i.e., PAHs in the DWAO (Beltrán et al. 1998, Lehto et al. 2000). After addition of 18 mg/L of Corexit 9500A, the intensities of all the identified peaks were notably enhanced compared to those without the dispersant, i.e., more PAHs remained after ozonation, which is consistent with the results shown in **Figure 148**.



**Figure 148. Effects of Corexit EC9500A on ozonation of PAHs in DWAO.**

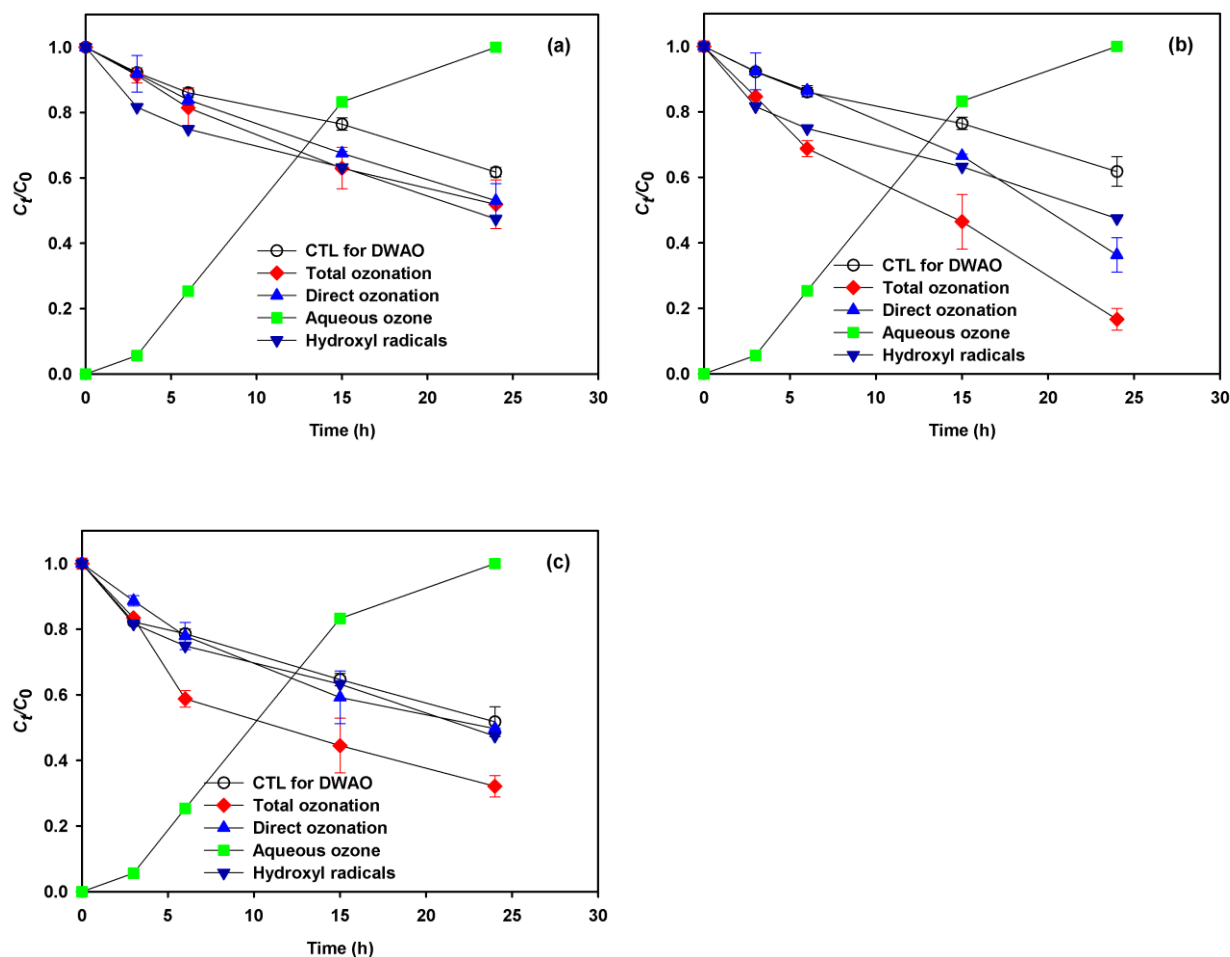
(a) Ozonation of PAHs in DWAO in the presence of various concentrations of Corexit EC9500A, and (b) distributions of PAHs in DWAO after 24 h ozonation at various dispersant concentrations. Experimental conditions: initial TPHs = 149.7 mg/L, *n*-alkanes = 79.3 mg/L, and TPAHs = 6.2 mg/L (in DWAO with Corexit EC9500A), gas flow rate = 4 mL/min, ozone = 86 ppbv, temperature = 22±1 °C, volume of solution = 250 mL, solution pH = 8.1±1, salinity = 2 wt.%.



**Figure 149. Fluorescence EEM spectra of DWAO.**  
 (a) With 18 mg/L of Corexit 9500A, and (b) without dispersant after 24 hours of ozonation.

### 6.2.3. Ozonation mechanisms of DWAO

**Figure 150a** compares the total ozonation and direct ozonation rates of TPHs, *n*-alkanes and total PAHs. To determine the relative roles of direct ozonation against indirect ozonation, para-chlorobenzoic acid (*p*CBAs) was used as an OH<sup>•</sup> radical probe compound during the ozonation based on its very slow direct reaction with ozone and fast reaction with OH<sup>•</sup> radicals. In the absence of *p*CBAs, the total ozonation rate constant of TPHs was 0.016 h<sup>-1</sup>; in the presence of the *p*CBAs, the ozonation (direct ozonation) rate constant of TPHs was reduced to 0.0085 h<sup>-1</sup>, i.e., direct ozonation accounted for 53% of the total ozonation based on the first order rate constant. Therefore, the contributions of direct and indirect ozonation are comparable. **Table 41** gives the respective rate constants for TPHs removal due to volatilization and the different ozonation mechanisms. **Figure 150b** profiles the volatilization, total ozonation and direct ozonation of *n*-alkanes in DWAO under the same gas flow rate with or without *p*CBAs, and **Table 41** gives the respective rate constants for the various processes. In the absence of the *p*CBAs, the total ozonation rate of *n*-alkanes was 0.0333 h<sup>-1</sup>; in the presence of the *p*CBAs, the ozonation rate of *n*-alkanes was reduced to 0.0184 h<sup>-1</sup>, namely, 55% of the total ozonation was attributed to direct ozonation, which is similar to that for TPHs ozonation.



**Figure 150. Transient concentrations of oil components, ozone and hydroxyl radicals.**

(a) TPHs, (b) *n*-alkanes, and (c) total PAHs; and dissolved ozone and hydroxyl radicals in the batch reactor during ozonation of DWAO. Experimental conditions: initial TPHs = 149.7 mg/L, *n*-alkanes = 79.3 mg/L, TPAHs = 6.2 mg/L, gas flow rate = 4 mL/min, ozone in air = 86 ppbv, temperature = 22±1 °C, volume of solution = 250 mL, solution pH = 8.1±1, salinity = 2%.

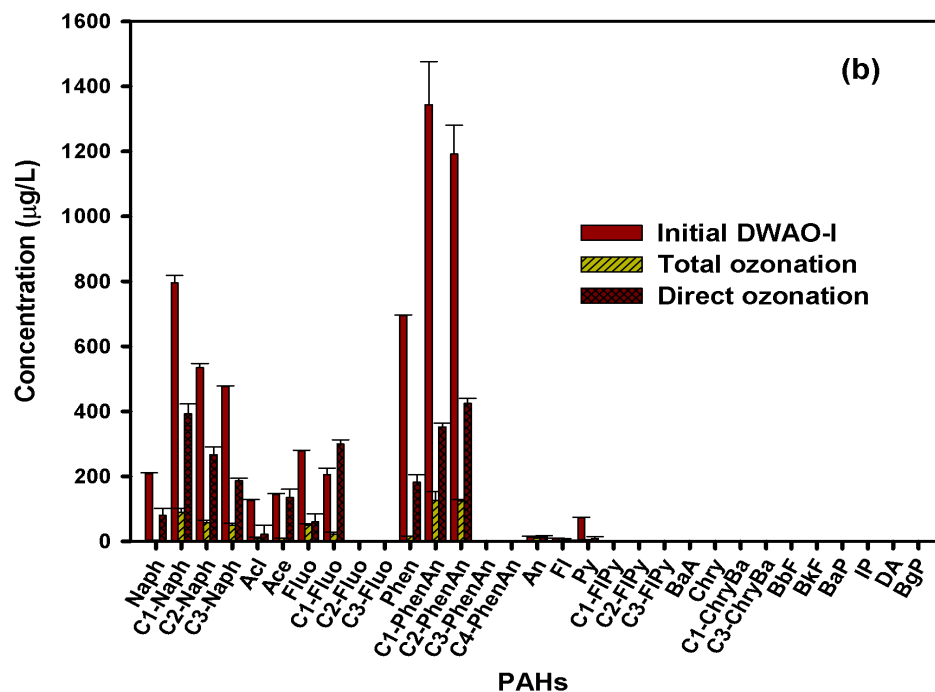
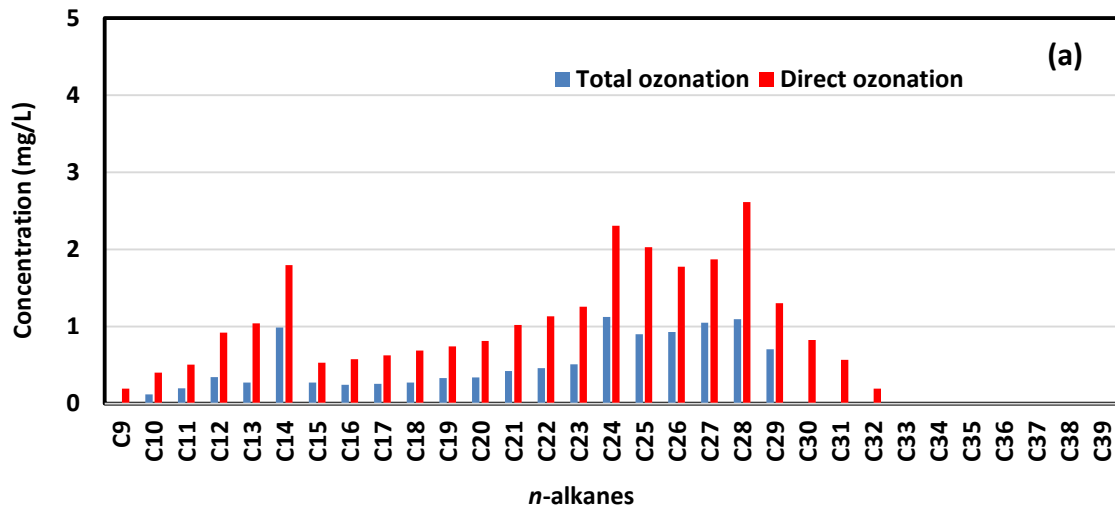
**Table 41. First-order ozone oxidation rate constants for TPHs, *n*-alkanes and TPAHs in DWAO**

Components		Volatilization		Overall dissipation		Ozonation		
		$k_v$ (h <sup>-1</sup> )	$R^2$	$k$ (h <sup>-1</sup> )	$R^2$	$k_o$ (h <sup>-1</sup> )	$k_R$ (h <sup>-1</sup> )	$k_D$ (h <sup>-1</sup> )
TPHs	Total ozonation	0.0177	0.9920	0.0337	0.9752	0.0160	0.0075	-
	Direct ozonation	0.0177	0.9920	0.0262	0.9989	0.0085	0	0.0085
<i>n</i> -alkanes	Total ozonation	0.0095	0.9994	0.0510	0.9835	0.0415	0.0231	
	Direct ozonation	0.0095	0.9994	0.0361	0.9564	0.0184	0	0.0184
TPAHs	Total ozonation	0.0146	0.9642	0.0625	0.9655	0.0479	0.0264	
	Direct ozonation	0.0146	0.9642	0.0361	0.9564	0.0215	0	0.0215

Ozone can react with the C-H bonds in alkanes (Fokin and Schreiner 2002). The initial attack of ozone on alkanes is centered on the  $\sigma$ -bonding between C and H atoms, which includes two major pathways: 1,3-dipolar insertion and radical reactions (Hellman and Hamilton 1974). For the ozonation of *n*-alkanes in DWAO, 1,3-dipolar insertion corresponds to the direct ozonation, whereas the reaction with  $\bullet\text{OH}$  radicals relates to the indirect ozonation. Furthermore, the 1, 3-dipolar insertion is affected by the electronegative properties of atoms. In the presence of the dispersant (Corexit EC9500A), the various groups of *n*-alkanes, i.e., HMWHs, MMWHs and LMWHs, may have different electronegative characteristics. Consequently, different fractions of the *n*-alkanes were degraded to various rates and extents (**Figure 150a**). In addition, it was reported that alkanes, especially LMWHs, can undergo oxidative transformation by hydroxyl radicals (Vikhorev et al. 1978). The ozonation can convert the more persistent HMWHs to MMWHs and then to the more degradable LMWHs. However, the LMWHs in DWAO may undergo further decomposition by indirect ozonation.

**Figure 150c** shows the volatilization, total ozonation and direct ozonation of PAHs under the same gas flow rate with or without *p*CBA, and **Table 41** gives the respective rate constants for various processes. In the absence of *p*CBA, the total ozonation rate constant of PAHs was  $0.0264 \text{ h}^{-1}$ ; in the presence of *p*CBA, the ozonation rate constant was lowered to  $0.0071 \text{ h}^{-1}$ , indicating that direct ozonation only contributed 26.9% to the total ozonation. Therefore, for ozonation of PAHs in DWAO, the indirect ozonation was the dominant mechanism.

Compared to *n*-alkanes, PAHs require more energy to be directly degraded by molecular ozone. On the other hand, hydroxyl radicals are more powerful, non-specific oxidizing agents compared to  $\text{O}_3$ . As a result, oxidation by hydroxyl radicals played a more important role. **Figure 151b** shows that indirect ozonation contributed more than direct ozonation to the ozonation of the 2-ring PAHs (naphthalene, acenaphthylene and acenaphthene).



**Figure 151. Distributions of oil components upon total and direct ozonation.**  
 (a) *n*-alkanes, and (b) PAHs.

### 6.3. Removal of DWAOs by combined ozonation and photodegradation

Though catalytic photolysis and ozonation can each tackle persistent organic compounds through ROS, the rather different yields and types of ROS generated and the reaction mechanisms enable the two processes to be synergistically supplementary (Agustina et al., 2005), i.e., ROS produced in photolysis may prime persistent oil and PAHs to the active intermediates to ease ozonation, and on the other hand, ozonation can also facilitate photodegradation. Such synergistic effects can be further augmented in the presence of catalysts and oil dispersants. Because photolysis, ozonation and catalysis are concurrently



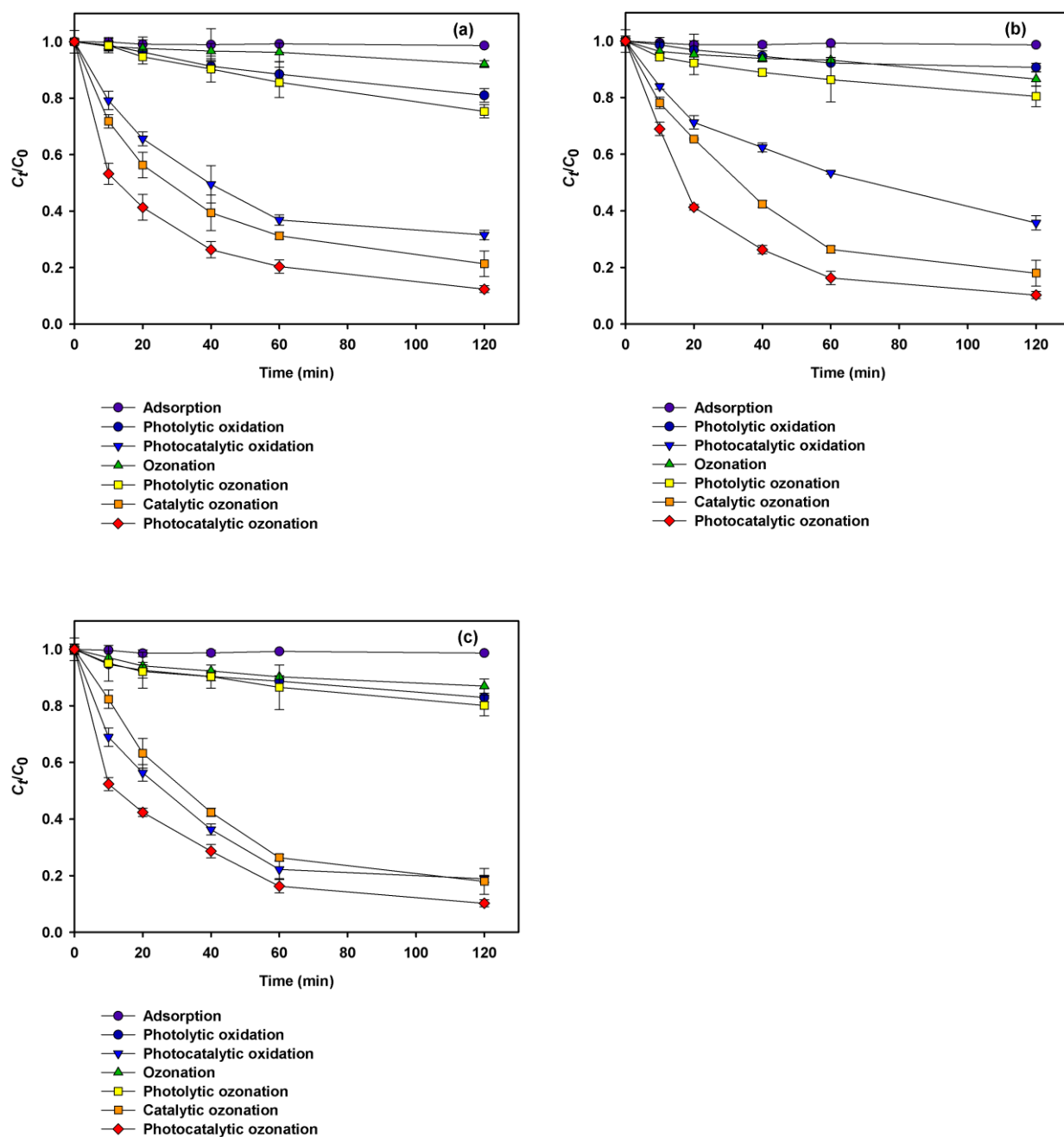
present in the Gulf Coast ecosystems, it is of pivotal importance to determine the contribution of combined catalytic photolysis and ozonation to the overall weathering of oil and PAHs, which has been largely ignored in the research community.

Studies have reported the synergistic effect of catalytic photolysis and ozonation for degradation of organic compounds. Beltrán et al. (2005) observed that the degradation effectiveness of fluorene follows the sequence of:  $\text{TiO}_2$ -catalyzed photolysis and ozonation ( $\text{TiO}_2/\text{UVA}/\text{O}_3$ ) > photolysis and ozonation ( $\text{UVA}/\text{O}_3$ ) > ozonation ( $\text{O}_3$ )  $\approx$   $\text{TiO}_2$ -catalyzed ozonation ( $\text{TiO}_2/\text{O}_3$ )  $\approx$   $\text{TiO}_2$ -catalyzed photolysis ( $\text{TiO}_2/\text{UVA}$ ) > adsorption ( $\text{TiO}_2$ ). Li et al. (2003) found that combined photocatalysis with UV irradiation and ozonation ( $\text{TiO}_2/\text{UV}/\text{O}_3$ ) considerably increased the removal rate of catechol compared to combined photocatalysis with UV irradiation and oxygen oxidation ( $\text{TiO}_2/\text{UV}/\text{O}_2$ ), ozonation alone ( $\text{O}_3$ ) process, combined ozonation and UV irradiation ( $\text{UV}/\text{O}_3$ ). García-Araya et al. (2010) reported that ozonation alone resulted in incomplete oxidation of diclofenac, while photolytic  $\text{TiO}_2$  catalyzed ozonation was more effective in mineralizing diclofenac. Parrino et al. (2014) found that combined photocatalytic ozonation was more efficient for oxidizing organics and reducing hazardous bromate than either photocatalysis or ozonation alone. Though the latest science predicts that a combination of catalysis, photolysis and ozonation will synergistically accelerate weathering of persistent oil components and, though these important abiotic processes are known to take place concomitantly in the Gulf Coast environment, information has been lacking on the roles and mechanisms of such processes and on the roles of oil dispersants and naturally existing catalysts (e.g., metal ions, metal oxides, sulfides and sands) in combined weathering processes.

A series of batch kinetic tests were conducted to further investigate the combined ozonation and photodegradation rates and extent of DWAO in the presence of the  $\text{TiO}_2/\text{SiO}_2$ -800 composite material described in Section 5.3.1. The degradation experiments were carried out in a new glass cylinder reactor that can facilitate both ozonation and photodegradation, and an ozone generator as described in Section 6.1.1.

In each test, 250 mL of a solution was loaded in the reactor along with a known mass of the photocatalyst under constant magnetic stirring at 400 rpm, resulting in a surface area of  $50 \text{ cm}^2$ . For the tests with ozonation only or adsorption, the reactor was kept in the dark, while the reactor was exposed to simulated solar light for reactions involving both ozonation and photocatalytic mechanisms. At predetermined times, each 20 mL of the solution was sampled and extracted with DCM in three consecutive steps (20 mL solution with 5 mL DCM in each step) according to EPA Method 3510C, and then the extracts were filtered through a glass column packed with 5 g of anhydrous sodium sulfate and concentrated to 4 mL under a gentle nitrogen flow. The samples were filtered through a PTFE membrane ( $0.22 \mu\text{m}$ ) filter and separated into amber glass vials with equal volumes (labeled as B1 and B2). B1 was analyzed for *n*-alkanes and PAHs using GC-MS, and B2 for TPHs using GC-FID. Specifically, the 16 parent PAHs (as specified in EPA Method 610) and *n*-alkanes (C9–C40) in the DWAO before and after reactions were targeted. More details on the analytical methods can be found in Section 3.3.1.5.

**Figure 152** shows the adsorption, photolytic oxidation, photocatalytic oxidation, ozonation, photolytic ozonation, catalytic ozonation and photocatalytic ozonation of DWAO in the presence or absence of atmospheric ozone and visible light. The first order kinetic model was used to interpret the kinetic data and **Table 42** lists the best-fitted model parameters. The combined photolysis and ozonation displayed the highest degradation rate for all types of oil components in DWAO, indicating a clear synergistic effect between the catalytic photodegradation and the ozonation processes.  $\text{TiO}_2/\text{SiO}_2$ -800 showed low adsorptive removal of DPHs (including *n*-alkanes and TPAHs) during the adsorption stage, while DPHs in the aqueous phase decreased by 90% in the reaction state, indicating that all the removal was due to photocatalytic ozonation (**Figure 152**).



**Figure 152. Removal of oil components by combined ozonation and photodegradation.**

(a) TPHs, (b) *n*-alkanes and (c) total PAHs in DWAO (Corexit EC9500A) solution. Experimental conditions: initial TPHs in DWAO = 149.7 mg/L, *n*-alkanes = 79.3 mg/L, TPAHs = 6.2 mg/L, gas flow rate = 4 mL/min, ozone in air = 86 ppbv, temperature =  $22 \pm 1$  °C, volume of solution = 250 mL, solution pH =  $8.1 \pm 1$ , salinity = 2 wt.%. Experimental data are plotted as mean of duplicates and error bars are calculated as the standard deviation to indicate data reproducibility.

**Table 42. First-order reaction rate constants for TPHs, *n*-alkanes and TPAHs in DWAO for different reaction mechanisms**

Systems	TPHs		<i>n</i> -alkanes		TPAHs	
	$k_1$ (h <sup>-1</sup> )	$R^2$	$k_2$ (h <sup>-1</sup> )	$R^2$	$k_3$ (h <sup>-1</sup> )	$R^2$
Adsorption	0.0001	0.8236	0.0001	0.8236	0.0001	0.8236
Ozonation	0.0006	0.9678	0.0011	0.9400	0.0011	0.8878
Photolytic oxidation	0.0018	0.9833	0.0008	0.8858	0.0014	0.9023
Photolytic ozonation	0.0024	0.9938	0.0017	0.9184	0.0017	0.9420
Photocatalytic oxidation	0.0135	0.9139	0.0092	0.9555	0.0236	0.9487
Catalytic ozonation	0.0192	0.9327	0.020	0.9794	0.0203	0.9791
Photocatalytic ozonation	0.0351	0.9145	0.0351	0.9735	0.0356	0.9307

## 7. Summary and Observations

The key findings and observations from this research project are summarized as follows:

- 1) A new method was established to determine the Corexit EC9500A concentration in seawater by measuring the surface tension of the dispersant solutions and by means of the linear correlation between surface tension and  $\ln$ [dispersant concentration]. The most-suitable dispersant concentration range is 0.5 to 23.5 mg/L for this method. Minor changes in solution salinity (< 0.3%), pH (7.0–9.0), and DOM (< 1.5 mg/L as TOC) had negligible effects on the surface tension measurements
- 2) A revised UV-based approach for measuring CMCs of an array of surfactants or oil dispersants was developed and tested. This method determines CMCs for a wide range of surfactants and dispersants using the critical red shift concentration corresponding to the strongest UV peak, and, for more accurate measurements, by means of the maximum measurable peak difference as a function of surfactant concentration.
- 3) Increasing dispersant concentration proportionally increases the concentration of oil *n*-alkanes and PAHs in WAO. However, the dissolution process is selective, i.e., different dispersants disperse different fractions of oil alkanes and PAHs in seawater. The dispersant SPC 1000 is much more effective than Corexit EC9500A and Corexit EC9527A at dispersing various oil components and at desorbing aged oil components from marine sediment.
- 4) Increasing dispersant concentration progressively enhances sediment uptake of oil and PAHs, and the presence of oil dispersants during desorption results in remarkable sorption hysteresis. SOM plays a key role in sorption of oil dispersants and dispersed oil; the dispersant effects increase with increasing SOM content. The presence of dispersed oil substantially increases sediment sorption of PAHs.
- 5) Deepwater conditions reduce solubilization of PAHs and lessen the dispersant effects on PAHs uptake. Sorption of oil dispersants on sediment is favored at higher salinities while inhibited at lower temperatures (4 °C). When dispersed oil is subjected to sorption by sediment, *n*-alkanes of C27–C32 are more favorably taken up by the sediment, though the sorption rate of different fractions of *n*-alkanes is comparable.
- 6) The content of TPHs in a 5-year-old sediment that was contaminated by the *DwH* oil spill was 2.310 mg/g-sediment, with the total *n*-alkanes accounting for ~50% of the TPHs. The C27 *n*-alkane was the most abundant single *n*-alkane and MMW *n*-alkanes (C21–C30) made up 76.61% of the total *n*-alkanes. The total parent and alkylated PAHs concentrations were 11.934 and 8.110 µg/g-sediment, respectively, in which the 3-ring and 4-ring PAHs constitute more than 80% of the total PAHs. The presence of oil dispersants desorbed more oil components, with SPC 1000 being more effective than Corexit EC9500A in desorption of various oil components from the aged sediment.
- 7) Both oil and Corexit EC9500A enhance the formation of marine snow. The formation of marine oil snow involves interactions between specific oil components, dispersant, microorganisms, and natural suspended particulate matter. Lower molecular-weight *n*-alkanes (C9–C18) are more favorably partitioned in MOS than in the aqueous phase in the presence of the dispersant. The presence of oil dispersant results in much more and smaller MOS and transfers more LMW oil in MOS, which enhances the buoyancy, i.e., incorporation of oil and dispersant in the particles inhibits sinking of MS and MOS or may reverse the transport direction.

**8)** Oil dispersants accelerate the settling velocity of suspended sediment particles. The nonionic surfactants (Tween 80 and Tween 85) are the most important dispersant components that enhance the aggregation and sedimentation of sediment particles by masking the negative zeta potential of the sediment particles and enhancing the particle aggregation. The presence of DWAO accelerates the settling of sediment particles, and the addition of dispersant greatly increases the sediment-facilitated transport of oil and PAHs.

**9)** Photodegradation plays an important role in weathering oil and PAHs. Common oil alkanes and PAHs are degraded in hours. The presence of Corexit EC9500A promotes photodegradation of pyrene, anthracene and 9,10-DMA due to enhanced formation of superoxide or hydroxyl radicals. Methylated PAHs are more vulnerable to photolysis than their parent PAHs. Higher ionic strength and temperature and lower DOM favor pyrene photodegradation.

**10)** A new class of cobalt-deposited TNTs (Co-TNTs) photocatalysts was synthesized through hydrothermal treatment of a commercial  $\text{TiO}_2$  followed by calcination at 600 °C. Co-TNTs-600 is a nanocomposite consisting of titanate, anatase and CoO. At a dosage of 1 g/L, the material can degrade 98.6% of phenanthrene in 12 h under solar light with an apparent first-order rate constant ( $k_1$ ) of  $0.39 \text{ h}^{-1}$ , which is ~23 times higher than that of TNTs and ~10 times that of conventional  $\text{TiO}_2$  P25 (the precursor). The CoO nanoparticles in Co-TNTs-600 can not only facilitate effective utilization of visible light for production of electron-hole pairs, but also serve as an electron transfer mediator that inhibits recombination of the pairs. Co-TNTs-600 can be efficiently separated via gravity-settling and reused.

**11)** A new class of platinum-deposited TNTs (Pt-TNTs) photocatalysts was prepared through hydrothermal treatment of  $\text{TiO}_2$ , deposition of Pt, and calcination at 600 °C. Both Pt(0)-TNTs-600 and Pt(IV)-TNTs-600 exhibited high photocatalytic activity for degradation of phenanthrene under solar light, with a first-order rate constant ( $k_1$ ) being 3 and 1.5 times of that of the parent  $\text{TiO}_2$ , respectively. For both materials, Pt(0) transfers the excited electrons, thereby inhibiting the electron-hole recombination; for Pt(IV)-TNTs-600, PtO acts as an electron-hole trap, which also inhibits the recombination of electron-hole pairs though less effective than Pt(0). Pt(0)-TNTs-600 can be separated through gravity sedimentation and reused in multiple cycles of operations with minimal loss in the photocatalytic activity.

**12)** A new class of silica aerogel supported  $\text{TiO}_2$  ( $\text{TiO}_2/\text{SiO}_2$ ) composite materials was developed through initial sol-gel method and subsequent calcination, in which  $\text{TiO}_2$  acts as the primary photocatalyst and silica serves as the support for nano- $\text{TiO}_2$ . Higher calcination temperature leads to lower adsorption capacity but higher photocatalytic activity. Although only 5.2% of phenanthrene was removed through adsorption by  $\text{TiO}_2/\text{SiO}_2$ -800, 100% degradation was achieved through photocatalysis within 3 h. 100% of phenanthrene still could be removed by  $\text{TiO}_2/\text{SiO}_2$ -800 after 5 times of repeated uses of the same material.

**13)** A novel composite material, TNTs@AC, was synthesized through a simple hydrothermal process based on low-cost commercial AC and  $\text{TiO}_2$ . TNTs@AC offer not only rapid adsorption, but also high adsorption capacity for phenanthrene due to the ink-bottle-shaped pores in the micro-AC modified TNTs and capillary condensation. TNTs@AC displayed superior photocatalytic activity, which allowed for rapid degradation of adsorbed phenanthrene. TNTs@AC performed well over a broad pH range, at elevated ionic strength, and displayed excellent resistance to organic fouling. TNTs@AC hold great potential to substantially advance current practices in treating spilled oil from water or seawater. More than 99.5% of TPHs, *n*-alkanes and PAHs could be adsorbed at 1.25 g/L TNTs@AC, and then, 98.0%, 94.8% and 98.4% of the pre-concentrated TPHs, *n*-alkanes and PAHs could be degraded within 4 h under UV irradiation.

**14)** The oil dispersant Corexit EC9500A enhances ozonation of oil PAHs. The ozonation rate constants for 1-methylnaphthalene and 1-methylfluorene were increased by 3.6 and 1.45 times in the presence of 18 mg/L Corexit EC9500A at an atmospheric ozone concentration of 200 µg/L, respectively. Mechanically, the presence of the dispersant (18 mg/L) increased both direct ozonation rate (by 60% for 1-methylnaphthalene and 20% for 1-methylfluorene) and indirect ozonation rate (by 6.8 times for 1-methylnaphthalene and 1.8 times for 1-methylfluorene).

**15)** Corexit EC9500A accelerates the ozonation of TPHs, *n*-alkanes and TPAHs in a simulated seawater-oil system. The ozonation rate of TPHs, *n*-alkanes and TPAHs were increased by 2.2, 1.01 and 1.96 times in the presence of 18 mg/L Corexit EC9500A and at a ozone concentration of 86 ppbv. Alkylated PAHs were more degradable than parent PAHs in WAO and DWAO by ozonation. Increasing pH slightly enhanced ozonation, while elevated HA inhibited the reaction. Direct ozonation accounted for 53%, 55% and 45% of the total ozonation for TPHs, *n*-alkanes and TPAHs, respectively.

**16)** A strong synergistic effect was observed in the presence of TiO<sub>2</sub>/SiO<sub>2</sub>-800 when ozonation and photocatalytic degradation of DPHs in DWAO were combined. The ozonation rate constants of TPHs, *n*-alkanes and TPAHs through combined ozonation and photodegradation were increased by 57.5, 30.1, and 31.4 times, respectively, compared to those for ozonation alone, and increased by 18.5, 42.9, and 24.4 times compared to those for photocatalytic oxidation only.

## 8. References

- Abbriano, R.M., Carranza, M.M., Hogle, S.L., Levin, R.A., Netburn, A.N. 2011. *Deepwater Horizon* oil spill: A review of the planktonic response. *Oceanography* 24(3), 294-301.
- Abdel-Shafi, A.A. and Wilkinson, F. 2000. Charge transfer effects on the efficiency of singlet oxygen production following oxygen quenching of excited singlet and triplet states of aromatic hydrocarbons in acetonitrile. *Journal of Physical Chemistry A* 104(24), 5747-5757.
- Adamson, A.W. 2001. The physical chemistry of surfaces. Abstracts of Papers of the American Chemical Society 221, U320-U320.
- Adebajo, M.O., Frost, R.L., Klopogge, J.T., Carmody, O. and Kokot, S. 2003. Porous materials for oil spill cleanup: A review of synthesis and absorbing properties. *Journal of Porous Materials* 10(3), 159-170.
- ADEM (Alabama Department of Environmental Management) 2014. Safeguarding Alabama's air quality. Available at: <http://adem.alabama.gov/programs/air/airquality/ozone/8HourOzoneData.pdf> (accessed August 15, 2016)
- Ahn, C.K., Woo, S.H. and Park, J.M. 2010. Selective adsorption of phenanthrene in nonionic-anionic surfactant mixtures using activated carbon. *Chemical Engineering Journal* 158(2), 115-119.
- Agustina, T.E., Ang, H.M. and Vareek, V.K. 2005. A review of synergistic effect of photocatalysis and ozonation on wastewater treatment. *Journal of Photochemistry and Photobiology C: Photochemistry Reviews* 6(4), 264-273.
- Akbay, C., Wilmot, N., Agbaria, R.A. and Warner, I.M. 2004. Characterization and application of sodium di (2-ethylhexyl) sulfosuccinate and sodium di (2-ethylhexyl) phosphate surfactants as pseudostationary phases in micellar electrokinetic chromatography. *Journal of Chromatography A* 1061(1), 105-111.
- Akhavan, O. and Ghaderi, E. 2010. Toxicity of graphene and graphene oxide nanowalls against bacteria. *ACS Nano* 4(10), 5731-5736.
- Aksnes, G. and Vagstad, B.H. 1979. Photooxidation of 9, 10-dimethylanthracene in two phase system: Benzene-water. *Acta Chemica Scandinavica B* 33(1979), 47-51.
- Alila, S., Aloulou, F., Beneventi, D. and Boufi, S. 2007. Self-aggregation of cationic surfactants onto oxidized cellulose fibers and coadsorption of organic compounds. *Langmuir* 23(7), 3723-3731.
- Allan, S.E., Smith, B.W. and Anderson, K.A. 2012. Impact of the *Deepwater Horizon* oil spill on bioavailable polycyclic aromatic hydrocarbons in Gulf of Mexico coastal waters. *Environmental Science & Technology* 46(4), 2033-2039.
- Allredge, A.L. and Silver, M.W. 1988. Characteristics, dynamics and significance of marine snow. *Progress in Oceanography* 20(1), 41-82.
- Amat, A.M., Arques, A., Miranda, M.A., Vincente, R. and Segui, S. 2007. Degradation of two commercial anionic surfactants by means of ozone and/or UV irradiation. *Environmental Engineering Science* 24(6), 790-794.
- An, Y.J. and Carraway, E.R. 2002. PAH degradation by UV/H<sub>2</sub>O<sub>2</sub> in perfluorinated surfactant solutions. *Water research* 36(1), 309-314.
- An, Y.J. 2001. Photochemical treatment of a mixed PAH/surfactant solution for surfactant recovery and reuse. *Environmental Progress* 20(4), 240-246.

- Andrews, S.S., Caron, S. and Zafiriou, O.C. 2000. Photochemical oxygen consumption in marine waters: A major sink for colored dissolved organic matter. *Limnology and Oceanography* 45(2), 267-277.
- Aumann, E., Hildemann, L.M. and Tabazadeh, A. 2010. Measuring and modeling the composition and temperature-dependence of surface tension for organic solutions. *Atmospheric Environment* 44(3), 329-337.
- Bandara, U.C., Yapa, P.D. and Xie, H. 2011. Fate and transport of oil in sediment laden marine waters. *Journal of Hydro-environment Research* 5(3), 145-156.
- Barbetta, A. and Cameron, N.R. 2004. Morphology and surface area of emulsion-derived (PolyHIPE) solid foams prepared with oil-phase soluble porogenic solvents: Span 80 as surfactant. *Macromolecules* 37(9), 3188-3201.
- Basu Ray, G., Chakraborty, I. and Moulik, S.P. 2006. Pyrene absorption can be a convenient method for probing critical micellar concentration (cmc) and indexing micellar polarity. *Journal of Colloid and Interface Science* 294(1), 248-254.
- Batchu, S.R., Ramirez, C.E. and Gardinali, P.R. 2014. Stability of dioctyl sulfosuccinate (DOSS) towards hydrolysis and photodegradation under simulated solar conditions. *Science of the Total Environment* 481(0), 260-265.
- Baumard, P., Budzinski, H., Garrigues, P., Sorbe, J.C., Burgeot, T. 1998. Concentrations of PAHs (polycyclic aromatic hydrocarbons) in various marine organisms in relation to those in sediments and to trophic level. *Marine Pollution Bulletin* 36(12), 951-960.
- Bavykin, D.V., Friedrich, J.M., Lapkin, A.A. and Walsh, F.C. 2006. Stability of aqueous suspensions of titanate nanotubes. *Chemistry of Materials* 18(5), 1124-1129.
- Beltrán, F.J., Ovejero, G., Garcia-Araya, J.F. and Rivas, J. 1995. Oxidation of Polynuclear Aromatic Hydrocarbons in water. 2. UV radiation and ozonation in the presence of UV radiation. *Industrial & Engineering Chemistry Research* 34(5), 1607-1615.
- Beltrán, F.J., Rivas, F.J., Gimeno, O. and Carbajo, M. 2005. Photocatalytic enhanced oxidation of fluorene in water with ozone. Comparison with other chemical oxidation methods. *Industrial & engineering chemistry research* 44(10), 3419-3425.
- Beltrán, J.L., Ferrer, R. and Guiteras, J. 1998. Multivariate calibration of polycyclic aromatic hydrocarbon mixtures from excitation–emission fluorescence spectra. *Analytica Chimica Acta* 373(2-3), 311-319.
- Benner Jr, R.A., El Said, K.R., Jester, E.L.E., Flurer, R.A., Boyd, B.L. 2010. Investigation of Corexit 9500 dispersant in Gulf of Mexico seafood species. US Food and Drug Administration. Available at: <<http://www.fda.gov/downloads/Food/FoodSafety/Product-SpecificInformation/Seafood/UCM250307.pdf>> (accessed August 15, 2016)
- Bejarano, A. C., Edwin L. and Alan J. M. 2013. Effectiveness and potential ecological effects of offshore surface dispersant use during the *Deepwater Horizon* oil spill: A retrospective analysis of monitoring data. *Environmental Monitoring and Assessment* 185(12), 10281-10295.
- Besra, L., Sengupta, D., Roy, S. and Ay, P. 2004. Influence of polymer adsorption and conformation on flocculation and dewatering of kaolin suspension. *Separation and Purification Technology* 37(3), 231-246.
- Boehm, P.D., Murray, K.J. and Cook, L.L. 2016. Distribution and attenuation of polycyclic aromatic hydrocarbons in Gulf of Mexico seawater from the *Deepwater Horizon* oil accident. *Environmental Science & Technology* 50(2), 584-592.
- Bojes, H.K. and Pope, P.G. 2007. Characterization of EPA's 16 priority pollutant polycyclic aromatic



- hydrocarbons (PAHs) in tank bottom solids and associated contaminated soils at oil exploration and production sites in Texas. *Regulatory Toxicology and Pharmacology* 47(3), 288-295.
- Borisov, O.V., Ji, J., Wang, Y., Vega, F. and Ling, V. 2011. Toward understanding molecular heterogeneity of polysorbates by application of liquid chromatography-mass spectrometry with computer-aided data analysis. *Analytical Chemistry* 83(10), 3934-3942.
- Bouloubassi, I., Mejanelle, L., Pete, R., Fillaux, J., Lorre, A. 2006. PAH transport by sinking particles in the open Mediterranean Sea: A 1 year sediment trap study. *Marine Pollution Bulletin* 52(5), 560-571.
- Bouyoucos, G.J. 1962. Hydrometer method improved for making particle size analyses of soils. *Agronomy Journal* 54(5), 464-465.
- Boyle, E.S., Guerriero, N., Thiallet, A., Vecchio, R.D. and Blough, N.V. 2009. Optical properties of humic substances and CDOM: Relation to structure. *Environmental Science & Technology* 43(7), 2262-2268.
- Braida, W.J., White, J.C., Ferrandino, F.J. and Pignatello, J.J. 2001. Effect of solute concentration on sorption of polyaromatic hydrocarbons in soil: uptake rates. *Environmental Science & Technology* 35(13), 2765-2772.
- Brandt, C.A., Becker, J.M. and Porta, A. 2002. Distribution of polycyclic aromatic hydrocarbons in soils and terrestrial biota after a spill of crude oil in Trecate, Italy. *Environmental Toxicology and Chemistry* 21(8), 1638-1643.
- Braun, A.M., Maurette, M.T. and Oliveros, E. 1991. *Photochemical Technology*, John Wiley and Sons Ltd, Hoboken, NJ.
- Bruheim, P., Bredholt, H. and Eimhjellen, K. 1999. Effects of surfactant mixtures, including Corexit 9527, on bacterial oxidation of acetate and alkanes in crude oil. *Applied and Environmental Microbiology* 65(4), 1658-1661.
- Burgeth, G. and Kisch, H. 2002. Photocatalytic and photoelectrochemical properties of titania-chloroplatinate(IV). *Coordination Chemistry Reviews* 230(1-2), 41-47.
- Bzdusek, P.A., Christensen, E.R., Li, A. and Zou, Q. 2004. Source apportionment of sediment PAHs in Lake Calumet, Chicago: Application of factor analysis with nonnegative constraints. *Environmental Science & Technology* 38(1), 97-103.
- Cai, J., Zhu, Y., Liu, D., Meng, M., Hu, Z. 2015. Synergistic effect of titanate-anatase heterostructure and hydrogenation-induced surface disorder on photocatalytic water splitting. *ACS Catalysis* 5(3), 1708-1716.
- Cai, Z., Gong, Y., Liu, W., Fu, J., O'Reilly, S. 2016. A surface tension based method for measuring oil dispersant concentration in seawater. *Marine Pollution Bulletin* 109(1), 49-54.
- Camilli, R., Reddy, C.M., Yoerger, D.R., Van Mooy, B.A.S., Jakuba, M.V. 2010. Tracking hydrocarbon plume transport and biodegradation at *Deepwater Horizon*. *Science* 330(6001), 201-204.
- Chakraborty, I. and Moulik, S.P. 2007. Self-aggregation of ionic C10 surfactants having different headgroups with special reference to the behavior of decyltrimethylammonium bromide in different salt environments: A calorimetric study with energetic analysis. *The Journal of Physical Chemistry B* 111(14), 3658-3664.
- Chatterjee, A., Moulik, S.P., Sanyal, S.K., Mishra, B.K. and Puri, P.M. 2001. Thermodynamics of micelle formation of ionic surfactants: A critical assessment for sodium dodecyl sulfate, cetyl pyridinium chloride and dioctyl sulfosuccinate (Na salt) by microcalorimetric, conductometric, and tensiometric measurements. *Journal of Physical Chemistry B* 105(51), 12823-12831.

- Chelme-Ayala, P., El-Din, M.G., Smith, D.W. and Adams, C.D. 2011. Oxidation kinetics of two pesticides in natural waters by ozonation and ozone combined with hydrogen peroxide. *Water Research* 45(8), 2517-2526.
- Chen, H., Lo, S. and Ou, H. 2013. Catalytic hydrogenation of nitrate on Cu–Pd supported on titanate nanotube and the experiment after aging, sulfide fouling and regeneration procedures. *Applied Catalysis B: Environmental* 142, 65-71.
- Chen, H., Ku, Y. and Kuo, Y. 2007a. Effect of Pt/TiO<sub>2</sub> characteristics on temporal behavior of o-cresol decomposition by visible light-induced photocatalysis. *Water Research* 41(10), 2069-2078.
- Chen, J., Chen, W. and Zhu, D. 2008. Adsorption of nonionic aromatic compounds to single-walled carbon nanotubes: Effects of aqueous solution chemistry. *Environmental Science & Technology* 42(19), 7225-7230.
- Chen, K., Zhu, L. and Yang, K. 2015a. Acid-assisted hydrothermal synthesis of nanocrystalline TiO<sub>2</sub> from titanate nanotubes: Influence of acids on the photodegradation of gaseous toluene. *Journal of Environmental Sciences* 27, 232-240.
- Chen, Q., Zhou, W., Du, G. and Peng, L. 2002. Trititanate nanotubes made via a single alkali treatment. *Advanced Materials* 14(17), 1208-1211.
- Chen, W., Duan, L. and Zhu, D. 2007b. Adsorption of polar and nonpolar organic chemicals to carbon nanotubes. *Environmental Science & Technology* 41(24), 8295-8300.
- Chen, X. and Burda, C. 2008. The electronic origin of the visible-light absorption properties of C-, N- and S-doped TiO<sub>2</sub> nanomaterials. *Journal of the American Chemical Society* 130(15), 5018-5019.
- Chen, X., Liu, L. and Huang, F. 2015b. Black titanium dioxide (TiO<sub>2</sub>) nanomaterials. *Chemical Society Reviews* 44(7), 1861-1885.
- Chen, X. and Mao, S. 2007. Titanium dioxide nanomaterials: Synthesis, properties, modifications, and applications. *Chemical Reviews* 107(7), 2891-2959.
- Cheng, K. and Wong, J.W.C. 2006. Combined effect of nonionic surfactant Tween 80 and DOM on the behaviors of PAHs in soil–water system. *Chemosphere* 62(11), 1907-1916.
- Chilom, G., Bruns, A.S. and Rice, J.A. 2009. Aggregation of humic acid in solution: Contributions of different fractions. *Organic Geochemistry* 40(4), 455-460.
- Chingombe, P., Saha, B. and Wakeman, R.J. 2005. Surface modification and characterisation of a coal-based activated carbon. *Carbon* 43(15), 3132-3143.
- Choi, M. and Yong, K. 2014. A facile strategy to fabricate high-quality single crystalline brookite TiO<sub>2</sub> nanoarrays and their photoelectrochemical properties. *Nanoscale* 6(22), 13900-13909.
- Chu, W., Chan, K. and Graham, N.J.D. 2006. Enhancement of ozone oxidation and its associated processes in the presence of surfactant: Degradation of atrazine. *Chemosphere* 64(6), 931-936.
- Chu, W. and Jia, J. 2009. The photodegradation and modeling of a typical NAPL, trichloroethene, by onochromatic UV irradiations. *Environmental Science & Technology* 43(5), 1455-1459.
- Chu, W. and Kwan, C.Y. 2002. The direct and indirect photolysis of 4,4'-dichlorobiphenyl in various surfactant/solvent-aided systems. *Water Research* 36(9), 2187-2194.
- Cirin, D.M., Posa, M.M., Krstonosic, V.S. and Milanovic, M.L. 2012. Conductometric study of sodium dodecyl sulfate-nonionic surfactant (Triton X-100, Tween 20, Tween 60, Tween 80 or Tween 85) mixed micelles in aqueous solution. *Hemijaska Industrija* 66(1), 21-28.

- Clark, C.D., De Bruyn, W.J., Ting, J. and Scholle, W. 2007. Solution medium effects on the photochemical degradation of pyrene in water. *Journal of Photochemistry and Photobiology A: Chemistry* 186(2-3), 342-348.
- Clark, C.D. and Hoffman, M.Z. 1997. Effect of solution medium on the rate constants of excited-state electron-transfer quenching reactions of ruthenium(II)-diimine photosensitizers. *Coordination Chemistry Reviews* 159(0), 359-373.
- D'Auria, M., Emanuele, L., Racioppi, R. and Velluzzi, V. 2009. Photochemical degradation of crude oil: Comparison between direct irradiation, photocatalysis, and photocatalysis on zeolite. *Journal of Hazardous Materials* 164(1), 32-38.
- Dabestani, R. and Ivanov, I.N. 1999. A compilation of physical, spectroscopic and photophysical properties of polycyclic aromatic hydrocarbons. *Photochemistry and Photobiology* 70(1), 10-34.
- Dąbrowski, A., Podkościelny, P., Hubicki, Z. and Barczak, M. 2005. Adsorption of phenolic compounds by activated carbon-a critical review. *Chemosphere* 58(8), 1049-1070.
- Dahl, M., Liu, Y. and Yin, Y. 2014. Composite titanium dioxide nanomaterials. *Chemical Reviews* 114(19), 9853-9889.
- Dai, G., Liu, S., Liang, Y. and Luo, T. 2013. Synthesis and enhanced photoelectrocatalytic activity of p-n junction  $\text{Co}_3\text{O}_4/\text{TiO}_2$  nanotube arrays. *Applied Surface Science* 264(0), 157-161.
- Davies, B.E. 1974. Loss-on-Ignition as an estimate of soil organic-matter. *Soil Science Society of America Journal* 38(1), 150-151.
- de Bruyn, W.J., Clark, C.D., Ottelle, K. and Aiona, P. 2012. Photochemical degradation of phenanthrene as a function of natural water variables modeling freshwater to marine environments. *Marine Pollution Bulletin* 64(3), 532-538.
- de la Pena O'Shea, V.A., Alvarez Galvan, M.C., Platero Prats, A.E., Campos-Martin, J.M. and Fierro, J.L.G. 2011. Direct evidence of the SMSI decoration effect: the case of  $\text{Co}/\text{TiO}_2$  catalyst. *Chemical Communications* 47(25), 7131-7133.
- Delvigne, G.A.L. and Sweeney, C.E. 1988. Natural dispersion of oil. *Oil and Chemical Pollution* 4(4), 281-310.
- Diaz, M., Luiz, M., Bertolotti, S., Miskoski, S. and Garcia, N.A. 2004. Scavenging of photogenerated singlet molecular oxygen and superoxide radical anion by sulphadiazine-Kinetics and mechanism. *Canadian Journal of Chemistry-Revue Canadienne De Chimie* 82(12), 1752-1759.
- Diemand, R. 2011. Dispersants for crude oil spills: Dispersant behavior studies, Worcester Polytechnic Institute.
- Diercks, A.R., Highsmith, R.C., Asper, V.L., Joung, D.J., Zhou, Z. 2010. Characterization of subsurface polycyclic aromatic hydrocarbons at the *Deepwater Horizon* site. *Geophysical Research Letters* 37(20).
- Doong, R., Chang, S. and Tsai, C. 2013. Enhanced photoactivity of Cu-deposited titanate nanotubes for removal of bisphenol A. *Applied Catalysis B-Environmental* 129, 48-55.
- Driessen, M.D. and Grassian, V.H. 1998. Photooxidation of trichloroethylene on  $\text{Pt}/\text{TiO}_2$ . *Journal of Physical Chemistry B* 102(8), 1418-1423.
- Eastoe, J. and Dalton, J.S. 2000. Dynamic surface tension and adsorption mechanisms of surfactants at the air-water interface. *Advances in Colloid and Interface Science* 85(2-3), 103-144.
- Echaniz, S.A. and Vignatti, A.M. 2011. Seasonal variation and influence of turbidity and salinity on the

- zooplankton of a saline lake in central Argentina. *Latin American Journal of Aquatic Research* 39(2), 306-315.
- Edwards, D.A., Luthy, R.G. and Liu, Z. 1991. Solubilization of polycyclic aromatic hydrocarbons in micellar nonionic surfactant solutions. *Environmental Science & Technology* 25(1), 127-133.
- Ehrhardt, M. and Petrick, G. 1993. On the composition of dissolved and particle-associated fossil fuel residues in Mediterranean surface water. *Marine chemistry* 42(1), 57-70.
- EPA (Environmental Protection Agency), 1996. Acid digestion of sediments, sludges, and soils, Method 3050B, Revision 2; USEPA. Washington, DC, USA.
- EPA (Environmental Protection Agency), 2010. Dispersants. <<http://www.epa.gov/bpspill/dispersants.html#chemicals>> (accessed July 07, 2013).
- EPA (Environmental Protection Agency), 2013. National Contingency Plan product schedule toxicity and effectiveness summaries. <[http://www.epa.gov/emergencies/content/ncp/tox\\_tables.htm](http://www.epa.gov/emergencies/content/ncp/tox_tables.htm)> (accessed November 11, 2013).
- Erdem, N.S., Alawani, N. and Wesdemiotis, C. 2014. Characterization of polysorbate 85, a nonionic surfactant, by liquid chromatography vs. ion mobility separation coupled with tandem mass spectrometry. *Analytica Chimica Acta* 808, 83-93.
- Evans, D.F., Allen, M., Ninham, B.W. and Fouda, A. 1984. Critical micelle concentrations for alkyltrimethylammonium bromides in water from 25 to 160 °C. *Journal of Solution Chemistry* 13(2), 87-101.
- Fallahtafi, S., Rantanen, T., Brown, R. S., Snieckus, V., and Hodson, P. V. 2012. Toxicity of hydroxylated alkyl-phenanthrenes to the early life stages of Japanese medaka (*Oryzias latipes*). *Aquatic Toxicology* 106, 56-64.
- Fang, J., Shan, X., Wen, B., Lin, J., Lu, X. 2008. Sorption and desorption of phenanthrene onto iron, copper, and silicon dioxide nanoparticles. *Langmuir* 24(19), 10929-10935.
- Fasnacht, M.P. and Blough, N.V. 2002. Aqueous photodegradation of polycyclic aromatic hydrocarbons. *Environmental Science & Technology* 36(20), 4364-4369.
- Fasnacht, M.P. and Blough, N.V. 2003. Mechanisms of the aqueous photodegradation of polycyclic aromatic hydrocarbons. *Environmental Science & Technology* 37(24), 5767-5772.
- Feng, C., Teng, F., Liu, Z., Chang, C., Zhao, Y. 2015. A newly discovered BiF<sub>3</sub> photocatalyst with a high positive valence band. *Journal of Molecular Catalysis A: Chemical* 401(0), 35-40.
- Fokin, A.A. and Schreiner, P.R. 2002. Selective alkane transformations via radicals and radical cations: Insights into the activation step from experiment and theory. *Chemical Reviews* 102(5), 1551-1594.
- Foote, C.S. and Wexler, S. 1964. Singlet oxygen. A probable intermediate in photosensitized autoxidations. *Journal of the American Chemical Society* 86(18), 3880-3881.
- Fornasiero, D. and Grieser, F. 1990. Study of the absorption spectra of pyrene complexed to paraquat in pentanol-sodium dodecylsulphate micelles. *Journal of the Chemical Society, Faraday Transactions* 86(17), 2955-2960.
- Franklin, C.L. and Warner, L.J. 2011. Fighting chemical with chemicals: The role and regulation of dispersants in oil spill response. *Natural Resources & Environment* 26(2), 7.
- Frimmel, F.H. 1994. Photochemical aspects related to humic substances. *Environment International* 20(3), 373-385.

- Fu, J., Cai, Z., Gong, Y., O'Reilly, S.E., Hao, X. 2015. A new technique for determining critical micelle concentrations of surfactants and oil dispersants via UV absorbance of pyrene. *Colloids and Surfaces A: Physicochemical and Engineering Aspects* 484, 1-8.
- Fu, J., Gong, Y., Zhao, X., O'Reilly, S.E. and Zhao, D. 2014. Effects of oil and dispersant on formation of marine oil snow and transport of oil hydrocarbons. *Environmental Science & Technology* 48(24), 14392-14399.
- Fujii, M., Imaoka, A., Yoshimura, C. and Waite, T.D. 2014. Effects of molecular composition of natural organic matter on ferric iron complexation at circumneutral pH. *Environmental Science & Technology* 48(8), 4414-4424.
- Furukawa, Y., Watkins, J.L., Kim, J., Curry, K.J. and Bennett, R.H. 2009. Aggregation of montmorillonite and organic matter in aqueous media containing artificial seawater. *Geochemical Transactions* 10(1), 1.
- Gandra, N., Chiu, P.L., Li, W., Anderson, Y.R., Mitra, S. 2009. Photosensitized singlet oxygen production upon two-photon excitation of single-walled carbon nanotubes and their functionalized analogues. *Journal of Physical Chemistry C* 113(13), 5182-5185.
- Gao, H., Zhao, S., Mao, S., Yuan, H., Yu, J. 2002. Mixed micelles of polyethylene glycol (23) lauryl ether with ionic surfactants studied by proton 1D and 2D NMR. *Journal of Colloid and Interface Science* 249(1), 200-208.
- Garcia, M.T., Campos, E., Marsal, A. and Ribosa, I. 2009. Biodegradability and toxicity of sulphonate-based surfactants in aerobic and anaerobic aquatic environments. *Water Research* 43(2), 295-302.
- Garcia, T., Murillo, R., Cazorla-Amoros, D., Mastral, A.M. and Linares-Solano, A. 2004. Role of the activated carbon surface chemistry in the adsorption of phenanthrene. *Carbon* 42(8-9), 1683-1689.
- Gauthier, T.D., Shane, E.C., Guerin, W.F., Seitz, W.R. and Grant, C.L. 1986. Fluorescence quenching method for determining equilibrium constants for polycyclic aromatic hydrocarbons binding to dissolved humic materials. *Environmental Science & Technology* 20(11), 1162-1166.
- Gearing, P.J., Gearing, J.N., Pruell, R.J., Wade, T.L. and Quinn, J.G. 1980. Partitioning of No. 2 fuel oil in controlled estuarine ecosystems. Sediments and suspended particulate matter. *Environmental Science & Technology* 14(9), 1129-1136.
- Gehlen, M.H. and De Schryver, F.C. 1993. Fluorescence quenching in micelles in the presence of a probe-quencher ground-state charge-transfer complex. *The Journal of Physical Chemistry* 97(43), 11242-11248.
- Ghita, D., Rosca, P. and Ezeanu, D.S. 2012. Synthesis and characterization of Pt catalysts supported on mesoporous matters. *Revista De Chimie* 63(10), 1056-1061.
- Ghosh, S. 2001. Surface chemical and micellar properties of binary and ternary surfactant mixtures (cetyl pyridinium chloride, Tween-40, and Brij-56) in an aqueous medium. *Journal of Colloid and Interface Science* 244(1), 128-138.
- Ghosh, S. and Moulik, S.P. 1998. Interfacial and micellization behaviors of binary and ternary mixtures of amphiphiles (Tween-20, Brij-35, and sodium dodecyl sulfate) in aqueous medium. *Journal of Colloid and Interface Science* 208(2), 357-366.
- Glover, A.G. and Smith, C.R. 2003. The deep-sea floor ecosystem: Current status and prospects of anthropogenic change by the year 2025. *Environmental Conservation* 30(3), 219-241.
- Gong, Y., Fu, J., O'Reilly, S.E. and Zhao, D. 2015. Effects of oil dispersants on photodegradation of pyrene in marine water. *Journal of Hazardous Materials* 287(0), 142-150.

- Gong, Y., Zhao, X., Cai, Z., O'Reilly, S.E., Hao, X. 2014a. A review of oil, dispersed oil and sediment interactions in the aquatic environment: Influence on the fate, transport and remediation of oil spills. *Marine Pollution Bulletin* 79(1-2), 16-33.
- Gong, Y., Zhao, X., O'Reilly, S., Qian, T. and Zhao, D. 2014b. Effects of oil dispersant and oil on sorption and desorption of phenanthrene with Gulf Coast marine sediments. *Environmental Pollution* 185, 240-249.
- Gong, Y., Liu, Y., Xiong, Z., Kaback, D. and Zhao, D. 2012. Immobilization of mercury in field soil and sediment using carboxymethyl cellulose stabilized iron sulfide nanoparticles. *Nanotechnology* 23(29), 294007.
- Gordon, D.C. 1970. A microscopic study of organic particles in the North Atlantic Ocean. In *Deep Sea Research and Oceanographic Abstracts* 17(1), 175-185. Elsevier.
- Graham, W.M., Condon, R.H., Carmichael, R.H., D'Ambra, I., Patterson, H.K. 2010. Oil carbon entered the coastal planktonic food web during the *Deepwater Horizon* oil spill. *Environmental Research Letters* 5(4), 045301.
- Grandcolas, M., Cottineau, T., Louvet, A., Keller, N. and Keller, V. 2013. Solar light-activated photocatalytic degradation of gas phase diethylsulfide on WO<sub>3</sub>-modified TiO<sub>2</sub> nanotubes. *Applied Catalysis B: Environmental* 138, 128-140.
- Griffiths, P., Hirst, N., Paul, A., King, S., Heenan, R. 2004. Effect of ethanol on the interaction between poly (vinylpyrrolidone) and sodium dodecyl sulfate. *Langmuir* 20(16), 6904-6913.
- Guetzloff, T.F. and Rice, J.A. 1994. Does humic acid form a micelle? *Science of the Total Environment* 152(1), 31-35.
- Guo, W., He, M., Yang, Z., Lin, C., Quan, X. 2007. Distribution of polycyclic aromatic hydrocarbons in water, suspended particulate matter and sediment from Daliao River watershed, China. *Chemosphere* 68(1), 93-104.
- Gupta, A., Sender, M., Fields, S. and Bothun, G.D. 2014. Phase and sedimentation behavior of oil (octane) dispersions in the presence of model mineral aggregates. *Marine Pollution Bulletin* 87(1-2), 164-170.
- Guyomarch, J., Merlin, F.X. and Bernanose, P. 1999. Oil interaction with mineral fines and chemical dispersion: Behaviour of the dispersed oil in coastal or estuarine conditions, pp. 137-150, Minister of Supply and Services, Canada.
- Guyomarch, J., Le F., S. and Merlin, F.X. 2002. Effect of suspended mineral load, water salinity and oil type on the size of oil–mineral aggregates in the presence of chemical dispersant. *Spill Science & Technology Bulletin* 8(1), 95-100.
- Hadgiivanova, R. and Diamant, H. 2009. Premicellar aggregation of amphiphilic molecules: Aggregate lifetime and polydispersity. *The Journal of Chemical Physics* 130(11), 114901.
- Harayama, S., Kishira, H., Kasai, Y. and Shutsubo, K. 1999. Petroleum biodegradation in marine environments. *Journal of Molecular Microbiology and Biotechnology* 1(1), 63-70.
- Harris, D.C. 2010. *Quantitative Chemical Analysis*, Macmillan.
- Hayworth, J.S. and Clement, T.P. 2012. Provenance of Corexit-related chemical constituents found in nearshore and inland Gulf Coast waters. *Marine Pollution Bulletin* 64(10), 2005-2014.
- Hazen, T.C., Dubinsky, E.A., DeSantis, T.Z., Andersen, G.L., Piceno, Y.M., 2010. Deep-sea oil plume enriches indigenous oil-degrading bacteria. *Science* 330(6001), 204-208.

- He, Y., Yediler, A., Sun, T. and Kettrup, A. 1995. Adsorption of fluoranthene on soil and lava-effects of the organic-carbon contents of adsorbents and temperature. *Chemosphere* 30(1), 141-150.
- Heil, D. and Sposito, G. 1993a. Organic-matter role in illitic soil colloids flocculation. 1. Counter Ions and Ph. *Soil Science Society of America Journal* 57(5), 1241-1246.
- Heil, D. and Sposito, G. 1993b. Organic-matter role in illitic soil colloids flocculation. 2. Surface-Charge. *Soil Science Society of America Journal* 57(5), 1246-1253.
- Hellman, T.M. and Hamilton, G.A. 1974. Mechanism of alkane oxidation by ozone in the presence and absence of iron(III) chloride. *Journal of the American Chemical Society* 96(5), 1530-1535.
- Hemmer, M.J., Barron, M.G. and Greene, R.M. 2011. Comparative toxicity of eight oil dispersants, Louisiana sweet crude oil (LSC), and chemically dispersed LSC to two aquatic test species. *Environmental Toxicology and Chemistry* 30(10), 2244-2252.
- Hinze, J.O. 1955. Fundamentals of the hydrodynamic mechanism of splitting in dispersion processes. *AIChE Journal* 1(3), 289-295.
- Ho, Y.S. and McKay, G. 1998. Sorption of dye from aqueous solution by peat. *Chemical Engineering Journal* 70(2), 115-124.
- Ho, Y.S. and McKay, G. 1999. Pseudo-second order model for sorption processes. *Process Biochemistry* 34(5), 451-465.
- Hoang Anh, L., Le Thuy, L., Chin, S. and Jung, J. 2012. Photocatalytic degradation of methylene blue by a combination of TiO<sub>2</sub>-anatase and coconut shell activated carbon. *Powder Technology* 225, 167-175.
- Hu, Y. and Dai, J. 2003. Hydrophobic aggregation of alumina in surfactant solution. *Minerals Engineering* 16(11), 1167-1172.
- Hu, Y., Song, X., Jiang, S. and Wei, C. 2015. Enhanced photocatalytic activity of Pt-doped TiO<sub>2</sub> for NO<sub>x</sub> oxidation both under UV and visible light irradiation: A synergistic effect of lattice Pt<sup>4+</sup> and surface PtO. *Chemical Engineering Journal* 274, 102-112.
- Hu, Y., Tsai, H.L. and Huang, C. 2003. Effect of brookite phase on the anatase-rutile transition in titania nanoparticles. *Journal of the European Ceramic Society* 23(5), 691-696.
- Huang, W., Tang, X., Wang, Y., Kolytyn, Y. and Gedanken, A. 2000. Selective synthesis of anatase and rutile via ultrasound irradiation. *Chemical Communications* (15), 1415-1416.
- Hunter, R.J. 2013. *Zeta Potential in Colloid Science: Principles and Applications*, Academic Press.
- Ikehata, K. and El-Din, M.G. 2004. Degradation of recalcitrant surfactants in wastewater by ozonation and advanced oxidation processes: A review. *Ozone-Science & Engineering* 26(4), 327-343.
- Innocente, N., Biasutti, M., Venir, E., Spaziani, M. and Marchesini, G. 2009. Effect of high-pressure homogenization on droplet size distribution and rheological properties of ice cream mixes. *Journal of Dairy Science* 92(5), 1864-1875.
- Inoue, Y., Kubokawa, T. and Sato, K. 1991. Photocatalytic activity of alkali-metal titanates combined with Ru in the decomposition of water. *Journal of Physical Chemistry* 95(10), 4059-4063.
- Inoue, Y., Niiyama, T. and Sato, K. 1994. Photocatalysts using hexa- and octa-titanates with different tunnel space for water decomposition. *Topics in Catalysis* 1(1-2), 137-144.
- Jacob, S.M. and Bergman, R.E. 2001a. Water based oil dispersant, U.S. Polychemical Marine Corp.
- Jensen, G.V., Lund, R., Gummel, J., Monkenbusch, M., Narayanan, T. 2013. Direct observation of the

- formation of surfactant micelles under nonisothermal conditions by synchrotron SAXS. *Journal of the American Chemical Society* 135(19), 7214-7222.
- Jeong, I.S., Kim, J.H. and Im, S. 2003. Ultraviolet-enhanced photodiode employing n-ZnO/p-Si structure. *Applied Physics Letters* 83(14), 2946-2948.
- Jia, H., Zhao, J., Fan, X., Dilimulati, K. and Wang, C. 2012. Photodegradation of phenanthrene on cation-modified clays under visible light. *Applied Catalysis B: Environmental* 123-124(0), 43-51.
- Jin, Z., Xi, C., Zeng, Q., Yin, F., Zhao, J. 2003. Catalytic behavior of nanoparticle  $\alpha$ -PtO<sub>2</sub> for ethanol oxidation. *Journal of Molecular Catalysis A: Chemical* 191(1), 61-66.
- Johansen, O. 2003. Development and verification of deep-water blowout models. *Marine Pollution Bulletin* 47(9-12), 360-368.
- Johnson, A.C., Ternes, T., Williams, R.J. and Sumpter, J.P. 2008. Assessing the concentrations of polar organic microcontaminants from point sources in the aquatic environment: Measure or model? *Environmental Science & Technology* 42(15), 5390-5399.
- Jones-Hughes, T. and Turner, A. 2005. Sorption of ionic surfactants to estuarine sediment and their influence on the sequestration of phenanthrene. *Environmental Science & Technology* 39(6), 1688-1697.
- Jonker, M.T.O., Sinke, A.J.C., Brils, J.M. and Koelmans, A.A. 2003. Sorption of polycyclic aromatic hydrocarbons to oil contaminated sediment: Unresolved complex? *Environmental Science & Technology* 37(22), 5197-5203.
- Joshi, O., McGuire, J. and Wang, D. 2008. Adsorption and function of recombinant factor VIII at solid-water interfaces in the presence of Tween-80. *Journal of Pharmaceutical Sciences* 97(11), 4741-4755.
- Kahan, T.F. and Donaldson, D.J. 2007. Photolysis of polycyclic aromatic hydrocarbons on water and ice surfaces. *Journal of Physical Chemistry A* 111(7), 1277-1285.
- Kalyanasundaram, K. and Thomas, J.K. 1977. Environmental effects on vibronic band intensities in pyrene monomer fluorescence and their application in studies of micellar systems. *Journal of the American Chemical Society* 99(7), 2039-2044.
- Kamil, M. and Siddiqui, H. 2013. Experimental study of surface and solution properties of gemini-conventional surfactant mixtures on solubilization of polycyclic aromatic hydrocarbon. *Modeling and Numerical Simulation of Material Science* 3(04), 17.
- Karapanagioti, H.K., Sabatini, D.A., Kleinedam, S., Grathwohl, P. and Ligouis, B. 1999. Phenanthrene sorption with heterogeneous organic matter in a landfill aquifer material. *Physics and Chemistry of the Earth Part B-Hydrology Oceans and Atmosphere* 24(6), 535-541.
- Kasprzyk-Hordern, B., Ziolek, M. and Nawrocki, J. 2003. Catalytic ozonation and methods of enhancing molecular ozone reactions in water treatment. *Applied Catalysis B: Environmental* 46(4), 639-669.
- Kawaguchi, H. 1993. Rates of sensitized photo-oxidation of 2,4,6-trimethylphenol by humic acid. *Chemosphere* 27(11), 2177-2182.
- Kepner, R. and Pratt, J.R. 1994. Use of fluorochromes for direct enumeration of total bacteria in environmental samples: Past and present. *Microbiological Reviews* 58(4), 603-615.
- Kester, D.R., Duedall, I.W., Connors, D.N. and Pytkowic, R.M. 1967. Preparation of artificial seawater. *Limnology and Oceanography* 12(1), 176-179.
- Khairy, M.A. and Lohmann, R. 2012. Field Validation of polyethylene passive air samplers for parent and



- alkylated PAHs in Alexandria, Egypt. *Environmental Science & Technology* 46(7), 3990-3998.
- Khan, M.A., Jung, H. and Yang, O. 2006. Synthesis and characterization of ultrahigh crystalline TiO<sub>2</sub> nanotubes. *The Journal of Physical Chemistry B* 110(13), 6626-6630.
- Khelifa, A., Fieldhouse, B., Wang, Z., Yang, C., Landriault, M.E.B.C. 2008. Effects of chemical dispersant on oil sedimentation due to oil-SPM flocculation: Experiments with the NIST standard reference material 1941. *International Oil Spill Conference 2008*(1), 627-631.
- Khelifa, A. and Hill, P.S. 2006. Models for effective density and settling velocity of flocs. *Journal of Hydraulic Research* 44(3), 390-401.
- Khelifa, A., Stoffyn-Egli, P., Hill, P.S. and Lee, K. 2002. Characteristics of oil droplets stabilized by mineral particles: Effects of oil type and temperature. *Spill Science & Technology Bulletin* 8(1), 19-30.
- Khelifa, A., Stoffyn-Egli, P., Hill, P.S. and Lee, K. 2005. Effects of salinity and clay type on oil-mineral aggregation. *Marine Environmental Research* 59(3), 235-254.
- Kim, K.H., Jahan, S.A., Kabir, E. and Brown, R.J.C. 2013. A review of airborne polycyclic aromatic hydrocarbons (PAHs) and their human health effects. *Environment International* 60, 71-80.
- Kim, S., Kim, M., Hwang, S. and Lim, S.K. 2012. Enhancement of photocatalytic activity of titania-titanate nanotubes by surface modification. *Applied Catalysis B: Environmental* 123, 391-397.
- Kjørboe, T. 1997. Small-scale turbulence, marine snow formation, and planktivorous feeding. *Scientia Marina* 61, 141-158.
- Kirsten, W.J. 1979. Automated methods for the simultaneous determination of carbon, hydrogen, nitrogen, and sulfur, and sulfur alone in organic and inorganic materials. *Analytical Chemistry* 51, 1173-1179.
- Klemas, V. 2010. Tracking oil slicks and predicting their trajectories using remote sensors and models: case studies of the Sea Princess and *Deepwater Horizon* oil spills. *Journal of Coastal Research*, 789-797.
- Kline, S.R. and Kaler, E.W. 1994. Colloidal interactions in water/2-butoxyethanol solvents. *Langmuir* 10(2), 412-417.
- Ko, S.O., Schlautman, M.A. and Carraway, E.R. 1998a. Effects of solution chemistry on the partitioning of phenanthrene to sorbed surfactants. *Environmental Science & Technology* 32(22), 3542-3548.
- Ko, S.O., Schlautman, M.A. and Carraway, E.R. 1998b. Partitioning of hydrophobic organic compounds to sorbed surfactants. 1. Experimental Studies. *Environmental Science & Technology* 32(18), 2769-2775.
- Konova, P., Stoyanova, M., Naydenov, A., Christoskova, S. and Mehandjiev, D. 2006. Catalytic oxidation of VOCs and CO by ozone over alumina supported cobalt oxide. *Applied Catalysis A: General* 298, 109-114.
- Kou, J., Li, Z., Yuan, Y., Zhang, H., Wang, Y. 2009. Visible-light-induced photocatalytic oxidation of polycyclic aromatic hydrocarbons over tantalum oxynitride photocatalysts. *Environmental Science & Technology* 43(8), 2919-2924.
- Kou, J., Zhang, H., Yuan, Y., Li, Z., Wang, Y. 2008. Efficient photodegradation of phenanthrene under visible light irradiation via photosensitized electron transfer. *The Journal of Physical Chemistry C* 112(11), 4291-4296.
- Kover, S.C., Rosario-Ortiz, F.L. and Linden, K.G. 2014. Photochemical fate of solvent constituents of

- Corexit oil dispersants. *Water Research* 52, 101-111.
- Kretzschmar, R., Hesterberg, D. and Sticher, H. 1997. Effects of adsorbed humic acid on surface charge and flocculation of kaolinite. *Soil Science Society of America Journal* 61(1), 101-108.
- Kretzschmar, R., Holthoff, H. and Sticher, H. 1998. Influence of pH and humic acid on coagulation kinetics of kaolinite: A dynamic light scattering study. *Journal of Colloid and Interface Science* 202(1), 95-103.
- Kretzschmar, R., Robarge, W.P. and Weed, S.B. 1993. Flocculation of kaolinitic soil clays - Effects of humic substances and iron-oxides. *Soil Science Society of America Journal* 57(5), 1277-1283.
- Kujawinski, E.B., Kido Soule, M.C., Valentine, D.L., Boysen, A.K., Longnecker, K. 2011. Fate of dispersants associated with the *Deepwater Horizon* oil spill. *Environmental Science & Technology* 45(4), 1298-1306.
- Kuribayashi, K. and Kitamura, S. 2001. Preparation of Pt-PtO<sub>x</sub> thin films as electrode for memory capacitors. *Thin Solid Films* 400(1-2), 160-164.
- Lam, C.W., James, J.T., McCluskey, R., Arepalli, S. and Hunter, R.L. 2006. A review of carbon nanotube toxicity and assessment of potential occupational and environmental health risks. *Critical Reviews in Toxicology* 36(3), 189-217.
- Lam, M.W., Tantuco, K. and Mabury, S.A. 2003. PhotoFate: A new approach in accounting for the contribution of indirect photolysis of pesticides and pharmaceuticals in surface waters. *Environmental Science & Technology* 37(5), 899-907.
- Leahy, J.G. and Colwell, R.R. 1990. Microbial degradation of hydrocarbons in the environment. *Microbiological Reviews* 54(3), 305-315.
- Lee, C., Wang, C., Lyu, M., Juang, L., Liu, S. 2007. Effects of sodium content and calcination temperature on the morphology, structure and photocatalytic activity of nanotubular titanates. *Journal of Colloid and Interface Science* 316(2), 562-569.
- Lee, J. and Hildemann, L.M. 2013. Surface tension of solutions containing dicarboxylic acids with ammonium sulfate, D-glucose, or humic acid. *Journal of Aerosol Science* 64, 94-102.
- Legrini, O., Oliveros, E. and Braun, A.M. 1993. Photochemical processes for water treatment. *Chemical Reviews* 93(2), 671-698.
- Lehr, B., Bristol, S. and Possolo, A. 2010. Oil Budget Calculator-*Deepwater Horizon*, technical documentation: a report to the National Incident Command. Coastal Response Res. Cent. <[http://www.restorethegulf.gov/sites/default/files/documents/pdf/OilBudgetCalc\\_Full\\_HQ-Print\\_111110.pdf](http://www.restorethegulf.gov/sites/default/files/documents/pdf/OilBudgetCalc_Full_HQ-Print_111110.pdf)> (accessed August 15, 2013)
- Lehto, K., Vuorimaa, E. and Lemmetyinen, H. 2000. Photolysis of polycyclic aromatic hydrocarbons (PAHs) in dilute aqueous solutions detected by fluorescence. *Journal of Photochemistry and Photobiology A: Chemistry* 136(1-2), 53-60.
- Lessard, R.R. and Demarco, G. 2000. The significance of oil spill dispersants. *Spill Science & Technology Bulletin* 6(1), 59-68.
- Li, F. and Li, X. 2002. The enhancement of photodegradation efficiency using Pt-TiO<sub>2</sub> catalyst. *Chemosphere* 48(10), 1103-1111.
- Li, H., He, X., Kang, Z., Huang, H., Liu, Y. 2010. Water-soluble fluorescent carbon quantum dots and photocatalyst design. *Angewandte Chemie International Edition* 49(26), 4430-4434.
- Li, P., Li, Z., Shen, H., Thomas, R.K., Penfold, J. 2013a. Application of the Gibbs Equation to the

- adsorption of nonionic surfactants and polymers at the air-water interface: Comparison with surface excesses determined directly using neutron reflectivity. *Langmuir* 29(30), 9324-9334.
- Li, R., Dong, G. and Chen, G. 2015. Synthesis, characterization and performance of ternary doped Cu-Ce-B/TiO<sub>2</sub> nanotubes on the photocatalytic removal of nitrogen oxides. *New Journal of Chemistry* 39(9), 6854-6863.
- Li, X., Cao, X., Wu, G., Temple, T., Coulon, F. 2014. Ozonation of diesel-fuel contaminated sand and the implications for remediation end-points. *Chemosphere* 109, 71-76.
- Li, Y., Duan, X., Li, X. and Zhang, D. 2013b. Photodegradation of nonylphenol by simulated sunlight. *Marine Pollution Bulletin* 66(1-2), 47-52.
- Libby, B. and Monson, P. 2004. Adsorption/desorption hysteresis in inkbottle pores: a density functional theory and Monte Carlo simulation study. *Langmuir* 20(10), 4289-4294.
- Librando, V., Bracchitta, G., de Guidi, G., Minniti, Z., Perrini, G. 2014. Photodegradation of anthracene and benzo[a] anthracene in polar and apolar media: New pathways of photodegradation. *Polycyclic Aromatic Compounds* 34(3), 263-279.
- Lima, A.L.C., Farrington, J.W. and Reddy, C.M. 2005. Combustion-derived polycyclic aromatic hydrocarbons in the environment: A review. *Environmental Forensics* 6(2), 109-131.
- Lin, C., Chao, J., Liu, C., Chang, J. and Wang, F. 2008. Effect of calcination temperature on the structure of a Pt/TiO<sub>2</sub> (B) nanofiber and its photocatalytic activity in generating H<sub>2</sub>. *Langmuir* 24(17), 9907-9915.
- Lin, C., Zhang, W., Yuan, M., Feng, C., Ren, Y. 2014. Degradation of polycyclic aromatic hydrocarbons in a coking wastewater treatment plant residual by an O<sub>3</sub>/ultraviolet fluidized bed reactor. *Environmental Science and Pollution Research* 21(17), 10329-10338.
- Lin, H., Chiu, H.C., Tsai, H.C., Chien, S.H. and Wang, C. 2003. Synthesis, characterization and catalytic oxidation of carbon monoxide over cobalt oxide. *Catalysis Letters* 88(3-4), 169-174.
- Linsebigler, A.L., Lu, G.Q. and Yates, J.T. 1995. Photocatalysis on TiO<sub>2</sub> surfaces: Principles, mechanisms and selected results. *Chemical Reviews* 95(3), 735-758.
- Lippold, H., Gottschalch, U. and Kupsch, H. 2008. Joint influence of surfactants and humic matter on PAH solubility. Are mixed micelles formed?. *Chemosphere* 70(11), 1979-1986.
- Liss, S.N., Droppo, I.G., Leppard, G.G. and Milligan, T.G. 2004. *Flocculation in Natural and Engineered Environmental Systems*, CRC Press, Boca Raton, Florida.
- Liu, W., Borthwick, A.G.L., Li, X. and Ni, J. 2014a. High photocatalytic and adsorptive performance of anatase-covered titanate nanotubes prepared by wet chemical reaction. *Microporous and Mesoporous Materials* 186, 168-175.
- Liu, W., Ni, J. and Yin, X. 2014b. Synergy of photocatalysis and adsorption for simultaneous removal of Cr(VI) and Cr(III) with TiO<sub>2</sub> and titanate nanotubes. *Water Research* 53, 12-25.
- Liu, W., Sun, W., Borthwick, A.G.L. and Ni, J. 2013a. Comparison on aggregation and sedimentation of titanium dioxide, titanate nanotubes and titanate nanotubes-TiO<sub>2</sub>: Influence of pH, ionic strength and natural organic matter. *Colloids and Surfaces A: Physicochemical and Engineering Aspects* 434(0), 319-328.
- Liu, W., Wang, T., Borthwick, A.G., Wang, Y., Yin, X. 2013b. Adsorption of Pb<sup>2+</sup>, Cd<sup>2+</sup>, Cu<sup>2+</sup> and Cr<sup>3+</sup> onto titanate nanotubes: Competition and effect of inorganic ions. *Science of the Total Environment* 456, 171-180.

- Liu, W., Zhao, X., Borthwick, A.G., Wang, Y. and Ni, J. 2015a. Dual-enhanced photocatalytic activity of Fe-deposited titanate nanotubes used for simultaneous removal of As(III) and As(V). *ACS Applied Materials & Interfaces* 7(35), 19726-19735.
- Liu, W., Zhao, X., Wang, T., Fu, J. and Ni, J. 2015b. Selective and irreversible adsorption of mercury(II) from aqueous solution by a flower-like titanate nanomaterial. *Journal of Materials Chemistry A* 3(34), 17676-17684.
- Liu, X., Sheng, G., Luo, H., Zhang, F., Yuan, S. 2010. Contribution of extracellular polymeric substances (EPS) to the sludge aggregation. *Environmental Science & Technology* 44(11), 4355-4360.
- Liu, X., Wang, M., Zhang, S. and Pan, B. 2013c. Application potential of carbon nanotubes in water treatment: a review. *Journal of Environmental Sciences* 25(7), 1263-1280.
- Liu, Y., Shu, W., Chen, K., Peng, Z. and Chen, W. 2012a. Enhanced photothermocatalytic synergetic activity toward gaseous benzene for Mo plus C-codoped titanate nanobelts. *ACS Catalysis* 2(12), 2557-2565.
- Liu, Y., Zhong, L., Peng, Z., Cai, Y., Song, Y. 2011. Self-assembly of Pt nanocrystals/one-dimensional titanate nanobelts heterojunctions and their great enhancement of photocatalytic activities. *CrystEngComm* 13(17), 5467-5473.
- Liu, Z., Liu, J., Zhu, Q. and Wu, W. 2012b. The weathering of oil after the *Deepwater Horizon* oil spill: insights from the chemical composition of the oil from the sea surface, salt marshes and sediments. *Environmental Research Letters* 7(3), 035302.
- Logan, B.E. 2012. *Environmental Transport Processes*, John Wiley & Sons, Hoboken, New Jersey.
- Lombard, F., Guidi, L. and Kiorboe, T. 2013. Effect of type and concentration of ballasting particles on sinking rate of marine snow produced by the appendicularian *Oikopleura dioica*. *Plos One* 8(9), e75676.
- Lopez-Cervantes, J.L., Gracia-Fadrique, J., Calvo, E. and Amigo, A. 2013. Surface tensions, densities, and speeds of sound for aqueous solutions of lauryl ether ethoxylates. *Fluid Phase Equilibria* 356, 193-200.
- Lorphensri, O., Intravijit, J., Sabatini, D.A., Kibbey, T.C.G., Osathaphan, K. 2006. Sorption of acetaminophen, 17 alpha-ethynyl estradiol, nalidixic acid, and norfloxacin to silica, alumina, and a hydrophobic medium. *Water Research* 40(7), 1481-1491.
- Lu, D., Fang, P., Liu, X., Zhai, S., Li, C. 2015. A facile one-pot synthesis of TiO<sub>2</sub>-based nanosheets loaded with Mn<sub>x</sub>O<sub>y</sub> nanoparticles with enhanced visible light-driven photocatalytic performance for removal of Cr(VI) or RhB. *Applied Catalysis B: Environmental* 179, 558-573.
- Lu, L. and Zhu, L.Z. 2012. Effect of soil components on the surfactant-enhanced soil sorption of PAHs. *Journal of Soils and Sediments* 12(2), 161-168.
- Lunkenheimer, K. and Wantke, K.D. 1981. Determination of the surface-tension of surfactant solutions applying the method of Lecomte-Du-Nouy (Ring Tensiometer). *Colloid and Polymer Science* 259(3), 354-366.
- Lytle, D.A. and Peckarsky, B.L. 2001. Spatial and temporal impacts of a diesel fuel spill on stream invertebrates. *Freshwater Biology* 46(5), 693-704.
- Mackay, D. and Hossain, K. 1982. Interfacial tensions of oil, water, chemical dispersant systems. *The Canadian Journal of Chemical Engineering* 60(4), 546-550.
- Mahdi, E.S., Sakeena, M.H.F., Abdulkarim, M.F., Abdullah, G.Z., Sattar, M.A. 2011. Effect of surfactant

- and surfactant blends on pseudoternary phase diagram behavior of newly synthesized palm kernel oil esters. *Drug Design Development and Therapy* 5, 311-323.
- Majhi, P.R., Mukherjee, K., Moulik, S.P., Sen, S. and Sahu, N.P. 1999. Solution properties of a saponin (Acaciaside) in the presence of Triton X-100 and Igepal. *Langmuir* 15(20), 6624-6630.
- Malato, S., Fernandez-Ibanez, P., Maldonado, M.I., Blanco, J. and Gernjak, W. 2009. Decontamination and disinfection of water by solar photocatalysis: Recent overview and trends. *Catalysis Today* 147(1), 1-59.
- Marin, R.P., Kondrat, S.A., Gallagher, J.R., Enache, D.I., Smith, P. 2013. Preparation of fischer-tropsch supported cobalt catalysts using a new gas anti-solvent process. *ACS Catalysis* 3(4), 764-772.
- Martino, A. and Kaler, E.W. 1995. The stability of lamellar phases in water, propylene glycol, and surfactant mixtures. *Colloids and Surfaces A: Physicochemical and Engineering Aspects* 99(2), 91-99.
- Masrat, R., Maswal, M. and Dar, A.A. 2013. Competitive solubilization of naphthalene and pyrene in various micellar systems. *Journal of Hazardous Materials* 244, 662-670.
- Masten, S.J. and Davies, S.H. 1994. The use of ozonation to degrade organic contaminants in wastewaters. *Environmental Science & Technology* 28(4), 180A-185A.
- McGenity, T.J. 2014. Hydrocarbon biodegradation in intertidal wetland sediments. *Current Opinion In Biotechnology* 27, 46-54.
- Menger, F.M., Shi, L. and Rizvi, S.A.A. 2009. Re-evaluating the gibbs analysis of surface tension at the air/water interface. *Journal of the American Chemical Society* 131(30), 10380-10381.
- Mill, T., Mabey, W.R., Lan, B.Y. and Baraze, A. 1981. Photolysis of polycyclic aromatic-hydrocarbons in water. *Chemosphere* 10(11-1), 1281-1290.
- Miller, J.S. and Olejnik, D. 2001. Photolysis of polycyclic aromatic hydrocarbons in water. *Water Research* 35(1), 233-243.
- Mittal, K.L. 2000. *Acid-Base Interactions: Relevance to Adhesion Science and Technology*, VSP, Leiden Netherlands.
- Mohamed, A. and Mahfoodh, A.S.M. 2006. Solubilization of naphthalene and pyrene by sodium dodecyl sulfate (SDS) and polyoxyethylenesorbitan monooleate (Tween 80) mixed micelles. *Colloids and Surfaces A: Physicochemical and Engineering Aspects* 287(1), 44-50.
- Mondal, S. and Ghosh, S. 2012. Role of curcumin on the determination of the critical micellar concentration by absorbance, fluorescence and fluorescence anisotropy techniques. *Journal of Photochemistry and Photobiology B: Biology* 115, 9-15.
- Moulik, S.P. and Ghosh, S. 1997. Surface chemical and micellization behaviours of binary and ternary mixtures of amphiphiles (Triton X-100, Tween-80 and CTAB) in aqueous medium. *Journal of Molecular Liquids* 72(1-3), 145-161.
- Mukerjee, P. and Mysels, K.J., 1971. Critical micelle concentrations of aqueous surfactant systems (No. NSRDS-NBS-36). National Standard reference data system.
- Murov, S.L., Carmichael, I. and Hug, G.L. 1993. *Handbook of photochemistry*, second edition, Taylor & Francis.
- Muschenheim, D.K. and Lee, K. 2002. Removal of oil from the sea surface through particulate interactions: Review and prospectus. *Spill Science & Technology Bulletin* 8(1), 9-18.

- Muthukumar, M. and Selvakumar, N. 2004. Studies on the effect of inorganic salts on decolouration of acid dye effluents by ozonation. *Dyes and Pigments* 62(3), 221-228.
- Myers, D. 1988. *Surfactant science and technology*, VCH Publishers, New York.
- Myers, D. 1999. *Surfaces, interfaces, and colloids*, Wiley, New York, NY, USA.
- Nalco, C. 2010. *Corexit ingredients*, Nalco Company.
- Nam, J.J., Thomas, G.O., Jaward, F.M., Steinnes, E., Gustafsson, O. 2008. PAHs in background soils from Western Europe: Influence of atmospheric deposition and soil organic matter. *Chemosphere* 70(9), 1596-1602.
- Naspinski, C., Lingenfelter, R., Cizmas, L., Naufal, Z., He, L., 2008. A comparison of concentrations of polycyclic aromatic compounds detected in dust samples from various regions of the world. *Environment International* 34(7), 988-993.
- Nel, A., Xia, T., Madler, L. and Li, N. 2006. Toxic potential of materials at the nanolevel. *Science* 311(5761), 622-627.
- Neta, P., Huie, R.E. and Ross, A.B. 1988. Rate constants for reactions of inorganic radicals in aqueous-solution. *Journal of Physical and Chemical Reference Data* 17(3), 1027-1284.
- Neville, E.M., MacElroy, J.M.D., Thampi, K.R. and Sullivan, J.A. 2013. Visible light active C-doped titanate nanotubes prepared via alkaline hydrothermal treatment of C-doped nanoparticulate TiO<sub>2</sub>: Photo-electrochemical and photocatalytic properties. *Journal of Photochemistry and Photobiology A: Chemistry* 267, 17-24.
- Newell, C.R., Pilskalns, C., Robinson, S. and MacDonald, B. 2005. The contribution of marine snow to the particle food supply of the benthic suspension feeder, *Mytilus edulis*. *Journal of Experimental Marine Biology and Ecology* 321(2), 109-124.
- Nicodem, D.E., Guedes, C.L.B., Fernandes, M.C.Z., Severino, D., Correa, R.J. 2001. Photochemistry of petroleum. *Progress in Reaction Kinetics and Mechanism* 26(2-3), 219-238.
- Ning, B., Graham, N.J.D. and Zhang, Y.P. 2007a. Degradation of octylphenol and nonylphenol by ozone - Part I: Direct reaction. *Chemosphere* 68(6), 1163-1172.
- Ning, B., Graham, N.J.D. and Zhang, Y.P. 2007b. Degradation of octylphenol and nonylphenol by ozone - Part II: Indirect reaction. *Chemosphere* 68(6), 1173-1179.
- Ning, X., Shen, L., Sun, J., Lin, C., Zhang, Y. 2015. Degradation of polycyclic aromatic hydrocarbons (PAHs) in textile dyeing sludge by O<sub>3</sub>/H<sub>2</sub>O<sub>2</sub> treatment. *RSC Advances* 5(48), 38021-38029.
- Noüy, P.L.d. 1925. An interfacial tensiometer for universal use. *The Journal of General Physiology* 7(5), 625-631.
- NRC (National Research Council) 2003. *Oil in The Sea III: Inputs, Fates, and Effects*. The National Academies Press, Washington, D.C.
- NRC (National Research Council) 2005a. *National Research Council: Understanding Oil Spill Dispersant: Efficacy and Effects*, National Academies Press, Washington, D.C.
- NRC (National Research Council) 2005b. *National Research Council: Oil Spill Dispersants: Efficacy and Effects*, The National Academies Press, Washington, D.C.
- NRC (National Research Council) 2005c. *National Research Council: Understanding Oil Spill Dispersants: Efficacy and Effects*, The National Academies Press, Washington, D.C.
- Omotoso, O.E., Munoz, V.A. and Mikula, R.J. 2002. Mechanisms of crude oil-mineral interactions. *Spill*

- Science & Technology Bulletin 8(1), 45-54.
- OSAT (Operational Science Advisory Team) 2010. Summary Report for Sub-Sea and Sub-Surface Oil and Dispersant Detection: Sampling and Monitoring.  
[https://www.restorethegulf.gov/sites/default/files/documents/pdf/OSAT\\_Report\\_FINAL\\_17DEC.pdf](https://www.restorethegulf.gov/sites/default/files/documents/pdf/OSAT_Report_FINAL_17DEC.pdf)  
 (accessed May 13, 2015)
- OSB (Ocean Studies Board) 2005. Oil spill dispersants: efficacy and effects. The National Research Council of the National Academies. The National Academies Press, Washington, D.C.
- OSIR (Oil Spill Intelligence Report) 1980. Volume III, Center for Short-Lived Phenomena, Cambridge, MA.
- Ou, H., Liao, C., Liou, Y., Hong, J. and Lo, S. 2008. Photocatalytic oxidation of aqueous ammonia over microwave-induced titanate nanotubes. *Environmental Science & Technology* 42(12), 4507-4512.
- Ou, H. and Lo, S. 2007. Effect of Pt/Pd-doped TiO<sub>2</sub> on the photocatalytic degradation of trichloroethylene. *Journal of Molecular Catalysis A: Chemical* 275(1-2), 200-205.
- Owens, E.H. 1999. The interaction of fine particles with stranded oil. *Pure and Applied Chemistry* 71(1), 83-93.
- Owens, E.H. and Lee, K. 2003. Interaction of oil and mineral fines on shorelines: Review and assessment. *Marine Pollution Bulletin* 47(9-12), 397-405.
- Pallardy, R. 2016. *Deepwater Horizon* oil spill of 2010. < <https://www.britannica.com/event/Deepwater-Horizon-oil-spill-of-2010> > (Accessed May 24, 2013).
- Pan, B. and Xing, B. 2008. Adsorption mechanisms of organic chemicals on carbon nanotubes. *Environmental Science & Technology* 42(24), 9005-9013.
- Pan, G., Jia, C., Zhao, D., You, C., Chen, H. 2009. Effect of cationic and anionic surfactants on the sorption and desorption of perfluorooctane sulfonate (PFOS) on natural sediments. *Environmental Pollution* 157(1), 325-330.
- Pan, X., Chen, X. and Yi, Z. 2016. Defective, porous TiO<sub>2</sub> nanosheets with Pt decoration as an efficient photocatalyst for ethylene oxidation synthesized by a C<sub>3</sub>N<sub>4</sub> templating method. *ACS Applied Materials & Interfaces* 8(16), 10104-10108.
- Paria, S. and Khilar, K.C. 2004. A review on experimental studies of surfactant adsorption at the hydrophilic solid-water interface. *Advances in Colloid and Interface Science* 110(3), 75-95.
- Paris, C.B., Le Henaff, M., Aman, Z.M., Subramaniam, A., Helgers, J. 2012. Evolution of the Macondo well blowout: Simulating the effects of the circulation and synthetic dispersants on the subsea oil transport. *Environmental Science & Technology* 46(24), 13293-13302.
- Park, J.W. and Jaffe, P.R. 1993. Partitioning of three nonionic organic compounds between adsorbed surfactants, micelles, and water. *Environmental Science & Technology* 27(12), 2559-2565.
- Park, O.K. and Kang, Y. 2005. Preparation and characterization of silica-coated TiO<sub>2</sub> nanoparticle. *Colloids and Surfaces A: Physicochemical and Engineering Aspects* 257-58, 261-265.
- Parlett, C.M., Wilson, K. and Lee, A.F. 2013. Hierarchical porous materials: catalytic applications. *Chemical Society Reviews* 42(9), 3876-3893.
- Passow, U., Ziervogel, K., Asper, V. and Diercks, A. 2012. Marine snow formation in the aftermath of the *Deepwater Horizon* oil spill in the Gulf of Mexico. *Environmental Research Letters* 7(3), 035301.

- Pavlostathis, S.G. and Mathavan, G.N. 1992. Desorption kinetics of selected volatile organic compounds from field contaminated soils. *Environmental Science & Technology* 26(3), 532-538.
- Payne, J.R., Clayton Jr, J.R. and Kirstein, B.E. 2003. Oil/suspended particulate material interactions and sedimentation. *Spill Science & Technology Bulletin* 8(2), 201-221.
- Payne, J.R., Clayton Jr., J.R., McNabb Jr., G.D., Kirstein, B.E., Clary, C.L. 1989. Oil-Ice Sediment Interactions during Freeze-up and Break-up: Final Report, pp. 1-382, US Department of Commerce, NOAA.
- Pelaez, M., Nolan, N.T., Pillai, S.C., Seery, M.K., Falaras, P., 2012. A review on the visible light active titanium dioxide photocatalysts for environmental applications. *Applied Catalysis B: Environmental* 125, 331-349.
- Peng, S., Wu, W. and Chen, J. 2011. Removal of PAHs with surfactant-enhanced soil washing: influencing factors and removal effectiveness. *Chemosphere* 82(8), 1173-1177.
- Perez, L., Pinazo, A., Rosen, M.J. and Infante, M.R. 1998. Surface activity properties at equilibrium of novel gemini cationic amphiphilic compounds from arginine, Bis(Arg). *Langmuir* 14(9), 2307-2315.
- Persson, C.M., Jonsson, A.P., Bergstrom, M. and Eriksson, J.C. 2003. Testing the gouy-chapman theory by means of surface tension measurements for SDS-NaCl-H<sub>2</sub>O mixtures. *Journal of Colloid and Interface Science* 267(1), 151-154.
- Pignatello, J.J. 1998. Soil organic matter as a nanoporous sorbent of organic pollutants. *Advances in Colloid and Interface Science* 76-77(0), 445-467.
- Pignatello, J.J., Kwon, S. and Lu, Y. 2006. Effect of natural organic substances on the surface and adsorptive properties of environmental black carbon (char): Attenuation of surface activity by humic and fulvic acids. *Environmental Science & Technology* 40(24), 7757-7763.
- Pignatello, J.J. and Xing, B. 1995. Mechanisms of slow sorption of organic chemicals to natural particles. *Environmental Science & Technology* 30(1), 1-11.
- Portet-Koltalo, F., Ammami, M.T., Benamar, A., Wang, H., Le Derf, F. 2013. Investigation of the release of PAHs from artificially contaminated sediments using cyclolipopeptidic biosurfactants. *Journal of Hazardous Materials* 261, 593-601.
- Prosser, A.J. and Franses, E.I. 2001. Adsorption and surface tension of ionic surfactants at the air-water interface: Review and evaluation of equilibrium models. *Colloids and Surfaces A: Physicochemical and Engineering Aspects* 178(1-3), 1-40.
- Puziy, A.M., Poddubnaya, O.I., Socha, R.P., Gurgul, J. and Wisniewski, M. 2008. XPS and NMR studies of phosphoric acid activated carbons. *Carbon* 46(15), 2113-2123.
- Qiao, R., Zhang, X., Qiu, R., Kim, J.C. and Kang, Y. 2009. Morphological transformation of Co(OH)<sub>2</sub> microspheres from solid to flowerlike hollow core-shell structures. *Chemistry-A European Journal* 15(8), 1886-1892.
- Quinones, D.H., Rey, A., Alvarez, P.M., Beltran, F.J. 2014. Enhanced activity and reusability of TiO<sub>2</sub> loaded magnetic activated carbon for solar photocatalytic ozonation. *Applied Catalysis B: Environmental* 144, 96-106.
- Raber, B., Kogel-Knabner, I., Stein, C. and Klem, D. 1998. Partitioning of polycyclic aromatic hydrocarbons to dissolved organic matter from different soils. *Chemosphere* 36(1), 79-97.
- Radding, S.B., Mill, T., Gould, C., Liw, D. and Johnson, H. 1976. The environmental fate of selected



- poly-nuclear aromatic hydrocarbons. Available from the National Technical Information Service, Springfield VA 22161 as PB-250 948, Price codes: A 07 in paper copy, A 01 in microfiche. Report EPA-560/5-75-009, February, 1976, 122, 31.
- Ramachandran, S.D., Hodson, P.V., Khan, C.W. and Lee, K. 2004. Oil dispersant increases PAH uptake by fish exposed to crude oil. *Ecotoxicology and Environmental Safety* 59(3), 300-308.
- Ray, G.B., Chakraborty, I. and Moulik, S.P. 2006. Pyrene absorption can be a convenient method for probing critical micellar concentration (CMC) and indexing micellar polarity. *Journal of Colloid and Interface Science* 294(1), 248-254.
- Reddy, C.M., Arey, J.S., Seewald, J.S., Sylva, S.P., Lemkau, K.L. 2012a. Composition and fate of gas and oil released to the water column during the *Deepwater Horizon* oil spill. *Proceedings of the National Academy of Sciences of the United States of America* 109(50), 20229-20234.
- Reddy, C.M., Arey, J.S., Seewald, J.S., Sylva, S.P., Lemkau, K.L. 2012b. Science applications in the *Deepwater Horizon* oil spill special feature: Composition and fate of gas and oil released to the water column during the *Deepwater Horizon* oil spill. *Proceedings of the National Academy of Sciences of the United States of America*, 1101242108.
- Redman, J.A., Walker, S.L. and Elimelech, M. 2004. Bacterial adhesion and transport in porous media: role of the secondary energy minimum. *Environmental Science & Technology* 38(6), 1777-1785.
- Reichert, M.D. and Walker, L.M. 2013. Interfacial tension dynamics, interfacial mechanics, and response to rapid dilution of bulk surfactant of a model oil-water-dispersant system. *Langmuir* 29(6), 1857-1867.
- Rey, A., Quinones, D.H., Alvarez, P.M., Beltran, F.J. and Plucinski, P.K. 2012. Simulated solar-light assisted photocatalytic ozonation of metoprolol over titania-coated magnetic activated carbon. *Applied Catalysis B: Environmental* 111, 246-253.
- Ribeiro, A.C., Lobo, V.M., Valente, A.J., Azevedo, E.F., Miguel, M.d.G. 2004. Transport properties of alkyltrimethylammonium bromide surfactants in aqueous solutions. *Colloid and Polymer Science* 283(3), 277-283.
- Riegelman, S., Allawala, N.A., Hrenoff, M.K. and Strait, L.A. 1958. The ultraviolet absorption spectrum as a criterion of the type of solubilization. *Journal of Colloid Science* 13(3), 208-217.
- Rodríguez-Cruz, M.S., Sanchez-Martin, M.J. and Sanchez-Camazano, M. 2005. A comparative study of adsorption of an anionic and a non-ionic surfactant by soils based on physicochemical and mineralogical properties of soils. *Chemosphere* 61(1), 56-64.
- Ruckmani, K., Jayakar, B. and Ghosal, S.K. 2000. Nonionic surfactant vesicles (niosomes) of cytarabine hydrochloride for effective treatment of leukemias: Encapsulation, storage, and in vitro release. *Drug Development and Industrial Pharmacy* 26(2), 217-222.
- Rufier, C., Collet, A., Viguier, M., Oberdisse, J. and Mora, S. 2011. Influence of surfactants on hydrophobically end-capped poly(ethylene oxide) self-assembled aggregates studied by SANS. *Macromolecules* 44(18), 7451-7459.
- Ryu, J. and Choi, W. 2004. Effects of TiO<sub>2</sub> surface modifications on photocatalytic oxidation of arsenite: The role of superoxides. *Environmental Science & Technology* 38(10), 2928-2933.
- Saeed, T., Ali, L.N., Al-Bloushi, A., Al-Hashash, H., Al-Bahloul, M. 2011. Effect of environmental factors on photodegradation of polycyclic aromatic hydrocarbons (PAHs) in the water-soluble fraction of Kuwait crude oil in seawater. *Marine Environmental Research* 72(3), 143-150.
- Sahoo, D. and Smith, J.A. 1997. Enhanced trichloroethene desorption from long-term contaminated soil

- using triton X-100 and pH increases. *Environmental Science & Technology* 31(7), 1910-1915.
- Sammarco, P.W., Kolian, S.R., Warby, R.A.F., Bouldin, J.L., Subra, W.A. 2013. Distribution and concentrations of petroleum hydrocarbons associated with the BP/*Deepwater Horizon* Oil Spill, Gulf of Mexico. *Marine Pollution Bulletin* 73(1), 129-143.
- Scelfo, G.M. and Tjeerdema, R.S. 1991. A simple method for determination of corexit 9527® in natural waters. *Marine Environmental Research* 31(1), 69-78.
- Schick, M.J. 1963. Effect of Temperature on the critical micelle concentration of nonionic detergents. Thermodynamics of micelle formation. *The Journal of Physical Chemistry* 67(9), 1796-1799.
- Schierbaum, K.D., Fischer, S., Torquemada, M.C., DeSegovia, J.L., Roman, E. 1996. The interaction of Pt with TiO<sub>2</sub>(110) surfaces: A comparative XPS, UPS, ISS, and ESD study. *Surface Science* 345(3), 261-273.
- Schneider, J., Matsuoka, M., Takeuchi, M., Zhang, J., Horiuchi, Y. 2014. Understanding TiO<sub>2</sub> photocatalysis: Mechanisms and materials. *Chemical Reviews* 114(19), 9919-9986.
- Schwarzenbach, R.P., Gschwend, P.M. and Imboden, D.M. 2003. An introduction to environmental organic chemicals. *Environmental Organic Chemistry*, 13-54.
- Shankar, R., Shim, W.J., An, J.G. and Yim, U.H. 2015. A practical review on photooxidation of crude oil: Laboratory lamp setup and factors affecting it. *Water Research* 68, 304-315.
- Shemer, H. and Linden, K.G. 2007. Aqueous photodegradation and toxicity of the polycyclic aromatic hydrocarbons fluorene, dibenzofuran, and dibenzothiophene. *Water Research* 41(4), 853-861.
- Shen, C., Li, B., Huang, Y. and Jin, Y. 2007. Kinetics of coupled primary- and secondary-minimum deposition of colloids under unfavorable chemical conditions. *Environmental Science & Technology* 41(20), 6976-6982.
- Shen, L., Guo, A. and Zhu, X. 2011. Tween surfactants: Adsorption, self-organization, and protein resistance. *Surface Science* 605(5-6), 494-499.
- Shen, Y. 1999. Sorption of natural dissolved organic matter on soil. *Chemosphere* 38(7), 1505-1515.
- Sigman, M.E., Schuler, P.F., Ghosh, M.M. and Dabestani, R.T. 1998. Mechanism of pyrene photochemical oxidation in aqueous and surfactant solutions. *Environmental Science & Technology* 32(24), 3980-3985.
- Simister, E.A., Thomas, R.K., Penfold, J., Aveyard, R., Binks, B.P. 1992. Comparison of neutron reflection and surface-tension measurements of the surface excess of tetradecyltrimethylammonium bromide layers at the air-water-interface. *Journal of Physical Chemistry* 96(3), 1383-1388.
- Simpson, A.J. 2002. Determining the molecular weight, aggregation, structures and interactions of natural organic matter using diffusion ordered spectroscopy. *Magnetic Resonance in Chemistry* 40(13), S72-S82.
- Simpson, M.J., Simpson, A.J. and Hatcher, P.G. 2004. Noncovalent interactions between aromatic compounds and dissolved humic acid examined by nuclear magnetic resonance spectroscopy. *Environmental Toxicology and Chemistry* 23(2), 355-362.
- Singer, M., George, S. and Tjeerdema, R. 1995. Relationship of some physical properties of oil dispersants and their toxicity to marine organisms. *Archives of Environmental Contamination And Toxicology* 29(1), 33-38.
- Singer, M.M., Aurand, D., Bragin, G.E., Clark, J.R., Coelho, G.M., 2000. Standardization of the preparation and quantitation of water-accommodated fractions of petroleum for toxicity testing.

- Marine Pollution Bulletin 40(11), 1007-1016.
- Sirisaksoontorn, W., Thachepan, S. and Songsasen, A. 2009. Photodegradation of phenanthrene by N-doped TiO<sub>2</sub> photocatalyst. *Journal of Environmental Science and Health, Part A* 44(9), 841-846.
- Slaga, T., Gleason, G., Mills, G., Ewald, L., Fu, P. 1980. Comparison of the skin tumor-initiating activities of dihydrodiols and diol-epoxides of various polycyclic aromatic hydrocarbons. *Cancer Research* 40(6), 1981-1984.
- Solak Erdem, N., Alawani, N. and Wesdemiotis, C. 2014. Characterization of polysorbate 85, a nonionic surfactant, by liquid chromatography vs. ion mobility separation coupled with tandem mass spectrometry. *Analytica Chimica Acta* 808(0), 83-93.
- Sorial, G., Chandrasekar, S. and Weaver, J.W. 2004. Characteristics of spilled oils, fuels, and petroleum products: 2a. dispersant effectiveness data for a suite of environmental conditions-The effects of temperature, volatilization, and energy. EPA/600/R - 04/119. <http://www.epa.gov/athens/research/projects/eros>. (accessed August 15, 2013)
- Srivastava, A. and Ismail, K. 2014. Solubilization of polycyclic aromatic hydrocarbons in aqueous sodium dioctylsulfosuccinate solutions. *Journal of Molecular Liquids* 195(0), 105-109.
- Stahelin, J. and Hoigne, J. 1985. Decomposition of ozone in water in the presence of organic solutes acting as promoters and inhibitors of radical chain reactions. *Environmental Science & Technology* 19(12), 1206-1213.
- Standeker, S., Novak, Z. and Knez, Z. 2007. Adsorption of toxic organic compounds from water with hydrophobic silica aerogels. *Journal of Colloid and Interface Science* 310(2), 362-368.
- Steffy, D.A., Nichols, A.C. and Kiplagat, G. 2011. Investigating the effectiveness of the surfactant dioctyl sodium sulfosuccinate to disperse oil in a changing marine environment. *Ocean Science Journal* 46(4), 299-305.
- Steffy, D.A., Nichols, A.C., Morgan, L.J. and Gibbs, R. 2013. Evidence that the *Deepwater Horizon* oil spill caused a change in the nickel, chromium, and lead average seasonal concentrations occurring in sea bottom sediment collected from the Eastern Gulf of Mexico continental shelf between the years 2009 and 2011. *Water Air And Soil Pollution* 224(11), 1-11.
- Stoermer, S., G. Butler, C. Henry 2001. Application of dispersants to mitigate oil spills in the Gulf of Mexico: The Poseidon pipeline spill case study. *International Oil Spill Conference Proceedings* 2001(2), 1227-1229.
- Stylidi, M., Kondarides, D.I. and Verykios, X.E. 2004. Visible light-induced photocatalytic degradation of acid orange 7 in aqueous TiO<sub>2</sub> suspensions. *Applied Catalysis B: Environmental* 47(3), 189-201.
- Sun, X. and Li, Y. 2003. Synthesis and characterization of ion-exchangeable titanate nanotubes. *Chemistry-A European Journal* 9(10), 2229-2238.
- Sung-Suh, H.M., Choi, J.R., Hah, H.J., Koo, S.M. and Bae, Y.C. 2004. Comparison of Ag deposition effects on the photocatalytic activity of nanoparticulate TiO<sub>2</sub> under visible and UV light irradiation. *Journal of Photochemistry and Photobiology A: Chemistry* 163(1), 37-44.
- Tan, H., Zhao, Z., Niu, M., Mao, C., Cao, D. 2014. A facile and versatile method for preparation of colored TiO<sub>2</sub> with enhanced solar-driven photocatalytic activity. *Nanoscale* 6(17), 10216-10223.
- Tanhaei, B., Saghatoleslami, N., Chenar, M.P., Ayati, A., Hesampour, M. 2013. Experimental study of CMC evaluation in single and mixed surfactant systems, using the UV-Vis spectroscopic method. *Journal of Surfactants and Detergents* 16(3), 357-362.

- Tansel, B., Fuentes, C., Sanchez, M., Predoi, K. and Acevedo, M. 2011. Persistence profile of polyaromatic hydrocarbons in shallow and deep Gulf waters and sediments: Effect of water temperature and sediment-water partitioning characteristics. *Marine Pollution Bulletin* 62(12), 2659-2665.
- Theurich, J., Bahnemann, D., Vogel, R., Ehamed, F., Alhakimi, G. 1997. Photocatalytic degradation of naphthalene and anthracene: GC-MS analysis of the degradation pathway. *Research on Chemical Intermediates* 23(3), 247-274.
- Thibodeaux, L.J., Valsaraj, K.T., John, V.T., Papadopoulos, K.D., Pratt, L.R. 2011. Marine oil fate: Knowledge gaps, basic research, and development needs; A perspective based on the *Deepwater Horizon* spill. *Environmental Engineering Science* 28(2), 87-93.
- Thornton, D.C.O. 2002. Diatom aggregation in the sea: Mechanisms and ecological implications. *European Journal of Phycology* 37(2), 149-161.
- Tian, Y., Shi, G., Liu, G., Guo, C., Peng, X. 2014. Source contributions and spatiotemporal characteristics of PAHs in sediments: Using three-way source apportionment approach. *Environmental Toxicology and Chemistry* 33(8), 1747-1753.
- Tokuoka, Y., Uchiyama, H., Abe, M. and Christian, S.D. 1995. Solubilization of some synthetic perfumes by anionic-nonionic mixed surfactant systems. 1. *Langmuir* 11(3), 725-729.
- Tomaszewska, M., Mozia, S. 2002. Removal of organic matter from water by PAC/UF system. *Water Research* 36, 4137-4143.
- Tombacz, E., Libor, Z., Illes, E., Majzik, A. and Klumpp, E. 2004. The role of reactive surface sites and complexation by humic acids in the interaction of clay mineral and iron oxide particles. *Organic Geochemistry* 35(3), 257-267.
- Tomiyasu, H., Fukutomi, H. and Gordon, G. 1985. Kinetics and mechanism of ozone decomposition in basic aqueous-solution. *Inorganic Chemistry* 24(19), 2962-2966.
- Tonnesen, H.H., Masson, M. and Loftsson, T. 2002. Studies of curcumin and curcuminoids. XXVII. Cyclodextrin complexation: Solubility, chemical and photochemical stability. *International Journal of Pharmaceutics* 244(1-2), 127-135.
- Tooby, P.F., Wick, G.L. and Isaacs, J.D. 1977. The motion of a small sphere in a rotating velocity field: A possible mechanism for suspending particles in turbulence. *Journal of Geophysical Research* 82(15), 2096-2100.
- Tremblay, L., Kohl, S.D., Rice, J.A. and Gagne, J.P. 2005. Effects of temperature, salinity, and dissolved humic substances on the sorption of polycyclic aromatic hydrocarbons to estuarine particles. *Marine Chemistry* 96(1-2), 21-34.
- Tuckermann, R. 2007. Surface tension of aqueous solutions of water-soluble organic and inorganic compounds. *Atmospheric Environment* 41(29), 6265-6275.
- Tuller, M., Or, D. and Dudley, L.M. 1999. Adsorption and capillary condensation in porous media: Liquid retention and interfacial configurations in angular pores. *Water Resources Research* 35(7), 1949-1964.
- Turro, N.J. and Yekta, A. 1978. Luminescent probes for detergent solutions. A simple procedure for determination of the mean aggregation number of micelles. *Journal of the American Chemical Society* 100(18), 5951-5952.
- UGA 1983. Reference Soil Test Methods for the Southern Region of the United States, Southern Cooperative Series Bulletin 289, 1983, University of Georgia College of Agriculture Experiment

- Stations, Athens, GA, 30602.
- Ullah, I., Baloch, M.K., Ullah, I. and Mustaqeem, M. 2014. Enhancement in aqueous solubility of mefenamic acid using micellar solutions of various surfactants. *Journal of Solution Chemistry* 43(8), 1360-1373.
- Ullman, E.F. and Baumann, N. 1968. Photosensitization of wavelength-dependent lactones. Influence of orbital symmetries on triplet energy transfer. *Journal of the American Chemical Society* 90(15), 4158-4160.
- Underberg, W.J.M. and Lingeman, H. 1983. Aspects of the Chemical-stability of mitomycin and porfiromycin in acidic solution. *Journal of Pharmaceutical Sciences* 72(5), 549-553.
- US EPA 2014. Toxic and Priority Pollutants Under the Clean Water Act: Priority pollutant list. <  
<https://www.epa.gov/eg/toxic-and-priority-pollutants-under-clean-water-act>> (accessed August 15, 2016)
- Vader, F.V. 1960. Adsorption of detergents at the liquid-liquid interface .1. *Transactions of the Faraday Society* 56(7), 1067-1077.
- Valderrama, C., Gamisans, X., De las Heras, X., Farran, A. and Cortina, J. 2008. Sorption kinetics of polycyclic aromatic hydrocarbons removal using granular activated carbon: Intraparticle diffusion coefficients. *Journal of Hazardous Materials* 157(2), 386-396.
- Vankayala, R., Kuo, C.L., Sagadevan, A., Chen, P.H., Chiang, C.S. 2013. Morphology dependent photosensitization and formation of singlet oxygen by gold and silver nanoparticles and its application in cancer treatment. *Journal of Materials Chemistry B* 1(35), 4379-4387.
- Veldurthi, N.K., Velchuri, R., Pola, S., Prasad, G., Muniratnam, N.R. 2015. Synthesis, characterization and silver/copper-nitrogen substitutional effect on visible light driven photocatalytic performance of sodium hexatitanate nanostructures. *Journal of Chemical Technology and Biotechnology* 90(8), 1507-1514.
- Vikhorev, A.A., Syroezhko, A.M., Proskuryakov, V.A. and Yakovlev, A.S. 1978. Oxidation of Normal Decane by Ozone-air Mixtures. *Journal of Applied Chemistry of the Ussr* 51(11), 2448-2451.
- Voice, T.C. and Weber Jr, W.J. 1983. Sorption of hydrophobic compounds by sediments, soils and suspended solids-I. Theory and background. *Water Research* 17(10), 1433-1441.
- von Gunten, U. 2003. Ozonation of drinking water: Part I. Oxidation kinetics and product formation. *Water Research* 37(7), 1443-1467.
- von Szyszkowski, B. 1908. Experimental studies on capillary properties of aqueous solutions of fatty acids. *Zeitschrift für Physikalische Chemie* 64, 385-414.
- Wade, T.L., Sweet, S.T., Sericano, J.L., Guinasso, N.L., Diercks, A.R.R. 2011. Analyses of water samples from the *Deepwater Horizon* oil spill: Documentation of the subsurface plume. *Monitoring and Modeling the Deepwater Horizon oil spill: a record-breaking enterprise*, 77-82.
- Wan, L. and Lee, P.F. 1974. CMC of polysorbates. *Journal of Pharmaceutical Sciences* 63(1), 136-137.
- Wang, D., McLaughlin, E., Pfeffer, R. and Lin, Y. 2012. Adsorption of oils from pure liquid and oil-water emulsion on hydrophobic silica aerogels. *Separation and Purification Technology* 99, 28-35.
- Wang, J., Chen, Z. and Chen, B. 2014. Adsorption of polycyclic aromatic hydrocarbons by graphene and graphene oxide nanosheets. *Environmental Science & Technology* 48(9), 4817-4825.
- Wang, P. and Keller, A.A. 2008. Particle-Size Dependent sorption and desorption of pesticides within a water-soil-nonionic surfactant system. *Environmental Science & Technology* 42(9), 3381-3387.

- Wang, S., Li, P., Liu, H., Li, J. and Wei, Y. 2010. The structure and optical properties of ZnO nanocrystals dependence on Co-doping levels. *Journal of Alloys and Compounds* 505(1), 362-366.
- Wang, T., Liu, W., Xiong, L., Xu, N. and Ni, J. 2013a. Influence of pH, ionic strength and humic acid on competitive adsorption of Pb (II), Cd (II) and Cr (III) onto titanate nanotubes. *Chemical Engineering Journal* 215, 366-374.
- Wang, T., Liu, W., Xu, N. and Ni, J. 2013b. Adsorption and desorption of Cd (II) onto titanate nanotubes and efficient regeneration of tubular structures. *Journal of Hazardous Materials* 250, 379-386.
- Wang, W., Zheng, Y. and Lee, K. 2013c. Role of the hydrophobicity of mineral fines in the formation of oil-mineral aggregates. *Canadian Journal of Chemical Engineering* 91(4), 698-703.
- Wang, X., Lu, J. and Xing, B. 2008. Sorption of organic contaminants by carbon nanotubes: Influence of adsorbed organic matter. *Environmental Science & Technology* 42(9), 3207-3212.
- Wang, X., Yu, J., Yip, H., Wu, L., Wong, P. 2005. A mesoporous Pt/TiO<sub>2</sub> nanoarchitecture with catalytic and photocatalytic functions. *Chemistry-A European Journal* 11(10), 2997-3004.
- Wang, Y., Hsieh, M., Lee, J. and Yang, C. 2013d. Nonaqueous synthesis of CoO<sub>x</sub>/TiO<sub>2</sub> nanocomposites showing high photocatalytic activity of hydrogen generation. *Applied Catalysis B: Environmental* 14-143(0), 626-632.
- Wang, Z. and Fingas, M. 1997. Developments in the analysis of petroleum hydrocarbons in oils, petroleum products and oil-spill-related environmental samples by gas chromatography. *Journal of Chromatography A* 774(1), 51-78.
- Wang, Z., Friedrich, D.M., Beversluis, M.R., Hemmer, S.L., Joly, A.G. 2001. A fluorescence spectroscopic study of phenanthrene sorption on porous silica. *Environmental Science & Technology* 35(13), 2710-2716.
- Wang, Z., Hollebone, B., Fingas, M., Fieldhouse, B., Sigouin, L. 2003. Characteristics of spilled oils, fuels, and petroleum products: 1. Composition and properties of selected oils, US EPA Report. < [nepis.epa.gov/Exe/ZyPURL.cgi?Dockey=P1000AE6.TXT](http://nepis.epa.gov/Exe/ZyPURL.cgi?Dockey=P1000AE6.TXT) >
- Wang, Z., Li, K., Lambert, P. and Yang, C. 2007. Identification, characterization and quantitation of pyrogenic polycyclic aromatic hydrocarbons and other organic compounds in tire fire products. *Journal of Chromatography A* 1139(1), 14-26.
- Wang, Z., Zhao, J., Song, L., Mashayekhi, H., Chefetz, B. 2011. Adsorption and desorption of phenanthrene on carbon nanotubes in simulated gastrointestinal fluids. *Environmental Science & Technology* 45(14), 6018-6024.
- Wang, C., Yediler, A., Peng, A. and Kettrup, A. 1995. Photodegradation of phenanthrene in the presence of humic substances and hydrogen peroxide. *Chemosphere* 30(3), 501-510.
- Walter, T., Ederer, H.J., Först, C. and Stieglitz, L. 2000. Sorption of selected polycyclic aromatic hydrocarbons on soils in oil-contaminated systems. *Chemosphere* 41(3), 387-397.
- Wen, S., Zhao, J., Sheng, G., Fu, J. and Peng, P.a. 2002. Photocatalytic reactions of phenanthrene at TiO<sub>2</sub>/water interfaces. *Chemosphere* 46(6), 871-877.
- Wen, S., Zhao, J.C., Sheng, G.Y., Fu, J.M. and Peng, P.A. 2003. Photocatalytic reactions of pyrene at TiO<sub>2</sub>/water interfaces. *Chemosphere* 50(1), 111-119.
- Wenk, J., von Gunten, U. and Canonica, S. 2011. Effect of dissolved organic matter on the transformation of contaminants induced by excited triplet states and the hydroxyl radical. *Environmental Science & Technology* 45(4), 1334-1340.

- Weromshaw, R.L. 1994. Membrane-micelle model for humus in soils and sediments and its relation to humification, US Geological Survey; USGPO. < [pubs.usgs.gov/wsp/2410/report.pdf](http://pubs.usgs.gov/wsp/2410/report.pdf) >
- White, H.K., Hsing, P.Y., Cho, W., Shank, T.M., Cordes, E.E. 2012. Impact of the *Deepwater Horizon* oil spill on a deep-water coral community in the Gulf of Mexico. *Proceedings of the National Academy of Sciences of the United States of America* 109(50), 20303-20308.
- White, J.C. and Pignatello, J.J. 1999. Influence of Bisolute Competition on the Desorption Kinetics of Polycyclic Aromatic Hydrocarbons in Soil. *Environmental Science & Technology* 33(23), 4292-4298.
- Wilén, B.-M., Jin, B. and Lant, P. 2003. The influence of key chemical constituents in activated sludge on surface and flocculating properties. *Water research* 37(9), 2127-2139.
- Woan, K., Pyrgiotakis, G. and Sigmund, W. 2009. Photocatalytic carbon-nanotube-TiO<sub>2</sub> composites. *Advanced Materials* 21(21), 2233-2239.
- Woo, O.T., Chung, W.K., Wong, K.H., Chow, A.T. and Wong, P.K. 2009. Photocatalytic oxidation of polycyclic aromatic hydrocarbons: Intermediates identification and toxicity testing. *Journal of Hazardous Materials* 168(2-3), 1192-1199.
- Wu, S.C. and Gschwend, P.M. 1986. Sorption kinetics of hydrophobic organic compounds to natural sediments and soils. *Environmental Science & Technology* 20(7), 717-725.
- Wu, Z., Dong, F., Zhao, W., Wang, H., Liu, Y. 2009. The fabrication and characterization of novel carbon doped TiO<sub>2</sub> nanotubes, nanowires and nanorods with high visible light photocatalytic activity. *Nanotechnology* 20(23).
- Xia, X., Li, G., Yang, Z., Chen, Y. and Huang, G. 2009. Effects of fulvic acid concentration and origin on photodegradation of polycyclic aromatic hydrocarbons in aqueous solution: Importance of active oxygen. *Environmental Pollution* 157(4), 1352-1359.
- Xing, B., Pignatello, J.J. and Gigliotti, B. 1996. Competitive sorption between atrazine and other organic compounds in soils and model sorbents. *Environmental Science & Technology* 30(8), 2432-2440.
- Xiong, L., Chen, C., Chen, Q. and Ni, J. 2011a. Adsorption of Pb(II) and Cd(II) from aqueous solutions using titanate nanotubes prepared via hydrothermal method. *Journal of Hazardous Materials* 189(3), 741-748.
- Xiong, L., Sun, W., Yang, Y., Chen, C. and Ni, J. 2011b. Heterogeneous photocatalysis of methylene blue over titanate nanotubes: Effect of adsorption. *Journal of Colloid and Interface Science* 356(1), 211-216.
- Xiong, L., Yang, Y., Mai, J., Sun, W., Zhang, C. 2010. Adsorption behavior of methylene blue onto titanate nanotubes. *Chemical Engineering Journal* 156(2), 313-320.
- Xu, H., Li, P.X., Ma, K., Thomas, R.K., Penfold, J. 2013. Limitations in the application of the gibbs equation to anionic surfactants at the air/water surface: Sodium dodecylsulfate and sodium dodecylmonooxyethylenesulfate above and below the CMC. *Langmuir* 29(30), 9335-9351.
- Xu, Q., Ma, Y., Zhang, J., Wang, X., Feng, Z. 2011. Enhancing hydrogen production activity and suppressing CO formation from photocatalytic biomass reforming on Pt/TiO<sub>2</sub> by optimizing anatase-rutile phase structure. *Journal of Catalysis* 278(2), 329-335.
- Xu, Z., Jing, C., Li, F. and Meng, X. 2008. Mechanisms of photocatalytical degradation of monomethylarsonic and dimethylarsinic acids using nanocrystalline titanium dioxide. *Environmental Science & Technology* 42(7), 2349-2354.

- Xue, G., Liu, H., Chen, Q., Hills, C., Tyrer, M. 2011. Synergy between surface adsorption and photocatalysis during degradation of humic acid on TiO<sub>2</sub>/activated carbon composites. *Journal of Hazardous Materials* 186(1), 765-772.
- Xue, J.L., Yu, Y., Bai, Y., Wang, L. and Wu, Y. 2015. Marine oil-degrading microorganisms and biodegradation process of petroleum hydrocarbon in marine environments: A Review. *Current Microbiology* 71(2), 220-228.
- Yang, D., Sarina, S., Zhu, H., Liu, H., Zheng, Z.. 2011a. Capture of radioactive cesium and iodide ions from water by using titanate nanofibers and nanotubes. *Angewandte Chemie International Edition* 50(45), 10594-10598.
- Yang, G.P., Zhao, Y.H., Lu, X.L. and Gao, X.C. 2005. Adsorption of methomyl on marine sediments. *Colloids and Surfaces A: Physicochemical and Engineering Aspects* 264(1-3), 179-186.
- Yang, H.G., Sun, C.H., Qiao, S.Z., Zou, J., Liu, G. 2008. Anatase TiO<sub>2</sub> single crystals with a large percentage of reactive facets. *Nature* 453(7195), 638-641.
- Yang, K., Wang, X., Zhu, L. and Xing, B. 2006a. Competitive sorption of pyrene, phenanthrene, and naphthalene on multiwalled carbon nanotubes. *Environmental Science & Technology* 40(18), 5804-5810.
- Yang, K., Wu, W., Jing, Q., Jiang, W. and Xing, B. 2010. Competitive adsorption of naphthalene with 2,4-dichlorophenol and 4-chloroaniline on multiwalled carbon nanotubes. *Environmental Science & Technology* 44(8), 3021-3027.
- Yang, K. and Xing, B. 2007. Desorption of polycyclic aromatic hydrocarbons from carbon nanomaterials in water. *Environmental Pollution* 145(2), 529-537.
- Yang, K., Zhu, L. and Xing, B. 2006b. Enhanced soil washing of phenanthrene by mixed solutions of TX100 and SDBS. *Environmental Science & Technology* 40(13), 4274-4280.
- Yang, Y., Chiang, K. and Burke, N. 2011b. Porous carbon-supported catalysts for energy and environmental applications: A short review. *Catalysis Today* 178(1), 197-205.
- Yates, L.M. and von Wandruszka, R. 1999. Effects of pH and metals on the surface tension of aqueous humic materials. *Soil Science Society of America Journal* 63(6), 1645-1649.
- Yehia, A. 1992. Adsorption of dioctyl sodium sulphosuccinate on some synthetic carbonate apatites. *Minerals Engineering* 5, 707-714.
- Yim, U.H., Ha, S.Y., An, J.G., Won, J.H., Han, G.M. 2011. Fingerprint and weathering characteristics of stranded oils after the Hebei Spirit oil spill. *Journal of Hazardous Materials* 197, 60-69.
- Yin, F., John, G.F., Hayworth, J.S. and Clement, T.P. 2015a. Long-term monitoring data to describe the fate of polycyclic aromatic hydrocarbons in *Deepwater Horizon* oil submerged off Alabama's beaches. *Science of the Total Environment* 508, 46-56.
- Yin, F., John, G.F., Hayworth, J.S. and Clement, T.P. 2015b. Long-term monitoring data to describe the fate of polycyclic aromatic hydrocarbons in *Deepwater Horizon* oil submerged off Alabama's beaches. *Science of the Total Environment* 508, 46-56.
- Yu, D., Kang, N., Bae, W. and Banks, M.K. 2007. Characteristics in oxidative degradation by ozone for saturated hydrocarbons in soil contaminated with diesel fuel. *Chemosphere* 66(5), 799-807.
- Yu, H., Yu, J., Cheng, B. and Zhou, M. 2006a. Effects of hydrothermal post-treatment on microstructures and morphology of titanate nanoribbons. *Journal of Solid State Chemistry* 179(2), 349-354.
- Yu, H., Zhao, Y., Zhou, C., Shang, L., Peng, Y.. 2014. Carbon quantum dots/TiO<sub>2</sub> composites for



- efficient photocatalytic hydrogen evolution. *Journal of Materials Chemistry A* 2(10), 3344-3351.
- Yu, J., Yu, H., Cheng, B., Zhao, X. and Zhang, Q. 2006b. Preparation and photocatalytic activity of mesoporous anatase TiO<sub>2</sub> nanofibers by a hydrothermal method. *Journal of Photochemistry and Photobiology A: Chemistry* 182(2), 121-127.
- Yuan, S., Shu, Z., Wan, J. and Lu, X. 2007. Enhanced desorption of hexachlorobenzene from kaolin by single and mixed surfactants. *Journal of Colloid and Interface Science* 314(1), 167-175.
- Yukselen, Y. and Kaya, A. 2003. Zeta potential of kaolinite in the presence of alkali, alkaline earth and hydrolyzable metal ions. *Water Air And Soil Pollution* 145(1), 155-168.
- Zafiriou, O.C., Jousotdubien, J., Zepp, R.G. and Zika, R.G. 1984. Photochemistry of natural waters. *Environmental Science & Technology* 18(12), A358-A371.
- Zepp, R.G. and Schlotzhauer, P.F. 1979. Polynuclear aromatic hydrocarbons: Third international symposium on chemistry and biology-carcinogenesis and mutagenesis. . Jones P.W., L., P. (ed), pp. 141-158, Ann Arbor Science, Ann Arbor, MI.
- Zhang, G., Huang, H., Li, W., Yu, F., Wu, H. 2012. Enhanced photocatalytic activity of CoO/TiO<sub>2</sub> nanotube composite. *Electrochimica Acta* 81(0), 117-122.
- Zhang, H.P., Khatibi, M., Zheng, Y., Lee, K., Li, Z.K. a 2010. Investigation of OMA formation and the effect of minerals. *Marine Pollution Bulletin* 60(9), 1433-1441.
- Zhang, J., Zhang, Y., Lei, Y. and Pan, C. 2011a. Photocatalytic and degradation mechanisms of anatase TiO<sub>2</sub>: a HRTEM study. *Catalysis Science & Technology* 1(2), 273-278.
- Zhang, J.H. and He, M.C. 2011. Effect of surfactants on sorption and desorption of phenanthrene onto black carbon. *Water Environment Research* 83(1), 15-22.
- Zhang, J., Zeng, J., and He, M. 2009. Effects of temperature and surfactants on naphthalene and phenanthrene sorption by soil. *Journal of Environmental Sciences-China* 21(5), 667-674.
- Zhang, L., Li, P., Gong, Z. and Li, X. 2008. Photocatalytic degradation of polycyclic aromatic hydrocarbons on soil surfaces using TiO<sub>2</sub> under UV light. *Journal of Hazardous Materials* 158(2-3), 478-484.
- Zhang, M. and Zhu, L.Z. 2010. Effect of SDBS-Tween 80 mixed surfactants on the distribution of polycyclic aromatic hydrocarbons in soil-water system. *Journal of Soils and Sediments* 10(6), 1123-1130.
- Zhang, X., Wang, F., Huang, H., Li, H., Han, X. 2013. Carbon quantum dot sensitized TiO<sub>2</sub> nanotube arrays for photoelectrochemical hydrogen generation under visible light. *Nanoscale* 5(6), 2274-2278.
- Zhang, Y., Jiang, Z., Huang, J., Lim, L.Y., Li, W.. 2015. Titanate and titania nanostructured materials for environmental and energy applications: A review. *RSC Advances* 5(97), 79479-79510.
- Zhang, Y., Wang, F., Yang, X., Gu, C., Kengara, F.O.. 2011b. Extracellular polymeric substances enhanced mass transfer of polycyclic aromatic hydrocarbons in the two-liquid-phase system for biodegradation. *Applied Microbiology and Biotechnology* 90(3), 1063-1071.
- Zhang, Y., Wong, J.W.C., Liu, P. and Yuan, M. 2011c. Heterogeneous photocatalytic degradation of phenanthrene in surfactant solution containing TiO<sub>2</sub> particles. *Journal of Hazardous Materials* 191(1-3), 136-143.
- Zhao, B., Zhu, L., Li, W. and Chen, B. 2005. Solubilization and biodegradation of phenanthrene in mixed anionic-nonionic surfactant solutions. *Chemosphere* 58(1), 33-40.

- Zhao, D., Hunter, M., Pignatello, J.J. and White, J.C. 2002a. Application of the dual-mode model for predicting competitive sorption equilibria and rates of polycyclic aromatic hydrocarbons in estuarine sediment suspensions. *Environmental Toxicology and Chemistry* 21(11), 2276-2282.
- Zhao, D., Hunter, M., Pignatello, J.J. and White, J.C. 2002b. Application of the dual-mode model for predicting competitive sorption equilibria and rates of polycyclic aromatic hydrocarbons in estuarine sediment suspensions. *Environmental Toxicology and Chemistry* 21(11), 2276-2282.
- Zhao, D., Pignatello, J.J., White, J.C., Braida, W. and Ferrandino, F. 2001a. Dual-mode modeling of competitive and concentration-dependent sorption and desorption kinetics of polycyclic aromatic hydrocarbons in soils. *Water Resources Research* 37(8), 2205-2212.
- Zhao, D.Y., Pignatello, J.J., White, J.C., Braida, W. and Ferrandino, F. 2001b. Dual-mode modeling of competitive and concentration-dependent sorption and desorption kinetics of polycyclic aromatic hydrocarbons in soils. *Water Resources Research* 37(8), 2205-2212.
- Zhao, J., Wang, Z., Zhao, Q. and Xing, B. 2014. Adsorption of phenanthrene on multilayer graphene as affected by surfactant and exfoliation. *Environmental Science & Technology* 48(1), 331-339.
- Zhao, W., Shi, H. and Wang, D. 2004. Ozonation of Cationic Red X-GRL in aqueous solution: degradation and mechanism. *Chemosphere* 57(9), 1189-1199.
- Zhao, W., Liu, F., Yang, Y., Tan, M. and Zhao, D. 2011. Ozonation of Cationic Red X-GRL in aqueous solution: Kinetics and modeling. *Journal of Hazardous Materials* 187(1-3), 526-533.
- Zhao, W.R., Wu, Z.B. and Wang, D.H. 2006. Ozone direct oxidation kinetics of Cationic Red X-GRL in aqueous solution. *Journal of Hazardous Materials* 137(3), 1859-1865.
- Zhao, X., Cai, Z., Wang, T., O'Reilly, S., Liu, W.. 2016a. A new type of cobalt-deposited titanate nanotubes for enhanced photocatalytic degradation of phenanthrene. *Applied Catalysis B: Environmental*, 187, 134-143.
- Zhao, X., Gong, Y., O'Reilly, S.E. and Zhao, D. 2015. Effects of oil dispersant on solubilization, sorption and desorption of polycyclic aromatic hydrocarbons in sediment-seawater systems. *Marine Pollution Bulletin* 92(1-2), 160-169.
- Zhao, X., Liu, W., Fu, J., Cai, Z., O'Reilly, S.. 2016b. Dispersion, sorption and photodegradation of petroleum hydrocarbons in dispersant-seawater-sediment systems. *Marine Pollution Bulletin* 109(1), 526-538.
- Zheng, O. and Zhao, H.X. 2006. Solubilization of pyrene in aqueous micellar solutions of gemini surfactants C<sub>12-5</sub>-C<sub>12</sub>.2Br. *Journal of Colloid and Interface Science* 300(2), 749-754.
- Zheng, X., Shen, G., Li, Y., Duan, H., Yang, X. 2013. Self-templated synthesis of microporous CoO nanoparticles with highly enhanced performance for both photocatalysis and lithium-ion batteries. *Journal of Materials Chemistry A* 1(4), 1394-1400.
- Zhou, W. and Zhu, L. 2005. Distribution of polycyclic aromatic hydrocarbons in soil-water system containing a nonionic surfactant. *Chemosphere* 60(9), 1237-1245.
- Zhou, W., Li, J., Wei, W., Su, Z. and Ma, G. 2011. Effect of solubilization of surfactant aggregates on pore structure in gigaporous polymeric particles. *Colloids and Surfaces A-Physicochemical and Engineering Aspects* 384(1-3), 549-554.
- Zhu, L. and Feng, S. 2003. Synergistic solubilization of polycyclic aromatic hydrocarbons by mixed anionic-nonionic surfactants. *Chemosphere* 53(5), 459-467.
- Zhu, L. and Chiou, C.T. 2001. Water solubility enhancements of pyrene by single and mixed surfactant

solutions. *Journal of Environmental Sciences-China* 13(4), 491-496.

Zoller, U. 2008. *Handbook of Detergents, Part E: Applications*, Taylor & Francis.

Zuijdgheest, A. and Huettel, M. 2012. Dispersants as used in response to the MC252-spill lead to higher mobility of polycyclic aromatic hydrocarbons in oil-contaminated Gulf of Mexico sand. *PLoS One* 7(11), e50549.



### ***The Department of the Interior Mission***

As the Nation's principal conservation agency, the Department of the Interior has responsibility for most of our nationally owned public lands and natural resources. This includes fostering sound use of our land and water resources; protecting our fish, wildlife, and biological diversity; preserving the environmental and cultural values of our national parks and historical places; and providing for the enjoyment of life through outdoor recreation. The Department assesses our energy and mineral resources and works to ensure that their development is in the best interests of all our people by encouraging stewardship and citizen participation in their care. The Department also has a major responsibility for American Indian reservation communities and for people who live in island territories under US administration.



### ***The Bureau of Ocean Energy Management***

As a bureau of the Department of the Interior, the Bureau of Ocean Energy (BOEM) primary responsibilities are to manage the mineral resources located on the Nation's Outer Continental Shelf (OCS) in an environmentally sound and safe manner.

### ***The BOEM Environmental Studies Program***

The mission of the Environmental Studies Program (ESP) is to provide the information needed to predict, assess, and manage impacts from offshore energy and marine mineral exploration, development, and production activities on human, marine, and coastal environments.